

AD-A082 207

BATTELLE COLUMBUS LABS OH
RESEARCH TO DEVELOP PROCESS MODELS FOR PRODUCING A DUAL PROPERTY--ETC(U)
DEC 79 G D LAHOTI, T ALTAN

F/G 11/6

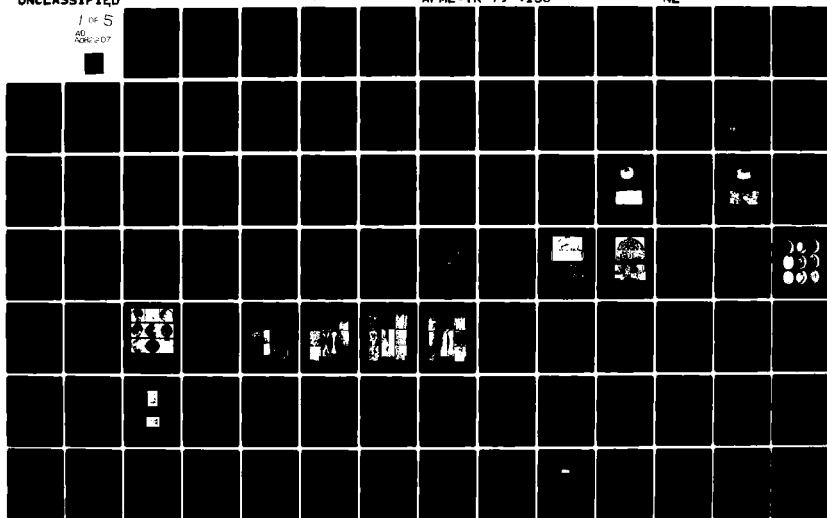
F33615-78-C-5025

UNCLASSIFIED

AFML-TR-79-4156

NL

1 of 5
AD
A082 207



AD A082207

18 19
AFML TR-79-4156

LEVEL

2

6
RESEARCH TO DEVELOP PROCESS MODELS
FOR PRODUCING A DUAL PROPERTY TITANIUM
ALLOY COMPRESSOR DISK

16 G.D. Lahoti and T. Altan

DTIC
ELECTE
MAR 21 1980

Battelle's Columbus Laboratories
Columbus, Ohio 43201

11
DECEMBER 1979

12 400

13 F33615-78-C-5025

Interim Annual Report August 1, 1978 — July 31, 1979

1 Aug 78 - 31 Jul 79

16 2306

Approved for public release; distribution unlimited.

17 P17

AIR FORCE MATERIALS LABORATORY
AIR FORCE WRIGHT AERONAUTICAL LABORATORIES
AIR FORCE SYSTEMS COMMAND
WRIGHT-PATTERSON AIR FORCE BASE
OHIO 45433

407080

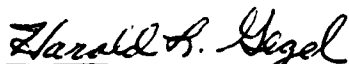
80 3 20 031

DDC FILE COPY

NOTICE

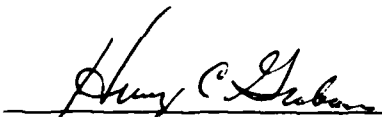
When Government drawings, specifications, or other data are used for any purpose other than in connection with a definitely related Government procurement operation, the United States Government thereby incurs no responsibility nor any obligation whatsoever; and the fact that the government may have formulated, furnished, or in any way supplied the said drawings, specifications, or other data, is not to be regarded by implication or otherwise as in any manner licensing the holder or any other person or corporation, or conveying any rights or permission to manufacture, use, or sell any patented invention that may in any way be related thereto.

This technical report has been reviewed and is approved for publication.



Dr. Harold L. Gegel
Project Engineer

FOR THE DIRECTOR



Dr. H. C. Graham, Chief

Chief,
Processing and High Temperature Materials Branch
Metals and Ceramics Division

"If your address has changed, if you wish to be removed from our mailing list, or if the addressee is no longer employed by your organization please notify AFWAL/MLLM, W-PAFB, OH 45433 to help us maintain a current mailing list."

Copies of this report should not be returned unless return is required by security considerations, contractual obligations, or notice on a specific document.

SECURITY CLASSIFICATION OF THIS PAGE (When Data Entered)

REPORT DOCUMENTATION PAGE		READ INSTRUCTIONS BEFORE COMPLETING FORM												
1. REPORT NUMBER AFML-TR-79-4156 ✓	2. GOVT ACCESSION NO.	3. RECIPIENT'S CATALOG NUMBER												
4. TITLE (and Subtitle) RESEARCH TO DEVELOP PROCESS MODELS FOR PRODUCING A DUAL PROPERTY TITANIUM ALLOY COMPRESSOR DISK		5. TYPE OF REPORT & PERIOD COVERED Interim Annual Technical Report, 8/1/78 to 7/31/79												
		6. PERFORMING ORG. REPORT NUMBER												
7. AUTHOR(s) G. D. Lahoti and T. Altan		8. CONTRACT OR GRANT NUMBER(s) F33615-78-C-5025												
9. PERFORMING ORGANIZATION NAME AND ADDRESS Battelle's Columbus Laboratories ✓ 505 King Avenue Columbus, Ohio 43201		10. PROGRAM ELEMENT, PROJECT, TASK AREA & WORK UNIT NUMBERS 2306 P7 03												
11. CONTROLLING OFFICE NAME AND ADDRESS		12. REPORT DATE August 1979												
		13. NUMBER OF PAGES												
14. MONITORING AGENCY NAME & ADDRESS (if different from Controlling Office)		15. SECURITY CLASS. (of this report) Unclassified												
		15a. DECLASSIFICATION/DOWNGRADING SCHEDULE												
16. DISTRIBUTION STATEMENT (of this Report) Approved for public release; distribution unlimited.														
17. DISTRIBUTION STATEMENT (of the abstract entered in Block 20, if different from Report)														
18. SUPPLEMENTARY NOTES														
19. KEY WORDS (Continue on reverse side if necessary and identify by block number) <table border="0"> <tr> <td>Process Modeling</td> <td>Interface Effects</td> <td>Dual-Property Disk</td> </tr> <tr> <td>Constitutive Equation</td> <td>Integrated System</td> <td>Disk Forging</td> </tr> <tr> <td>Formability</td> <td>Computer Modeling</td> <td>Ti-6242 Alloy</td> </tr> <tr> <td>Workability</td> <td>Processing Conditions</td> <td>Microstructure/Properties</td> </tr> </table>			Process Modeling	Interface Effects	Dual-Property Disk	Constitutive Equation	Integrated System	Disk Forging	Formability	Computer Modeling	Ti-6242 Alloy	Workability	Processing Conditions	Microstructure/Properties
Process Modeling	Interface Effects	Dual-Property Disk												
Constitutive Equation	Integrated System	Disk Forging												
Formability	Computer Modeling	Ti-6242 Alloy												
Workability	Processing Conditions	Microstructure/Properties												
20. ABSTRACT (Continue on reverse side if necessary and identify by block number) <p>This program is aimed at developing a science-based methodology for analyzing, optimizing, and designing metal-deformation processes to control microstructure and properties in a finished part. The validity and application of this approach will be demonstrated by developing forging process for a compressor disk from Ti-6242 alloy, as an example.</p>														

DD FORM 1473

1 JAN 73

EDITION OF 1 NOV 65 IS OBSOLETE

SECURITY CLASSIFICATION OF THIS PAGE (When Data Entered)

Material behavior under processing conditions is being characterized by developing constitutive equations, formability and workability indices, and processing condition-microstructure-property maps. Computerized process models for compression of cylinders from rate-sensitive materials were developed. A test procedure for determining interface heat-transfer and friction coefficients is being developed. Once the material, process, and interface models are complete, an integrated system of computer programs will be developed for designing and optimizing the forging process for a compressor disk.

Accession For	
NTIS GRA&I	<input checked="checked" type="checkbox"/>
DDC TAB	<input type="checkbox"/>
Unannounced	<input type="checkbox"/>
Justification	
By _____	
Distribution/	
Availability Codes	
Dist	Available and/or special
A	

SUMMARY

This interim annual report describes the work performed during the first year of this program by Battelle's Columbus Laboratories (prime contractor) and its subcontractors, namely, Wyman-Gordon Company, Wright State University, University of Pittsburgh, University of California, Los Alamos Scientific Laboratories, and Dr. L. J. Teutonico, Consultant. In order to develop a science-based methodology for analyzing, optimizing and designing metal-deformation processes to control microstructure and properties in a finished part, detailed mathematical models of the workpiece material, the forming process, and the tool-workpiece interface are being developed. The applicability and validity of these models will be illustrated by developing a forging process for a Ti-6242 compressor disk with dual properties.

Uniform compression tests are being conducted to develop constitutive equations for Ti-6242 under normal forging conditions. For this purpose, low strain rate tests are being conducted at Wright State University, and high strain rate tests are being conducted in a plastometer at Los Alamos Scientific Laboratory. In addition, use of a mechanical press to obtain high strain rate data was demonstrated at Battelle. Similarly, use of an MTS machine to obtain high strain rate data is being investigated at the University of Pittsburgh.

The microstructure of the uniformly compressed specimens will be characterized to develop processing conditions/microstructure maps. In addition, a series of pancake forging tests are being conducted at Wyman-Gordon to determine the forgeability and optimum heat treat conditions, and to characterize microstructure/property relationships for the alloy under investigation.

Theoretical development of forming limit curves (FLC) for sheet metal, conducted earlier under Air Force sponsorship, is being extended to the right hand side and the effect of strain rate, strain path and anisotropy are being included. For this purpose the Marciniak-Kuczynski model is being used. Further, workability indices for massive forming, especially for forging process, are being developed at the University of Pittsburgh.

In order to establish process models, mathematical and computer models are being developed to simulate metal flow that occurs during forging of axisymmetric components, such as a compressor disk. For this purpose, the finite-element method is being used at the University of California, and the

upper-bound method is being used at Battelle. Once developed, these process models will be implemented in an interactive system of computer programs with graphics capabilities.

The tool-workpiece interface conditions are being characterized by determining friction factors and interface heat transfer coefficients for selected lubrication systems and forging conditions. At Battelle, a test procedure and fixture is being developed to determine the interface heat transfer coefficient during forging.

Once the material, process, and interface models, described above, are available, they will be integrated in a system to design and optimize the forging process for a subscale compressor disk. A subscale disk will be forged and its properties/microstructures will be evaluated to illustrate the application and validity of this processing science program.

FOREWORD

This interim Annual Technical Report covers the work performed under Contract No. F33615-78-C-5024, from August 1, 1978 to July 31, 1979. It is published for technical information only and does not necessarily represent the recommendations, conclusions, or approval of the Air Force. This contract with Battelle's Columbus Laboratories, Columbus, Ohio, was initiated under the project "Research to Develop Process Models for Producing a Dual-Property Titanium Alloy Compressor Disk". It is being conducted under the direction of Dr. Harold L. Gegel/LLM, Air Force Materials Laboratory, Wright-Patterson Air Force Base, Ohio. Battelle's Columbus Laboratories is the prime contractor on this program with Wyman-Gordon Company, Wright State University, University of Pittsburgh, University of California, and Los Alamos Scientific Laboratories as subcontractors. At Battelle, Dr. T. Altan, Senior Research Leader, and Dr. G. D. Lahoti, Principal Research Scientist are the program manager and principal investigator, respectively.

This report represents the work done by a team of organizations and individuals given below:

- Battelle's Columbus Laboratories, Columbus, Ohio
Dr. T. Altan (Program Manager)
Dr. G. D. Lahoti (Principal Investigator)
Drs. S. L. Semiatin and S. I. Oh
Dr. E. W. Collings
- Wyman Gordon Company, Worcester, Massachusetts
Dr. C. C. Chen
- Wright State University, Dayton, Ohio
Dr. J. F. Thomas, Jr.
Dr. P. Dadras
- University of Pittsburgh, Pittsburgh, Pennsylvania
Dr. H. A. Kuhn
- University of California, Berkeley, California
Dr. S. Kobayashi
- Los Alamos Scientific Laboratories, New Mexico
Dr. J. E. Hockett
- Dr. L. J. Teutonico, Consultant

TABLE OF CONTENTS

SECTION		PAGE
I	INTRODUCTION	1
II	PROGRAM PURPOSE AND OBJECTIVES	3
III	PROGRAM HIGHLIGHTS	4
	Phase I - Material Behavior Under Processing Conditions	4
	Phase II - Process Modeling for Disk Type Forging. . .	5
	Phase III - Interface Effects.	5
	Phase IV - Integration of Material and Process Models.	6
	Phase V - Property/Microstructure Relationships in the Forged Disks.	6
IV	PROGRAM PROGRESS	9
V	MATERIAL BEHAVIOR UNDER PROCESSING CONDITIONS.	11
	Material Characterization and Development of Constitutive Equations (Task 1.1)	11
	Characterization of Dynamic Metallurgical Behavior Under Processing Conditions (Processing-Microstructural Relation- ships) (Task 1.2)	34
	Theoretical and Experimental Forming Limit Representation (Task 1.3)	50
VI	PROCESS MODELING FOR DISK TYPE FORGING	53
	Process Modeling With Finite-Element Method (Task 2.1).	53
	Process Modeling With Upper-Bound and Finite- Difference Method (Task 2.2).	54
	Development of an Interactive System to Predict Metal Flow and Temperatures (Task 2.3).	60

TABLE OF CONTENTS (CONT'D)

SECTION		PAGE
VII	INTERFACE EFFECTS	62
	Selection of Lubricants for Disk Forging (Task 3.1)	63
	Determination of Heat Transfer Co- efficients and Interface Effects (Task 3.2)	63
	Analysis of Metal Flow and Tempera- tures in Ring and Flange Type Configurations (Task 3.3).	67
VIII	INTEGRATION OF MATERIAL AND PROCESS MODELS	69
IX	PROPERTY/MICROSTRUCTURE RELATIONSHIPS IN THE FORGED DISK.	70
X	FUTURE WORK	71
	Material Behavior Under Processing Conditions	71
	Process Modeling For Disk Type Forging	71
	Interface Effects	72
	Property/Microstructure Relationships in the Forged Disk	72
APPENDIX A:	LOW STRAIN RATE TESTS AND DEVELOPMENT OF CONSTITUTIVE EQUATIONS	73
APPENDIX B:	RESEARCH ON THE HOT WORKABILITY OF Ti-6242.	105
APPENDIX C:	DETERMINATION OF HIGH-STRAIN-RATE-FLOW- STRESS DATA FOR Ti-6242 USING A MECHANICAL PRESS	214
APPENDIX D:	DETERMINATION OF HIGH STRAIN RATE FLOW STRESS DATA FOR Ti-6242 BY USING AN MTS MACHINE.	241
APPENDIX E:	PROCESSING, STRUCTURE, AND PROPERTIES OF Ti-6Al-2Sn-4Zr-2Mo-0.1Si ALLOY FORGINGS	254

TABLE OF CONTENTS (CONT'D)

SECTION	PAGE
APPENDIX F: FINITE-ELEMENT ANALYSIS OF AXISYMMETRIC FORGING OF RATE-SENSITIVE MATERIALS	337
APPENDIX G: DESCRIPTION OF THE COMPUTER PROGRAM 'MATRIX'.	353
APPENDIX H: DESIGN OF THE HEAT TRANSFER EXPERIMENT	369

LIST OF ILLUSTRATIONS

FIGURE		PAGE
1	Program Approach For the Project on Process Modeling to Produce a Dual Property Titanium Alloy Compressor Disk	7
2	Outline of the Dual Property Compressor Disk Program	8
3	Microstructure of As-Received Mults	12
4	Engineering Stress-Strain Curves for Ti-6242 (β) at 565 C (1050 F) Vs. Strain Rate	17
5	Engineering Stress-Strain Curves for Ti-6242 (β) at 815 C (1500 F) and 10^{-2} and 10^{-4} sec^{-1}	18
6	Engineering Stress-Strain Curves for Ti-6242 (β) at 10^{-2} sec^{-1} Vs. Temperature	19
7	Fixture used in Uniform Isothermal Compression Tests.	23
8	(a) Plan View and (b) Macro-Section of $\alpha+\beta$ Isothermal Compression Specimen Deformed at 913 C (1675 F), $\dot{\epsilon} \approx 2 \text{ sec}^{-1}$	24
9	Stress Vs. Strain and Strain Rate Vs. Strain Plots for $\alpha+\beta$ -Preform Microstructure at 913 C (1675 F) at Nominal Strain Rate of 2 sec^{-1}	25
10	(a) Plan View and (b) Macro-Section of β Isothermal Compression Specimen Deformed at 913 C (1675 F), $\dot{\epsilon} \approx 10 \text{ sec}^{-1}$	26
11	Stress Vs. Strain and Strain Rate Vs. Strain Plots for β -Preform Microstructure at 913 C (1675 F) at Nominal Strain Rate of 2 Sec^{-1}	28
12	True Stress-Strain Curves for Ti-6242 for Tests Run at Strain Rates of (a) 2 sec^{-1} and (b) 10 sec^{-1}	29
13	Isothermal Compression Die and Furnace, Lower Half.	30
14	True Stress-Strain Curve for Ti-6242 at T=913 C (1675 F), $\dot{\epsilon}=10 \text{ sec}^{-1}$	32
15	True Stress-Strain Curves for Ti-6242	33
16	Triple Point Crack in β Preform Compression Specimen After Deformation	35

LIST OF ILLUSTRATIONS (CONT'D)

FIGURE		PAGE
17a	Macro- and Microstructures of the ($\alpha+\beta$) Preforms Used for Producing Pancake Forging	37
17b	Macro- and Microstructures of the β -Preforms Used for Producing Pancake Forging	38
18	Top View of Pancake Forgings Produced From Nine Different Combinations of Forging Variables	41
19a	Influence of Forge Temperatures and Preform Micro- structures on the Yielding and Stress-Strain Behavior of Isothermally Forged Pancakes.	42
19b	Effect of Forge Temperatures and Preform Micro- structures on the Yielding Forge Pressure and Stress-Strain Behavior of Isothermally Forged Pancakes	43
20	Macrostructures at the Top Surface of the Pancake Forgings Produced from Nine Different Combinations of Forging Variables	44
21a	Effect of Preform Structure on the Macrostructures and Microstructures of Isothermally ($\alpha+\beta$) Forged Pancakes	46
21b	Effect of Preform Structure on the Macrostructures and Microstructures of Conventionally ($\alpha+\beta$) Forged Pancakes	47
21c	Comparison of Macrostructures and Microstructures Between Isothermally and Conventionally β -Forged Pancakes	48
21d	Comparison of Macrostructures and Microstructures Between Isothermally and Near-Conventionally ($\alpha+\beta$) Forged Pancakes.	49
22	Comparison of the Finite-Element Rigid-Plastic Analysis (xxxx) With the Dynamic Analysis (----) and Experiment (——)	55
23	Comparison of the Finite-Element Rigid-Viscoplastic Analysis (xxxx) With the Dynamic Analysis (----) and Experiment (——).	56
24	Visioplasticity Specimen (a) Before and (b) After Isothermal Compression	58

LIST OF ILLUSTRATIONS (CONT'D)

FIGURE		PAGE
25	Distorted Gridlines, Strains, Strain Rates, and Temperatures as Predicted By FORGTM	59
26	Various Types of Plots Generated by the Graphical Display Routine for Compression of Ti-6242 Cylindrical Specimen at 1750°F	61
27	Design of the Experimental Fixture for Determining Interface Heat Transfer Coefficient	64
28	One Dimensional Dynamic Temperature Distribution in Response to the Application of Heat Source at Temperature T_s to a Long Bar at Initial Temperature T_i	65

LIST OF TABLES

TABLE		PAGE
1	Program Schedule and Progress Under Various Phases.	10
2	Processing Conditions for Specimen Material	13
3	Conditions for Uniform Compression Tests.	15
4	Conditions for Tensile Tests.	15
5	Tensile Test Parameters for Ti-6242 (Beta).	16
6	Forging Variables Used for the 18 Pancakes.	39
7	Times Required to Attain Various Temperatures at Various Depths.	66

SECTION I

INTRODUCTION

A large number of aerospace components are manufactured by means of one or more material deformation processes followed by heat treatment and machining. This is the case especially for highly stressed critical engine and airframe parts such as disks, blades, vanes, and structural rib-web type components. The manufacturing cost of these components, used in Air Force systems, continues to rise. Therefore, innovations are sought to reduce the processing and life cycle costs of such products while improving material utilization and properties. Such innovations can be achieved by the combined application of materials science, mechanics, and mechanical engineering disciplines to develop advanced metal processing techniques, more productive and less costly than the state-of-the-art methods.

Recognizing the need for innovative techniques in deformation processing, the Air Force has initiated a new effort on processing research and development. This effort includes an appropriate combination of basic and applied research, a coordinated application of materials data, process analysis, computer-aided simulation of metal flow, and equipment behavior. This new approach is expected to encourage innovative approaches for the future application and development of metal forming technology.

In order to implement the computer-aided design and manufacturing (CAD/CAM) approach, detailed mathematical models of the workpiece material, the forming process, and the workpiece-tool interface conditions are required. However, these models do not now exist in a sufficiently complete form. Hence, the overall objective of this program is to develop and verify the required models and integrate them to form an interactive computer program for process design. The process models are to be developed to a level of sophistication sufficient to allow the control of microstructure and properties in addition to the shape of the finished part. Although the methodology to be developed will be generally applicable to a range of deformation processes, the validation and application will be restricted to the forging process for a Ti-6Al-2Sn-4Zr-2Mo (designated as Ti-6242 hereafter) turbine compressor disk. Since the optimal properties of a compressor disk vary from the bore to the rim, a gradient in

microstructure and properties ("dual property") is desired for the final disk. The program goal is to produce a subscale Ti-6242 compressor disk with high tensile and high low-cycle fatigue properties at the bore region, and good creep and high stress rupture properties at the rim region.

SECTION II

PROGRAM PURPOSE AND OBJECTIVES

The overall purpose of this program is to develop an innovative scientific approach for the analysis and practical application of metal-deformation processes. This new approach must consider a deformation process as a system which includes the metallurgy, mechanics, interface effects, finished shape and microstructure. The program will (a) illustrate how to bring metallurgy and mechanics together, (b) establish the interaction and control of microstructure-property relationships in the finished product, and (c) demonstrate the feasibility for applying a scientific methodology to solve relevant industrial deformation processing problems.

The specific objective of the program is to develop a science-based methodology for analyzing, optimizing and designing metal-deformation processes to control microstructure and properties in a finished shape. The methodology to be developed in this program will be generally applicable to all deformation processes. The validity and application of the scientific methodology, being developed in this program, will be illustrated using the forging process for an engine disk from Ti-6242 alloy, as an example.

Thus, the specific objectives of this program will be achieved by performing the following five tasks:

- (1) Generate data on material behavior under processing conditions
- (2) Develop a computerized model for simulating and optimizing disk-type forging processes
- (3) Develop quantitative data and analysis to characterize material-die interface effects
- (4) Integrate material and process models and apply the computerized model to a disk forging
- (5) Evaluate the properties and microstructure of the forged disks and illustrate the application of the computerized approach developed in this program.

SECTION III

PROGRAM HIGHLIGHTS

Battelle's Columbus Laboratories is the prime contractor on this program with Wyman-Gordon Company, Wright State University, University of Pittsburgh, University of California, and Los Alamos Scientific Laboratories acting as subcontractors. This program is being conducted in the following five phases:

Phase I - Material Behavior Under Processing Conditions

Phase II - Process Modeling for Disk Type Forging

Phase III - Interface Effects

Phase IV - Integration of Material and Process Models

Phase V - Property/Microstructure Relationships on the Forged Disk

The Scope of Work defined in the RFP No. F33615-78-R-5025 serves as the basis for detailed approach in this study. The various tasks and subtasks in each phase are given in the following.

Phase I. Material Behavior Under Processing Conditions

Task 1.1. Material Characterization and Development of Constitutive Equations

Subtask 1.1.1. Low Strain Rate Tests and Development of Constitutive Equations

Subtask 1.1.2. High Strain-Rate Plastometer Tests and Development of Constitutive Equations

Subtask 1.1.3. Use of a Mechanical Press in Obtaining High Strain-Rate Compression Data

Subtask 1.1.4. Use of an MTS Machine in Obtaining High Strain-Rate Compression Data

Subtask 1.1.5. Accuracy, Reliability and Manageability of Constitutive Equations

Task 1.2. Characterization of Dynamic Metallurgical Behavior Under Processing Conditions (Processing-Microstructure Relationships)

Subtask 1.2.1. Structural and Microstructural Evaluation of Uniformly Compressed Samples under Task 1.1.

Subtask 1.2.2. Pancake Forging Tests for Microstructure-Property Evaluation

Task 1.3. Theoretical and Experimental Forming Limit Representation (Workability)

Subtask 1.3.1. Theoretical Formability for Sheet Metal and Bulk Forming Processes

Subtask 1.3.2. Experimental and Theoretical Investigation of Forming Limit Criteria in Disk Forging

Phase II. Process Modeling for Disk Type Forging

Task 2.1. Process Modeling with Matrix Method

Task 2.2. Process Modeling with Upper Bound and Finite-Difference Methods

Task 2.3. Development of an Interactive System to Predict Metal Flow and Temperatures

Phase III. Interface Effects

Task 3.1. Selection of Lubricants for Disk Forging

Task 3.2. Determination of Heat Transfer Coefficients and Interface Effects

Task 3.3. Analysis of Metal Flow and Temperatures in Ring and Flange (Spike) Type Configurations

Phase IV. Integration of Material and Process Models

Task 4.1. Establishment of Forging Process Conditions,
Speed, Temperatures, Contact Times

Task 4.2. Computer-Aided Design of the Preform Shape

Task 4.3. Development of a Process Plan and
Forging of Subscale Disks

Task 4.4. Improvement of the Interactive Process
Design System and Development of an Economic
Model

Phase V. Property/Microstructure Relationships in the Forged Disks

Task 5.1. Evaluation of Microstructures and
Comparison with Predictions

Task 5.2. Evaluation of Mechanical Properties and
Comparison with Predictions

Task 5.3. Titanium Alloy Selection

The program approach is illustrated in Figure 1. The overall plan for conducting this program is summarized in a block diagram given in Figure 2.

PROCESSING SCIENCE PROGRAM

PROGRAM APPROACH

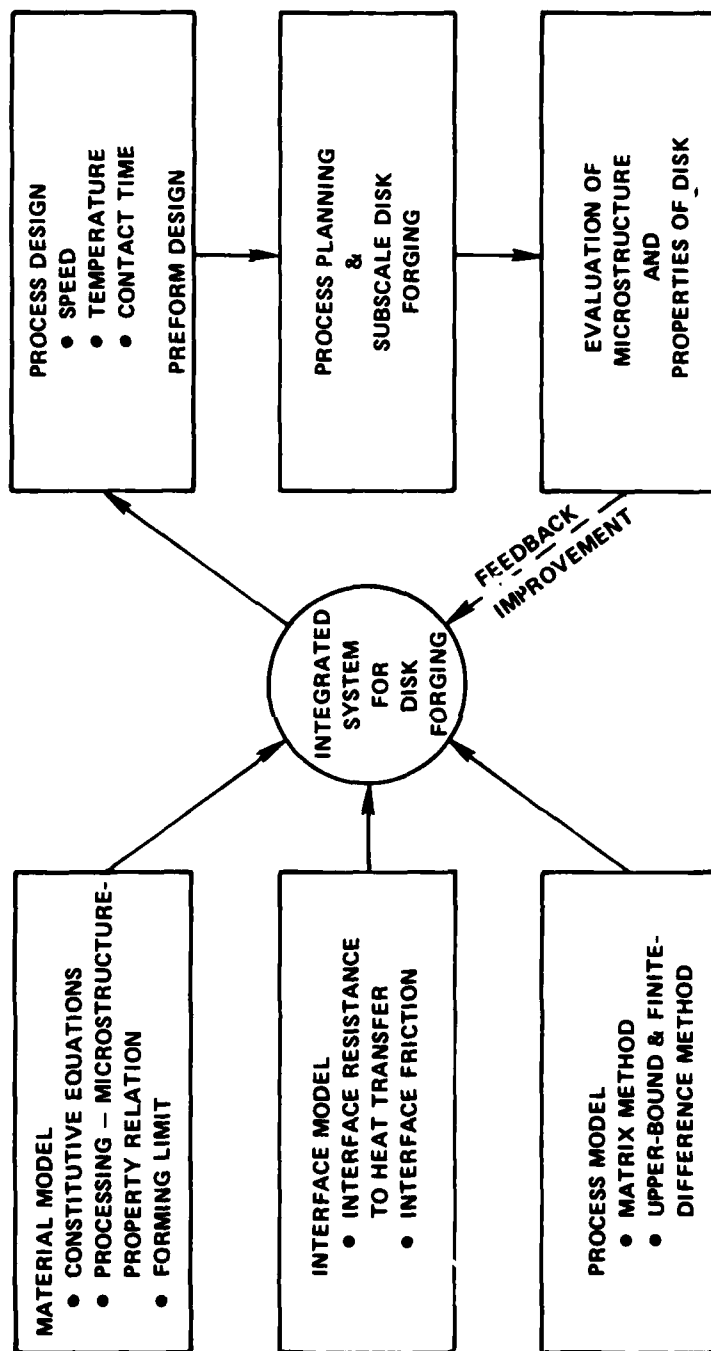


FIGURE 1. PROGRAM APPROACH FOR THE PROJECT ON PROCESS MODELING TO PRODUCE A DUAL PROPERTY TITANIUM ALLOY COMPRESSOR DISK

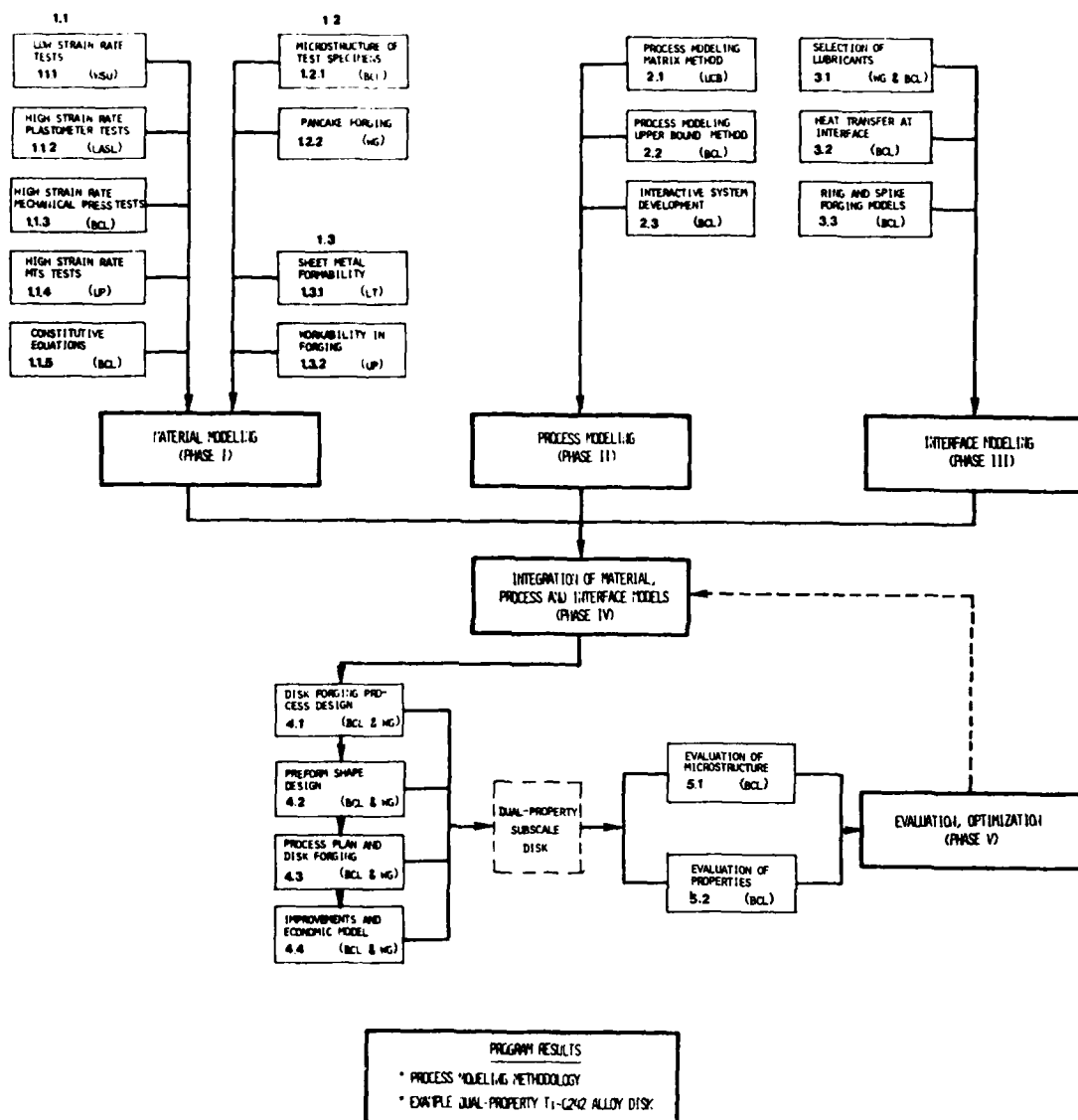


FIGURE 2. OUTLINE OF THE DUAL-PROPERTY COMPRESSOR DISK PROGRAM (BCL = BATTELLE-COLUMBUS, WG = WYMAN GORDON, UCB = UNIVERSITY OF CALIFORNIA, BERKELEY, UP = UNIVERSITY OF PITTSBURGH, LASL = LOS ALAMOS SCIENTIFIC LABORATORY, LT = DR. L. J. TEUTONICO, CONSULTANT). NUMBERS INDICATE VARIOUS TASKS AND SUBTASKS.

SECTION IV

PROGRAM PROGRESS

The program schedule and progress under the various phases of the program are given in Table 1. As per schedule, the work on Phases I, II and III started during the first year. No work was scheduled and conducted on Phases IV and V during the first year of the program. In Table 1, the progress under each phase and each task is assessed by estimated percent of completed work. Detailed description of the progress under each phase and each task of the program are given in the following sections.

TABLE 1
PROGRAM SCHEDULE AND PROGRESS UNDER VARIOUS PHASES
(MONTHS AFTER START OF CONTRACT)

	0	6	12	18	24	30	36	42	Percent Complete
<u>PHASE I</u>									
Task 1.1. Material Behavior Constitutive Equations									
Subtask 1.1.1									25
1.1.2									50
1.1.3									100
1.1.4									25
1.1.5									0
Task 1.2 Process/Microstructural Relationships									
Subtask 1.2.1									10
1.2.2									30
Task 1.3 Forming Limits									
Subtask 1.3.1									50
1.3.2									0
<u>PHASE II</u>									
Task 2.1 Model/Matrix Method									25
Task 2.2 Model/Upper Bound									25
Task 2.3 Interactive Systems and Appl. to Disk									0
<u>PHASE III</u>									
Task 3.1 Lubrication/Selection									50
Task 3.2 Heat Transfer Coefficient									25
Task 3.3 Ring/Flange Analyses									25
<u>PHASE IV</u>									
Task 4.1 Forging Conditions									0
Task 4.2 Forging Trials									0
Task 4.3 Microeconomic Model									0
<u>PHASE V</u>									
Task 5.1 Evaluation of Microstructures									0
Task 5.2 Mechanical Properties									0
Task 5.3 Titanium Alloy Selection									0

SECTION V

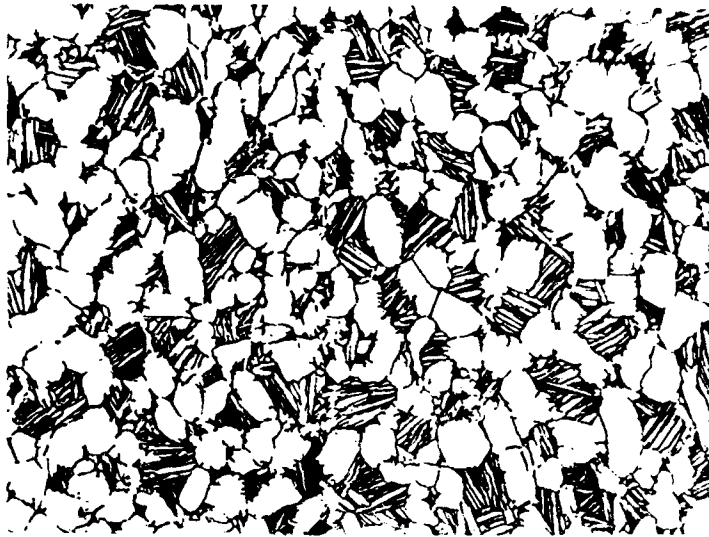
MATERIAL BEHAVIOR UNDER PROCESSING CONDITIONS

In order to develop usable predictive models for a deformation process, it is necessary to determine quantitative relationships which describe the behavior of an engineering alloy under deformation processing conditions. Under the present program, Ti-6242 was selected as a candidate alloy to produce a dual-property compressor disk. Thus, the work under this phase of the program is focused on the development of material models for the titanium alloy Ti-6242.

The material required for all the test specimens under this phase was supplied in the form of 112.65 mm (4.75 inch) diameter x 152.4 mm (6 inch) long multis to Battelle by Wyman-Gordon Company in two different initial (preform) microstructures ($\alpha + \beta$ and β), as shown in Figure 3. They were converted from as-received 203.2 mm (8 in.) diameter billet on a Wyman-Gordon 13.34 MN (1500 ton) press at 4.23 mm/s (10 inch/min) speed. The details of the processing conditions are given in Table 2. These multis were cut into square bars at Battelle, and each bar was marked with its location in the mult it originated. Various types of specimens for compression and tension tests were machined from these bars.

Material Characterization and Development of Constitutive Equations (Task 1.1.)

A process simulation model, which takes into account the influence of material properties on the stress and strain distribution, during deformation, requires the flow stress data on the material as input. The basic information needed is a plastic flow law, or a constitutive equation, expressing the dependence of the flow stress on strain, strain rate, temperature and one or more explicitly history-dependent state variables. These constitutive equations describing the plastic deformation of a material enter the forming analysis in two distinct ways. In the first place, they are required for the forming process model in order to determine the required loads and predict the strain-strain rate temperature path for each element of the deformation zone. The design process requires that this be done as a function of process variables



(a) $\alpha + \beta$ preform microstructure (500x)



(b) β preform microstructure (500x)

FIGURE 3. MICROSTRUCTURE OF AS-RECEIVED MULTS

TABLE 2
PROCESSING CONDITIONS FOR SPECIMEN MATERIAL

Mult Serial No.	Preform Microstructure	Processing Conditions	
		Forge Condition	Heat Treat Condition
A11, A12, A13, A14	$\alpha + \beta$	954 C (1750 F)/ Air Cool	968 C (1775 F)/2 hrs/ Air Cool
A21, A22	β	1037 C (1900 F)/ Air Cool	1024 C (1875 F)/2 hrs/ Air Cool

Note: Further details are given in Appendix E.

such as temperature, ram rate, and preform shape. The strain-strain rate-temperature path will determine the microstructure and properties of each element of the finished part. In the second place, the constitutive equation is used to determine workability indices, such as strain rate sensitivity, which can be used in workability models which predict the maximum strains that the workpiece can undergo without failure.

Under this task, the constitutive equations for Ti-6242 are being developed, primarily by conducting uniform compression tests at various forging temperatures and strain rates, by various members of the team, as shown in Table 3. In addition, as given in Table 4, a limited number of tension tests are being conducted by Wright State University.

Low Strain Rate Tests and Development of Constitutive Equations

Work under this part of the program is being conducted at Wright State University, and the details of this study are included in Appendix A. During this reporting period, the work consisted of determination of (a) tensile properties of Ti-6242 beta preform structure, and (b) effect of heat treatment and protective coating on Ti-6242 alloy.

Tension Tests: Tensile tests were conducted on button-head specimens at temperatures from 565 to 815 C (1050 to 1500 F) and strain rates from 10^{-4} to 10^{-2} sec^{-1} . All specimens were machined from mult A21, which had the transformed beta preform microstructure. The tests were conducted in air with the specimens protected by a thin layer of FelPro C100 (MoS_2 - based lubricant).

The engineering stress-strain curves have been used to compute a number of standard tensile test parameters. These are summarized in Table 5. In this table, σ_y is the engineering stress at 0.2 percent non-elastic strain, σ_{UTS} is the engineering stress at maximum load, ϵ_{unif} is the true, non-elastic strain at maximum load, and ϵ_{tot} is the engineering strain at fracture.

The engineering stress-strain curves in Figures 4 to 6 illustrate strain rate and temperature dependencies. Figure 4 illustrates strain rate dependence at 565 C (1050), and shows an inverted strain rate effect at 10^{-2} sec^{-1} . In general, the strain rate dependence is fairly small at this temperature. Figure 5 shows the strain rate dependence at 815 C (1500 F). The large strain rate dependence of the flow stress and the large apparent elongation at 10^{-4} sec^{-1} suggest conditions approaching superplastic behavior.

TABLE 3
CONDITIONS FOR UNIFORM COMPRESSION TESTS

Test Temperatures (F)		1650	1675	1700	1750	1800	1850	1900
Institution	Preform Microstr.	Test Strain Rates (sec. ⁻¹)						
Los Alamos	$\alpha + \beta$	0.1, 1, 10	---	0.1, 1, 10, 100	0.1, 1, 10	0.1, 1, 10, 100	0.1, 1, 10, 100	0.1, 1, 10, 100
	β	0.1, 1, 10	---	0.1, 1, 10, 100	0.1, 1, 10	0.1, 1, 10, 100	---	---
University of Pittsburgh	$\alpha + \beta$	---	0.01, 0.1, 1, 10	---	0.01, 0.1, 1, 10	0.01, 0.1, 1, 10	0.01, 0.1, 1, 10	---
	β	---	---	---	---	---	---	---
Wright State University	$\alpha + \beta$	$10^{-3}, 10^{-2}, 10^{-1}$	---	$10^{-3}, 10^{-2}, 10^{-1}$	$10^{-3}, 10^{-2}, 10^{-1}$	$10^{-3}, 10^{-2}, 10^{-1}$	$10^{-3}, 10^{-2}, 10^{-1}$	---
	β	$10^{-3}, 10^{-2}, 10^{-1}$	---	$10^{-3}, 10^{-2}, 10^{-1}$	$10^{-3}, 10^{-2}, 10^{-1}$	$10^{-3}, 10^{-2}, 10^{-1}$	---	---
Battelle	$\alpha + \beta$	---	2, 10	---	2, 10	2, 10	2, 10	2, 10
	β	---	2, 10	---	2, 10	2, 10	---	---

TABLE 4

CONDITIONS FOR TENSILE TESTS (ALL TO BE PERFORMED BY WSU USING SPECIMENS WITH β PREFORM MICROSTRUCTURE)

- Stress relaxation tests at T's between 1000 and 1650 F
- Tensile tests at T's = 1050, 1650 F, $\dot{\epsilon}$'s = 10^{-4} , 10^{-3} , 10^{-2} sec.⁻¹
- Additional tensile tests at $\dot{\epsilon}$ = 10^{-2} sec.⁻¹ and T's = 1250, 1500, 1700, 1750, 1800 F

TABLE 5
TENSILE TEST PARAMETERS FOR Ti-6242 (BETA)

Bar	Temperature C(F)	Strain Rate sec ⁻¹	σ_y MPa	σ_{UTS} MPa	ϵ_{unif}	ϵ_{tot} %
4	565 (1050)	10 ⁻⁴	463	554	0.047	9.4
3	565 (1050)	10 ⁻³	478	578	0.057	11.1
3	565 (1050)	10 ⁻²	464	557	0.041	7.0
11	677 (1250)	10 ⁻²	448	520	0.029	10.0
11	732 (1350)	10 ⁻²	389	457	0.019	8.3
5	815 (1500)	10 ⁻²	251	301	0.018	7.1
5	815 (1500)	10 ⁻⁴	106	111	0.013	-

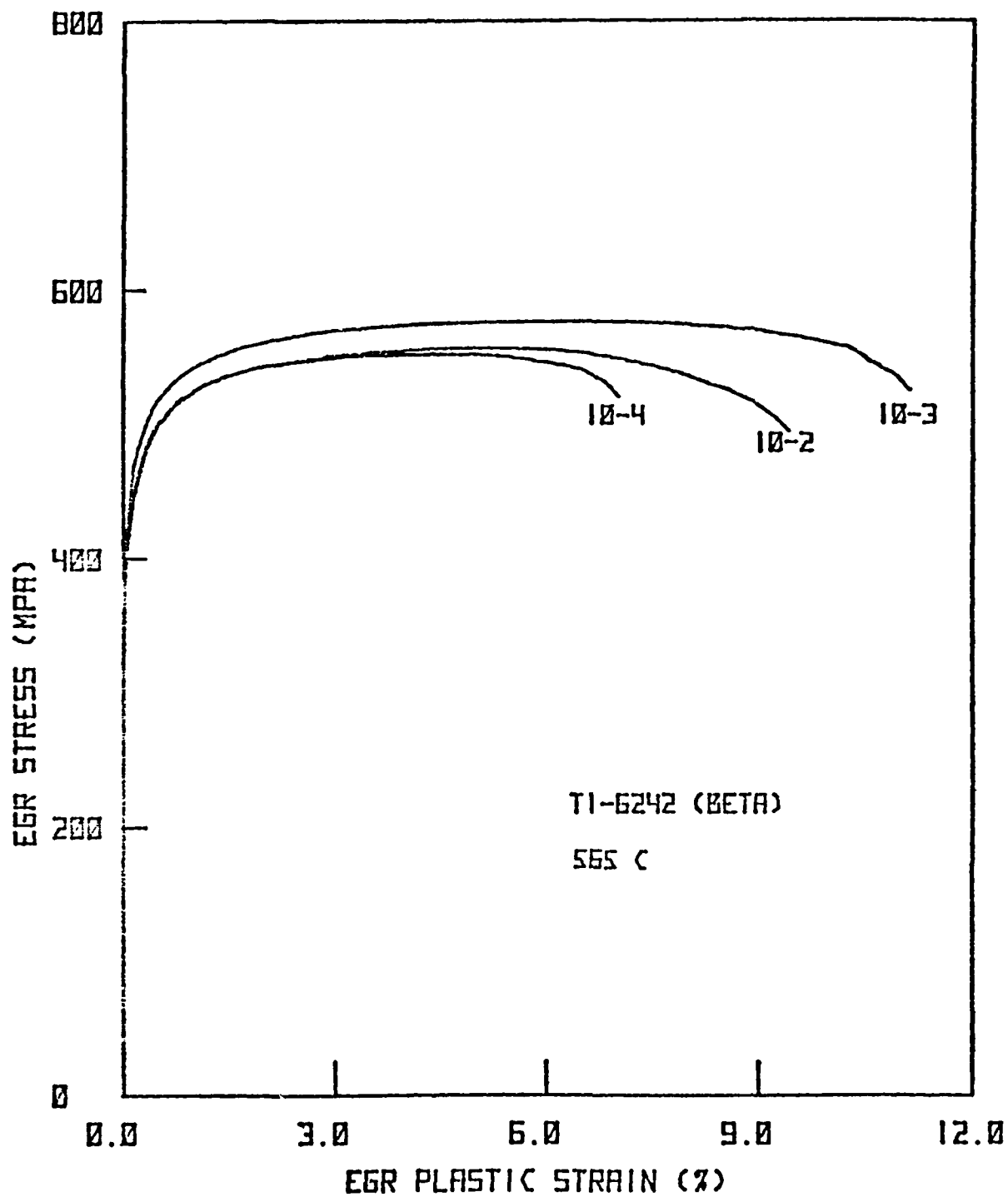


FIGURE 4. ENGINEERING STRESS-STRAIN CURVES FOR Ti-6242 (β) AT 565 C (1050 F) VS. STRAIN-RATE.

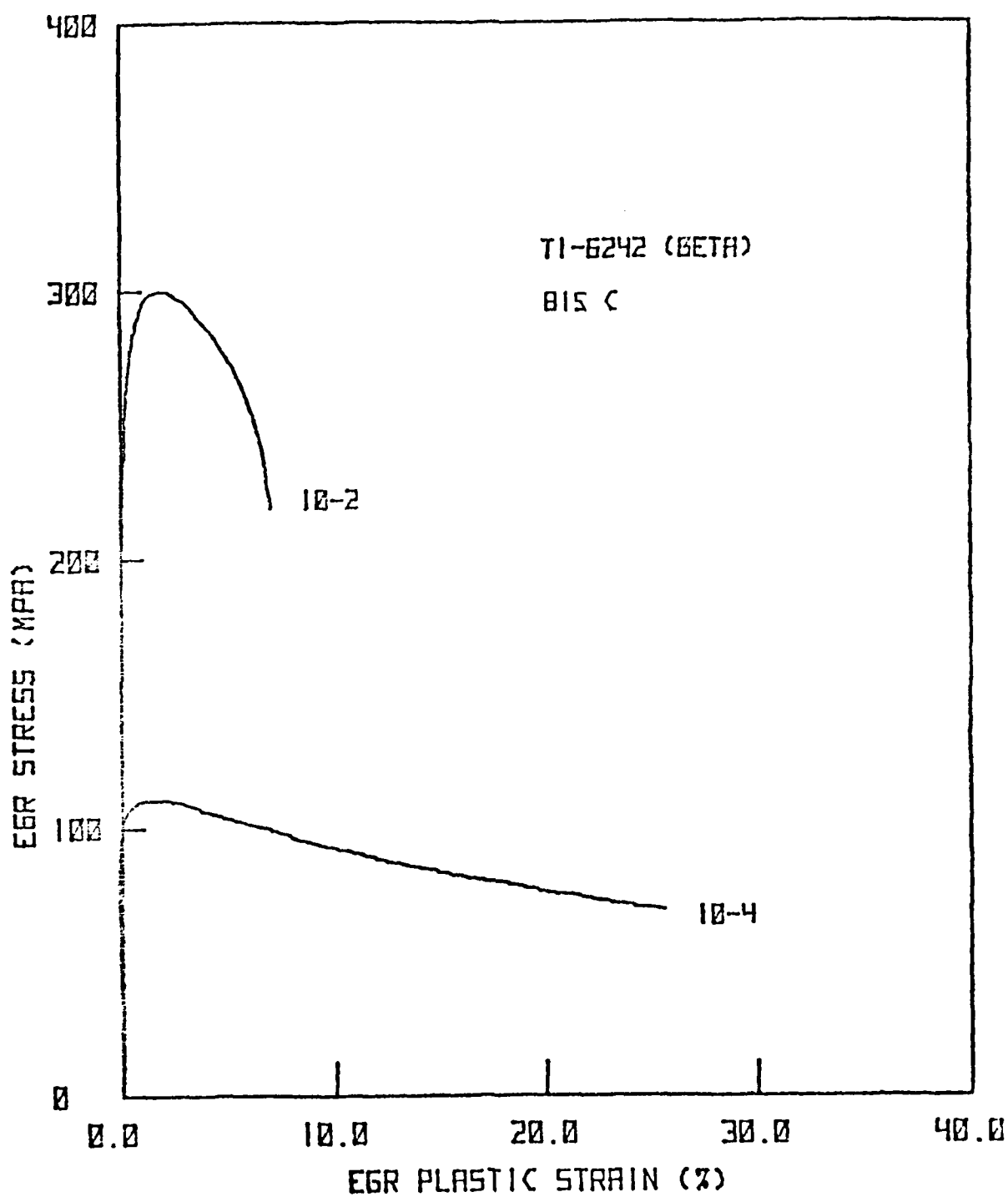


FIGURE 5. ENGINEERING STRESS-STRAIN CURVES FOR Ti-6242 (β) AT 815 C (1500 F) AND 10^{-2} AND 10^{-4} SEC $^{-1}$.

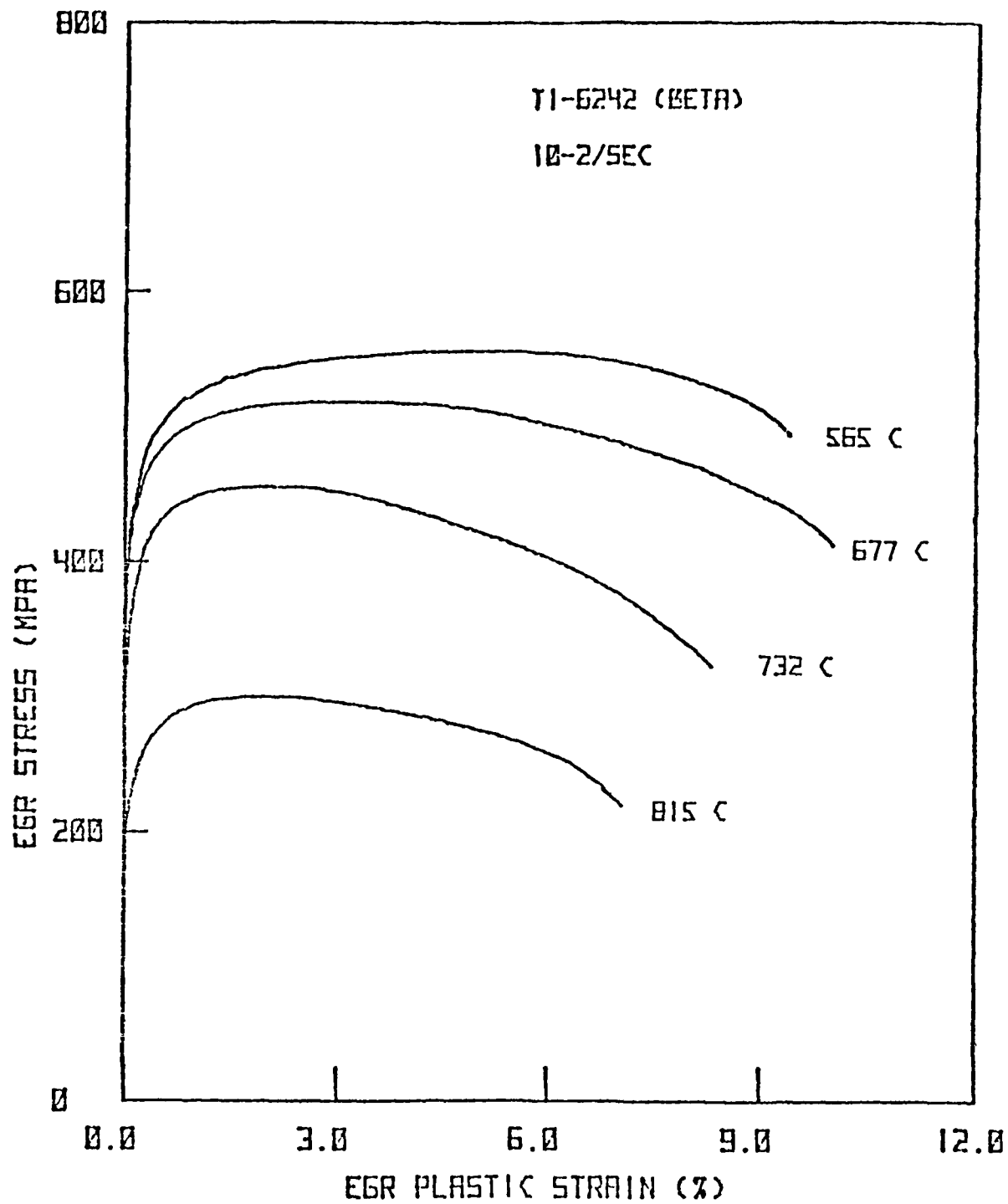


FIGURE 6. ENGINEERING STRESS-STRAIN CURVES FOR Ti-6242 (β) AT 10^{-2} SEC^{-1} VS. TEMPERATURE.

Figure 6 illustrates the temperature dependence at strain rate of 10^{-2} . It is seen that the flow stress only begins to fall off appreciably above 677 C (1250 F).

Metallographic Study of Tensile Specimens: The deformed structure of the tensile specimens tested at a strain rate of 10^{-2} sec^{-1} and at 565, 677, 732 and 815 C (1050, 1250, 1350, and 1500 F) were examined and the following general conclusions were obtained.

1. As a result of deformation, no noticeable change in (a) the size, shape and the distribution of the primary β -colonies, and (b) the general morphology of the transformed β -structure was observed.
2. In all cases studied, the fracture was predominantly intergranular. Also, grain boundary separation, with no evidence of grain boundary sliding was mostly observed.
3. Free surface wrinkling and orange peel topography was observed as a result of the relative displacement of the large ($\sim 1\text{mm}$) primary β -grains.

Fractography of Tensile Specimens: The SEM observations provided further evidence regarding the fracture characteristics of the transformed β microstructure. In the temperature range of 565 to 815 C (1050 to 1500 F) and for a constant strain rate of 10^{-2} sec^{-1} , the fracture is predominantly intergranular. For all the specimens, grain boundary separation is prevalent and grain boundary sliding is not observed. In isolated cases, transgranular cracks formed by interconnecting cavities are noticed. Such cracks, however, do not extend from grain wall to grain wall and their contribution to the eventual failure is considered inconsequential.

High Strain Rate Plastometer Tests and Development of Constitutive Equations

This part of the program is being conducted at the Los Alamos Scientific Laboratory. The purpose of this study is to conduct constant strain rate compression tests (a) to determine the dependence of flow stress on strain rate and temperature, (b) to investigate strain hardening and flow softening behavior, and (c) to characterize the structures produced by hot-working both $\alpha + \beta$ and β preform microstructures as a function of strain, strain rate and temperature.

Uniform compression tests with Ti-6242 specimens are under progress at the Los Alamos Scientific Laboratory. The various strain rates and temperature conditions for these tests are given in Table 3. The details of this study are not available yet and will be reported later.

Hot Workability of Ti-6242 Alloy

This part of the program was conducted at the Air Force Materials Laboratory and the details are given in Appendix B.

Hot compression tests at various temperatures were conducted on AFML's 500-ton hydraulic press using dies made from alloy 713C. The specimens were coated with Delta Glaze 69, which acted both as a lubricant and a coating to prevent oxidation of the surfaces. The specimens were reduced to approximately half of their initial height under a ram speed of one inch per second. Microstructures were examined at different points in the cross sections of the forged specimens to characterize the structural changes accompanying the high strain rate and high temperature deformation. The results showed clearly that in both $\alpha + \beta$ preform and β preform, when forged in the $\alpha + \beta$ temperature range just below the β -transus, geometrical nonuniformities appeared in the form of a kink resulting in an instability condition which could lead to shear-band formation. This instability condition was proven to result from a microstructural instability during forging.

A dual property disk was fabricated by using a composite ring preform, where the hub portion was made from $\alpha + \beta$ preform structure and the rim portion was made from β preform structure materials of the same alloy. The preform was stiffened through geometric design and were isothermally forged at 1700 and 1900F. The specimen during deformation behaved as one unit since there was good matching of flow lines for the two different compositions. However, the flow of the case material appeared to be more sensitive to temperature.

Use of a Mechanical Press in Obtaining High Strain Rate Compression Data

This part of the program was conducted at Battelle and the details are given in Appendix C.

Uniform compression tests were conducted on Battelle's 4.45 MN (500 ton) mechanical press. For this purpose, a fixture shown in Figure 7 was used. The specimens were heated together with the container under a protective argon atmosphere, and the surface of the carbide platens and the specimens with grooved-ends were coated with glass lubricants appropriately selected for a temperature range. Data were obtained, at various test temperatures and strain rates summarized in Table 3, for Ti-6242 specimens having two different microstructures, namely equiaxed α in a transformed matrix, the $\alpha + \beta$ microstructure, and a microstructure consisting solely of transformed β , the β microstructure. The flow behavior of the two microstructures differed markedly and can be summarized as follows:

- (1) In compression, the $\alpha + \beta$ microstructure deformed stably, as shown in Figure 8, with monotonically increasing load-stroke curves. Reducing this data to stress-strain data, as shown in Figure 9, the flow behavior was shown to exhibit softening which could be attributed to adiabatic heating and a decreasing strain rate as the deformation proceeded, a characteristic of compression tests run in the mechanical press. Adjusting the data for this softening, it was shown that the dependence of flow stress on strain is weak, and hence, the flow stress is a function primarily of strain rate and temperature. This is a characteristic of metals which dynamically recover during hot working and has been observed in other $\alpha + \beta$ titanium alloys tested at much lower strain rates than those of the present tests. It appears, however, that the flow stress is a function of strain-rate history as shown by comparing strain-rate sensitivity data obtained through two different deformation schemes.
- (2) The compressive deformation of β specimens gave rise to non-uniform, unstable flow, as shown in Figure 10, characterized by decreasing load stroke curves. The stress-strain curves for this microstructure show an additional amount of flow softening

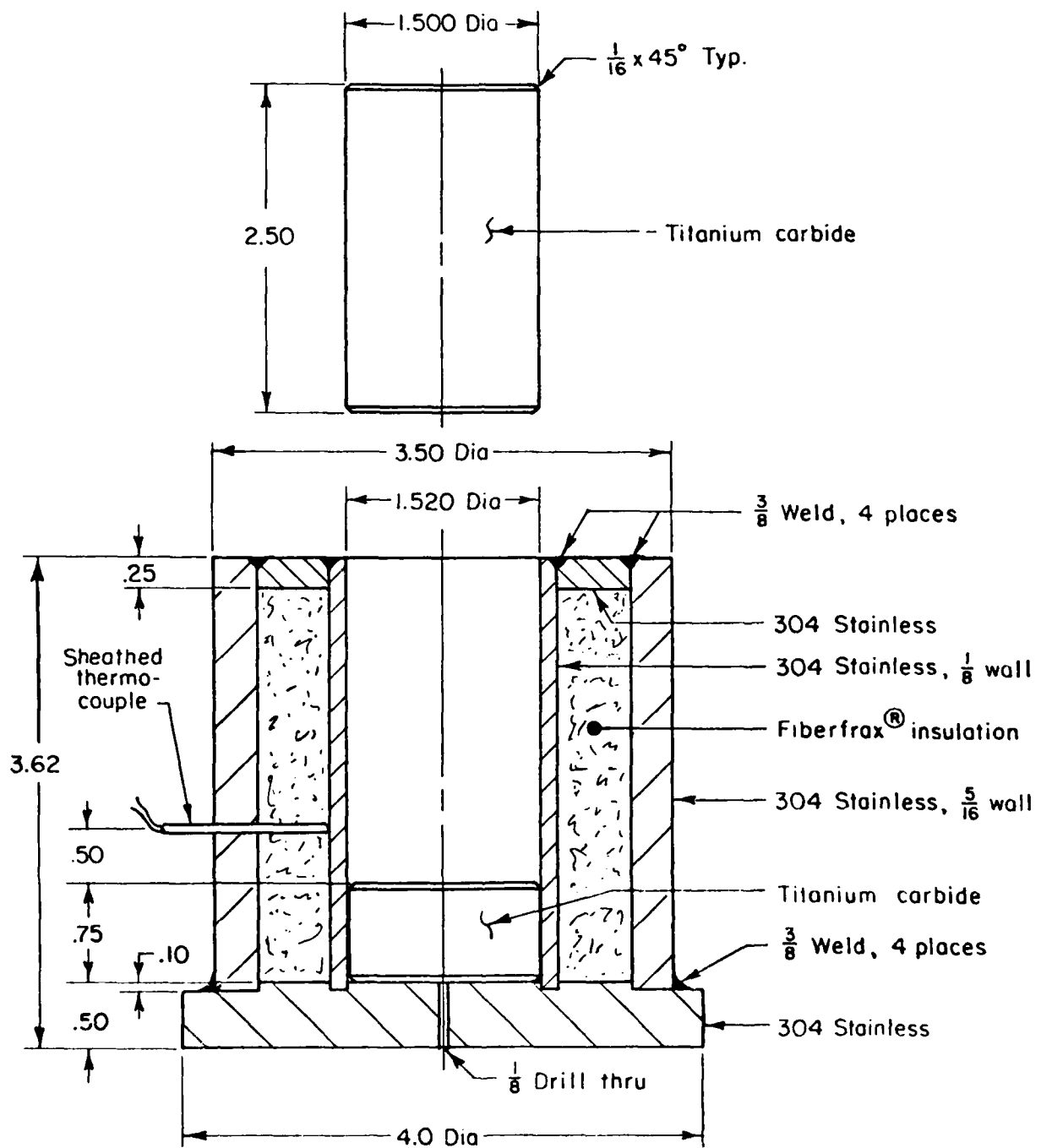


FIGURE 7. FIXTURE USED IN UNIFORM
ISOTHERMAL COMPRESSION TESTS

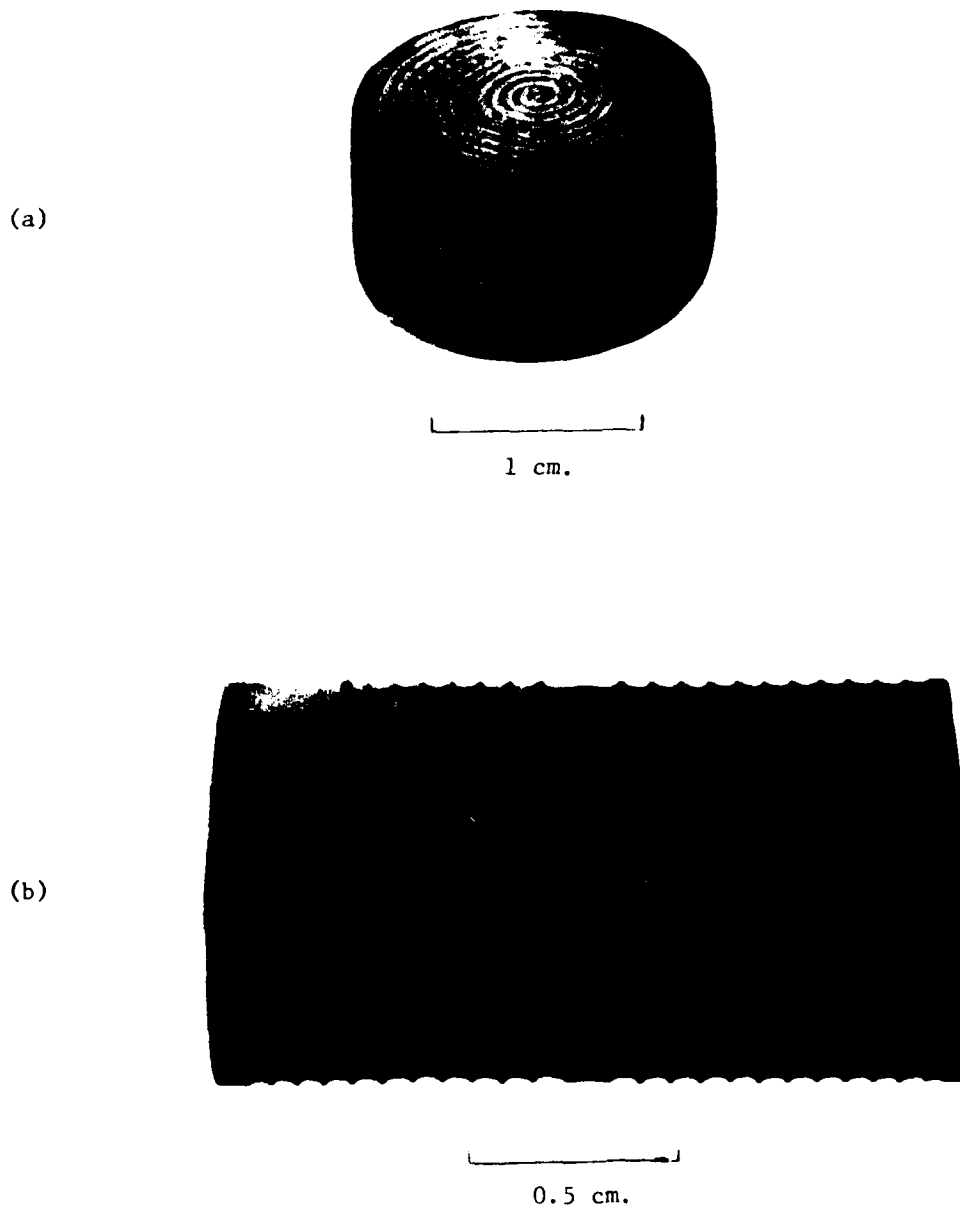


FIGURE 8. (a) PLAN VIEW AND (b) MACRO-SECTION OF $\alpha + \beta$ ISOTHERMAL COMPRESSION SPECIMEN DEFORMED AT 913 C (1675 F), $\dot{\epsilon} \approx 2 \text{ Sec.}^{-1}$

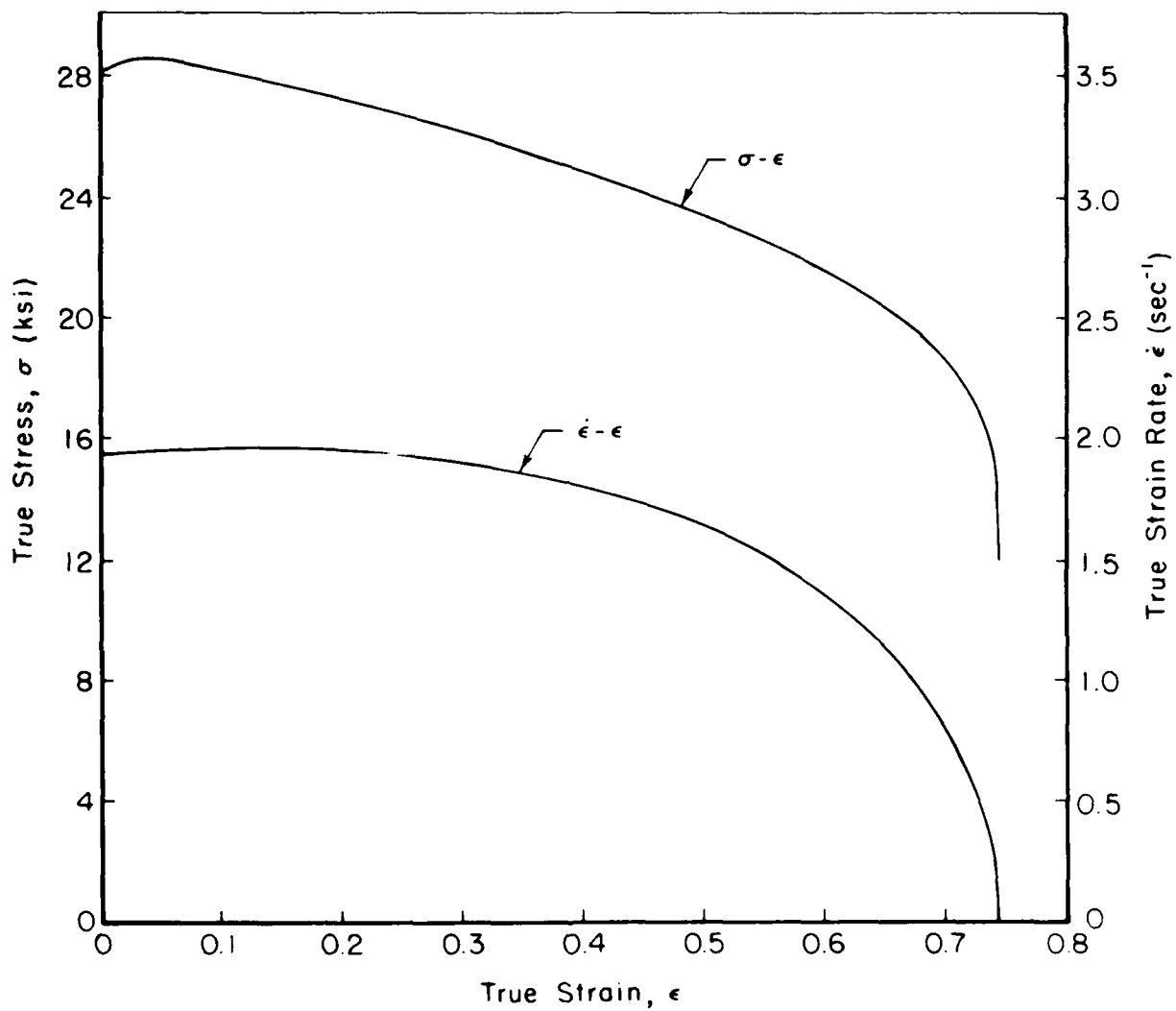
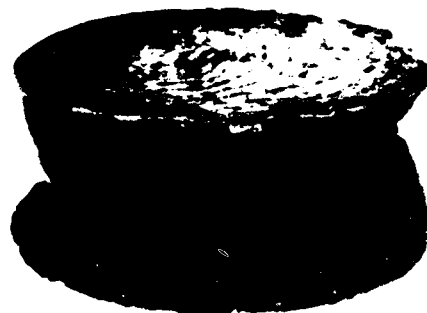


FIGURE 9. STRESS VERSUS STRAIN AND STRAIN RATE VERSUS STRAIN PLOTS FOR $\alpha + \beta$ -PREFORM MICROSTRUCTURE AT 913 C (1675 F) AT NOMINAL STRAIN RATE OF 2 Sec⁻¹.



1 cm.

(a)



0.5 cm.

(b)

FIGURE 10. (a) PLAN VIEW AND (b) MACRO-SECTION OF β ISOTHERMAL COMPRESSION SPECIMEN DEFORMED AT 913 C (1675 F), $\dot{\epsilon} \approx 10 \text{ sec.}^{-1}$

in excess of that observed for the $\alpha+\beta$ microstructure, as shown in Figure 11. This increment has been attributed to breakdown of the β microstructure and recrystallization to yield the equilibrium α phase at test temperatures below the β transus temperature. It is also believed that development of a softer texture may have caused some of the observed flow softening. The true stress-strain curves for Ti-6242 from this study are summarized in Figure 12.

Use of an MTS Machine in Obtaining High Strain Rate Compression Data

These tests are being conducted at the University of Pittsburgh. The details of this study are given in Appendix D.

Under this study, the validity of using an MTS machine to obtain flow stress data for Ti-6242 alloy is being determined. The isothermal compression test apparatus used is shown in Figure 13. The high temperature tooling is enclosed within a radiant heating furnace so that the test specimen and the dies may be heated to the same temperature. The upper and lower dies and the specimen are fitted with thermocouples to record the temperature.

The dies are preheated to the required temperature and then the lubricated specimen is heated in-situ on the lower platen. When the specimen reaches the desired temperature, the test is performed at a prescribed strain rate and to a prescribed total strain through the control system on the MTS machine. To achieve constant strain rate, the stroke is controlled by using the dual slope setting on the function generator. The desired exponential relationship of stroke and time are approximated by two linear segments. During the test, the instantaneous strain rate may vary about 20 percent from the nominal value.

The load and stroke data are converted to digital form on a data logger. The stroke is corrected for the lubricant thickness and machine compliance, and the digital data is processed using an on-line computer terminal. The results obtained are in the form of:

- (a) True Stress vs True Strain Curves,
- (b) Stroke vs Time Curves, and
- (c) Strain Rate vs Strain Curves.

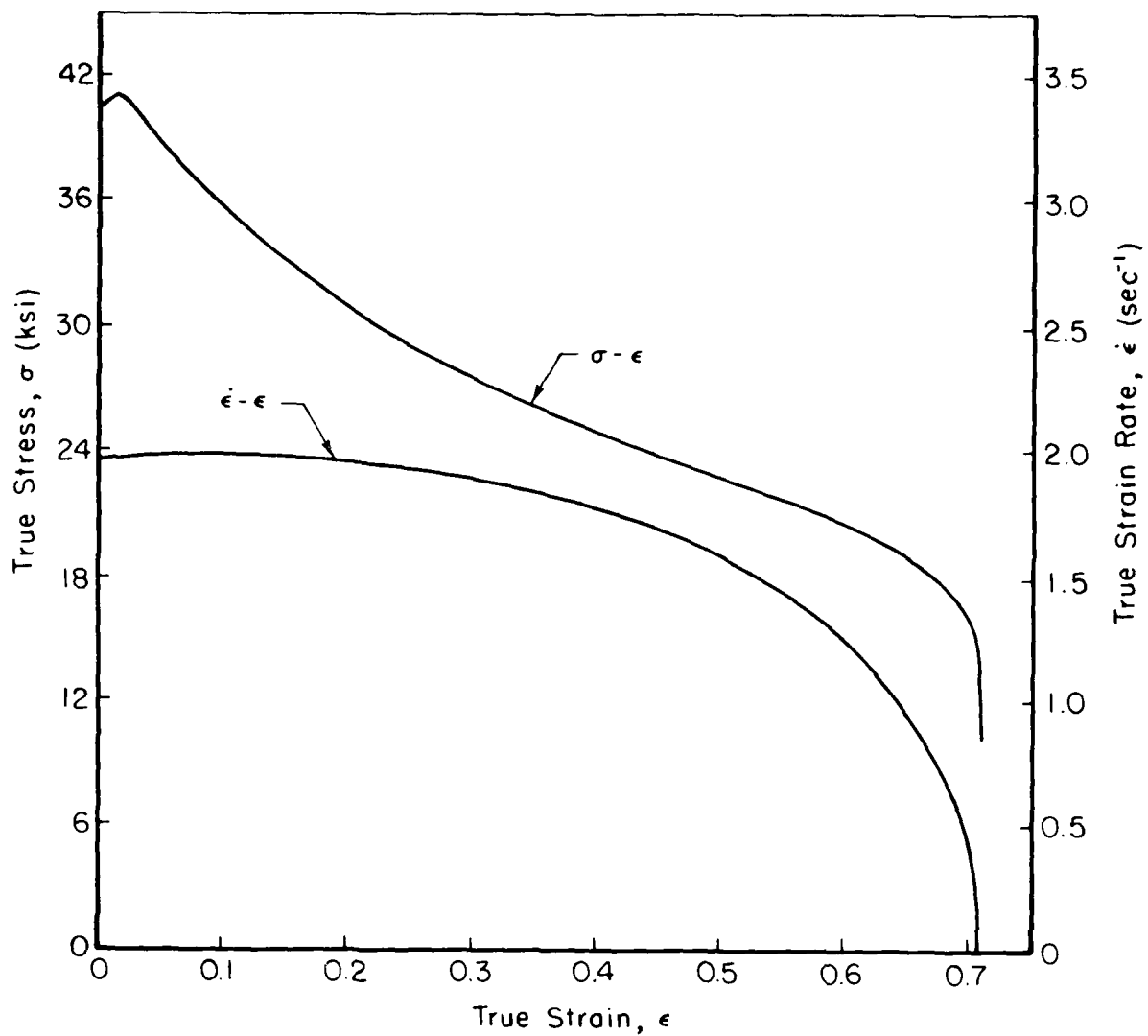


FIGURE 11. STRESS VERSUS STRAIN AND STRAIN RATE VERSUS STRAIN PLOTS FOR β -PREFORM MICROSTRUCTURE AT 913 C (1675 F) AT NOMINAL STRAIN RATE OF 2 Sec⁻¹.

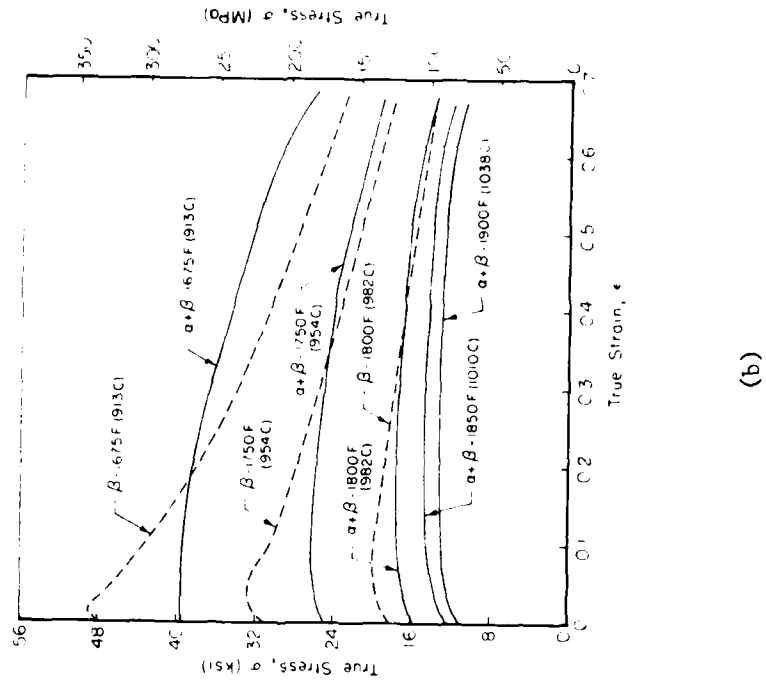
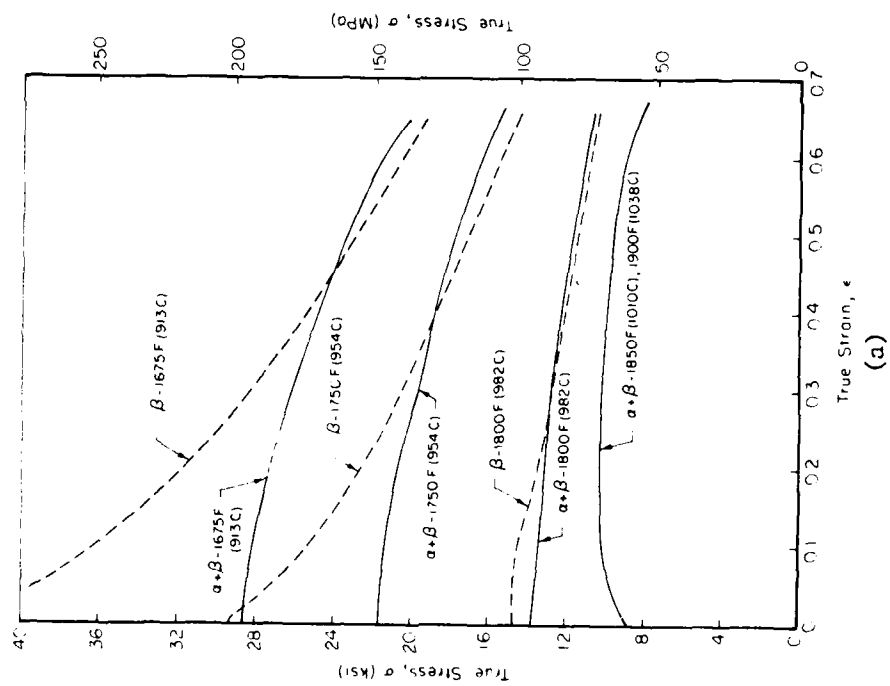
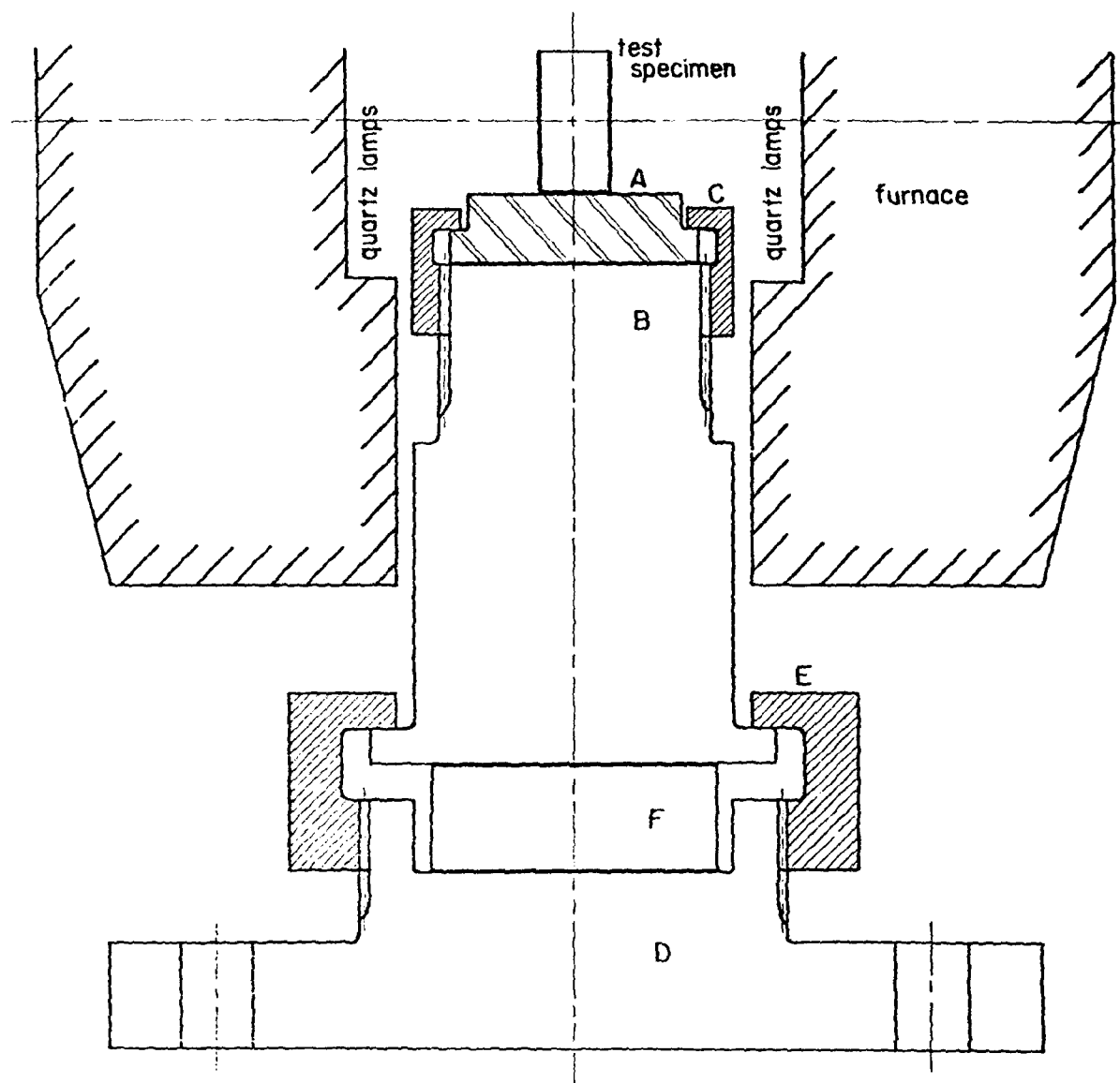


FIGURE 12. TRUE STRESS-STRAIN CURVES FOR Ti-6242 FOR TESTS RUN AT STRAIN RATES OF (a) 2 sec.⁻¹ and (b) 10 sec.⁻¹



- | | |
|-----------------------------|--|
| A die insert, Incoloy | D base, stainless steel |
| B die holder, Waspalloy | E collar, stainless steel |
| C retaining ring, Waspalloy | F ceramic insulator, hot-pressed Al_2O_3 |

FIGURE 13. ISOTHERMAL COMPRESSION DIE AND FURNACE, LOWER HALF.

An example of a true stress-strain curve, as obtained through the data read-out system described above, is given in Figure 14. There is some noise in the load-cell output, which is reflected as noise in the calculated true stress-strain plot. The reproducibility of these plots is very good. Figure 15 shows some stress-strain curves developed using this system. However, the stress values here are approximately half of those given in Figure 12. This discrepancy is being investigated currently.

Accuracy, Reliability and Manageability of Constitutive Equations

The aim of this part of the program is to develop a constitutive equation which is accurate, reliable, and manageable for use in a computerized process model of disk forging. For this purpose, the uniform compression test data developed by various team members will be used. The various types of constitutive equations are being investigated currently. One such equation under study is due to Hart⁽¹⁾. The flow law can be stated as

$$\sigma = \sigma^*(\dot{\epsilon}, T) \quad (1)$$

where σ^* is a hardness state parameter, $\dot{\epsilon}$ is strain rate and T is temperature. The single most important feature of this constitutive relation formulation is the identification of state parameters which evolve with deformation history and partially determine the future response of the material. In addition, it is recognized that the plastic strain is not a state parameter, but rather a path variable, albeit an important one for most process calculations. However, for a description according to Equation (1), it is possible to measure the current value of hardness parameter σ^* .

Hart's formulation has been shown to be valid at low strain rates (10^{-2} sec^{-1} and lower). Under a separate study, its validity at moderate and high strain rates ($10^{-1}, 1, 10 \text{ sec}^{-1}$) is being investigated by conducting compression tests using Al 1100-0 test specimens.

(1) Hart, E. W., "A Phenomenological Theory for Plastic Deformation of Polycrystalline Metals", Acta Metallurgical, Vol. 18, p. 599 (1970).

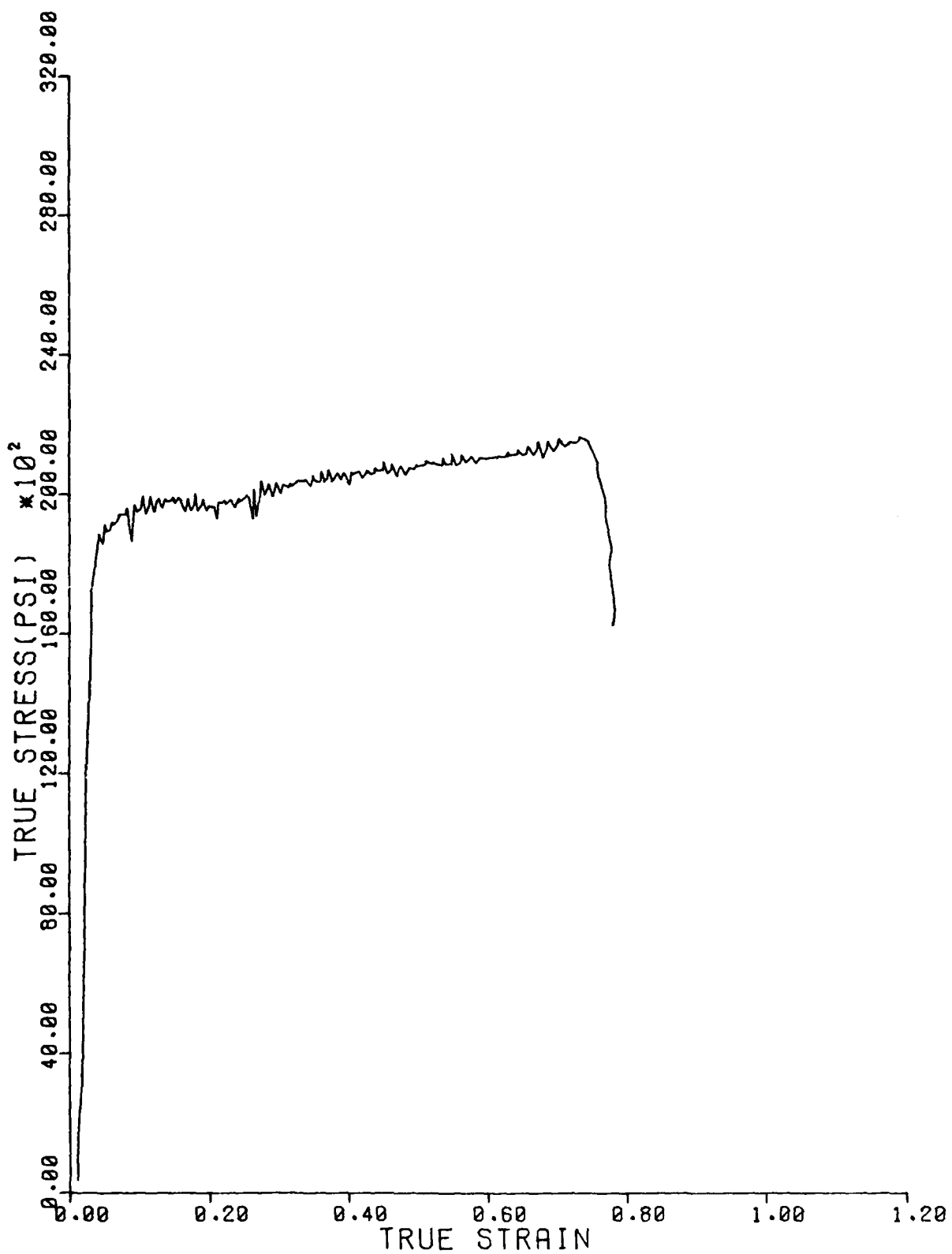


FIGURE 14. TRUE STRESS-STRAIN CURVE FOR Ti-6242 AT $T=913$ C(1675 F), $\dot{\epsilon}=10 \text{ sec}^{-1}$

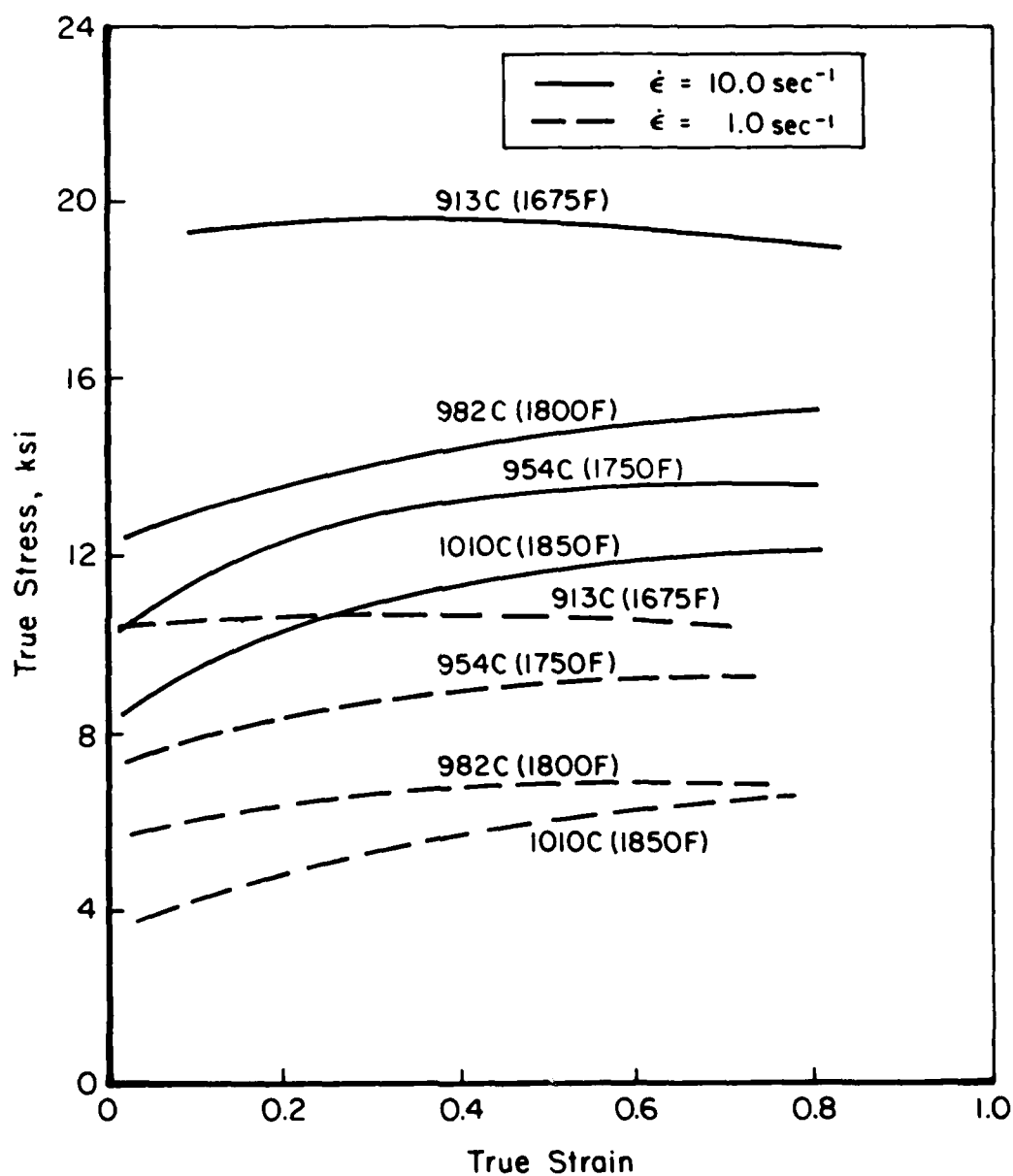


FIGURE 15. TRUE STRESS-STRAIN CURVES FOR Ti-6242.

Characterization of Dynamic Metallurgical Behavior
Under Processing Conditions (Processing-Microstructure Relationships)
(Task 1.2)

In titanium alloys, the microstructure can be quite varied, resulting in a wide range of properties. The microstructure of $\alpha+\beta$ titanium alloys strongly depends on both processing history and on heat treatment. A variety of transformation products can be formed in these alloys; the morphology, volume fraction, and distribution of these can be altered by the appropriate combination of heat treatment and processing. The resultant microstructural variations can influence both strength and fracture behavior. The trade-off between increases in strength and decreases in fracture toughness are well known, but there are limited data which allow a proper selection of microstructure to obtain desired mechanical properties in service.

Structural and Microstructural Evaluation of
Uniformly Compressed Samples

The work under this task will be conducted at Battelle after the uniformly compressed specimens from Wright State University, University of Pittsburgh and Los Alamos Scientific Laboratory are received. The uniformly compressed specimens from the mechanical press tests, conducted at Battelle, were briefly examined for microstructural changes. Figure 3 shows the initial microstructures ($\alpha+\beta$ and β) of the specimens used in these tests. The microstructure in specimens with $\alpha+\beta$ preform structure remained essentially unchanged after deformation at various temperatures and strain rate conditions given in Table 3. However, the microstructure of specimens with β preform structure changed significantly after deformation. The basketweave colonies had broken up into somewhat smaller colonies, and, more importantly, it was noted that small recrystallized alpha grains had been formed. In one instance, triple point cracks were also observed, as shown in Figure 16. Further studies are needed in order to establish relationships between processing conditions and resulting microstructures.

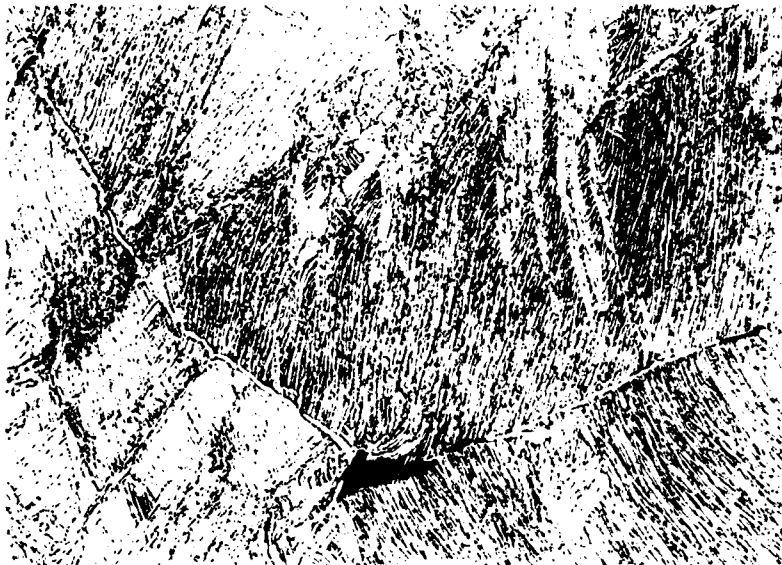


FIGURE 16. TRIPLE POINT CRACK IN β PREFORM COMPRESSION SPECIMEN AFTER DEFORMATION (500x)

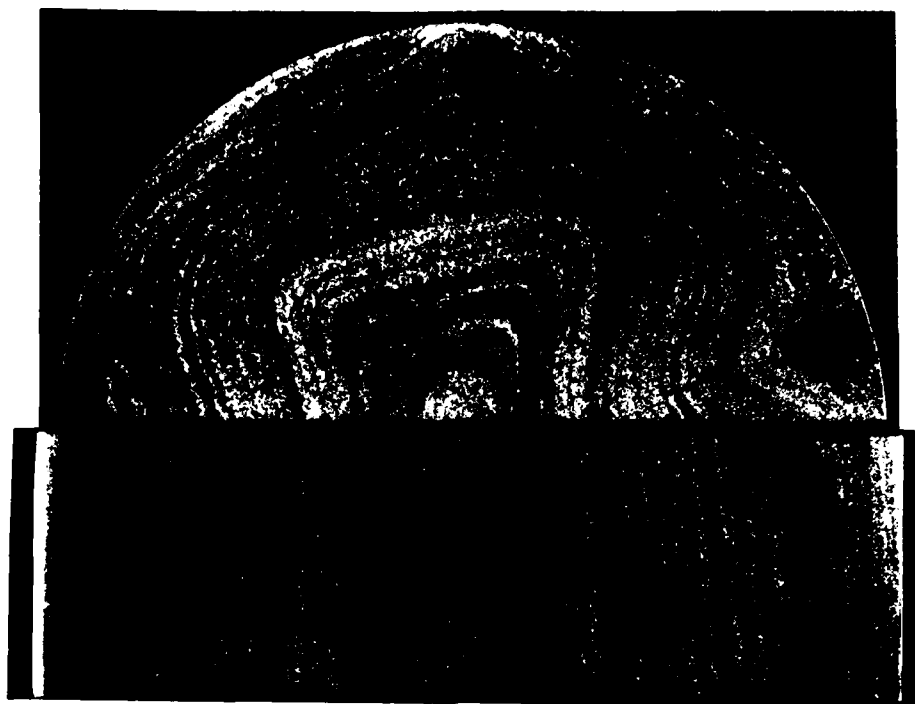
Pancake Forging Tests For Microstructure-Property Evaluation

This part of the program is being conducted at Wyman-Gordon Company. The details are included in Appendix E. A series of 18 pancake forgings were produced to characterize the forgeability, the metal flow characteristics, and the resultant microstructure and properties of the pancakes. The main purpose of this portion of the program is to determine the forgeability and optimum heat treat conditions, and to characterize the microstructure/property relationships of the alloy forgings.

(a) Forge Processing

Approximately 91 kg (200 lb) of 203.2 mm (8 inch) round Ti-6242 billets were converted to 88.9 mm (3.5 inch) round bars. They were heat treated to produce ($\alpha + \beta$) and β -preforms (see Table 2), and then machined to 18 of 82.55 mm (3.25 inch) round x 82.55 mm (3.25 inch) thick preforms for forging evaluations, and two of 82.55 mm (3.25 inch) x 25.4 mm (1 inch) thick samples for structural evaluations. Typical macro- and microstructures of the ($\alpha + \beta$) and β -preforms produced are given in Figures 17a and 17b, respectively.

The forging operations were conducted on a 1.78 MN (200 ton) isothermal forging press, and TZM flat dies were used. These forgings were produced both isothermally and conventionally, both subtransus and supertransus. The multiples were first coated with BN coating about 0.13 mm (5 mil) thick per side, and then preheated for the aim temperature prior to forging. The dies were induction heated. The strain rates used were 0.1 min.^{-1} ($1.7 \times 10^{-3} \text{ s}^{-1}$) for isothermal forging and 3.0 min.^{-1} ($5.0 \times 10^{-2} \text{ s}^{-1}$) for conventional forging; these strain rates are comparable with those used in industrial press forging. The forge operations were accomplished by one-stage forging from 82.55 mm (3.25 inch) to a final thickness of about 31.75 mm (1.25 inch). This is equal to a total deformation of 60% reduction in thickness. The thickness:diameter ratio of the initial preform is 1:1, an acceptable ratio for production preforms. After the forging operation, the forgings were air-cooled. The forgings have a diameter of 139.7 mm (5.5 inch) and a plan view area of 24 square inches. The forging variables used for the forge processings are given in Table 6. Two pancakes per condition were produced.



($\alpha+\beta$)-preform

1 inch
2.54 cm

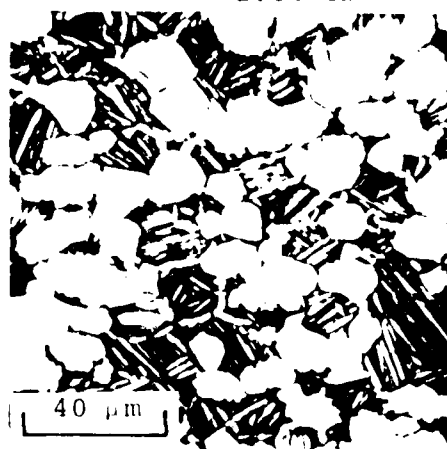
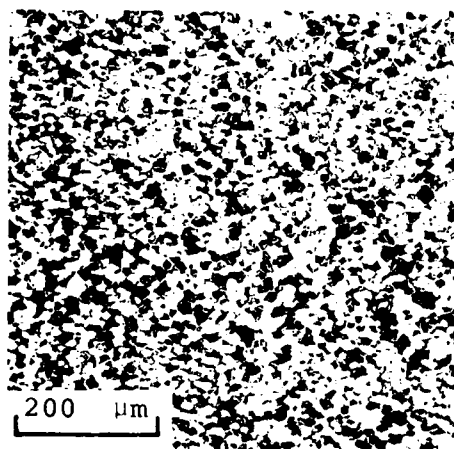
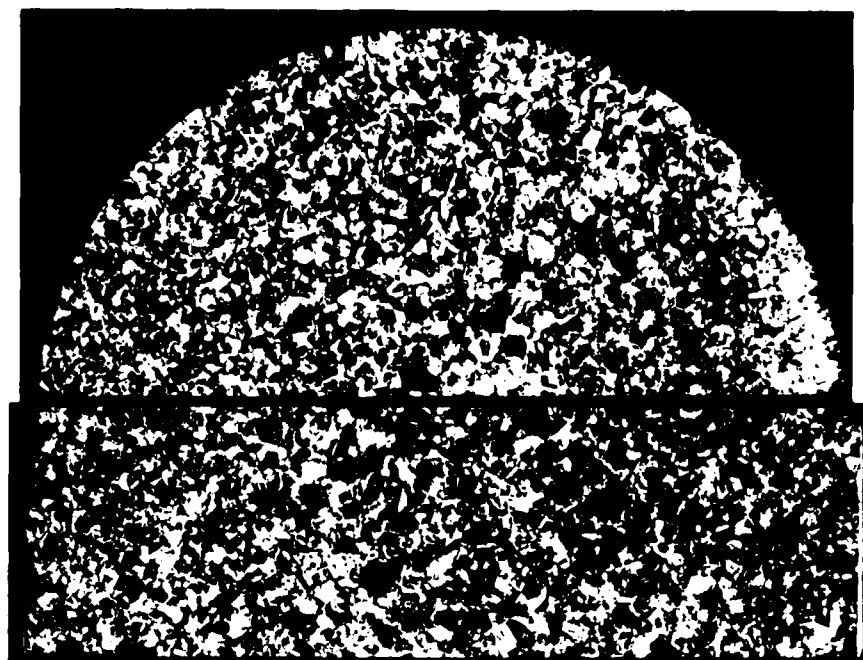


FIGURE 17a. MACRO- AND MICROSTRUCTURES OF THE ($\alpha+\beta$) PREFORMS SET FOR PRODUCING PANCAKE FORGING.



B-preform

1 inch
2.54 cm

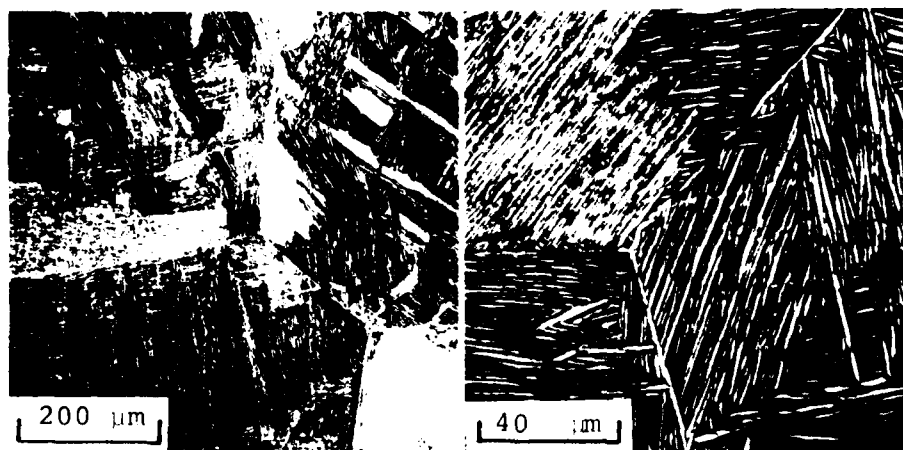


FIGURE 17b. MACRO- AND MICROSTRUCTURES OF THE B-PREFORMS USED FOR PRODUCING PANCAKE FORGINGS.

TABLE 6
 FORGING VARIABLES USED FOR THE 18 PANCAKES:
 TWO PANCAKES PER CONDITION WERE PRODUCED

Serial No.	Preform Micro- Structure	Stock Temp. C(F)	Die Temp. C(F)	Strain Rate 1/Min.
P1	$\alpha + \beta$	968 (1775)	968 (1775)	0.1
P2	$\alpha + \beta$	927 (1700)	927 (1700)	0.1
P3	$\alpha + \beta$	968 (1775)	371 (700)	3.0
P4	$\alpha + \beta$	1024 (1875)	1024 (1875)	0.1
P5	$\alpha + \beta$	1024 (1875)	371 (700)	3.0
P6	β	968 (1775)	968 (1775)	0.1
P7	β	927 (1700)	927 (1700)	0.1
P8	β	968 (1775)	371 (700)	3.0
P9	β	968 (1775)	649 (1200)	3.0

During forge processing, both forge load and displacement were recorded and the forgeability of the alloy were determined. The forge pressures as a function of percent reduction of pancake thickness were analyzed, and the influence of processing variables was examined. Figure 18 illustrates examples of the pancakes produced through nine different combinations of forging variables. Heavy surface wrinkles are observable for isothermal ($\alpha+\beta$) forgings using α -preforms (P6 and P7). Severity of surface cracking for conventional ($\alpha+\beta$) forgings using β -preforms depends strongly on the die temperatures used (P8 and P9).

Figure 19a presents the average forge-load versus displacement curves for isothermally forged pancakes, illustrating the effect of forge temperatures and preform microstructures on the yielding and load-displacement behavior. The true stress-strain curves at various forge temperatures for pancake forgings using $\alpha+\beta$ and β -preforms are calculated from the average load versus displacement curves and are further illustrated in Figure 19b.

It is seen from Figure 19b that the true stress-strain curves obtained for ($\alpha+\beta$) forgings were smooth and the deformation proceeded at relatively constant forge pressure for ($\alpha+\beta$) preforms and at a continuous softening for β -preforms. The deformation for β -forgings continued at only a slight increase in forge pressure up to about a true strain of 1.0.

Figure 19b also demonstrates that the values of yielding forge pressures for pancake forgings using β -preforms are higher than those of ($\alpha+\beta$) preforms. However, the stress-strain relationship showed that a more appreciable forge-pressure drop in the stress-strain curves for β -preform microstructures. The degree of softening during forging of ($\alpha+\beta$) and β -preforms increases as the forge temperature decreases. At the end of the forging, the forge pressure required for ($\alpha+\beta$) preforms is beyond that for β -preforms.

(b) Structural Characterization

Figure 20 illustrates the effects of forge temperature, die temperature, and preform microstructure on the macrostructures at the top surface of the pancakes. Approximately 3.18 mm (0.125 inch) of the top surface was removed by machining prior to etching to reveal the macrostructures.

It is seen from Figure 20 that microstructural uniformity of the forgings varies significantly with the forging variables, such as forge temperature, die temperature, and preform microstructure. In particular, the effects of lowering die temperature and/or using β -preforms are most obvious. As is

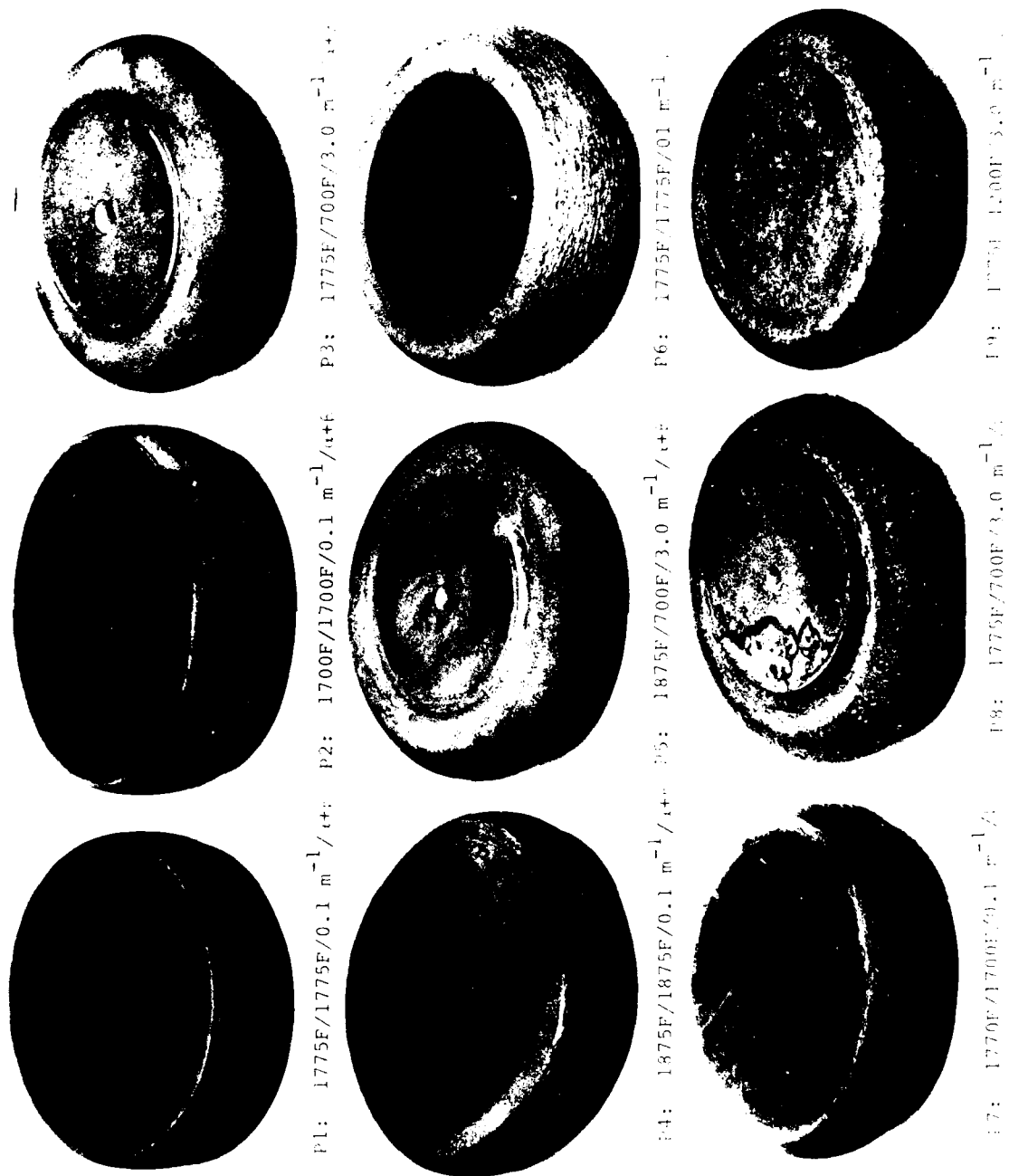


FIGURE 18. TOP VIEW OF PANGAKE FORGINGS PRODUCED FROM NINE DIFFERENT COMBINATIONS OF FORGING VARIABLES

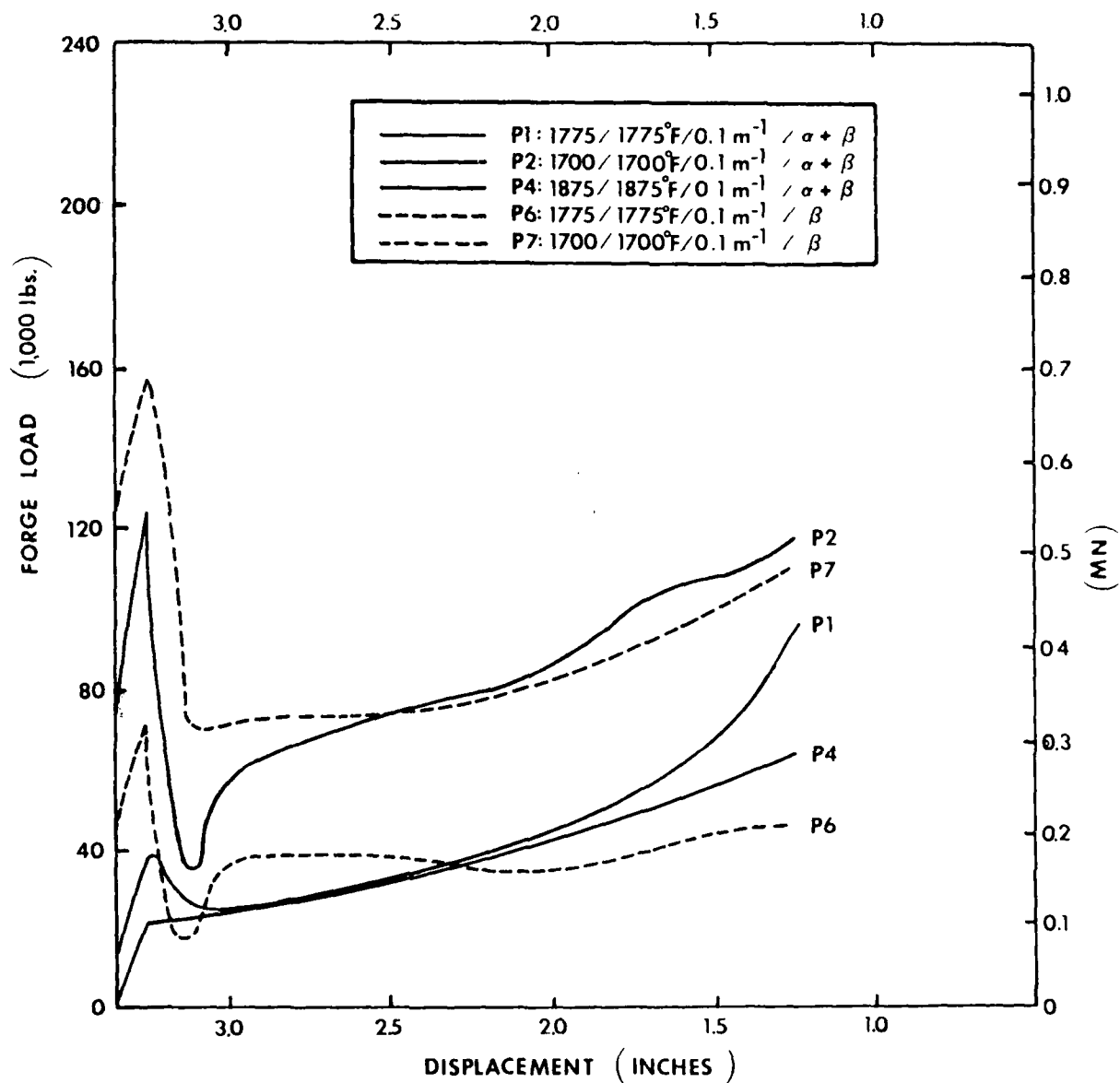


FIGURE 19a. INFLUENCE OF FORCE TEMPERATURES AND PREFORM MICROSTRUCTURES ON THE YIELDING AND STRESS-STRAIN BEHAVIOR OF ISOTHERMALLY FORGED PANCAKES.

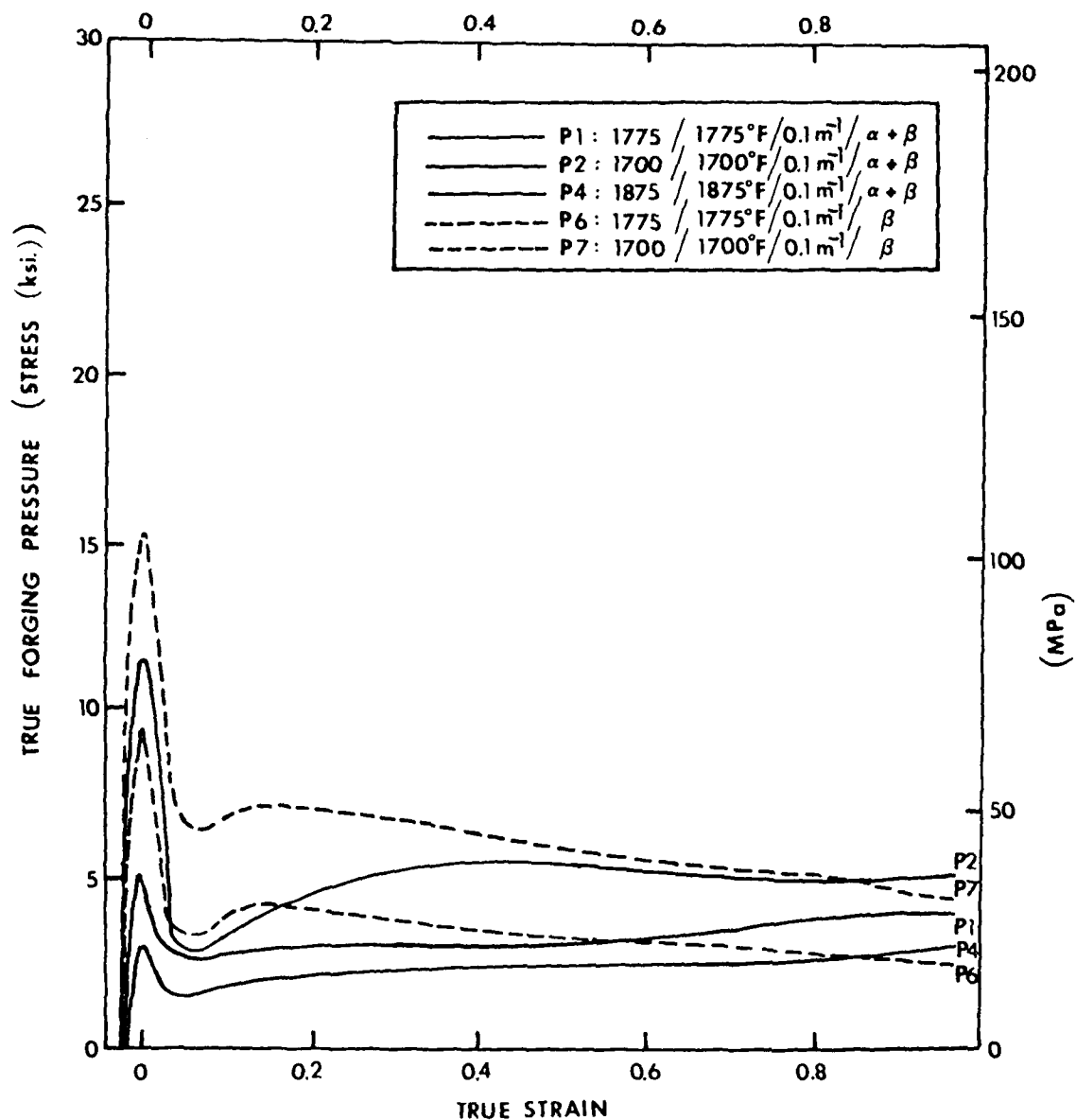
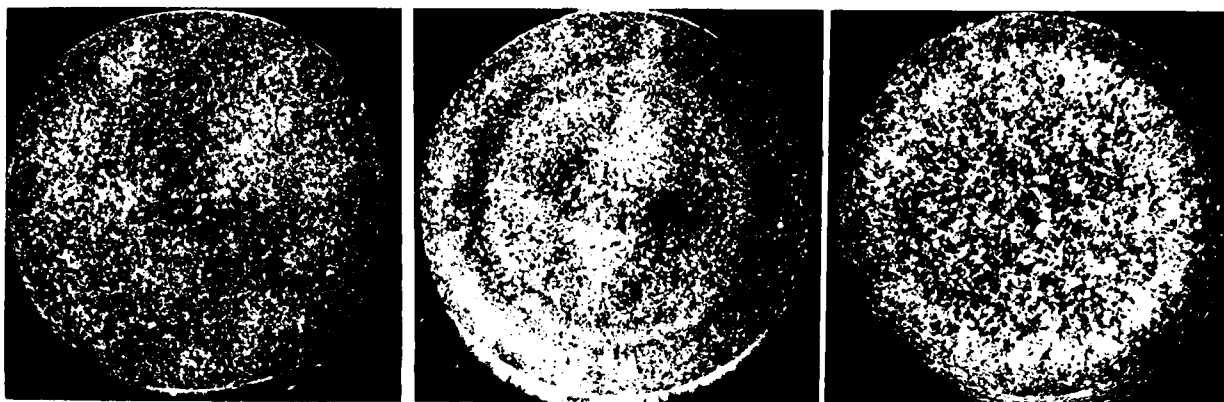


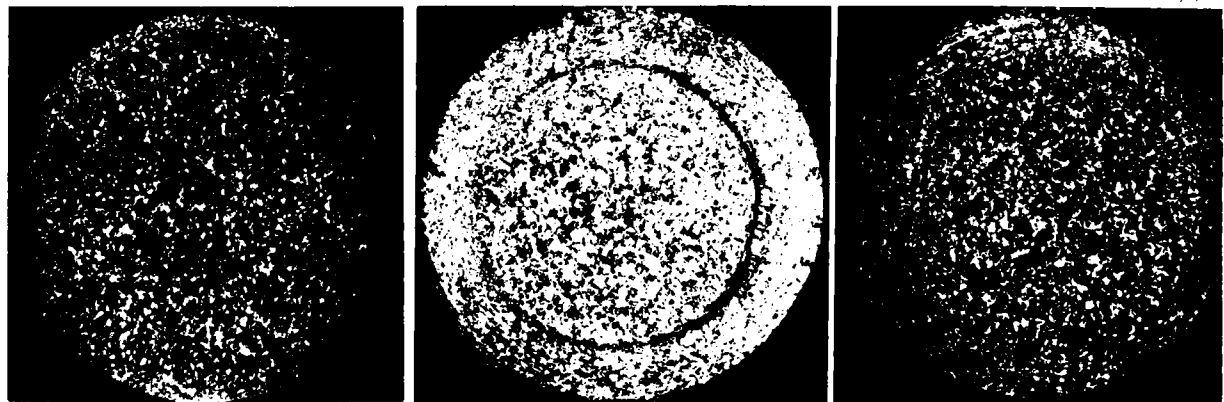
FIGURE 19b. EFFECT OF FORGE TEMPERATURES AND PREFORM MICROSTRUCTURES ON THE YIELDING FORCE PRESSURE AND STRESS-STRAIN BEHAVIOR OF ISOTHERMALLY FORGED PANCAKES.



P1: 1775F/1775F/0.1 m⁻¹/α+β P2: 1700F/1700F/0.1 m⁻¹/α+β P3: 1775F/700F/3.0 m⁻¹/α+β



P4: 1875F/1875F/0.1 m⁻¹/α+β P5: 1875F/700F/3.0 m⁻¹/α+β P6: 1775F/1775F/0.1 m⁻¹/β



P7: 1700F/1700F/0.1 m⁻¹/β P8: 1775F/700F/3.0 m⁻¹/β P9: 1775F/1200F/3.0 m⁻¹/β

2 inch
5.08 cm

FIGURE 20. MACROSTRUCTURES AT THE TOP SURFACE OF THE PANCAKE FORGINGS PRODUCED FROM NINE DIFFERENT COMBINATIONS OF FORGING VARIABLES.

expected, the fully recrystallized macrostructures of β -forgings are quite uniform throughout the forgings under isothermal forging conditions.

The variation of transverse macrostructures and microstructures with preform structure are given in Figures 21a and 21b for isothermal forging and conventional forging, respectively. It is seen that the preform structures have a significant influence on the flow characteristics and the microstructure of the $(\alpha+\beta)$ forgings. Good flow lines are observable for $(\alpha+\beta)$ preforms, and significant variations in microstructural features are seen for β -preforms from one location to another. Localized flow is clearly seen for conventional forgings.

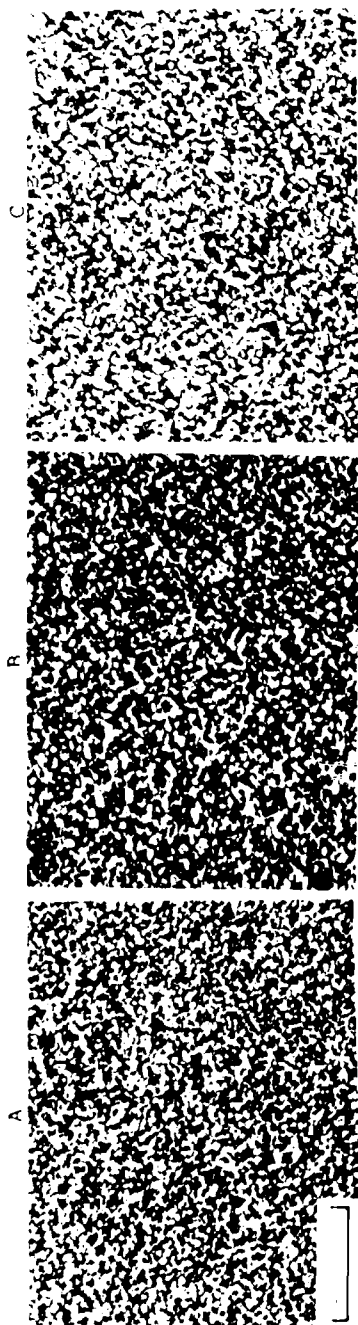
A direct comparison of the transverse macrostructures between isothermally forged and conventionally forged pancakes (Figures 21c and 21d) showed that excellent uniformity of macrostructure and microstructure for isothermal forgings. Very extended surface layers (characterized by large recrystallized grains) are observable for conventional forgings. The increased shear band and reduced metal flow due to die chill are very profound.

(c) Heat Treatments

Sixteen pancake forgings (P1, P2, P3, P4, P5, P6, P7, P9) were sectioned into half-pancakes and subjected to five heat treat cycles; this gives a total of 32 forge-heat treat combinations for the 32 half-pancakes. The four half-pancakes per forge condition were produced and identified as A, B, C, and D. The heat treatments included: (a) direct age; (b) $(\alpha+\beta)$ -ST/AC and Age; (c) $(\alpha+\beta)$ -ST/WQ + Age; (d) β -ST/AC + Age; (e) β -ST/WQ + Age. Note that the solution-treatment was made in both $(\alpha+\beta)$ and β -phase regions, and the aging was done at 593 C (1100 F)/8 hours/AC for all conditions. After heat treatment, they were blast-cleaned to remove the coating. Details of heat treat variables are given in Appendix E (Table E-6).

(d) Property and Structural Characterizations

A series of mechanical property evaluations and microstructural characterizations of the heat-treated pancakes are being conducted, and the results will be compiled in the next reporting period. These results will include: (1) macro- and microstructural characterizations for the 32 half-pancakes (52 macros and 126 micros), (2) Room temperature tensiles (one each for 32 conditions), (3) 510 C (950 F) tensiles (one each for six conditions), (4) 566 C (1050 F) tensiles (one each for six conditions),



P2: 1700F/1700F
0.1 min. -1 1/2

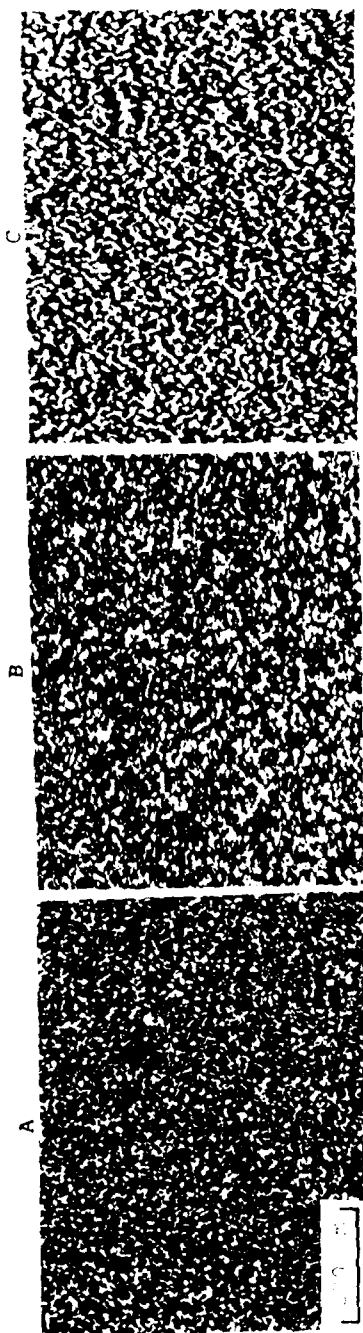


2.54 cm
1 inch

P7: 1700F/1700F
0.1 min. -1 1/2



FIGURE 21a. EFFECT OF PREFORM STRUCTURE ON THE MACROSTRUCTURES AND MICROSTRUCTURES OF ISOTHERMALLY (α+β) FORCED PANGARES



F3: 1775F/700F

2.0 mm



2.54 cm
1 inch

F4: 1775F/700F

2.0 mm



FIGURE 216. LEFT: OF PORE STRUCTURE IN THE MACRO-POROUS AND MICRO-POROUS OF CONVENTIONALLY CURED EPOXY RESIN



P4: 1875F/1875F
0.1 min. $-1/1+$



2.54 cm
1 inch

P5: 1875F/700F
3.0 min. $-1/1+$



FIGURE 21c. COMPARISON OF MACROSTRUCTURES AND MICROSTRUCTURES BETWEEN ISOTHERMALLY AND CONVENTIONALLY 8-FORGED PANCAKES

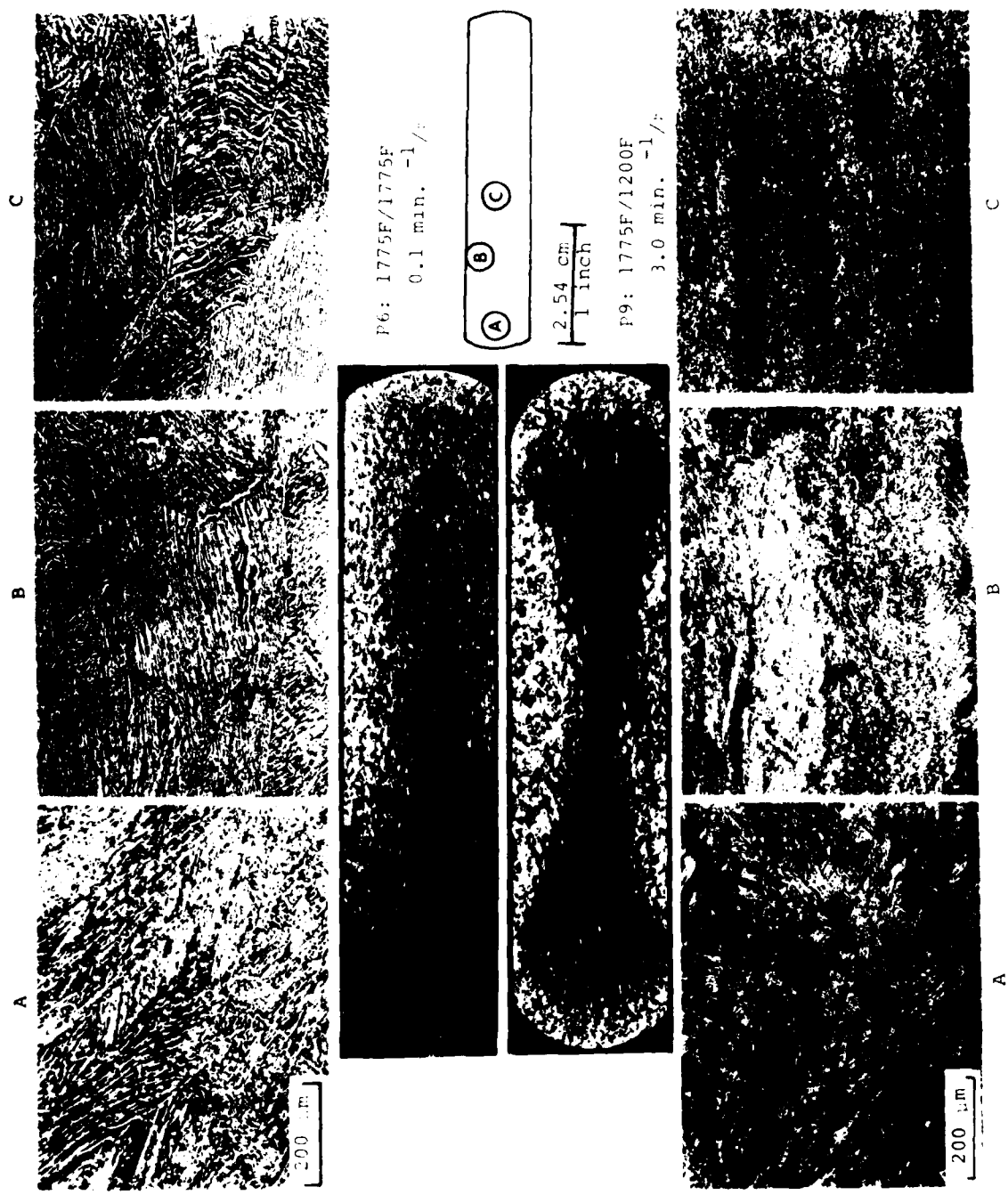


FIGURE 21d. COMPARISON OF MACROSTRUCTURES AND MICROSTRUCTURES BETWEEN ISOTHERMALLY AND NEAR-CONVENTIONALLY ($\alpha + \beta$)-FORGED PANCAKES

(b) creep at 510 C/241 MPa/0.2% (950 F/35 ksi/0.2%), one each for six conditions, (c) creep at 566 C/172 MPa/0.2% (1050 F/24 ksi/0.2%), one per each for 32 conditions, (7) stress rupture at 510 C/448 MPa (950 F/65 ksi), one per each for six conditions, and (8) post creep tensiles (a total of 38 tests).

based on the results of property testings, the six best forge-heat treat cycles will be selected. Wyman-Gordon then will produce six more pancakes using the selected cycles. These pancakes will be delivered to BCL for da/dn and LCF testings.

(c) Further Examination of Heat-Treatment for Selected Forge Practice

In order to develop a successful processing model for manufacturing disk forgings with dual properties, an additional effort is necessary during Phase I effort to refine heat treat practice for the optimized forge cycles. A total of 12 pancake forgings will be produced to examine the two best forge-heat treat cycles. Both structural characterizations (macros and micros), and mechanical property testings (tensile, creep, stress rupture, post-creep tensile at Wyman-Gordon, and da/dn, LCF at BCL) will be subsequently carried out to determine optimum cycles for the best properties.

Theoretical and Experimental Forming Limit Representation (Task 1.3)

Theoretical development of a forming limit curve (FLC) requires three distinct steps: (1) Failure criteria must be identified, (2) FLC's must be computed in terms of relevant material properties for each failure criterion, (3) the lowest FLC appropriate for a particular material must be applied. In sheet metal forming, plastic instability and ductile fracture are the two primary modes of failure. Constitutive relationships, (including strain-rate sensitivity), the yield function, and the strain path are the material and process variable that must be included in the formability analysis for a given failure criterion.

In massive forming, workability indices are required for two separate types of material failure criteria, plastic instability and ductile fracture. In forging processes, plastic instability can result in defects such as shear bands and internal folds. Ductile fracture would most likely occur as surface cracks which open up under large tensile hoop stresses.

Although ductile fracture may be the most critical failure mode for forgings, fracture and instability considerations usually cannot be separated, since the voids which initiate ductile fracture can affect the plastic flow behavior of the material. In high temperature deformation, in addition to plastic instability and ductile fracture, the flow softening effect must also be considered.

Theoretical Formability for Sheet Metal

Under Air Force sponsorship, Dr. L. J. Teutonico developed a theoretical analysis for FLC's based on the failure criterion of localized necking. This analysis is limited in application to negative minor strains and also the effects of strain rate and strain path were not included. The work under the present program is aimed at developing a generalized formability analysis which includes (a) a failure criterion applicable to tension-tension quadrant of the limiting strain diagram and (b) the effects of strain rate, strain path, and anisotropy on FLC.

A critical review of studies on localized necking was conducted to establish the approach for developing the generalized FLC analysis. Here a summary of this review is presented. To account for localization of deformation in those states for which both principal strains are positive, two approaches have been taken. The first, due to Marciniak and Kuczynski⁽²⁾ and extended by Hutchinson and Neale⁽³⁾, postulates the existence of an initial non-homogeneity in the form of a narrow band across the sheet. The second approach, first proposed by Storen and Rice and later modified by Hutchinson and Neale, incorporates a deformation theory of plasticity into a classical bifurcation analysis; the bifurcation mode corresponding to localized deformation in a narrow band, similar to Hill's analysis.

(2) Marciniak, Z., Kuczynski, K., and Pokora, T., Int. J. Mech. Sci., 15, 789 (1973)

(3) Hutchinson, J. W., and Neale, K. W., Reports DAS M-4, M-5, Division of Applied Sciences, Harvard University, Aug 1977.

The Marciniak-Kuczynski (M-K) model has been applied to both the left hand side and the right hand side of forming limit diagrams by Hutchinson and Neale. Also the strain rate effects can be included. The main drawback of the M-K model is that the limit strains are sensitive to the choice of the inhomogeneity parameter which cannot be established without some tests. In spite of this drawback, the M-K approach appears to be the most promising for developing a generalized formability analysis for sheet metal. The following improvements/refinements have to be made to the existing M-K model.

1. The present analysis applies only for power-law dependence of stress on strain and strain rate. The analyses need to be generalized to allow for an arbitrary flow law, $\sigma = \sigma(\epsilon, \dot{\epsilon})$. Ultimately, in line with the goal of this program, one must introduce a constitutive relation (Hart-type) which allows for evolutionary material parameters.
2. Both planar and normal anisotropy should be introduced in the present analysis, which applies only to isotropic materials.
3. The present analysis considers only proportional (linear) strain paths. Non-linear paths approximating paths encountered in actual forming processes should be considered.
4. If possible, a rationale for choosing the value of the inhomogeneity parameter should be established.

Experimental and Theoretical Investigation of Forming Limit Criteria in Disk Forging

This part of the program will be conducted at the University of Pittsburgh, and it involves application of workability analysis to forging of compressor disks from Ti-6242 alloy, with the objective of specifying the process conditions for accomplishing the desired structure without failure. Results from this part of the program will also interface with other parts of the program.

During this reporting period, no work was scheduled under this task and consequently no work has been conducted yet.

SECTION VI

PROCESS MODELING FOR DISK TYPE FORGING

Under this phase of the program, mathematical and computer models of axisymmetric compression are being developed to simulate metal flow that occurs during forging of axisymmetric components, such as a compressor or a turbine disk, while taking into consideration the problem of non-steady-state heat transfer in a moving incompressible medium with heat sources. These models also take into consideration the dependence of material behavior on strain, strain rate, and temperature, and it is expected that analyses provide information on these parameters so that the properties of the deformed materials may be predicted. This effort is being carried out by using an "exact" method (finite-element method) and an "approximate" method (upper-bound method) in parallel. Further, these developments are being implemented in an interactive system of computer programs for design and optimization of the forging process.

Process Modeling With Finite-Element Method (Task 2.1)

Work under this part of the program is being conducted at the University of California, Berkeley. The details are given in Appendix F.

The present research is aimed at establishing the finite-element formulation for the analysis of axisymmetric forging of rate-sensitive materials. Although the residual stress calculation is an important aspect in metal working, equally important is the flow analysis during deformation. An accurate determination of flow characteristics under various processing conditions is a prime requirement for proper design and design of any metal-working process. Therefore, with this view, the behavior of materials under the present investigation is characterized as rigid-viscoplastic.

Under this task, first an approach for construction of a constitutive equation for rigid-viscoplastic materials was developed. Then, the extremum principle, as a basis for the finite-element formulation of the flow behavior problem was developed. Finally a finite-element method code was written and applied to the analysis of simple axisymmetric compression.

The calculated overall quantities are compared with experimental data and with the numerical dynamic analysis of Klemz and Hashmi⁽⁴⁾ in Figures 22 and 23. Some observations can be made from the figures. The results for non-strain-rate-sensitive analysis (Figure 22) tends to follow those by the analysis of Klemz and Hashmi, which did not take into account strain-rate effects, but was based on a dynamic analysis. The agreement of the two indicates that the dynamic effect is negligible. However, both solutions show poor agreement with experiments. The analysis which includes strain-rate sensitivity shows good agreement with experiments (Figure 23). No "rigid" zones were formed at such a low value of friction in either rate-sensitive or rate-insensitive cases.

Process Modeling With Upper-Bound and Finite-Difference Method
(Task 2.2)

The work under this part of the program is being conducted at Battelle. The objectives of this task are to develop an upper-bound analysis to simulate metal flow in disk-type forgings, and to incorporate a finite-difference temperature analysis so that the material behavior can be considered as a function of strain, strain rate and temperature.

A numerical upper-bound technique, coupled with a finite-difference temperature algorithm, was developed at Battelle for a detailed investigation of metal flow and temperatures in simple compression.⁽⁵⁾ This upper-bound analysis for predicting metal flow considers the material flow stress as a function of strain, strain rate and temperature. The temperatures are calculated by taking into account simultaneously the heat generation due to deformation and friction, and the heat transfer. The process of heat generation, transportation, and conduction is approximated as taking place in two consecutive steps. During a time interval, Δt , the heat generation and transportation are regarded as occurring instantaneously, followed by a time interval, Δt , in which conduction takes place as for a stationary medium.

(4) Klemz, F. B., and Hashmi, S. J., "Simple Upsetting of Cylindrical Billets: Experimental Investigation and Theoretical Prediction," Proc. 18th MTDR Conference, London, 1977.

(5) Lahoti, G. D., and Altan, T., "Prediction of Temperature Distributions in Axisymmetric Compression and Torsion", Trans. ASME, J. Eng. Industry, 1979 p. 113.

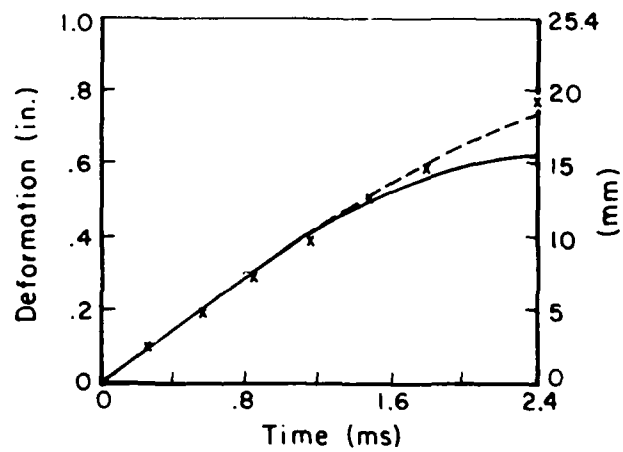
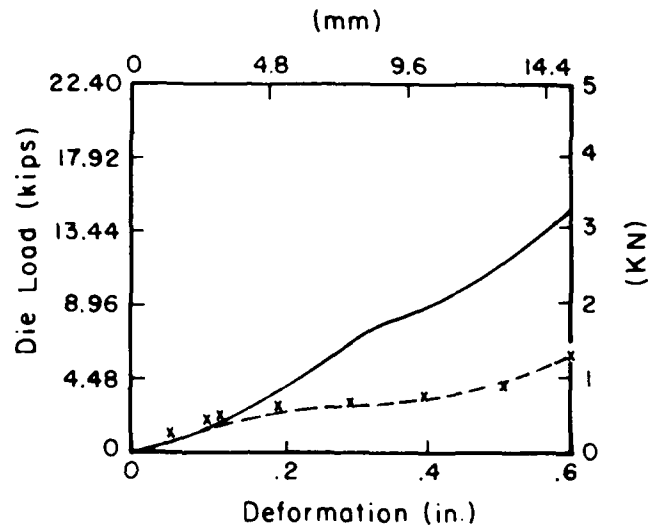


FIGURE 22. COMPARISON OF THE FINITE-ELEMENT RIGID-PLASTIC ANALYSIS (xxxx) WITH THE DYNAMIC ANALYSIS (-----) AND EXPERIMENT (——).

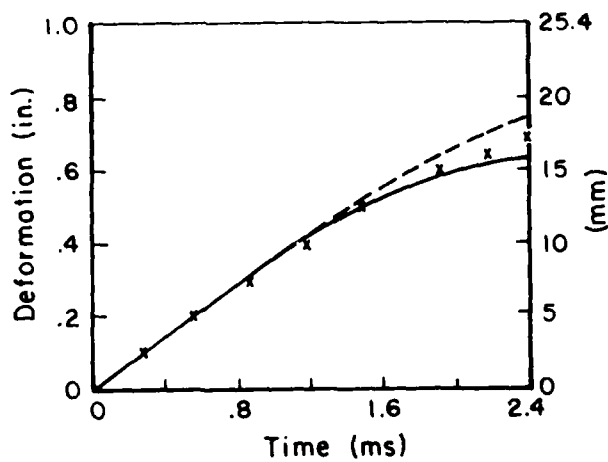
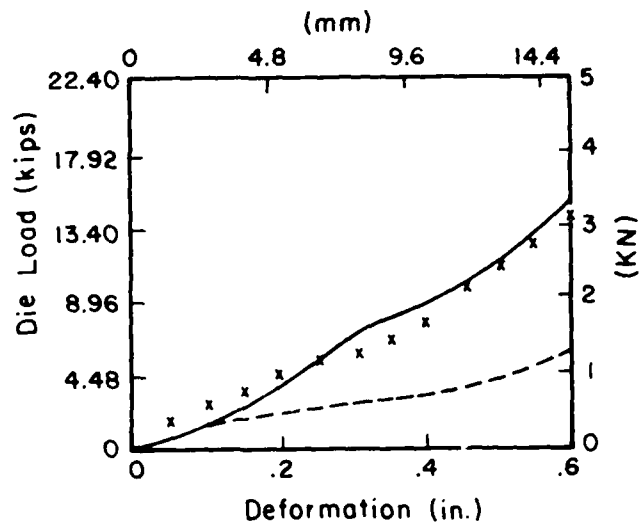


FIGURE 23. COMPARISON OF THE FINITE-ELEMENT RIGID-VISCOPLASTIC ANALYSIS (xxxx) WITH THE DYNAMIC ANALYSIS (----) AND EXPERIMENT (—).

During this reporting period, the computer programs, FORGTM, based on the above mentioned analysis of simple compression, were used to evaluate viscoplasticity studies conducted at the Air Force Materials Laboratory (AFML). A Ti-6242 cylindrical specimen of 25.4 mm (1.00) diameter x 46.7 mm (1.84 inch) height was split in two halves along a diametral plane, and square grid lines were etched on the flat surface as shown in Figure 24(a). The two halves were assembled and were kept together by a hollow cylinder of 2.54 mm (0.100 inch) wall thickness. The ends of this composite cylinder were lubricated with Delta Glaze 69, and it was compressed isothermally at 871 C (1600 F) to a height of 30.48 mm (1.200 in.). The two halves of the deformed specimens were opened after cooling the specimen. The deformed grid lines are shown in Figure 24(b).

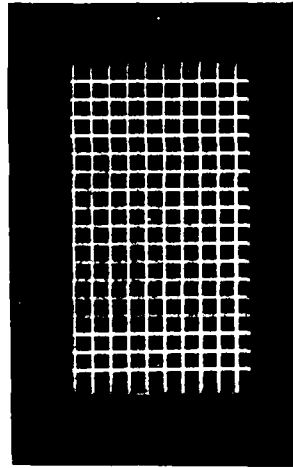
This deformation in simple compression was simulated by using the computer program FORGTM. The deformed grid lines at the end of deformation, as predicted by FORGTM, are shown in Figure 25. For this purpose, an average value of friction factor, $m = 0.1$, was taken from a previous study⁽⁶⁾. The value of strain, strain rate and temperatures at the grid points are also given in Figure 25.

Although the model does not predict bowing of horizontal grid lines, especially near the die surface, the overall agreement seems to be good except near the corners. This later discrepancy is believed to be mostly due to a separation between the cylinder halves and the retainer tube. It is believed that if the retainer tube is bonded to the cylinder halves, the agreement between theory and experiment will improve considerably.

Currently, under this task, a concept of a general approximate method, which combines the features of both the upper-bound method and the finite-element method, for analyzing axisymmetric deformation processes is being developed.

Since the two methods of analysis are based on the same mathematical principles, it is possible to combine the two methods. The combined method should provide a systematic way of solution of a wide class of problems with little or no modification. It should also improve the calculation efficiency by relaxing the strictness of the finite-element method.

⁽⁶⁾Chen, C. C., "Evaluation of Lubrication System for Isothermal Forging of Alpha-Beta and Beta Titanium Alloys", Technical Report AFML-TR-77-8, 1977.



(a)



(b)

FIGURE 24. VISOPLASTICITY SPECIMEN (a) BEFORE AND (b) AFTER ISOTHERMAL COMPRESSION (1x)

Die Speed = 0.762 mm/s
Friction Factor m = 0.10

Die: 731 C.
Specimen: 871 C.

Scale: 10X

899	899	899	898	891 °C	Temperature Strain Strain Rate
.341	.341	.342	.344	.346 mm/mm-1	
.02597	.02597	.02597	.02597	.02597 sec-1	
912	912	911	911	907	
.369	.369	.370	.371	.372	
.02588	.02588	.02588	.02588	.02588	
916	916	916	915	913	
.392	.393	.393	.394	.395	
.02560	.02559	.02559	.02558	.02558	
920	920	919	919	917	
.413	.413	.413	.414	.414	
.02514	.02512	.02510	.02509	.02509	
923	923	922	922	921	
.429	.429	.429	.429	.430	
.02448	.02444	.02441	.02438	.02438	
925	925	925	924	924	
.441	.441	.441	.442	.442	
.02361	.02355	.02350	.02347	.02346	
926	926	926	926	925	
.450	.450	.450	.450	.450	
.02255	.02244	.02237	.02233	.02231	
927	927	927	927	926	
.455	.455	.455	.455	.456	
.02125	.02111	.02100	.02094	.02092	
928	928	928	927	927	
.457	.457	.457	.457	.457	
.01973	.01952	.01938	.01920	.01926	

FIGURE 25. DISTORTED GRIDLINES, STRAINS, STRAIN RATES, AND TEMPERATURES AS PREDICTED BY FORGTM

Development of an Interactive System to Predict Metal
Flow and Temperatures (Task 2.3)

This part of the program is being conducted at Battelle. The objective of this task is to develop a versatile computerized system for the design and analysis of axisymmetrical forging components. The interactive computer program will utilize both the finite-element method and the upper-bound method for analyzing the mechanics of deformation.

An interactive computer program, named MATRIX, was developed for analyzing mechanics of deformation in simple compression. This program utilized analysis by the finite-element method developed at the University of California, and has graphical display capabilities. As shown in Figure 26, various plots can be obtained at the user's command. Any of the four types of plots shown in Figure 26 can also be enlarged on a single page for more detailed information. The details of computer program MATRIX are given in Appendix G.

In the future, it is planned to expand this graphical display capability to obtain contour plots of strain, strain rate and temperature distribution at any instant of deformation, and to incorporate such capabilities for analysis of disk-type forgings.

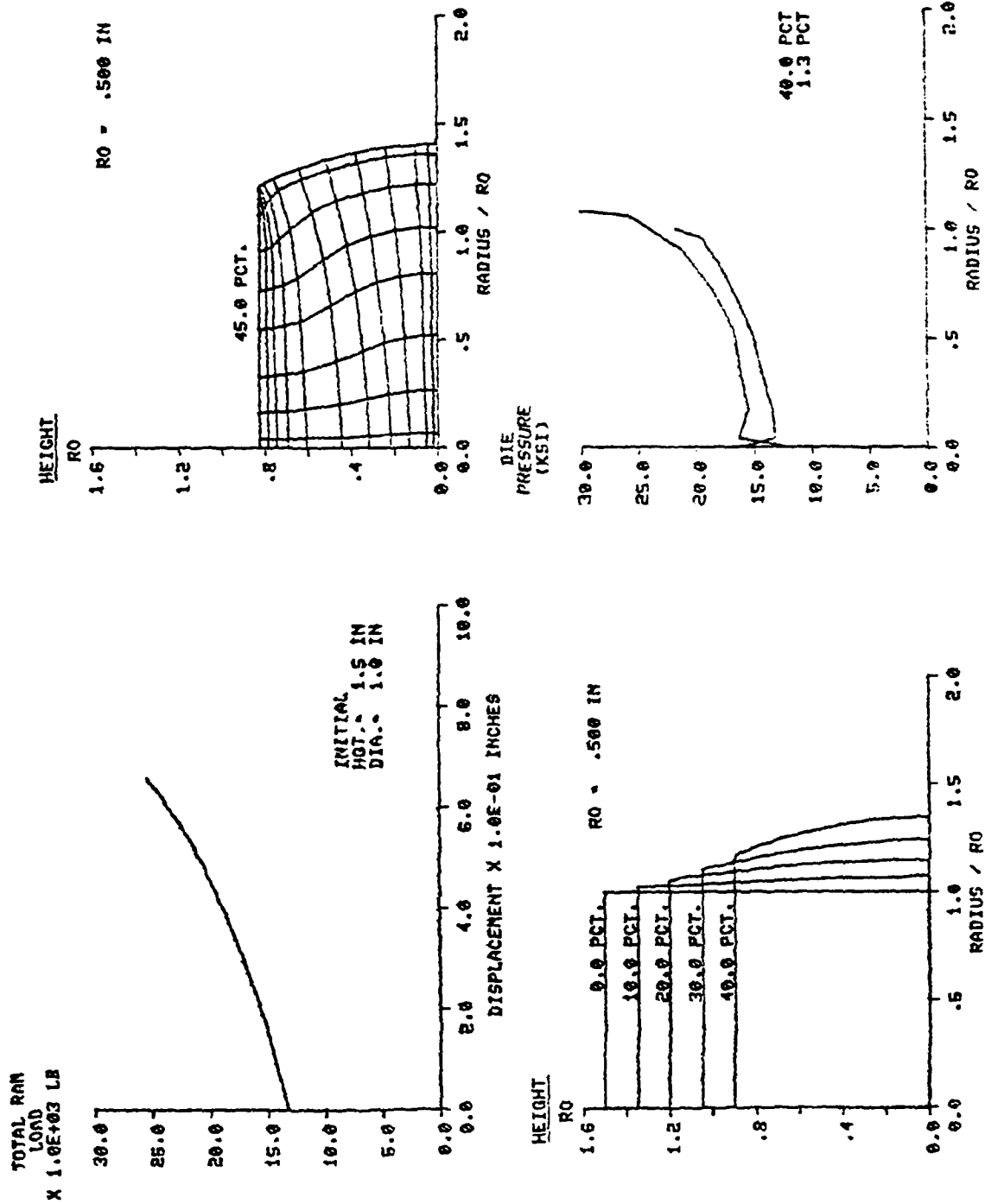


FIGURE 26. VARIOUS TYPES OF PLOTS GENERATED BY THE GRAPHICAL DISPLAY ROUTINE FOR COMPRESSION OF T1-6242 CYLINDRICAL SPECIMEN AT 1750°F

SECTION VII

INTERFACE EFFECTS

In metal-deformation processing, and in particular in forging, the lubricant at the material-die interface plays several important roles: (a) it controls the heat transfer from the workpiece into the dies and the temperature gradients within the deforming metal, and (b) it influences the friction conditions at the interface. The net effect is to change the velocity fields, or metal flow, within the deformation zone and to strongly influence the limiting strain to failure. In addition, lubricants directly influence such factors as part surface quality, metal flow, grain structure, mechanical properties, dimensional consistency, and load and energy requirements. Further, lubricants which provide effective separation and thermal insulation between the sliding metal and the die promote long die life.

During forging, heat is lost from the billet by conduction and radiation through the lubricant. Laboratory insulation tests can be performed to measure the thermal conductivity of lubricant/interface layer. In these tests, a lubricant film is squeezed between two flat punches, simulating the forging dies (same material, surface finish and temperature as the forging die). The pressure and temperature conditions created at the interface layer are similar to those present in the actual forging. During the test, the surface temperature and temperatures at various depths from the interface are measured. These data, analyzed together with pressure, interface layer temperature, and lubricant thickness give quantitative information on thermal conductivity of the lubricant under various conditions.

The objective of this phase of program is to characterize the interface effects in axisymmetric compression of disk-type forgings. This includes characterization of heat transfer coefficients and the friction conditions at the tool-workpiece interface.

Selection of Lubricants for Disk Forging (Task 3.1)

This task is being conducted jointly by Wyman-Gordon Company and Battelle. Several excellent lubricants have been recently evaluated by Wyman-Gordon for isothermal forging of alpha-beta titanium alloys.⁽⁶⁾ Based on this study and the forging conditions for dual-property disk from Ti-6242, several lubricants will be selected. These lubricants will be further evaluated by conducting the ring tests.

Determination of Heat Transfer Coefficients and Interface Effects (Task 3.2)

This part of the program is being conducted at Battelle. The details are given in Appendix H. The objective of this task is to develop a procedure for calculation of an effective heat transfer coefficient for the lubricated tool/material interface, and to determine the values of these coefficients for the particular combinations of lubricant and die materials to be used under this program.

In order to measure the interface heat transfer coefficient, a test fixture as shown in Figure 27 was designed. It consists of a pair of IN100 dies, screwed to a pair of superalloy supports. The supports rest on alumina blocks which act as insulators. The lower and upper end of the fixture are water-cooled. The thermocouples will be imbedded in the dies in such a way that they will lie underneath the alloy sample which is being deformed. The dimensions of the dies are so selected that a standard ring specimen can be used. The entire length of the fixture between the lower and upper supports will be enclosed in a clam-shell furnace to heat the dies and the specimen to desired temperatures.

The duration of the forging experiments lies between 10ms and 0.25 sec. Therefore, the depth-locations of the thermocouples in the dies are important. For this purpose, one dimensional dynamic temperature analysis was carried out. A typical response at any time t is shown in Figure 28. For a given tool (371 C [700 F]) and workpiece temperature (927 C [1700 F]), the times required to observe 38, 149, and 427 C (100, 300 and 800 F) at various depths in the die block are given in Table 7. The details of the analysis are given in Appendix H.

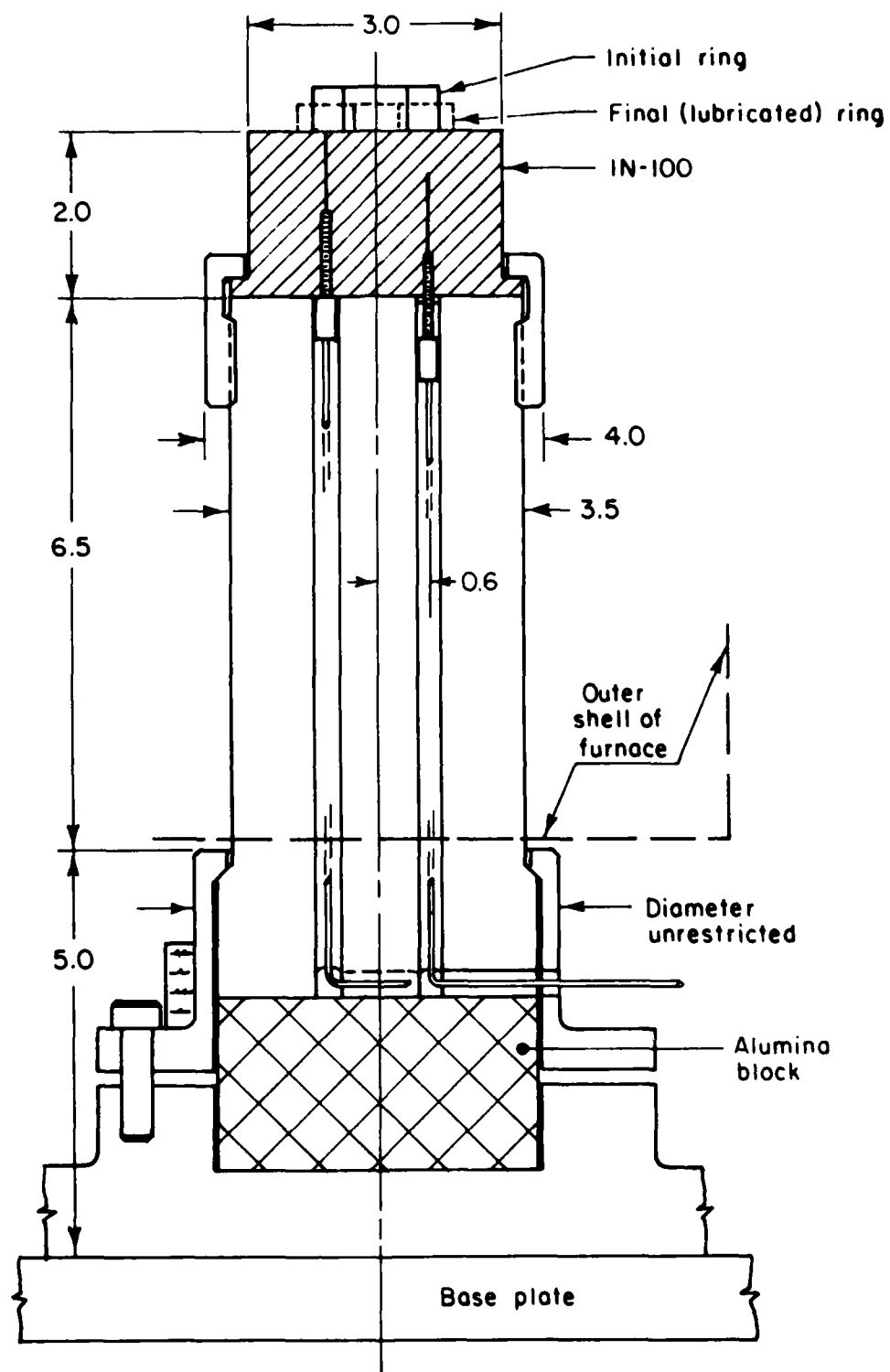


FIGURE 27. DESIGN OF THE EXPERIMENTAL FIXTURE FOR DETERMINING INTERFACE HEAT TRANSFER COEFFICIENT

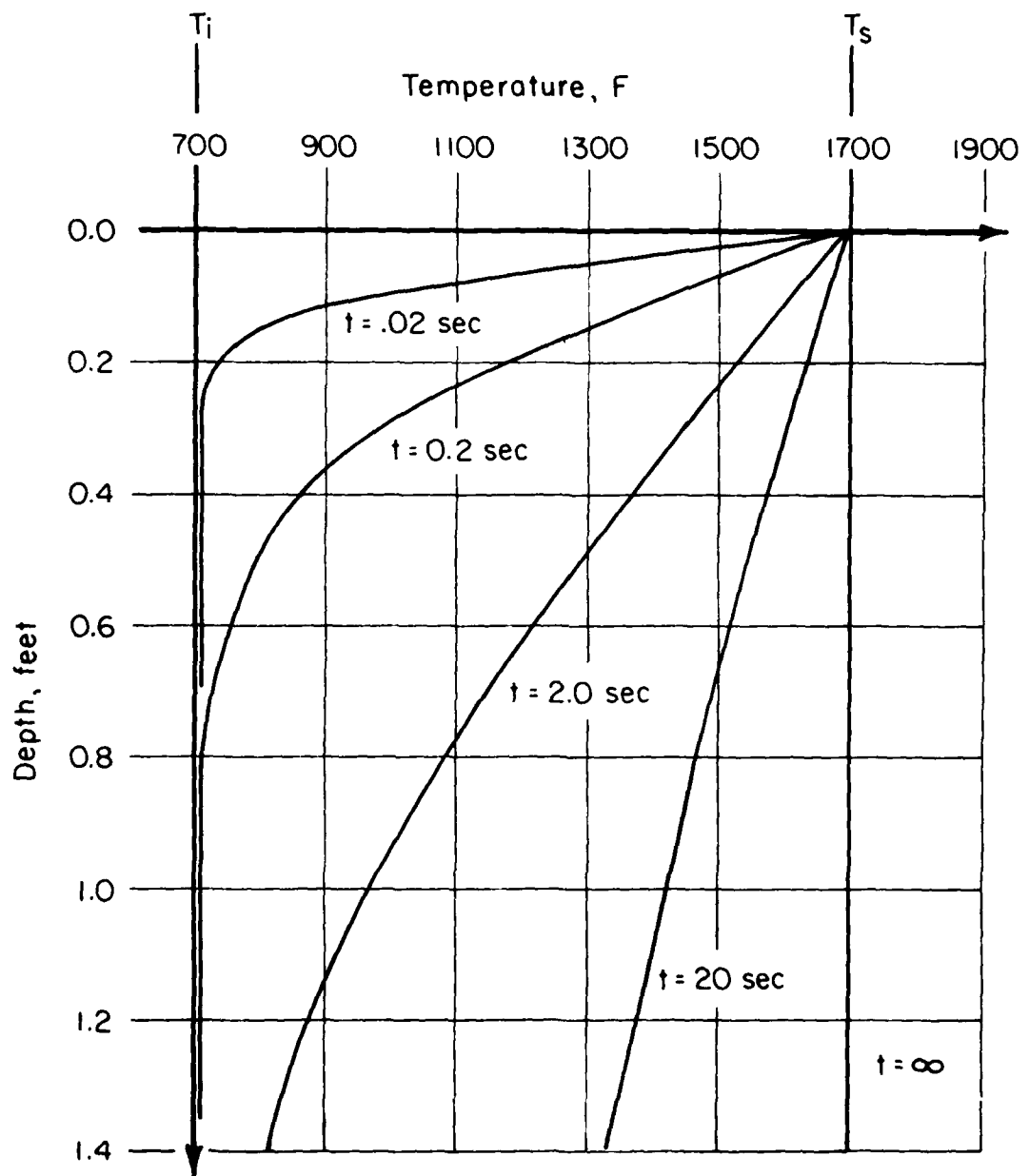


FIGURE 28. ONE DIMENSIONAL DYNAMIC TEMPERATURE DISTRIBUTION IN RESPONSE TO THE APPLICATION OF HEAT SOURCE AT TEMPERATURE T_s TO A LONG BAR AT INITIAL TEMPERATURE T_i

TABLE 7
TIMES REQUIRED TO ATTAIN VARIOUS
TEMPERATURES AT VARIOUS DEPTHS

Depth, mm (in)	Times to attain the following temperature increments			Time Units
	38C (100°F)	149C (300°F)	427C (800°F)	
0.76 (0.03)	21	50	860	ms
1.27 (0.05)	58	139	2.4	
2.54 (0.10)	233	556	9.6	
5.08 (0.20)	933	2.2	38.2	s
10.16 (0.40)	3.7	8.9	152.9	

Currently, the materials for various components of the fixture have been ordered. The fixture will be fabricated and the experiments will be conducted during the next reporting period.

Analysis of Metal Flow and Temperatures in Ring
and Flange Type Configurations (Task 3.3)

This part of the program is being conducted at Battelle. Forging of a ring geometry and a flange type configuration have been used for characterizing friction conditions in metal processing and for evaluating lubricants. The variation in internal diameter of a ring during compression or the height of spike in compression of flange type configuration is a good indication of the frictional conditions at the tool/material interface. These tests are very easy to conduct since the technique requires either measuring the internal diameter of a ring or the height of the spike after forging.

A numerical method for simultaneous prediction of metal flow and temperatures in upset forging of rings was developed at Battelle.⁽⁷⁾ For this purpose, an improved upper-bound analysis was developed to predict metal flow, and it was combined with a finite-difference algorithm to predict temperature distributions. Currently, a finite-element analysis to predict metal flow and temperatures in ring compression is being developed at the University of California. These analyses will be used (a) in evaluating the lubricants under Task 3.1, and (b) to determine heat transfer coefficients under Task 3.2.

A numerical upper-bound method to predict metal flow in spike forging was also developed at Battelle.⁽⁸⁾ A set of interactive computer programs was developed for dividing the cross section of a forging systematically into modular elements. Analytical expressions for velocity fields in each elements were developed. By properly assembling the various elements, the lowest upper-bound on the energy rate is determined through numerical minimization techniques, and thereby determining the best velocity field from the selected class.

(7) Nagpal, V., Lahoti, G. D., and Altan, T., "A Numerical Method for Simultaneous Prediction of Metal Flow and Temperatures in Upset Forging of Rings", Trans. ASME, J. Engrg. Industry, 100, 1978, p 413.

(8) Altan, T., Clauer, A. H., Lahoti, G. D., Rosenfield, A. R., and Subramanian, T. L., "Effect of Hot Forging Variables Upon Microstructure and Properties of Metals and Alloys", Final Report to AFOSR, Grant No. AFOSR-76-2971, 1979.

Once the velocity field is developed, strain rates within the modular elements are estimated. Strains within the elements are determined by integrating the continuous strain rate functions with respect to time over the elapsed time interval. The temperature analysis in this case is very involved and will be conducted in the next reporting period.

SECTION VIII

INTEGRATION OF MATERIAL AND PROCESS MODELS

The objective of this phase of the program is to develop an interactive computer program which will integrate the material behavior models with the process model to investigate the interaction of the basic components of this analytical processing system. This system will be used to design forging preform, dies, calculate loads, temperature distributions, metal flow patterns and to predict microstructural changes.

During this reporting period, no work was scheduled under this phase of the program, and thus, no work has yet been conducted under this phase of the program.

SECTION IX

PROPERTY/MICROSTRUCTURE RELATIONSHIPS IN THE FORGED DISK

The objective of this phase of the program is to investigate metallurgically the forgings designed and produced under this program to determine whether the microstructure and the mechanical properties pertinent to design requirements for the dual property disk correspond to the predictions. This will involve detailed metallographic examination of the forged disk, and determination of mechanical properties (tensile, creep, LCF, fracture toughness) of the forged material. During this reporting period, no work was scheduled under this phase of the program. Consequently, no work was conducted under this phase of the program.

SECTION X

FUTURE WORK

During the next twelve months, the following work is planned to be conducted under this program:

Material Behavior Under Processing Conditions

- (a) The low strain rate tests at Wright State University will be completed.
- (b) The high strain rate plastometer tests at Los Alamos Scientific Laboratory will be completed and the results will be summarized.
- (c) The MTS machine tests at University of Pittsburgh will be completed and the results will be summarized.
- (d) The work on development of material constitutive equations will be completed.
- (e) The work on structural and microstructural evaluation of uniformly compressed specimens will be started.
- (f) The second series of pancake forging tests will be conducted, and actual forging process variables will be defined.
- (g) The work on sheet metal formability study (computerization of Marciniak's approach) will be completed.
- (h) The workability study of Ti-6242 will continue at the University of Pittsburgh.

Process Modeling For Disk Type Forging

- (a) The work on process modeling with the finite-element method will continue at the University of California. Capabilities to predict temperature distribution in cylinder and ring compression will be included.
- (b) The work on process modeling with the upper-bound and the finite-difference method will continue at Battelle. A procedure for preform design will be developed.

- (c) An interactive system of computer programs will be developed using the process models developed in (a) and (b) above. This system will have graphical display capability, and will be used in design of forging processes for dual property disks.

Interface Effects

- (a) Several isothermal forging lubricants will be selected and evaluated by conducting the ring test.
- (b) The fixture for the heat transfer study will be fabricated and tests will be conducted to measure the heat transfer coefficient at the interface.
- (c) Analysis of temperatures in spike forging will be included.

Integration of Material and Process Models

- (a) Based on the pancake tests, process modeling studies, and interface effects studies, conditions for forging of a subscale disk will be defined.
- (b) The disk forging tests will be planned and scheduled.

Property/Microstructure Relationships in the Forged Disk

No activity is planned under this phase of the program.

APPENDIX A

LOW STRAIN RATE TESTS AND
DEVELOPMENT OF CONSTITUTIVE EQUATIONS

J.F. Thomas, Jr., and P. Dadras

Wright State University
Dayton, Ohio 45435

APPENDIX A

LOW STRAIN RATE TESTS AND DEVELOPMENT OF CONSTITUTIVE EQUATIONS

Application of a Material Model in the Process Model of a Disk Forging

Introduction. A fundamental assumption behind the U.S. Air Force Processing Science Program is that the technology of massive forming of metals and alloys is at a point where significant advances can be accomplished through computer-aided design and manufacturing (CAD/CAM) methods. However, in order to implement the CAD/CAM approach, detailed mathematical models of the workpiece material, the forming process, and the workpiece-tool interface conditions are required, and these models do not now exist in a sufficiently complete form. Hence, a primary objective of this Program is to develop and verify the required models and to integrate them to form an interactive computer program for process design. The process models are to be developed to a level of sophistication sufficient to allow the control of microstructure and properties in addition to the shape of the finished part. Although the methodology to be developed will be generally applicable to a range of deformation processes, the validation and application will be restricted to the forging process for a Ti-6242 turbine compressor disk. Since the optimal properties of a compressor disk vary from the bore to the rim, a gradient in microstructure and properties ("dual property") is desired for the final disk.

Process Model for a Disk Forging. In order to provide a basis for further discussion, an abbreviated outline of a process model of a disk forging is presented below in terms of the necessary inputs and expected output information:

Input

- Material Model

Constitutive relations for non-elastic flow, characterization of the initial structure, workability criteria and limits

- Interface Conditions
 - Friction factors, heat transfer coefficients
- Geometries
 - Preform shape, grid system, velocity field, final shape
- Process Variables
 - Ram speed, starting temperatures

Output

- Force and Energy Requirements
- Form/Fail Prediction
- Strain, Strain-Rate, Temperature of any Material Element vs. Time
- Final Structure of any Element
- Total Elapsed Time

The interaction of the material, interface, geometrical and process variables is extremely complex. Together they determine the local metal flow necessary to achieve the final shape. However, if the strain, strain rate, temperature of any specific material element can be followed in a process model calculation, the constitutive relations should provide for the calculation of some local properties of the finished part. Knowledge of the generation and multiplication of defects will be required for a complete characterization.

Components of the Material Model. The constitutive relations for non-elastic flow, characterization of the initial structure, and characterization of the final structure of the workpiece will be discussed in terms of application to the design of a compressor disk. The workability-criteria and limits component is considered in other sections of this report and is only considered here as needed to discuss characterization of initial and final structure.

The constitutive relations to be discussed here are those proposed by E.W. Hart (1-3). We will emphasize the general features of the constitutive relations rather than specific functional forms:

- A flow law

$$\sigma = \sigma(\sigma^*, \dot{\epsilon}, T) \quad (A-1)$$

based upon evolutionary state parameters (σ^*),

- Conceptual separation of the non-elastic strain into plastic and anelastic portions,
- Provision for an incremental deformation path,

$$d \ln \sigma = \gamma d \epsilon + \nu d \ln \dot{\epsilon}, \quad (A-2)$$

with γ and ν defined by considering $d \ln \sigma$ as an exact differential,

- Evolution of the hardness state of the workpiece

$$d \ln \sigma^* = \Gamma d \epsilon - R dt \quad (A-3)$$

in terms of both strain-induced (Γ) and time-dependent (R) mechanisms,

- Fully three dimensional formulation based upon a yield function, associated flow law, and microstructural anisotropy.

The single most important feature of this constitutive relation formulation is the identification of state parameters which evolve with deformation history and partially determine the future response of the material. In addition, it is recognized that the plastic strain ϵ is not a state parameter, but rather a path variable, albeit an important one for most process calculations. Plastic strain is not a state parameter because there is no way to measure the current value of the accumulated plastic strain. On the other hand, for a description according to Eq. (A-1), it is possible to measure the current value of a hardness state parameter σ^* .

Application of the constitutive equations for a specific deformation process would then take the following general form:

- (1) A specific functional form of the flow law, Eq. (A-1), will define one or more state parameters of the type σ^* . These, then, must be measured to characterize the initial state of the material. Generally, this could be done through a few simple tests at

carefully selected temperatures.

- (2) Empirical relations which govern the evolution of the hardness state, Eq. (A-3) must be known. The process model must then provide for the continual updating of the hardness parameters as deformation proceeds. This requires the calculation of local temperature as well as strain and strain-rate.
- (3) The final values (distribution) of the state parameters from the process model can be used to calculate some aspects of the mechanical behavior of the final product. These would include stress-strain curves, stress relaxation behavior, and primary and secondary creep rates. For a complete characterization of the final state, other properties such as low cycle fatigue, fracture toughness, or stress rupture which depend upon defects would have to be measured separately.

Many features of the constitutive relation framework have been verified to date⁽²⁾ including some work on titanium alloys^(4,5). Generally, this work has not been at hot working conditions. It is expected that deformation behavior associated with thermally assisted evolution of the state parameters evident through features such as flow softening will be the most difficult to approach.

Phenomenological Aspects of Flow Instability in Compression

When β -transformed preforms are forged at a temperature range of 815-927 C, flow softening and plastic instability are usually observed (Fig. A-1). Similar behavior has been reported for other alloys that have been processed in a thermodynamically metastable condition^(6,7). Due to instability, flow localization and adverse structural inhomogeneities develop that usually persist during subsequent final forming operations.

For ideal compression, instability criteria have been developed⁽⁸⁾ from the application of the Considère relation $(\frac{1}{\sigma} \frac{d\sigma}{d\varepsilon} = 1)$ ⁽⁹⁾, Hart's flow localization theory $(\gamma = 1 - \nu)$ ⁽¹⁰⁾, or Jonas' strain localization condition $((\gamma-1)/\nu < 0)$ to the compression stress-strain curve. Here, $\gamma = \frac{1}{\sigma} \frac{\partial \sigma}{\partial \varepsilon}$, and $\nu = \frac{\partial \ln \sigma}{\partial \ln \dot{\varepsilon}}$. In Fig. (A-2), a schematic representation of typical σ - ε curves in compression and the necessary constructions for determination of instability are shown. Instability is predicted only for case (c), and in the limited strain interval of ε_A to ε_B . Case (c) is characterized by a rapid rate of flow softening from a highly stressed state, complementary conditions which insure large positive values for γ . This example indicates that, unlike the tension test where instability is always imminent, in compression testing the condition for even a limited instability is very specific. In fact, applying the instability criteria to the data on the $(\alpha+\beta)$ forging of Ti-6Al-4V preforms⁽¹¹⁾ indicates that, in spite of appreciable flow softening at certain temperatures, the deformation remains stable throughout (Fig. A-3).

The theoretical instability criteria are developed for ideal compression where F is the same at all points of the specimen. As a result, the variation of stress expressed as:

$$\delta\sigma = \frac{\partial\sigma}{\partial\varepsilon} \delta\varepsilon + \frac{\partial\sigma}{\partial\dot{\varepsilon}} \delta\dot{\varepsilon} \quad (A-4)$$



Material, Ti-6242 ($\alpha + \beta$)
Specimen Temp., 955 C
Die Temp., 871 C
Lubricant, DG-69
Ram Speed, 25.4 mm/s

Fig. A-1. Plastic instability in Ti-6242, ($\alpha + \beta$) structure. (Courtesy of H.L. Giegel and S. Nativ).

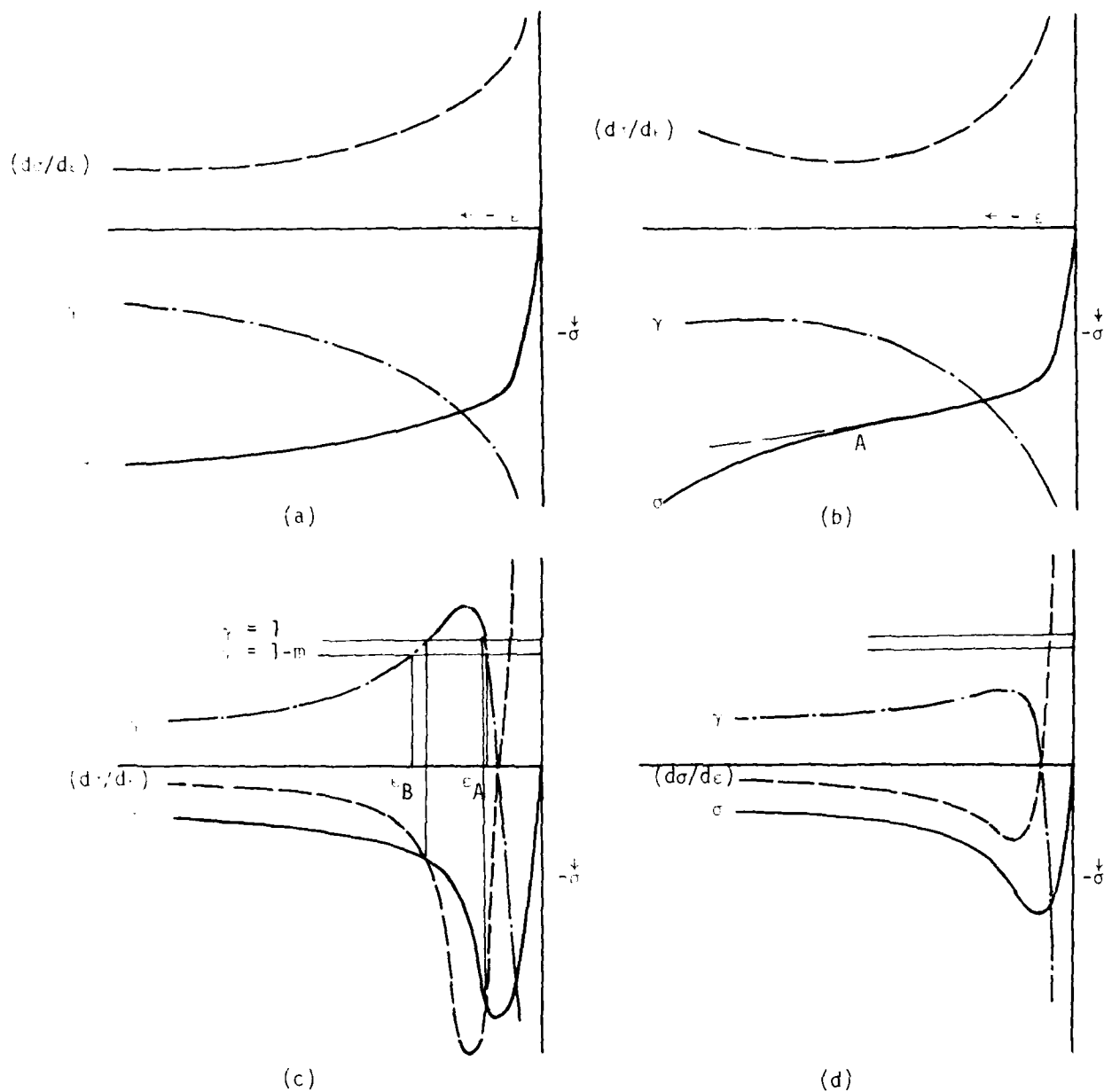
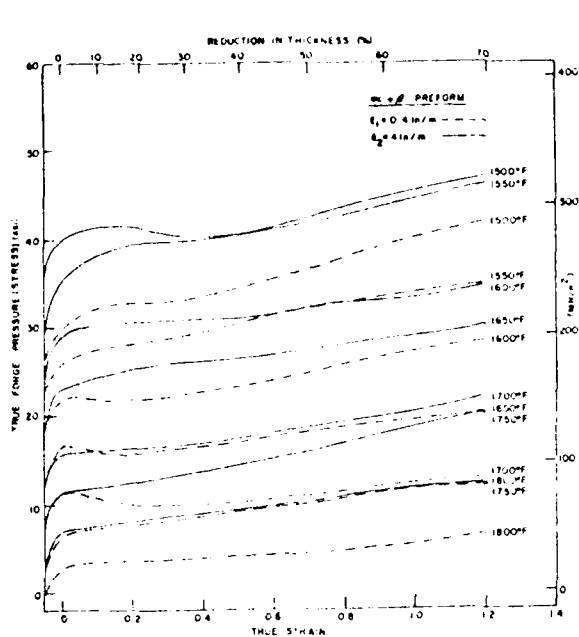
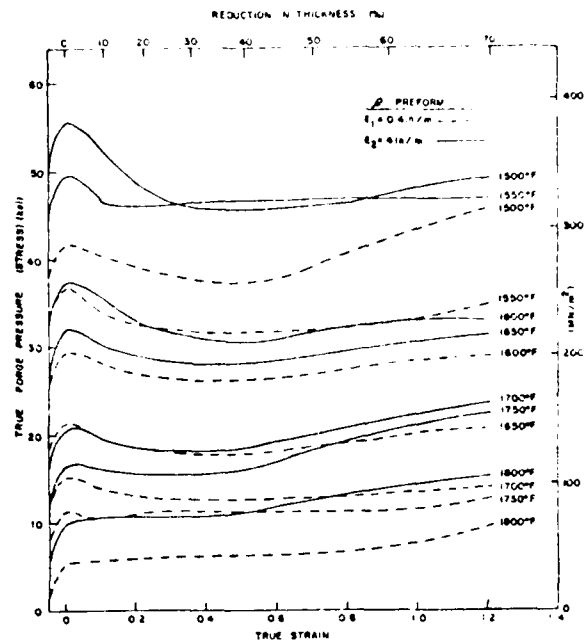


Fig. A-2. Schematic representations of typical stress-strain behavior and the variations of γ and $(d\sigma/d\epsilon)$ in compression testing. (a) Stable flow of a well-lubricated billet, (b) stable flow of a billet exhibiting foldover starting at point A, (c) flow of a material characterized by an appreciable amount of deformation induced softening; flow is unstable in the strain interval of ϵ_A to ϵ_B , and (d) stable flow in the presence of deformation-induced softening.



(a)



(b)

Fig. A-3 (a). True stress-strain curves for isothermal forging of pancakes using $\alpha + \beta$ preforms at various forge temperatures, and
 (b). true stress-strain curves for isothermal forging of pancakes using β preforms at various forge temperatures.(11)

is independent of the spatial coordinates of the specimen. In forging, due to the existence of complex interfacial friction forces, and imposed as well as deformation-induced temperature gradients, inhomogeneous strain and strain rate fields develop and stress variations in axial and radial directions result. Because of this, and due to the difficulty of determining ν for a material that is undergoing a structural transformation, the theoretical instability criteria are of limited application to forging.

The changes with strain of four representative parameters, namely stress σ , cross-sectional area A , strain rate $\dot{\epsilon}$, and hardness H , for two forgings (stable and unstable) are shown in Fig. A-4. In each case, a bulge (B) of area $A_b > A_a$, where A_a is the area of an element (A) outside of the bulge, is considered. Moreover, it is assumed that these bulges are formed during the initial stages of deformation and prior to the onset of any softening. For isothermal forging, and in the presence of strain hardening (case (a), and case (b) up to point C), the intrinsic strength and hardness of B (material properties) increase with strain and are greater than the corresponding values for A. In spite of this, as well as the increased resistance offered by a larger A_b and a greater $\dot{\epsilon}_b$, the deformation continues at a faster rate at the bulge. This is a direct consequence of the particular stress distribution in forging which produces a larger effective stress in the region of the bulge. When a softening mechanism becomes operative (Fig. A-4, case (b)), the bulge region transforms to a soft structure and A_b will then grow at faster rates.

Depending on material and process variables, different mechanisms such as recovery, recrystallization, phase transformations and rearrangements can be responsible for the observed flow softening. In general, for all such mechanisms, the rate of reaction can be enhanced, sometimes substantially,

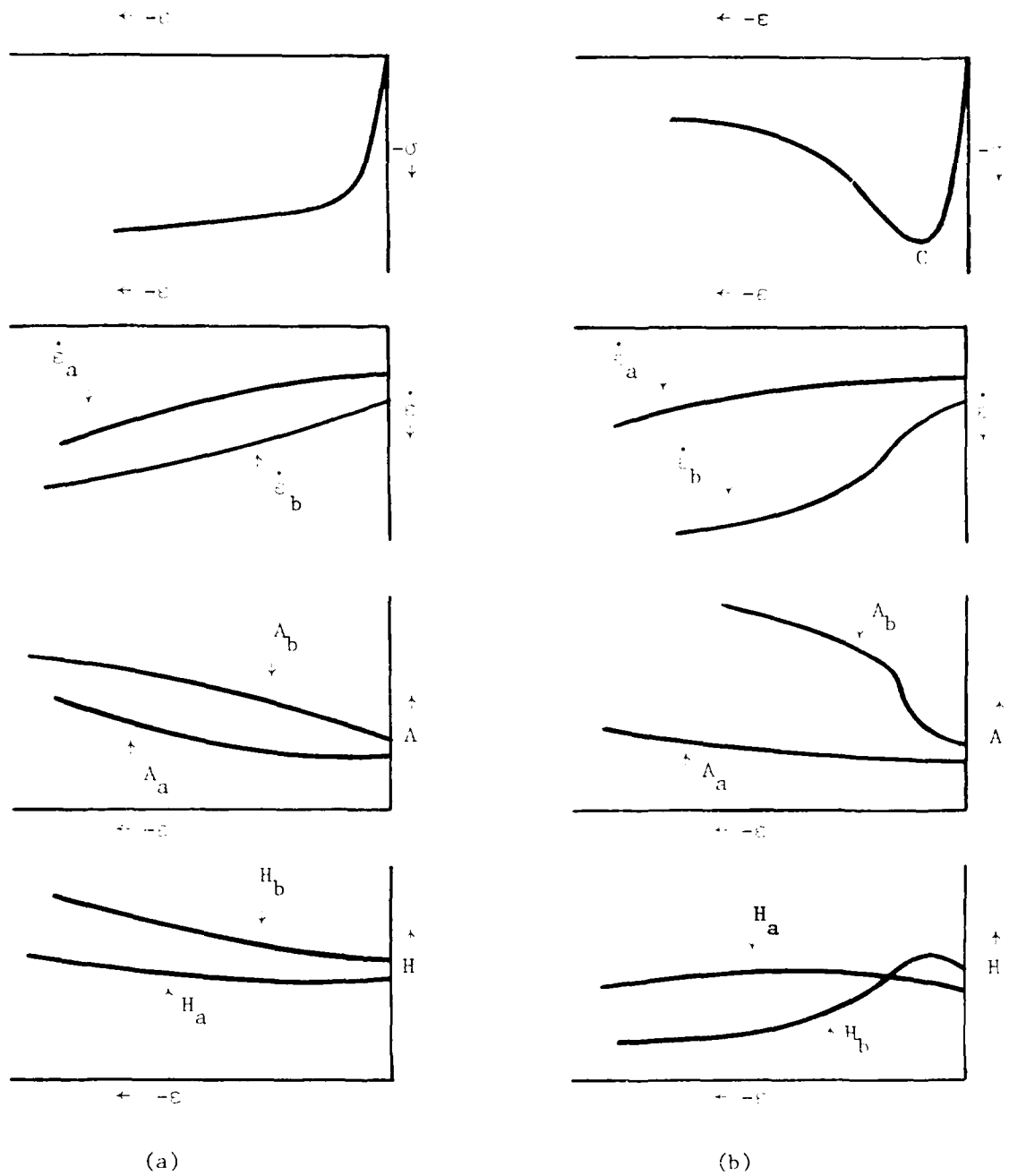


Fig. A-4. Schematic representation of the changes with strain of stress, strain rate, area and hardness in: (a) a stable forging, and (b) an unstable forging operation.

AD-A082 207

BATTELLE COLUMBUS LABS OH

F/G 11/6

RESEARCH TO DEVELOP PROCESS MODELS FOR PRODUCING A DUAL PROPERTY--ETC(U)

DEC 79 G D LAHOTI, T ALTAN

F33615-78-C-5025

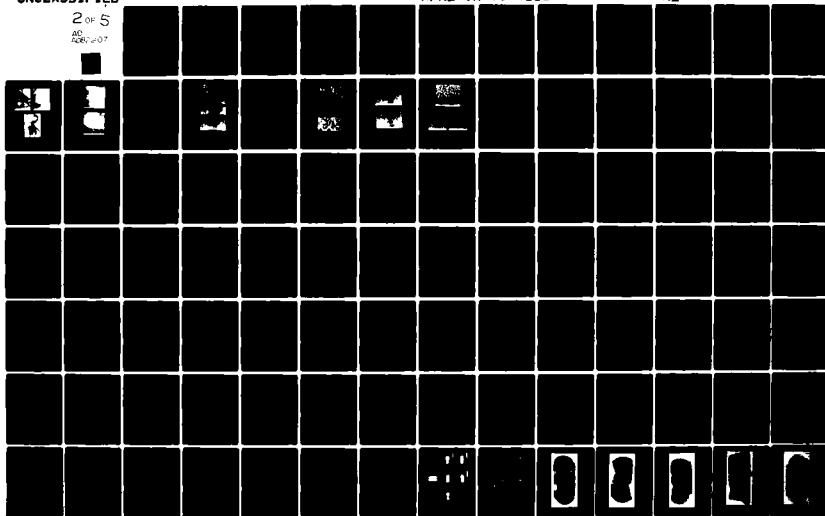
UNCLASSIFIED

AFML-TR-79-4156

NL

2 OF 5

AD
A082 207



by concurrent deformation. For example, the spheroidization of a eutectoid steel, which takes many hours at 700°C, can be accomplished in a few minutes by warm working at the same temperature⁽¹²⁾. Deformation-induced flow softening is most pronounced when, with respect to the imminent softening mechanism, the starting structure is potentially unstable. Moreover, the operation of the softening mechanism should not proceed by thermal activation alone, rather it should depend strongly on the assistance from the concurrent deformation.

For forging at high temperatures (for example 982 C for the β -transformed billets), where most of the softening is due to thermal activation, a soft and macroscopically uniform structure is expected to result. At such a high temperature, the material is characterized by low flow stress, small rate of work hardening, and high ductility. These properties are not conducive to the development of highly localized stressed regions during the deformation, and material-related strain localization and plastic instability cannot be expected. On the other hand, for the class of materials where deformation-induced flow softening can occur during the initial stages of straining, inhomogeneities in deformation caused by the interface and process conditions are likely to develop. Deformation-induced softening mechanisms will then become operative only in the highly stressed regions that are thus produced. The localized soft zones in turn will accommodate more strain, thereby, encouraging more strain localization and perhaps even plastic instability.

The nature of the induced localized stresses and strains is also of great significance. For example, in a material that exhibits flow softening due to the break up of a Widmanstatten structure, large displacements, produced by the shear components of stress, will be most effective. In contrast,

a high hydrostatic stress field may retard diffusion-controlled processes⁽¹³⁾ such as recovery and particle coarsening, thereby reducing the rate and the extent of flow softening.

Tensile Properties of Ti-6242 Beta Preform Structure

Tensile tests have been conducted on button-head specimens at temperatures from 1050° to 1500°F (565° to 815°C) and strain rates from 10^{-4} to 10^{-2} sec⁻¹. All specimens were machined from billet A-21 which has the transformed beta preform microstructure (forge 1037 C, air cool; heat treat 1024 C, 2 hours, air cool). The specimen bars were taken from the rim region of the billet, and two specimens were obtained from each bar. The tests were conducted in air with the specimens protected by a thin layer of FelPro C100 (MoS₂-based) lubricant which is rated for use to 1316 C.

The engineering stress-strain curves have been used to compute a number of standard tensile test parameters. These are summarized in Table A-1. In this table, σ_y is the engineering stress at 0.2 percent non-elastic strain, σ_{UTS} is the engineering stress at maximum load, ϵ_{unif} is the true, non-elastic strain at maximum load, and e_{tot} is the engineering strain at fracture.

TABLE A-1
Tensile Test Parameters for Ti-6242 (Beta)

Bar	T(C)	Rate(sec ⁻¹)	σ_y (MPa)	σ_{UTS} (MPa)	ϵ_{unif}	e_{tot} (%)
4	565	10^{-4}	463	554	0.047	9.4
3	565	10^{-3}	478	578	0.057	11.1
3	565	10^{-2}	464	557	0.041	7.0
11	677	10^{-2}	448	520	0.029	10.0
11	732	10^{-2}	389	457	0.019	8.3
5	815	10^{-2}	251	301	0.018	7.1
5	815	10^{-4}	106	111	0.013	---

The inverted strain rate dependence at 565 C and 10^{-2} sec⁻¹ is obtained concurrently with noticeable load serrations and is attributed to dynamic strain

aging. The variations in e_{tot} with strain rate at 565 C are not thought to be significant.

The engineering stress-strain curves and true stress-strain curves combined so as to illustrate the temperature and strain-rate dependencies are shown in Figs. A-5 to A-9. Figs. A-5 and A-6 illustrate the strain-rate dependence at 565 C and show the inverted strain rate effect at 10^{-2} sec^{-1} . In general, the strain rate dependence is quite small at this temperature. Figs. A-7 and A-8 illustrate the temperature dependence of the stress-strain behavior at a strain-rate of 10^{-2} sec^{-1} . It is seen that the flow stress only begins to fall off appreciably above 677 C. Fig A-9 shows the strain-rate dependence at 815 C. The large strain-rate dependence of the flow stress and the large apparent elongation at 10^{-4} sec^{-1} suggest conditions approaching superplastic behavior. However, the large prior beta grain size (~1mm) compared to the gauge diameter (4.5mm) led to a partial rupture of the specimen while the load was still decreasing in a gradual manner.

Strain Hardening. For the tests at 565 C, the true stress-true strain curves (up to maximum load) have been used to investigate the strain hardening behavior in terms of the dependence of the strain hardening coefficient γ on flow stress σ . A characteristic plot of $\log \gamma$ vs $\log \sigma$ for the test at 10^{-3} sec^{-1} is shown in Fig A-10. It is seen that $\log \gamma$ varies linearly with $\log \sigma$ above a stress that corresponds to a strain of approximately 1%. Similar behavior has recently been reported for Ti-6Al-4V⁽⁵⁾ and 2024-0 aluminum⁽¹⁴⁾. The linear dependence of $\log \gamma$ on $\log \sigma$,

$$\log \gamma = \log A - B \log \sigma, \quad (\text{A-5})$$

implies a stress-strain law of the form

$$\sigma = K(\epsilon_0 + \epsilon)^n, \quad (\text{A-6})$$

with $K = (AB)^{1/B}$, $n = 1/B$, and $\epsilon_0 = \sigma_0^B / AB$ where σ_0 is the stress at $\epsilon = 0$ ⁽⁵⁾.

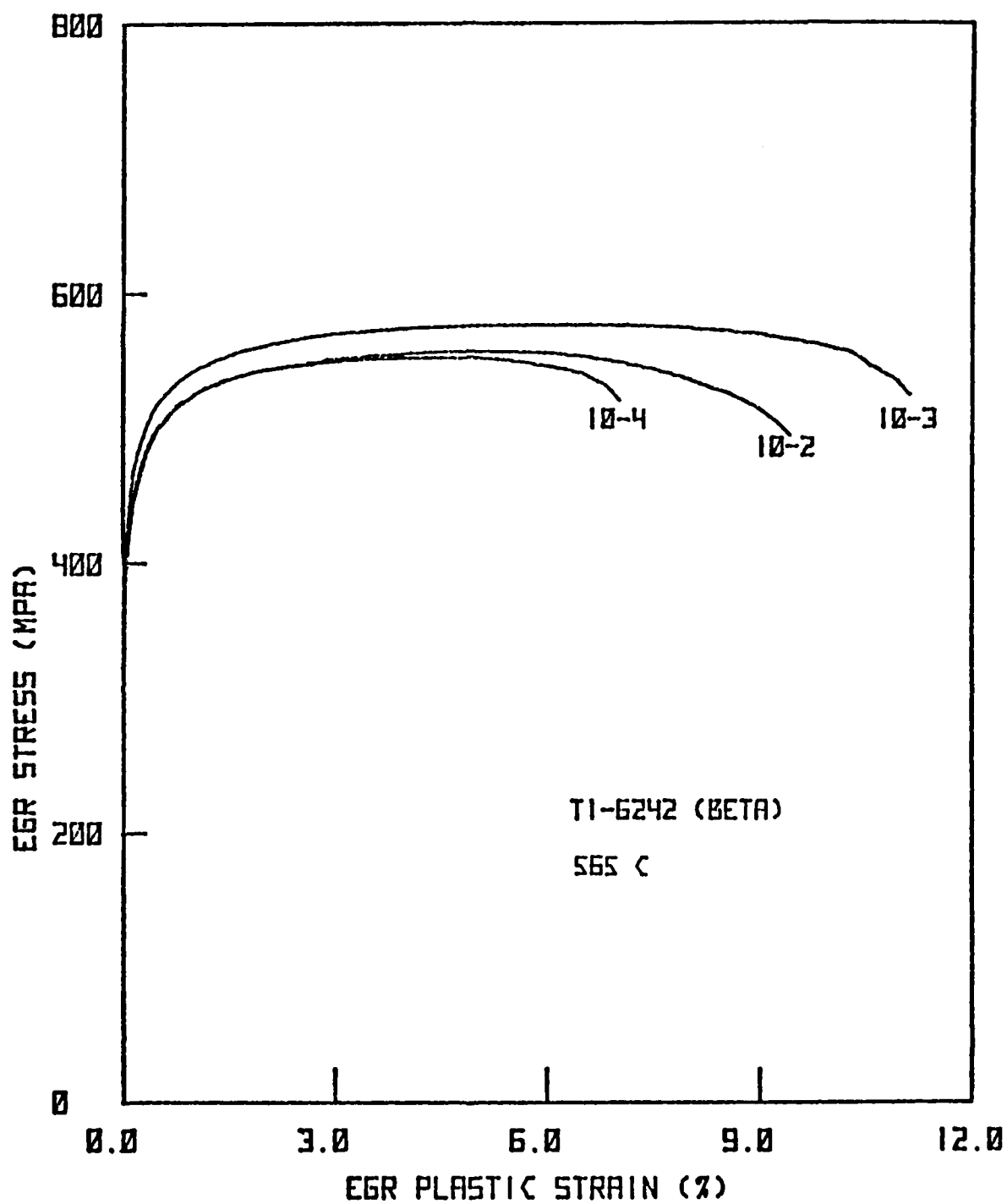


Fig. A-5. Engineering Stress-Strain Curves for Ti-6242 (B) at 565 C vs. Strain-Rate.

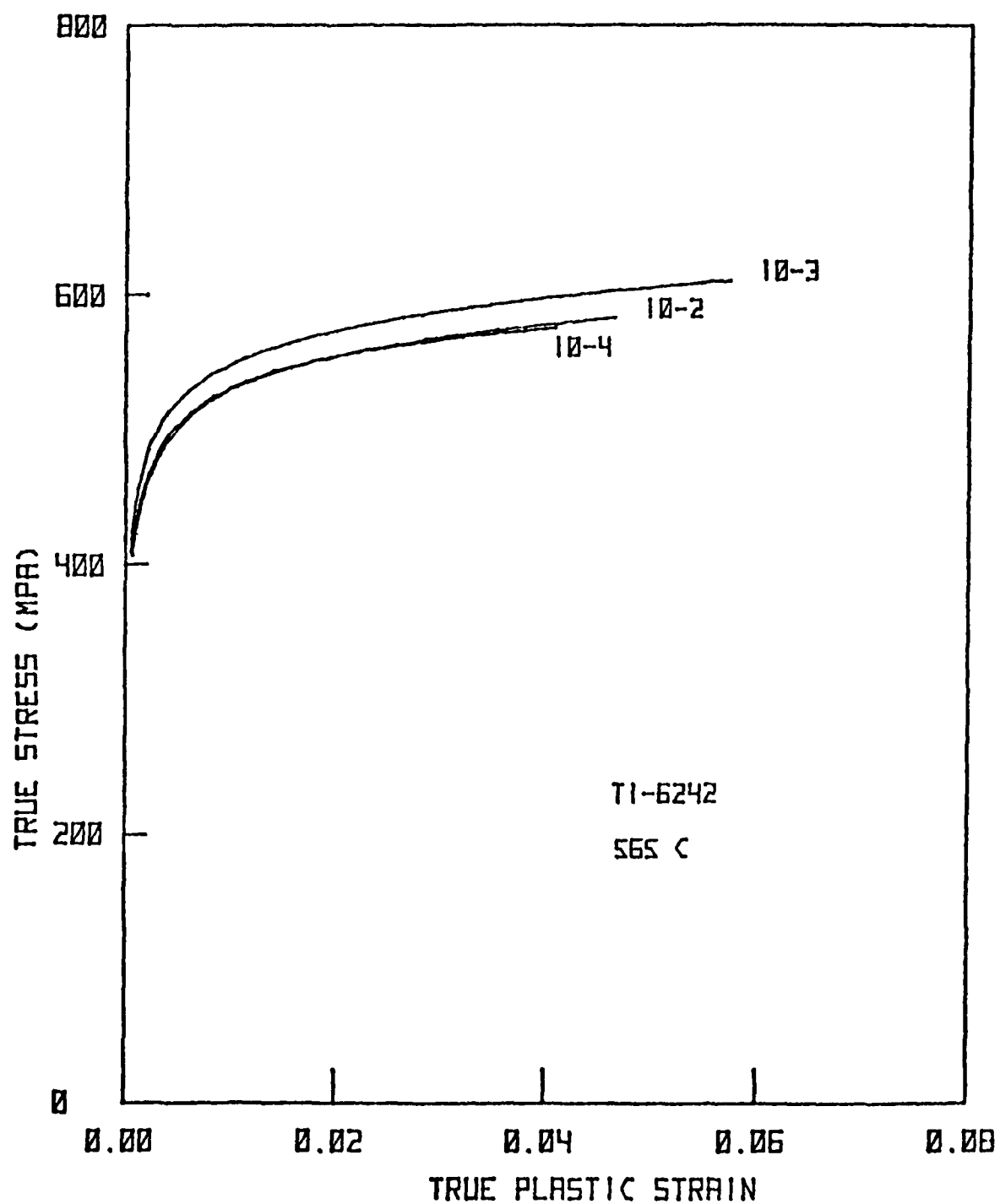


Fig. A-6. True Stress-Strain Curves for Ti-6242 (β) at 565 °C
vs. Strain-Rate.

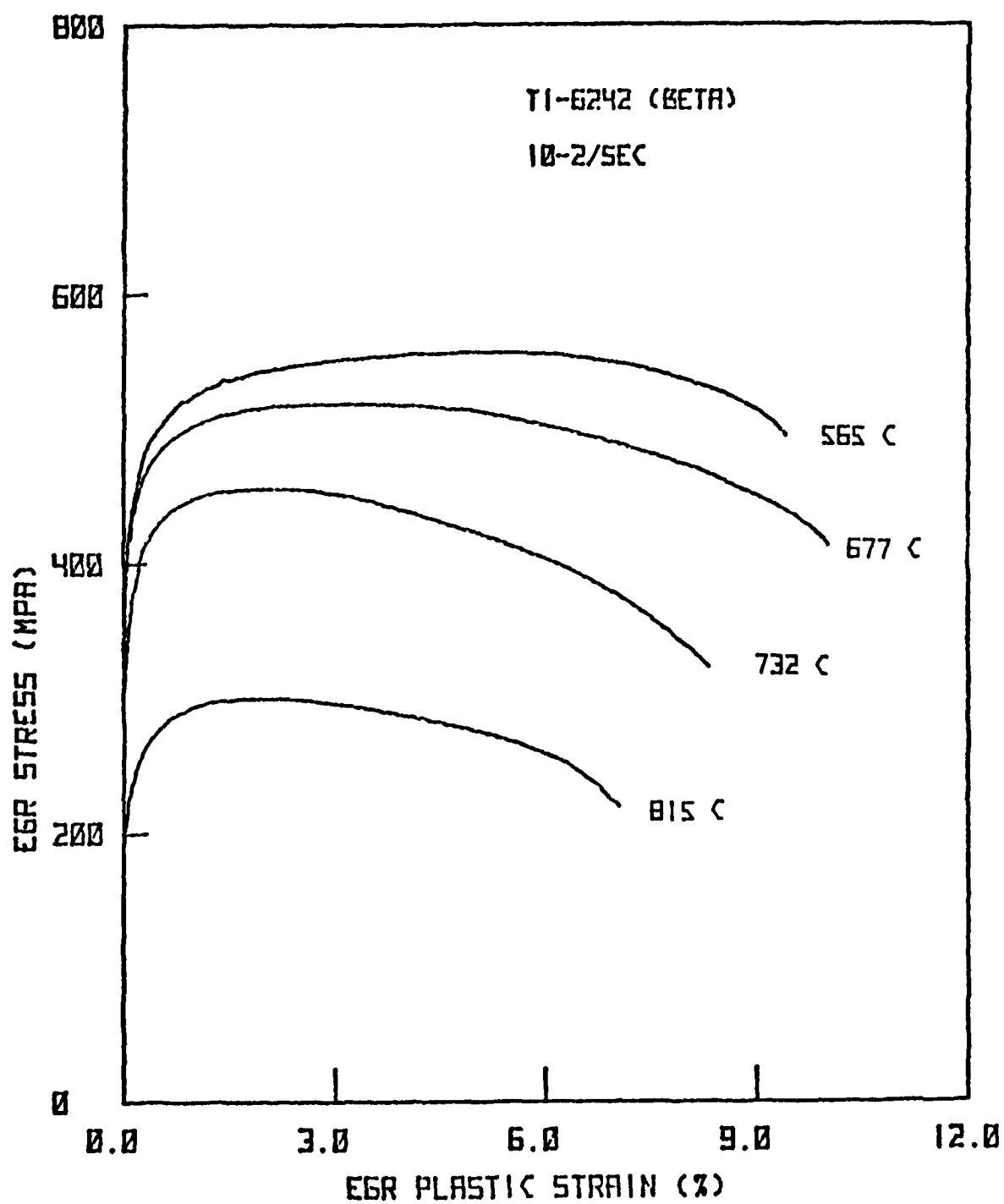


Fig. A-7. Engineering Stress-Strain Curves for Ti-6242 (B) at
10⁻² sec⁻¹ vs. Temperature.

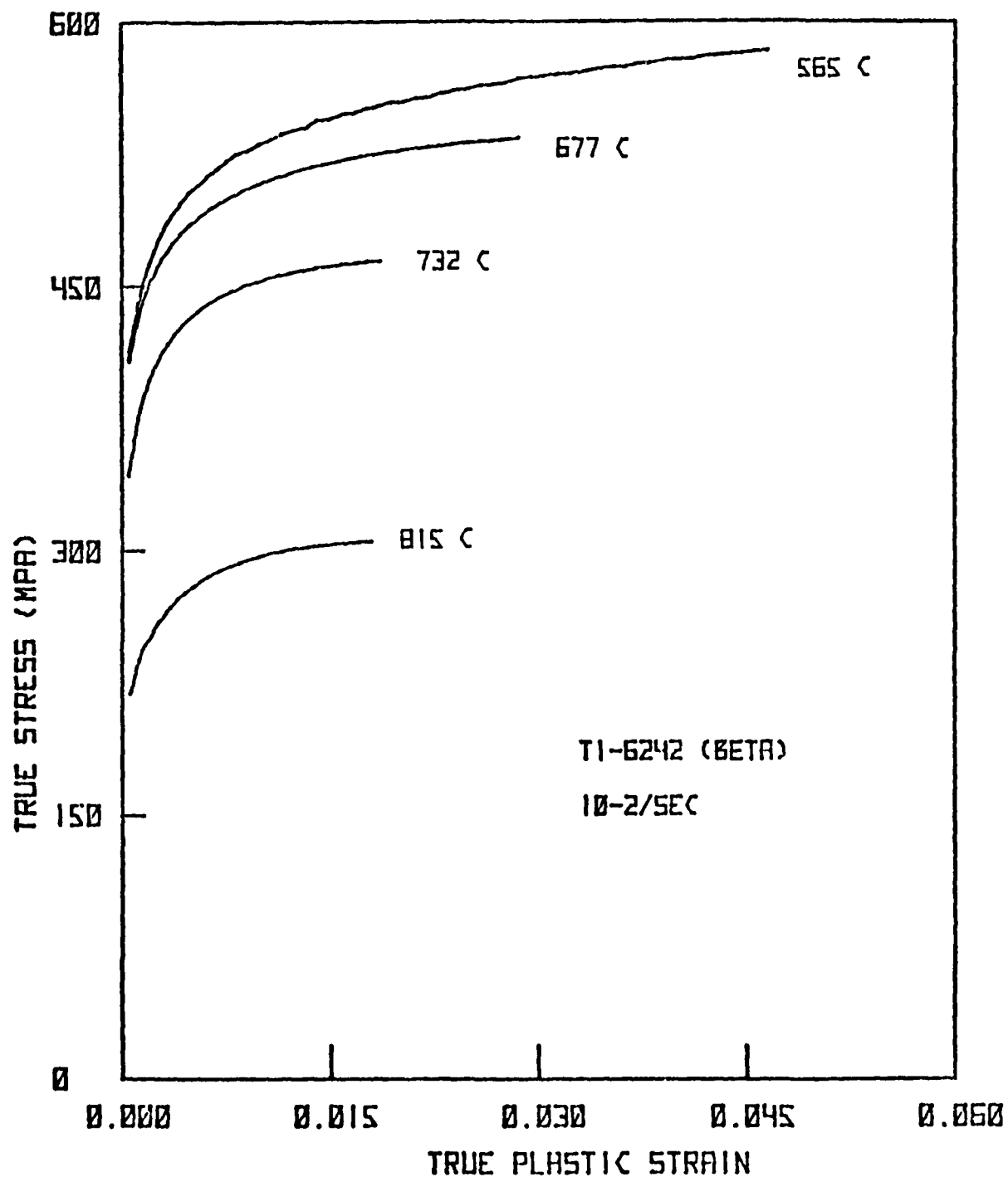


Fig. A-8. True Stress-Strain Curves for Ti-6242 (B) at 10^{-2} sec $^{-1}$ vs. Temperature.

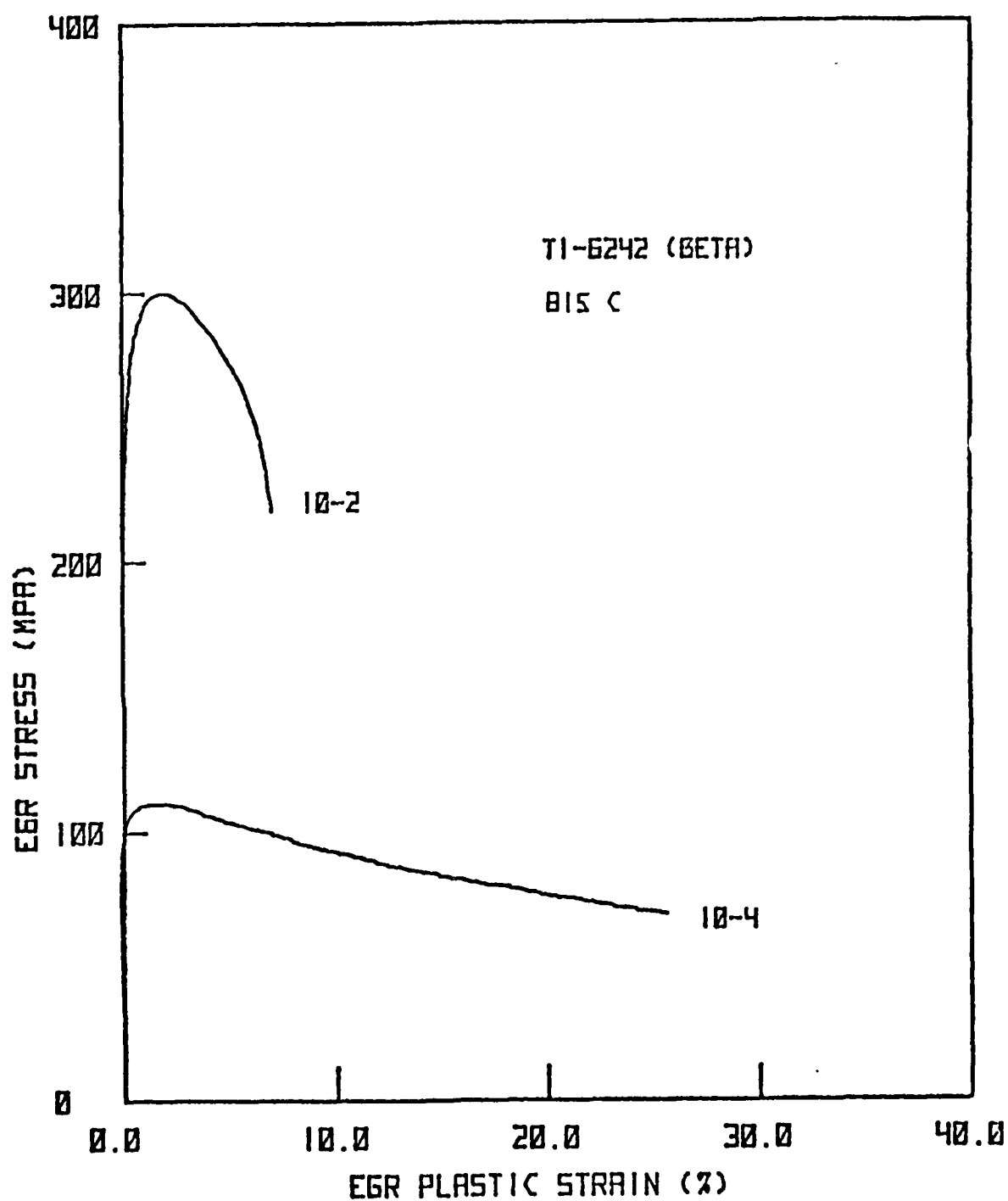


Fig. A-9. Engineering Stress-Strain Curves for Ti-6242 (β) at 815 C and 10^{-2} and 10^{-4} sec $^{-1}$.

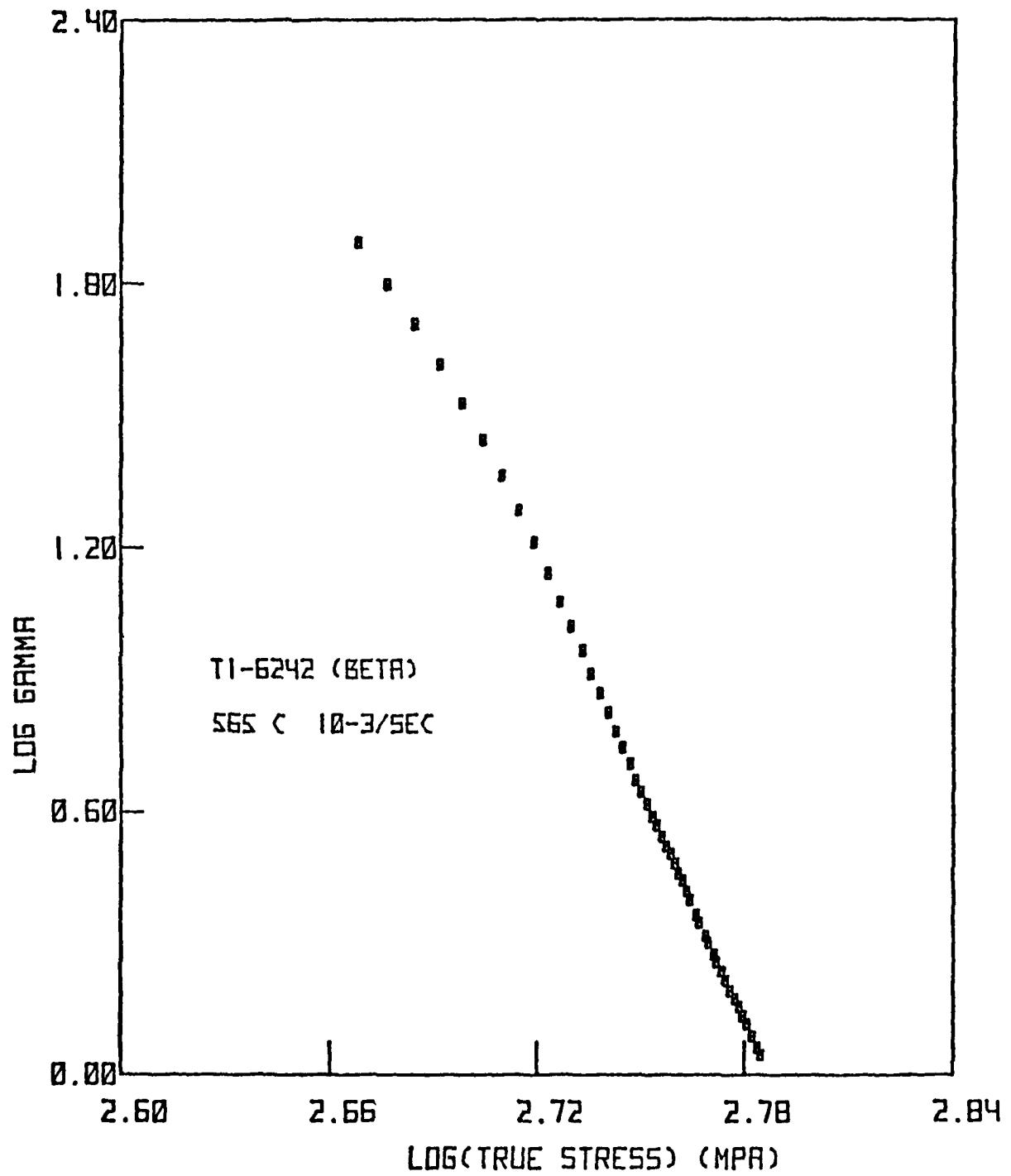


Fig. A-10. Strain Hardening Behavior Presented as $\log \gamma$ vs. $\log \sigma$
for Ti-6242 (β) at 565°C and 10^{-3} sec^{-1} .

The true stress-strain data for 10^{-3} sec^{-1} are shown in Fig. A-11 along with a theoretical curve based on Eq.(A-6). The parameter values are $n = 0.0568$, $K = 720.6 \text{ MPa}$, and $\epsilon_0 = -1.66 \times 10^{-3}$. The fit is seen to be excellent for true strains above 0.01.

Metallographic Examination of Deformed Tensile Specimens. The deformed structures of the tensile specimens tested at a strain rate of 10^{-2} sec^{-1} and at 565 C, 677 C, 732 C, and 815 C were examined and the following general conclusions were obtained:

1. As a result of deformation, no noticeable change in (a) the size, shape and the distribution of the primary β -grains, (b) the configuration of the transformed β -colonies, and (c) the general morphology of the transformed β -structure was observed. This is illustrated in Fig. A-12.
2. In all cases studied, the fracture was predominantly intergranular as shown in Fig.A-13. Also, grain boundary separation, with no evidence of grain boundary sliding, was mostly observed.
3. Free surface wrinkling and orange peel topography was observed as a result of the relative displacement of the large ($\sim 1\text{mm}$) primary β -grains.

Fractography of the Tensile Specimens. The SEM observations provided further evidences regarding the tensile fracture characteristics of the β -transformed microstructure. In Fig. A-14, it is shown that in the temperature range of 565 C to 815 C and for a constant extension rate of 10^{-2} sec^{-1} , the fracture is predominantly intergranular. For all the specimens, grain boundary separation is prevalent and grain boundary sliding is not observed. In isolated cases(Fig. A-15) transgranular cracks, formed by interconnecting cavities are noticed. Such cracks, however, do not extend from grain wall to grain wall and their contribution to the eventual failure is considered

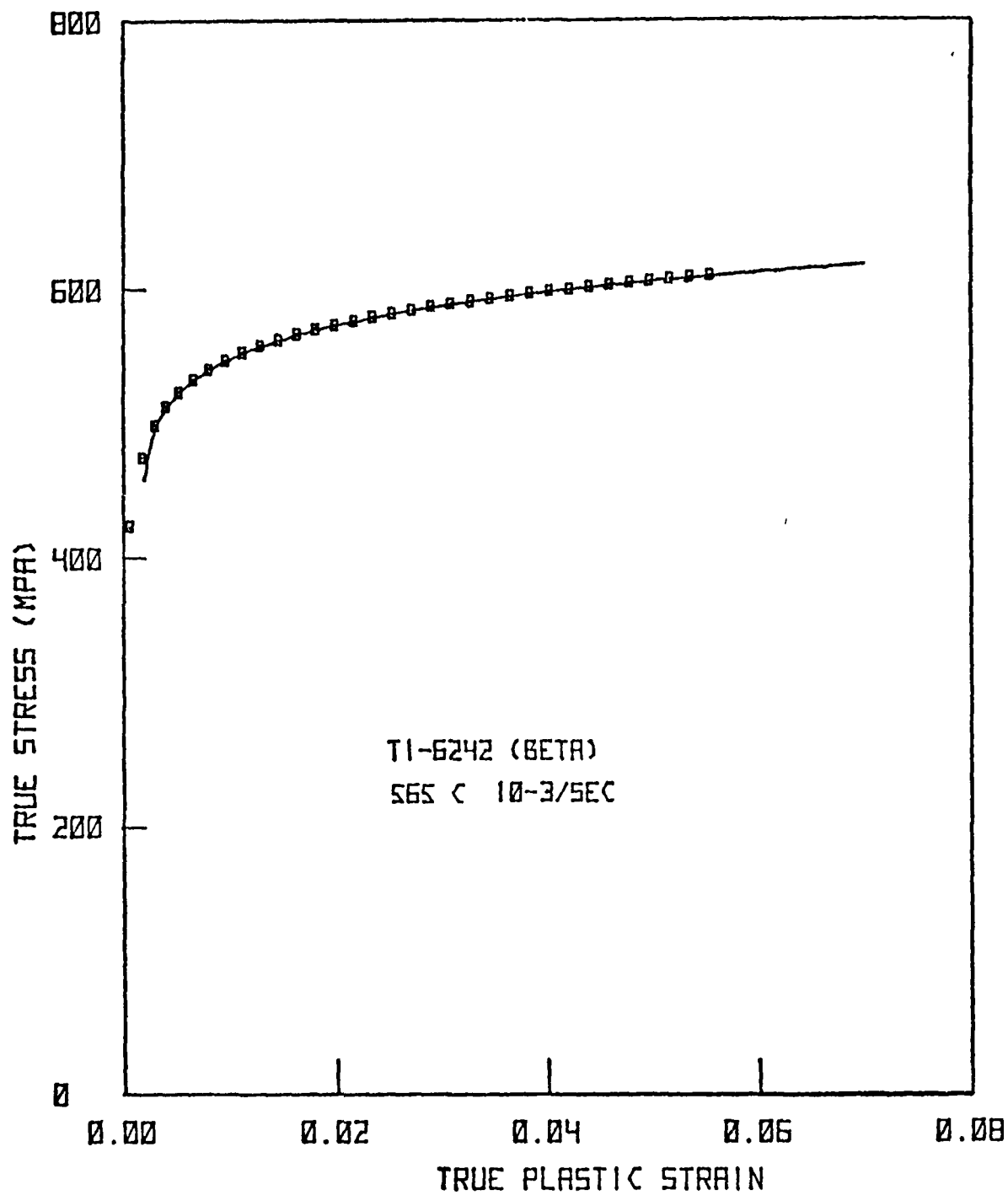


Fig. A-11. True Stress-Strain Data for Ti-6242 (β) at 565 C and 10^{-3} sec^{-1} with Theoretical Fit.



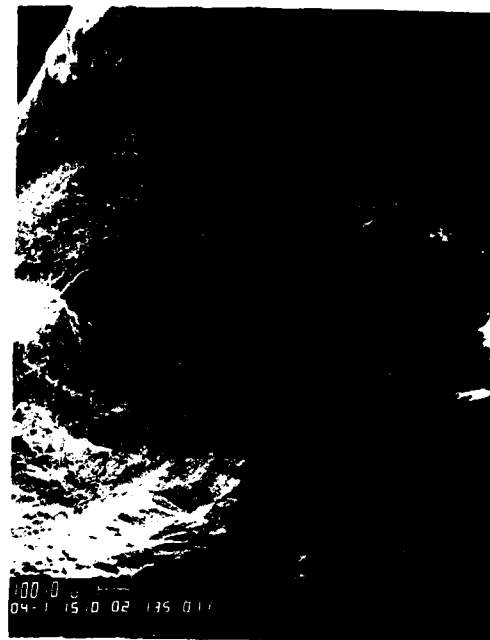
Fig A-12. Deformed structure of a Ti-6242(α) tensile specimen after loading to fracture at 815 C and $\dot{\epsilon} = 10^{-2}/\text{sec.}$ (400x)



Fig. A-13. Intergranular fracture in Ti-6242(β) structure at 815 C. (200x)



(a)



(b)



(c)

Fig. A-14. Intergranular fracture in Ti-6242(β) tensile specimens, $\dot{\epsilon} = 10^{-2}/\text{sec}$. (a) $T = 363^\circ\text{C}$, (b) $T = 732^\circ\text{C}$, and (c) $T = 815^\circ\text{C}$.



Fig. A-15. Occasional transgranular crack in Ti-6242(β) tensile specimen,
 $T = 815\text{ C}$, $\dot{\epsilon} = 10^{-2}/\text{sec}$.

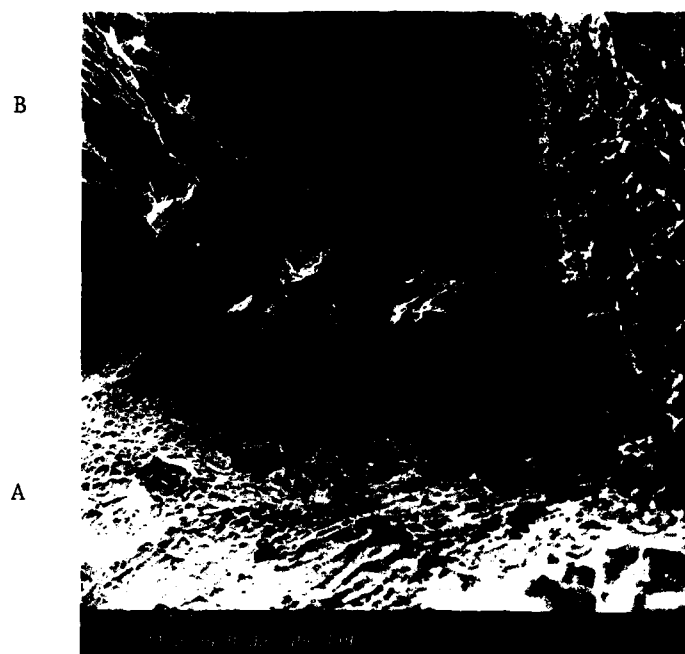


Fig. A-16. Configuration of dimples in Ti-6242(β).

inconsequential.

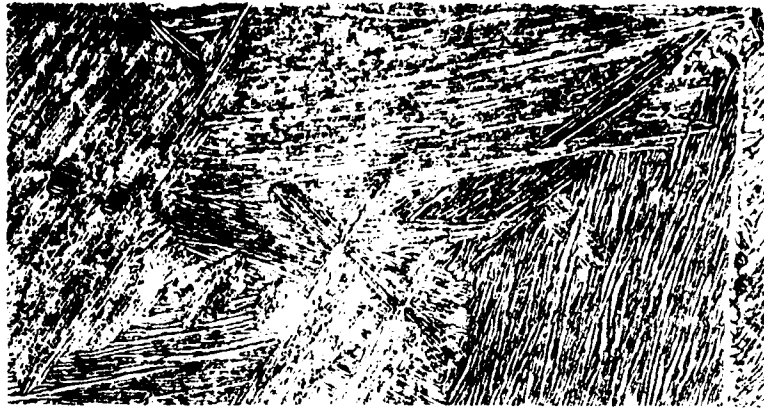
The existence of dimples on the separated grain boundaries indicates that all the specimens have fractured in a ductile mode. This is illustrated in Fig. A-16. The configuration of the dimples may depend on the orientation of the α -platelet colonies and the angle that they make with the separated grain walls. For large angles, numerous small dimples are expected to form (area A, Fig. A-16) while for small angles, or when the platelets are almost parallel to the grain walls, a flat serrated topography (area B, Fig. A-16) may develop.

Effect of Heat Treatment and Protective Coatings on Ti-6242

As-received Microstructures. A microstructural characterization of all the specimens used in the program is of utmost importance. Such a characterization involves specimen identification in regard to its particular location in the billet as well as nominal microstructure ($\alpha + \beta$, transformed- β) which is a function of the known process histories.

A metallographic investigation of the as-received microstructure of the β -transformed rods was conducted. Although the machinability of these rods was found to vary with their location in the mult, no conclusive evidence of microstructural differences was found. The microstructural variations existing within a rod contributed to the difficulty of this study.

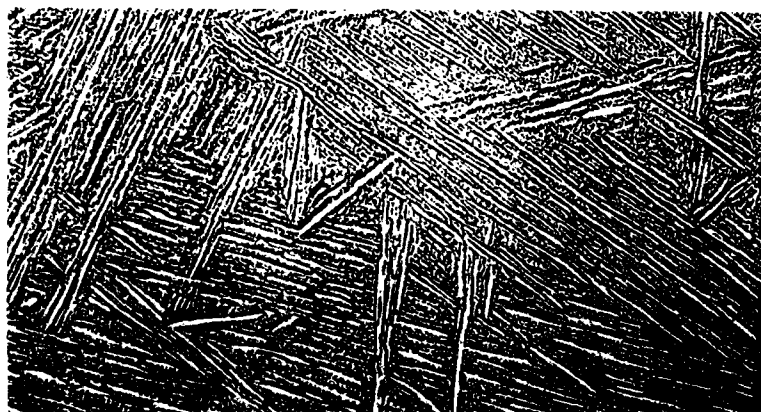
Thermal Soaking. Depending on test temperature and soak time, the microstructure at the start of the loading may be considerably different from the as-received microstructure. For the β -transformed microstructure, which is thermally more stable than the $\alpha + \beta$ structure, this is of less consequence. In Fig. A-17 the β -transformed microstructures in the as-received condition and after a soak time of 1 1/2 hours at 955 C and 815 C are compared. No differences are observed at this magnification nor at 1000X. In contrast, the



(a)



(b)



(c)

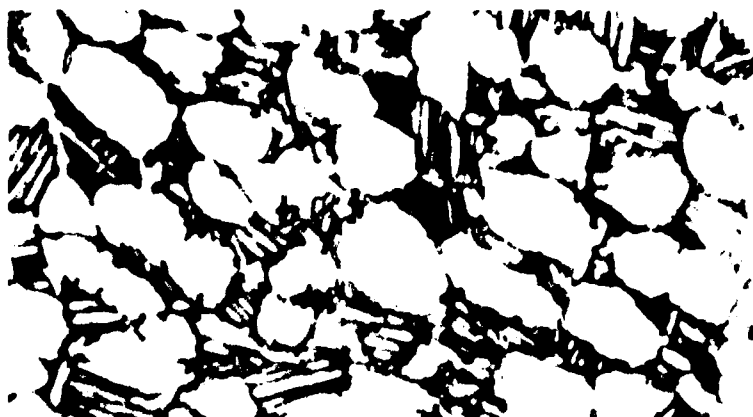
Fig. A-17. Effect of soak cycle on the microstructure of Ti-6242(β).
(a) as-received, (b) 1 1/2 hrs. at 815 C, and (c) 1 1/2
hrs. at 955 C. (400x)

$\alpha + \beta$ microstructure undergoes some noticeable changes during a similar soak cycle (Fig. A-18). A coarsening of the acicular- α structure at 815 C, and a transformation of the acicular- α structure to a martensitic structure after air cooling from 955 C, are the main features of the resulting microstructures.

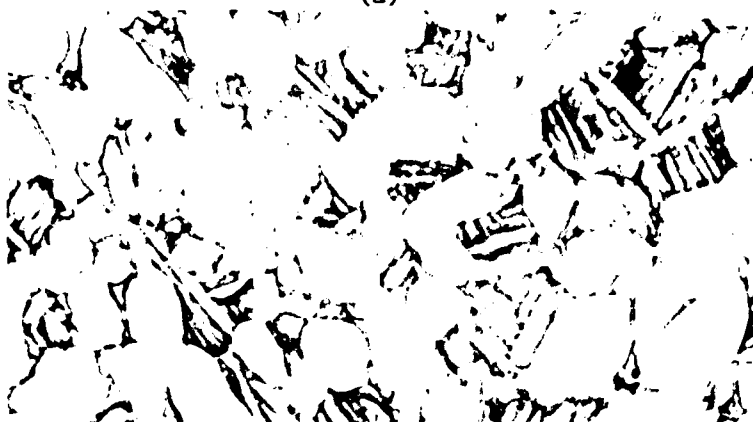
Protective Coatings. To prevent oxidation at high test temperatures the effectiveness of the following coatings was evaluated:

- 1 - Delta Glaze 93 glass lubricant
- 2 - Delta Glaze 69 glass lubricant
- 3 - FelPro C100 high temperature anti-galling compound.

The cleaned specimens were coated by dipping or brushing and after curing were heated at the desired temperature in air. Based on microscopic observations, it appears that, in general, any of the above coatings can provide sufficient oxidation prevention for the β -transformed samples (Fig A-19). On the other hand, for the $\alpha + \beta$ samples (Fig. A-20), the only effective coating is provided by DG-69. For the other coatings, extensive oxidation evidenced by substantial (~100u) α -casings were observed.



(a)

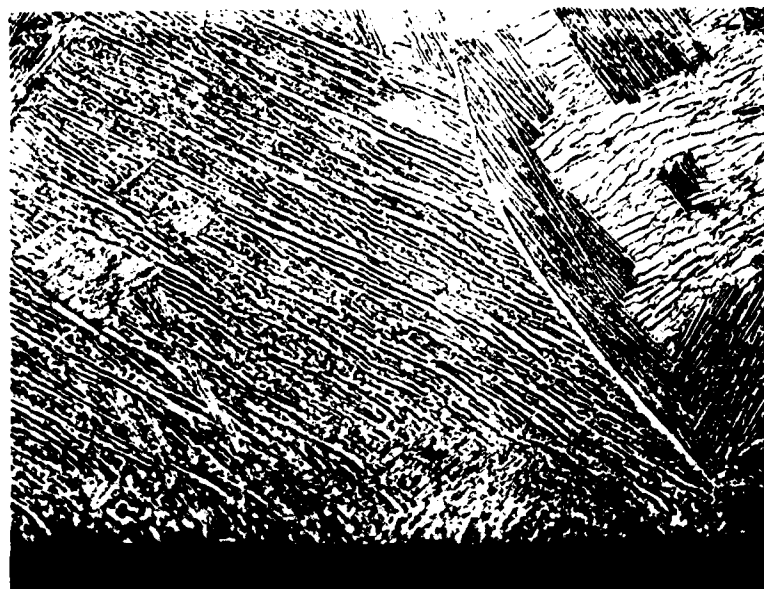


(b)



(c)

Fig. A-18. Microstructural changes due to soaking treatment of Ti-6242($\alpha + \beta$). (a) as-received, (b) 1 1/2 hrs. at 815 C, and (c) 1 1/2 hrs. at 955 C. (1000x)

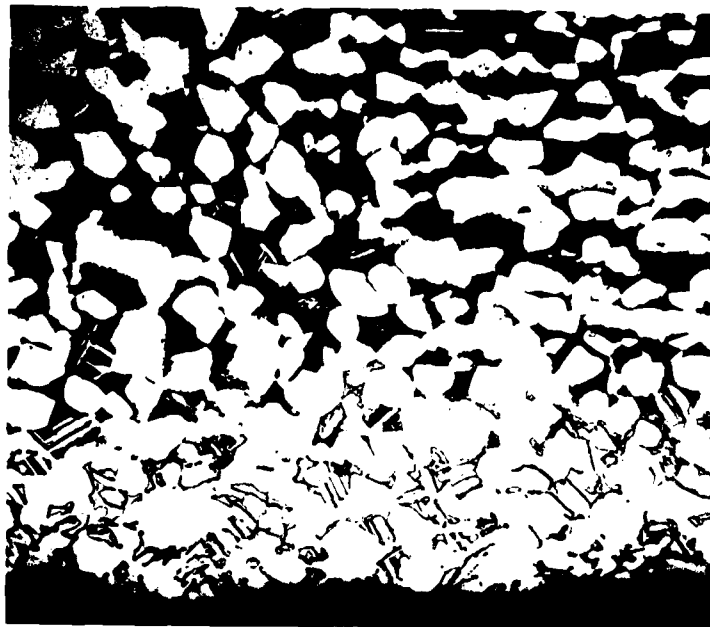


(a)

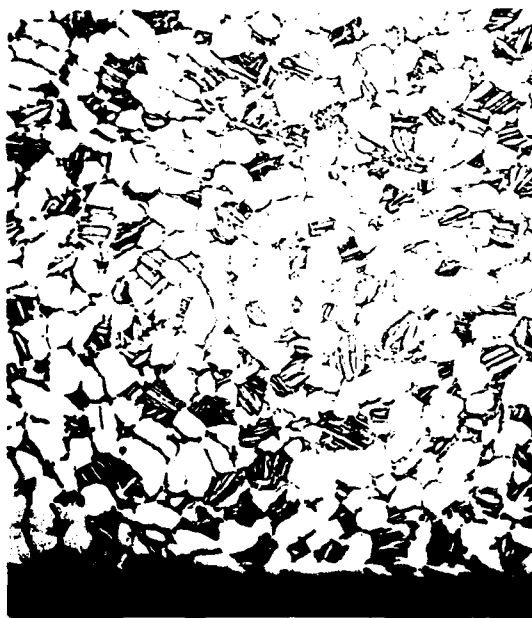


(b)

Fig. A-19. Effect of protective coatings on Ti-6242(β) (a) 1 1/2 hrs. at 955 C, DG-93, and (b) 1 1/2 hrs. at 955 C, Fel-Pro C100. (400x)



(a)



(b)



(c)

Fig. A-20. Effect of protective coatings on Ti-6242, ($\alpha + \beta$) (a) 1 1/2 hrs. at 955 C, DG-93, (b) 1 1/2 hrs. at 815 C, DG-69, and (c) 1 1/2 hrs. at 955 C, DG-69. (400x)

References

1. E. W. Hart, *Acta Metallurgical*, Vol. 18, p. 599 (1970).
2. E. W. Hart, C. Y. Li, H. Yamada, and G. L. Wire, in *Constitutive Equations in Plasticity*, A. S. Argon, Ed., MIT Press, p. 149 (1975).
3. E. W. Hart, *ASME Journal of Engineering Materials and Technology*, Vol. 98, p. 193 (1976).
4. J. F. Thomas, Jr., "Determination of Constitutive Equations for Titanium Alloys Applicable to Sheet Metal Formability", Report WSU-550F, Wright State University (1978).
5. J. F. Thomas, Jr., "Determination of Constitutive Equations for High Strength Aluminum and Titanium Alloys Applicable to Sheet Metal Formability", AFML-TR-79-4042 (1979).
6. J. J. Jonas and M. J. Luton, *Twenty-First Sagamore Conference on Advances in Deformation Processing* (1974).
7. J. J. Jonas, B. Heritier, and M. J. Luton, *Metallurgical Transactions*, Vol. 7A, p. 611 (1979).
8. J. J. Jonas, R. A. Holt, and C. E. Coleman, *Acta Metallurgica*, Vol. 24, p. 911 (1976).
9. A. Considere, *Ann. des Ponts & Chaussees*, Vol. 9, p. 574 (1885).
10. E. W. Hart, *Acta Metallurgica*, Vol. 15, p. 351 (1967).
11. C. C. Chen, and J. E. Coyne, *Metallurgical Transactions*, Vol. 7A, p. 1931 (1976).
12. J. L. Robbins, O. C. Shephard, and O. D. Sherby, *J. Iron Steel Inst.*, Vol. 202, p. 804 (1964).
13. J. Hudson, and R. Hoffman, *Trans. AIME*, Vol. 221, p. 761 (1961).
14. V. Nagpal, B. S. Shabel, J. F. Thomas, Jr., and H. L. Gegel, Proceedings NAMRC-VII, Society of Manufacturing Engineers, 1979.

APPENDIX B

RESEARCH ON THE HOT WORKABILITY OF T1-6242

S. Nativ, H.L. Gegel and J. Morgan
Metals and Ceramics Division
Air Force Materials Laboratory (LLM)
Wright-Patterson AFB, OH 45433

APPENDIX B

RESEARCH ON THE HOT WORKABILITY OF Ti-6242

Introduction

This report deals with a study, a part of a major program to apply scientific methods for controlling microstructure and properties in finished shapes produced by deformation processing. The end product will be an interactive computer program for designing a dual property disk for the compressor of a jet engine that will have a controlled set of microstructures and mechanical properties, (concentrating on tensile strength, low cycle fatigue and creep resistance). The alloy selected for this program was Ti-6242, a near- α titanium alloy that was believed to be stable under processing conditions, and has no trace-element effect. The program has different phases of which the first is concerned with the metallurgical area dealing with the material behavior under hot forging conditions and aims at defining the hot-workability properties. The results of the first phase should support future development of inelastic constitutive equations in terms of strain, strain-rate, and temperature, which are necessary for developing a process model that will describe the time-temperature deformation path throughout the processing. This is important for the manufacturing of a disk that will have a set of wanted microstructures and mechanical properties.

In order to characterize the dynamic metallurgical behavior under the processing conditions, hot-deformation studies were conducted to

characterize the microstructural changes that occur during hot-working. The conditions that developed during hot-working had to be related to the microstructure that developed due to subsequent phase-transformations. Flow-softening due to processes such as dynamic recrystallization, break-up of Widmanstatten and martensitic structures, and transformation induced plasticity were related to the development of geometric non-uniformity and adiabatic shear band formation. Flow-softening during hot-working has practical implication, because it will lead to plastic instability under compressive loading during processing; and later on, it will lead to failure under service conditions.

The specific alloy of interest has been characterized by compression testing in the range of strain-rates and temperatures used in commercial hot forging processes. The results thus obtained will be correlated with a mathematical analysis of upset forging that will be carried out by a group of continuum mechanics scientists, who will determine what the actual conditions of flow were during the compression. Microstructures were examined at different points in the cross sections of the forged specimens to characterize the structural changes accompanying the high strain-rate and high temperature deformation. The results, as presented in the present report, show clearly that in both ($\alpha + \beta$) preforms and β preforms, when forged in the ($\alpha + \beta$) range of temperatures just below the β -transus, geometrical non-uniformities appear in the form of a kinked specimen (away from symmetry) and instability conditions develop that will lead to shear-band formation. This instability condition was proven to result from microstructural instability during the forging, which is due to several factors such as (a) high-temperature dependency of the flow-stress, (b) transformation-induced plasticity (flow softening),

and (c) low-rigidity of the β -phase during the hot-working. The results have shown that unless the forging preform is stiffened by some method, as suggested in the report, the near-alpha titanium alloys have poor hot-workability in certain temperature and strain-rate regimes. The findings suggest that predictive calculations based on empirical constitutive equations are not always reliable or straightforward, as the possibility for the occurrence of plastic instabilities must be taken into account. Although the scope of the present report is of an exploratory nature, it may suggest, for example, that upperbound theorems cannot always be satisfactorily used in continuum mechanics calculations of metal flow. More realistic results can be obtained by using the matrix method for the analysis. Many of the metallographic features, such as flow-lines patterns, particle shape distortion, chilling-affected non-deformed zones, folding-over flow patterns, and tangential discontinuity velocity bands may provide a hint for better predictive calculations. This report is based on macroscopic and microscopic studies of the structures developed while forging cylinders and disks under different conditions of processing. A part concerned with textural studies is still missing due to lack of adequate x-ray equipment. These studies will be carried out in the near future when the equipment becomes available. Visioplasticity studies are also being considered for evaluating the accuracy of the process model predictions. A dual property disc is now being fabricated, by using a composite ring forging preform, where the hub portion is made from $(\alpha + \beta)$ -preform structure and the rim from β -preform structure materials of the same alloy. The preform was stiffened through geometric design.

Experimental

The Material

The near alpha titanium alloys were developed for improved high-temperature performance and weight reduction of jet-engine components. The use of Ti-6Al-2Sn-4Zr-2Mo alloy (Designated Ti-6242) extended the useful temperature range to 900°F, where both creep and fatigue resistivities are of critical importance. The addition of 0.1% silicon increases the high-temperature properties without any undesirable effects. The 6% aluminium in the alloy is a potent alpha phase stabilizer, while the 2% molybdenum is a moderate beta stabilizer. The tin and zirconium are solid-solution strengthening agents and are neutral with respect to the phase stabilization. The combination of alloying elements result in a weakly beta-stabilized, alpha-beta alloy (referred to as "near alpha" alloy). The β -transus temperature is about 1815°F. The aluminium promotes high-strength at elevated temperatures and the molybdenum increases still further the high-temperature tensile strength. The combination of aluminium, tin and zirconium maintain good creep restivity. Tin, zirconium, and molybdenum increase the toughness. The silicon addition results in precipitation of silicides, which increases further the high temperature creep resistivity. The material can be forged either above or below the β -transus. When forged above it, the end structure observed at room temperature consists of an acicular structure resembling plate martensite, known as β -transformed structure, since it actually differs from the former by having retained beta plates appearing between and parallel with the alpha plates. (This structure may sometimes be termed: discontinuous

Widmanstatten structure). The previous β -grain boundaries can always be observed, having elongated forms due to the deformation. These boundaries are sometimes covered by a thin continuous alpha film. The $(\alpha + \beta)$ structure is composed of primary alpha particles embedded in a continuous β -transformed matrix, except that the particles become elongated after hot working. Also, after the forging (or any other type of hot working), acicular particles of "secondary alpha" may appear within the β -transformed matrix (This structure may sometimes be termed: continuous Widmanstatten structure. The terms continuous or discontinuous are related to the matrix). The transformed β -structure, has better creep strength, while $(\alpha + \beta)$ is believed to have better low-cycle-fatigue endurance. Comparison of properties between the different structures, without any special heat-treatment subsequent to the hot-working show the following:

<u>Room-temp. Properties</u>				<u>Creep-data</u>		
Forging	0.2% YS	RA	K_{IC}	Temp	stress	Time for 2% strain
<u>condition</u>	<u>KSI</u>	<u>%</u>	<u>KSI \sqrt{in}</u>	<u>$^{\circ}F$</u>	<u>KSI</u>	<u>hrs.</u>
$\alpha + \beta$	160	42	32	1000	35	39
β	146	29	52	1000	35	77

Extrusion

A 5.5 lb. billet made from Ti-6242 (0.1 Si) with an $(\alpha + \beta)$ microstructure, and with dimensions of 2.95" diameter by 5 1/8" length, having 90° half inch bevel on one end, was machined from stock material. Extrusion took place on a 700 ton horizontal extrusion press. A conical tool steel die, with opening angle of 90° and final diameter of 1.210"

was used for reduction ratio of 6.5:1. The internal die surface was coated with Zirconia applied by flame spraying, and both the container liner and the die surface were lubricated just prior to the extrusion with graphite in calcium-base grease (Fiske 640), and maintained at 500°F. The billet was coated with 0.03: thick commercial potash-soda-lead lubrication glass (Corning 0010) applied with a brush, and heated prior to the extrusion for 1 hour at 1775°F in a globar furnace under a positive pressure of Argon. Transfer time of specimen from the furnace to the extrusion press was about 10 seconds. Extrusion was done with an average ram speed of 1.85 ips, and minimum pressure of 65 Ksi, resulting in a bar of 30 1/2" length which was air-cooled to room-temperature. Metallographic examination on a lengthwise cross-section, polished and etched by Kroll's Reagent, revealed a fibrous microstructure composed of elongated primary alpha particles, embedded in β -transformed matrix. Very little α -case was observed near the surface which was later removed during specimens preparation. Hardness measurements along a diameter line through the bar cross-section resulted in average value of 67.5 Rockwell "A".

Upset-Forging

The extruded bar, after sand-blast cleaning of the surface to remove the glass coating, was machined by turning into specimens of 1 inch diameter by 1.5 inch length. These cylindrical specimens were used for the compression upset-forging tests.

The specimens were forged on a 500 ton vertical hydraulic press. The upper and lower die blocks were kept constantly at 1600°F during the forging, while the wall surrounding the forging space was kept at

1700°F. Die-inserts 3 3/4" by 3 3/4" made of 713C tool-steel were used. The bare die inserts were heated to the predetermined temperature in a separate furnace and moved to their positions on the die blocks just before forging. The specimens were coated with DG-69 Commercial glass by dipping. It was used to lubricate to prevent free-surface oxidation during the forging. They were kept for 1/2 hour at a predetermined temperature in a globar furnace under positive pressure of Argon before forging. The tongues for specimen transfer were heated to dull red color prior to operation. Specimen transfer from furnace to the press took about 15 seconds, and the forging operation took somewhat between 5 and 7 seconds. Then, the specimens were air-cooled to room-temperature. The glass coating was not damaged during the total operation, and almost no α -case formation was noticed. For isothermal forging the die-insert with the specimen already on top of it was placed in the forging press to minimize temperature gradients development during the isothermal forging. Nevertheless, formation of small temperature differences (up to 20°F) between the upper and lower specimen surfaces was inevitable.

The specimens were reduced by the upset forging down to about half of their initial height under ram-speed of one inch per second. The hydraulic press pressure changes and the forging force build-up (by means of load-cell situated beneath the lower die-insert) versus time were recorded by a Honeywell visicorder device. Table I gives the details of the different specimens forged. In all specimens, except the isothermally forged (ISO) the lubrication film thickness was 0.006 inch, while in the ISO specimens it was 0.028 inch. It is seen in Table B-1, that the peak load for specimens forged in the ($\alpha + \beta$) phase field was twice that for specimens

forged in the β -phase field. The forging temperatures of the later were 150 to 200°F higher. In section (b) of Table B-1, composite structure specimens which were isothermally forged are described. In view of the final aim of the project of producing a dual-property disk, the combination chosen for the composite upset forging specimens was one having a central inner part made of Ti-6246, known for its better Low-cycle fatigue properties, and an outer rim-part made of Ti-6242 alloy with better creep resistance properties. The specimen glass coating was removed by sand-blasting before preparation for metallographic examination.

TABLE B-1
Upset-Forging

(a) Starting material: Ti-6242 (0.1 Si), ($\alpha + \beta$) structure after extrusion at 1775°F.
Reduction from 3" down to 1.2"
 ϕ 1" x 1.5"
Start Dimensions:
Specimen - D.G. 69, Die-bare
Lubrication: 30 minutes (Globar Furnace, Argon atmosphere)
Soaking time before forging: 0.5" per second
Ram speed: 15 seconds
Transfer time: 7 seconds
Total press time:

Air Cooling After Forging

Specimen No.	Die Temp. °F	Specimen Temp. °F	Peak Loads Tons	Final Dimensions Max O.D.	Height	Final Microstructure
75	700	1750	off-scale	1.639	0.700	($\alpha + \beta$)
76	700	1900	17	1.615	0.753	trans. β
77	1600	1750	27	1.535	0.700	($\alpha + \beta$)
78	1800	1750	21	1.525	0.690	($\alpha + \beta$)
79	1600	1900	12	1.570	0.690	trans. β
80	1800	1900	14	1.570	0.685	trans. β
ISO 1700	1700	1700	25	1.580	0.685	($\alpha + \beta$)
ISO 1900	1900	1900	13	1.545	0.692	trans. β

(b) Starting material: Ti-6246-Hub, Ti-6242-Rim, ($\alpha + \beta$) structure for both after combined extrusion.

All parameters as in section (a)

ISO 1700	1700	1700	24	1.568	0.695	($\alpha + \beta$)
ISO 1900	1900	1900	13	1.560	0.681	trans. β

Macro-Metallographic Examination

General Macroscopic Features

The upset forged specimens were cut in half along the compression axis direction, using an abrasive cutting wheel under its own weight (without any manual enforcement), while the specimen was completely immersed in a coolant liquid bath, kept at room temperature. The cutting procedure is very important since induced cold-work deformation on the cut surfaces ("surface burning") will leave marks that can not be removed by manual grinding, and will obscure the forging flow-lines pattern. One-half of the specimen was used for examining axial flow-lines pattern on the "along-the-compression-axis" direction cross-section, which is supposed to give an axisymmetrical shape. The other half was cut again, this time across the specimen (normal to the compression-axis direction) for examination of concentric structural variations along a radial line.

The specimens were roughed manually on a sequence of wet emery papers, each with smaller particle size. Then, they were polished manually on a rotating wheel covered with a suitable cloth, using an alumina slurry. No polishing with diamond paste was necessary. Finally, polishing with the alumina slurry took place for several hours on a "vibromet" (vibrating plate) device. The specimens were finally washed and cleaned in a ultrasonic-bath.

The outer surfaces of the specimens forged in the β phase field were rough ("Orange-Peel" appearance) due to surface reliefs of previous β -grains. Those forged in the $(\alpha + \beta)$ phase field show relatively smooth surfaces. The polished surfaces were macro-etched with the following

reagent: 5% HF, 10% HNO₃ in water.

Then, the specimens were photographed, with only slight magnification, using a "Polaroid" camera, under oblique lighting focused on the specimen's surface. The photographs are shown in Fig B-1, and in Fig B-2 for the ISO specimens. (No attention was made in the figures to put the specimens in the right upside direction relative to the upper and lower die-insert positions in the forging press).

Specimens #75, and #76, which were forged with die-inserts kept at 700°F, show strong chilling-effect in the form of upper and lower non-deformed zones (sometimes referred in literature on theory of plasticity as "false-head" zones). These zones have "triangular" boundaries in the ($\alpha + \beta$) forged specimen (#75). The previous contact surfaces with the die-inserts (outer surfaces of the non-deformed zones) show traces of the original cylindrical form dimensions of the specimen before the forging, pointing towards the existence of "sticking friction" between the specimen and the die-inserts during forging. The bulging curvature is high, and it expresses itself by the larger maximum outside dimension relative to other specimens (Table I).

Specimens 77 and 78, both forged in the ($\alpha + \beta$) phase field, show deviation from axisymmetrical form. The non-deformed zones moved apart from the specimen central-line axis. In specimen #77, strong kinking developed. Specimen #78 shows better uniformity, although due to probable temperature differences during forging between upper and lower surfaces, the deviation is more of a conical form. In contrast, specimens 79 and 80, which were forged in the β phase field, show highly uniform axisymmetrical forms.

The specimens that were forged in technical isothermal conditions (Fig B-2) show little bulging, but conical deviation in axisymmetry is observed. This results most probably from temperature differences between upper and lower die-inserts, since the upper one was put first into the die-block and had some time to cool down before the lower die-insert, with the specimen on top if it were inserted next. The estimated temperature difference might be as low as 20°F. However, the reason for the relatively large difference in radial expansion between the upper and lower sides of the specimen stems from the high temperature dependency of the flow-stress in the temperature range between 1600° and 1900°F for this material; this effect will be discussed later.

The ISO 1700 specimen (Fig B-2), forged in the ($\alpha + \beta$) phase field, shows pronounced deviation from axisymmetrical form (to be called "non-uniformity" later). The strongly developed kinking almost turned into a shear-band, running obliquely from the upper right corner through the specimen into the lower left corner. This behavior is shown in Fig B-2. The ISO 1700 composite structure (6242 + 6246 alloys) shows better uniformity (due to some stifening-effect to be discussed later), as do specimens ISO 1900 (both 6242 and composite 6242 + 6246). Following through the sequence of specimens (Figs B-1 and B-2): 75, 77, 78 and ISO 1700, all were forged in ($\alpha + \beta$) phase field, and they differ only by the die-insert temperatures. All specimens show a tendency to develop kinking and to become non-uniform during the forging. This stems from the low rigidity of the β -phase in the temperature range between 1600°F and the β -transus temperature. This will be discussed later.

In the next step, the same specimens were used for macroscopic examination of their flow lines. The flow line patterns give information on the amount of displacement each elementary unit-volume of the material experienced during the deformation. In cold-worked materials, the flow-lines can be easily detected since the macro-etching reagent reacts to the amount of locally-accumulated elastic-strain energy (either by selective amounts of etching, or selective amounts of depositions of a reactive constituent). In the case of hot-forged materials, especially titanium alloys which lack observable non-metallic inclusions, the flow-lines are difficult to detect. However, they can be followed through microstructural changes when observed at low-magnification. Continuum mechanics scientists usually prefer to scribe a grid pattern on the specimens cut into two parts along the axisymmetrical axis. The two parts are diffusion bonded back together again and subsequently processed to check the distorted part after the deformation. This may help to evaluate the effective strain and amount of displacement each elementary unit-volume of the material experienced during the processing. This is a tedious, step-wise viscoplastic technique, especially in upset forging that is required for determining the accuracy of numerical flow line predictions. It would be much easier, in a qualitative way, to appreciate these parameters by using some naturally observed flow-lines in the material.

Since in our case the starting material was extruded to develop the $(\alpha + \beta)$ microstructure, the primary- α grains are naturally elongated and situated along flow-lines in a fibrous microstructural appearance. This microstructure pattern can be used as a reference grid for distortion studies during upset forging in the $(\alpha + \beta)$ phase field.

If deformation takes place in the β phase field, the previous deformed β -grain boundaries, as seen within the β -transformed structure at room temperature, may also give clear information on the flow-line patterns.

After repolishing, all specimens were etched by a procedure that was found to enhance the visual appearance of the flow-lines, which are specially difficult to be seen in the $(\alpha + \beta)$ forged specimens due to the fineness of the primary- α grain size. The polished specimen was first immersed in a solution of 5% HF in water. (etching process can be observed by the large amount of bubble formation on the surface). When the surface started to turn black, the specimen immediately was transferred into a solution of 10% HNO_3 in water. This brightened the surface to some extent, and the residue film on it was in turn washed away by a strong stream of tap water. The procedure was repeated several times, until the flow-line pattern could be seen to exist with the naked eye (or with a magnifying glass) in the sun light.

In order to record macroscopically the specimen flow-line patterns, a macroscope with incident-beam illumination (shadowless) had to be used. Oblique illumination will blur the details. For this purpose a Nikon Photomacrography Multiphot with half-reflecting mirror for a 65 milimeter lens was used. However, due to the specimen size, three shots across the specimen had to be taken; one was taken in the center, and two were shot on each side. These three photographs had to be matched later into one complete macrograph. A 35 mm camera was used with high contrast film. The macrographs can be seen in Figs B-3 - B-12.

Macroscopic Flow-Line Patterns:
($\alpha + \beta$)-Forging Conditions

Fig B-3 shows the vertical flow line pattern of specimen 75 (die temp 700°F, Table I). Chilling-affected non-deformed zones exist on both ends of the specimen, having "triangular" (actually conical) form. The flow-lines within them are comprised mostly of those that existed in the original "as-extruded" material, since strong "sticking friction" actually existed between the specimen and die-inserts. The central part of the flow-line pattern, in the middle part of the specimen, show strong "squeeze-out" displacements due to the high compressive loading which exists there. The flow-lines bend sharply and tend to run parallel to the radial direction. This tendency diminishes for flow-lines which are situated further radially from the central axisymmetrical axis. Actually, somewhere further away from the direct compressive loading influence and approaching the circumferential free bulging surface, only bending of the flow-lines took place under. Conditions of tension probably dominated other stress states in this region. Thus, three major zones can be distinguished:

- "a". chilling-affected non-deformed zone.
- "b". central highly-compressed zone under confined stress conditions.
- "c". circumferential bulging zone (Barrelling) under nonconfined stress conditions.

In zone "a", no metal flow in the lateral direction took place whatsoever. In zone "b", high effective compressive strains with large lateral displacements occurred, while in zone "c" lateral material motion predominated.

Since almost no direct compressive loading exists in this region, the effective strains are small and a small tensile component may appear there. These zones were evaluated microscopically, and they are described in the next few paragraphs.

Fig B-4 shows the vertical flow-line pattern of specimen 77 (die temp 1600°F, Table B-1). Chilling-affected non-deformed zones do exist, although smaller than in specimen 75. The most important feature is the fact that these zones moved apart and away from the axisymmetrical vertical axis. Some kinking developed, as the upper part tended to move more to the left; and the lower part moved more to the right, resulting in non-uniform bulging. This kinking, as can be seen by following the flow-lines, is actually a forerunner of a shear bend, which might have been formed with higher reduction, from the upper left end, to the lower right end of the specimen in question.

Fig B-5 shows the vertical flow-lines pattern of specimen 78 (die temp 1800°F, Table B-1). Although the die-insert temperature technically was higher than that of the specimen, the flow line pattern shows that the dies were actually colder than the specimen. The evidence for this deduction is the occurrence of a chilling-affected, partially non-deformed zone on the upper side of the specimen. The size of this zone on the lower side is much smaller. The specimen expanded laterally (radially) along the friction surfaces. This was done by either incremental displacement of the lateral spacings between the vertical flow-lines within the chilling-affected zone, or it occurred mostly by lateral flow of the material parallel to the friction surfaces outside the chilling-affected zones, as is shown by the horizontal flow lines. The specimens have a

somewhat conical appearance with much lower bulging in comparison to specimen 77. The upper and lower lateral motions of the material along the friction surfaces took place in opposite directions. Although the specimen geometry looks uniform, kinking in the flow lines pattern can be observed, which could have been turned into a shear bend (from the upper right end to the lower left end of the specimen) with further reduction.

Fig B-6 shows the vertical flow-line pattern of specimen ISO 1700 (Table I). The lateral distortion of the specimen was higher compared with previous specimens #77, and #78. This specimen differs from the others in that the lubrication glass coating film was thicker: 0.028" against 0.006". The high lateral distortion shows large lateral spacings between the vertical flow-lines, indicative of horizontal material flow. This is shown for-example, by the flow-lines on the upper right side of the specimen. The specimen shows somewhat conical distortion, since the upper die-insert which was put first into the die block had more time to cool down than the lower die-insert with the specimen on top of it. The lower die and specimen were inserted just before the forging. The specimen shows that the external rim zone differs from the central part probably because it is under a less confined system of stress. This was confirmed by micro-metallography, and will be described later. However, the most important feature is the start of shear-band formation, as shown clearly by the excess of lateral material flow at the lower left end of the specimen. The highly kinked flow line pattern within the specimen center clearly shows this. The flow line pattern of the protruding material is complicated, and it resembles in-part that of the folding

pattern observed in specimen 75 (Fig B-3) at the lateral ends of the chilling-affected non-deformed zones, where, due to "sticking friction", the flow-lines curved over the ends before lateral material flow could proceed.

Macroscopic Flow Line Patterns:
 β -Forging Conditions

Fig B-7 shows the appearance of flow-lines based upon deformed β -grains, since the forging took place at a temperature above the β -transus. Although the microstructure transformed upon cooling to room-temperature, the previous β -grain boundaries gives information on the local effective strains, as well as flow lines. These flow lines differ from those observed for the $(\alpha + \beta)$ forging conditions in that they show the actual changes that took place in original imaginary horizontal reference lines, which were normal to the vertical flow line pattern of the $(\alpha + \beta)$ forgings. Fig B-7 is for specimen 76 (die temp 700°F, Table B-1). The chilling effect was strong, especially at the upper surface of the specimen, where the original diameter of the as-extruded bar before forging can be observed. Three major zones can be distinguished, as was the case for specimen 75. The horizontal flow lines in zones "b" and "c" can be highly appreciated, showing their spreading away from each other upon passing from zone "b" to zone "c". The boundaries of zone "a" are not triangular (conical), as they were in the $(\alpha + \beta)$ -forging conditions. The boundaries of zone "a" have a "parabolic" appearance. The folding over flow line patterns at the lateral ends of the non-deformed zones (zone "a"), which appear as a result of "sticking friction" between the specimen end surfaces and the die inserts, show the concave folding characteristics over the ends by means of high, local compressive straining.

Fig B-8 shows the appearance of the originally horizontal flow lines in specimen #79 (die temp 1600°F , Table B-1), and Fig B-9 shows the appearance of same flow lines in specimen #80 (die temp 1800°F , Table B-1). Both specimens have a highly uniform axisymmetrical geometrical form. Lateral expansion with pronounced folding at the ends took place in the partially non-deformed zones. The boundaries between these zones and the central part of the specimen are not truly "parabolic", but they have more of a wavy nature. The upper and lower boundaries are complementary in their wavy form.

The high geometrical uniformity manifests the high structural stability of the β -phase above the β -transus during forging. This negates the observation of the $(\alpha + \beta)$ microstructure below the β -transus during forging, where the tendencies for kinking and shear-band formation were observed as described above. It means that the $(\alpha + \beta)$ microstructure was unstable in the forging temperature range of between 1600° and 1800°F .

Fig B-10 shows the appearance of the flow-line pattern in ISO 1900 (Table B-1). The glass coating used for lubrication was somewhat thicker than the specimen thickness of the glass coating used on previous specimens (0.028" instead of 0.006"). The specimens show some conical distortion, since the upper surface was somewhat cooler than the lower one. The chill affected, non-deformed zone was almost absent. The central compressed zone is wide with moderate compression effective-strains. The circumferential zone is narrow with only a very small amount of bulging. Horizontal flow-lines could be seen almost all the way to the lower end-surface of the specimen. The lateral motion there actually consists of mini-folding pattern configurations.

Composite Alloy Forgings

Since the major goal of this project is to develop a dual property compressor disk, one that would have better creep resistance at the rim and better low-cycle fatigue resistance in the hub, it became apparent that this may call for forging a combined structure composed of two different alloys for the hub and rim regions. One choice was a combination of Ti-6242 and Ti-6246 alloys.

The Ti-6246 core material ($\alpha + \beta$ microstructure) of 1.45 " diameter was force-fitted into a Ti-6242 sleeve ($\alpha + \beta$ microstructure) of 2.9" outer diameter and 5" long. The end shape of the billet was turned into a $90^\circ - 1/2"$ bevel. The composite billet was extruded through a 1.1" die for a reduction ratio of 7.8:1 at 1675°F . The ram speed was 1.0 ips. The billet was diffusion bonded for 5 hours at 1500°F before extrusion. The coatings used for lubrication in extrusion were the same as previously described. The extruded composite bar was machined into specimens 1" diameter by 1.5" length. One specimen was isothermally upset forged at 1700°F , while the other specimens were forged at 1900°F (Table B-1 b).

Fig B-11 shows the appearance of the flow-line pattern in the ISO 1700 composite (Table B-1 b) specimen, and Fig B-12 shows it for the ISO 1900 composite (Table B-1 b) specimen. There is a good matching of flow-lines for the two different compositions. The specimens during deformation thus behave as one unit. However, the Ti-6246 core material seems to be more sensitive to temperature, since its conical distortion seems to be higher. The "weldability" of the two materials called for micrometallography examination, and this aspect of the problem will be described later.

Lateral Cross-Sections

Figs B-13 and B-14 are lateral cross-sections through the mid height of specimens 75 and 80. Fig B-3 is for an ($\alpha + \beta$) forging. The boundary between the central compressed zone (zone "b") and the circumferential bulging zone (zone "c") can actually be seen as a brighter contrast and to some extent concentric band. As it will be explained later, microstructural changes take place across this boundary. The microstructural changes seem to be due to discontinuities in the velocity (displacement-rate) field, which locally shows microstructures characteristic of higher temperatures. Fig 2.14 is for a β forging condition. In the central compressed zone larger equi-axed β -grains do exist while in the circumferential zone the grains are small and elongated along the circumferential concentric lines. In both cases the existence of a concentric flow-line pattern is proven.

Microscopic Metallographic Examination

The continuous material between the primary α -grains in the ($\alpha + \beta$) microstructure with its active slip systems actually carries the deformation of the specimen. With primary α -grain distortion conforming with it a way is provided to evaluate the local effective strains at the termination of processing. The long axis of a primary α -grain will point to the direction of maximum tensile distortion, whereas the short axis most probably is oriented towards the direction of maximum compression distortion. The direction of the large axis is most often coincidental with that of the flow-line, which in turn indicates the major displacement direction. The qualitative evaluation of both the state of effective strains and the displacements is simple, since the specimen is predominantly

(by magnitude) under compressive axial loading. If, however, shear-type loading becomes effective, as when kinking takes place or shear-bands form; slip-line patterns rather than flow-line patterns must be considered in order to understand the distortion of the primary- α grains. In any case, the amount of mean-free-path between the primary- α particles (spacing between flow-lines), as well as their possible alignment along other directions which do not coincide with the flow-lines direction must also be considered and carefully studied.

It is well known that part of the plastic energy is converted during the processing into heat. Adiabatic heating can only be reasonably considered as a realistic phenomenon found during local deformation or very high-rate straining (such as in shear-band formation), during the occurrence of discontinuities in the velocity field gradients, or during straining at shock wave propagation rates, etc. However, in bulk plastic deformation with the relatively "low" strain rates experienced during actual forging, it does not seem plausible that the temperature will increase high enough to cause drastic structural changes. Most of the generated heat will dissipate to the surroundings. But, if the material in the range of forging temperatures is not stable in the sense that it may recrystallize under dynamic conditions or undergo a phase-transformation, the plastic energy, instead of being dissipated as heat, may be consumed by accelerating the phenomenon. This is to say that both phenomena may be coupled in one and the same event, such as transformation-induced-plasticity (TRIP), shear-induced-transformation (SHIT), etc. This will express itself by local microstructural changes. In $(\alpha + \beta)$ -forging, forging changes the primary- α particle form and size, as well as the

surrounding material morphology. These changes may explain the micro-structural instability expressed by the specimen geometrical non-uniformity shown in the previous paragraphs.

$\alpha + \beta$ Forging Conditions

The metallography of the $\alpha + \beta$ forging conditions was systematically investigated by (a) following changes which take place in the flow-line directions, and (b) by the shape changes of primary α -particles that take place along predetermined lines on the specimen cross-sections that were previously used for the macroscopic study of flow-line patterns, or (c) by systematically following a chosen flow-line all the way from the upper non-deformed zone, through the specimen center into the lower non-deformed zone. This investigation was conducted by manually manipulating the microscope stage and simultaneously observing on the screen that the flow-line always will pass through the cross-line marker scribed in the middle of it. Exposures were taken occasionally along the flow-line without accurately fixing the position. A microscope stage that can be moved in two normal directions by means of micrometer screws will not facilitate the position fixing problem, since it will still be tedious and difficult to correlate two such readings with an accurate positioning of the specimen on the microscope stage.

In order to accurately position and continuously record the coordinates of the flow lines, two Linear-Voltage-Differential-Transformers (LVDT), should be mounted on the stage and normal to each other to follow the motion of the stage resulting from the manipulation of the micrometer screws. This type of position recording equipment will accurately fix the exposure positions and enable them to be recorded on an X-Y recorder.

Since such an X-Y manipulator-recorder system was not available, exposure position was only qualitatively determined to give a general idea of the metallurgical phenomena along the flow-lines in the different zones of the specimen. The magnifications chosen depended much on the actual primary α -grain size. For example, magnifications up to 100x were sufficient to observe flow-line directionality. 250x was found in most cases to give good evaluation of primary α -grain shape, as may be needed for the evaluation of the local effective strain. It also provided good resolution for the details of the secondary α -particles (the acicular-Widmanstatten pattern within the β -transformed structure). Also an appreciation of the distortion of previous β -grain boundaries could be obtained.

Quantitative measurements were carried out using a Quantimet 720 instrument and an epidiastope device for obtaining high-contrast prints from the same negatives used for the regular metallography. The different parameters were measured within a small live frame (360 x 360 points) chosen for the best part of the print (magnifications were 200x or 240x). First, the intercepts were measured in different directions on the print starting from the horizontal specimen direction, and other directions follow each other by 15° rotation. Finally, the vertical direction (forging direction) was investigated. The direction with the maximum number of intercepts was found to be normal to the flow-line direction.

The average aspect-ratio (AR) of primary α -particles along the flow-line direction was evaluated following an equation proposed by Underwood. (1) Accordingly, the aspect ratio (AR) is defined by:

$$\frac{\bar{L}}{\bar{L}} = \frac{\bar{d}}{\bar{L}} \quad \text{where:} \quad \bar{L} = \frac{L_L}{N_L} \quad \text{and,} \quad \bar{d} = \frac{\bar{A}}{L_L}$$

\bar{L} - average lineal intercept

L_L - length of lineal intercepts per unit length of test line

N_L - number of interception of features per unit length of test line

\bar{A} - average areal intercept

$$\bar{A} = \frac{A_A}{N_A} \quad (A_A - \text{area-fraction, and} \\ N_A - \text{Number of particles} \\ \text{per unit area})$$

$$\text{Therefore: } AR = \frac{\bar{A}}{(\bar{L})^2} = \frac{A_A}{N_A} \left\{ \frac{N_L}{L_L} \right\}^2 = \frac{P_P}{N_A} \frac{\{P_L\}^2}{2} \left\{ \frac{1}{P_P} \right\}^2$$

Where $P_L = 2N_L$, number of point intersections per unit length of test line.

$P_P = L_L = A_A$, point fraction, number of points (in areal features) per test point,

$$\text{which brings to: } AR = \frac{\{P_L\}^2}{4 \cdot N_A \cdot P_P}$$

Following the Quantimet strategy:

$$P_L = \frac{2 I_h}{L} \quad N_A = \frac{I_h}{A}$$

$L = A$ in the Quantimet, while I_h - is the number of horizontal intersections between the picture point matrix and the detected features.

Thus:

$$AR = \frac{\{I_h\}^2}{C \cdot A_\alpha}$$

Where C (= Count) is the number of features in the live frame field. A_α is the number of points falling within the α -phase in the live frame field. For specimen 75, Fig B-15 shows the form of the α -particles along a vertical line, which is situated a little aside from the vertical center line. (a) shows the original "as extruded" structure that was preserved in the chill affected non-deformed zone (major axis direction 90° , aspect ratio 2.33).

(b) shows strong bending as flow lines move outside the non-affected zone (major axis direction 30° , aspect ratio 2.41)

(c) shows the strong effect of compression, almost in the specimen's center (major axis direction 0° , aspect ratio 1.7). The elongated primary α -grains of the original structure became more equiaxed, and they tend to elongate along the horizontal-radial direction, which is the flow-lines' new direction. It is interesting to note that the secondary α -particles orientation is random spreading in all directions without preference to the direction of the flow lines. (In (b) some tendency to align with the flow lines was noticed). The previous β -grains are seen to be of the same order of magnitude as the size of the primary- α particles. Nothing much can be said about their deformation.

In Fig B-16, the shape of the α -particles along the specimen's horizontal center line changes in different positions.

(a) shows the microstructure near the specimen center; both the primary- α and the secondary acicular α -particles tend to align along the horizontal centerline. Aspect ratio of 2.36 is a biased value, since it is influenced by the secondary acicular α -particles.

(b) is from a position farther away radially along the center line. A local adiabatic thermal band appears in which the amount of primary α -particles is reduced and the amount of secondary α -particles increase drastically. This change in the amount of primary α -particles and secondary α -phase results from a discontinuity in the monotonously changing gradient of the velocity field. The extra energy is released during the deformation and transformed into heat that raises the local temperature and increases the local amount of the β -phase. The secondary acicular α -particles are aligned along the horizontal (radial) flow-lines direction, and bias the evaluation possibility of the aspect-ratio of the primary α -particles in the picture. (Since the pattern recognition mode for selected features measurements could not be used in our Quantimet instrument due to electronic instability of the function computer network, there was no way to get rid of the secondary particles effect. For example, in (b) the measured aspect ratio was 4.25. The thermal band is not concentric nor continuous, and it appears to form because of some local discontinuity in the flow-line pattern (presumably of textural origin). The thermal bands are found mostly near transition localities between zones "b" and "c" where a change in the state of strains takes place gradually.

(c) shows the structure appearance in zone "c", where vertically elongated grains reappear (major axis direction 75° , aspect ratio 1.55). These features can be interpreted to mean that the α -particles were not compressed very much, since the flow lines

in zone "c" follow concentric lines. Following metallographically a flow line running all the way from zone "a" to zone "c" at the specimen's mid-height center line, the aspect ratio of the primary α -particles did not change very much. However, the spacing between the flow-lines (Mean Free Path between the α -particles) was diminishing. The decrease in the spacing between the flow lines means, in addition to the strong outward material displacement, some radial compressive straining took place.

In the folding-over zone region of specimen 75, Fig B-17, flow lines running around the edge form a groove having many intrusions and extrusions at its surface. Each of these is bound to very localized shear bands. The folding was caused by die chilling which produced a deformation free zone and high sticking friction.

In specimen 77, the primary- α particles are smaller, and the volume fraction of the β -transformed material around them is larger than in specimen 75 (Fig B-18). At the center of the specimen where the compressive strains have maximum values, the primary α -particles are much finer and almost equiaxed in appearance (Fig B-18 c). (Compare with the "as-extruded" elongated particles (of Fig B-18 a). The secondary acicular α -particles are aligned in the horizontal flow direction. Along the horizontal center line, the primary α -particles tend to become coarser outward from the center direction (Fig B-19), and they lose alignment with respect to the horizontal direction of the flow-lines. This behavior occurred because the specimen became unstable and formed a kink (Fig B-19 b). This is better observed in specimen ISO 1700.

ISO 1700 micrographs were taken along a horizontal line just above the protruding material at the lower end of the starting shear band (Fig B-6) and parallel to the end surfaces. Going from left to right in Fig B-6, the microstructures in Fig B-20 (a) and (b) show flow-lines going from the upper right to the lower left of the micrograph in the external peripheral zone of the specimen. We assume that the peripheral zone is under a non-confining stress condition. At (c) the flow-lines' descending direction is diverted from left to right on passing from the external zone to the internal one, which is assumed to have a more confined stress condition. The flow-lines in the internal zone are shown in (d). In (e), a thermal discontinuity band can be seen running parallel to the flow-lines, but a more important feature is related to the primary α -particles. These α -particles tend to align themselves also in another direction. The impression of another aligning direction results from the α -particles having the same spacing between them along their flow line, as well as on each parallel flow line in an ordered manner. The second alignment direction results from a tendency to build a fibrous structure parallel with the direction of shear deformation. In (f), the ordered distribution of α -particles is completely disturbed. It is typical for the microstructure in the middle of a kinked zone. In (g) the α -particles start to resume their alignment along the flow-lines, and, in (h) and (i), the alignment is completely resumed. The microstructure in (h) and (i), like in (a) and (b), belong to the external peripheral zone of the specimen. In it, the primary α -particles are considerably elongated as in the case for the microstructures shown in (c) and (d), which belong to the internal zone. The α -particles

tend to become equiaxed and finer in the kinked zone, as seen in (e), (f) and (g).

Fig B-21 (a) shows the flow-lines at the right corner of the lower end surface. This part of the specimen was not affected at all during the forging. (b) shows the microstructure near the center of the lower end surface, where, due to high compressive strains, the α -particles tend to become equiaxed. The lateral displacement of the material seems to disturb the flow-lines pattern. Careful observation shows that the α -particles tend to align themselves along two sets of opposite slip directions, each about 45° from the normal to the end surface. The combined slip effect permits the lateral displacement of the material, which is visualized by the increment of spacing between α -particles in the lateral direction. Adjacent to the surface, mini folding-over configurations build up one after another in the radial direction. (c) shows the flow-lines near the left side of the lower end-surface approaching the lateral protruding part of the specimen. The flow-lines pattern resembles an incomplected major folding-over configuration. This is the same all the way through the cross section of the protruding part, where the flow-lines are absolutely not parallel to these surfaces, as is the case following folding-over due to sticking friction (specimens 77 and 78) where the flow-lines run parallel to the surfaces. It should be noted that the α -particles still remain equiaxed.

Fig B-22 (a) shows the microstructure of the kinked zone at 250x magnification in the middle of the ISO 1700 specimen. The primary α -particles are situated on flow lines running obliquely from the upper

left to the lower right corners of the micrograph. The α -particles form a fibrous structure in the direction from the upper right to the lower left corner of the micrograph, because they are aligned along the shear direction and parallel to the β -transformed strips. (b) and (c) micrographs show the α -particle alignment in two opposite slip directions, each about 45° from the vertical direction, near the lower end surface of the specimen. Very near the surface, as in the lower side of micrograph (c), mini folding-over configurations of flow-line patterns may be observed.

It is important to note that whenever the displacement component of the deformation field in the specimen is higher than the straining component, the flow lines will be continuous in the different zones of the forged specimen. This was the case in specimens 75, 77, and 78. There the lateral motion of the material is with the flow-lines running parallel to the end surfaces. However, when the strain component is larger than the displacement one, the α -particles tend to align themselves with the slip-directions; the combined straining created the lateral motion. When external shear loading became effective in the deformation process, the

α -particles tend to align themselves also with the shear direction, and in some cases the original flow-line pattern may be disturbed. This was the case within the kinked zone of specimen ISO 1700.

β -Forging Conditions

Deformation takes place in the β -phase when the alloy is forged above the β -transus temperature. Each β -grain is distorted in accordance with the local state of effective strain. The maximum elongated axis of a grain points towards the direction of the major displacement flow. This

differs from the ($\alpha + \beta$) preform forged specimens, where the elongated axis of the deformed primary α -particles was the reference for tracking the distortion of the originally vertical reference lines (the so called vertical flow-lines); while the major displacement was actually in the direction normal to them. The vertical flow lines served mostly as a means for appreciating the overall specimen distortion. When the alloy was forged in the β phase field, the maximum elongated axes of previous β -grains serve to track the distortion of the originally horizontal reference lines (the so called horizontal flow-lines). The direction of major displacement coincide with them, so they provide a means for appreciating the mass-flow directions of the material. The β -grains were equiaxed before forging as a result of heating the specimen to the forging temperature, and they do not have any relationship to the original "as-extruded" microstructure of the material.

In Fig B-23 (a), the original microstructure of equiaxed β -grains, is preserved in the chilling affected non-deformed zone of specimen 80. In (b) along the vertical center line, the deformed material structure at the mid-height between the specimen center and the end-surface shows the compressive-deformed β -grains. Micrograph (c) was taken from near the specimen center. In Fig B-24 (a), the highly elongated grains in the horizontal, radial direction at the center of the specimen show a heavily compressed structure. In (b), on the horizontal center-line, midway between the specimen center and circumferential free-surface, the grains show less compressive distortion. In (c), taken near the circumferential free-surface, the grains are still compressively distorted. This differs appreciably from specimen 76 (which had high chilling effects) for which the grains near the free-surface were found to be almost equiaxed. In specimens 79 and 80,

the axial effective compressive strain is high everywhere on the mid-height and through the cross section of the specimen, while in specimens forged in the $(\alpha + \beta)$ phase field, the axial compressive strains near the free-surface are very small and the material there bends in the outward (buckling) direction. It can therefore be concluded that in β -forged specimens separation between central confined zone, and peripheral non-confined zone in terms of states of stress during forging have little meaning, resulting from both the lower flow-stress of the single β -phase and the higher forging temperature. (Compare with $(\alpha + \beta)$ structure, forged in $(\alpha + \beta)$ phase field) To summarize, the deformation process for specimens forged in the β -phase field, in view of the respective flow line patterns, is different from the observed mechanisms for specimens forged in the $(\alpha + \beta)$ -phase field.

Fig B-25 (a) shows distorted β -grains in specimen 76, at 100x magnification. (b) in specimen 80 (240x mag) shows that the α -plates in the β -transformed structure tend (with high probability) to align themselves normal to the elongated axis of the previous β -grains upon cooling after forging. (c) shows the same behavior in specimen 76 (400x mag). There is very little data available on the crystallographic details of the β -transformed microstructure. If one however accepts that the boundary between α and β neighbor plates is a trace of an alpha prismatic plane⁽²⁾, and regarding Buerger's crystallographic relationship between α and β , it means that during the deformation of the β -phase one of the slip (110) planes was actually parallel to the vertical flow-lines and therefore not active in the slip process. But it also means that the other active (110) slip planes were oriented in such a way that

a tangentially directed deformation along horizontal concentric lines was predominant. This was actually observed to be the case of lateral cross sections (see paragraph 2.24).

Composite Alloy Forging

Optical and Scanning Electron Microscopy of the boundary between the inner Ti-6246 part and outer Ti-6242 part in the as-extruded material shows the appearance of some α -case on both alloys. This probably results from entrapped air left between the two parts during preparation of the composite bar. In the Ti-6246 alloy, a Widmanstatten secondary alpha instead of the regular matrix of β -transformed structure occurred between the primary alpha particles, and in Ti-6242 the primary alpha particles became larger and equiaxed. Although the α -case is responsible partially to the microstructural appearance in the interface, there is proof that the zones adjacent to the boundary experienced higher temperature than the total specimen. After upset-forging in ($\alpha + \beta$) phase field, the microstructures did not change drastically near the boundary. The primary alpha grains became somewhat deformed on the Ti-6242 side and towards the outer direction. Adjacent to it the amount of primary alpha was reduced in comparison with the structure elsewhere. The Widmanstatten structure was finer on the Ti-6246 side, and the amount of primary α -phase was reduced adjacent to the Widmanstatten structure. The amount of primary alpha reduction proves that the temperature was higher near the boundary, probably arising from tangential velocity discontinuity in the velocity field since the two alloys differ in properties such as ductility, rigidity, etc. This means that each alloy deforms separately but in conformity with each other to preserve flow-line pattern continuity in the total specimen.

Discussion: Non-Uniformity and Instability

This discussion will summarize a study of the factors responsible for the geometrical instability of the specimens which manifests itself in the forms of kinking and shear-band formation. These instabilities take place during the forging in $(\alpha + \beta)$ -phase field, i.e., in the temperature range between 1600° and 1800° F. The instability phenomena was not found in forging done in the β -phase field (above 1815° F), where the specimens kept their axisymmetrical geometry. Friction and chilling effects are not the major cause for nonuniformity in metal flow, since they appear in all the cases. It is more logical to assume that the inhomogeneous flow stems from microstructural instability which appears in titanium alloys in the critical range of temperatures just mentioned. The instability arises from both the high temperature-dependency of the flow stress and the low rigidity of the β -phase in this temperature range. These two factors and their mutual effects will be discussed qualitatively in order to present a model for the explanation of inhomogeneity which forms under the conditions of forging in the $(\alpha + \beta)$ -phase field.

Friction and Chilling Effects

The compression of a cylindrical specimen between parallel dies shows that the friction which prevails over the end faces is an important factor in causing barreling of the specimen. However, cooling of the hot workpiece in contact with the colder dies has the same effect as friction, and separation of the chilling and friction effects is extremely difficult.

For the case of die chilling, the specimen exhibits considerable resistance to deformation, since the upper and lower faces are at lower temperatures than the central portion of the specimen. Schey (3) first noticed in hot forging of steel that the end faces may increase their areas by folding the cylindrical side over the ends of the end-faces and against the die interfaces. The folding-over mechanism is very important for the lateral deformation of the specimen if sticking friction prevails over most of the end surfaces. The shape development factors due to true barreling and due to folding-over of the side face are actually not separable. It was suggested that the lubricant, under the high compressive loading, develops a sufficiently high pressure which may cause plastic deformation in the central region of the end-faces, while the peripheral area will be more exposed to boundary contact conditions. The "squeezed-film" effect, measured by the entrapped film thickness, will be higher as the end-face surface diameter and the approaching velocity between the specimen end-face and the die-insert surface increase in magnitude. The hydrostatic pressure created by the thick lubricant film will support a considerable amount of the compression loading and give a lower coefficient of friction. A sticking friction zone may develop in the periphery of the end-faces with each increment of reduction since the lubricant film becomes thinner and thinner in this region. Folding-over flow eventually occurs when direct contact between the flowed workpiece and dies is made. Thus, the interface shear strength is expected to increase as a function of end-face lateral expansion. Steady state conditions are never achieved, as the lubricant is exposed to a pressure-temperature-velocity combination which changes continuously during the deformation.

The coefficient of friction is expressed by $\mu = \frac{F}{P} = \frac{\tau}{\rho}$, where F is the lateral force, and τ is the lateral (Tangential) stress resisting the relative motion between the workpiece and the die. P and ρ are respectively the load and stress normal to the surface. Now, $\tau = m\tau_0$ where τ_0 is the shear strength of the deforming material and m is a fraction making $\tau \leq \tau_0$. During the lateral motion τ increases and when it becomes equal to τ_0 the movement along the interface is arrested and the friction actually becomes "sticking friction". The lateral deformation then can only be continuous by the "folding-over" mechanism. The coefficient of friction may either remain constant or change with the increment of the stress normal to the surface. This means that there is no fully acceptable way for representing the frictional condition mathematically.

The chill affected zone expands laterally by horizontal displacement normal to the vertical flow lines in the $(\alpha + \beta)$ forged specimens until the m factor becomes equal to unity. In other words, the spacings between these flow lines increase. When m becomes equal to unity, folding-over flow takes place. Further horizontal displacement now takes place with the previous vertical flow-lines in the horizontal direction parallel to the specimen friction surface. This condition was shown in the previous section on microscopy. If the lateral resisting stress increases until m becomes equal to unity once again, another folding-over flow may take place to permit further continuous lateral motion along the end surface. This situation may repeat itself several times. The velocity of the lateral displacement and the local effective strains increase with the radius. No strain hardening of the $(\alpha + \beta)$ preform material occurs when forged below the β -transus temperature, but the lateral resisting stress may increase due to the high strain rate sensitivity of the alloy.

The end result could be specimen kinking and shear band formation, especially since this alloy exhibits low-rigidity. These points will be explained and discussed in the next paragraphs.

Temperature Dependency of Deformation Resistance

The forging stress is a function of the forging strain, strain-rate, temperature, microstructure, and chemical composition. Buhler and Wagener (4) have proven that pure titanium and all types of titanium alloys (α , ($\alpha + \beta$), and β), when compressed isothermally show that: (1) the forging stress increases with decreasing temperature and with increasing strain rate, and (2) the strain-hardening decreases with increasing temperature after yielding has been reached. In pure titanium above 1100° F, stress-strain curves show very little strain-hardening after some initial amount of straining, which decreases with increasing temperature, and tend to become horizontal. In α alloys (e.g., Ti-5Al 2.55Sn) above 1100°F and after some initial straining, the stress-strain curve actually shows some softening. It will become horizontal without softening only at 1650°F and above. In ($\alpha + \beta$) alloys (e.g., Ti-6Al4V), softening characteristically starts already above 400°F. The same is true for β -alloys (e.g. Ti-13V11Cr3Al). These curves will become horizontal without softening at 1650°F and above. The softening at the lower temperatures is due to recovery, while at about 1600°F, it is mostly due to dynamic recrystallization. At temperatures approaching the β -transus, it is most probably due to transformation-induced-plasticity, and this will be discussed below. (See Ti-6Al4V in Fig B-26).

The forging stress versus temperature curves (at given strains and strain-rates) show linear dependency (on log-linear scales) up to a certain temperature, then a sharp fall within a range of temperatures. This behavior followed again by a linear dependency of the flow stress on temperature above that range. In pure titanium the sharp fall range is between 1500° and 1650°F due to the allotropic phase transformation, and in the α -alloy it is between 1650° and 1800°F, which is dependent on the α -stabilizing effect of the different elements. In the ($\alpha + \beta$) alloy the range starts at 1500°F, and in the β -alloy at 1100°F, and the effect is attributed to phase-transformation. (Example for Ti-6Al-4V in Fig B-27).

A careful study on the differences encountered between ($\alpha + \beta$)-preforms and β -preforms during the isothermal forging of Ti-6Al-4V alloy below the β -transus temperature (1835°F) was carried out by Chen and Coyne.⁽⁵⁾ It was shown that the stress-strain curves for the ($\alpha + \beta$)-preforms exhibit very small strain-hardening, and they tend to become either horizontal or show slight softening. The stress-strain curves for the β -preforms show appreciable drop in the forging stress after going through a maximum flow stress, which is later followed by a horizontal (constant stress) part. This was observed at or below 1750°F, while above this temperature the curves tend to become completely horizontal. The yielding forging-stresses of the β -preforms are higher by some 20% than those of the ($\alpha + \beta$)-preforms at the various temperatures. This was found also for the finish forging-stresses which generally are higher in the β -preforms. It was suggested that the observations are consistent with the fact that the β -preform microstructures have greater creep resistance than those of the ($\alpha + \beta$)-preforms. The plots

of the forging stresses versus temperature for all the preforms in the critical range of temperatures between 1500°F and 1800°F show a very strong temperature dependency.

Based on the Ti-6Al-4V work just described, Chen⁽⁶⁾ carried out the same type of study on Ti-6242Si. Following his results (Fig B-28), the variation of yielding forging-stress with temperature for upset forging is shown. The descending slope of the curves in the critical range of temperatures below the β -transus is higher for the β -preforms than for the $(\alpha + \beta)$ -preforms. If the temperature dependence of the flow stress is taken as a measure for the cause of heterogeneous flow, the β transformed microstructure should show lower uniformity. This behavior is to be expected since small local temperature fluctuations will cause higher differences in deformation resistance than one would anticipate for $(\alpha + \beta)$ preform structures. Examples of true stress-strain curves for isothermal forgings of $(\alpha + \beta)$ and β -preforms are given (Fig B-29). They show a strong softening effect for the β -preforms and a low strain-hardening behavior for the $(\alpha + \beta)$ curves. It was noted that at 1800°F the β -preforms may require a lower forging stress than the $(\alpha + \beta)$ -preforms. Semiatin⁽¹³⁾ obtained the same type of true stress-strain curves for β - and $(\alpha + \beta)$ -preforms of Ti-6242Si alloy isothermally forged in different temperatures (Fig B-30). High softening is observed in the curves obtained for β -preforms at lower temperatures of the critical range of forging temperatures. The curves obtained for $(\alpha + \beta)$ preforms show very moderate softening.

The differences in the softening mode of the true stress-strain curves show that the β -transformed microstructure has much lower stability during forging than the $(\alpha + \beta)$ microstructure. In the

latter, the true stress everywhere will be kept almost at the same value. Although in different localities within the specimen the true strains are much different. These fluctuations in stress values may cause local crack formation. Thus, high stress differences caused by local temperature fluctuations and the instability of the β -preform microstructure combine to make forging difficult in the $(\alpha + \beta)$ phase field in the vicinity of the β -transus temperature.

The strong temperature dependence of the forging stress in the temperature range between 1600° and 1800°F stems from several factors. First, the β -transus line (shown in Fig B-31) at the lower values of the β -stabilizing elements concentration declines slowly with concentration increment. Thus, high concentration differences can occur along the β -transus line for small fluctuations in temperature. This was found to be the actual case in the critical range of temperatures concerned for Ti-6242. Small increments in temperature therefore cause large increases in the volume fraction of the β -phase with a corresponding reduction in its stabilizing element content. The flow-stress of hcp α -titanium is expected to be higher than that for bcc β -titanium phase for the same alloy at elevated temperatures. The flow stress of each phase usually shows a decrease in value that is inversely proportional to temperature. As a first approximation, the flow stress of $(\alpha + \beta)$ mixture of phases equals the simple addition of the values of the flow stresses of the separate phases in question each multiplied by its volume-fraction. The flow stress analysis is actually more complicated than implied by the law of mixtures, since it depends on (a) the structural morphology at each temperature; (b) the mode of deformation due to special compression

properties; and (c) the different concentrations of the β -phase which, as will be shown later, dictates the rigidity of the β -phase. Due to these complications, the stress should rather be called the forging-stress and not the flow-stress.

Softening of the β -preform stress-strain curves is due to the following different possible mechanisms:

1) The softening results mostly from dynamic recrystallization which may take place during the processing either by: (a) diffusion controlled α -platelet thickening in the β -transformed structure (of the material surrounding the primary- α grains in the $(\alpha + \beta)$ -preform case, or the total structure in the β -preform case) (b) grain-boundaries sliding along α/β interfaces or previous β -grain-boundaries.

2) The horizontal type curve seems to result from a transformation-induced-plasticity (TRIP effect), where, as a result of local high stress development, relaxation may take place by means of phase transformation. Locally, small colonies of transformed beta structure may transform to β , making it possible for grain boundary migration. In the $(\alpha + \beta)$ preforms, after upset forging, the microstructure between the primary α -grains has the appearance of many secondary acicular (Widmanstätten like) α -grains, whose orientation seldom bears any relationship to the flow-lines observed by means of the directionality of the deformed primary- α grains. Evidence for the increase in the amount of β -phase with forging temperature is provided by the fact that the primary- α grains in the $(\alpha + \beta)$ preforms were smaller with increasing forging temperature; or, in forgings of the same temperature, the lower was the chilling effect due to higher temperature of the die inserts. The secondary acicular- α grains seem to precipitate from the material surrounding the primary α -grains during forging and while cooling. Precipitation during the heating

period prior to forging does not seem reasonable, since no directionality was observed in their orientation.

There is very little information in the literature about the microstructural changes that take place during the hot working of $(\alpha + \beta)$ or β -transformed structures below the β -transus temperature. Based on our microstructural observation for the case of the $(\alpha + \beta)$ -preform having a transformed β -matrix, it is plausible to conclude that deformation during forging occurs by hardening and softening events that are in parallel. Deformation probably proceeds via the following events:

(a) The volume fraction of the β -phase increases while the α -plates unite and thicken into secondary acicular α -grains, rejecting the β -stabilizing elements. The β -phase precipitates heterogeneously and grows around the boundaries of the acicular α grains, while the latter's composition approaches the equilibrium value pertinent to that temperature. The β -phase then completely surrounds the secondary acicular α -grains and inhibits their recrystallization.

(b) The β -grains deform and rotate by means of grain-boundary sliding along the α/β grain boundaries.

In the upper part of the critical range of temperatures there seems to be enough thermal and mechanical energy to completely convert the β -transformed structure into β -phase. This β -phase subsequently transforms to acicular α -grains that coarsen with time. The deformation will follow the transformation events (Transformation-induced-plasticity) while the stress is kept almost constant. Little observed softening is due to grain boundary sliding and diffusion controlled

recrystallization. The amount of the β -phase formed, in view of the high forging load applied to the specimen, seems to increase above the thermal equilibrium amount. This behavior is presumably another means for stress relaxation. Pressure is another intensive parameter in this thermodynamic system, giving it an additional degree of freedom. This is equivalent to saying that the stress field reduces the β -transus temperature. The excess amount of the β -phase reduces after the forging and during cooling by accelerating the kinetics of precipitation of the secondary α -grains.

In the β -transformed structure, the sequence of events, during the forging in ($\alpha + \beta$) range of temperature, is to some extent different and will be discussed later.

Superplasticity and High Strain-Rate-Sensitivity

In the present study the ram speed used for upset forging was 0.5" per sec (ips). This is equivalent to a nominal strain rate of 0.5 sec^{-1} (true strain rate of 0.7 sec^{-1}) for the specimens in question. However, since it was found that the ($\alpha + \beta$) titanium alloys exhibit superplastic properties at very low nominal strain rates (about 10^{-4} sec^{-1}), it is of interest to briefly discuss the topic. It is also of interest because strain rate sensitivity of the alloy is an important factor which controls its deformation behavior during forging.

Lee and Backofen⁽⁷⁾ have shown for different titanium alloys, in the critical range of temperatures below the β -transus, that the measured values of strain-rate-sensitivity (SRS) for a given strain-rate depends strongly on temperature. SRS rapidly increases with increasing temperature. At each temperature, the maximum SRS value was observed

at a different strain rate. In order to get superplasticity, the strain-hardening factor must be very low, approaching zero, to avoid the deformation instabilities (e.g. necking in uniaxial test specimen). The strain-rate sensitivity must be high enough to inhibit localized flow or local plastic instability by the strain-rate hardening reaction of the material. In the Ti-6242 alloy studied, the strain-hardening factor is very small and negligible, while the SRS factor is relatively high as was shown by Chen.⁽⁶⁾ This is also true for other $(\alpha + \beta)$ alloys.⁽⁴⁾ The flow stress was shown to decrease sharply with increasing temperature in the critical range, and, in order to avoid raising of the flow stress due to strain-rate hardening, it is important to use very low strain-rates (note that $\dot{\sigma} = K\dot{\epsilon}^m$), of the order of 10^{-4} sec^{-1} . The theory of superplasticity states that during deformation a viscous flow component must be active in order to relax a possible hardening due to crystallographic flow. Lee and Backofen⁽⁷⁾ suggested possible mechanisms for the viscous flow: Newtonian viscous boundary shear; Herring-Nabarro diffusional creep; Coble grain-boundary diffusional creep. All three may account for dynamic recrystallization. They also mentioned the importance of deformation occurring within the range of transformation temperatures (Transformation-Induced-Plasticity). In order to obtain high SRS, the microstructural morphology must be very fine, so there will be strong hardening available in case the local strain-rate starts to change. The fine structure is also needed to avoid strain-hardening by permitting quick stress relaxation by means of short range diffusion. The average mean-free-path between the particles of the discontinuous phase (L) provides a relative measure for evaluating the microstructure. A general relationship for a viscous flow process is:

$\dot{\epsilon} = \frac{\sigma}{L^a kT} \exp\left(-\frac{\Delta H}{kT}\right)$. It means that for a given strain rate the flow stress is related to the mean-free-path by $\sigma \propto L^a$ (a is a constant that depends on the type of viscous flow mechanism). Since the activation energy found experimentally is for diffusion, the viscosity (the reciprocal of strain rate) is related to L^a/D (D is diffusivity). Higher diffusivities are obtainable at higher temperatures, while avoidance of structural coarsening calls for relatively short processing time. Phase transformation will increase diffusion rates. During ideal superplastic deformation grain size should not change, but in practice some grain growth is observed. This grain growth is probably due to an excess of mechanical energy over the thermal energy needed. If a still higher strain-rate is used, the deformed grains might be expected to strain rate harden and subsequently relax by recrystallization to form a smaller grain-size.

Paton and Hamilton⁽⁸⁾ stated that the microstructure of certain alloy systems cannot adequately be characterized by a single parameter such as grain size. The two phase ($\alpha + \beta$) titanium alloys are an example.

Microstructural parameters such as uniformity of grain-size, volume fraction of α and β phases, grain aspect ratio and volume fraction of transformed β are among the parameters which must be used for a complete description of factors which might influence superplasticity. Since the grain boundary contribution to superplastic deformation may be of the nature of grain boundary sliding and/or enhanced grain-boundary diffusion, the rate of deformation is enhanced as the grain-size is decreased. For a non-uniform grain size, the kinetics of the grain-boundary diffusion process will be much slower around larger grains; thereby affecting the

overall response of the material to the imposed strain rate at a given flow stress. The presence of primary α grains is a case of such non-uniformity. Elongated grain structure would also be expected to affect the superplastic deformation process, since the grains could not rotate. Also, the diffusion distances are large along the length of the grains and impede stress relaxation. A significant difference in the deformation characteristics of the two phases is likely, since the diffusion kinetics differs by as much as a factor of two. The β -phase exhibits the higher diffusion rates. It would therefore develop a more rapid deformation rate, if diffusion controlled mechanisms are dominating the process. Superplastic deformation causes an overall reduction in texture, and this has been interpreted to be caused by random grain boundary rotation arising from grain boundary sliding. Experimental results did indicate that the effect of α -phase texture on superplasticity is small, if it exists at all. The above mentioned microstructural features appear not to impair the high SRS value in Ti-6Al-4V alloy, but to intervene in the superplastic deformation process and reduce the total elongation by causing premature rupture.

Chen ⁽⁶⁾ evaluated SRS for the Ti-6242 Si alloy using relatively high strain rates 0.1" to 0.5" per minute (ipm). Accordingly (Fig B-32), the critical temperature range starts at 1500°F and the maximum values for the SRS were 0.4 and 0.3 for the ($\alpha+\beta$) and β -preforms, respectively. This means that significant recovery may not take place during the deformation at these rates. Inversion in SRS was observed above the β -transus temperature as expected.

The relatively high SRS may control the type of barreling an isothermally upset forged specimen will show. If on one hand the friction on the end surfaces is very low, and on the other hand, the strain-rate is high at the mid-height of the peripheral free surface, a geometry of

inward barreling may appear due to the strain rate hardening effect. High SRS may be the responsible cause for the $(\alpha + \beta)$ -preform kinking during the forging and for the formation of a shear-band. Assume that after folding-over, resulting from "sticking friction" at the end surfaces, the material continues its lateral expansion by flow parallel to these surfaces. The lateral friction resisting stresses will increase again, with the increment of the displacement velocity being in the radial direction. However, since the strain-rate of the deforming material may also be increased, the strain-rate hardening will add up to the lateral friction resisting stress and stop the displacement. Stopping of the displacement may appear in different places on the upper and lower end surfaces and a strong moment of forces will build up that is strong enough to cause the specimen to kink upon further reduction.

Rigidity of Beta and Alpha Phases

Fisher and Dever⁽⁹⁾ suggested that there is considerable evidence that the magnitude of the elastic shear modulus $C' = (C_{11} - C_{12})/2$ in metallic bcc structure is closely related to the occurrence of martensitic phase transformation, and it is thus a useful parameter for estimating the relative stability of bcc crystal structures. In bcc metals and alloys where unfilled d-electron shells are not involved, C' is quite small relative to the other principal shear modulus C_{44} and the ratio C_{44}/C' is in the range of 8 to 12 in the alkali metals and in disordered Cu and Au alloys. Their study dealt with the values of C' in bcc structure in group IVA of the periodic table, to which titanium belongs. These elements undergo bcc \rightarrow cph transformation upon cooling. The transformation temperature is depressed when transition element atoms of higher group number are added. They all have bcc structures, and their C' values are in most cases

greater than C_{44} (which is not the case in titanium). They have shown that the value of C' is very closely related to the d-electron concentration in titanium alloys and that the phase transitions from the β -phase is associated either with the vanishing of C' or its very small value (C' in pure titanium is considerably less than zero at room-temperature, explaining the inability of retaining bcc by quenching). The ω -phase appears in β -phase compositions equivalent to electrons per atom ratio of 4.14 (valence based on the total d plus s electrons in a free-atom configuration). The appearance of ω -phase markedly increases the elastic moduli. As for the influence of temperature on C' for the e/a ratio in the bcc-phase regime, it was shown that there appears to be no significant difference between e/a dependence of C' at room temperature and at 1800°F, since C' decreases linearly with increasing temperature. However, the e/a ratio at which C' becomes greater than zero decreases with increasing temperature with the result that pure bcc titanium becomes structurally stable at 883°C, with e/a = 4.0.

Collings and Gegel⁽¹⁰⁾ also suggested that the mechanical properties of pure metals and alloys are electronic properties. In proper description the metals and alloys are regarded as an assembly of positive ions stabilized in position by interaction with the conduction electrons. This description leads to the understanding of the interactions which control the ionic motion during deformation, and by that explain phase stability and solid solution strengthening. The interactions are expressed in terms of the cohesive energy (E_{coh}), a component of the internal energy (E), where : $E = E_{coh} + TS$ (T -temperature, S -entropy). The cohesive energy may be described by a series expansion into components representing contributions by the electron gas itself and by body interactions, as

follows: $E_{coh} = \sum_{i=1}^m E_i$. The first term is structure independent which represents the contribution by the electrons plus the self energy of the ions embedded in it. This is a dominant term which is responsible for the ductility of metallic solids. The second term depends on pairwise (central force) interactions, the third on triplet interactions between ions, and so on. The shear modulus would be zero were it not for the second and higher terms. The degree to which metals resist deformation depends on the degree to which the conduction electron states are perturbed by the presence of solute atoms. The theoretical implications are discussed by Collings, Gegel and Ho⁽¹²⁾. The relationship between phase stability and other physical properties, such as: electronic specific heat coefficient; Fermi density of states; Debye temperature and magnetic susceptibility are discussed by Collings, Ho and Jaffee⁽¹¹⁾.

Titanium alloys may reasonably be subdivided into two main classes: "Ti-T₂" alloys, where T₂ stands for another transition element (e.g. V, Cr, Fe, Mo), and "Ti-B" alloys, where B stands for non-transition element (e.g. Al, Ga, Sn). (The interstitially dissolved elements such as oxygen or nitrogen behave like B-elements, while hydrogen behaves like a T₂-element). The substitution of T₂ atom for titanium in the lattice brings about only relatively small perturbation of the electron states. Stabilization of the bcc β -phase is achieved by alloying with the T₂-elements, which add conduction electrons to titanium and increase the occupancy of the d-band. This makes the appearance of the hexagonal structure less favorable. The strengthening effect by T₂-elements is mostly attributed to "size-misfit" and "modulus-mismatch" factors. The perturbations in fact are so weak that the properties may often be indexed by the average number of valence electrons to atom ratio, rather than in

terms of the particular elements involved. An important property that can be so described is the structural phase stability, as was shown to be related to the elastic shear modulus C' . The shear modulus may therefore be used as an indicator for the bcc stability since it is a measure of the extent to which the lattice resists deformation at constant volume (Fig B-33). The maximum stability at room temperature is found at $e/a \approx 5.9$. The β -phase becomes increasingly soft to shear stress as e/a decrease in the β -regime. Stiffening may appear at $e/a = 4.3$ or below due to the precipitation of the ω -phase. Otherwise, with lower e/a ratios the single phase β -alloys exhibit pronounced softening of their elastic shear constants, and the vanishing at $e/a = 4.1$ coincides with the lowest limit of stability of the bcc phase, at which martensitic (shear) transformation takes place.

The addition of B-elements ("s-p" elements) to titanium results in a strong perturbation of the electronic states. The alpha titanium electrons tend to avoid the B-element cells; hence they are strongly scattered by them. Since the maximal d-wave function amplitudes remain at the transition metal ions sites the further addition of the solutes may be regarded as only "diluting" the lattice of the titanium atoms, the d-electron bonds between which become tighter and more directional. The solid solution remains basically "titanium-like" which explains the α -stabilizing effect of the B-elements. Strong non-central interaction between the ions result in a pronounced structure-dependent cohesive energy. As alloying proceeds, intermetallic compounds may be formed (such as α_2 - Ti_3Al). Readjustment of the energy states of a solute B-element in titanium through the formation of s, p, d hybridized bonds

will form strong interactions or directional bonding between B and its Ti neighbors. The localization of a large fraction of the conduction electrons occur, and the occupancy of the titanium d-band is reduced. Therefore, the electronic strengthening effect will increase with the atomic fraction of the B -elements. It was found that the effectiveness of the strengthening is proportional to the thermodynamic interaction strength parameter (I) which is defined by: $I = \Omega_{ij}$, where Ω_{ij} is a pairwise interaction parameter given by: $\Omega_{ij} = Z \left\{ E_{ij} + \frac{(E_{ii} + E_{jj})}{2} \right\}$ where: Z, the coordination number, and E_{ij} are the interaction energies between atom i and atom j. According to Collings and Gegel⁽¹⁰⁾ the strength promoted by the dissolved B -element in titanium is not only due to the highly structure dependent cohesive energy, but to the fact that local coordinative groups of Ti_xB are formed. These groups cause strong dislocation pinning, when B atoms along the dislocation line, by actually occupying sites of reduced symmetry, become part of the directionally bonded local groups. In comparison to binary "Ti-B" alloys, a significant improvement of tensile strength by multiple B -elements addition of equivalent total solute concentration was noted. It was assumed, based on the cohesive energy argument, that the more alloying elements are present, the higher order terms in the series-expansion description of the cohesive energy have to be taken into consideration. From the thermodynamic interaction approach one simply has to deal with all possible combinations of interaction strength parameters and an additive effect has been assumed as a first approximation. There is at present little more explanation for it. No data is available for the dependency of the elastic shear moduli on the concentration or electron per atom ratio in the α -phase (valence

is based on both the d and s electrons of Ti and s and p electrons of B). Collings et al⁽¹¹⁾ measured the values of Debye temperature with electron to atom ratio in the α -phase (Fig B-34). Since there is a direct resemblance between the characteristic of the Debye temperature and elastic shear modulus (C') with the e/a ratio curves, one can infer that C' decreases with the increase of the e/a ratio in the α -phase. The decrease becomes pronounced above e/a = 3.5, unless intermetallic compounds form (such as α_2 -Ti₃Al) which will increase the rigidity. (Possible similarities in the mechanical and electronic properties between α and α_2 phases were pointed out in reference (12)).

In a multicomponent β -phase the different elements have different stiffening effects, which will increase the C' value in a given temperature. Measurements of the Debye temperature in a set of Ti-Mo alloys⁽¹²⁾ to which different amounts of Fe and Al were added, while maintaining an average e/a, constant at 4.3 (aluminum was assumed not to contribute to the e/a ratio) have shown that replacement of Mo by Fe brings slight increase of the Debye temperature. Since a direct correlation exists between the characteristics of both "Debye temp with e/a" and " C' with e/a" curves, it means that Fe slightly stiffens the structure. A much greater degree of stiffening was observed accompanying the admixture of Al.

The most important factor for understanding the stability of the β -phase is the temperature dependency of the C' . Following Fisher and Dever⁽⁹⁾ the dependency might be better explained in a graphical presentation. According to them $\frac{dc'}{dt} = (\text{const} < 0)$, which means that in the " C' with e/a" diagram, the scale unit of the C' ordinate linearly expands with temperature rise, while the curve characteristic remains unchanged. This means that

each C' value is lowered by the same ratio as the temperature increases without changing the curve characteristic. This may be termed: "Temperature stiffness-softening". Parallel with it the point of $C' = 0$, which is at $e/a = 4.0$ at 883°C , for pure titanium starts to move left with the temperature rise. The $C' = 0$ point represents the M_s point (Martensite start) at the temperature in question and at the proper concentration in e/a units. The horizontal component of the motion follows the concentration change with temperature of the M_s line in the phase diagram. Let this be termed: "Transformation stiffening". It is felt, although not proven, that the negative value of $\frac{dc'}{dt}$ is not constant but actually depends on the temperature in accordance with the lever rule. In the "Alloy Stiffening" effect, expressed by the increment of the absolute value of C' at each e/a , the graphical presentation will have the unit scale decreased. This will not interfere with the "Temperature stiffness-softening effect".

In ($\alpha+\beta$) alloys the following is the sequence of α -rigidity lowering with e/a increase: Ti-6Al-4V, Ti-6242, Ti-6246. In the Ti-6Al-4V alloy, the appearance of α_2 may be favored. In the Ti-6246 alloy on the other hand twinning deformation in α may take place. This alloy in fact has orthorhombic martensite. Its retained- β in the β -transformed structure may have a high enough e/a value which may permit under suitable condition, such as high stress level, the formation of ω -phase. If correct, this may explain its observed low-fracture-toughness. All values of e/a lower than 4.1 have additions of α -stabilizing elements, as is the case with the near α -alloys. Their $C'=0$ point is at higher temperatures than that of pure titanium. Following the e/a ratio for them, the sequence of M_s points in the direction of lowering temperatures is once again:

Ti-6Al-4V, Ti-6242 and Ti-6246 (all still above that of pure Ti) which manifest the β -stabilization effect of molybdenum and vanadium.

Kinking and Shear Band Formation - A Proposed Model

Technically small temperature differences between the upper and lower end surfaces of the specimen during isothermal upset forging may explain the appearance of a conical-like distorted geometrical form. Relatively high strain rate sensitivity may control the type of bulging forms observed after isothermal forging. If the friction on the end surfaces is low while high strain rate develops at the middle height of the peripheral free surface, an inward buckling may develop due to strain rate hardening. The kinking of the $(\alpha + \beta)$ preforms during forging at the critical range of temperatures result from number of factors, and they will be discussed below:

(1) After a folding-over deformation process due to a "sticking friction" developed at the end surfaces, the material flowed further radially and parallel to the surfaces with the lateral resisting stresses increasing again. This build-up of the resisting stresses is caused by the friction increment as the displacement velocity along the surfaces increase in the radial direction causing strain rate hardening. Parallel with it the strain-rate of the deforming material also increases. These two phenomena add up and may stop the lateral motion in locations on the end surfaces where the displacement velocity is the highest. These locations mostly differ in position on the different end surfaces building up a resultant couple of forces sufficient to kink a specimen, if other favorable conditions exist as well.

(2) On the interfaces between the chill affected non-deformed zones and the central highly compressed zone, extra energy is released due to tangential velocity discontinuity⁽¹⁵⁾ in the displacement velocity field. This energy release will bring in turn a local temperature rise, since the hot forging time is very short and there is not enough time for gross heat dissipation by conduction. This is especially true because the heat conductivity of titanium is low. This is termed: "Thermal Band" formation. The temperature rise will cause local softening along the interfaces due to the high temperature dependence of the flow stress which together with the resultant couple of forces developed on the end surfaces (due to frictional effect and strain-rate hardening) may lead to the kinking and shear-band formation. All necessary conditions are still not met to cause kinking and shear-band formation, since such phenomenon was not observed when forging took place in the β -phase field, i.e., above 1815°F. The instability of the microstructure must also be considered.

(3) Lee and Backofen⁽⁷⁾ found that the plastic anisotropy index (the ratio between the width and thickness strains) in the critical temperature range below the β -transus decreases sharply with increasing temperature. It could therefore be inferred that it results from the incremental volume-fraction increase of the isotropic β -phase. This does not explain the kinking appearance in the same range of temperatures. The fact that no kinking was observed when the specimen was forged in the β -phase field has nothing to do with the isotropy of β -phase. Since kinking is a forerunner of shear-band formation, it is evidently the low-rigidity of the β -phase in the same range of temperatures which play a decisive role in the phenomenon. Still, at each temperature the equilibrium concentration for the β -phase (on the β -transus line) is relatively higher

than that needed for the low rigidity property ($C' = 0$). It is the non-equilibrium concentration which induces low rigidity properties to the structure.

(4) Since the true stress-strain curves show constant stress with strain relationship (almost horizontal curve), the plastic instability was attributed mostly to a TRIP-effect (Transformation-Induced-Plasticity). Since the hot-working time is very small, it is not enough time for the development of an equilibrium concentration at the moving micro-boundaries of transformation ("Nernst condition" is not obeyed). It is absolutely reasonable to assume that: (a) the transformation into β during the hot-working is of a shear type, opposite to the direction which formed the β -transformed structure in the source material, and (b) the composition of the newly formed β -phase is almost equal to that of the M_s value at the temperature in question. It is sound from fundamental thermodynamic principles, since: (a) The "Zener rule" states that a system upon transformation will choose the path of highest available rate of transformation, although it is not the one which will bring the highest gain in free-energy, and (b) the "Ostwald rule" states that instead of a transformation with high activation barrier which may lead to the formation of another stable phase, a set of transformations, each with lower activation barrier and which lead to metastable phase formation, is preferred. In our case the shear transformation into β is the first metastable one, followed next by the precipitation of secondary acicular α -particles from the β -phase, which will bring the later to the equilibrium concentration and volume-fraction. The metastable- β has very low-rigidity (almost $C' = 0$), while the β -phase will regain with the precipitation of secondary acicular-

its original rigidity at the temperature in question. The excess amount of metastable- β is also related to the hydrostatic component of the stress field that arises from the compressive loading. These components serve as another intensive parameter for the thermodynamic system, which seems to decrease the β -transus temperature relative to the one at thermal equilibrium. The flow-stress actually observed during the hot compression ($\sigma - \epsilon$ curve) stems from the rigidity of the primary α -grains. Otherwise the material would show Newtonian-flow type of deformation. It must be recalled again that the TRIP effect is responsible for a constant stress strains, so local deformation due to microstructural heterogeneities will not affect the homogeneity of the stress field and cause failure due to locally developed defects. (This is not the case in β -preforms. See para 3.6)

To summarize this discussion, the poor hot workability due to kinking and adiabatic shear in ($\alpha + \beta$) titanium alloys in the critical range of temperatures below the β -transus depends on four factors that have to be simultaneously satisfied. They are as follows:

- (a) Build-up of couple forces on the specimen during the forging (friction and/or strain-rate hardening effects).
- (b) Temperature rise (due to tangential velocity discontinuities) and local softening (due to high temperature dependency of flow stresses).
- (c) Low-rigidity of the β -phase (a decisive factor).
- (d) Transformation-induced-plasticity (TRIP effect) which forms the low-rigidity β , and keeps constant stress at increasing strains. (promotes homogenous stress field in spite of heterogeneous microstructure)

Continuum mechanics predictive calculations assume: $\Delta T = K \left(\frac{f}{\zeta c} \right) \frac{\Delta U_t}{U_p}$,
 where: ΔT is the adiabatic temperature rise; ζ is the density; c is the specific heat; f is the fraction of dissipated energy which cause

temperature rise; k is the yield shear stress; U is the tangential velocity change on interface of directional velocity discontinuity; and U_p is the velocity perpendicular to the discontinuity interface. It also assumes that $K = K(\epsilon, \dot{\epsilon}, T, S)$, where the dependency of ϵ (the strain) and $\dot{\epsilon}$ (the strain-rate) is through constant elastic moduli, which are fixed by the temperature, T , and the structural features, S , such as: morphological, textural and electronic. But, the instability phenomena results from kinetic changes of S . Mathematically, these are manifested by the changes of the elastic moduli during the process. Thus, for example, $K = K'(\dot{\epsilon}) \dot{\epsilon}^m$ must be considered and $K'(\dot{\epsilon})$ must be iterated in a numerical solution for the velocity field which develops in the specimen during hot working.

When an adiabatic shear band forms, the total deformation of the specimen will concentrate in the band, while the other parts of the specimen will move relative to each other almost like rigid bodies. The temperature rise and concentrated shear strain will produce an excess of vacancies; reduce the dislocation density; and even cause recrystallization. It is also possible to develop a new local texture. To certain extent, the local softening is counteracted by the high deformation-rate hardening, which in turn may explain the very fine grain structure which appears there.

Instability of β -Preforms Below The β -Transus

Semiatin⁽¹³⁾ found that the transformed- β preform is very unstable upon isothermal forging in the critical range of temperatures below the β -transus. Gross geometrical non-uniformity appeared (Fig B-35) and microstructural instability expressed by microcrack formation was observed (Fig B-36). The isothermal true stress-strain curves show very

high softening characteristics (Fig B-30) compared to that of the ($\alpha + \beta$) preforms at the same temperatures. The strain-rates used by him were higher than those used in the present study. The cracks that formed are typical grain boundary triple-point junction cracks, such as those often encountered in creep failure. Fig B-36 suggests that the softening was not caused by sliding on previous β -grain-boundaries, since they are covered by a continuous film of the α -phase (this could have been formed during the first stage of forging). This film to a certain extent inhibits local accommodation deformation near the triple-point junctions and along grain boundaries. However, the softening characteristics of the true stress-strain curves suggest that accommodation deformation in different localities actually took place. The softening characteristics of the true stress-strain curve serve to indicate the possibility of high microstructural instability during hot working.

One of the major aims of the project is the development of a dual-property compressor disk. The hub of the disk will have a microstructure that resists low-cycle fatigue failure, and the rim will have another that resists creep failure. Therefore, the hub will be made from the Ti-6242 alloy with the ($\alpha + \beta$) microstructure, while the rim be made of the same alloy in the β -transformed microstructure. A composite forging preform was designed having the respective microstructures in the bore and rim regions. The combined disk actually resembles a composite ring (Fig B-37). In order to avoid axial compression loading during the initial stages of forging on the rim, the composite preform was tapered so that only after 30% of reduction the specimen would attain completely flat surfaces faces. The specimens were isothermally forged at 1600° and

1700°F, and they were coated with DG-69 glass with a film thickness of about 0.01 inch. The ram speed was 0.03 ipm, and the peak load was about 80 tons. The forged specimens were geometrically uniform despite the fact that one of the microstructures in the composite forging preform was the low stability β -transformed structure. A macro cross section (Fig B-38) shows some inward material flow, indicating that some friction was involved. In the hub region, the flow-lines pattern of the $(\alpha + \beta)$ material shows that the dead zone region was not formed, and a symmetrical outward barrelling took place while being confined by the rim material. In the β -transformed rim zone, β -grain dimension changes took place. The largest grains were observed near the inner interface adjacent to the $(\alpha + \beta)$ bore material, but the smallest appeared where the radial stress was maximized. In the central rim zone the previous β -grains are equiaxed showing that a process like recrystallization took place. Near the "shear-interfaces" (boundaries between the dead zone and the central compressed zones) the previous β -grains are elongated in the direction of displacement flow. The observations seem to support a possibility, that although the forging took place below the β -transus, partial transformation to β took place, making it possible to observe grain size changes of the " β -grains" during hot working. Stress relaxation in local regions near grain boundaries and triple point junctions seemingly was enough to cause the β -transus to be lowered by a local increase in the hydrostatic component of stress.

Color optical metallography using polarized light shows that the structure within each previous β -grain is composed of irregular blocks of Widmanstatten Colonies having different orientations. Some colonies had

either a blue or yellow color that could be alternately changed by rotating the analyzer by 90° . Some of the colonies had a magenta color which did not change with rotation. The yellow and blue colors seem to result from Widmanstätten colonies that were present in the original

β -preform structure, while the magenta color is apparently related to a colony of Widmanstätten structure that resulted from a shear induced phase transformation $\alpha + \beta(A) \xrightarrow[\text{T}]{\text{stress}} \beta$ where $\alpha + \beta$ (A) denotes the acicular Widmanstätten structure and T is a temperature below the β -transus.

The magenta color structure has assumed a new orientation such that the cross sectioned area is almost parallel with the Widmanstätten plates (Fig B-39). In order to understand the origin of the magenta colonies, the raw material was annealed for 4 hours at 1900°F and water-quenched. Part of it was later annealed for 2 hours at 1700°F and air-cooled.

The martensite is a very fine "basket weave" like structure, also having the magenta color under polarized light. The annealed martensite has an appearance of coarse "basket weave" β -transformed structure which is largely magenta colored with some blue and yellow plates appearing.

These two structures are completely different from the blocky structure obtained after the short-term forging. Thus, the magenta blocks seem to result from the transformation of the original β -transformed structure in localized regime into β -phase during the forging that subsequently retransforms into a new β -transformed structure presumably of different orientation (Fig B-40).

Scanning electron microscopy (Fig 3.16) shows that the platelet structure of the β -transformed microstructure can undergo a large amount of plastic transformation. This behavior is revealed by the wavy-nature of the deformed plates. Accommodation deformation by localized shear near

previous β -grain boundaries and at triple point grain boundary junctions cause the local transformation to β -phase to take place, preventing grain boundary cracking. This type of phase transformation occurs at strain rates approaching 10^{-3} sec^{-1} and lower. This appears to be the major softening mechanism and the one most responsible for the instability and inhomogeneous flow of the β -preforms when forged below the β -transus in the neighborhood of 1700°F (927°C).

It should also be stated here that large β -forged structures may have the same structural blocky feature (!), but this is due to the relaxation of thermally induced stresses during cooling following beta forging. The transformed β -structure (as mentioned earlier), can accommodate large amounts of deformation by bending of the plates. This behavior seems to occur by a relative displacement of neighboring α -plates, due to the low rigidity β -phase situated between the plates.

The Detection of Metal Flow Instability During Hot Forging

Load and pressure measuring cells connected to the AFML forging press continuously recorded the compression load and hydraulic oil pressure during the upset forging of the specimens used in the present study (Fig B-42). It was observed that these measurements can be used to indicate whether the metal flow is stable or unstable during the process. The load versus time curves show that the load cell was not as sensitive as the pressure versus time curve for this purpose, since some of the load variations were dampened by layers of thermal insulation. The curve in the upper diagram is for the stable β -forging condition, and the one in the lower diagram for the unstable, $(\alpha + \beta)$ -forging condition.

The pressure versus time curve in the upper diagram shows a monotonic pressure increase during stable metal flow. For the case of unstable metal flow shown in the lower diagram, the pressure goes through a maximum value before it starts to rise again. The shape of this curve and the fluctuation of the signals result from kinking and shear-band formation in the specimen. The pressure declination is due to the localization of the metal flow (In a way, it resembles the discontinuity between upper and lower yield points in the stress-strain curve of a mild steel). Load and pressure sensors might be used in "smart" machines to prevent or detect the formation of shear band defects resulting from unstable metal flow.

The signals generated when the forging defects were produced are signatures that can be used as an on-line quality assurance tool or as a signal to control the rate of deformation. One approach to this problem could involve the development of a multiprocessor control system for forging presses that is capable of signature analysis. The design of such a system would require:

- (1) an understanding of the physical nature of the process to be controlled and analyzed;
- (2) identifying the phenomena that generate the signals that reflect the condition of the process;
- (3) sensors that provide signals which directly or indirectly result from the generating phenomena;
- (4) selecting computable measures which describe feature characteristics as scalar quantities, and
- (5) developing a decision routine or thresholds for classifying each condition using the scalar measures.

The first step involves developing models of both the process and the forging press. These models would provide knowledge of the phenomena in the normal operating state of the forge press as well as knowledge of the mechanism of each failure mode. The analytical models being developed under the current program should take care of the initial step. A suitable detection system would have to be selected from the standpoint of consistency of measurement, and this will be an important factor for on-line control and inspection. Based on the signals generated for the pressure-time and load-time curves, practical sensors for controlling the forging process should be available. Having a suitable sensor, it will then be necessary to collect the output for the various operating states to avoid overlooking any spectral information that might be useful for both process control and quality assurance. The signal analysis must then be carefully compared to the process models being developed for simulation purposes. A multiprocessor system design can then follow which involves detection of characteristics of the signals that correspond to specific operating states. This approach to process control contrasts to purely statistical alternatives.

A multiprocessor control system can potentially link together the physical nature of the process with inspection equipment and design engineering to increase:

(1) manufacturing design flexibility, (2) productivity, (3) product durability, and (4) the conservation of strategic materials and energy. Control systems that link together the physical nature of the process and the manufacturing equipment ultimately leads to increased economy in small batch processing, because it provides increased flexibility

for new design introduction; process development time is drastically reduced, and there is increased versatility in process control. The end result will be a lower rate of scrap production and the increased production of more durable parts.

The driving force behind the development of "smart" machines is the economics achieved through reduced life cycle costs that is made possible through repeatable production of controlled microstructures and properties in finished geometries.

The results of this study on hot workability of Ti-6242 alloy clearly points to the need to control the process in real time. It also shows that metallurgical instabilities can be used to advantage in meeting the objective of producing controlled properties/microstructures in finished shapes. However, this achievement will require the effective strain rates to be controlled in the strain rate regime of approximately 10^{-3} sec^{-1} to 10^{-4} sec^{-1} , and the temperature of the process should be near isothermal. When these process conditions are achieved it then becomes feasible to think in terms of increasing the productivity through the production of multiple forgings in a single operation that are near net shaped.

In summary, the development of "adequately elegant" material, process and equipment models that are linked together via a multiprocessor system will make it possible to achieve greater technological and economic goals that are now being demanded by world economic pressures.

REFERENCES

1. Underwood, E. E., Private Communication (through M. Rosenblum).
2. Shechtman, D. and Eylon, D., Met. Trans. 9A (1978) 10108.
3. Schey, J. A., Metal Deformation Processes, Friction and Lubrication, P. 608 (Fig. 9.2), Dekker, N.Y. 1970 (See also paragraphs 2.12 and 9.22).
4. Buhler, H. and Wagener, H. W., Deformation Properties of Titanium and Titanium Alloys, Royal Aircraft Est. Library Translation 1657. Farnborough 1972. (Translated from Bander Bleche Rohre 6 (1965)).
5. Chen, C. C. and Coyne, J. E., Met. Trans. 7A (1976) 1931.
6. Chen, C. C., Metallurgical Fundamentals to Ti-6242 (0.1) Alloy Forging, Report RD-77-110, Wyman-Gordon Co., Massachusetts 1977.
7. Lee, D. and Backofen, W. A., Trans. AIME 239 (1967) 1034.
8. Paton, N. E. and Hamilton, C. H., Met. Trans. 10A (1979) 241.
9. Fisher, E. S. and Dever, D., Acta Met. 18 (1970) 265.
10. Collings, E. W. and Gegel, H. L., Scripta Met. 7 (1973) 437.
11. Collings, E. W., Ho, J. C. and Jaffee, R. I., Titanium Science and Technology, Vol. 2 (Ed. R. I. Jaffee, H. M. Burte), P. 832, Plenum, NY.
12. Collings, E. W., Gegel, H. L. and Ho, J.C., Solid-Solution Strengthening and Fundamental Design of Titanium Alloys, AFML-TR-72-171, Ohio 1972.
13. Semiatin, S. L., Private Communication.
14. Khorev, A. I., Principle of Titanium Alloys Complex, 2nd International Conference on Titanium and Its Alloys, Moscow.
15. Johnson, W. and Mellor, P. B., Engineering Plasticity, paragraphs 13.4 and 13.11, Van-Nostrand, London 1973.

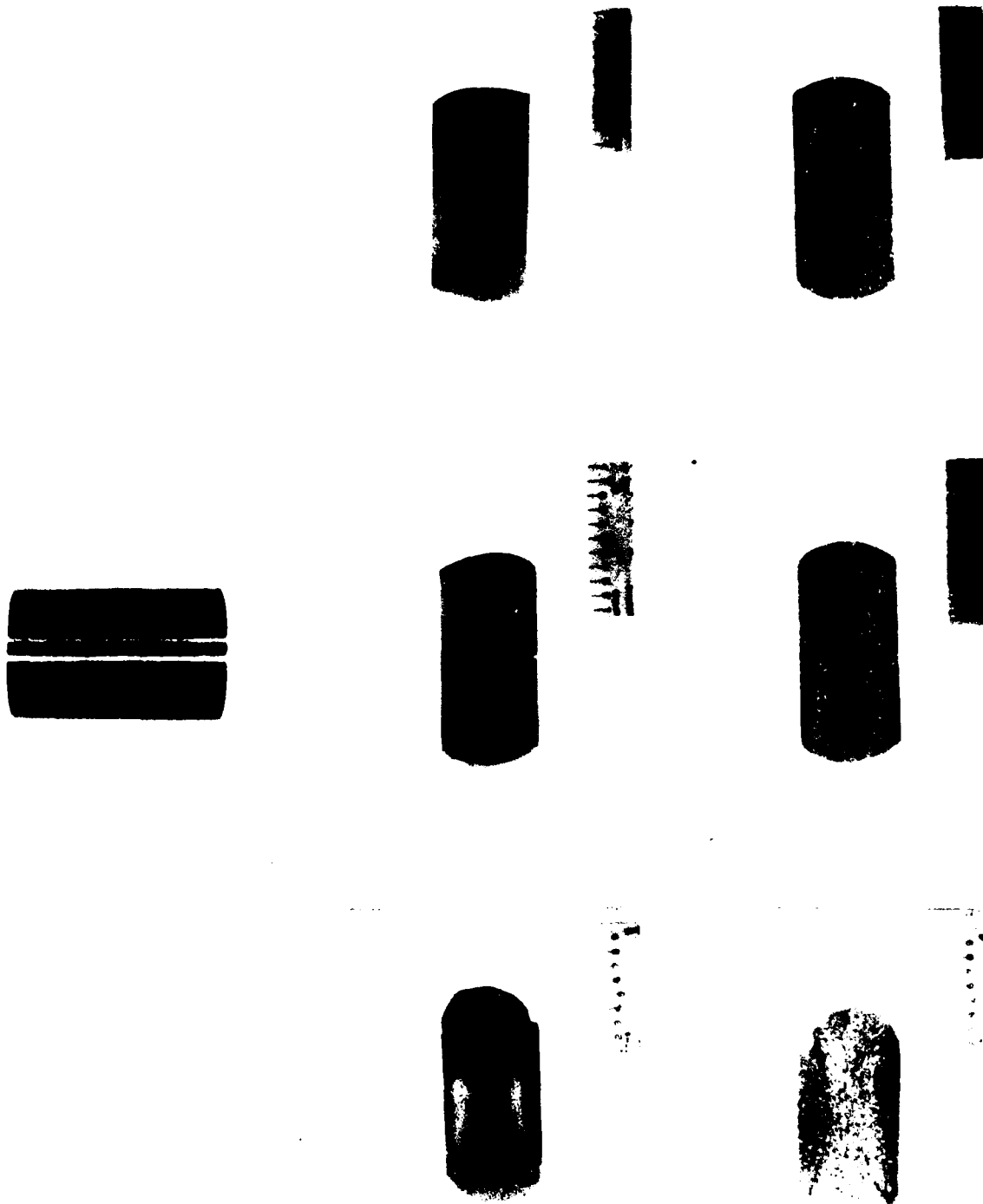


FIGURE B-1. Cross-sections of upset-forged specimens, photographed at low-magnification. For details see Table B-1.

Isothermal Forging

6242

6242+6246

**a+b
1700**



**tr.b
1900**

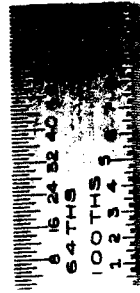
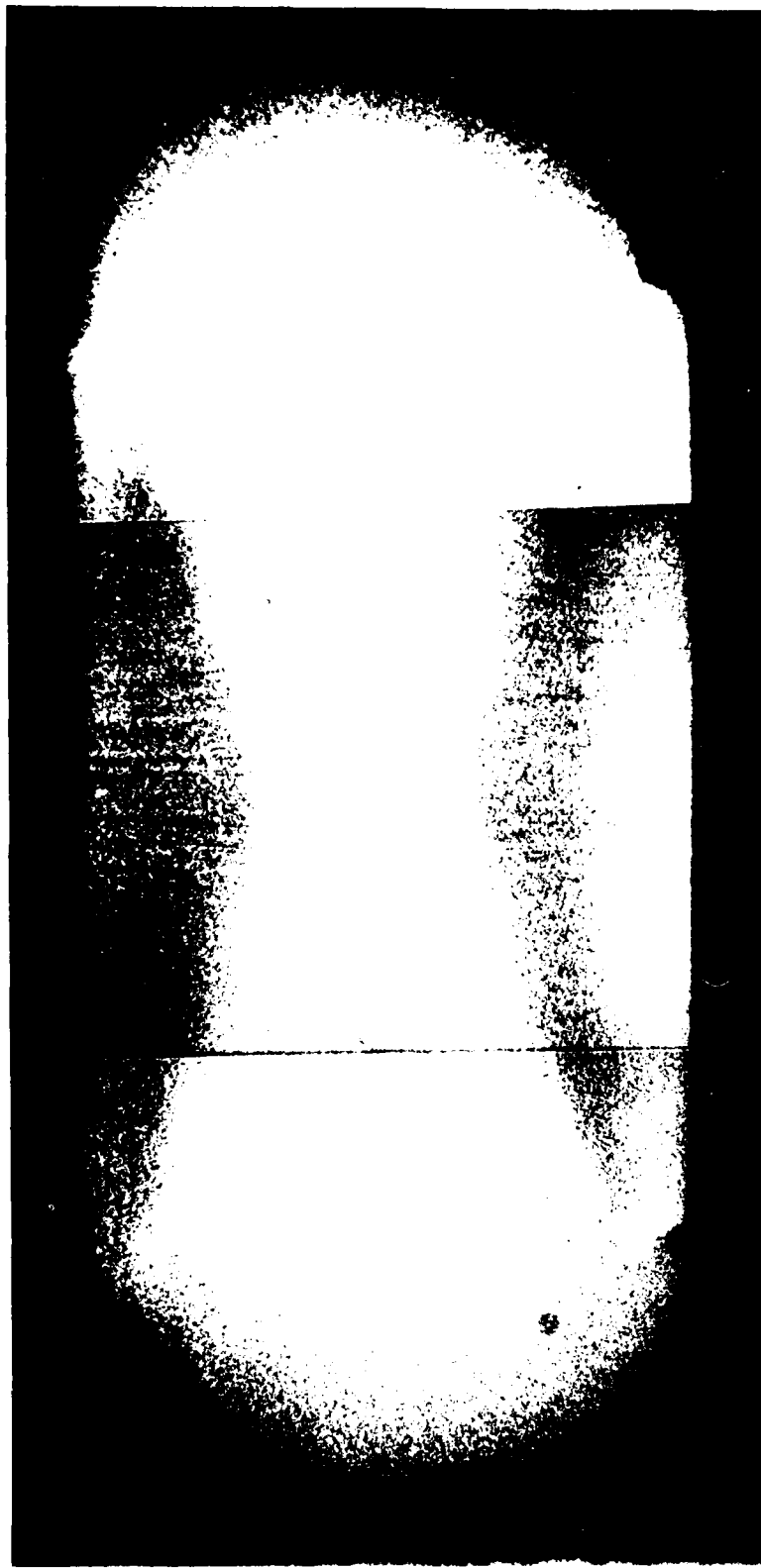
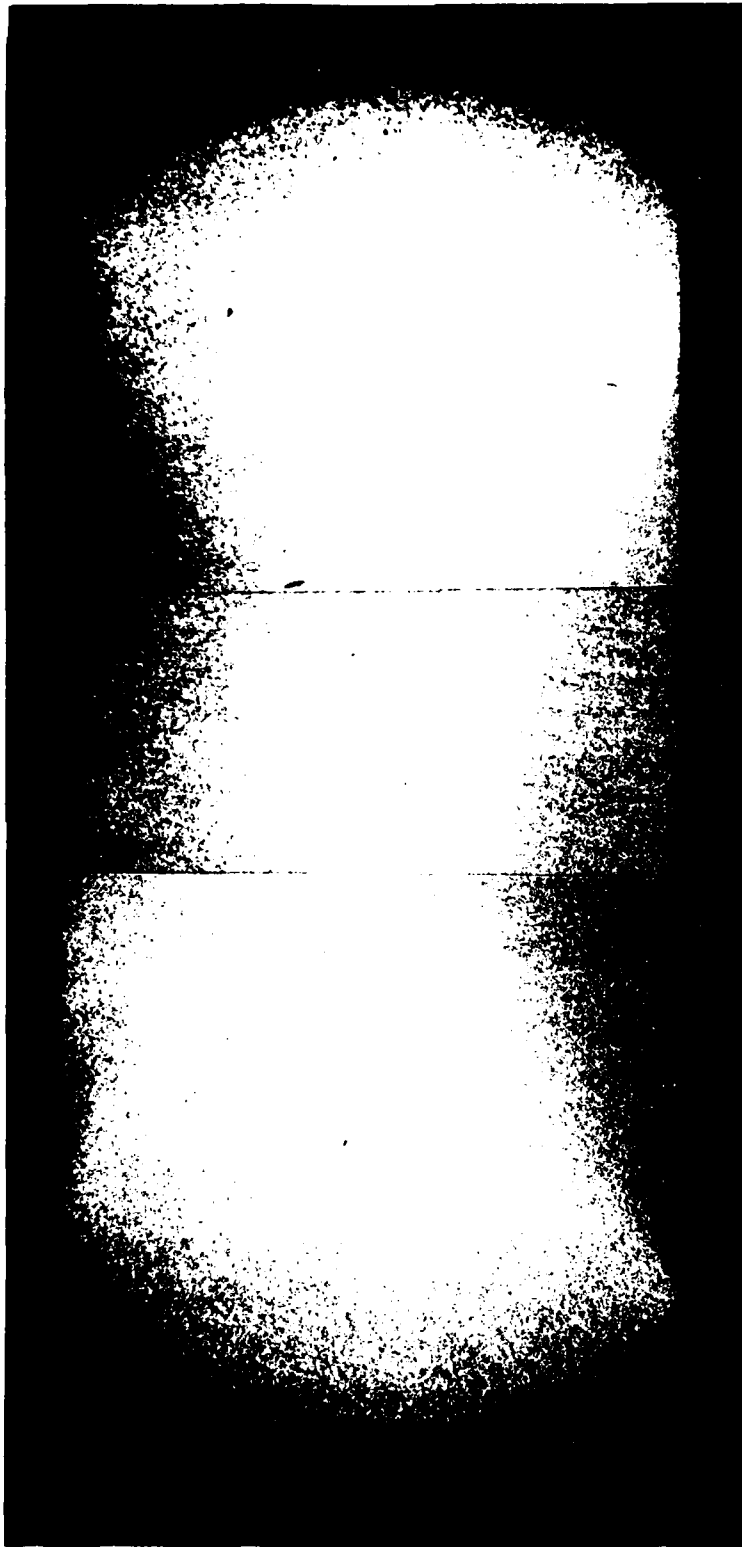


FIGURE B-2. Cross-sections of isothermally upset-forged specimens, photographed at low-magnification. For details see Table B-1.



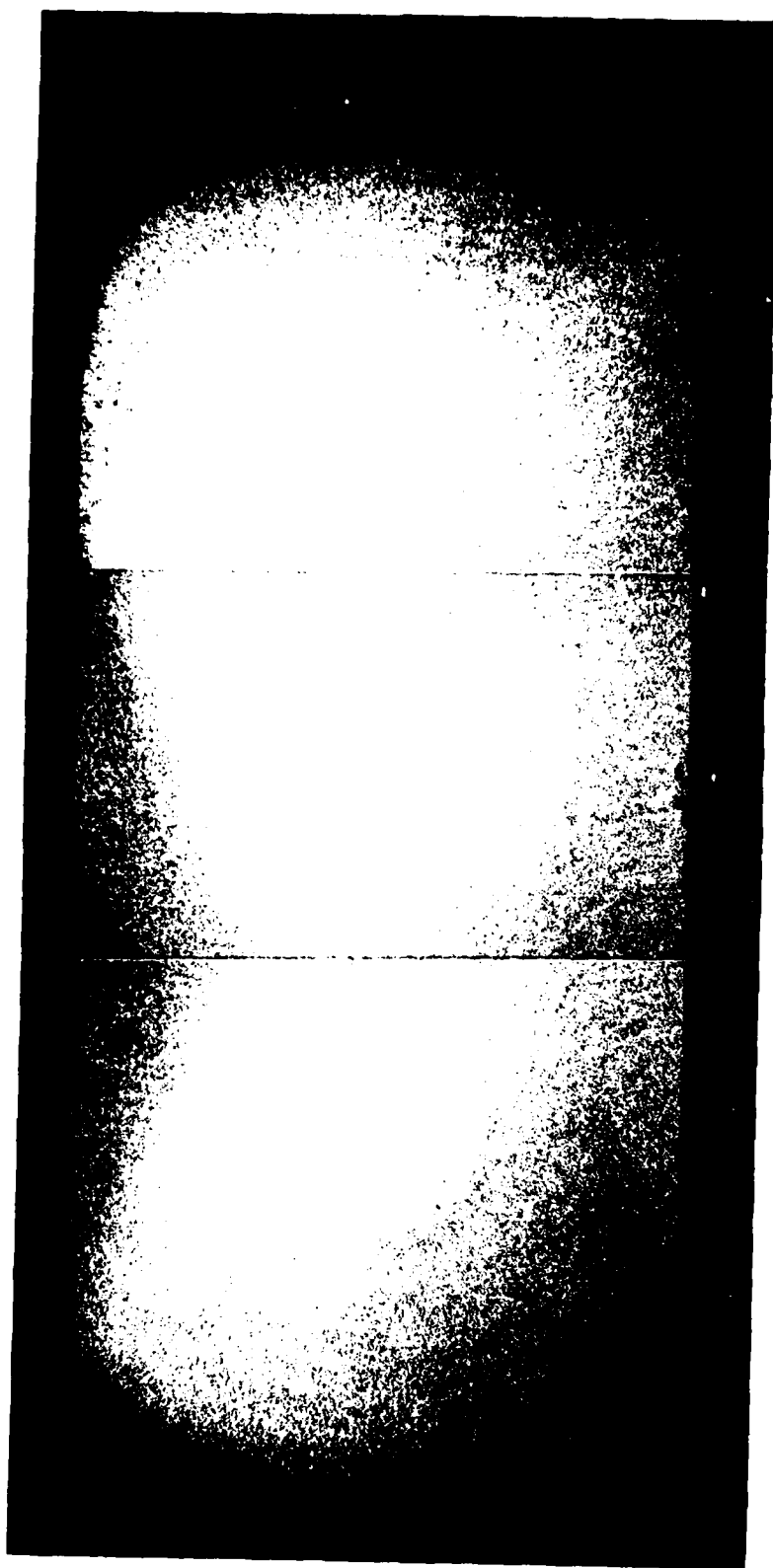
75

FIGURE B-3. Macroscopic flow-lines pattern of specimen No. 75 (curing-temperature 1750°F, dies temperature 700°F).



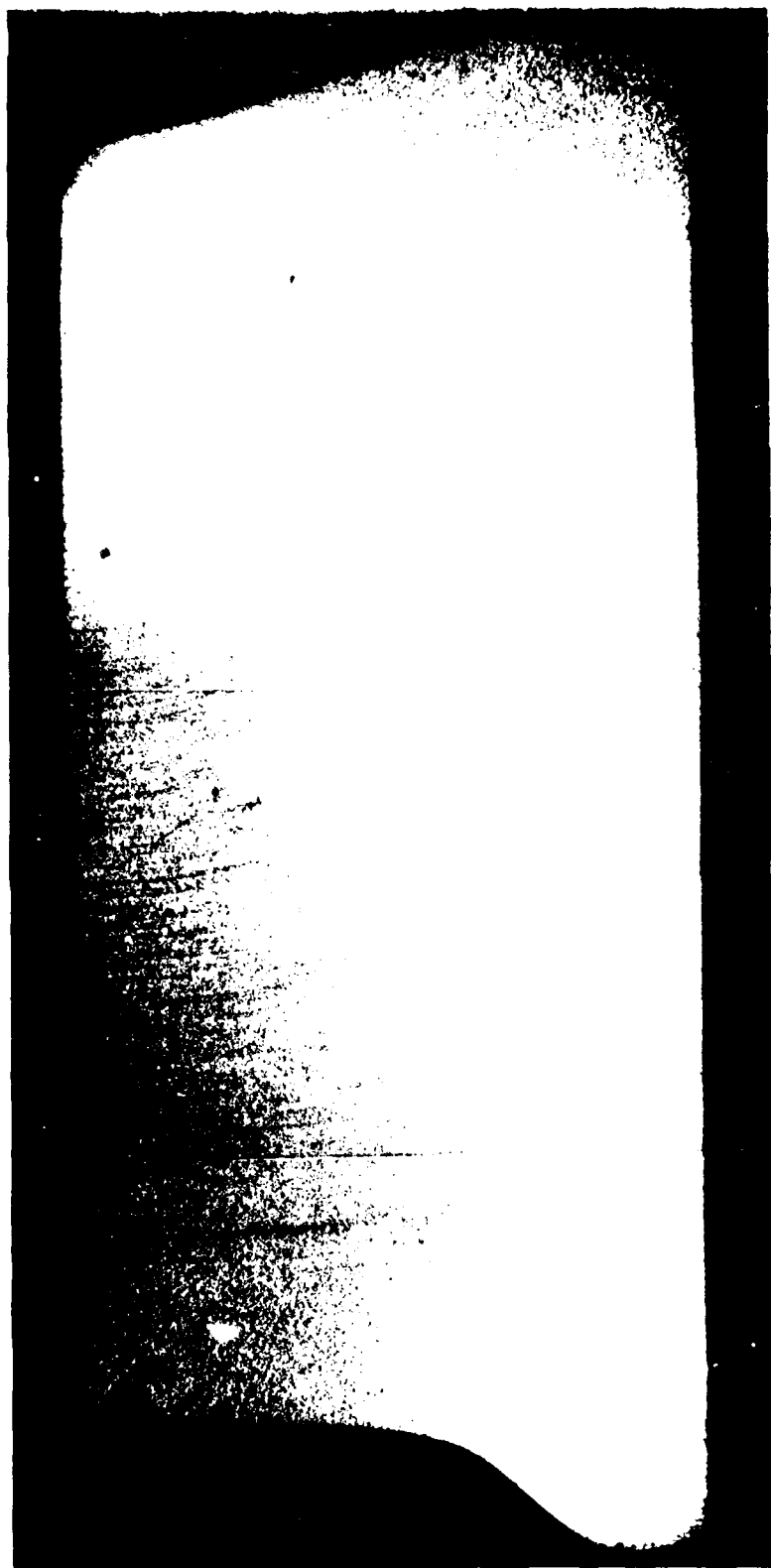
77

FIGURE B-4. Macroscopic flow-lines pattern of specimen No. 77 (forging temperature 1750°F, dies temperature 1600°F).



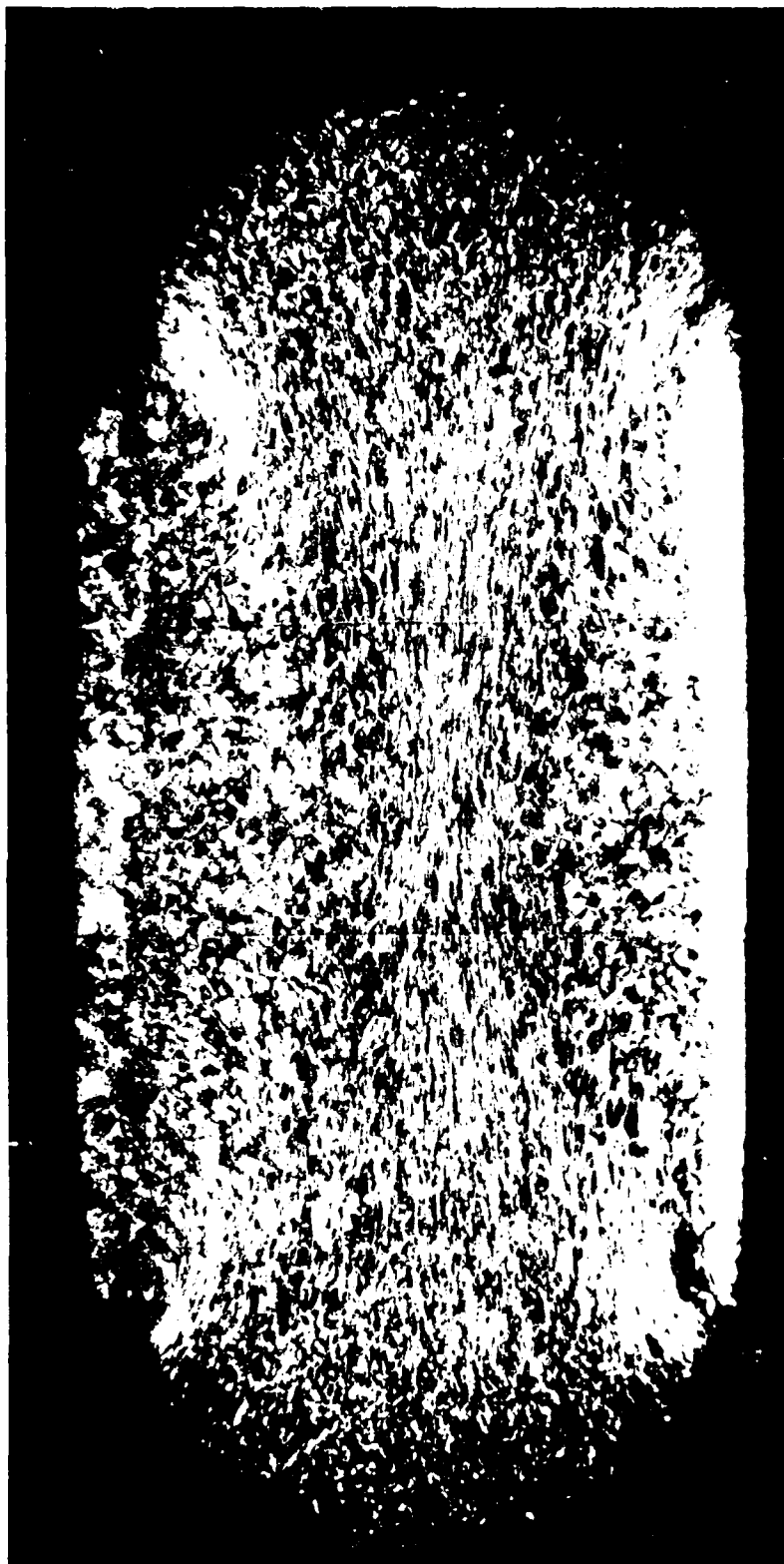
78

FIGURE B-5. Macroscopic flow-lines pattern of specimen No. 78 (forging temperature 1750°F, dies temperature 1800°F).



iso 1700

FIGURE B-6. Macroscopic view of pattern of ISO 1300 chloride temperature 1700°F, flex temperature 1700°F.



AD-A082 207

BATTELLE COLUMBUS LABS OH
RESEARCH TO DEVELOP PROCESS MODELS FOR PRODUCING A DUAL PROPERTY--ETC(U)
DEC 79 G D LAHOTI, T ALTAN

F/G 11/6

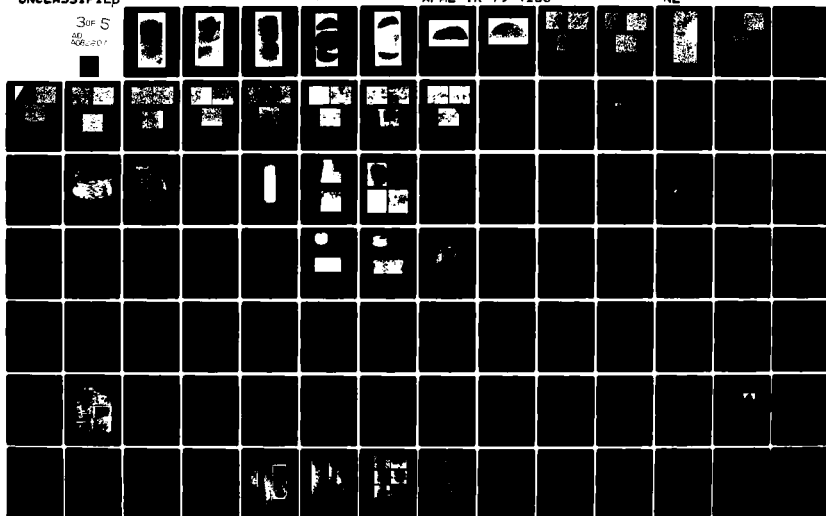
F33615-78-C-5025

UNCLASSIFIED

AFML-TR-79-4156

NL

30 S
40
406-207





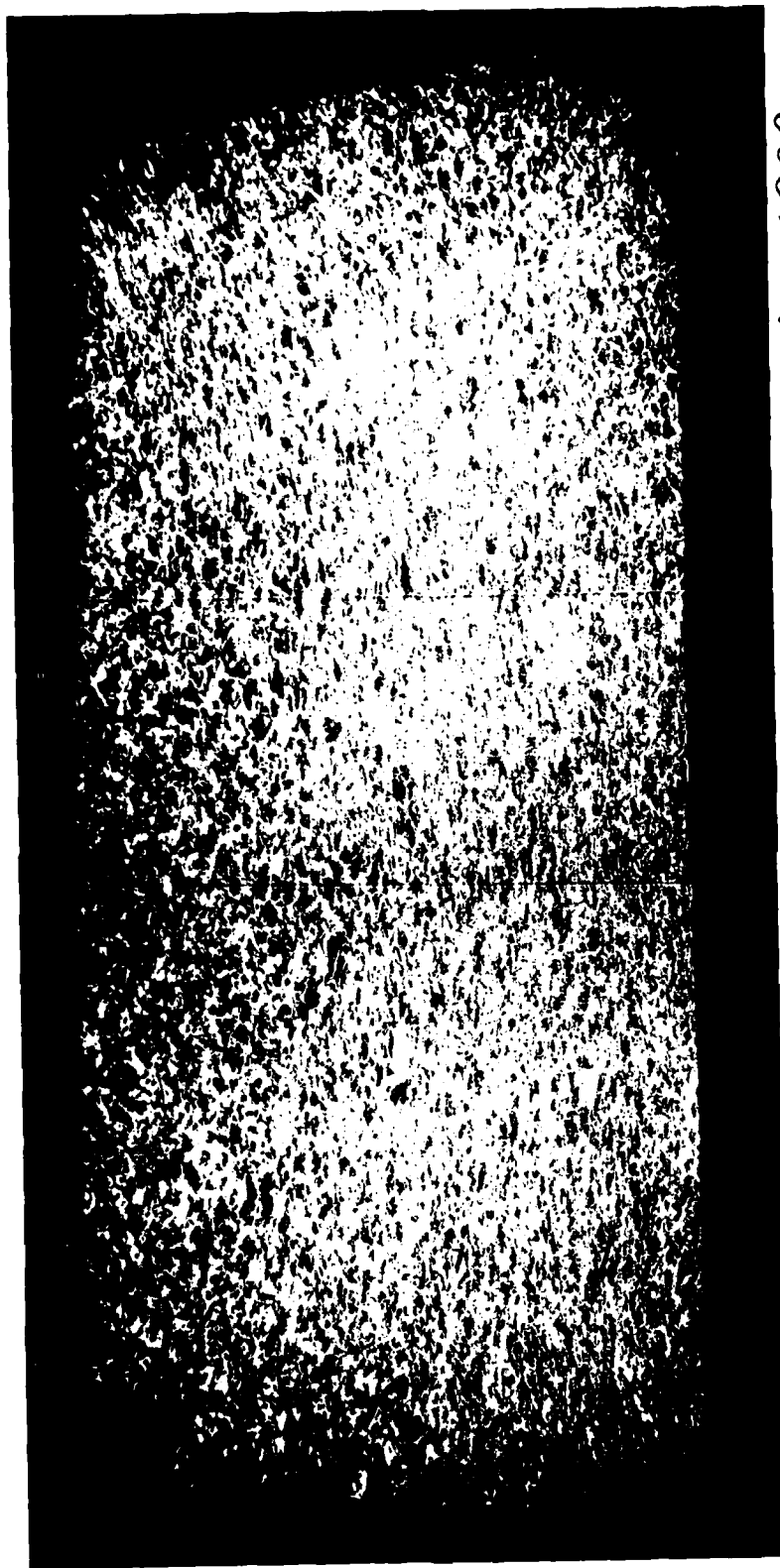
79

FIGURE B-8. Macroscopic flow-lines pattern of specimen No. 79 (forging temperature 1900°F, dies temperature 1600°F).



80

FIGURE B-9. Macroscopic flow-lines pattern of specimen No. 80 (forging temperature 1900°F).



iso 1900

FIGURE B-10. Macroscopic flow-lines pattern of specimen ISO 1900 (forging temperature 1900°F, dies temperature 1900°F).



iso 1700

FIGURE B-11. Macroscopic flow-lines pattern of combined alloys specimens (Hub-Ti6246, Rim-Ti6242). No. ISO 1700 (forging temperature 1700°F, dies temperature 1700°F).



iso 1900

FIGURE B-12. Macroscopic flow-lines pattern of combined alloys specimen (Hub-Ti6246, Rim-Ti6242). No. ISO 1900 (forging temperature 1900°F, dies temperature 1900°F).



FIGURE B-13. Lateral cross-section of an (c + f)-condition forged specimen (No. 75).

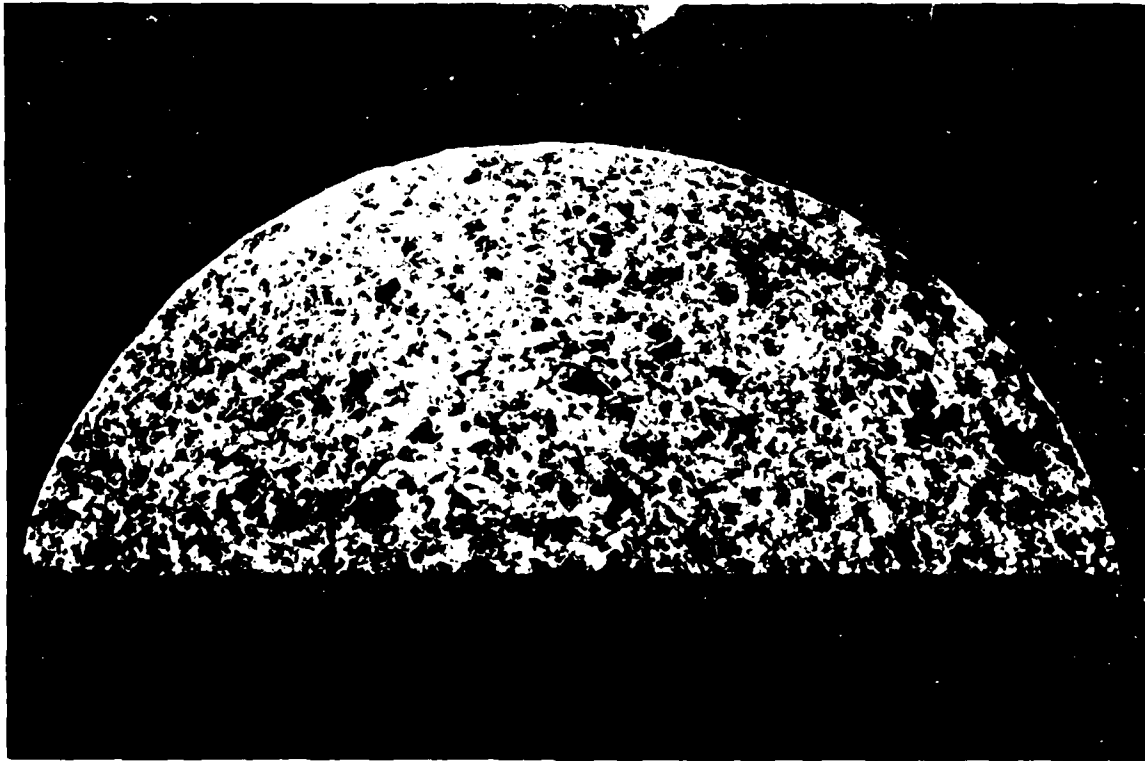
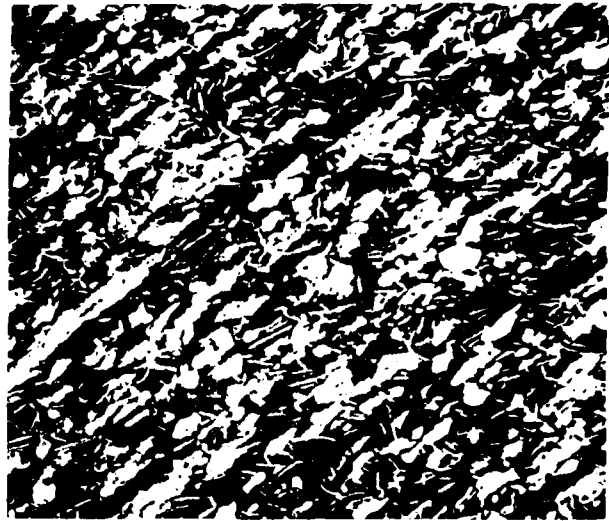


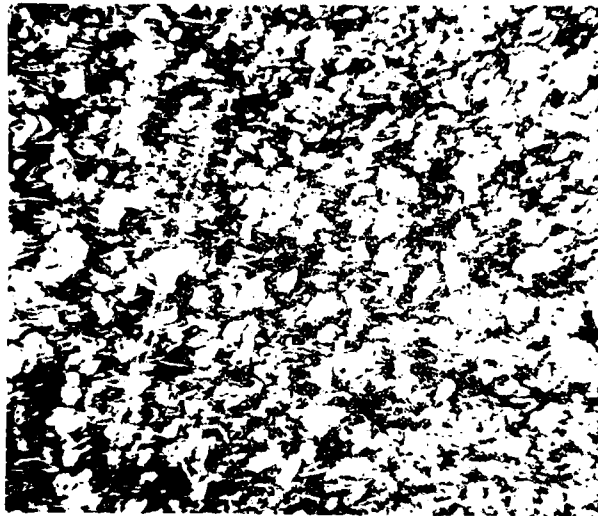
FIGURE B-14. Lateral cross-section of a γ -condition forged specimen (No. 80).



(a)



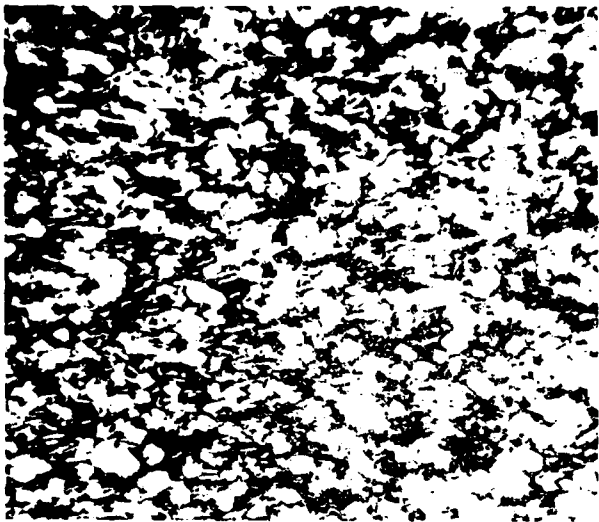
(b)



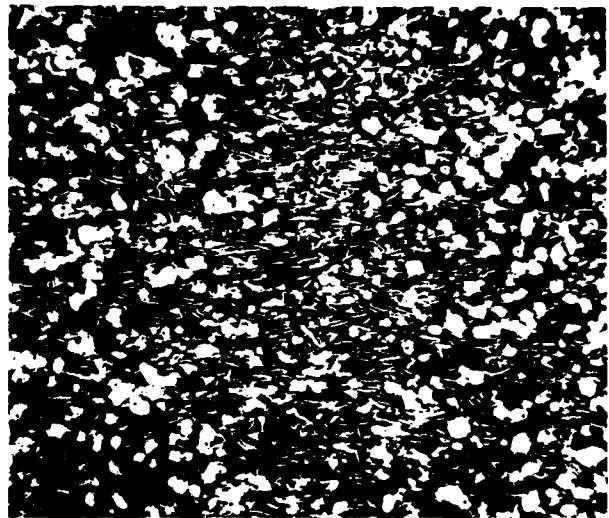
(c)

FIGURE B-15. Microscopy along the vertical centerline of specimen 75 cross-section. (Etched with Kroll's Reagent. Magnification: 240X)

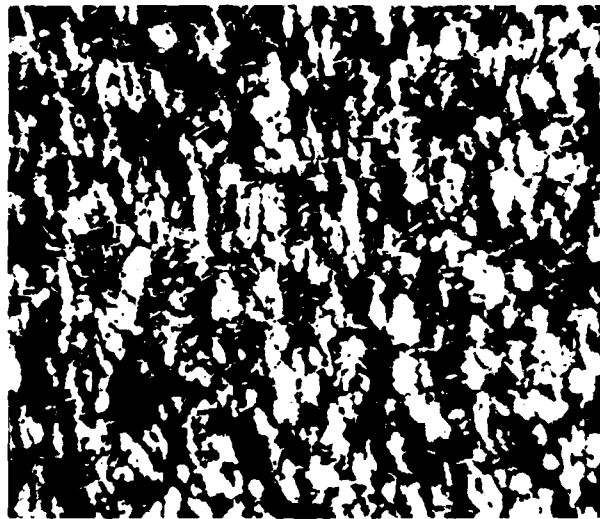
- (a) within upper chilling affected non-deformed zone (original "as-extruded" microstructure)
- (b) strong flow-lines bending below the non-deformed zone
- (c) strong compression-affected zone in the middle of the specimen



(a)



(b)



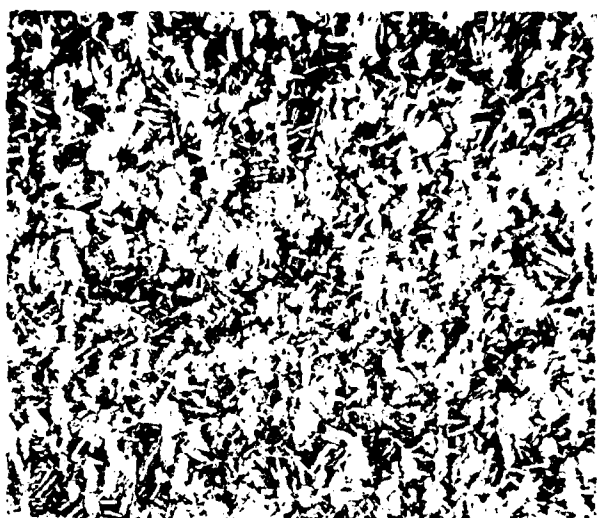
(c)

FIGURE B-16. Microscopy along the horizontal centerline of specimen 75 cross-section. (Etched with Kroll's Reagent. Magnification: 240X)

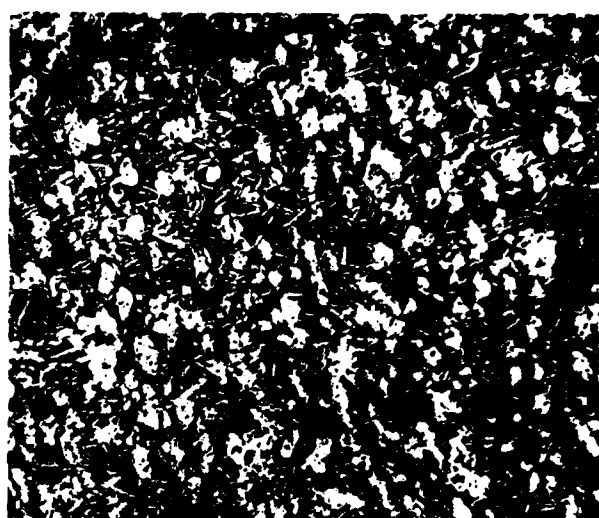
- (a) strong compression-affected zone in the middle of the specimen
- (b) appearance of adiabatic thermal band, horizontal-directed flow-lines
- (c) microstructure near the peripheral free-surface



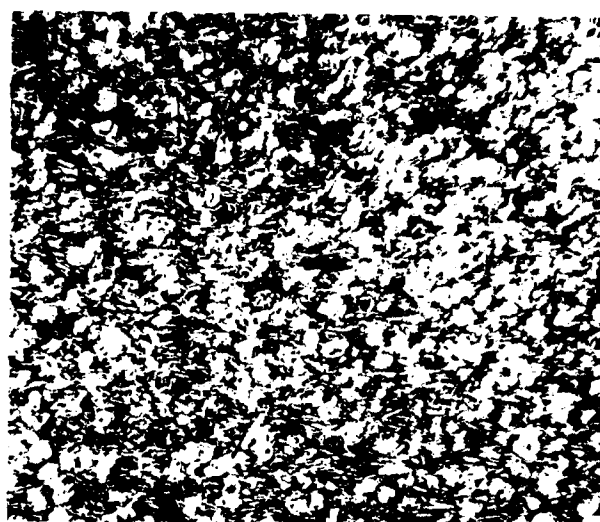
FIGURE B-17. Folding-over flow-lines pattern near the extreme end of the chilling-affected non-deformed zone (end of "sticking friction" area).



(a)



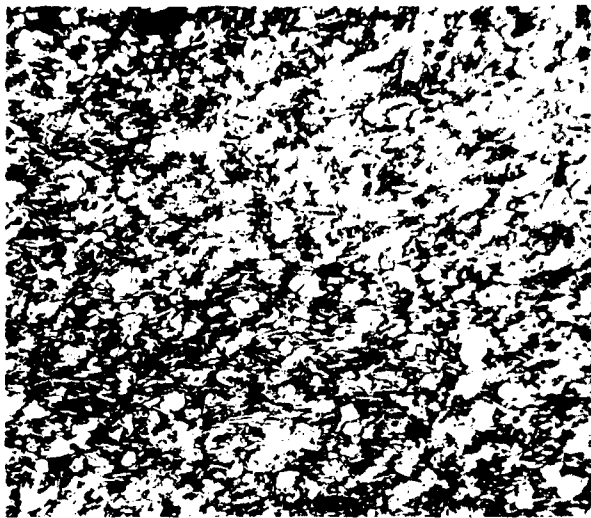
(b)



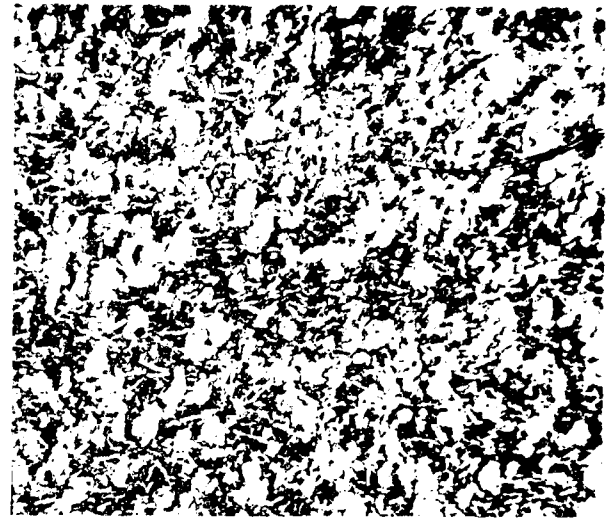
(c)

FIGURE B-18. Microscopy along the vertical centerline of specimen 77 cross-section. (Magnification: X240).

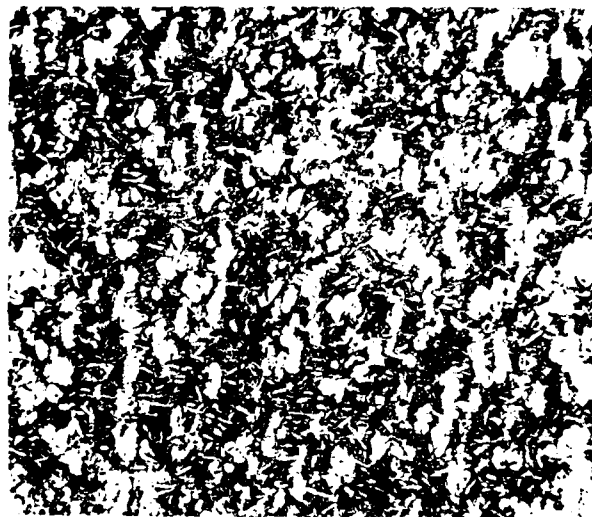
- (a) within upper chilling-affected non-deformed zone
- (b) within the compression-affected zone
- (c) strong compression-affected zone in the middle of the specimen



(a)



(b)



(c)

FIGURE B-19. Microscopy along the horizontal centerline of specimen 77 cross-section. (Magnification: X240).

- (a) near the middle of the specimen, along radially-directed, converging flow-lines
- (b) loosely-align radial flow-lines. Disturbance due to specimen kinking
- (c) near the peripheral free-surface

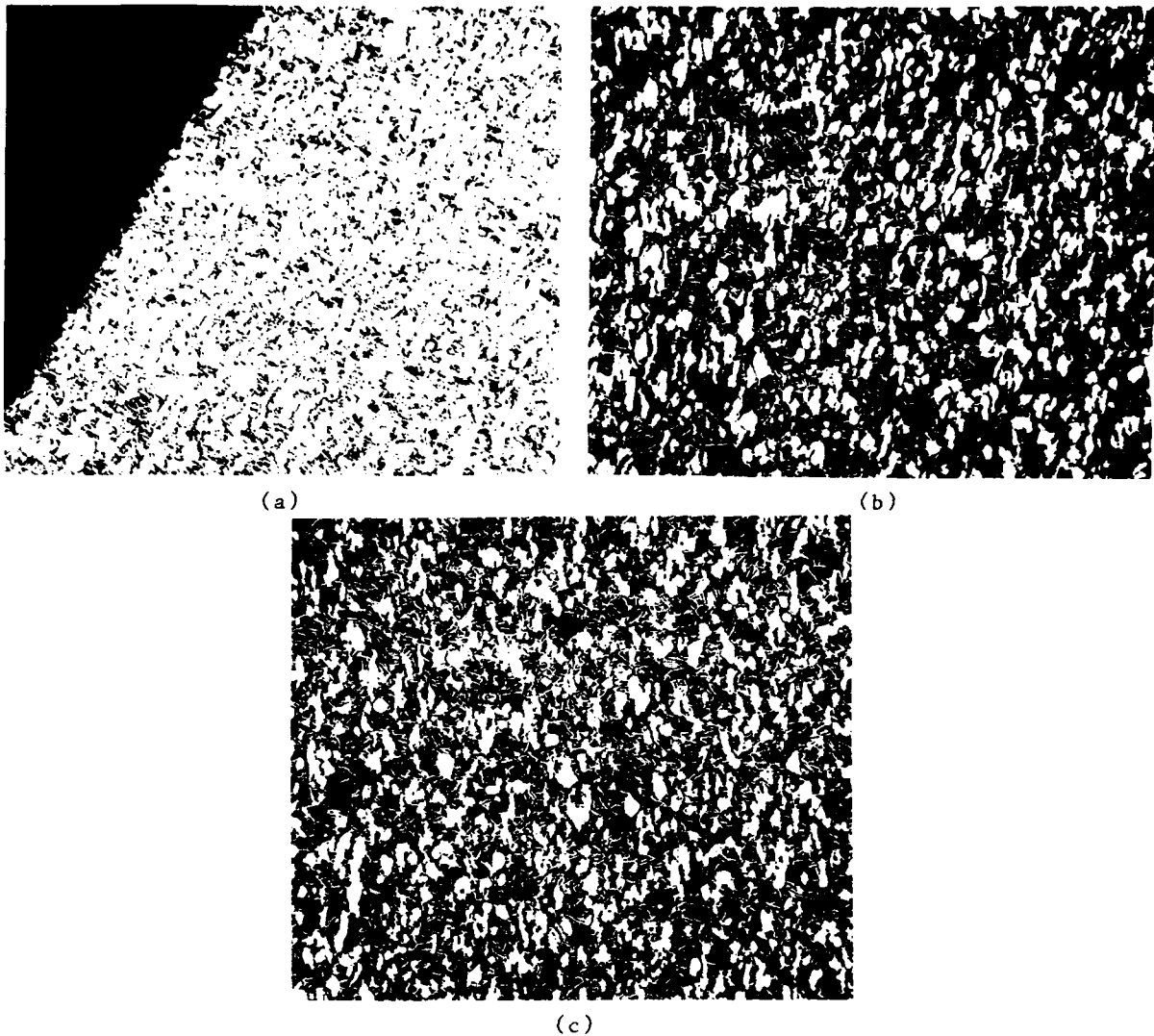
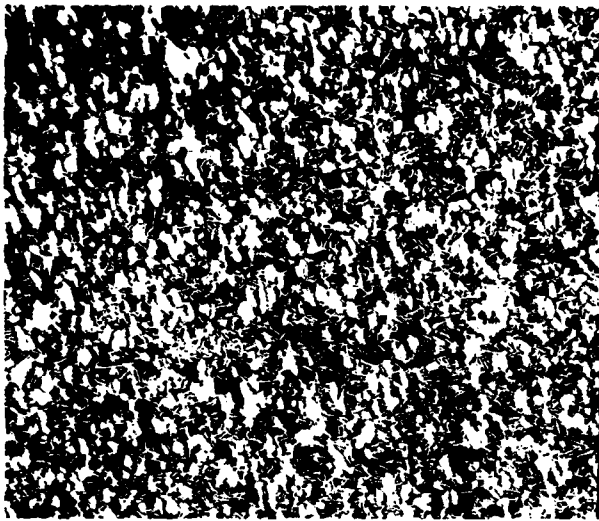
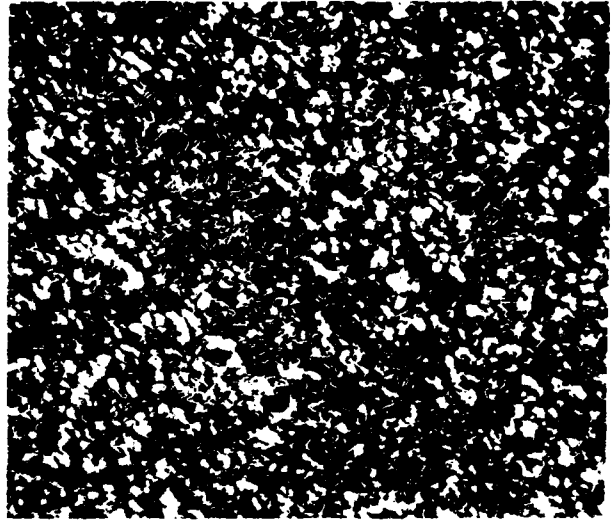


FIGURE B-20. Microscopy along horizontal line of specimen ISO 1700, just above the protruding material at the lower left-end of the cross-section. (See Fig. B-6). (Magnification: 240X)

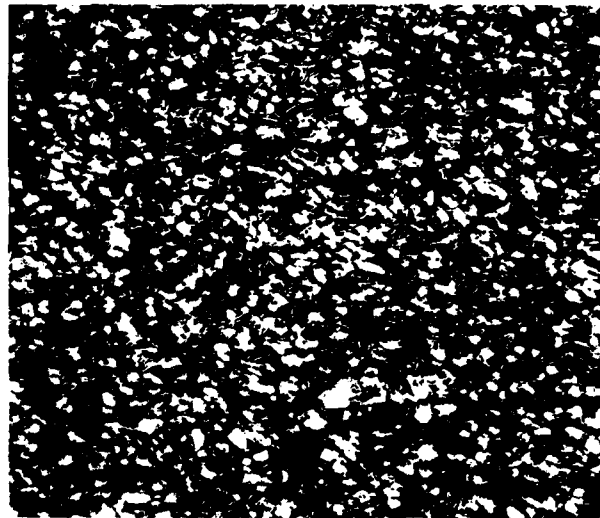
- (a) near the left-end free-surface
- (b) within the left-side non-confined stress-conditions zone
- (c) divergence of flow-lines direction on passing into the internal confined stress conditions zone
- (d) within the left-side of the confined stress-conditions zone
- (e) primary α -grains align themselves also along the shear direction of the kinking-affected zone
- (f) complete disturbance of flow-lines pattern in the middle of kinking-affected zone
- (g) resumption of flow-lines pattern within the right-side of the confined stress-conditions zone
- (h) within the right-side of non-confined stress-conditions zone
- (i) near the right-end free-surface



(d)

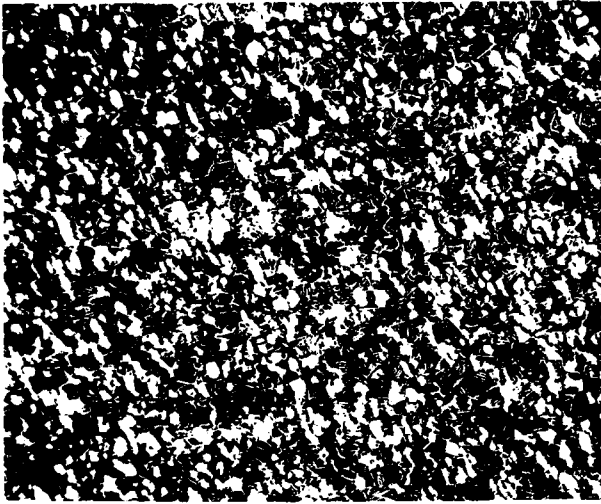


(e)

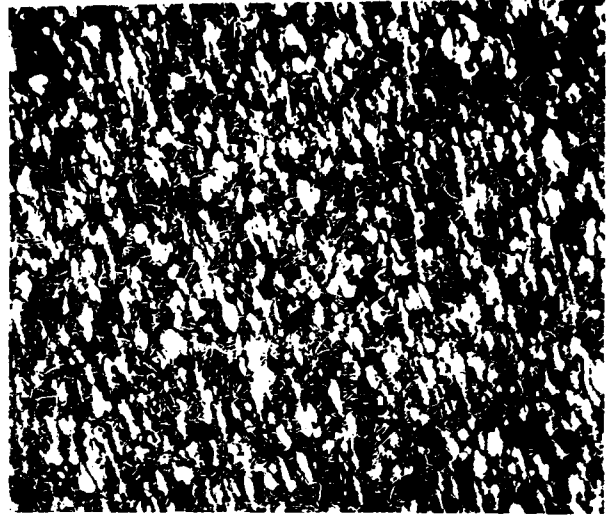


(f)

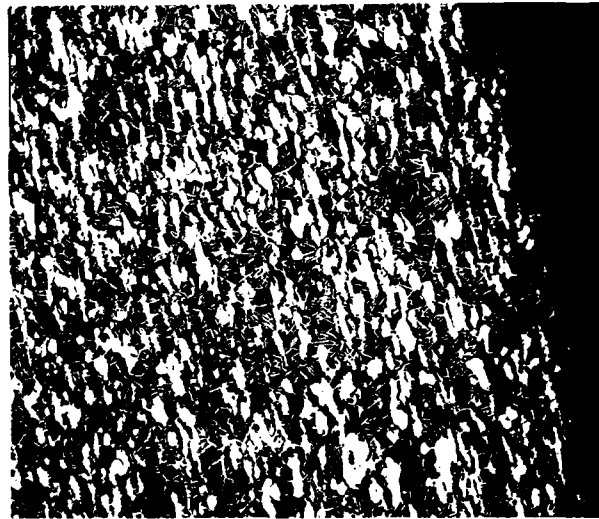
FIGURE B-20. (CONTINUED)



(g)

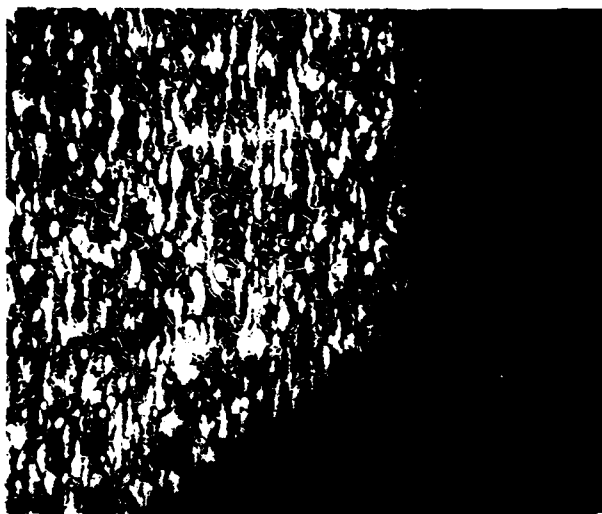


(h)

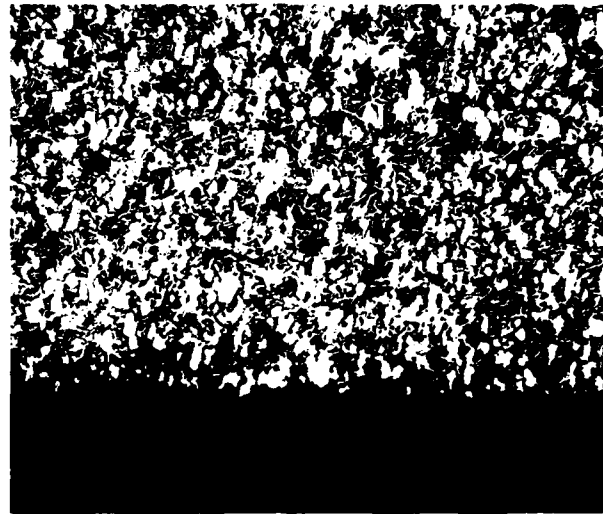


(i)

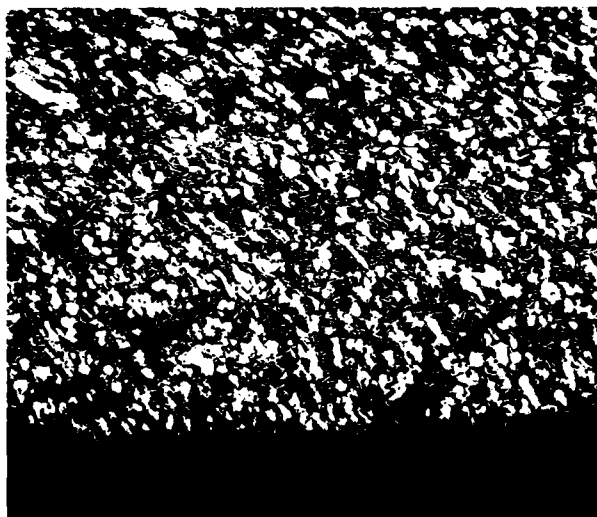
FIGURE B-20. (CONTINUED)



(a)



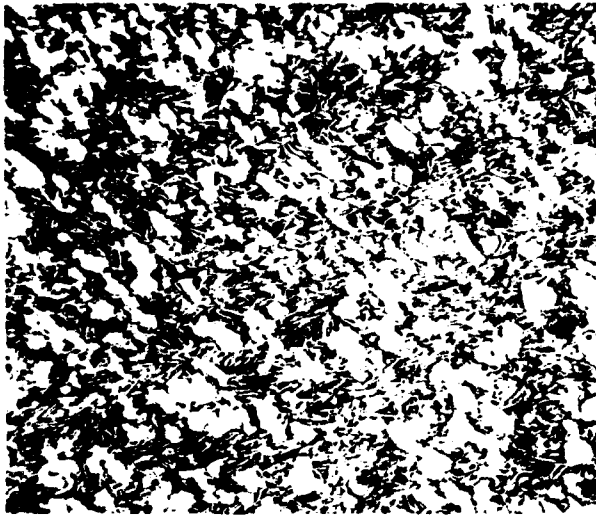
(b)



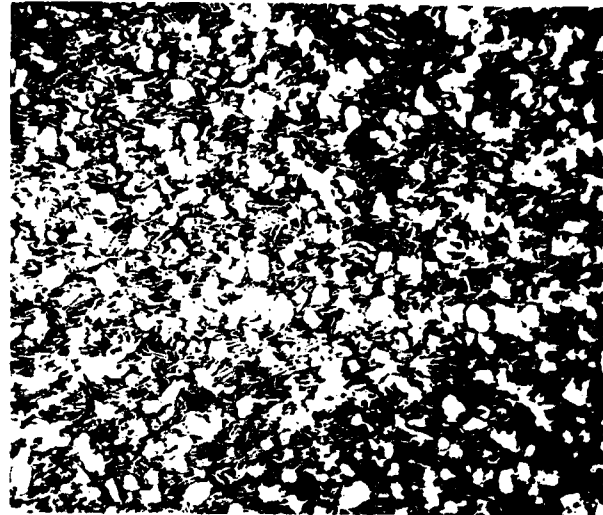
(c)

FIGURE B-21. Microscopy near the lower end-surface of specimen ISO 1800.
(Magnification: 240X)

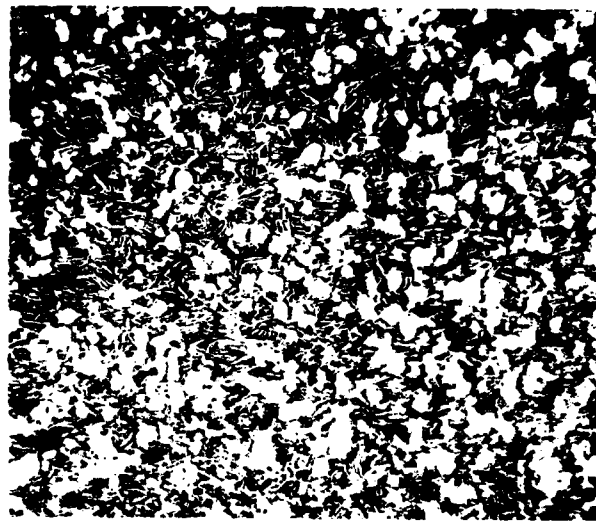
- (a) non-affected flow-lines pattern at the right cross-section corner.
- (b) near the vertical centerline where in highly compressed zone, primary α -particles align themselves along two sets of opposite slip directions (each 45° from the surface normal), as a mean for lateral displacement.
- (c) near the left-end within the protruding material (end of a shear-band), showing that flow-lines pattern has the folding-over characteristics



(a)



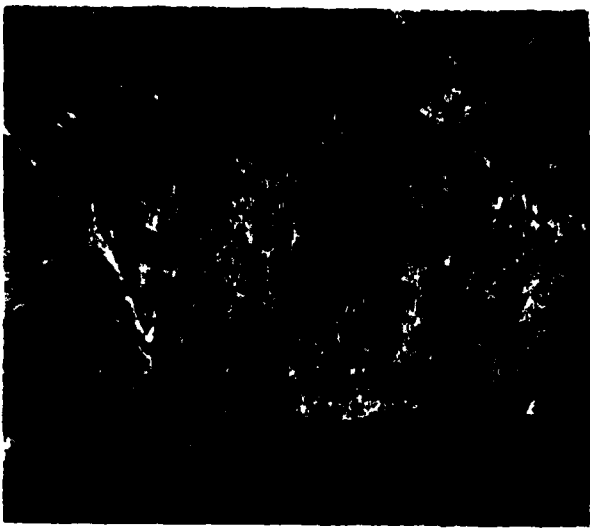
(b)



(c)

FIGURE B-22. Special microscopical features of specimen ISO 1700 (Magnification: X250).

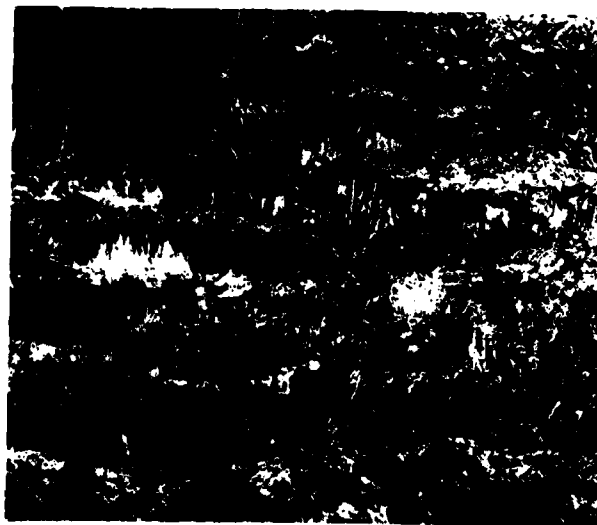
- (a) primary α -particles align themselves also along the shear direction within the kinking-affected zone (See also Fig. B-20e)
- (b) near the middle of lower end surface where primary α -particles align themselves along two sets of opposite slip directions
- (c) the same as (b), but nearer the end-surface where mini-folding-over flow-lines configurations may be seen along the surface



(a)



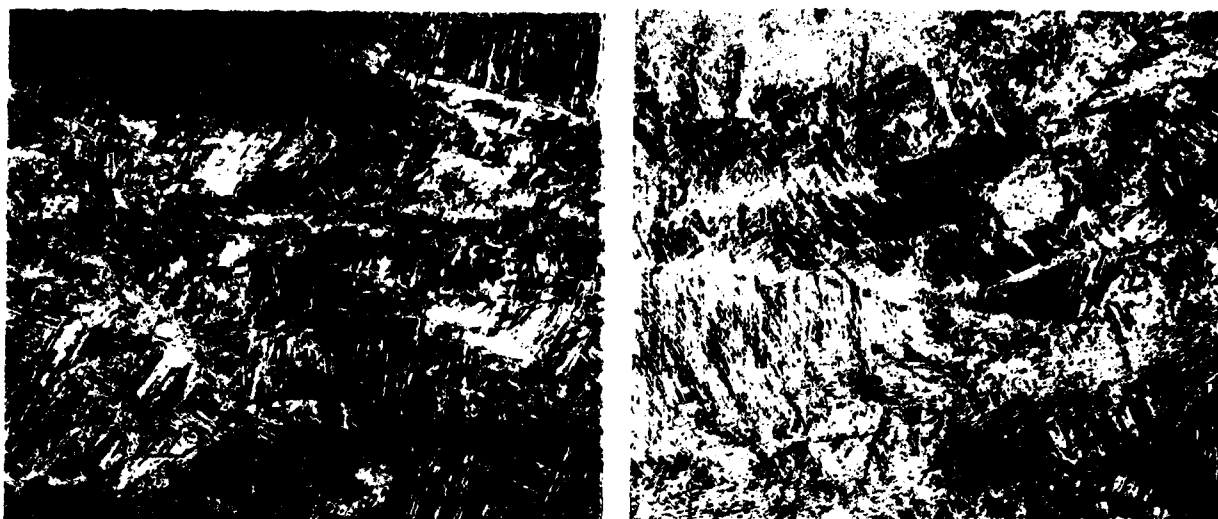
(b)



(c)

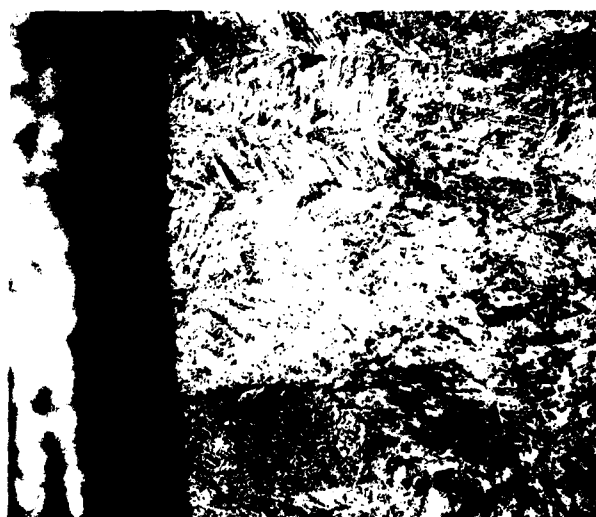
FIGURE B-23. Microscopy along the vertical centerline of specimen 80 cross-section. (Magnification: 100X)

- (a) original microstructure of equiaxed β -grains, preserved within the chilling-affected non-deformed zone
- (b) within the compression-affected zone
- (c) strong compression-affected zone near the middle of the specimen



(a)

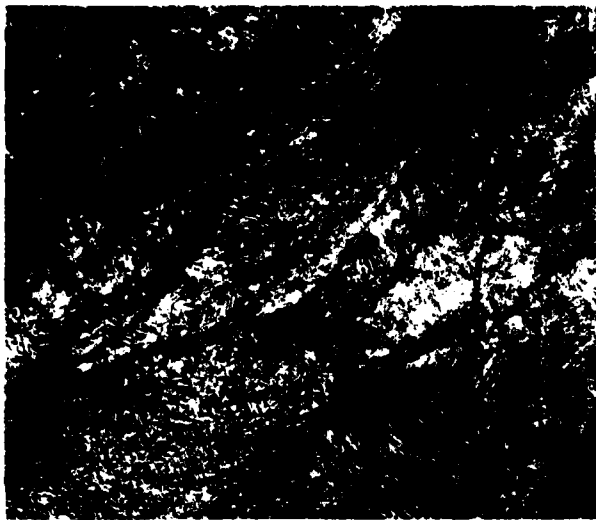
(b)



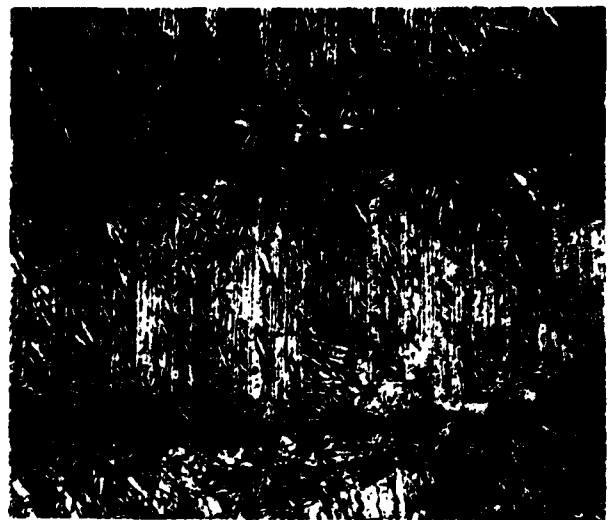
(c)

FIGURE B-24. Microscopy along the horizontal centerline of specimen 80 cross-section. (Magnification: 100X)

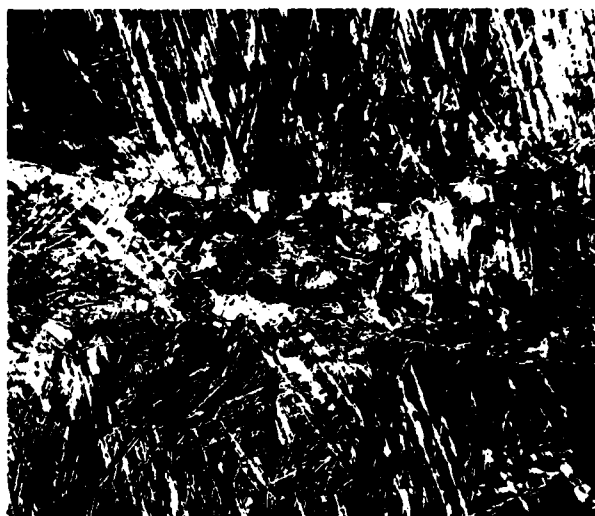
- (a) at the specimen center, high compression distortion of previous β -grains
- (b) along the radial direction. Lesser compression distortion of previous β -grains
- (c) near the peripheral free-surface



(a)



(b)



(c)

FIGURE B-25. Special microscopical features of specimens 80 and 76.

- (a) along obliquely-directed flow-line. (Magnification: X100). specimen No. 80
- (b) α -platelets within deformed previous γ -grains tend to align themselves normal to the maximum distortion direction (flow-line direction). (Magnification: X240). Specimen No. 80.
- (c) the same as in (b), but in specimen No. 76. (Magnification: X400).

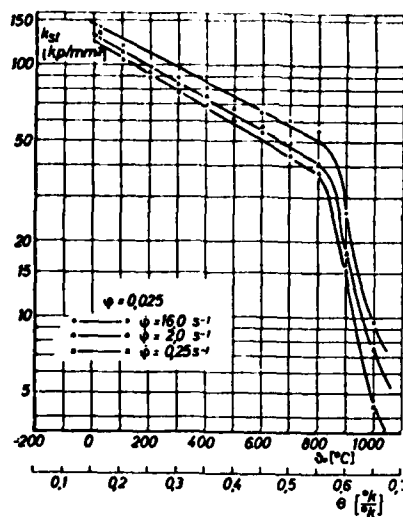


FIGURE B-26. Flow-stress temperature dependency at the critical range of $(\alpha + \beta)$ temperatures for Ti-6Al-4V. (Ref. 4).

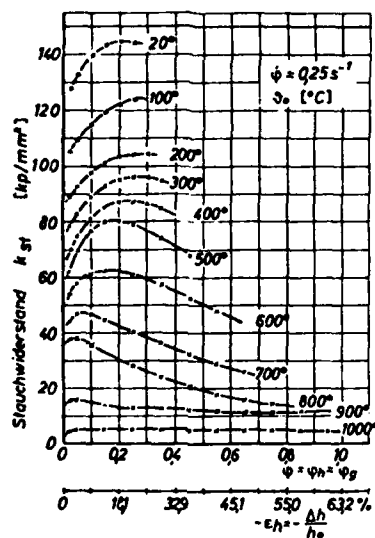


FIGURE B-27. True stress-strain curves for Ti-6Al-4V, at the critical range of $(\alpha + \beta)$ temperatures. (Ref. 4).

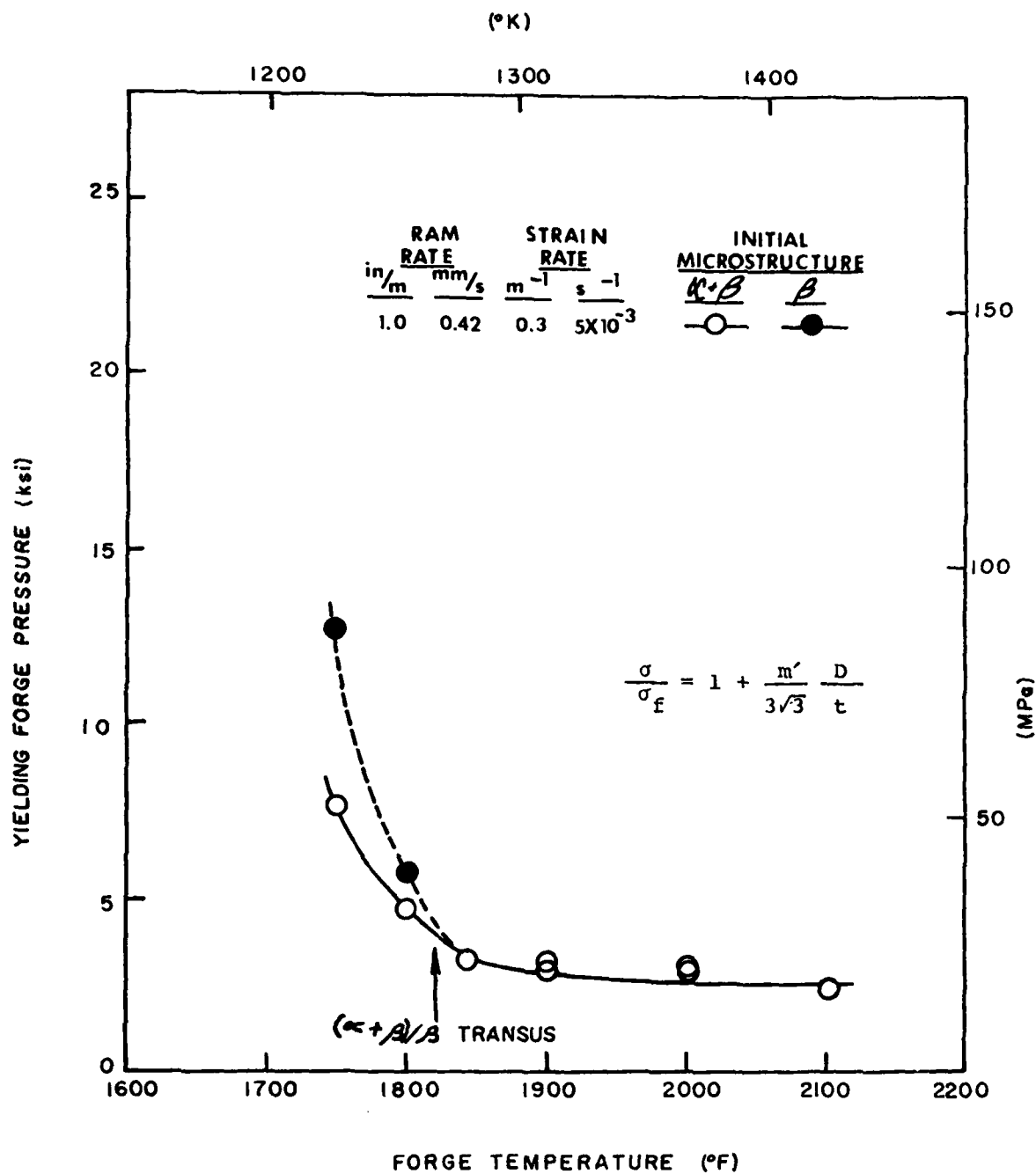
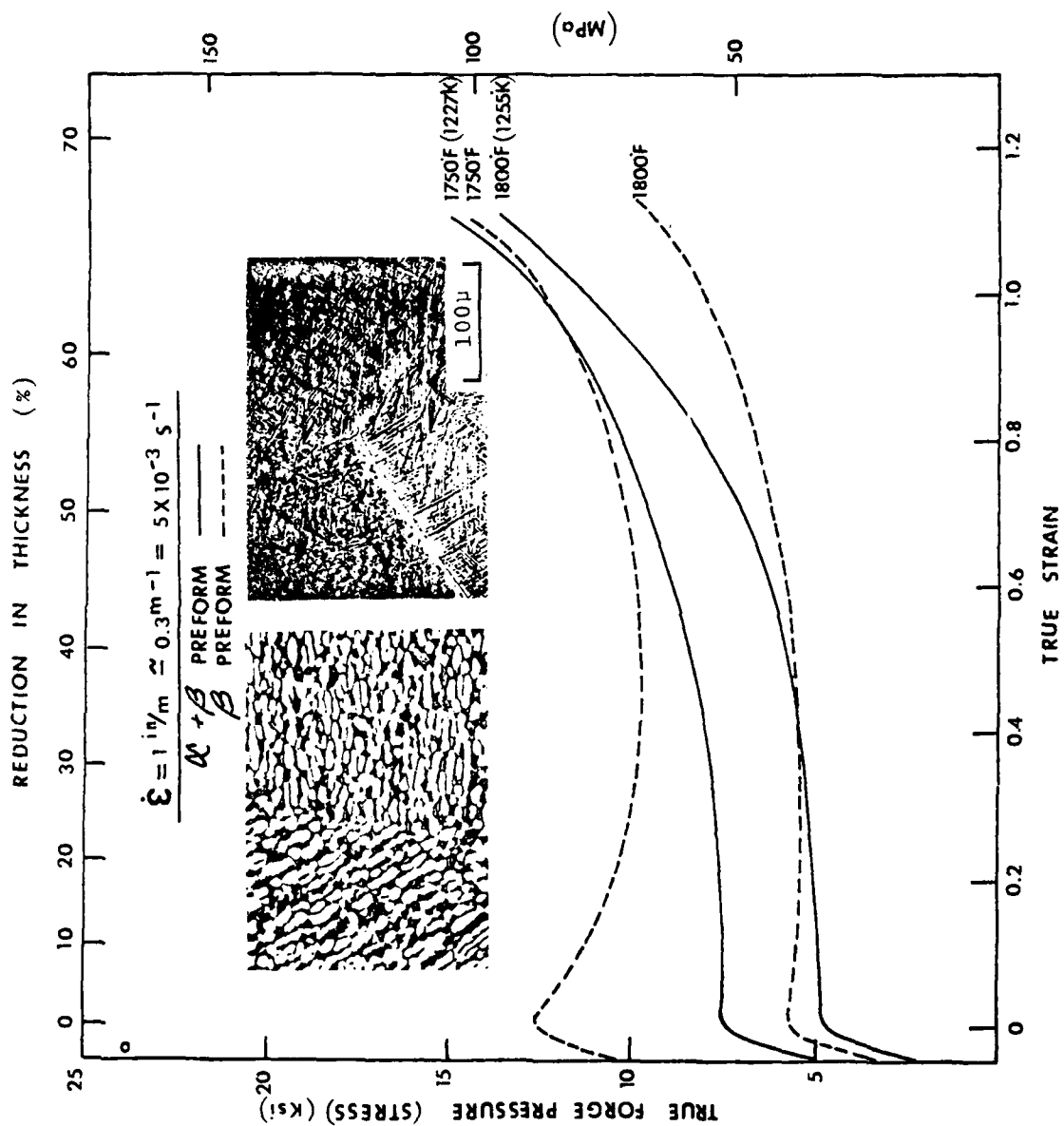


FIGURE B-28. Yielding forge-pressure versus temperature for Ti-6242. (Ref. 6).



B-29. True stress-strain curves for isothermal forging of Ti-6242 alloy, for both ($\alpha + \beta$) and β -preforms. (Ref. 6).

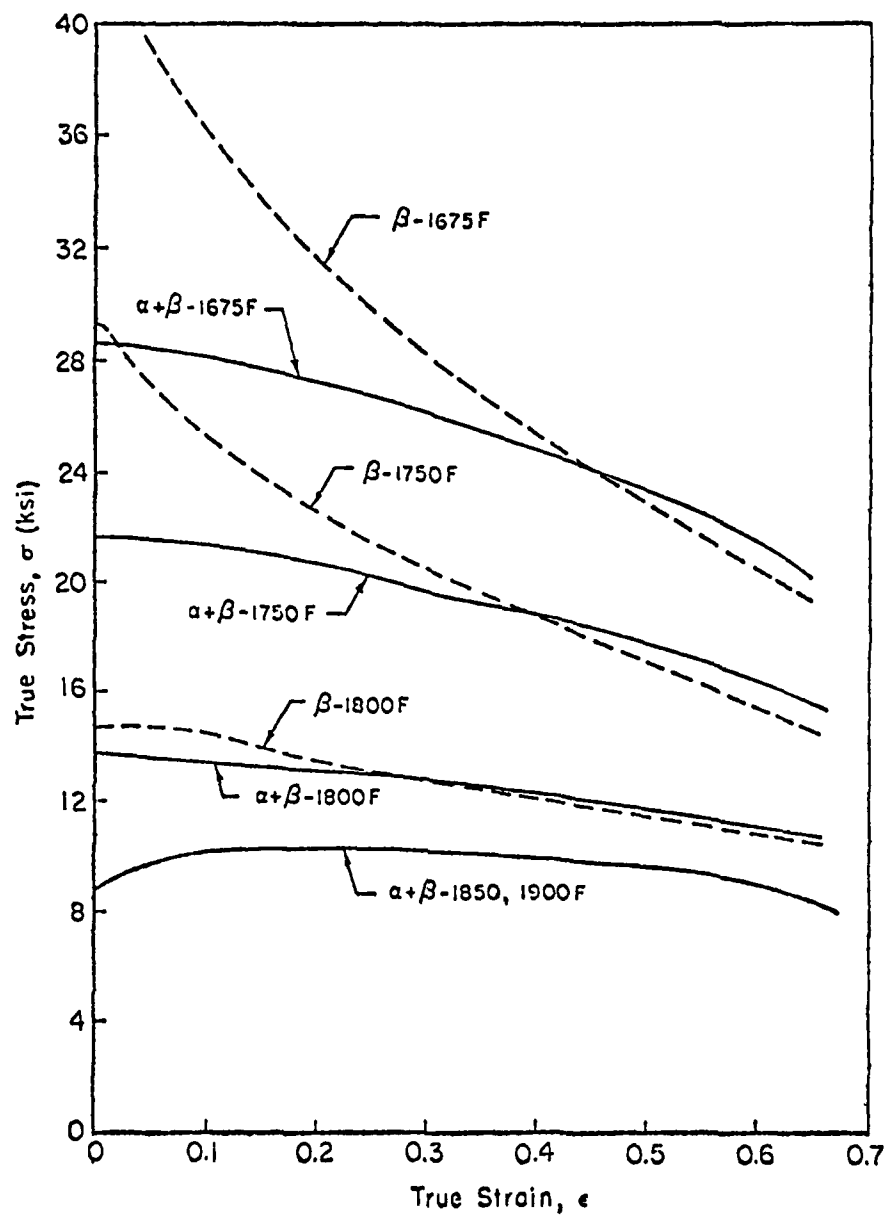


FIGURE B-30. True stress-strain curves for Ti-6242 (0.1 Si) at strain-rate of 10 sec.⁻¹. (Ref. 13).

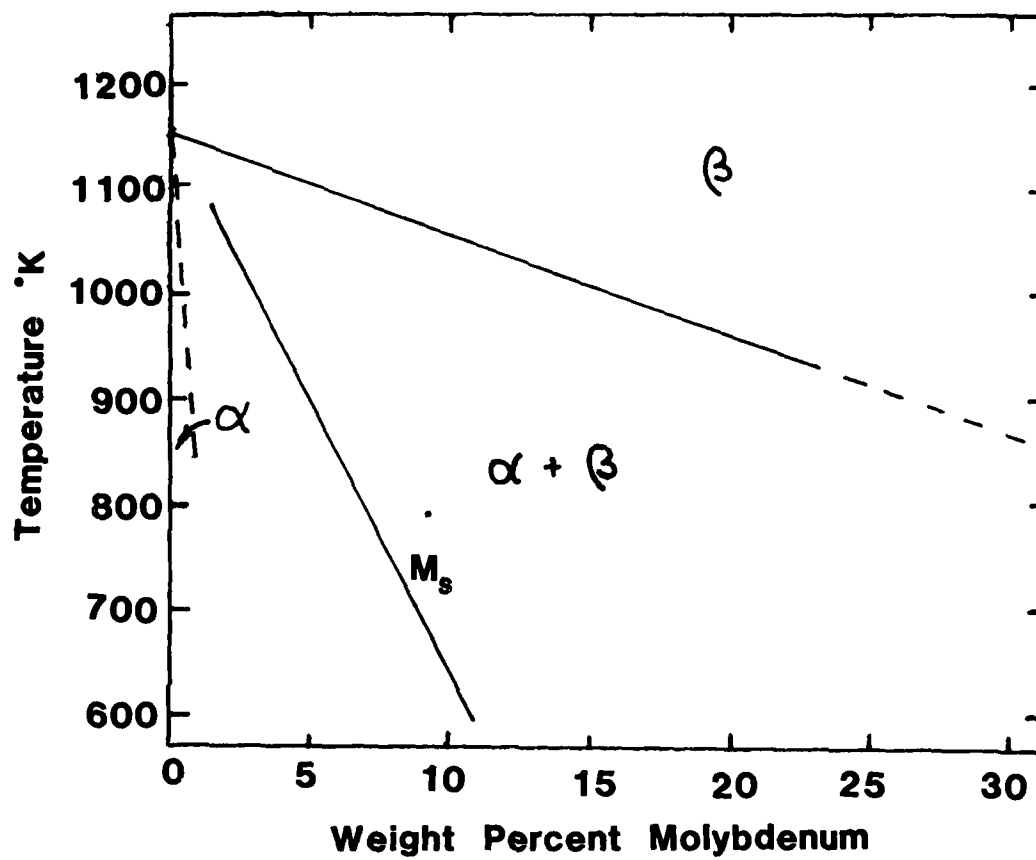


FIGURE B-31. Schematic presentation of isomorphous ($\alpha + \beta$) phase diagram.

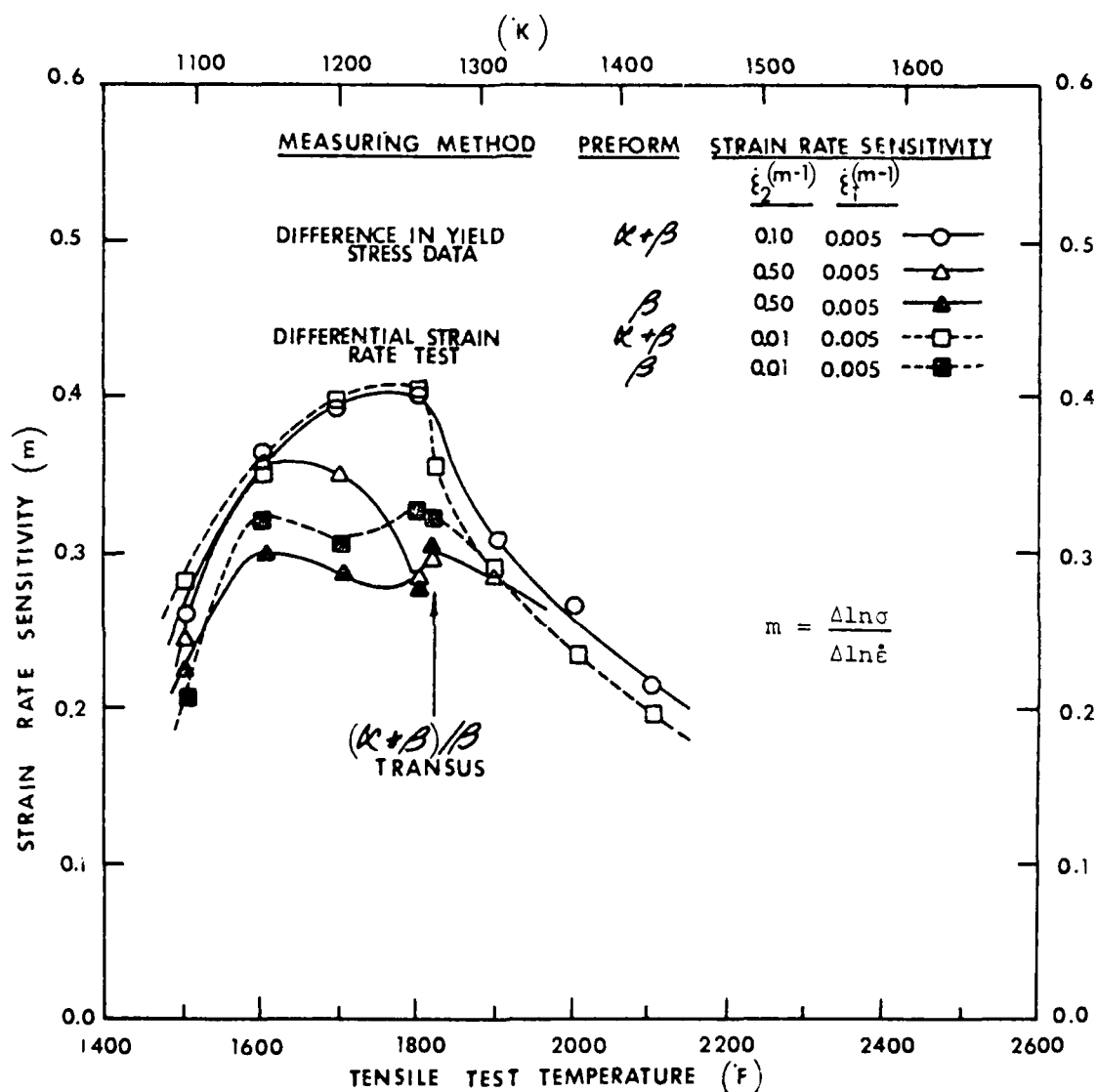


FIGURE B-32. Strain-rate sensitivity factor versus temperature for Ti-6242. (Ref. 6).

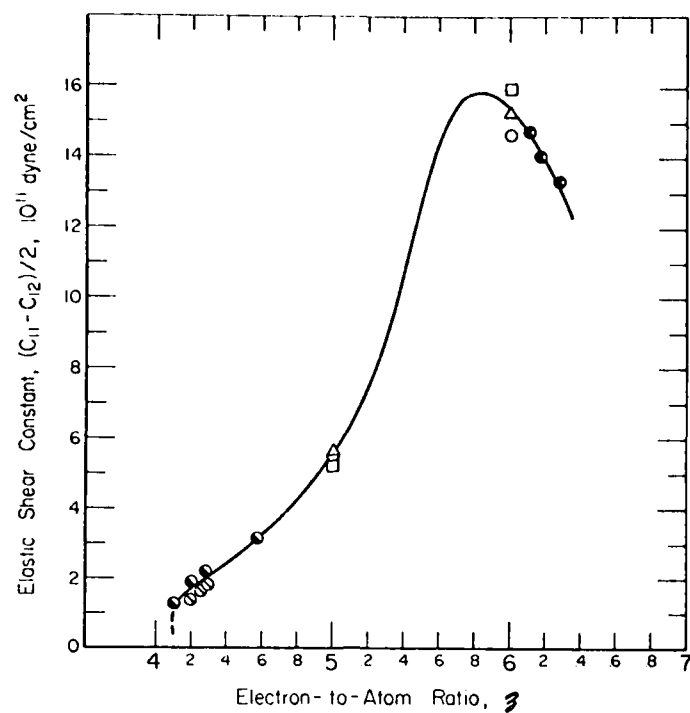


FIGURE B-33. Elastic shear modulus ($C' = (C_{11} - C_{12})/2$) for transition metals and binary alloys. (Ref. 10).

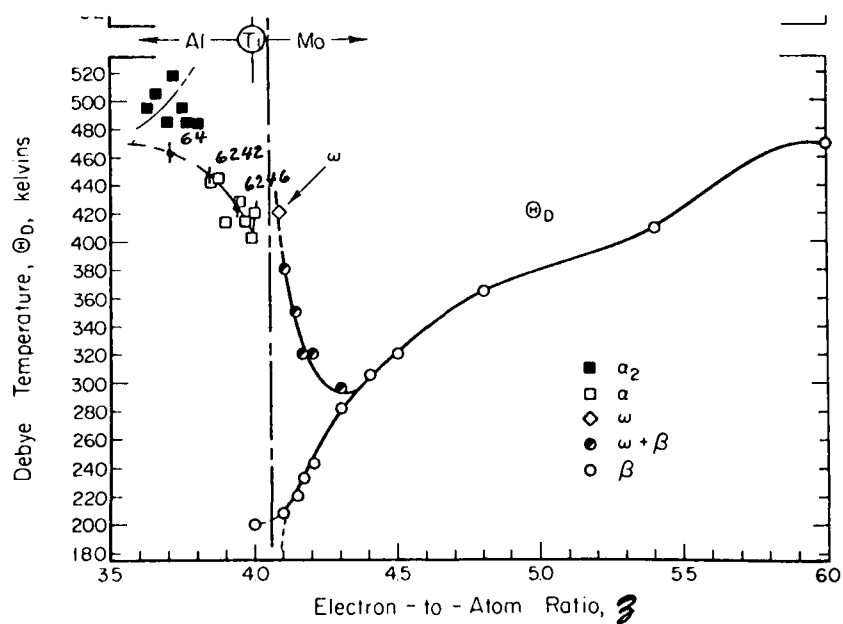


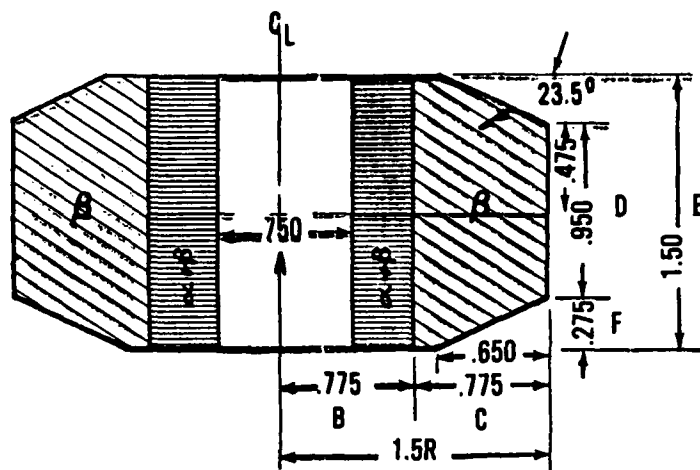
FIGURE B-34. Empirically-derived Debye-temperature as function of Electron-to-atom ratio for Ti-base alloys. (Ref. 11).



FIGURE B-35. Non-uniformity of ϵ -preform forged at $(\alpha + \epsilon)$ critical temperature.
(After Ref. 13).



FIGURE B-36. Structural non-stability of the non-uniform specimen of Fig. 3.10. Microcracks formation at triple-corner junctions. (After Ref. 13).



FORGING PREFORM

FIGURE B-37. Drawing of a combined-disc preform. The inner part made from $(\alpha + \beta)$, the outer part from β -microstructures.

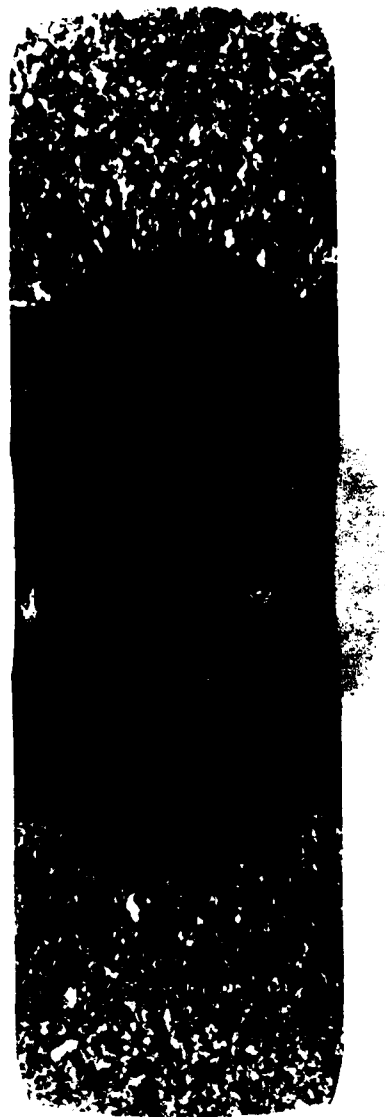


FIGURE B-38. Macro-cross-section of combined disc preform after forging at 1600°F.

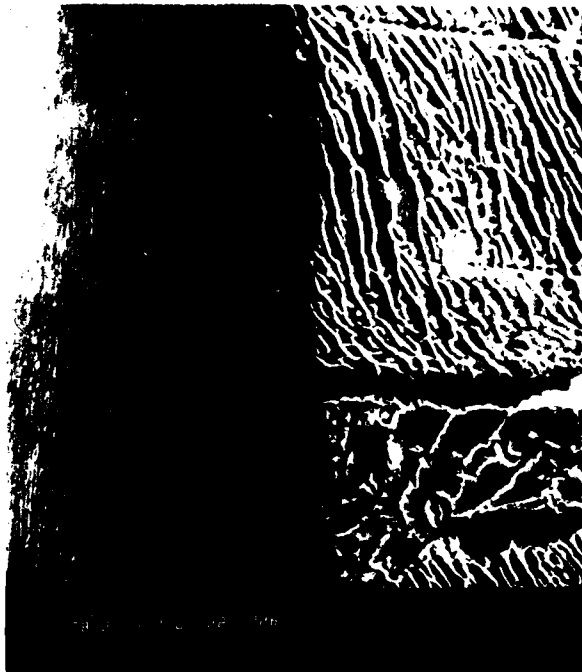
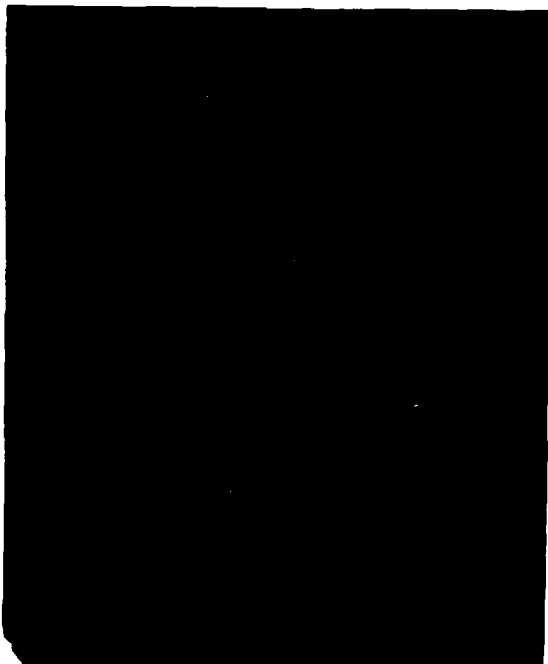


FIGURE B-39. Appearance of same β -transform microstructure at different directionally-cut cross-sections. Scanning-electron microscopy.



FIGURE B-41. Local transformation into β -phase resulting from accommodation deformations near triple-corner junction of previous β -grain-boundaries. Scanning-electron-microscopy.



(a)



(b)



(c)

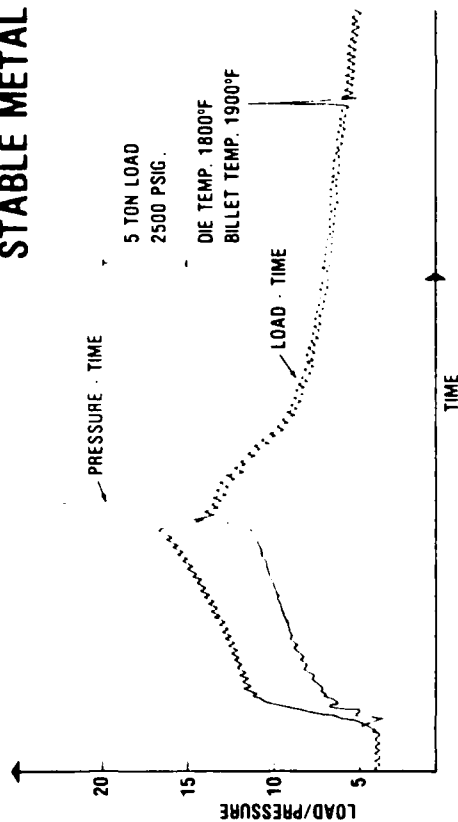
FIGURE B-40.

Microstructures (originally coloured, before black and white prints were made out of them) of 8-preforms under polarized light, after etching with Kroll's reagent.

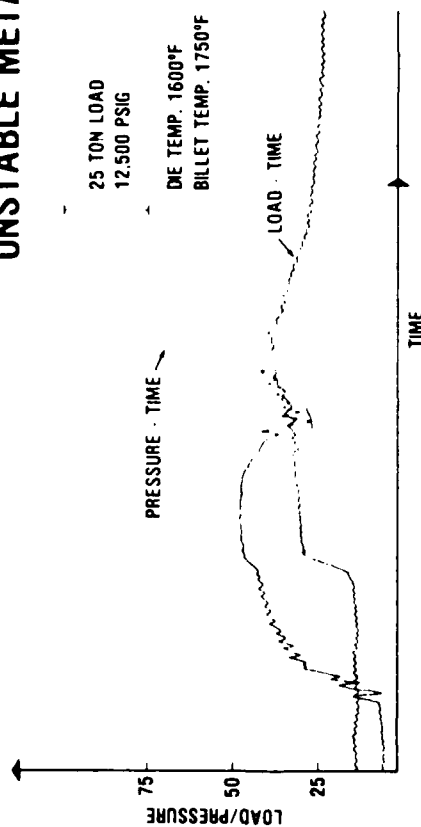
- (a) water-quenched martensite after 4 hours at 1900°F treatment of Ti-6242 alloy.
- (b) the martensite of (a) after 2 hours annealing at 1700°F. "Basket-Weave" microstructure
- (c) the 8-preform microstructure after 7 seconds hot-forging at 1600°F. Blocky martensite

LOAD AND PRESSURE SENSORS INDICATING STABLE AND UNSTABLE METAL FLOW FOR UPSET FORGING OF Ti - 6242 ALLOY ON AFML INSTRUMENTED FORGING PRESS

STABLE METAL FLOW



UNSTABLE METAL FLOW



BASIS FOR DEVELOPING "SMART" MACHINES

FIGURE B-42. Load and pressures sensors for stable ($\alpha + \beta$) and unstable [$(\alpha + \beta)$ - forgings] metal flow for upset-forging of Ti-6242 alloy on AFML instrumented forging press.

APPENDIX C

DETERMINATION OF HIGH-STRAIN-RATE-FLOW-STRESS
DATA FOR Ti-6242 USING A MECHANICAL PRESS

S. L. Semiatin, G. D. Lahoti, and T. Altan
Battelle's Columbus Laboratories
Columbus, Ohio 43201

APPENDIX C

DETERMINATION OF HIGH-STRAIN-RATE-FLOW-STRESS DATA FOR Ti-6242 USING A MECHANICAL PRESS

Introduction

The modelling and simulation of metal deformation processes is complex, requiring many inputs to achieve success. Among these are quantitative descriptions of the properties of the workpiece material such as its flow stress, fracture strain, and physical and thermal properties, on the one hand, and definition of process variables such as deformation rate and lubrication, on the other. Of the material properties mentioned, measurements of flow stress in the literature are very extensive. However, except in a few instances⁽¹⁾, these data are of little use in metal-forming because they were obtained at slow strain rates or under conditions which only roughly approximate actual forming conditions.

The torsion, tension, and compression tests⁽²⁻⁴⁾ have been used widely in obtaining flow stress data at hot working temperatures (temperatures above approximately one-half the melting or solidus temperature). Each test has its advantages and disadvantages. The main advantage of the uniaxial compression test is that the imposed stress state is close to that involved in actual bulk forming operations (e.g., forging, extrusion). In order to obtain reliable data, though, care must be exercised to maintain isothermal conditions (compression dies and specimen at the same temperature) and to ensure uniform deformation by having adequate lubrication throughout testing⁽⁵⁾.

In order to obtain a constant strain rate ($\dot{\epsilon}$) during uniform compression tests, a cam plastometer is needed. However, since cam plastometers are not readily available for use, a mechanical press can be used,

as it is done in the present study, to obtain flow stress data at nearly-constant strain rate⁽¹⁾. It has been shown that, for 50% reduction in height of the specimen, the strain rate during uniform compression tests in a mechanical press remains nearly constant up to a true strain ($\bar{\epsilon}$) of approximately 0.4. Thus, the stress-strain curve obtained in a mechanical press can be considered to be for a constant $\dot{\bar{\epsilon}}$ for strains up to $\bar{\epsilon} = 0.4$ and can be used for practical purposes.

The present work was undertaken to demonstrate that the conventional mechanical press can be used to obtain hot compression data for process modelling purposes. The $\alpha+\beta$ titanium alloy Ti-6Al-2Sn-4Zr-2Mo-0.1Si (hereafter referred to as Ti-6242) was tested in a mechanical press, which is commonly used in forge shops. By running the flywheel at various speeds, flow stress data were obtained as a function of strain rate as well as of strain and temperature. From these data, the operative softening mechanisms during deformation were determined, and insight into the constitutive relation of the alloy was gained.

Materials and Procedures

Materials

The Ti-6242 alloy used in the program was melted and broken down by RMI Company of Niles, Ohio, and had a composition of 6.1% Al, 2.1% Sn, 3.9% Zr, 2.1% Mo, 0.084% Si, balance titanium. Wyman-Gordon Company of Worcester, Massachusetts finish forged the material to 12.07 cm. (4.75 in.) diameter bar. Finish forging was done at either 954 C (1750 F) followed by annealing at 968 C (1775 F) (2 hours + air cool) or 1038 C (1900 F) followed by annealing at 1024 C (1875 F) (2 hours + air cool). From the former forge-heat treatment cycle a microstructure of globular alpha phase (α grain size = 10 μ) in a matrix of transformed beta phase was produced (Figure C-1a)⁽⁶⁾. This microstructure is referred to as the $\alpha+\beta$ microstructure. The second forge-heat treatment cycle was above the $\beta \rightarrow \alpha+\beta$ transus temperature 992 C (1817 F) and produced a transformed microstructure (Widmanstätten or basketweave microstructure) of prior β grain size $\approx 400 \mu$ (Figure C-1b)⁽⁷⁾. This microstructure is referred to as the β microstructure.

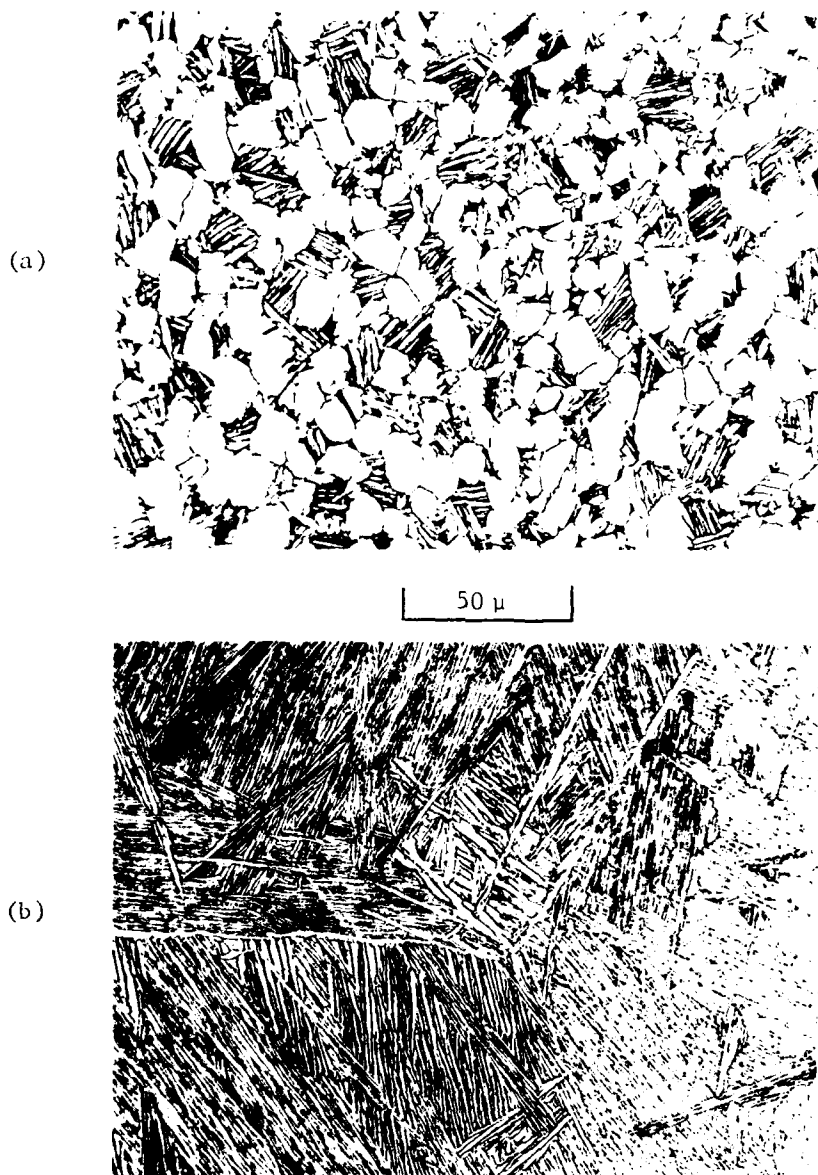


FIGURE C-1. AS-RECEIVED MICROSTRUCTURES OF (a) $\alpha + \beta$
AND (b) β MATERIAL

Experimental Procedures

Cylindrical uniaxial compression specimens with axes parallel to the bar axis were cut from the forged and heat treated materials received from Wyman-Gordon. Specimen dimensions were 1.98 cm. (0.780 in.) in height by 1.27 cm. (0.500 in.) diameter, giving a height to diameter ratio of 1.56:1⁽⁸⁾. Grooves, 0.25 mm (0.010 in.) deep and 0.51 mm (0.020 in.) apart, were put into the ends of the specimens to retain the glass lubricant.

The test conditions are given in Table C-1. Since both the microstructures revert to the single phase bcc, or β microstructure above the transus temperature of 992 C (1817 F), only the $\alpha+\beta$ specimens were tested above this temperature. The glasses were applied to warm test specimens (121 C [\sim 250 F]) using a slurry of finely ground glass in isopropyl alcohol.

Grooved compression samples were preheated and tested in a can-like superalloy jig with a stainless steel base⁽⁵⁾. Having TiC anvils, the jig had a hole in the sidewall to receive a thermocouple for monitoring the temperature of the jig and specimen, which were heated together in a muffle furnace under argon atmosphere. It was found that at temperatures above about 954 C (1750 F), microstructural changes were noticeable for heating times on the order of 10 minutes to 1-2 hours. For instance, the fraction of globular α in the transformed matrix for the $\alpha+\beta$ microstructure went from two-thirds as-received to one-half after 20 minutes at 977 C (1790 F) to one-fourth after 80 minutes at 977 C (1790 F). Furthermore, above the transus temperature, the transformation of the $\alpha+\beta$ microstructure to the β phase was sluggish. Complete transformation required approximately 15 minutes at 1010 C (1850 F). For these reasons, preheating times were kept constant at about 20 minutes for all tests.

The press used in running the experiments was an Erie 4.45 MN (500-ton) mechanical press (Model 10057) of scotch-yoke design. By controlling the angular velocity of the flywheel, the ram speed could be controlled to produce test strain rates of nominally 2 sec.⁻¹ and 10 sec.⁻¹. Details on the flywheel speed and stroke characteristics are given in References (5) and (9). To obtain load and stroke data, the press was equipped with a Sensotec 0.89 MN (100-ton) load cell (Model LCFB-5) and an LVDT made by Daytronic Corporation. Because of the high ram speeds in the tests, a high speed device to record the output data from these transducers was needed. For this, a light-beam oscillograph (Honeywell Visicorder, Model 1858) was employed.

TABLE C-1
TEST CONDITIONS OF THE UNIFORM COMPRESSION TESTS

Test Temperature, C (F)	Preform Microstructure	Nominal Strain Rate (Sec ⁻¹)	Nominal Maximum Strain	Lubricant Used and Its Chemical Composition
913 (1675)	$\alpha+\beta$ β	2, 10	0.75	Ceramic Color Glass 3KB (48.4% SiO ₂ , 27.3% B ₂ O ₃ , 3.78% Al ₂ O ₃ , 0.12% Fe ₂ O ₃ , 11.83% CaO, 0.21% MgO, 8.22% Na ₂ O, and 0.07% K ₂ O)
954 (1750)	$\alpha+\beta$ β	2, 10	0.75	"
982 (1800)	$\alpha+\beta$ β	2, 10	0.75	"
1010 (1850)	$\alpha+\beta$	2, 10	0.75	"
1038 (1900)	$\alpha+\beta$	2, 10	0.75	Saint Gobain Glass 71 (46.0% SiO ₂ , 19.0% B ₂ O ₃ , 6.5% CaO, 4.5% MgO, 25.0% K ₂ O)

The test procedure consisted of removing the test jig (holding the specimen) from the furnace, placing it on the die platen in the press, and activating the press in a single-press-stroke mode. At the end of the deformation (nominally 50% height reduction in all tests), the jig was removed from the press, and the top anvil was taken out to allow specimen removal. After the anvils were cleaned of excess glass, some fresh, ground glass was sprinkled on the bottom anvil, a lubricated sample was placed in the jig after which a small additional amount of glass powder was sprinkled on top of it, and the top anvil replaced. The jig was then replaced in the furnace for preheating. Care must be taken in selecting lubricants and anvil materials for testing different alloys. A poor selection can lead to rapid anvil corrosion at high temperature⁽⁵⁾. However, this was not a problem in the present series of experiments.

Data Reduction and Analysis

Stroke vs. Time Records. A sample light-beam oscillograph record is shown in Figure C-2. Since the derivative of the stroke as a function of time is needed to obtain the strain-rate history, an analytical function was fitted to the stroke versus time curves. The fitting was facilitated by the fact that these curves are sinusoidal functions because of the mechanical characteristics of the press. The amplitude of the fitted sine (or cosine) curve is one-half of the total press stroke (= 25.4 cm. [10 in.]) for the Erie press). Hence, the distance, y , of the ram from bottom dead center, BDC, follows a function of the form:

$$y = 12.7 - 12.7 \cos (\omega t + \phi), \text{ (cm.)} \quad , \quad (C-1)$$

in which ω denotes the flywheel angular velocity and ϕ the flywheel angle at specimen impact ($t = 0$). When the ram reaches the BDC, the specimen is at its final height, h_f . The instantaneous height of the specimen is, therefore, $h = y + h_f$:

$$h(t) = 12.7 + h_f - 12.7 \cos (\omega t + \phi) \text{ (cm.)} \quad . \quad (C-2)$$

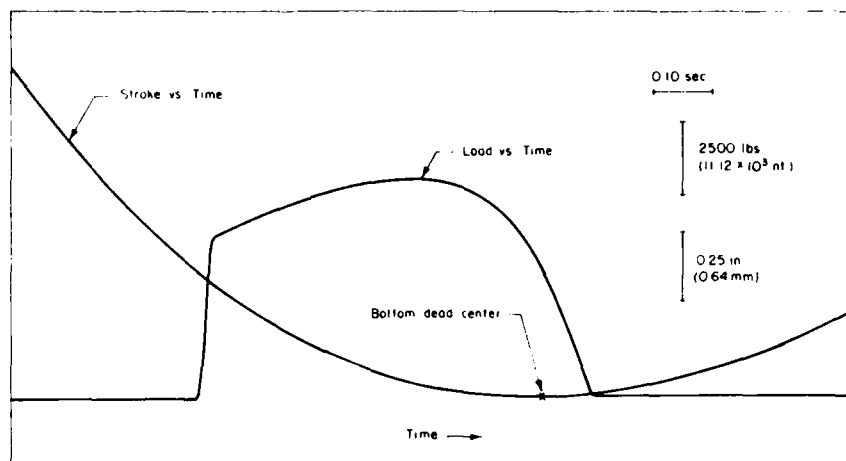


FIGURE C-2. SAMPLE STROKE VS. TIME AND LOAD VS. TIME CHART RECORD FOR HOT COMPRESSION TESTING OF Ti-6242 USING A MECHANICAL PRESS ($\alpha+\beta$ MICROSTRUCTURE, 913 C [1675 F], $\dot{\epsilon} \approx 2 \text{ sec.}^{-1}$)

From Equation (C-2), the true strain $\bar{\epsilon}$, velocity $v (= dh/dt)$, and true strain rate $\dot{\bar{\epsilon}} (= [dh/dt]/h)$ can be determined. In the actual experiments, the phase angle ϕ was determined by knowing the press stroke, initial specimen height, and final specimen height, and the angular velocity was determined from the phase angle and total time of deformation (off the chart records). A small correction (on the order of 5%) had to be made to the angular velocities so calculated to take into account various inertial and frictional effects involved in the press operation.

Load vs. Time Records. Load vs. time records off the light-beam oscillograph (Figure C-2) were reduced using a Summagraphics digitizer (Model ID-1-CTR-17). Load readings were taken at time increments of 0.01 seconds. Assuming uniform deformation and incompressibility, the instantaneous cross-sectional area and, thus, true stress σ could be calculated.

From the measured true stress-true strain data, work input into the compression samples was estimated, and it was assumed that 95% of the work was converted into heat. Since the strain rates in the tests were relatively high (2 and 10 sec.^{-1}), it was further assumed that the heating was adiabatic, and temperature rises, ΔT , were calculated from:

$$\Delta T = \frac{0.95 f \sigma d \epsilon}{\rho c J} \quad (C-3)$$

In this expression, ρ is the mass density and c the specific heat of Ti-6242 (at test temperatures), and J is the mechanical equivalent of heat.

Calculation of Strain-Rate-Sensitivity Parameters. It was assumed that at a given strain, the flow stress dependence on strain rate for Ti-6242 follows a power relation:

$$\sigma \propto \dot{\epsilon}^m \quad (C-4)$$

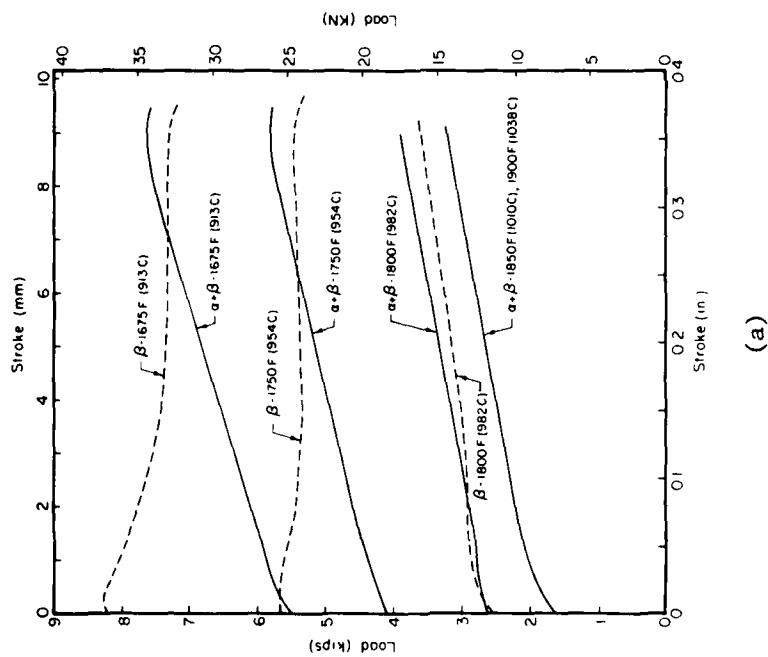
With this assumption, m , the strain-rate-sensitivity parameter, was obtained from the stress-strain data at nominal strain rates of 2 and 10 sec^{-1} . The relation $\{\log (\bar{\sigma}_1 / \bar{\sigma}_2) / \log (\dot{\epsilon}_1 / \dot{\epsilon}_2)\}$ (where $\bar{\sigma}_1$ is the stress at the strain rate $\dot{\epsilon}_1 \approx 10 \text{ sec}^{-1}$, and $\bar{\sigma}_2$ is the stress at the strain rate $\dot{\epsilon}_2 \approx 2 \text{ sec}^{-1}$) was applied at strains of $\bar{\epsilon} = 0.05, 0.15, 0.30, 0.50$, and 0.60 .

A second method of calculating the strain-rate-sensitivity parameter was made possible by the kinematics of the mechanical press. As the press ram approaches the BDC, its velocity v , drops sinusoidally to zero. Because the specimen height h is decreasing as well, the strain rate (v/h) is somewhat constant, except for the last 10 to 20% of the deformation. Here the strain rate drops from a value on the order of the nominal value to zero. Plotting the $\bar{\sigma}-\bar{\epsilon}$ data from these terminal portions of the stress-strain measurements on log-log graph paper allowed estimates of m for Ti-6242 to be obtained also. These plots were linear supporting the hypothesis of a power-law dependence of flow stress on strain rate.

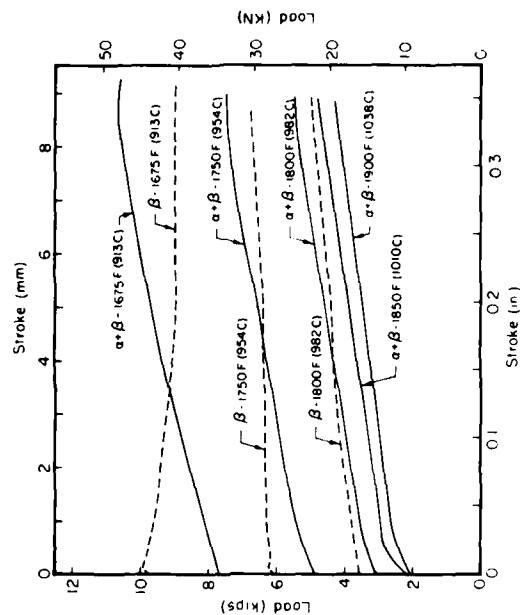
Results

Load-Stroke Characteristics and Deformation Features

The load-stroke plots for Ti-6242 tests run at nominal strain rates of 2 sec^{-1} and 10 sec^{-1} are shown in Figure C-3. The basic trends of the plot for a given temperature and microstructure are similar for the two strain rates. However, it can be noted that, at a given temperature, the load-stroke curves for the $\alpha+\beta$ microstructure are considerably different from those for the β microstructure, particularly at 913 and 954 C (1675 and 1750 F). The basic difference is that the $\alpha+\beta$ curves increase monotonically, whereas the β curves either pass through a maximum and decrease monotonically or deform under constant load.



(a)



(b)

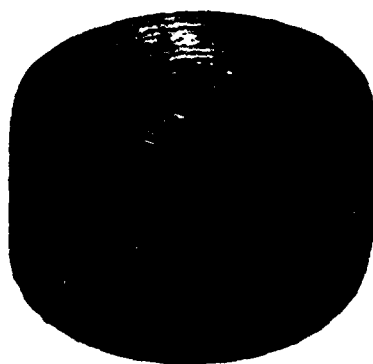
FIGURE C-3. LOAD-STROKE CURVES FOR Ti-6242-0.1 Si ISOTHERMAL COMPRESSION TESTS RUN AT
(a) 2 SEC.⁻¹ AND (b) 10 SEC.⁻¹

As is well known from tensile testing⁽¹⁰⁾, increasing load-stroke curves imply that deformation is stable and uniform. On the other hand, decreasing load-stroke curves, or deformation under falling load, can result in unstable, nonuniform flow even in compression⁽¹¹⁾. These generalizations were supported by the deformation features observed in the present investigation. In Figure C-4, a representative $\alpha+\beta$ compression specimen is shown in a plan view and etched macrosection. From these pictures, it can be inferred that the deformation was stable and that the small degree of nonuniformity in the cross section resulted from frictional effects. In contrast, the deformation of β specimens typically was grossly nonuniform (Figure C-5). In addition, the macroscopically nonuniform deformation of the β specimen was accompanied by microscopic grain-boundary and triple-point cracks (Figure C-6). The differences in load-stroke and deformation behavior are also evident in the stress-strain curves to be discussed next.

Stress-Strain Curves

As mentioned previously, load-stroke data were reduced to true stress-true-strain data assuming frictionless, uniform deformation. This is a good assumption for $\alpha+\beta$ microstructure data, but somewhat approximate for β microstructure, especially at 913 and 954 C (1675 and 1750 F). For both microstructures and strain rates, the stress-strain curves (Figure C-7) decrease monotonically with strain (i.e., flow soften), an effect especially pronounced for the β microstructures. It is estimated that the error limits for $\alpha+\beta$ data are +5%, -2% for stresses and ± 0.01 for the strains. The flow stress data for this microstructure are similar to those obtained previously in hydraulic and mechanical presses⁽⁵⁾. The error limits for the β microstructure are +10%, -2% for stresses and ± 0.01 for strains. However, it is thought that the basic trends in β stress-strain data are correct.

It can be noted that the flow stresses of this alloy (for both microstructures) are strongly dependent on temperature and strain rate at hot working temperatures. Furthermore, near the end of the deformations (i.e., at $\epsilon > 0.50$), the true stress drops rapidly for both $\alpha+\beta$ and β microstructures. This trend coincides with the rapid drop in strain rate at the end of the press stroke (Figure C-8).



(0.5 in.)
12.7 mm.

(a)



(0.2 in.)
5.08 mm

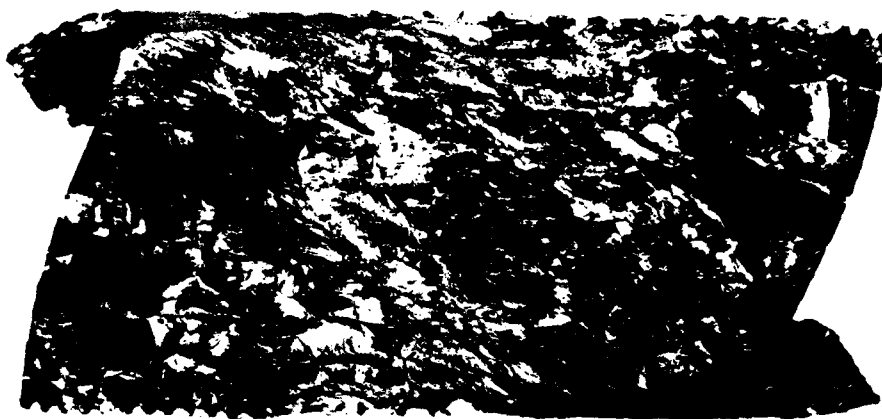
(b)

FIGURE C-4. (a) PLAN VIEW AND (b) MACRO-SECTION OF $\alpha+\beta$ ISOTHERMAL COMPRESSION SPECIMEN DEFORMED AT 913 C (1675 F), $\dot{\epsilon} \approx 2 \text{ sec.}^{-1}$



(0.5 in.)
12.7 mm

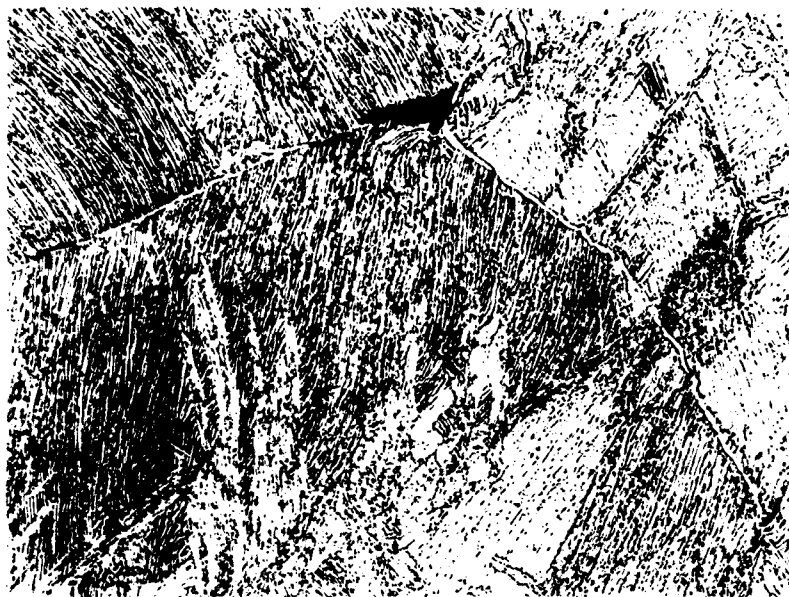
(a)



(0.2 in.)
5.68 mm

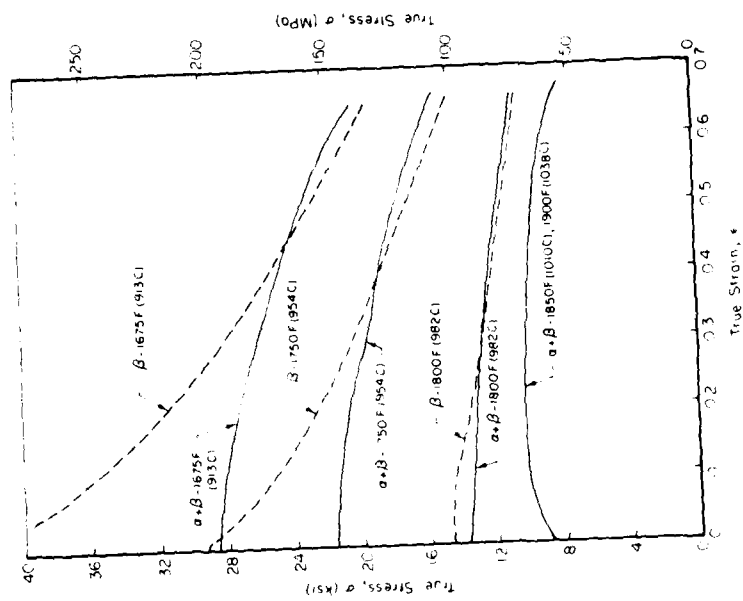
(b)

FIGURE C-5. (a) PLAN VIEW AND (b) MACRO-SECTION OF β ISOTHERMAL COMPRESSION SPECIMEN DEFORMED AT 913 C (1675 F), $\dot{\epsilon} \approx 10 \text{ sec.}^{-1}$

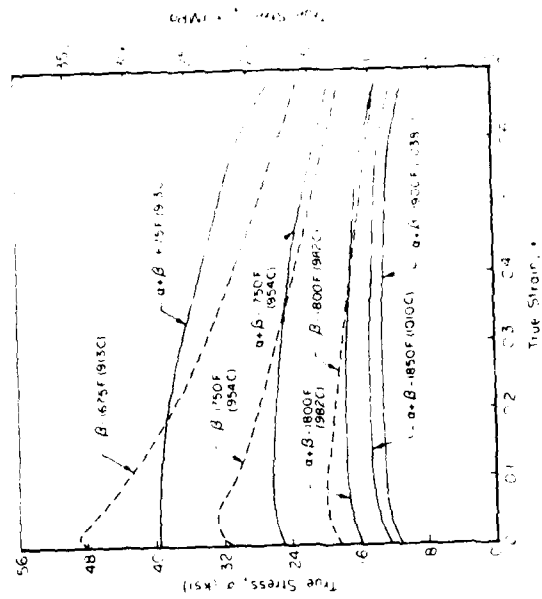


100μ

FIGURE C-6. TRIPLE-POINT CRACKING IN A β COMPRESSION SPECIMEN DEFORMED AT 913 C (1675 F), $\dot{\epsilon} \approx 2 \text{ sec.}^{-1}$

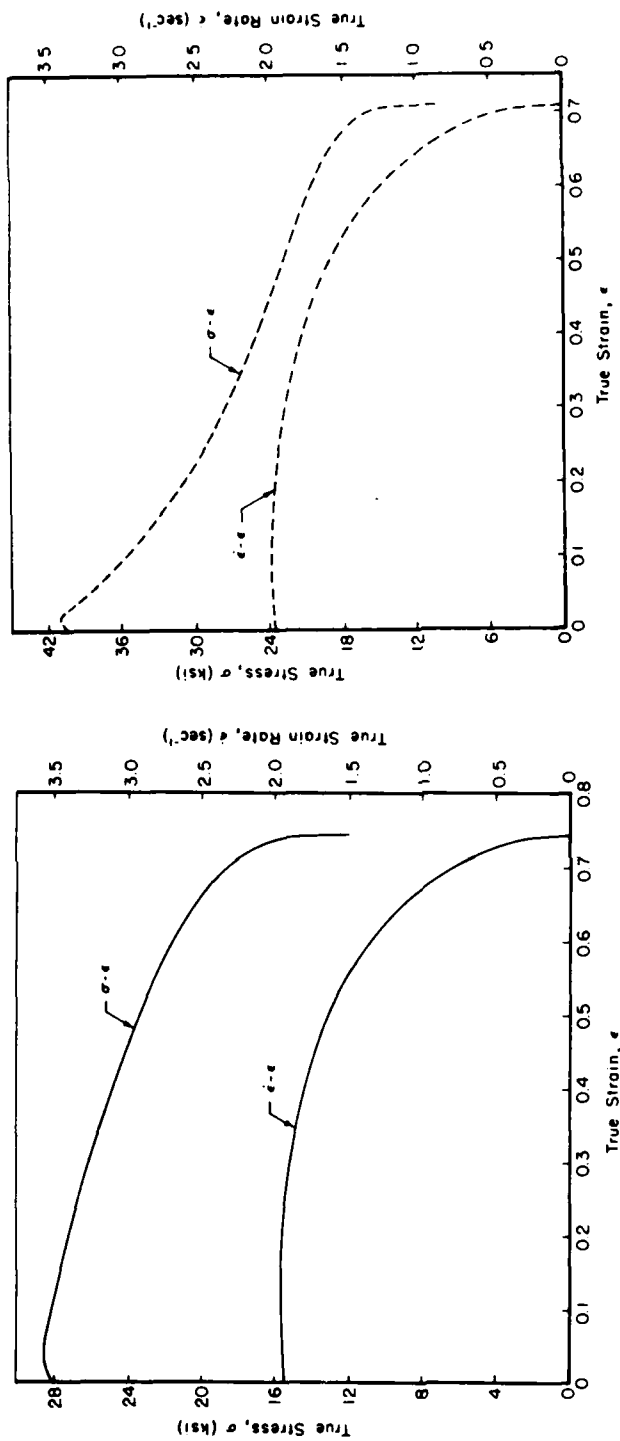


(a)



(b)

FIGURE C-7. TRUE STRESS-STRAIN CURVES FOR Ti-6242-0.1 Si FOR TESTS RUN AT STRAIN RATES OF (a) 2 sec.⁻¹ AND (b) 10 sec.⁻¹



(a)

(b)

FIGURE C-8. STRESS VERSUS STRAIN AND STRAIN RATE VERSUS STRAIN PLOTS AT 913 C (1675 F), $\dot{\epsilon} \approx 2 \text{ sec.}^{-1}$ FOR (a) $\alpha+\beta$ AND (b) β MICROSTRUCTURES

Strain-Rate-Sensitivities

Determined from tests at nominal strain rates of 2 sec.^{-1} and 10 sec.^{-1} , the strain-rate-sensitivity parameter, m , was found to show a non-negligible temperature dependence (Figure C-9). The dependence of m on strain is weak except at small strains for the $\alpha+\beta$ microstructure. The m values determined from the terminal portions of stress-strain curves are of similar magnitude as these m 's. However, they are (1) consistently lower for the $\alpha+\beta$ microstructure and (2) approximately the same for the β microstructure when compared to measurements from the former method (Table C-2). The lower values for the $\alpha+\beta$ microstructure can be rationalized from the viewpoint that the dislocation-substructure changes at the end of a particular deformation are less than the substructure differences obtained in two separate tests at different nominal strain rates. It is these dislocation substructures and changes in substructure which determine the flow stress and rate sensitivity of the flow stress⁽¹²⁾. The present $\alpha+\beta$ data are sketchy, and, therefore, full discussion of it as well as the β data must await further documentation.

TABLE C-2
STRAIN-RATE-SENSITIVITY PARAMETER m FOR
Ti6242 ALLOY AT VARIOUS TEMPERATURES

Micro-Structure	Temperature	m from Tests at 2 and 10 sec.^{-1} ($\bar{\epsilon} = 0.68$)	m from Terminal Portions of σ - ϵ Data (Avg. of $\bar{\epsilon}=2$ and 10 sec.^{-1} Data)
$\alpha+\beta$	913 C (1675 F)	0.206	0.181
	954 C (1750 F)	0.167	0.145
	982 C (1800 F)	0.201	0.176
	1010 C (1850 F)	0.259	0.145
	1038 C (1900 F)	0.217	0.173
β	913 C (1675 F)	0.134	0.153
	954 C (1750 F)	0.121	0.156
	982 C (1800 F)	0.190	0.153

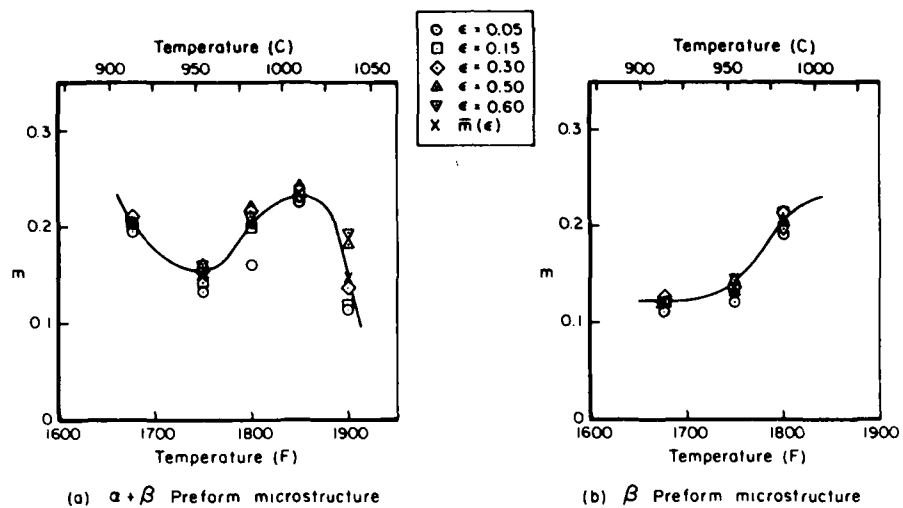


FIGURE C-9. STRAIN-RATE-SENSITIVITY PARAMETER, m , FOR (a) $\alpha + \beta$ MICROSTRUCTURE AND (b) β MICROSTRUCTURE

Discussion

Mechanisms of Flow Softening

At hot working temperatures, the stress-strain curves of most metals exhibit an initial work-hardening stage followed by a flow stress plateau or drop in flow stress, the latter phenomenon usually referred to as "flow softening". The flow softening in single phase metals usually results from one or a combination of the following⁽¹¹⁾:

- (a) Adiabatic heating - At high strain rates, most deformation work is converted into heat which raises the specimen temperature. In metals with sharp dependencies of flow stress on temperature, this leads to marked flow softening.
- (b) Dynamic recovery.
- (c) Dynamic recrystallization.
- (d) Generation of a softer texture during deformation.

For metals of two or more phases, the above softening mechanisms as well as others may operate at hot working temperatures⁽¹³⁾. Jonas and Luton⁽¹¹⁾ have listed examples of these softening mechanisms also:

- (a) Coarsening of Widmanstätten and martensitic structures.
- (b) Spheroidization of lamellar structures or precipitate coarsening.

The literature on $\alpha+\beta$ titanium alloys suggest that several of these dynamic softening mechanisms are operative in Ti-6242. For instance, the low strain-rate data of Griest, Sabroff, and Frost⁽¹⁴⁾ for Ti-6Al-4V exhibit a flow stress plateau after a short initial region of work hardening. As Jonas⁽¹⁵⁾ and others have shown, this behavior is indicative of softening principally through dynamic recovery. Analysis by Sulijoadikusumo and Dillon⁽¹⁶⁾ of various Ti-6Al-4V high strain-rate, stress-strain curves in the literature supports the theory that marked flow softening can arise from adiabatic heating for materials such as $\alpha+\beta$ titanium alloys which possess a marked temperature dependence of the flow stress. The present stress-strain data for Ti-6242 have been interpreted in light of these softening mechanisms.

Flow Softening in Ti-6242 - $\alpha+\beta$ Microstructure

Softening from Adiabatic Heating. It has been determined that the observed flow softening in $\alpha+\beta$ stress-strain data (Figure C-7) can be attributed largely to adiabatic heating. An example of how this conclusion can be drawn, consider the stress-strain data obtained at the nominal strain rate of 10 sec.^{-1} . (The findings for $\dot{\epsilon} = 2 \text{ sec.}^{-1}$ were similar.) The 10 sec.^{-1} data have been replotted to show the flow stress as a function of the nominal test temperature at given strain levels (Figure C-10). It appears that the flow stress is a function of strain and temperature for the given strain rate. After calculating the temperature rise associated with the measured level of deformation work [Equation (C-3)] and replotting each flow stress data point at the adjusted temperature (= nominal temperature plus temperature increase due to adiabatic heating), the flow stress versus temperature behavior appears as in Figure C-11. Because one flow stress versus temperature curve appears to fit all of the test data (except that for strains less than or equal to about 0.10), it may be surmised that the flow stress dependence on strain is weak. In other words, a high strain-rate, isothermal stress-strain curve for this material would show an initial region of work hardening followed by a stress plateau, as has been observed for low strain-rate, isothermal testing of similar $\alpha+\beta$ titanium alloys⁽¹⁴⁾.

Softening Due to Strain-Rate Effects Associated with Mechanical Press Testing. A further, small "correction" has been applied to the Ti-6242 flow stress data obtained using the mechanical press. This is a correction for the variation of strain rate during the deformation. The data obtained at nominally $\dot{\epsilon} = 10 \text{ sec.}^{-1}$ were adjusted by employing the power law expression, Equation (C-4), to obtain $\bar{\sigma} (10 \text{ sec.}^{-1}) = \sigma (\dot{\epsilon}) \left[\frac{10}{\dot{\epsilon}} \right]^m$. ($\dot{\epsilon}$ is the actual strain rate for a given flow stress data point, and m is the measured strain-rate-sensitivity parameter). Because of the drop in strain rate at the end of the deformation and the large rate sensitivity of the alloy, the flow stresses at strains greater than about 0.50 are much lower than would be obtained in a constant strain rate test. Flow stress data with this strain rate correction

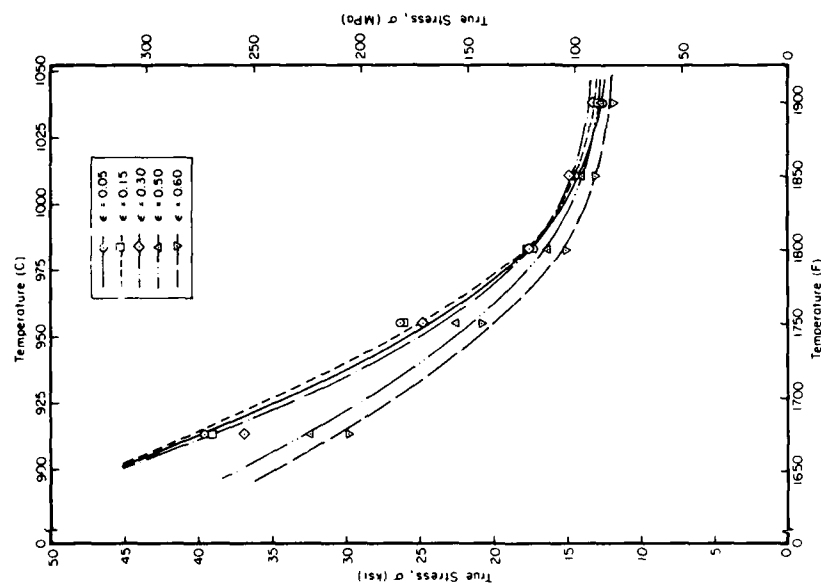


FIGURE C-10. FLOW STRESS DATA FOR Ti-6242
($\alpha+\beta$ MICROSTRUCTURE) RE-
PLOTED TO SHOW STRESS AS A
FUNCTION OF TEMPERATURE AT
DIFFERENT LEVELS OF STRAIN
($\dot{\epsilon} \approx 10 \text{ SEC.}^{-1}$)

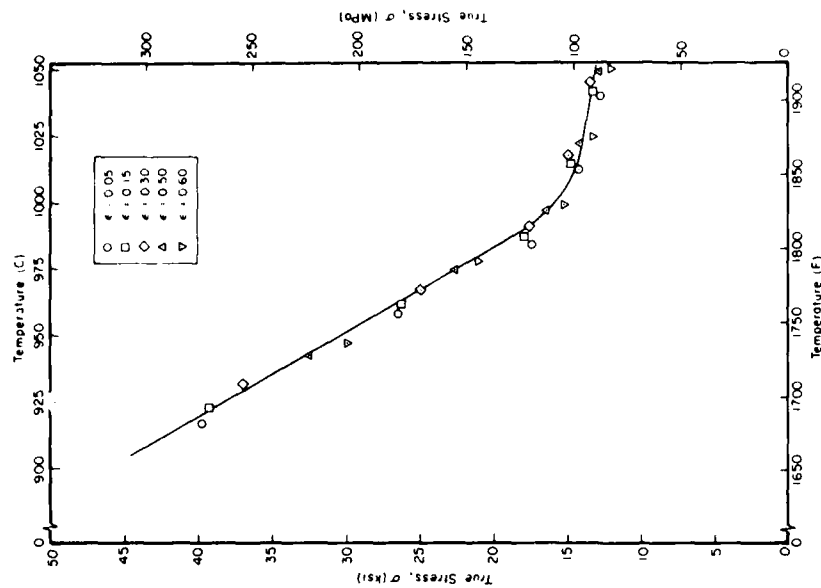


FIGURE C-11. FLOW STRESS DATA FOR Ti-6242
($\alpha+\beta$ MICROSTRUCTURE),
CORRECTED FOR ADIABATIC-
HEATING EFFECTS ($\dot{\epsilon} \approx 10$
 SEC.^{-1})

(Figure C-12) further enhances the conclusion drawn from Figure C-10. A constitutive relation for this microstructure would thus be simply $\bar{\sigma} = \bar{\sigma}(\dot{\epsilon}, T)$.

Flow Softening in Ti-6242 - β Microstructure

The flow softening noted in the stress-strain curves for Ti-6242 with the β microstructure (Figure C-7) is substantially greater than that for Ti-6242 of the $\alpha+\beta$ microstructure. As with the $\alpha+\beta$ microstructure, flow softening in the β microstructure can be attributed to adiabatic heating and, to a lesser extent, to the decreasing strain rate during tests in the mechanical press. However, other sources are needed to explain the total extent of flow softening for this microstructure.

An examination of polished sections of as-received and deformed compression specimens gave insight into the source of the additional softening. The as-received β material (Figure C-1b) consisted of a relatively fine acicular, basketweave microstructure in large prior β grains. After deformation at 913, 954, and 982 C (1675, 1750, 1800 F), however, the basketweave colonies had broken up into somewhat smaller colonies, and, more importantly, it was noted that small recrystallized alpha grains had been formed. This may be one of the reasons why, at a given temperature, the β stress-strain curves appear to approach the $\alpha+\beta$ stress-strain curves at large strains (Figure C-7). In some cases, at the larger strains, the β curves even fall below the $\alpha+\beta$ curves. This could be due to additional adiabatic heating resulting from the higher flow stresses for the β microstructure.

The metastable β microstructure is assisted by deformation in reaching the equilibrium microstructure (i.e., the $\alpha+\beta$ microstructure) at temperatures in the $\alpha+\beta$ field. However, it is unlikely that the flow softening at small strains (on the order of 0.05) is related to this mechanism inasmuch as dynamic recrystallization usually does not occur at these strain levels⁽¹²⁾. Another source of flow softening of the β microstructure which may occur at these strains is the generation of a softer texture. This effect can be significant because of the large plastic anisotropy of hexagonal metals. The fact that β grain-boundary and triple-point cracks were observed supports the conclusion that strong plastic anisotropy existed. Such anisotropy could generate

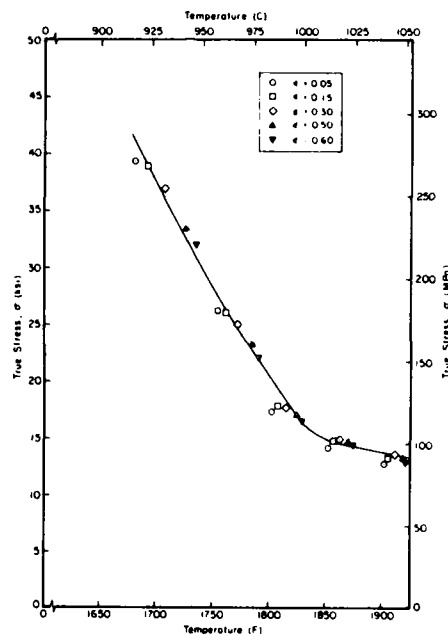


FIGURE C-12. FLOW STRESS DATA
FOR Ti-6242 ($\alpha+\beta$
MICROSTRUCTURE)
CORRECTED FOR
ADIABATIC-HEAT-
ING AND STRAIN-
RATE EFFECTS
($\dot{\epsilon} \approx 10 \text{ SEC.}^{-1}$)

the plastic incompatibility to produce such defects as well as cause the stress concentrations required for Widmanstätten colony breakup. That textural changes are indeed a source of softening is still conjecture at present, but it has been observed in a similar two-phase alloy, zirconium-5% tin⁽¹¹⁾.

Summary and Conclusions

A mechanical press has been used successfully to obtain high strain-rate compression flow stress data which can be used in modelling of deformation processes. Data were obtained at hot working temperatures for Ti-6242-0.1Si having two different microstructures—equiaxed α in a transformed matrix, the $\alpha+\beta$ microstructure, and a microstructure consisting solely of transformed β , the β microstructure. The flow behavior of the two microstructures differed markedly and can be summarized as follows:

- (1) In compression, the $\alpha+\beta$ microstructure deformed stably with monotonically increasing load-stroke curves. Reducing this data to stress-strain data, the flow behavior was shown to exhibit softening which could be attributed to adiabatic heating and a decreasing strain rate as the deformation proceeded, a characteristic of compression tests run in the mechanical press. Adjusting the data for this softening, it was shown that the dependence of flow stress on strain is weak, and, hence, the flow stress is a function primarily of strain rate and temperature. This is a characteristic of metals which dynamically recover during hot working and has been observed in other $\alpha+\beta$ titanium alloys tested at much lower strain rates than those of the present tests. It appears, however, that the flow stress is a function of strain-rate history as was shown by comparing strain-rate-sensitivity data obtained through two different deformation schemes.
- (2) The compressive deformation of β specimens gave rise to nonuniform, unstable flow characterized by decreasing load-stroke curves. The stress-strain curves for this

microstructure show an additional amount of flow softening in excess of that observed for the $\alpha+\beta$ microstructure. This increment has been attributed to breakup of the β microstructure and recrystallization to yield the equilibrium α phase at test temperatures below the β transus temperature. It is also believed that development of a softer texture may have caused some of the observed flow softening.

References

- (1) Altan, T., and Boulger, F. W., "Flow Stress of Metals and Its Application in Metal Forming Analyses", J. Eng. Ind., Trans. ASME, Vol. 95, 1973, p. 1009.
- (2) McQueen, H. J., and Jonas, J. J., "Hot Workability Testing Techniques", in Metal Forming - Interrelation Between Theory and Practice, A. L. Hoffmann, ed., Plenum Press, New York, 1971, p. 393.
- (3) Sellars, C. M., and Tegart, W.J. McG., "Hot Workability", Inter. Met. Rev., Vol. 17, 1972, p. 1.
- (4) Fulop, S., Cadien, K. C., Luton, M. J., and McQueen, H. J., "A Servo-Controlled Hydraulic-Torsion Machine for Hot Working Studies", J. Testing and Evaluation, Vol. 5, 1977, p. 419.
- (5) Douglas, J. R., and Altan, T., "A Study of Mechanics of Closed-Die Forging (Phase II)", Final Report on Contract No. DAAG46-71-C-0095, Battelle's Columbus Laboratories, Columbus, Ohio, November, 1972.
- (6) Chen, C. C., "Metallurgical Fundamentals to Ti-6Al-2Sn-4Ar-2Mo-0.01Si Alloy Forgings. I. Influence of Processing Variables on the Deformation Characteristics and the Structural Features of Ti-6242 Si Alloy Forgings", Report RD-77-110, Wyman-Gordon Company, Grafton, Mass., October, 1977.
- (7) Hammond, C., and Nutting, J., "The Physical Metallurgy of Superalloys and Titanium Alloys", in Forging and Properties of Aerospace Materials, The Metals Society, London, 1978, p. 75.
- (8) Private communication, J. E. Hockett, Los Alamos Scientific Laboratory, Los Alamos, New Mexico.
- (9) Altan, T., "Forging Equipment-Applications and Limitations", in Forging Equipment, Materials, and Practices, Report MCIC-HB-03, Battelle's Columbus Laboratories, Columbus, Ohio, October, 1973 (Chapter 1).

References (Continued)

- (10) Backofen, W. A., Deformation Processing, Addison-Wesley Publishing Company, Reading, Mass., 1972.
- (11) Jonas, J. J., and Luton, M. J., "Flow Softening at Elevated Temperatures", in Advances in Deformation Processing, Plenum Press, New York, 1978, p. 215.
- (12) Jonas, J. J., and McQueen, H. J., "Recovery and Recrystallization During High Temperature Deformation", in Treatise on Materials Science and Technology, Vol. 6: Plastic Deformation of Materials, R. J. Arsenault, ed., Academic Press, New York, 1975, p. 394.
- (13) Young, C. M., and Sherby, O. D., "Simulation of Extrusion Structures by Means of Torsion Testing for a High Strength Nickel-Base Alloy, Udimet 700", in Metal Forming - Interrelation Between Theory and Practice, A. L. Hoffmann, ed., Plenum Press, New York, 1971, p. 429.
- (14) Griest, A. J., Sabroff, A. M., and Frost, P. D., "Effect of Strain Rate and Temperature on the Compressive Flow Stresses of Three Titanium Alloys", Trans. ASM, Vol. 51, 1959, p. 935.
- (15) Jonas, J. J., "Recovery, Recrystallization, and Precipitation Under Hot Working Conditions", Proc. Fourth Inter. Conf. on the Strength of Metals and Alloys, Nancy, France, August 30-September 3, 1976, p. 976.
- (16) Sulijoadikusumo, A. U., and Dillon, O. W., Jr., "Work Softening of Ti-6Al-4V Due to Adiabatic Heating", in Metallurgical Effects at High Strain Rates, R. W. Rohde, et al., eds., Plenum Press, New York, 1973, p. 501.

APPENDIX D

DETERMINATION OF HIGH STRAIN RATE
FLOW STRESS DATA FOR Ti-6242
BY USING AN MTS MACHINE

H. A. Kuhn
University of Pittsburgh
Pittsburgh, Pennsylvania 15261

APPENDIX D

DETERMINATION OF HIGH-STRAIN RATE FLOW STRESS DATA FOR Ti-6242 BY USING AN MTS MACHINE

Introduction

At the University of Pittsburgh, research on Phase I of the program is being conducted to determine the validity of using an MTS machine to obtain flow stress data on the Ti-6242 alloy. Techniques to obtain the data from isothermal, uniform compression tests at constant true strain rate are being developed. Because of the high sensitivity of titanium alloys to temperature and strain rate, very careful control of these variables must be exercised during measurements of mechanical behavior. The isothermal compression test fixture at the University of Pittsburgh can provide such control, along with a cam plastometer at Los Alamos and a mechanical press at Battelle. Measurements from these three sources will be compared for evaluation of the test systems.

Experimental Procedure

Test Conditions

Isothermal compression tests are being conducted at all combinations of the four temperatures; 913, 954, 982, 1010 C, and strain rates 0.01, 0.1, 1.0, 10.0 sec⁻¹.

Material

The titanium 6242 alloy for testing is supplied by Battelle in the form of cylinders 12.7 mm (0.5 in.) diameter by 19.05 mm (0.75 in.) high. Each end face contained a spiral groove to aid lubricant entrapment and promote homogeneous flow.

Test Apparatus and Operation

The isothermal compression test apparatus is shown in Figure D-1. The high temperature tooling is enclosed within a radiant heating furnace so that the test specimen and compression dies may be heated to the same temperature to avoid die chilling and non-uniform temperature. The upper and lower dies and the specimen are fitted with thermocouples to record the temperature.

In practice, the dies are pre-heated to the required temperature. Next, the specimen, mounted on a thermocouple lead, attached to a

pneumatic cylinder, is positioned between the dies and the furnace halves are closed by pneumatic cylinders. The specimen, in contact with the dies, is heated to the test temperature. Continuous temperature measurements of the dies and specimen are made to indicate the proximity to isothermal conditions. (Typically, the upper and lower dies and specimen can be maintained within 5 C of the test temperature.) Then the test is performed at the prescribed strain rate and to the prescribed total strain through the MTS control system. When the test is completed, pneumatic cylinders separate the furnace halves and the pneumatic cylinder on which the specimen and thermocouple lead are mounted retracts the specimen from the furnace. If necessary, the pneumatic cylinder may be tripped by a release mechanism to rotate downward $\sim 45^\circ$, putting the specimen into a quench bath. Within one second, the specimen moves from the furnace to the quench bath.

Lubrication

Maintaining uniform, homogeneous deformation is of prime importance for determining true flow stress behavior of the material. Near perfect lubrication must be achieved for this purpose. For the test temperatures of interest here, Deltaglaze #19 was found to provide the closest approximation to homogeneous deformation. In addition, it was determined that the spiral grooves machined into each end face of the test cylinders received from Battelle were beneficial only for the low strain rate tests (0.01 and 0.1 sec^{-1}). For the higher strain rates (1.0 and 10.0 sec^{-1}) it was found that facing off the grooves so that each end face was smooth led to more homogeneous deformation.

Attainment of Constant Strain Rate

To achieve constant strain rate, the stroke should decrease exponentially with time. This is approximated by using the dual slope setting on the function generator. The desired exponential relationship of stroke and time is then approximated by two linear segments blending into a near exponential function: The instantaneous strain rate varies by about 20% from nominal during the test.

Correction for Lubricant Thickness and Machine Compliance

The stroke data which is used to determine the height of specimen at any instant is corrected for the thickness of the lubricant and the machine compliance. The difference between the initial actual height of specimen and the stroke value gives the initial thickness of the lubricant. Similarly, the difference between the final actual height of specimen and stroke gives the final thickness of lubricant and test machine compliance. A linear fit is assumed for the variation of lubricant thickness with strain. From this linear fit, the corrected stroke at any instant is given by:

$$S_t^c = S_t - T_t$$

where

S_t^c	=	corrected stroke at time, t
S_t	=	uncorrected stroke at time, t
T_t	=	thickness of lubricant plus machine compliance at time, t.

The corrected value of stroke then gives the actual specimen height at that instant of time and hence, is used to calculate true strain. Typically, the lubricant thickness varies from 3mm (0.12 in.) at $\epsilon = 0$ to 2.3mm (0.09 in.) at $\epsilon = 0.8$. The validity of the linear fit can be justified on the basis of the observation that, for two different tests under identical conditions, the slope of T (thickness of lubricant) vs ϵ remained almost constant.

Processing of MTS Data

The data from the load cell and LVDT (for measuring stroke) are converted to digital form and recorded on a custom built, data logger. Digital data are then processed using an on-line computer terminal. Computer programs have been developed to analyze the data from the data logger and give the results in the form of both digital values and plots. The results obtained are in the form of:

- (a) True stress - True strain
- (b) Stroke - Time
- (c) Strain Rate - Strain

Results

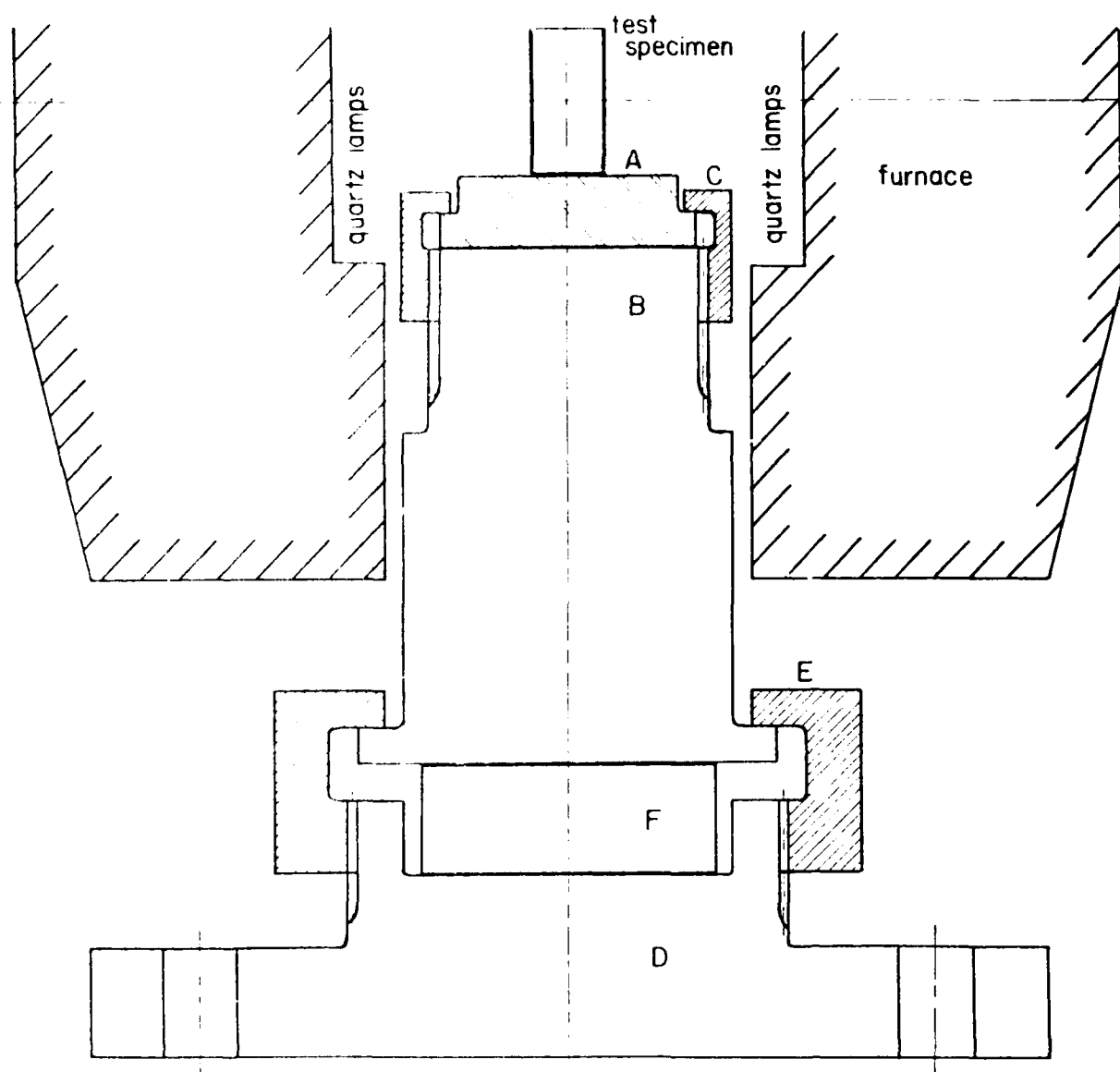
An example of a true stress-strain curve, as obtained through the data read-out system described in the previous section, is given in Figure D-2. There is some noise in the load cell output, which is reflected as noise in the calculated stress, but the data can easily be smoothed. Reproducibility of results is illustrated in Figure D-3, which gives the stress-strain curves for two tests under identical conditions superimposed on the same axes.

The effect of the lubricant thickness and machine compliance on the stress-strain curve is shown in Figure D-4. The correction reduces the curve slightly, reaching a maximum stress deviation of 5% at a strain of 0.8.

The stress-strain curves for all tests to date are summarized on Figure D-5. Increasing temperature and decreasing strain rate lead to the expected reduction of the stress-strain curves. Only the curve for 982 C and $\dot{\epsilon} = 10.0 \text{ sec}^{-1}$ seems out of line and may be due to a mistake in temperature or strain rate control. Assuming a power law relationship between stress and strain rate, the strain rate sensitivities can be calculated as a function of strain and temperature. As shown in Table D-1, the strain rate sensitivity is nearly uniform for all strains at a given temperature. As shown by other investigators, the strain rate sensitivity is minimum at 954 C.

TABLE D-1
Strain Rate Sensitivity for Ti-6242
at Various Temperatures and Strains

Temperature C (F)	Strain Rate Sensitivity Parameter, m		
	$\epsilon = 0.2$	$\epsilon = 0.4$	$\epsilon = 0.6$
913(1675)	0.27	0.27	0.26
954(1750)	0.18	0.18	0.17
1010(1850)	0.24	0.31	0.28



A: die insert, Inconel

B: die insert, Waspalloy

C: die insert, Waspalloy

D: base, stainless steel

E: collar, stainless steel

F: ceramic insulator, hot-pressed Al_2O_3

Figure D-1a. Hot-press die and furnace, lower half.

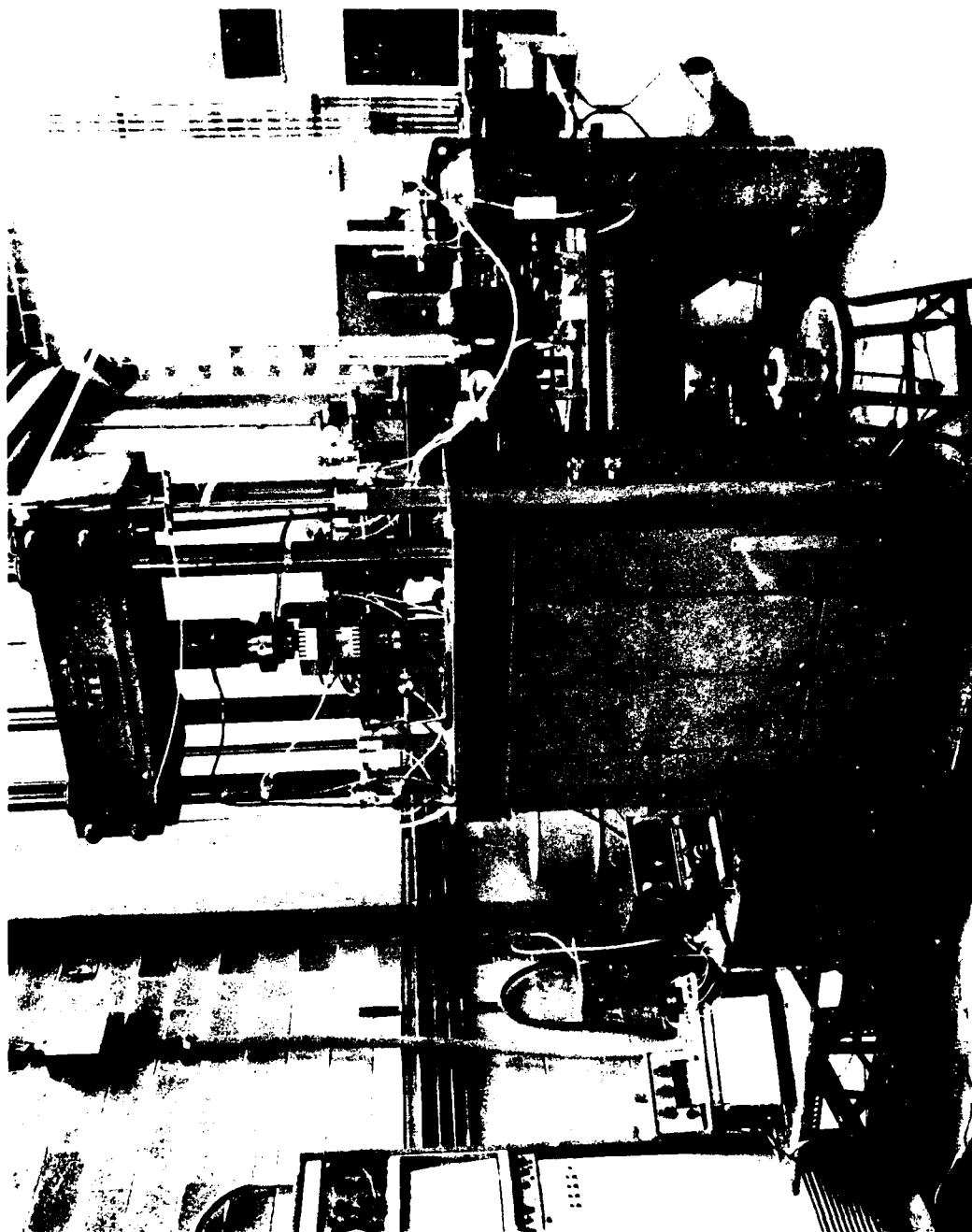


Figure 10-10. Vacuum and cooling mounted by U.S. for workability studies.

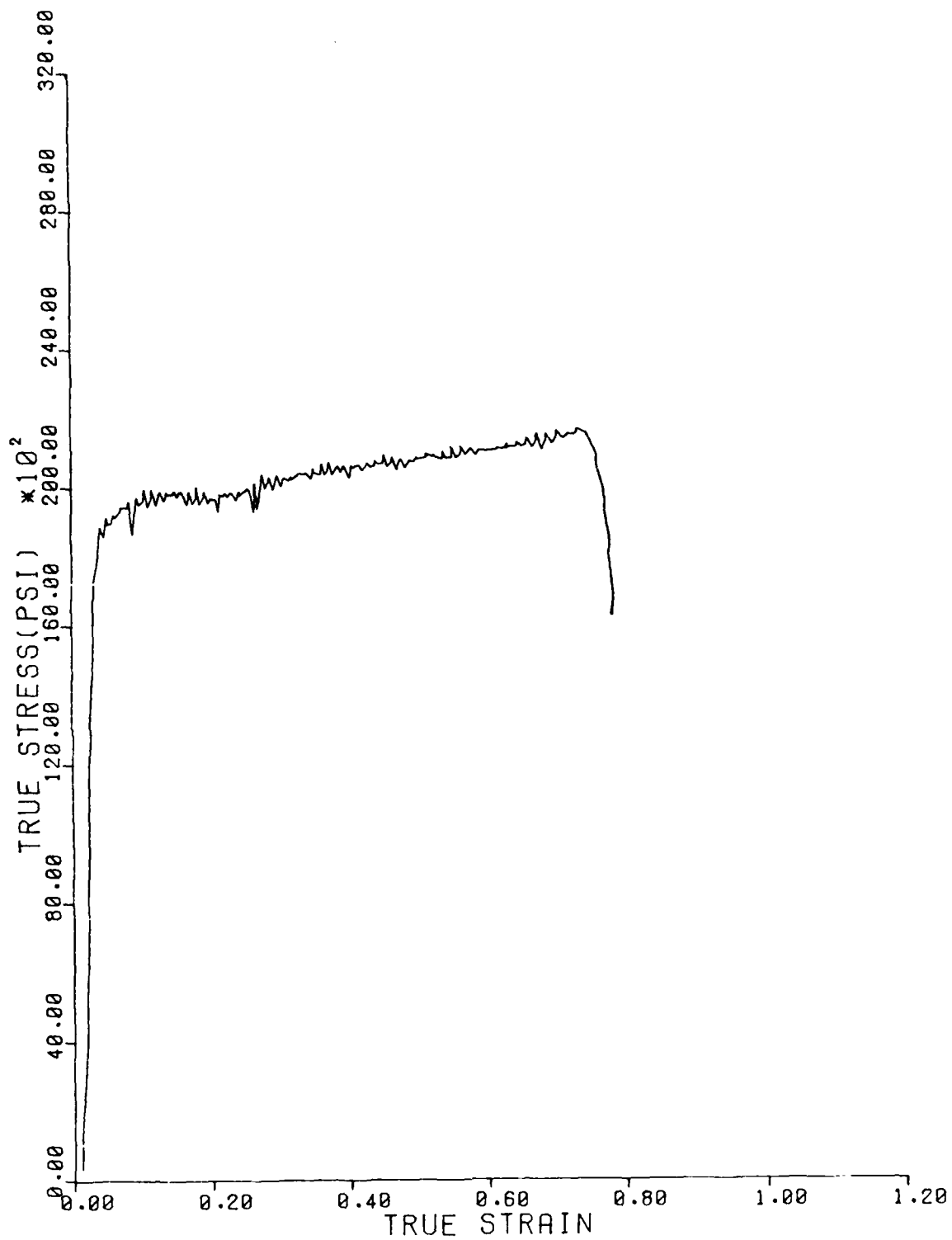


Figure D-2. True stress-strain curve for Ti-6242 at $T=913\text{ C}$ (1675 F), $\dot{\epsilon} = 10\text{ sec}^{-1}$.

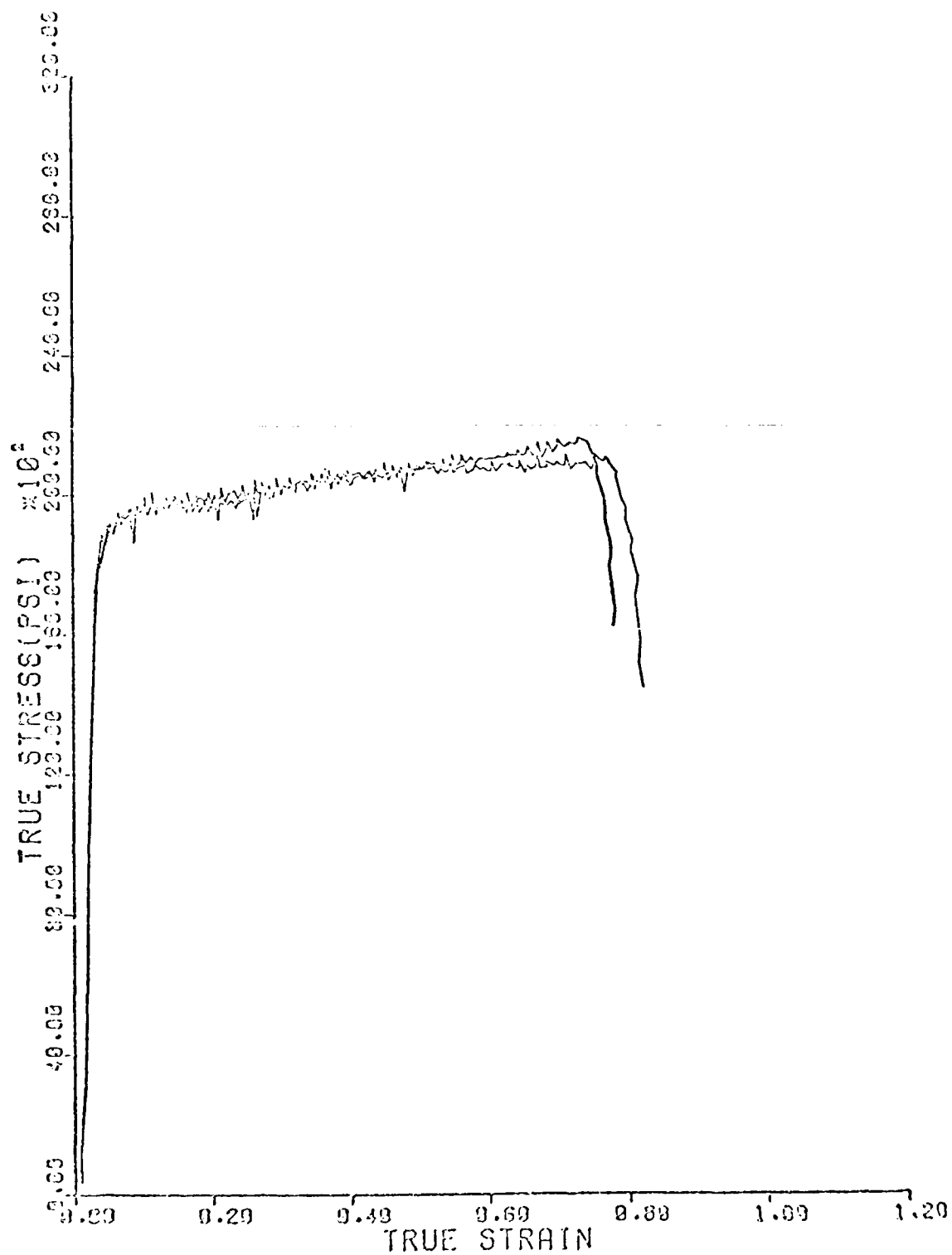


Figure D-3. True stress-strain curves for two tests at $1:913\text{ C}$, (1675 F), $\dot{\epsilon} = 10\text{sec}^{-1}$; shows good reproducibility of results.

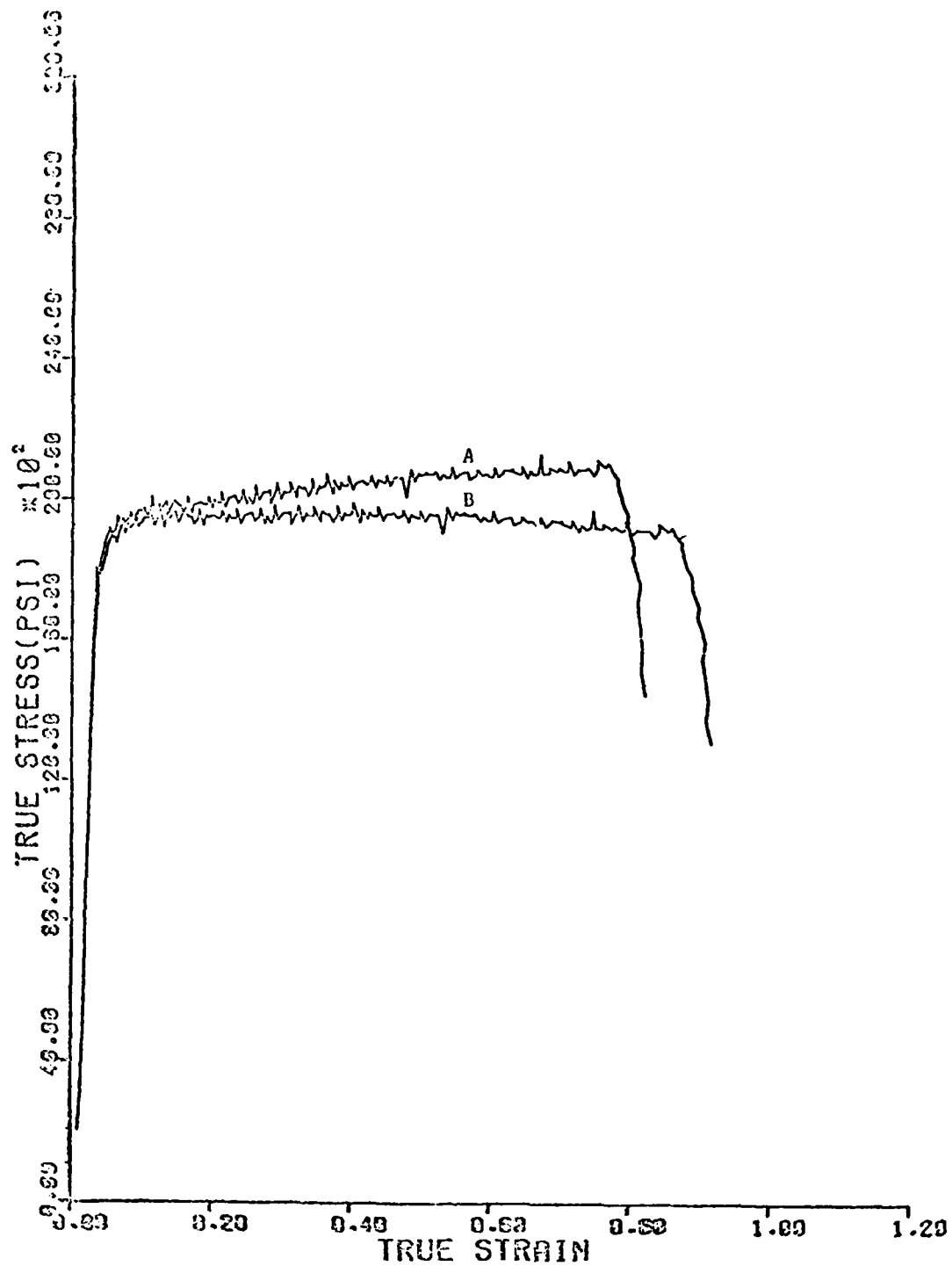


Figure D-4. Effect of correction for lubricant thickness and machine compliance
on true stress-strain curve at $T=913\text{ C}(1675\text{ F})$, $\dot{\epsilon} = 10\text{sec}^{-1}$;
A- uncorrected . B-corrected.

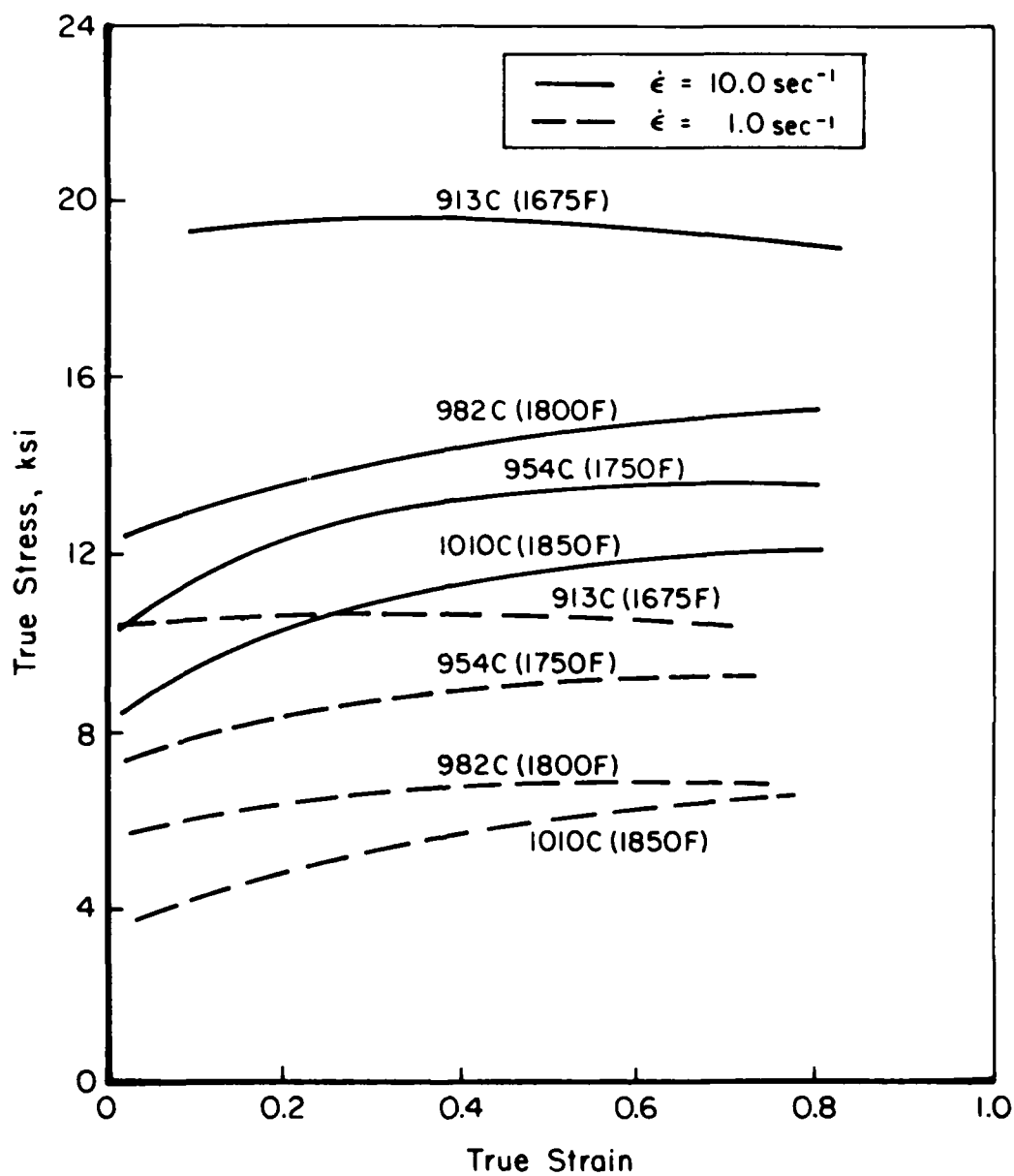


Figure D-5. True stress-strain curves for Ti-6242.

APPENDIX E

PROCESSING, STRUCTURE, AND PROPERTIES
OF Ti-6Al-2Sn-4Zr-2Mo ~ 0.1Si ALLOY
FORGINGS

C. C. Chen
Wyman-Gordon Company
North Grafton, Massachusetts 01536

APPENDIX E

PROCESSING, STRUCTURE, AND PROPERTY OF Ti-6Al-2Sn-4Zr-2Mo-0.1Si ALLOY FORGINGS

Introduction

Although it has been known that the processibility and the microstructure/property relationships of titanium alloy forgings can be optimized by exercising the metallurgical and mechanical interactions during forging deformation, the deformation processing for forging titanium alloys has always been highly experience-based technology. However, with recent improvement in the knowledge of processing technology, materials science, and mechanics, the development of a knowledge-oriented deformation processing has become feasible. At the present state of technology, it is highly desirable that a technical effort could be designed to develop a deformation processing system which could bring metallurgy and mechanics together for manufacturing titanium alloy forgings. Such developmental effort is particularly appropriate in order to support the Air Force goal of increasing efficient use of available resources, reducing the overall production cost of forging products, and permitting a better control of microstructures and mechanical properties of the forgings.

The objective of this program at Wyman-Gordon is to assist in developing an integrated total deformation forging model and to verify the model's usefulness when manufacturing titanium alloy disks through forging technology. The program goal is the development of the process model for producing a dual property titanium compressor or turbine disk for use in advanced gas turbine engines. The technical approach being taken by Wyman-Gordon consists of:

1. to supply the program materials with controlled processing history and microstructures,
2. to perform forging and heat-treat studies for obtaining the microstructures which will give selected properties,
3. to insure that appropriate processing variables, lubricants, and die materials are selected for manufacturing applicability,
4. to perform a series of pancake and subscale disk forgings for testing the usefulness and the validity of the developed processing model,
5. to characterize and to establish the property-microstructure relationships and dual property capability of the subscale compressor disks.

Program Description

The technical effort for the prime contract on "Research to Develop Process Models for Producing a Dual Property Titanium Alloy Compressor Disk" by BCL is divided into five phases according to the overall objectives of the program. The technical plan for the subcontract program at Wyman-Gordon is primarily designed to carry out the applied phases of the program to apply the knowledge-oriented deformation processing systems for manufacturing a Ti-6Al-2Sn-4Zr-2Mo-0.1%Si (designated as Ti-6242Si hereafter) alloy disk forging with dual properties. Since the structural variations are of great importance in hot forming of titanium alloys (1-4), this portion of the program emphasizes in particular the influence of metallurgical variables on the deformation properties and the resultant microstructures and properties. The feasibility for applying a process model to a manufacturing program will also be demonstrated from both technological and economic standpoints.

Material Behavior Under Processing Conditions (Phase I)

The program approach for Phase I is intended to supply the program materials with controlled processing history and microstructures for various phases of technical effort, and to extensively evaluate and establish the proper thermal-mechanical processing in terms of processing, and structural/property capabilities of the forgings through both isothermal and conventional forging techniques. A particular effort will be made to develop pancake forgings with microstructures of high creep, high stress rupture, good tensile, and higher low cycle fatigue properties by careful control of forge and heat treat practices. Both $\alpha+\beta$ and β -processings will be used to produce pancake forgings for this evaluation. Considerable work will be performed to explore the properties which could be potentially achieved by the combined operations of forging and subsequent heat treatment.

Process Modeling For Disk Type Forgings (Phase II)

In Phase II effort, the investigation is aimed to assist in formulating a practical simulation model with matrix method and upper-bound method for axisymmetric compression. Wyman-Gordon's experience in manufacturing (processing), structure, and property of the Ti-6242Si alloy should make a significant contribution for the team members to develop the process model for manufacturing application. Wyman-Gordon will assist to insure that appropriate forging variables such as forge temperature, die temperature, strain rate, microstructure, and preform shape are properly taken into consideration.

Interface Effects (Phase III)

The technical approach for Phase III will involve assisting Battelle to select appropriate lubricants, materials, and conditions for determining thermal lubricant properties. Limited ring compression tests will also be conducted at Wyman-Gordon to determine lubrication effectiveness and friction factor in the setup which will be used for forging subscale disks in Phase IV. Previous work ⁽⁵⁾ has demonstrated that the reproducibility and reliability of the lubricant effectiveness and performance could not be satisfactorily demonstrated before one tests such lubrications directly in actual performance conditions and requirements in the forge press.

Integration of Material and Process Models (Phase IV)

In Phase IV, Wyman-Gordon will attempt to apply the bodies of basic materials knowledge, process knowledge, and equipment behavior into manufacturing technology. Here application of metallurgical controls and production considerations will be emphasized. Three forging trials will be first conducted to test the validity of the developed processing model, and a forging run for the selected and optimized processing plans and forge-heat treat combinations will be finally made to produce the disk forgings. Both structural characteristics and property capability of the forgings will be examined after each forging trial, and a modification of the processing system, if necessary, will be made to develop an acceptable and applicable process model. A final analysis will be made on utilizing the developed processing model on manufacturing practice, cost saving element, and structural efficiency of the disk.

Property/Microstructure Relationships (Phase V)

The structural characterization in Phase V will include both macroflow characteristics and microstructures. The property evaluations will consist of room temperature, 950F, and 1050F tensiles, 950F/35 ksi/0.2% and 1050F/25 ksi/0.2% creeps, 950F/65 ksi and 1050F/55 ksi stress ruptures, post-creep tensiles, fracture toughness, room temperature, 950F, and 1050F low cycle fatigues, room temperature, 950F, and 1050F fatigue crack growth rates, and post $\frac{da}{dn}$ tensiles. The microstructure/property results obtained in Phase V will be analyzed to determine the capability of the achieved mechanical properties pertinent to the design requirements for the dual property disk.

Review of Previous Work

Titanium alloys are attractive alloy selections for jet engine and airframe components because of their higher strength-to-weight ratio and good corrosion resistance. During recent years, the increasing demands of higher temperature performance and lower weights of the jet engine components have brought about the development and use of near-alpha elevated temperature titanium alloys. As a result, the Ti-6242Si alloy has been mostly used for high temperature applications (6-8). The use of Ti-6242Si has extended the useful temperature range of titanium alloys to the 900F regime; here both creep and fatigue endurance properties at high temperatures are of critical factors. Very recently, the optimum processing and heat treating conditions have been established for producing Ti-6242Si alloy forgings that will extend the use of the forging to higher operational temperatures (i.e., 1100F) (1-3).

The current manufacturing forging practice for Ti-6242Si alloy are carried out at temperatures in both $\alpha+\beta$ and β -phase fields and the conventional forging processes have been generally used. Because of the significant influence of die chilling on both forging deformation and structural features of the forgings, the nature of the material response to the forging deformation and the structural characteristics has never been clearly illustrated for Ti-6242Si alloy through conventional forgings. However, (9-12), with recent development of isothermal forging technology, a systematic control of processing variables has become possible to produce the desired structure and property in forgings of Ti-6242Si.

Metallurgical Description of the Alloy

The alloy Ti-6242Si is a near alpha, alpha-beta titanium alloy (6, 7). The Al (6%) addition in the alloy is a potent α -phase stabilizer, while Mo (2%) represents a moderate quantity of β -phase stabilizer. The Sn (2%) and Zr (4%) are weak stabilizers and are relatively neutral with respect to α and β -phase stabilization, but they are solid solution strengthening elements for both α and β phases. Mo is believed to increase room- and elevated-temperature tensile strength and enhance stability and the combination of Al, Sn, and Zr improves the stability of long-time elevated-temperature strength. The addition of 0.1% Si to the alloy has been shown to significantly increase the high temperature properties without any apparent undesirable effects (8). The increase in density resulting from the 8% heavier metal additions (Sn, Zr, and Mo) is small, while the increase in toughness due to these additions is significant. Density of the alloy is 0.164 lb/in³ and the $(\alpha+\beta)/\beta$ transus temperature is about 1820F.

In the current forging practices, both $\alpha+\beta$ and β -forgings have been used to manufacture Ti-6242Si alloy forgings. The β -forging is used to acicularize the microstructure which results in a reduction in LCF and ductility, but increases in creep strength and fracture toughness. Solution-annealing is generally used for heat-treating the alloy forgings, followed by stabilization annealing at 1100F/air cool. Like other titanium alloys, the control of the nature and distribution of both globular- α and transformed products by thermal and mechanical processings are of great importance in determining the mechanical properties of the forgings.

Influence of Processing Variables on the Forging Deformation

A very extensive investigation was recently carried out to determine the influence of processing variables on the forge pressure and resultant structure of Ti-6242Si alloy pancake forgings⁽¹⁾; also the dependence of hot tensile properties on temperature, initial microstructure, and strain rate was characterized.

The results demonstrated that the forge pressure and the stress-strain behavior for the forging deformation were strongly dependent on the forge temperature, die temperature, ram rate, and preform microstructure; as illustrated from Figures E-1 through E-4. Here, the effect of preform microstructures on the deformation behavior was particularly emphasized. It was reported that the deformation characteristics under isothermal forging could be quantitatively related to the hot deformation properties of the alloy (Figures E-5 and E-6). On the basis of the hot-tensile results and the activation analysis, the rate-controlling deformation process in ($\alpha+\beta$) forgings was probably due to the dynamic softening. The very high values of activation energies obtained (137 Kcal/mole for ($\alpha+\beta$) preform and 107 Kcal/mole for β -preforms) indicated that the deformation process within ($\alpha+\beta$) phase field was rather predominantly dynamic recrystallization than more conventional rate-controlling mechanisms. This suggested that the structural changes occurred during forging deformation and the hot workability within commercial forging variables was a structure-sensitive problem.

Both macrostructure and microstructure of the forgings were sensitive to forge temperature, die temperature, ram rate, cooling rate, and preform microstructure, as given in Figures E-7 through E-10. Excellent uniformities in macro and microstructures were observed for isothermal forging and in β -forged conditions. The relationship between processing variables and structural inhomogeneities of the forgings was also presented.

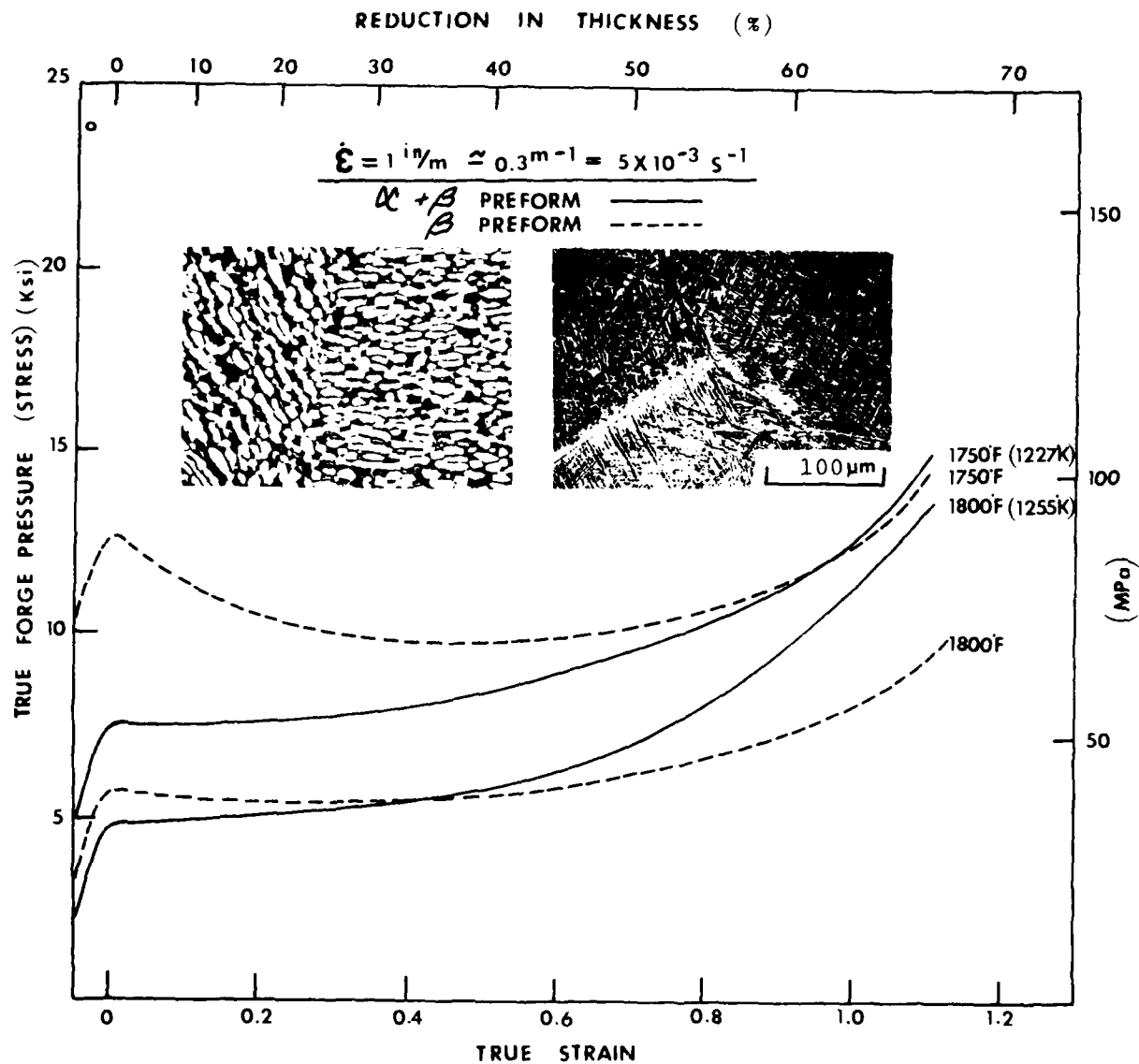


Figure E-1 Examples of true stress-strain curves for isothermal forging of Ti-6242Si alloy pancakes using $\alpha + \beta$ and β -preforms

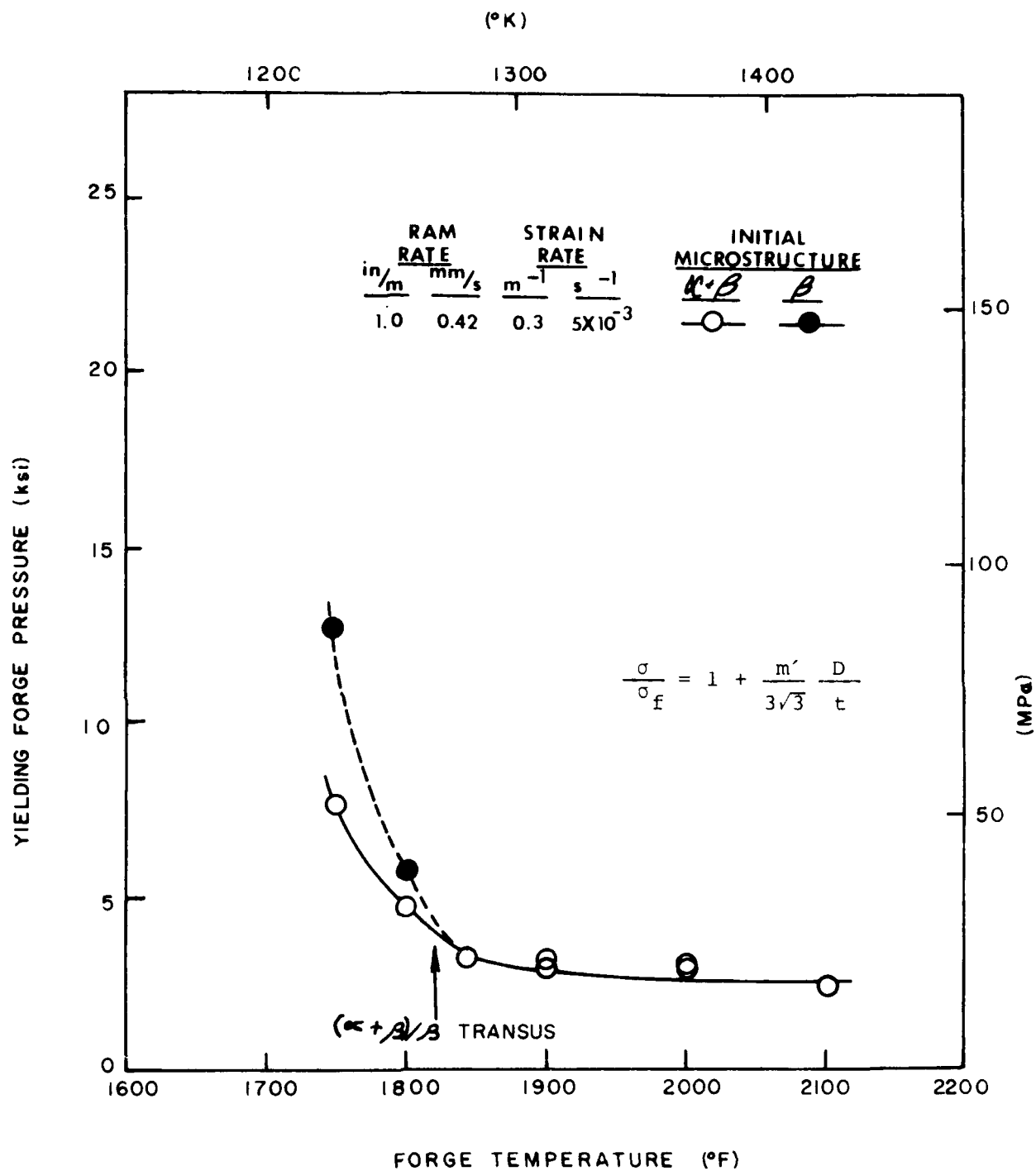


Figure E-2 Variation of Yielding forge pressure with temperature for Ti-6242Si alloy pancake forgings

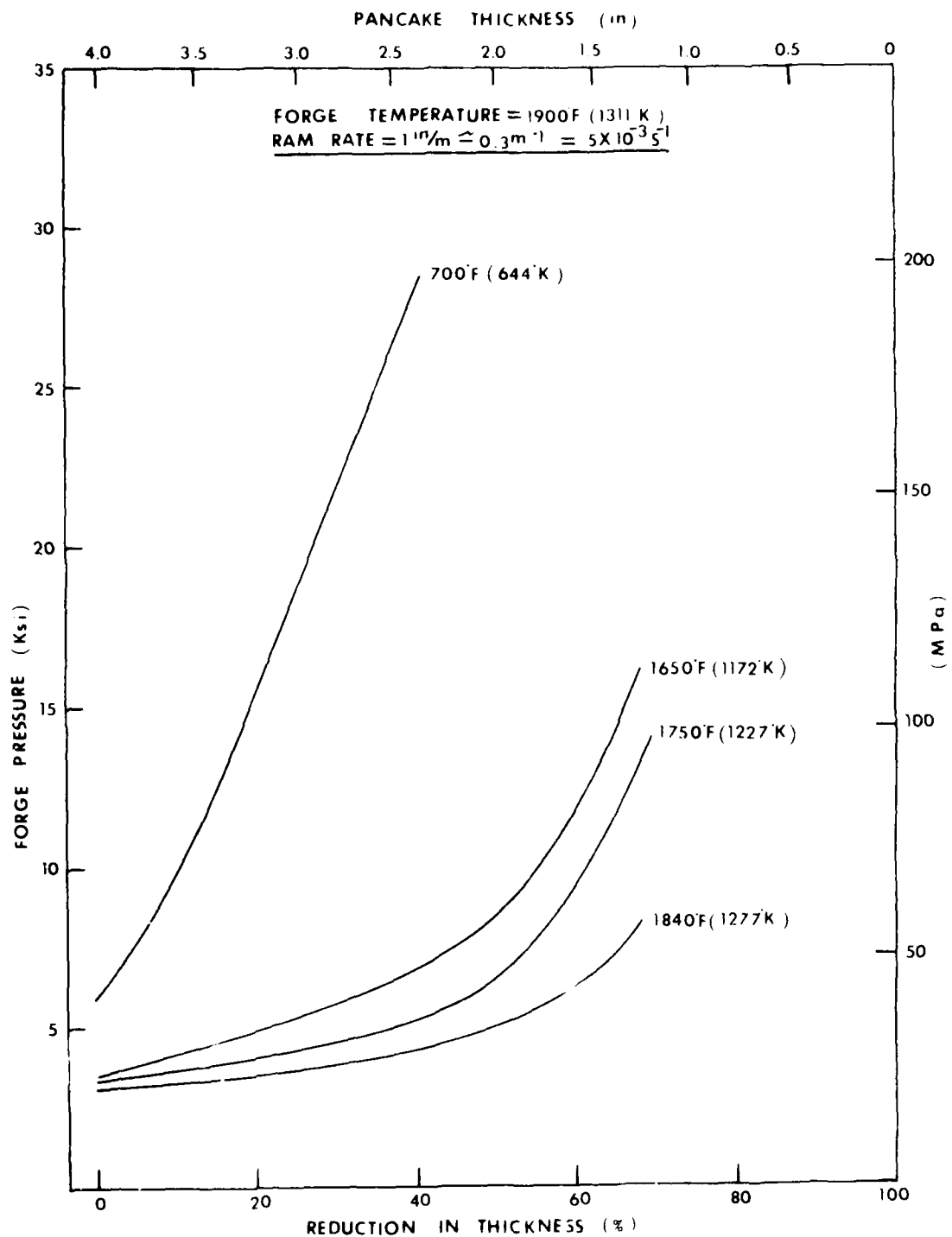


Figure II-3 Variation of forge pressure with pancake thickness for Ti-6242S alloy forgings at various die temperatures

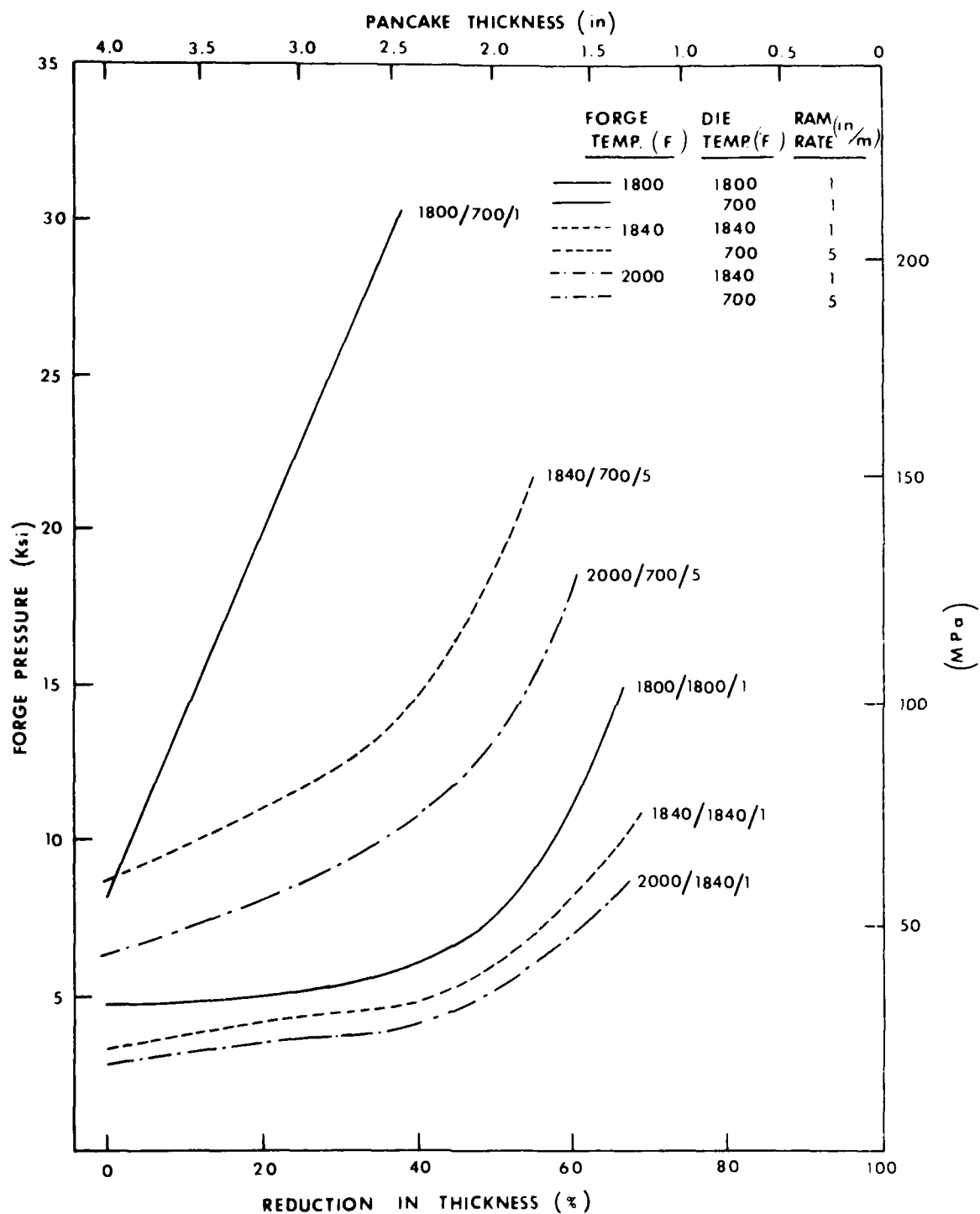


Figure E-4 Variation of forge pressure with pancake thickness for Ti-6242Si alloy forgings at various forge temperature-die temperature-ram rate combinations

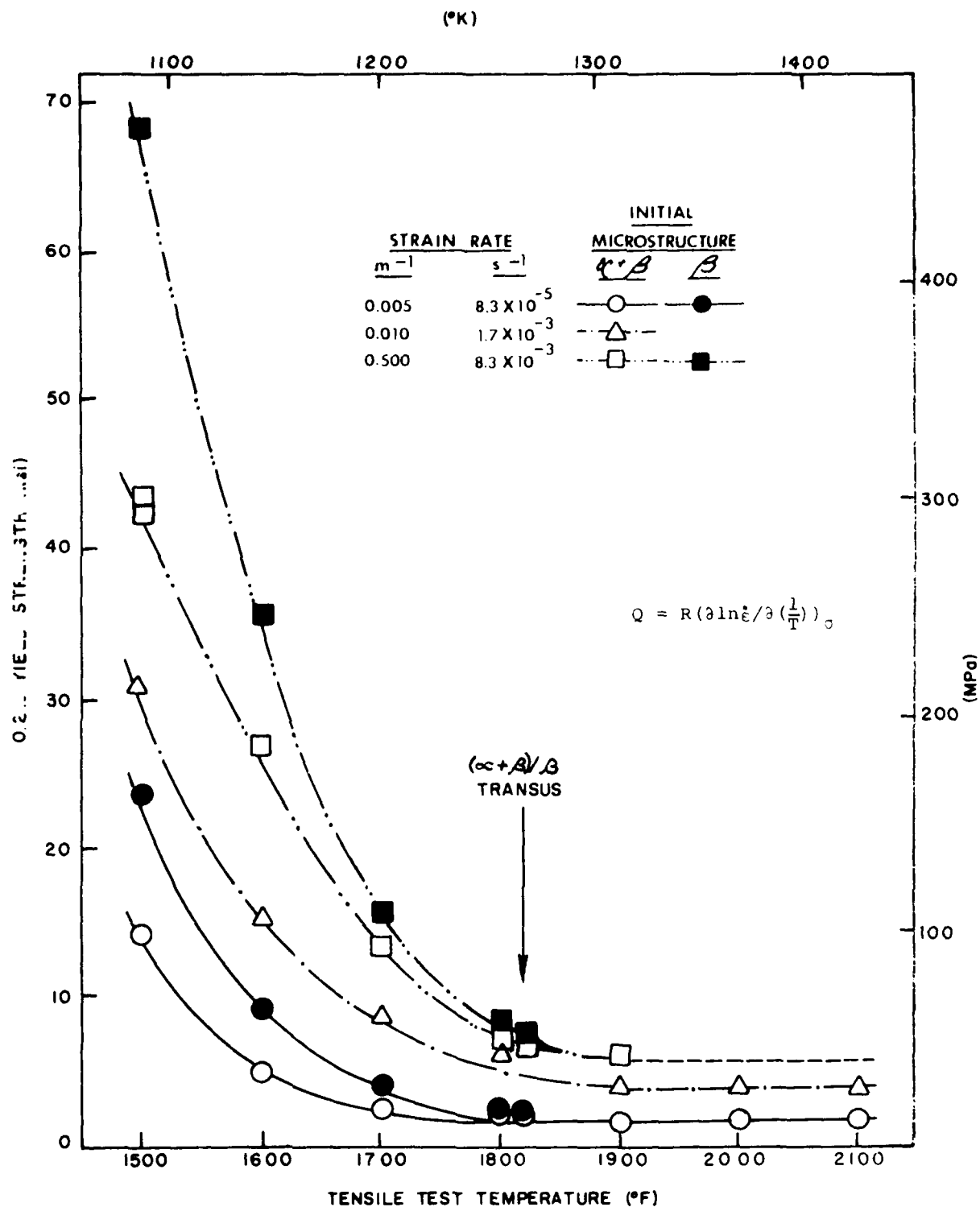


Figure F-5 Temperature dependence of yield strength for Ti-6242Si alloy

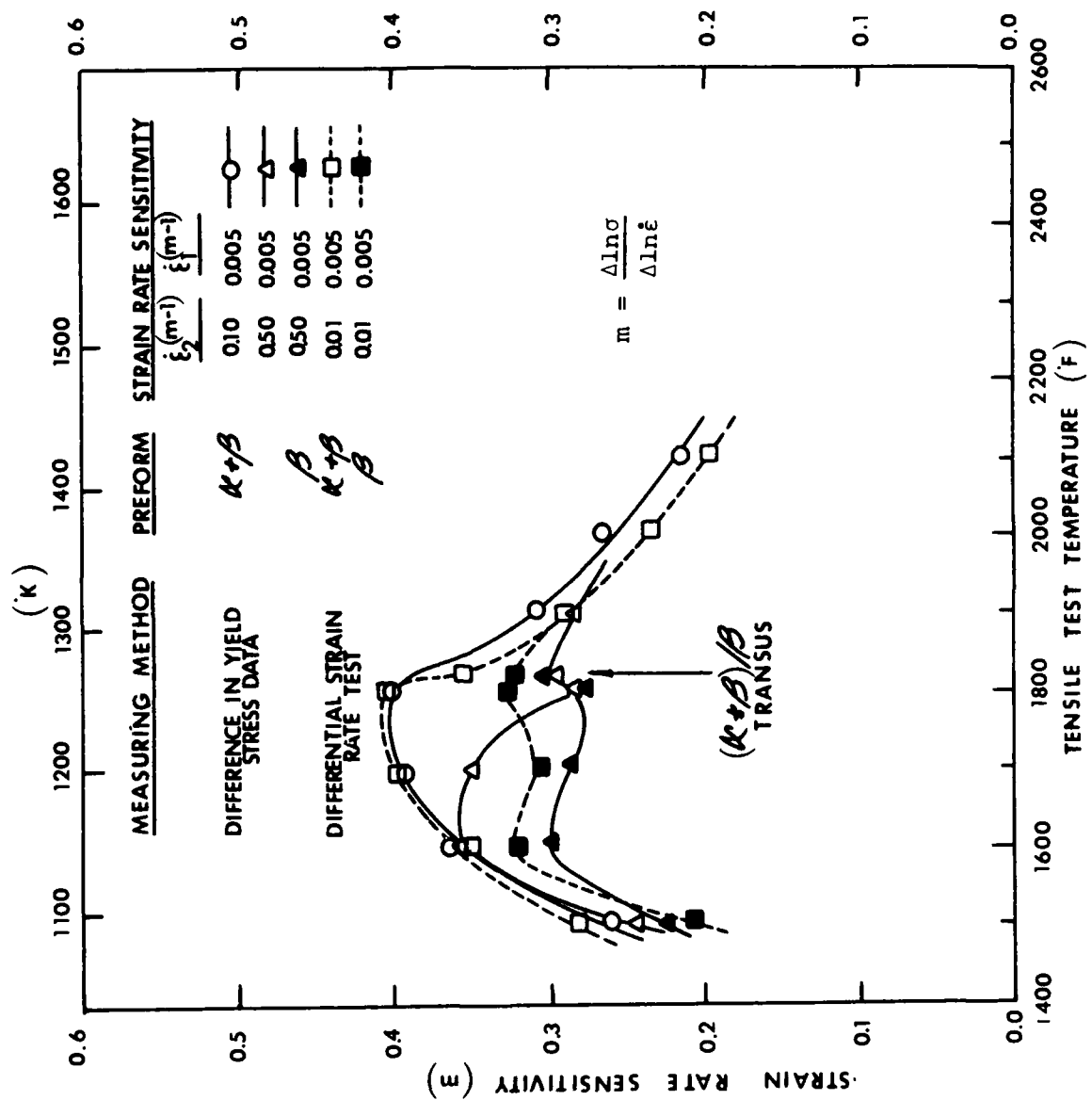


Figure E-6 Strain rate sensitivity versus temperature for Ti-6242Si alloy

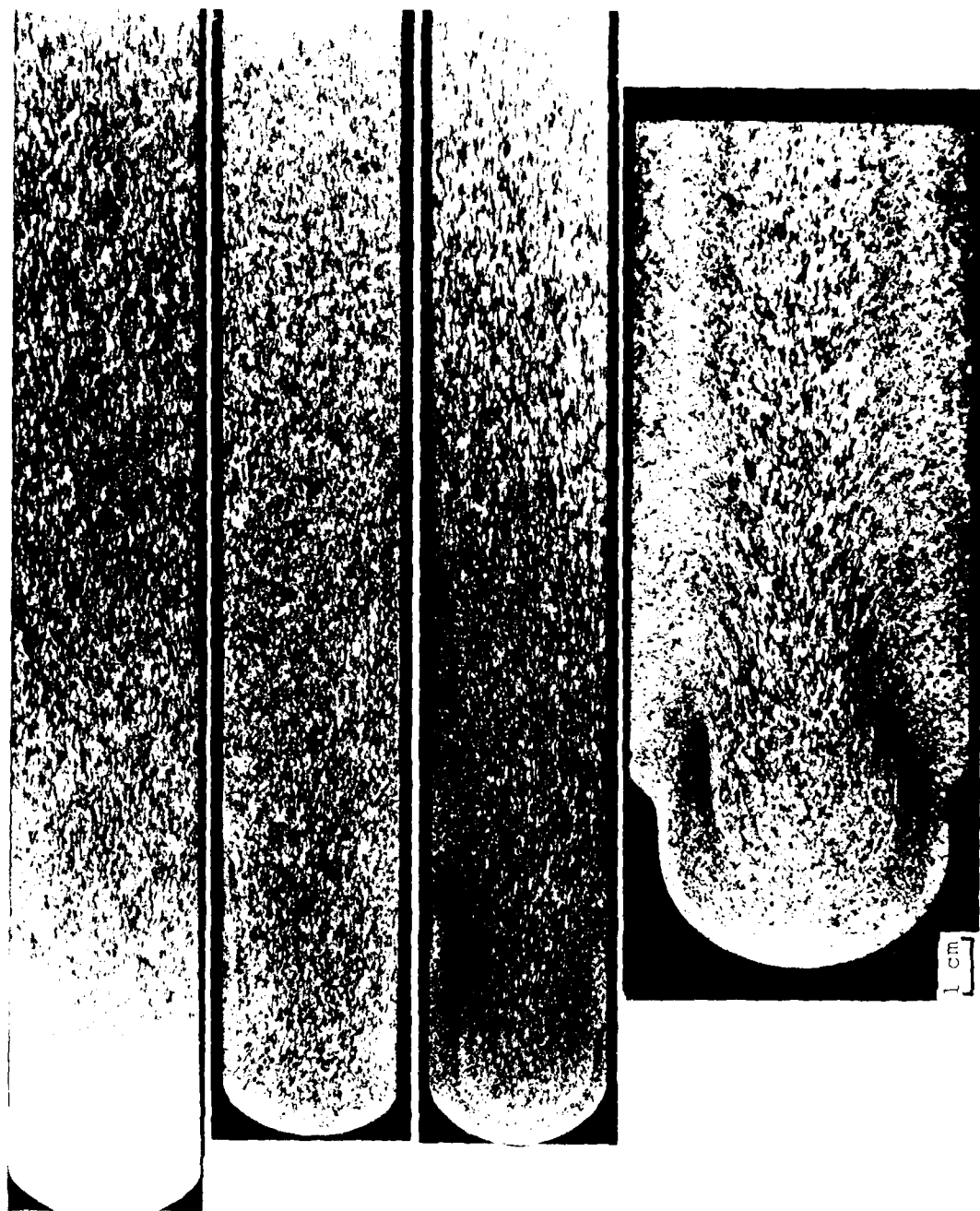


Figure E-7 Effect of die temperature on the macrostructure for die-forged pancakes



17.50F
17.50F
17.50F

17.50F
17.50F
17.50F

17.50F
17.50F
17.50F

17.50F
17.50F
17.50F

Figure E-8 Effect of preform structure on the macrostructure of (+)-formed pancakes



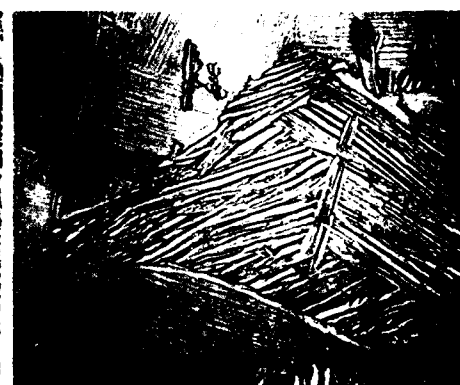
1750F/1750F/AC



1900F/1840F/AC



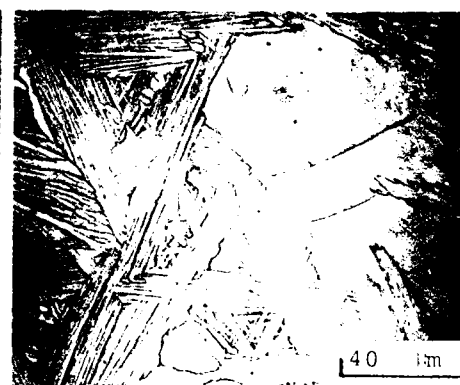
1800F/1800F/AC



2000F/1840F/AC



1840F/1840F/AC



2100F/1840F/AC

Figure E-9 Microstructures of isothermally forged Ti-6242Si alloy

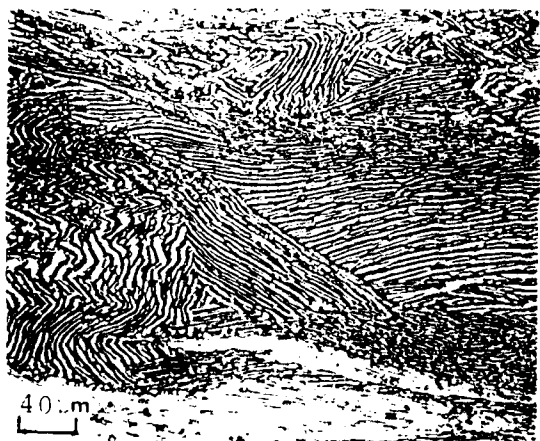


1750F/1750F/AC

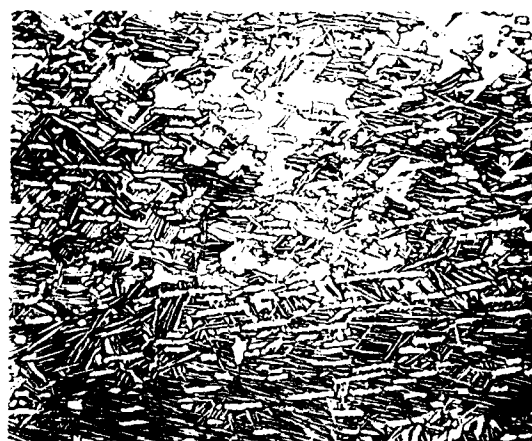


1800F/1800F/AC

$\alpha+\beta$
preform



1750F/1750F/AC



1800F/1800F/AC

β
preform

Figure E-10 Effect of β -preform structure on the microstructure

Effect of Processing Variables on the Mechanical Properties

In another phase of the program at Wyman-Gordon, an investigation was undertaken to determine the processing variable-mechanical property relationships of the forgings, and to elucidate the property capabilities for both $\alpha+\beta$ and β -forged Ti-6242Si alloy (10). The experimental observations included the influence of both forge variables (stock temperature, die temperature, preform microstructure, cooling method from the press), and heat treat variables (solution-treat temperature, time, and cooling method, aging time, intermediate annealing).

It was shown that excellent combination of creep, tensile, and fracture toughness properties can be achieved for both $\alpha+\beta$ and β forgings (Table E-1). The mechanical properties of Ti-6242Si alloy forgings have a complicated relation to the solution treat conditions. The control of solution temperature, time, and cooling method was of great importance for achieving optimum property combinations (Figure E-11 and Tables E-2a, E-2b, E-2c. The creep property appeared to be insensitive to aging time. Within the forge conditions investigated, the type of forging and forge temperature were found to have an important effect on creep properties. Since solution treatment for this alloy forgings has been generally made at very high temperatures, none of the die temperature, ram rate, cooling method from the press were detrimental to creep resistance.

For ($\alpha+\beta$) forgings, the β solution treatment may lower the tensile and fatigue properties, but a very significant improvement in creep resistance is achieved (Figure E-11). The use of ($\alpha+\beta$) solution treatment, β -preform microstructure or intermediate anneal, significantly degraded the creep properties. In the case of β -forgings, the ($\alpha+\beta$) solution treatment generally gave a better creep strength-ductility combination than that resulting from β -solution treatment.

Relationships Between Microstructure and Mechanical Property

The relationship between microstructures and mechanical properties of commercial-grade Ti-6242Si alloy forgings has also been previously investigated at Wyman-Gordon (11). Here the variation of creep properties with microstructure was particularly emphasized.

The results demonstrated that the creep resistance had an obvious variation with microstructure. The microstructure characterized by fine Widmanstätten colonies appeared to have the highest creep resistance if proper heat treatment was used; it also had excellent combinations of tensile and

TABLE E-1
ACHIEVABLE MECHANICAL PROPERTIES: Ti-6242Si ALLOY FORGING

Forge/ Heat Treat Conditions	Creep* (Hours to 0.2% Strain)	Creep** Rupture Time (Hours)	K _{IC} (ksi √in.)	RT		900F		Post-Creep	
				Tensiles YS (ksi)	El.%	Tensiles YS (ksi)	El.%	Tensiles YS (ksi)	El.%
(α+β)/β	199	325	74	131	13	78	13	129	10
(α+β)/β	169	-	~65***	134	10	82	11	-	-
(α+β)/(α+β)	56	-	~45***	138	14	86	15	-	-
(α+β)/β	19	-	~35***	155	3	124	5	-	-
(α+β)/(α+β)	164	-	~50***	130	14	82	17	-	-
β/(α+β)	185	-	~70***	135	11	84	17	-	-
β/(α+β)	160	-	~75***	136	10	-	-	-	-
β/(α+β)	116	-	76	130	11	82	15	134	12
β/β	134	275	72	122	7	80	12	128	12

* Creep condition: 1050F - 25 ksi

** Creep rupture: 1050F - 50 ksi

*** Estimated value

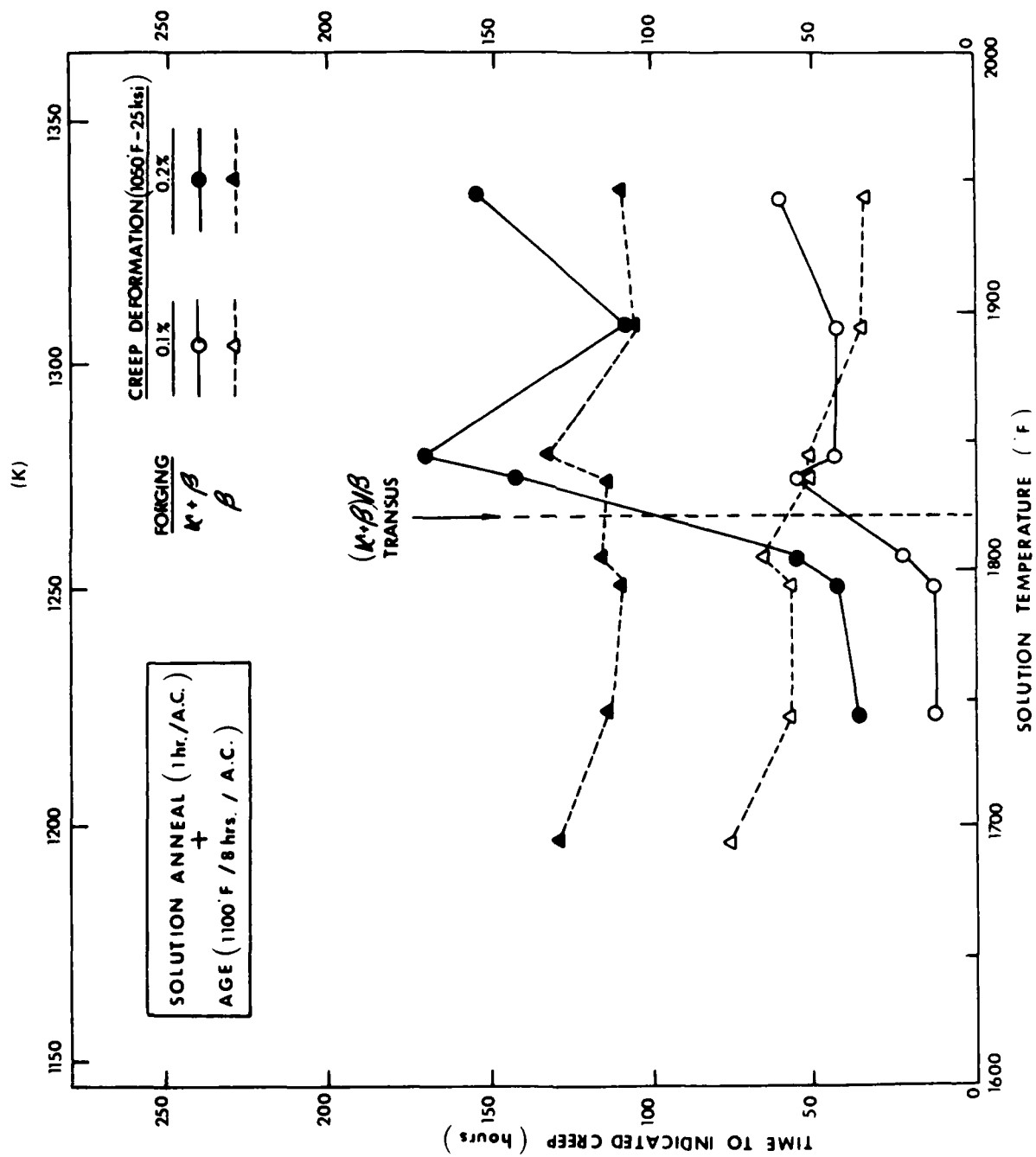


Figure E-11 Solution-temperature dependence of creep resistance for (n+t) and f-forgings

TABLE E-2a
EFFECT OF COOLING METHOD FROM THE SOLUTION TREATMENT:
Ti-6242Si ALLOY FORGING

Cooling from ST Temp.	Forge/ Solution Treat Condition	Creep (1050F - 25 ksi) (Hours to Indicated Creep)		R.T. Tensile Properties	
		0.1%	0.2%	Y.S. (ksi)	El. (%)
Air Cool	($\alpha+\beta$)/ β	67.5	168.5	134.0	10.0
Water Quench	($\alpha+\beta$)/ β	3.0	18.6	154.8	2.5

TABLE E-2b
EFFECT OF INTERMEDIATE ANNEAL:
Ti-6242Si ALLOY FORGING

Forge/Heat Treat Condition	Creep (1050F - 25 ksi) (Hours to Indicated Creep)		R.T. Tensile Properties	
	0.1%	0.2%	Y.S. (ksi)	El. (%)
($\alpha+\beta$)/(β -ST + Age)	42.5	171.0	131.2	10.2
($\alpha+\beta$)/(β -ST + Ann + Age)	3.2	24.2	133.8	10.0
($\alpha+\beta$)/(($\alpha+\beta$)-ST + Age)	11.5	43.0	136.4	13.7
($\alpha+\beta$)/(($\alpha+\beta$)-ST + Ann + Age)	1.5	8.3	-	-
β /(β -ST + Age)	32.0	101.0	124.0	7.4
β /(β -ST + Ann + Age)	3.8	26.5	128.0	9.5
β /(($\alpha+\beta$)-ST + Age)	45.5	94.5	125.2	11.6
β /(($\alpha+\beta$)-ST + Ann + Age)	4.3	26.7	128.0	12.3

TABLE E-2c
EFFECT OF PREFORM MICROSTRUCTURE FOR (α + β) FORGINGS:
Ti-6242Si ALLOY FORGING

Preform Micro- Structure	Forge/ Solution Treat Condition	Creep (1050F - 25 ksi) (Hours to Indicated Creep)		R.T. Tensile Properties		900F Tensile Properties	
		0.1%	0.2%	YS (ksi)	El.%	YS (ksi)	El.%
$\alpha+\beta$	(β_t-70)/ β	42.5	171.0	131.2	10.2	82.0	12.3
	(β_t-70)/($\alpha+\beta$)	11.5	43.0	136.4	13.7	80.4	15.1
β	(β_t-70)/ β	26.5	83.5	125.6	9.5	80.0	15.1
	(β_t-70)/($\alpha+\beta$)	10.5	37.0	134.4	12.3	82.4	17.9
$\alpha+\beta$	(β_t-20)/ β	48.5	134.0	126.0	11.6	78.0	12.3
	(β_t-20)/($\alpha+\beta$)	9.0	40.3	129.6	14.4	81.0	16.5
β	(β_t-20)/ β	37.0	126.0	127.8	9.0	81.4	13.0
	(β_t-20)/($\alpha+\beta$)	31.5	88.5	130.0	15.1	80.4	15.8

fracture toughness properties. Both transformed martensitic- α and globular- α appeared to significantly degrade the creep and fracture toughness properties (Figures E-12 through E-14). However, the presence of globular- α can significantly improve the low cycle fatigue of the alloy forgings.

In addition, it was observed that there was a definite variation between the creep resistance of the alloy, and the nature and size of incoherent precipitates (high Si and Sn) (Figures E-15 and E-16). It was suggested that immobilization of dislocations by either very fine silicides or silicon in solution dominated the rate controlling creep mechanism for the alloy. The thermal and mechanical history would obviously affect the state of silicon dissolution or silicon-solute clusters and limit the availability of silicon for improved creep properties. However, with adequate control of heat treat variables to eliminate such undesirable particles, an excellent combination of creep, tensile, and fracture toughness properties could be achieved for both $\alpha+\beta$ and β -forgings (Table I).

Program Status

Material Behavior Under Processing Conditions

In this reporting period, the technical effort has been primarily concentrated on Phase I effort. Wyman-Gordon produced and supplied all sample bars from the program materials with two distinctly different microstructures, designated as $(\alpha+\beta)$ and β -preform microstructures, for the team members. As stated earlier, the preform microstructure must be first controlled before one can adequately define the material behavior under processing conditions. Both chemistry and structural characteristics of the as-received billets were carefully evaluated and a series of pancake forgings was produced to determine the forgeability and the optimum heat-treat variables. The microstructure/property relationship for the pancakes will be characterized.

(a) Material Procurement

About 700 pounds of Ti-6242Si billet materials (8 inch round, premium grade for disks) was purchased for the program; 250 pounds for Phase I, 350 pounds for Phases III, IV, and V, and an additional 100 pounds for AFML in-house and other uses. The four mults (A, B, C, and D) were obtained from the same heat material, RMI heat number 996243. The relative locations of the billet materials used for various phases of the program are given in Figure E-17.

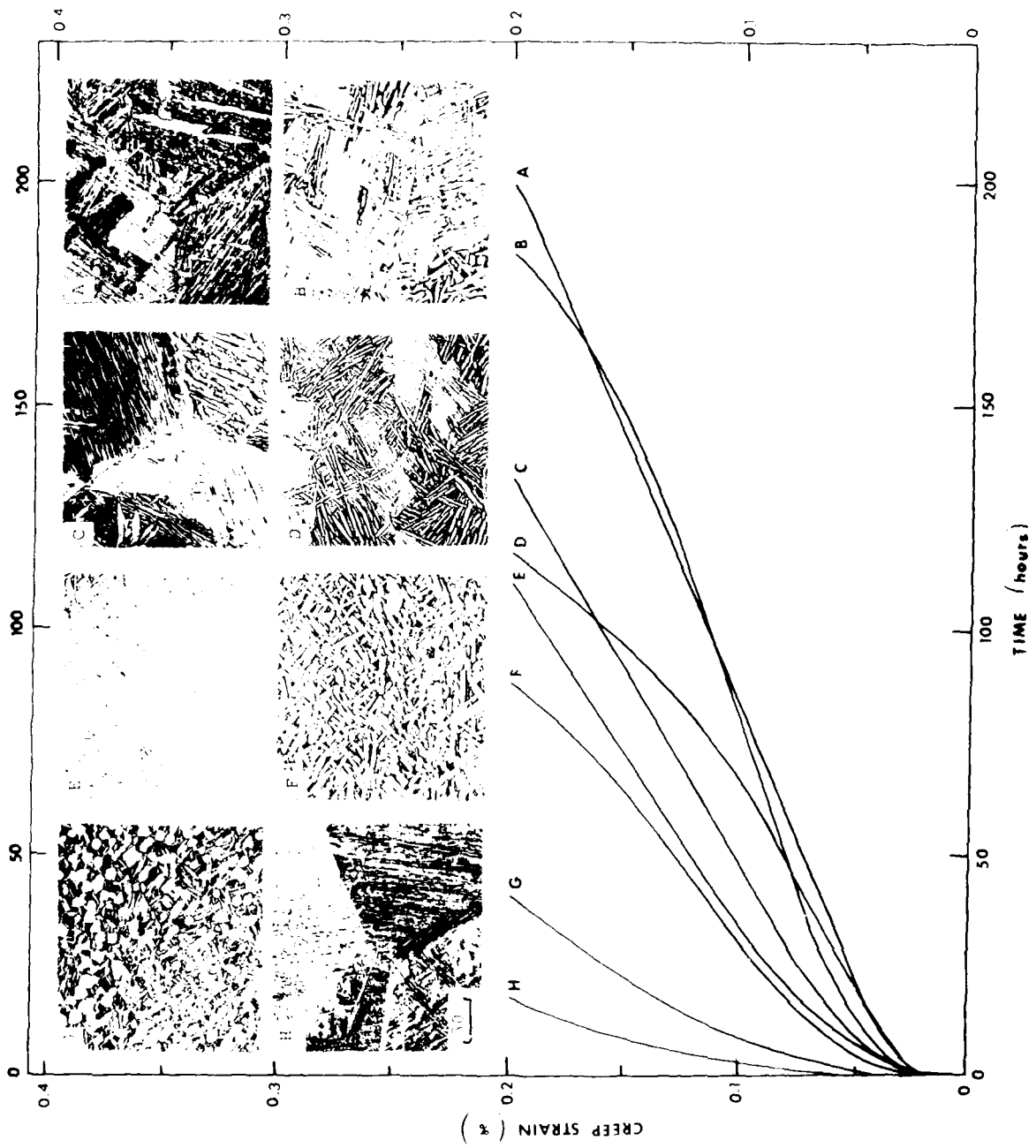


Figure E-12 Creep strain versus time curves for eight microstructural conditions of Ti-6242Si alloy pancakes

AD-A082 207

BATTELLE COLUMBUS LABS OH
RESEARCH TO DEVELOP PROCESS MODELS FOR PRODUCING A DUAL PROPERTY--ETC(U)
DEC 79 G D LAHOTI, T ALTAN

F/G 11/6

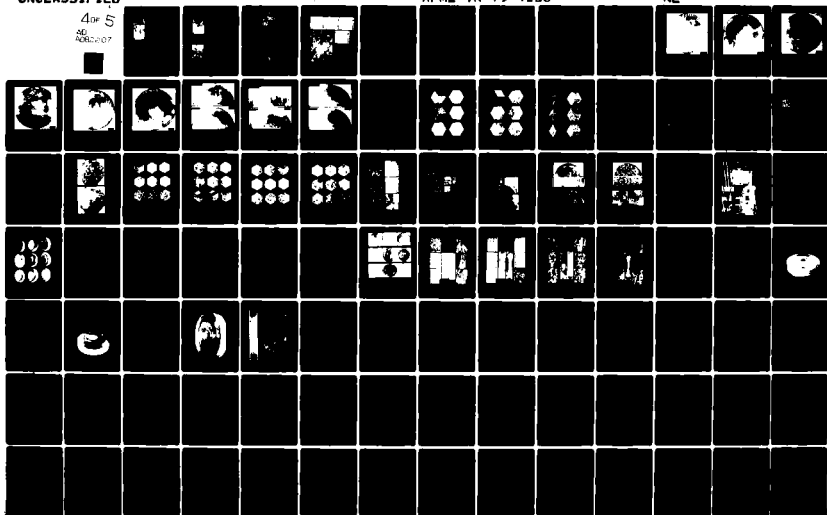
F33615-78-C-5025

UNCLASSIFIED

AFML-TR-79-4156

NL

4 of 5
AD A082 207



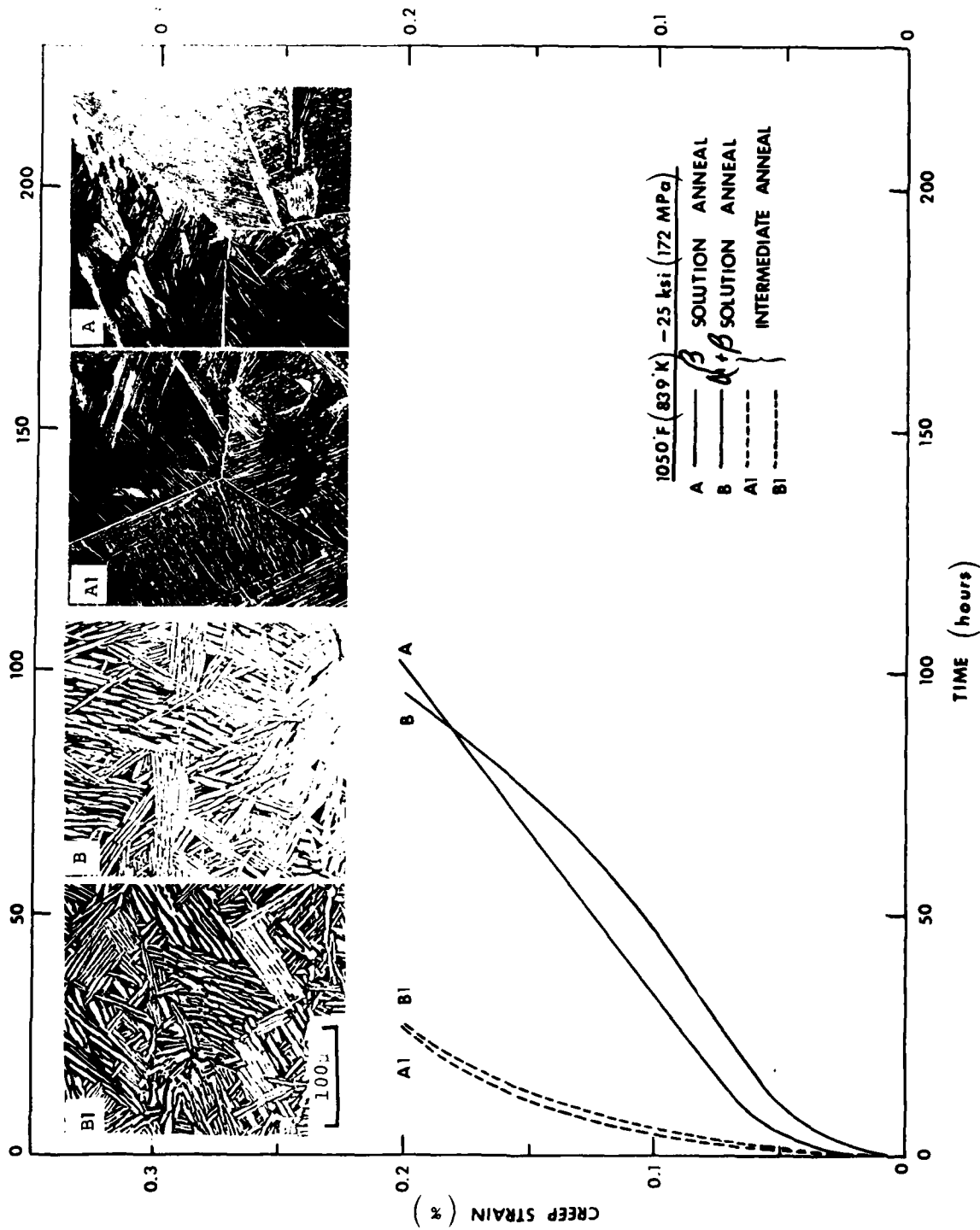


Figure F-13 Effect of intermediate anneal on creep resistance of Ti-6242Si alloy forgings

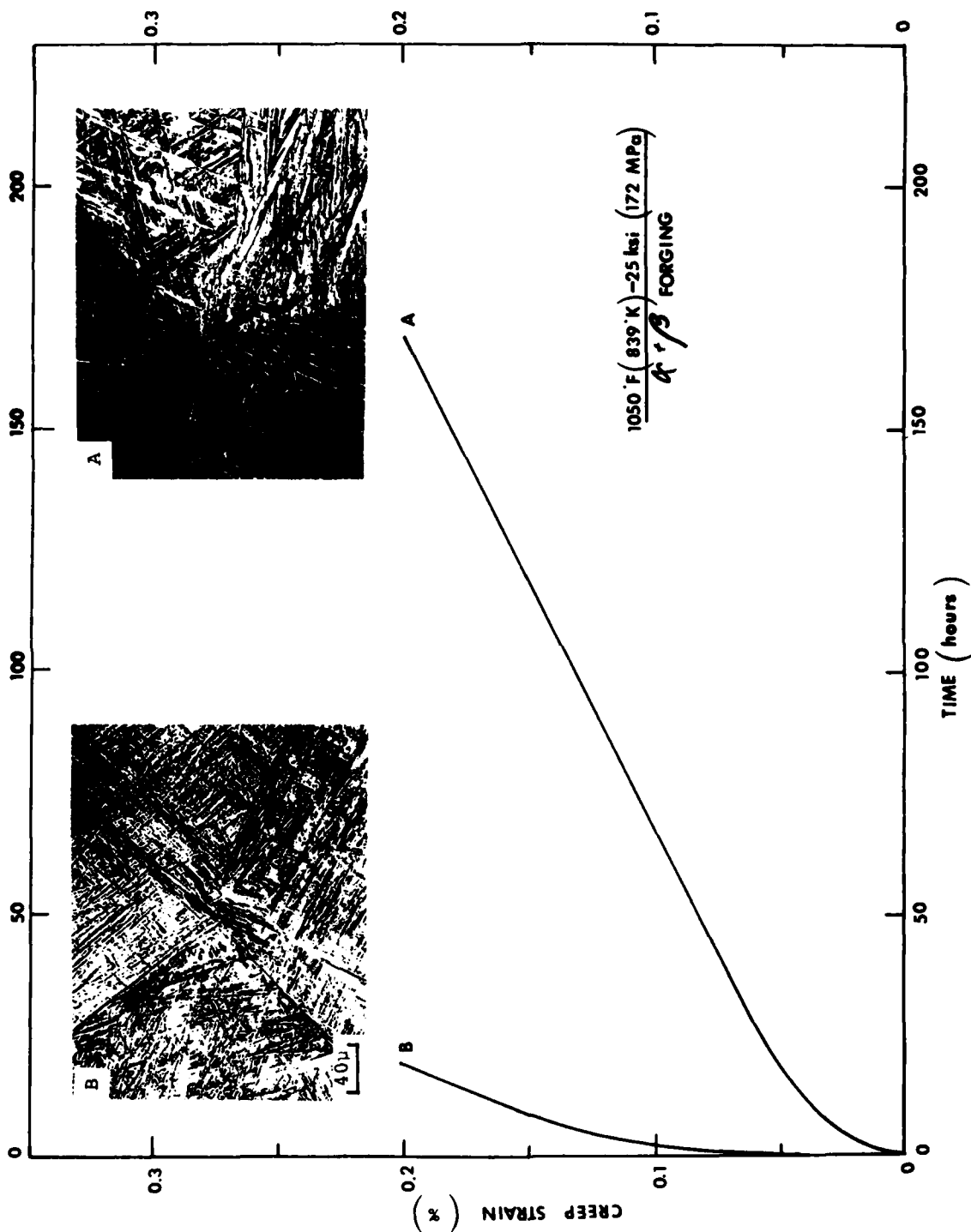


Figure E-14 Effect of cooling rate from solution-treat temperature on creep resistance of Ti-6242Si alloy forgings



0.2% creep: 199 hours
 K_{IC} : 74 ksi $\sqrt{\text{in.}}$
 RT YS: 131 ksi
 900F YS: 78 ksi
 Post-creep YS: 129 ksi

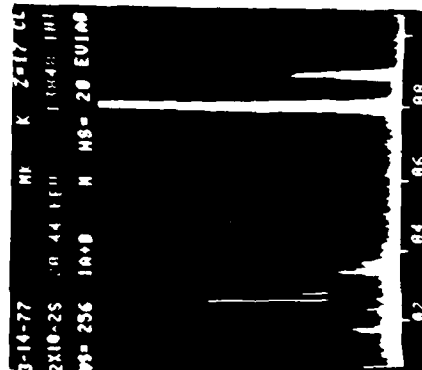
0.2% creep: 134 hours
 K_{IC} : 69 ksi $\sqrt{\text{in.}}$
 RT YS: 126 ksi
 900F YS: 78 ksi
 Post-creep YS: 124 ksi

0.2% creep: 40 hours
 K_{IC} : 50 ksi $\sqrt{\text{in.}}$
 RT YS: 130 ksi
 900F YS: 81 ksi
 Post-creep YS: 132 ksi

Figure E-15 Extraction replica showing the nature and distribution of precipitates in Ti-6242Si alloy pancakes at various processing conditions



(A) Extraction replica showing the nature and distribution of precipitates for intermediate-annealed condition



(a) group shot

(B) X-ray fluorescent analysis of extracted particles: (a) group shot in α -region, (b) large particles in β -region, (c) particles in α -region (d) small particles in β -region.

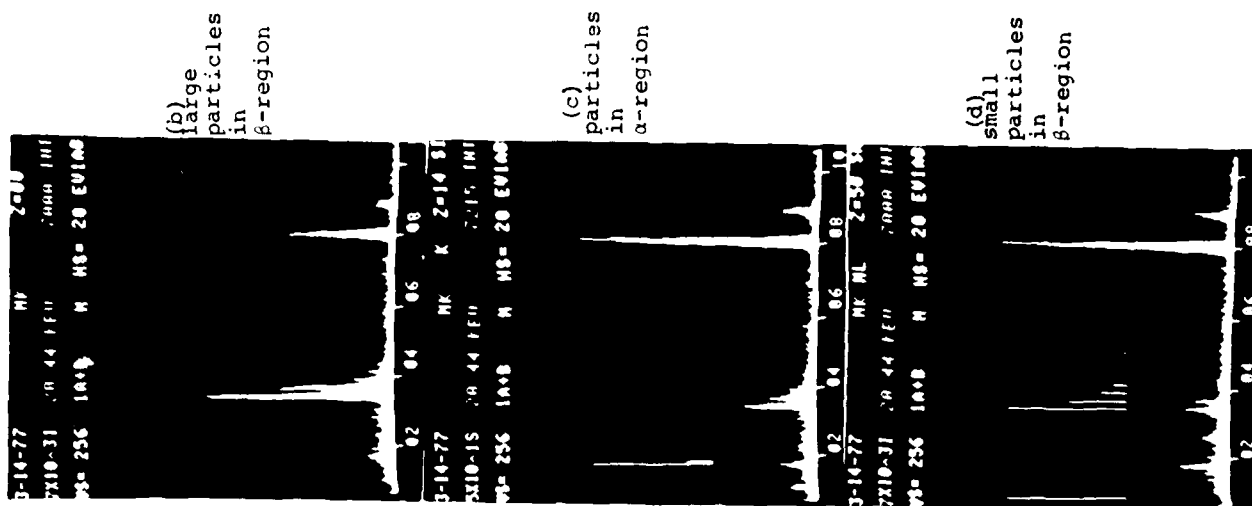


Figure E-16

PROGRAM MATERIAL: Ti-6Al-2Sn-4Zr-2Mo-0.1Si
8-INCH DIAMETER BILLET

"A" mult (517 pounds): Phases I, II, IV, and V -
test specimens, pancake
forgings, disk forgings

"B" mult (82 pounds): Phase III - interface effects

"C" mult (66 pounds): Future uses

"D" mult (67 pounds): AFML in-house program

A1, A2, A3, B1, C1, D1 slices: chemistry and
structural evaluations

R.M.I. HEAT - 996243

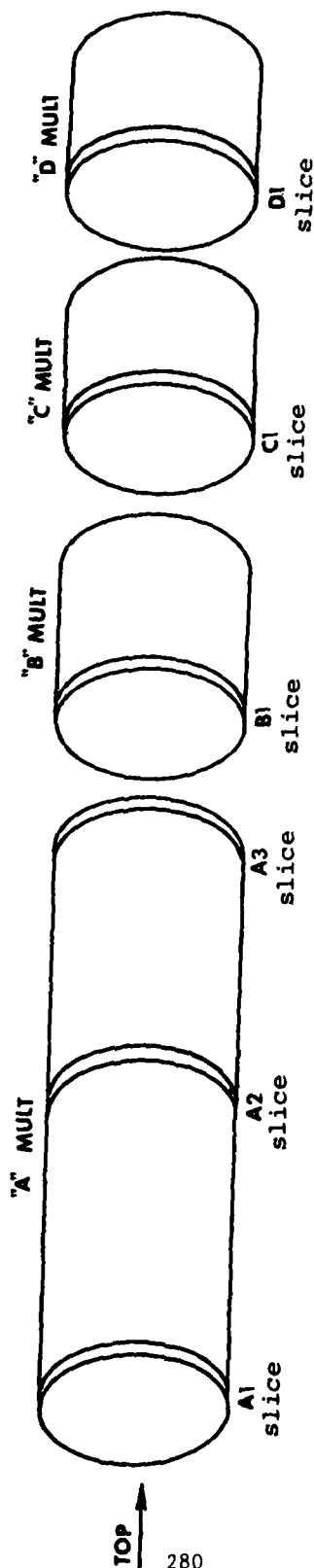


Figure E-17 Sketches of as-received 8 inch round billets showing the relative locations of the materials used for various phases of the program

(b) Billet Evaluations

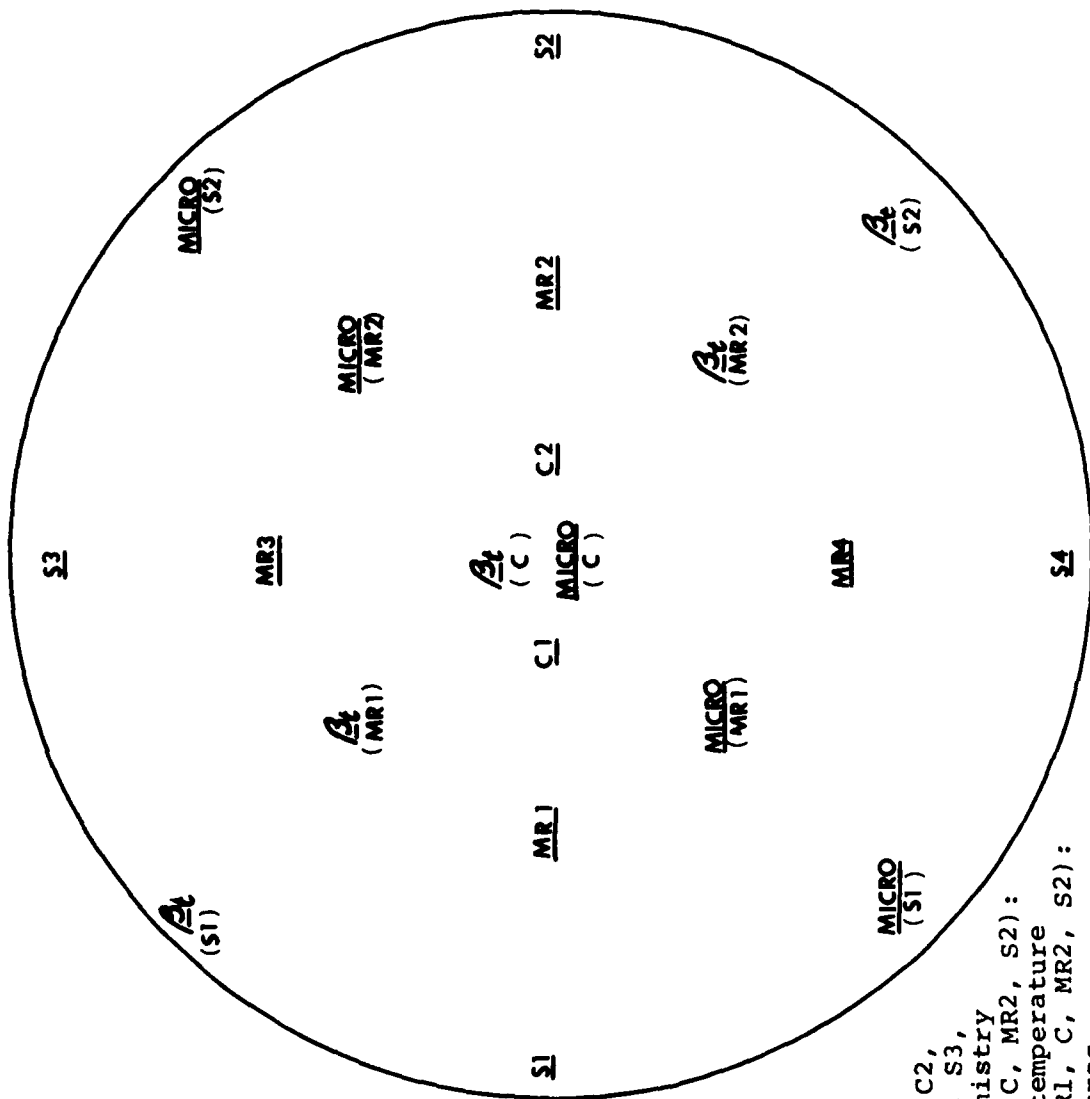
A detailed evaluation of the chemistry, structure, and β_t of the as-received billets was carried out to determine the quality of the program materials. It is known that the achievable mechanical properties of the titanium alloy forgings depend critically on the chemistry-homogeneity and structural uniformity of the initial ingot or billet (13).

Figure E-18 illustrates the relative locations of the materials used for chemistry, structural, and β_t evaluations of the billet slices; six slices were taken for this evaluation (see Figure E-17). The chemical analyses were made on aluminum, tin, zirconium, molybdenum, silicon, iron, carbon, nitrogen, oxygen, and hydrogen. The atomic absorption technique was used for Al, Sn, Zr, Mo, and Fe determination, Si was done by emission method, C was determined by combustion method, and N was analyzed by the Kjeldahl procedure. Oxygen analysis was made by inert gas fusion technique, and hydrogen content was determined by the hot-extraction method. The differential thermal analysis (DTA) method was used to determine the β_t -temperatures; this method is fast, economical, and an improvement in accuracy (1F/0.5C) over the conventional metallographic technique ($\pm 10F/5C$).

The results of chemical analyses and β_t -temperatures for the six billet slices (A1, A2, A3, B1, C1, and D1) are given in Tables E-3a and E-3b; the test reports regarding the chemistry and β_t -temperatures from both billet supplier and Wyman-Gordon's acceptance test are also included.

Several features from Table E-3 should be noted: (1) There is some variation in chemistry at different slices and different locations. The difference in Al, Zr, and Fe from one slice to another, and Si and H from one location to another are most obvious. This is expected in large production-size billets because large castings generally experience a wide range of localized freezing and cooling rates and result in nonuniform chemistry. (2) The information provided by the melter can only represent a macroscopic view of the bulk chemistry and β_t -temperature. (3) The program materials have acceptable uniformities in chemistry and β_t from a production standpoint, and are good production quality billets.

Figure E-19 illustrates examples of the macrostructures for several billet slices. It was shown that there is a significant variation in macroflow characteristics from one slice to another, but none of the slices has clear appearance of β -flecks. Figure E-20 further presents a comparison of macrostructures between modified Kroll etch and bifluoride etch; the bifluoride etch is excellent for revealing the details of flow characteristics for the billets.



S1, MR1, C1, C2,
MR2, S2, MR3, S3,
MR4, S4: Chemistry
β_t (S1, MR1, C, MR2, S2):
β -transus temperature
Micro (S1, MR1, C, MR2, S2):
microstructures

Figure E-18 Sketch of the as-received 8 inch round billet showing the relative locations of the materials used for chemistry, structural characterization, and β-transus evaluations

TABLE E-3a
RESULTS OF ALLOY CHEMISTRY ALONG WITH β -TRANSUS TEMPERATURE FOR
A1, A2, and A3, SLICES CUT FROM A-MULT BILLET

Serial Number (Slice)	Specimen Location	Chemical Composition (wt.%)										β_t (°F)
		Al	Sn	Zr	Mo	Si	Fe	C	N	O	H	
A1	S1	6.02	1.99	4.21	2.03	.084	.05	.014	.010	.073	.0068	1817
	S2	6.05	2.03	4.19	1.95	.089	.05	.020	.011	.076	.0091	1820
	S3	6.06	1.99	4.15	2.06	.068	.05	.014	.011	.076	.0090	-
	S4	6.02	1.99	4.27	1.99	.064	.05	.013	.010	.056	.0098	-
	MR1	5.90	2.05	4.16	1.99	.075	.04	.016	.009	.071	.0042	1815
	MR2	6.03	1.95	4.17	2.05	.091	.05	.013	.014	.071	.0065	1815
	MR3	5.62	1.92	4.28	1.80	.080	.04	.013	.010	.075	.0043	-
	MR4	6.16	1.97	4.33	1.95	.068	.07	.030	.011	.064	.0038	-
	Cl	6.05	1.98	4.35	1.95	.079	.05	.017	.009	.078	.0039	1821
	C2	6.02	1.99	4.25	1.97	.100	.05	.016	.013	.073	.0048	-
A2	S1	6.10	2.08	3.83	2.06	.086	.04	.021	.010	.075	.0092	1817
	S2	5.81	2.07	3.82	1.99	.072	.01	.018	.010	.080	.0097	1821
	S3	5.93	2.02	3.97	2.03	.068	.01	.019	.010	.084	.0087	-
	S4	6.05	2.05	3.95	2.01	.075	.01	.017	.011	.078	.0101	-
	MR1	6.07	2.01	4.03	2.05	.075	.01	.020	.010	.067	.0053	1816
	MR2	6.01	2.00	3.90	1.99	.071	.01	.017	.010	.080	.0052	1821
	MR3	5.95	2.03	3.90	1.97	.066	.01	.021	.020	.079	.0054	-
	MR4	6.03	1.97	4.02	2.08	.070	.01	.018	.013	.075	.0031	-
	Cl	6.01	1.98	3.85	2.02	.083	.01	.022	.021	.079	.0032	1821
	C2	5.85	1.96	3.91	2.02	.079	.01	.017	.009	.076	.0034	-
A3	S1	5.95	1.97	3.88	2.09	.087	.01	.017	.011	.070	.0086	1821
	S2	5.85	1.95	4.00	2.09	.076	.01	.014	.009	.092	.0092	1813
	S3	5.86	1.96	3.80	2.05	.074	.01	.013	.011	.069	.0069	-
	S4	6.01	2.01	3.75	2.08	.072	.01	.016	.013	.065	.0098	-
	MR1	6.02	2.00	3.88	2.05	.071	.01	.015	.010	.067	.0057	1813
	MR2	6.08	2.02	3.90	2.06	.066	.01	.016	.009	.078	.0046	1817
	MR3	5.97	2.02	3.81	2.09	.070	.01	.019	.011	.064	.0040	-
	MR4	5.86	2.03	3.85	1.98	.066	.01	.015	.013	.071	.0031	-
	Cl	6.00	1.98	3.80	2.06	.064	.01	.017	.010	.077	.0028	1816
	C2	5.92	2.06	3.85	2.07	.071	.01	.014	.010	.063	.0026	-
Test Report* (RMI)		6.1	2.1	3.9	2.1	.084	.05	.02	.010	.082 (T) .085 (B)	.0048 (MR) to .0092 (1/2" below)	1790±15
		6.1	2.1	3.9	2.1	.084	.05	.02	.010	.076 (T) .095 (B) to .0096 (S)	.0030 (C) to .0096 (S)	1810
Acceptance Report** (Wyman-Gordon)												
*	Cu = .01	Mn = .02	Y = < 10 ppm	B = < 30 ppm								
**	Cu = .03	Mn = .02	Y = < .0010	B = < .003								

TABLE 1-3b
RESULTS OF ALLOY CHEMISTRY ALONG WITH β -TRANSUS TEMPERATURE FOR
B1, C1, AND D1 SLICES CUT FROM B-, C-, D-MULT BILLETS, RESPECTIVELY

Serial Number (Slice)	Specimen Location	Chemical Composition (wt.%)										β_t (°F)
		Al	Sn	Zr	Mo	Si	Fe	C	N	O	H	
B1	S	6.05	1.97	3.90	1.99	.083	.04	.018	.009	.084	.0087	1819
	MR	6.03	2.02	4.11	1.97	.075	.04	.017	.009	.076	.0053	1819
	C	6.02	2.05	4.15	1.99	.072	.04	.011	.007	.076	.0034	1817
C1	S	6.03	2.03	4.01	1.98	.077	.04	.015	.010	.069	.0084	1815
	MR	6.09	2.07	4.15	1.99	.087	.04	.028	.009	.069	.0043	1810
	C	5.95	1.98	3.90	1.97	.091	.04	.039	.010	.069	.0037	1810
D1	S	5.96	2.01	3.92	2.00	.080	.04	.018	.009	.081	.0096	1817
	MR	6.09	1.98	4.15	1.99	.083	.04	.026	.009	.073	.0054	1819
	C	6.07	1.97	4.00	1.99	.083	.04	.014	.009	.076	.0043	1821
Test Report* (RMI)		6.1	2.1	3.9	2.1	.084	.05	.02	.010	.082 (T) .085 (B)	.0048 (MR) to .0092 (1/2" below)	1790±15
Acceptance Report** (Wyman-Gordon)		6.1	2.1	3.9	2.1	.084	.05	.02	.010	.076 (T) .095 (B)	.0030 (C) to .0096 (S)	1810

* Cu=<.01 Mn=.02 Y=<10 ppm B=<30 ppm
** Cu=.03 Mn=.02 Y=<.010 B=<.003

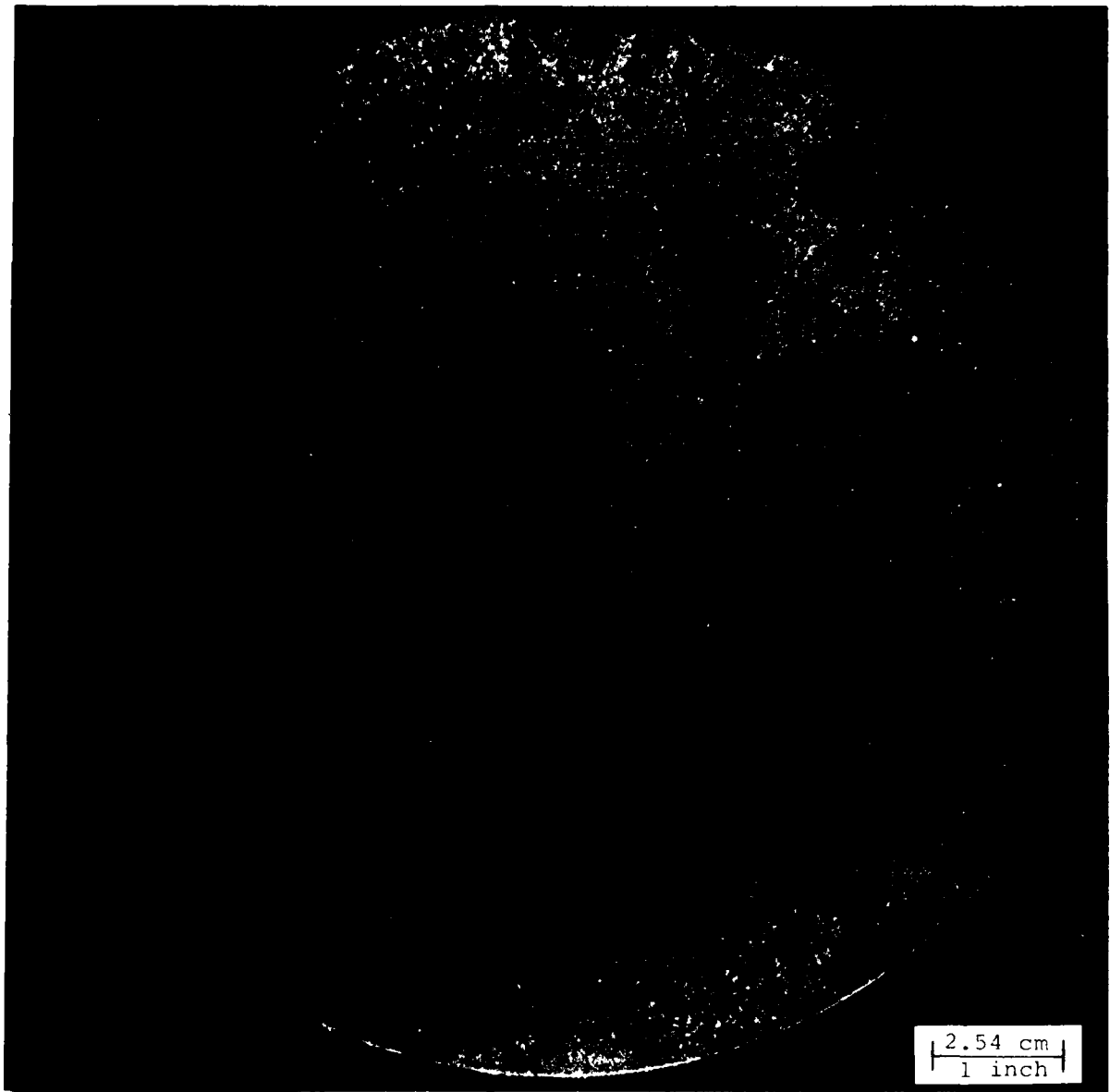


Figure E-19a

Transverse macrostructure for Al slice cut from
as-received 8 inch diameter A-mult billet;
bifluoride etch



Figure E-19b Transverse macrostructure for A2 slice cut from
as-received 8 inch diameter A-mult billet;
bifluoride etch

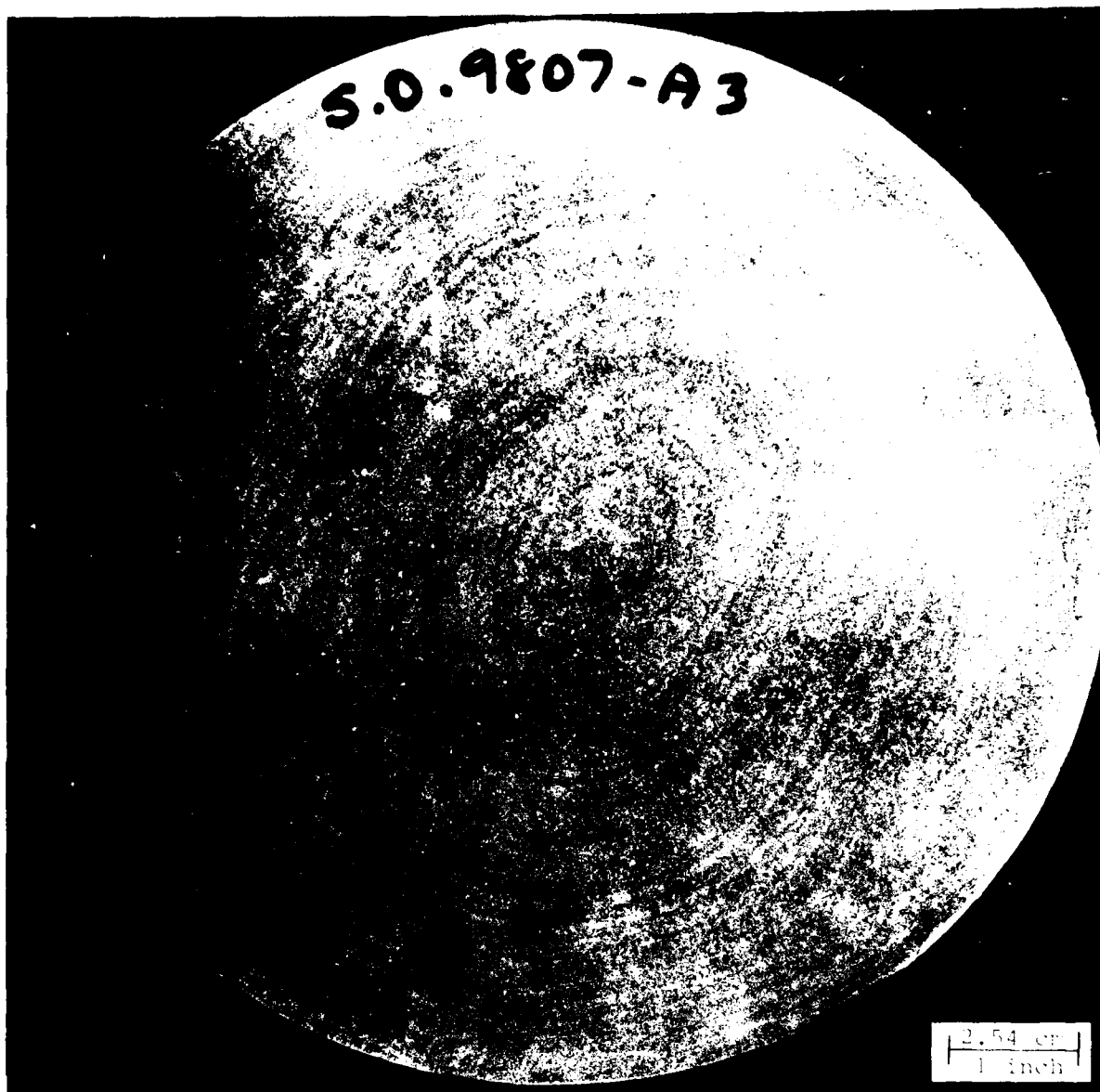


Figure E-19c

Transverse macrostructure for A3 slice cut from
as-received 8 inch diameter A-mult billet;
bifluoride etch

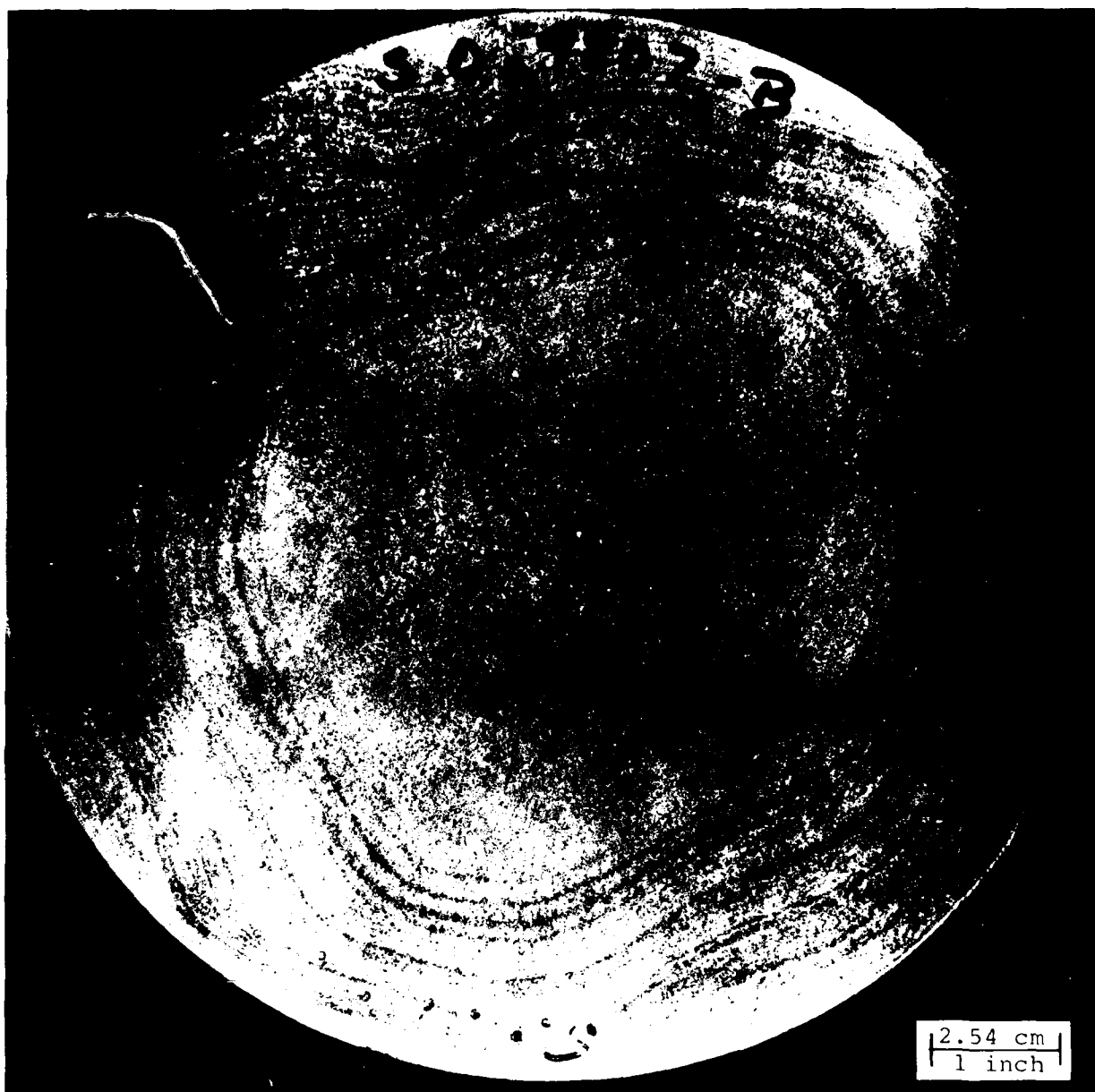


Figure E-19d

Transverse macrostructure for B1 slice cut from
as-received 8 inch diameter B-mult billet;
bismuth fluoride etch

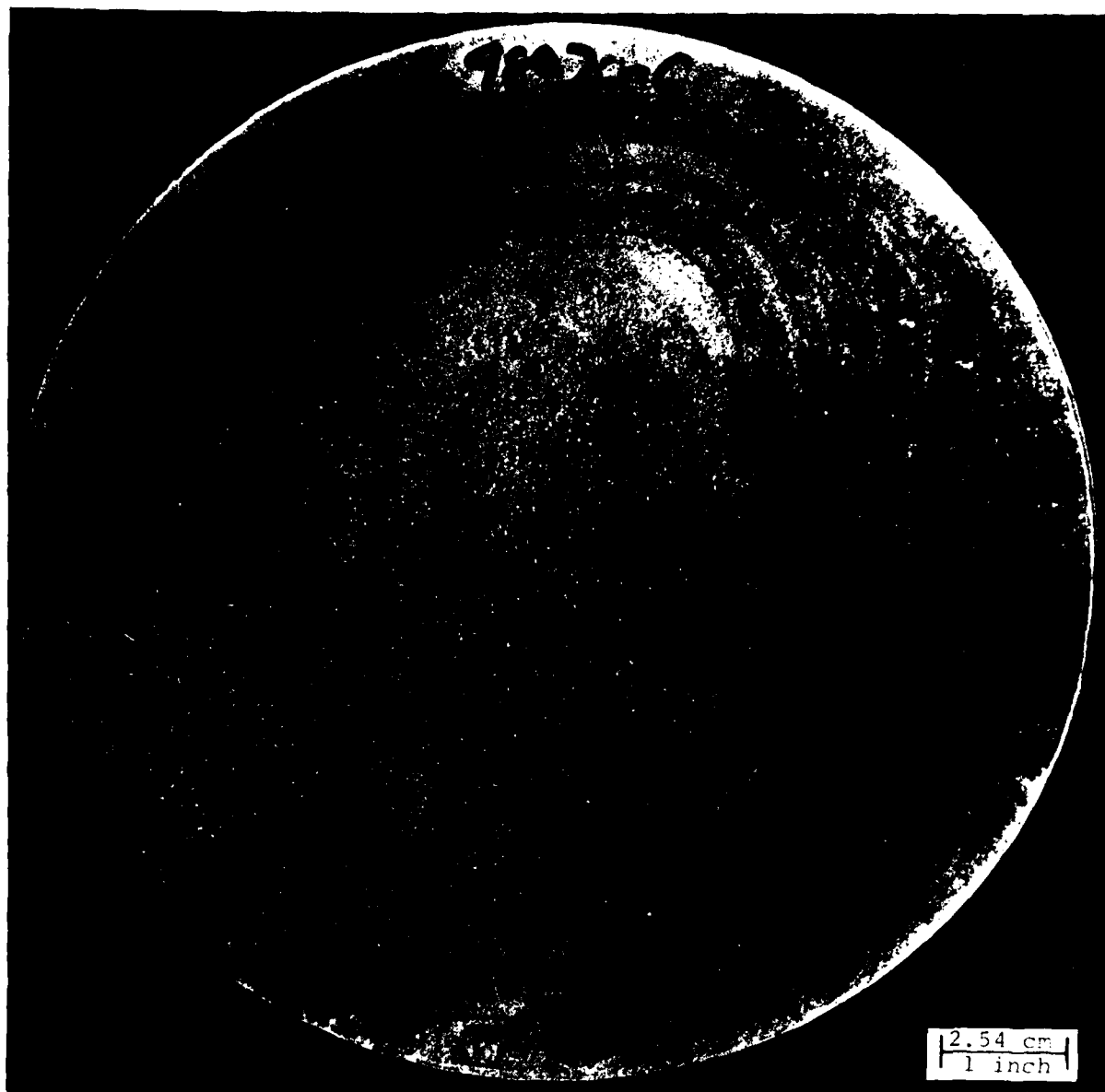


Figure E-19e Transverse macrostructure for C1 slice cut from
as-received 8 inch diameter C-mult billet;
bifluoride etch

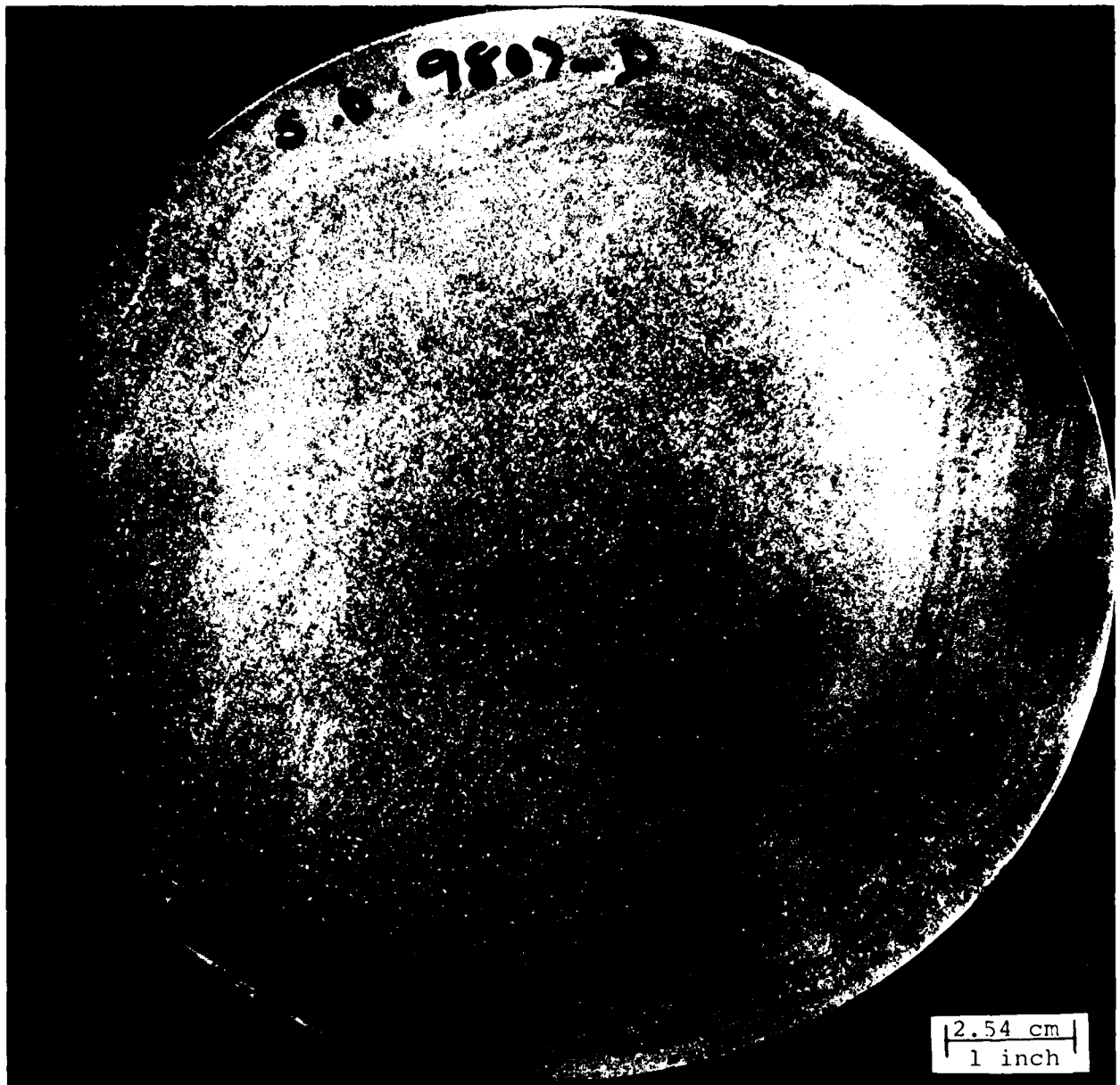


Figure E-19t Transverse macrostructure for D1 slice cut from
as-received 8 inch diameter D-mult billet;
bifluoride etch

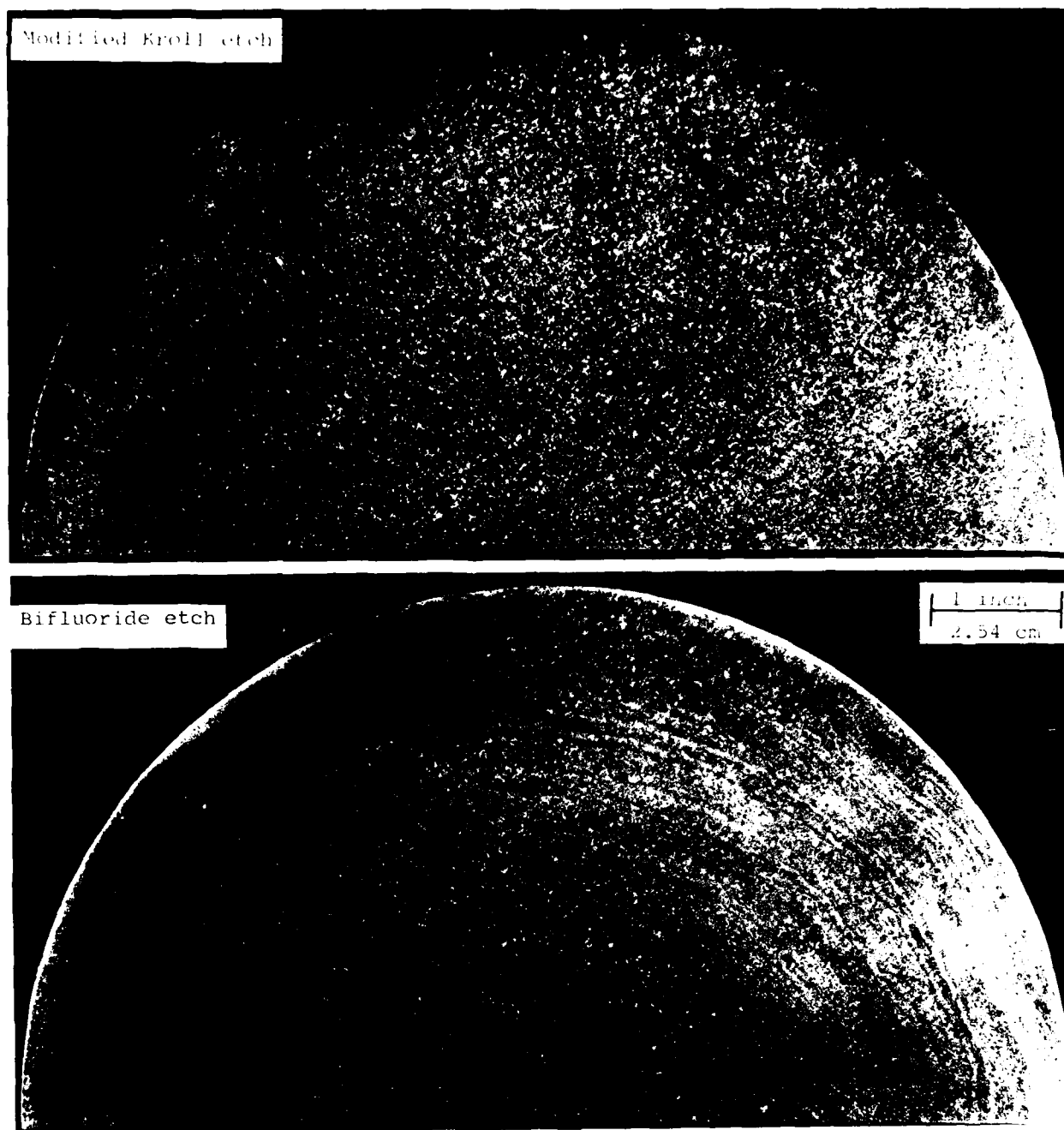
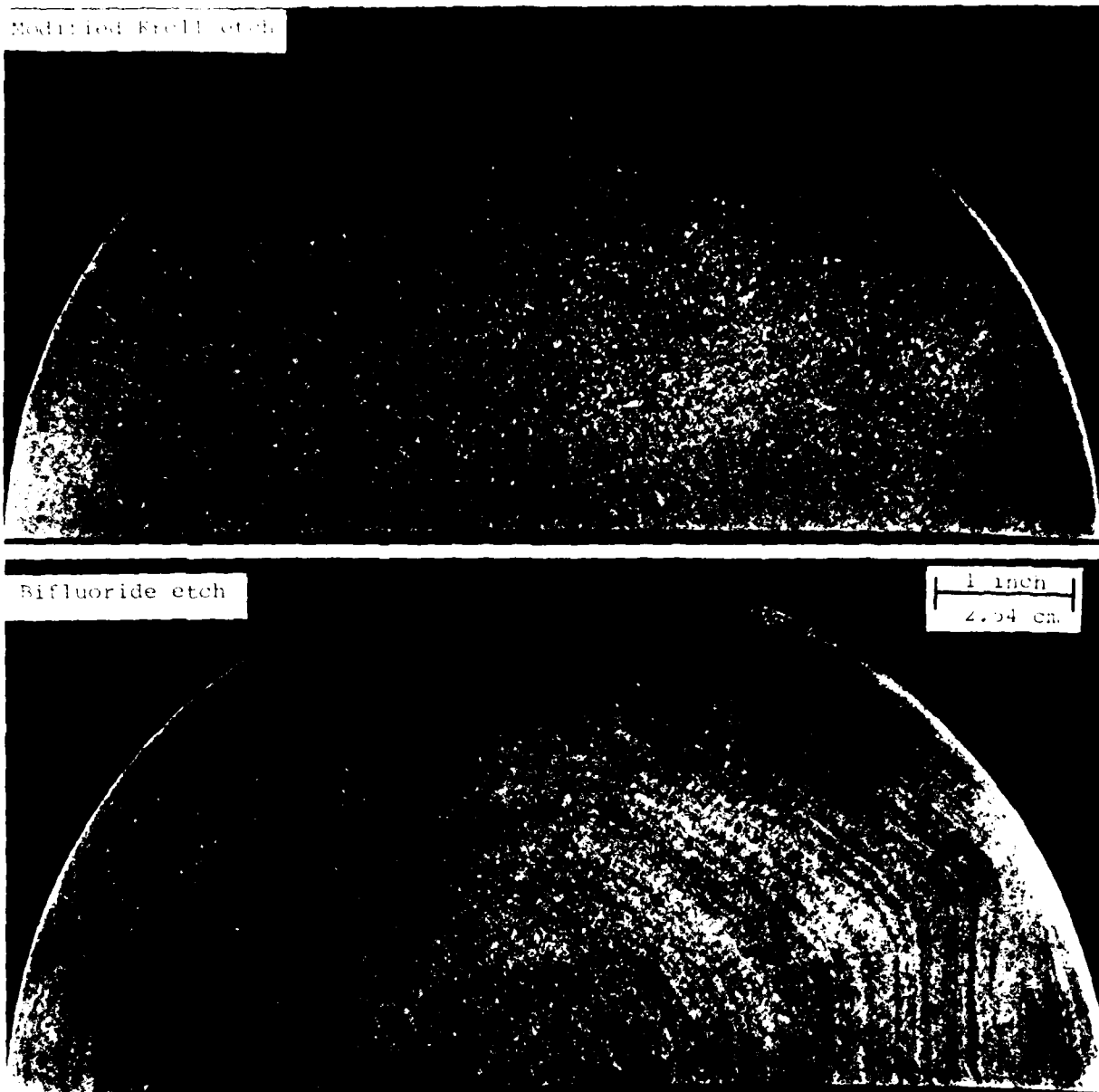


Figure E-20a Comparison of transverse macrostructures for as-received A2-slice as revealed by:
(a) modified Kroll etch, (b) Bifluoride etch



A2 - slice

Figure E-201 Comparison of transverse macrostructures for
as-received Al-slice as revealed by:
(a) modified Kroll etch, (b) Bifluoride etch

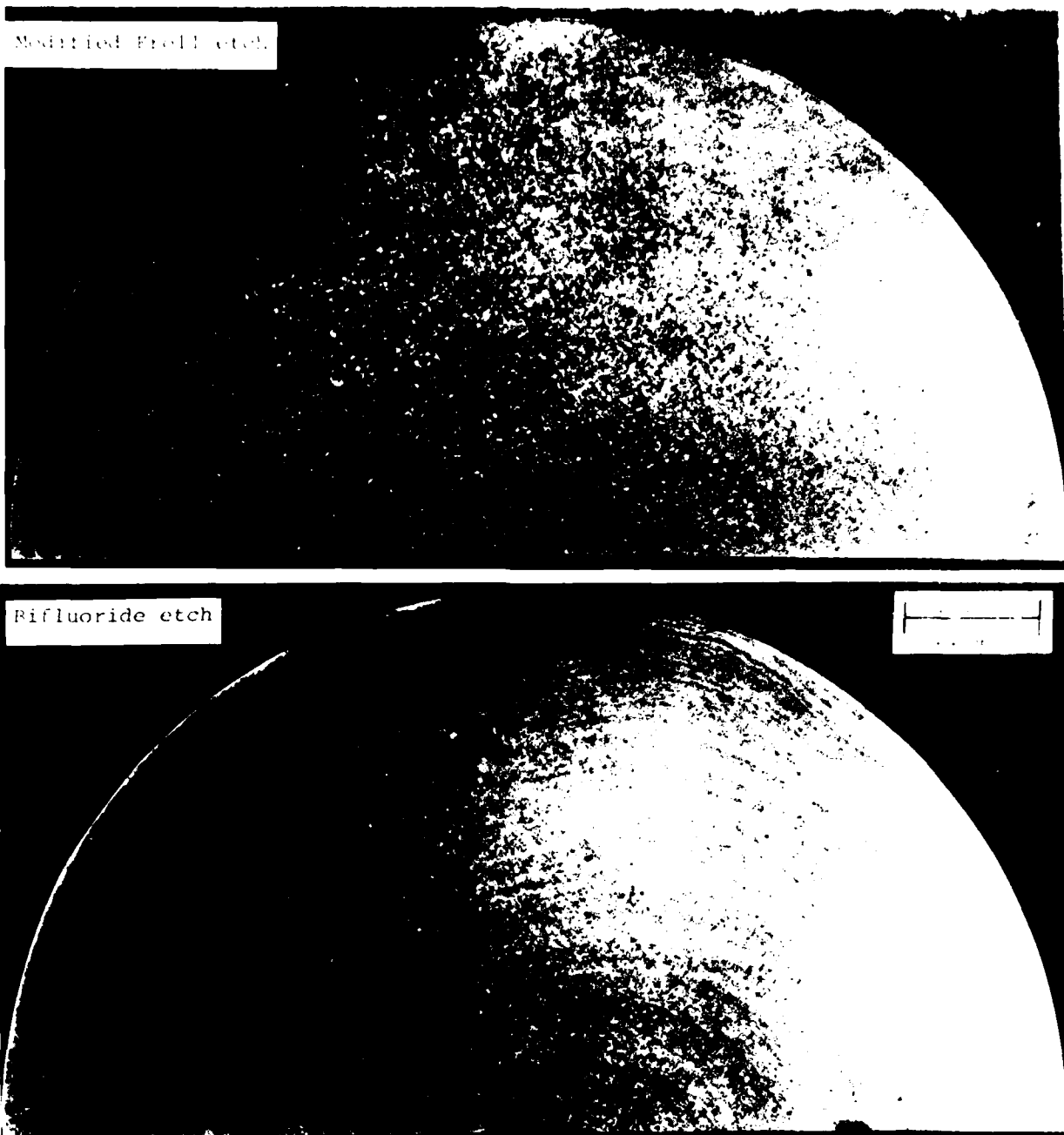


Figure E-20c Comparison of transverse macrostructures for as-received A3-slice as revealed by:
(a) modified Kroll etch, (b) Bifluoride etch

The initial microstructures for the as-received billet slices are given in Figure E-21; three locations (surface, midradius, center) per each slice were examined. A significant variation in microstructure with billet orientation can be seen from these three-dimensional micros at optical magnifications. Figures E-22 and E-23 further present the variation of microstructure with specimen location at five locations. Note that such small structural nonuniformity in billet slices are quite common for production billets.

(c) Billet Conversions

About 150-pound multiple was cut from the program material (A-mult). They were then sectioned into six (6) mults and converted conventionally to about 4-3/4 inch diameter x 6 inch long mults. These mults were prepared to Battelle's required size for the preparation of both compression and stress-relaxation specimens for other team members. They were converted from as-received 8 inch diameter billet on a Wyman-Gordon Research and Development 1500-ton hydraulic press. Before forge-operations, they were cut and chamfered, and preheated for two hours in an electric furnace at the given specific temperatures. The forge-operations were carried out at the average press head velocity of ten inches per minute with the average die temperature of 700F. After forge-operations, they were heat treated to produce two types of preform microstructures, i.e., four mults (s/n A11, A12, A13, A14) for ($\alpha+\beta$) preforms and two mults (s/n A21, A22) for β preforms. These preform blanks were delivered to Battelle for machining compression specimens, and for conducting both compression and stress-relaxation tests at Battelle, Wright-State, Los Alamos Laboratory, and the University of Pittsburgh. Processing variables for the six mults are given in Table E-4.

TABLE E-4
FORGE AND HEAT-TREAT VARIABLES USED
FOR THE SIX PREFORM MULTIPLES

Serial Number	Preform Micro-structure	Processing Condition	
		Forge Condition	Heat-Treat Condition
A11,A12, A13,A14	A1 Preform ($\alpha+\beta$)	1750F/Air cool	1775F/2 hours/Air cool
A21,A22	A2 Preform (β)	1900F/Air cool	1875F/2 hours/Air cool

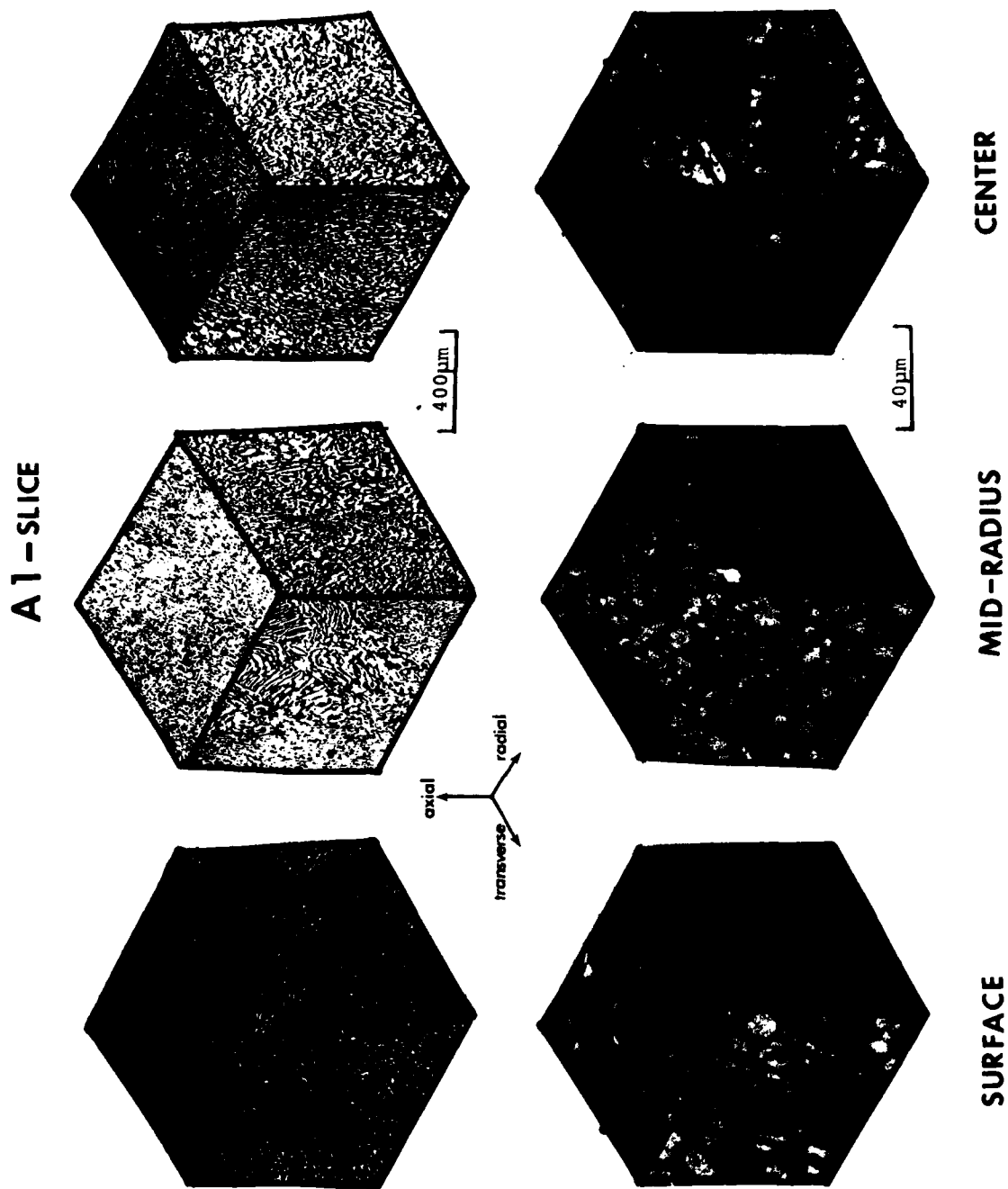
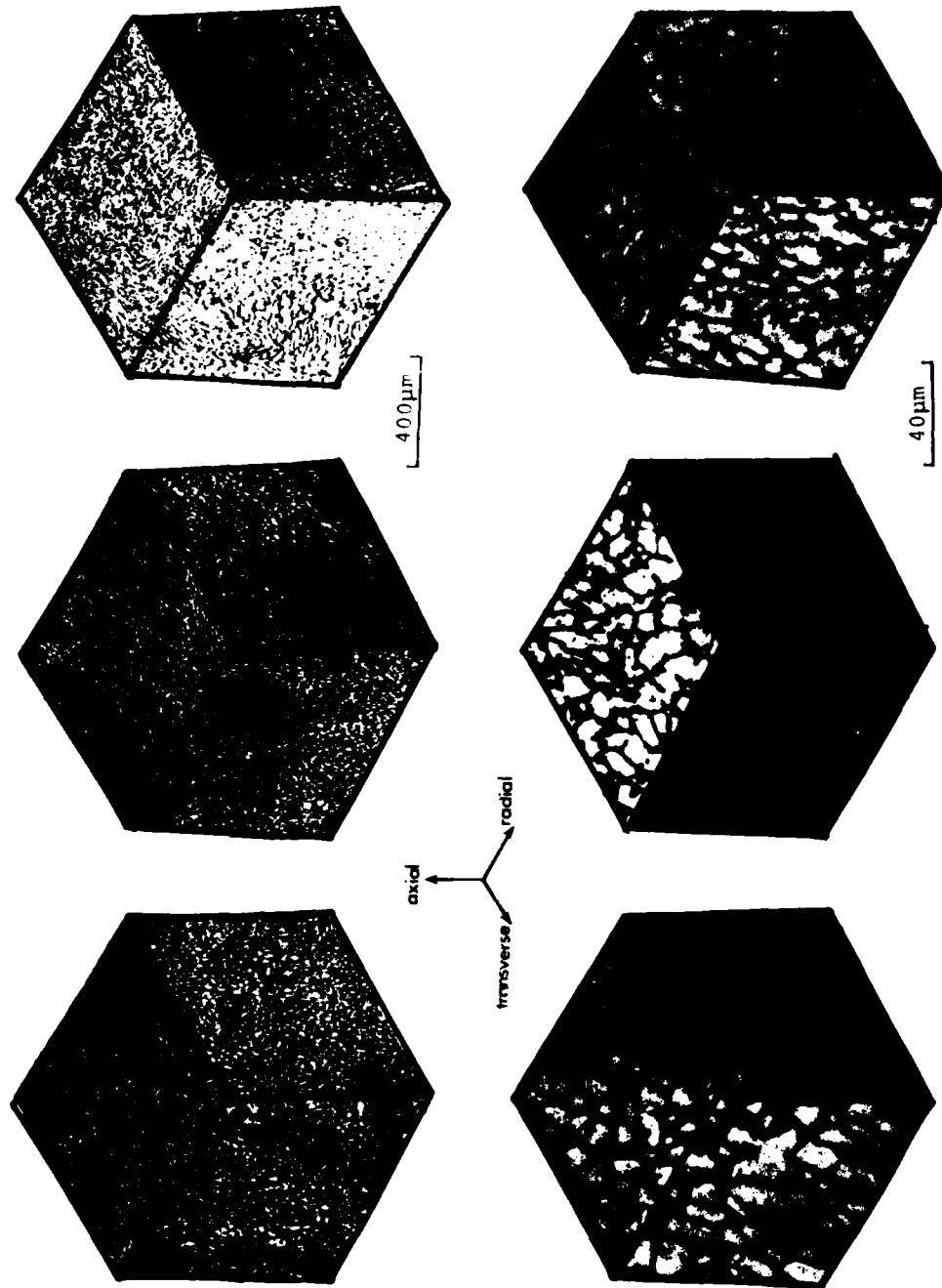


Figure E-21a Three-dimensional microstructures of Al billet slice

A2 - SLICE



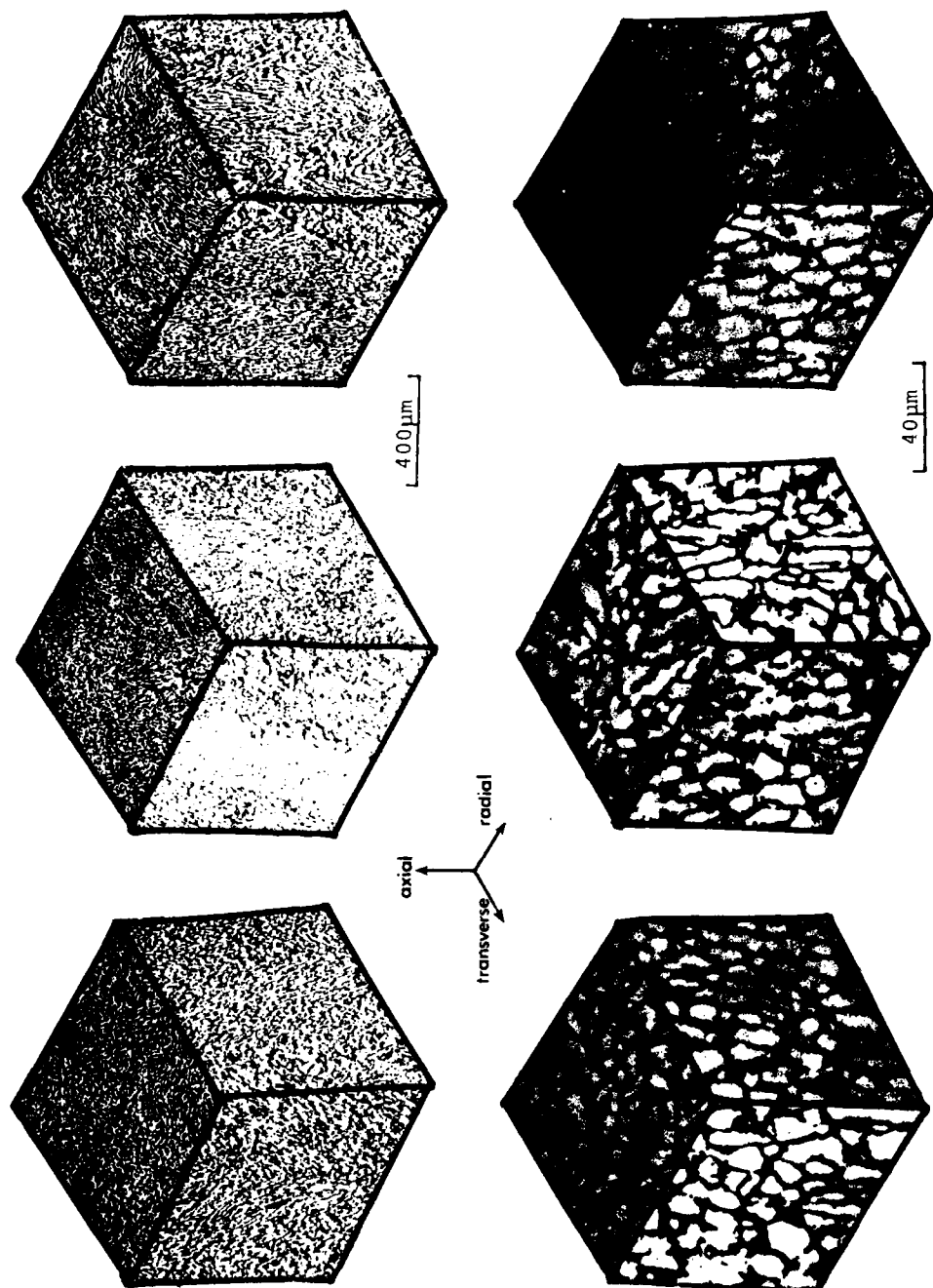
SURFACE

MID-RADIUS

CENTER

Figure E-21b Three-dimensional microstructures of A2 billet slice

A3-SLICE



SURFACE MID-RADIUS CENTER

Figure E-21c Three-dimensional microstructures of A3 billet slice

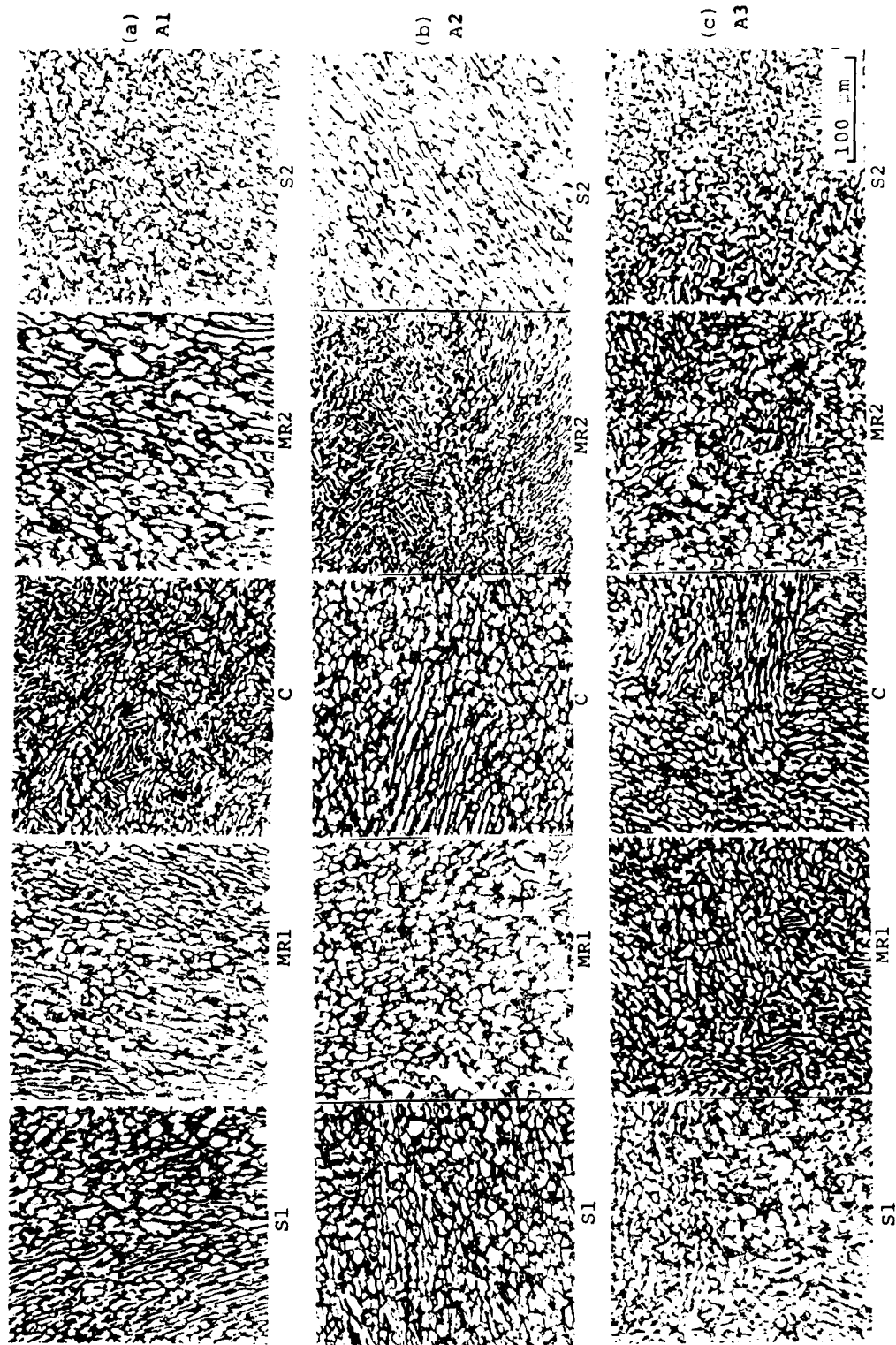


Figure E-22a Initial microstructure at various locations (surface, midradius, center) for the as-received A-mult billet:

(a) A1 slice, (b) A2 slice, (c) A3 slice

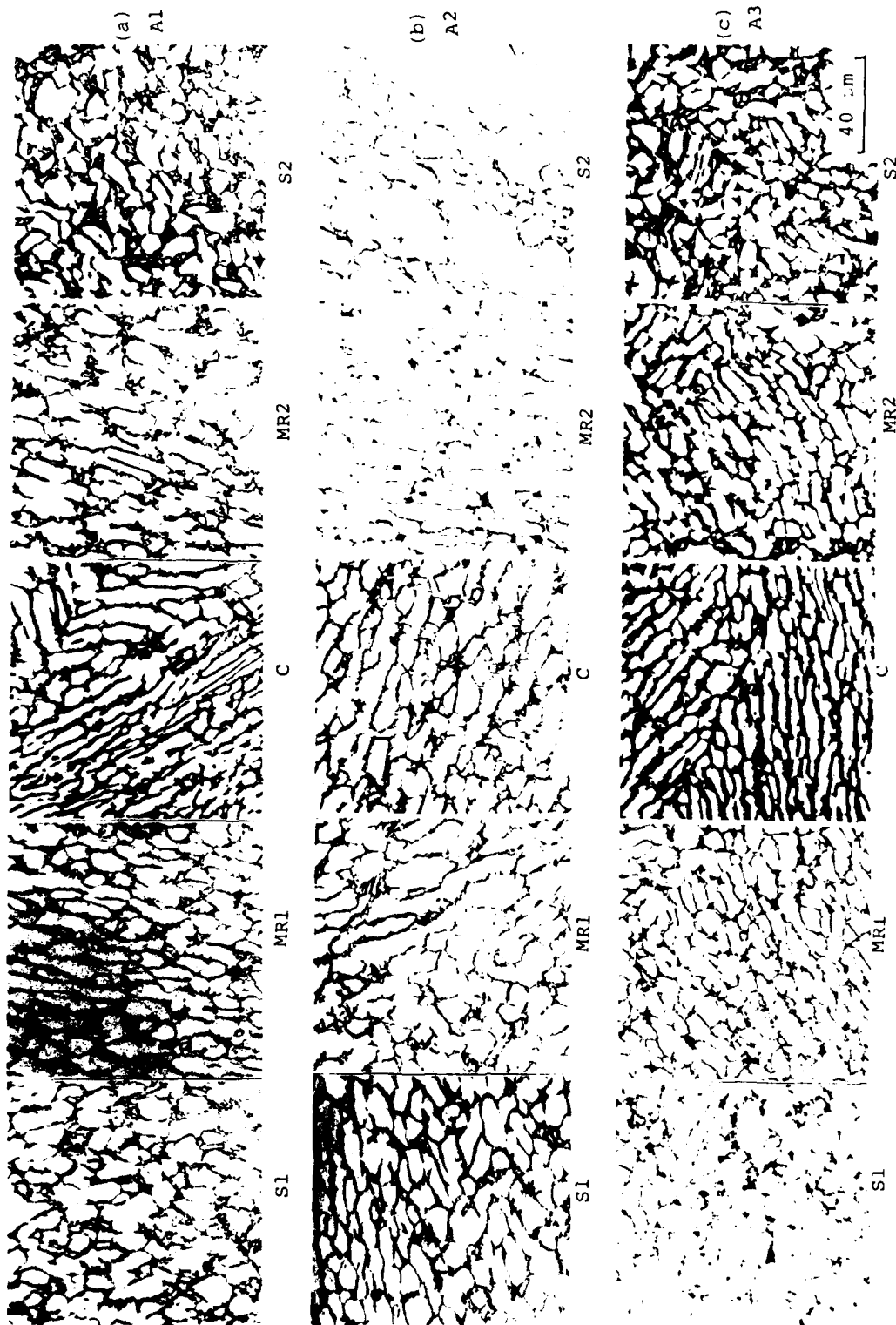


Figure E-22b Initial microstructure at various locations (surface, midradius, center) for the as-received A-mult billet:
 (a) A1 slice, (b) A2 slice, (c) A3 slice

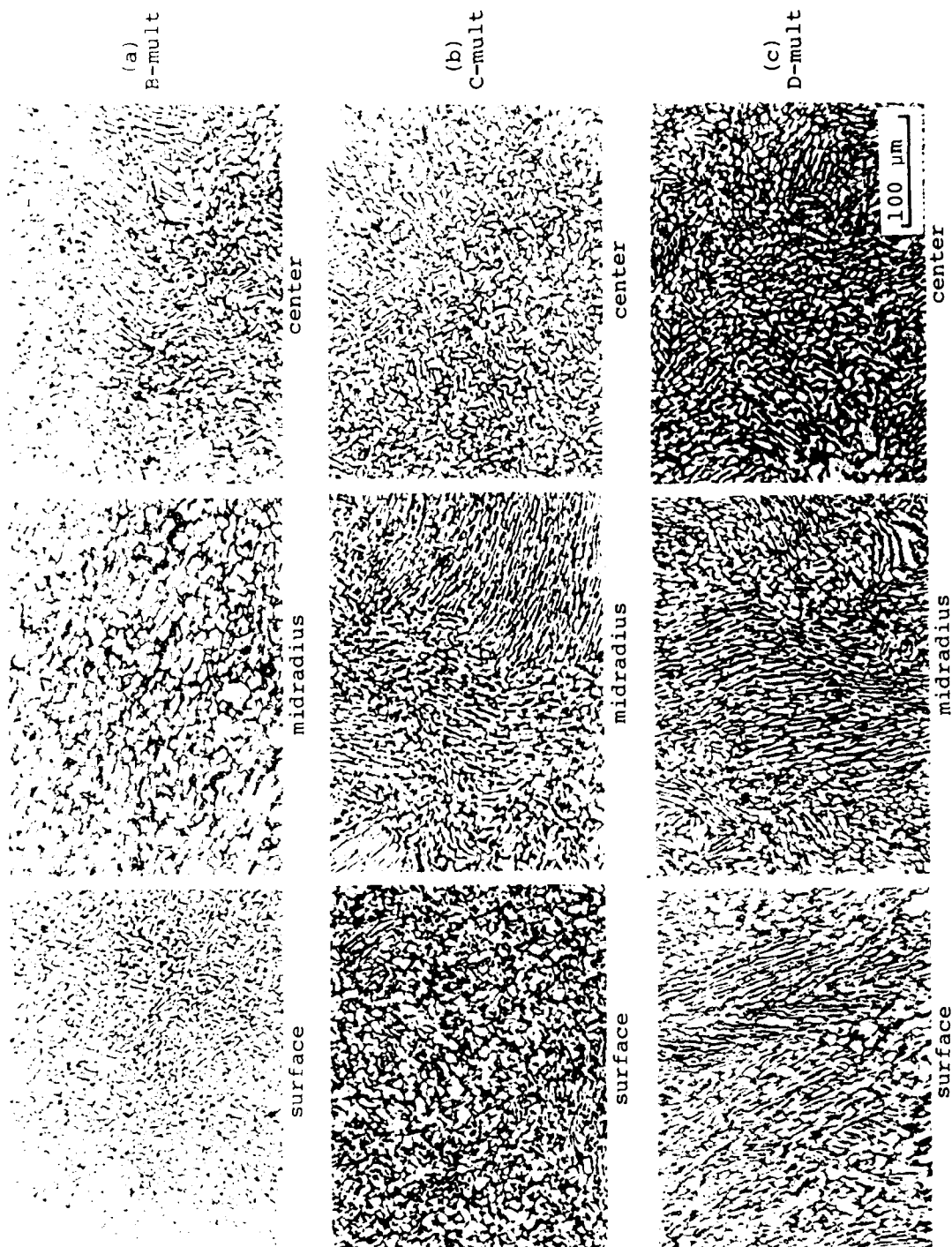


Figure E-23a Initial microstructures at surface, midradius, and center locations for the as-received billets: (a) B-mult, (b) C-mult, (c) D-mult

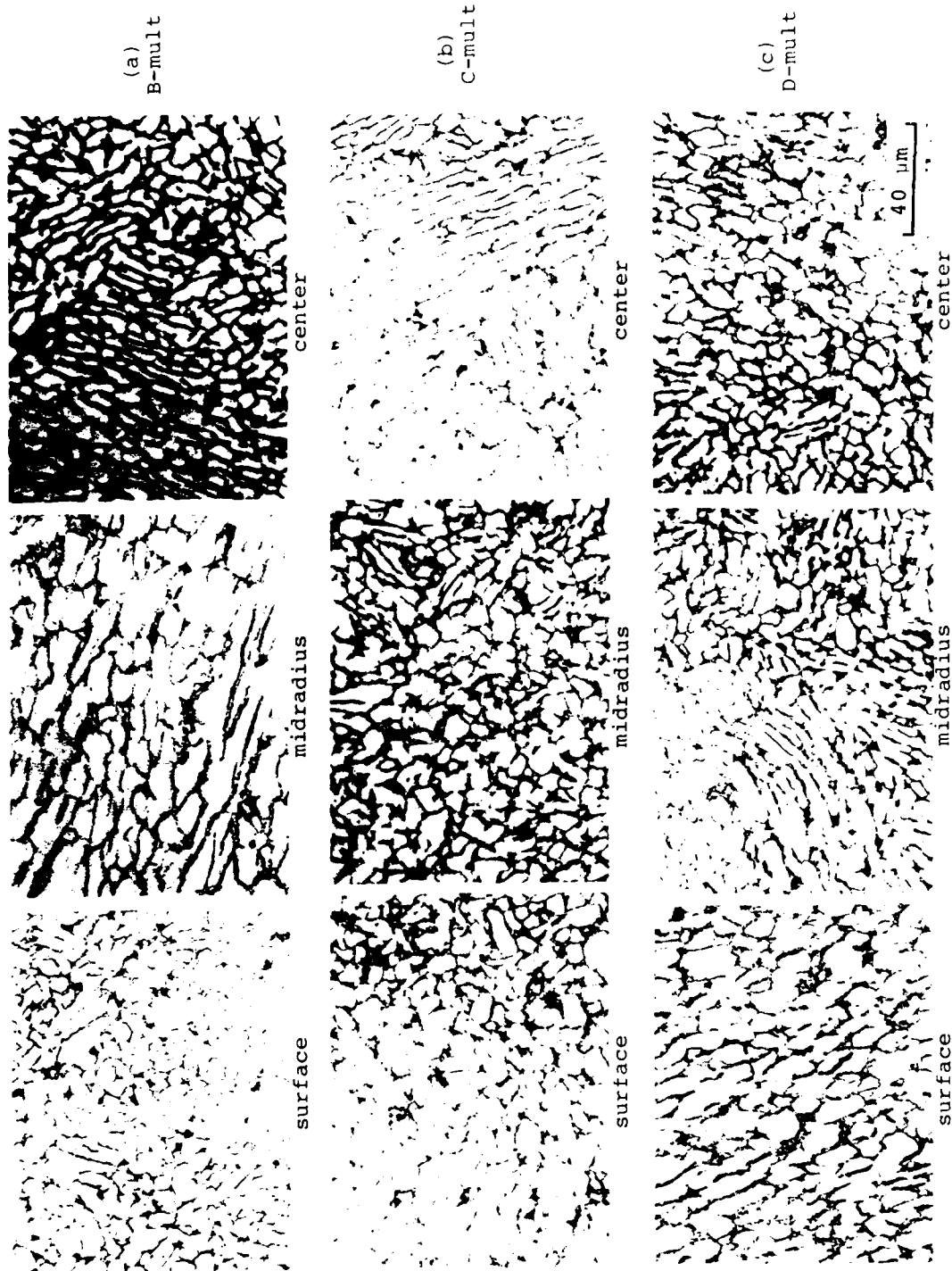


Figure E-23b Initial microstructures at surface, midradius, and center locations for the as-received billets: (a) B-mult, (b) C-mult, (c) D-mult

Figure E-24 presents examples of the transverse macrostructures of starting ($\alpha+\beta$) and β -preforms produced from the above conversion practice. Good flow pattern is revealed for ($\alpha+\beta$) preforms and uniform macrostructure for β -preform is clearly seen.

The transverse microstructures at various locations are illustrated in Figures E-25 and E-26. Excellent uniformity in microstructures from one location to another and from one orientation to another are observable. The ($\alpha+\beta$) preforms are characterized by 40-45% globular- α in the transformed- α matrix and the size of globular- α is in the 10 to 15 μm range. The β -grain size for the β -preforms is quite large, ranging from 500 to 700 μm .

In addition, about 40 pounds mult was cut from as-received D-mult billet and was converted into two of 3 inch round x 12 inches long bars; one of ($\alpha+\beta$) preform and one of β -preform. The two bars were sent to AFML for their in-house studies in conjunction with the present program. The processing conditions used for the two preforms (designated as D1 and D2) are the same as those used for A1 and A2 preforms (see Table IV). Figures E-25c, E-25d, and E-26c illustrate the typical microstructures of the D1 ($\alpha+\beta$) and D2 (β) preforms produced.

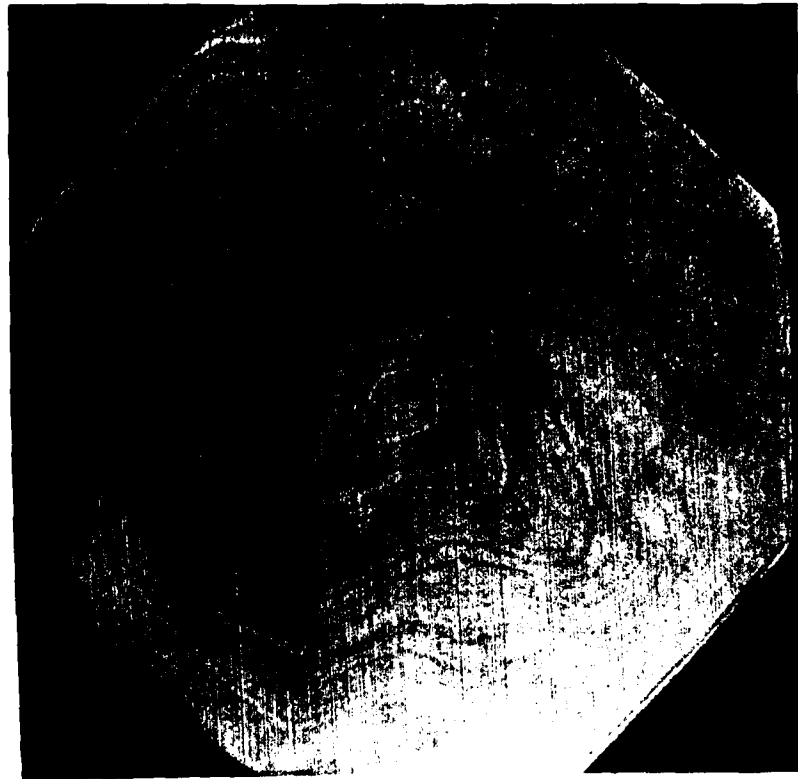
Verification Test Program - Pancake Forgings

A series of 18 pancake forgings were produced to characterize the forgeability, the metal flow characteristics, and the resultant microstructure and properties of the pancakes. As stated in the technical proposal, the main purpose of this portion of the program is to determine the forgeability and optimum heat treat conditions, and to characterize the microstructure/property relationships of the alloy forgings.

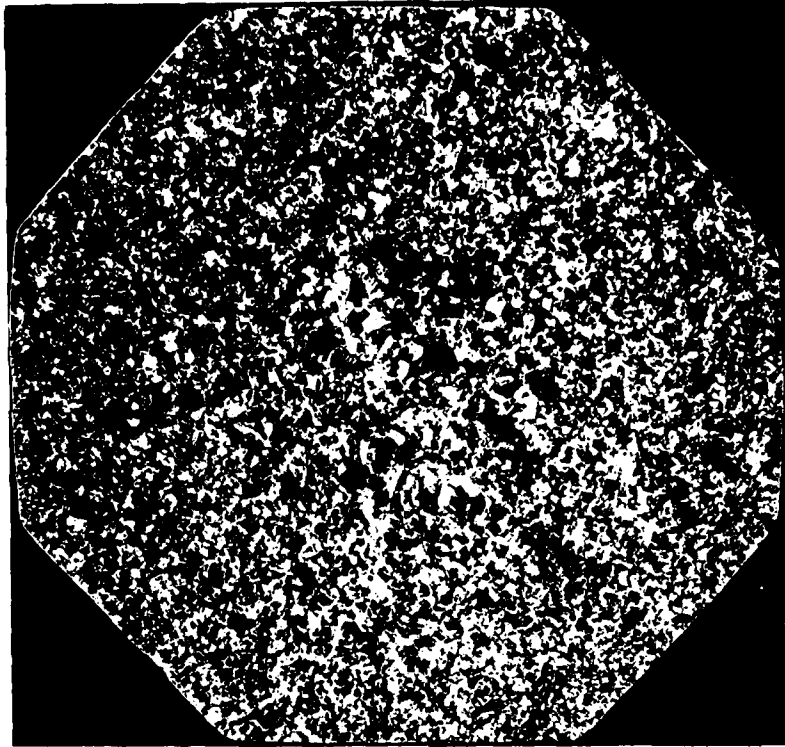
(a) Forge Processing

About 200 pounds of 8 inch round Ti-6242Si billets were converted to 3-1/2 inch round bars. They were heat treated to produce ($\alpha+\beta$) and β -preforms (see Table E-4), and then machined to 18 of 3-1/4 inch round x 3-1/4 inch thick preforms for forging evaluations, and two of 3-1/4 inch x 1 inch thick samples for structural evaluations. Typical macro- and microstructures of the ($\alpha+\beta$) and β -preforms produced are given in Figures E-27a and E-27b, respectively.

The forging operations were conducted on a 200-ton isothermal forging press, and TZM flat dies were used. These forgings were produced both isothermally and conventionally, both subtransus and supertransus. The multiples were first coated with BN coating for about 5 mils thick per side, and then preheated for the aim temperature prior to forging. The dies were induction heated. The strain rates used were 0.1 min.⁻¹ (1.7×10^{-3} s⁻¹) for isothermal forging and 3.0



(a) macrosection for (α+β) preform; A1 preform



(b) macrosection for γ-preform; A2 preform

2.54 cm
1 inch

Figure E-24 Examples of transverse macrostructures of
(a) starting (α+β) preforms,
(b) starting β-preforms produced from
this portion of the program

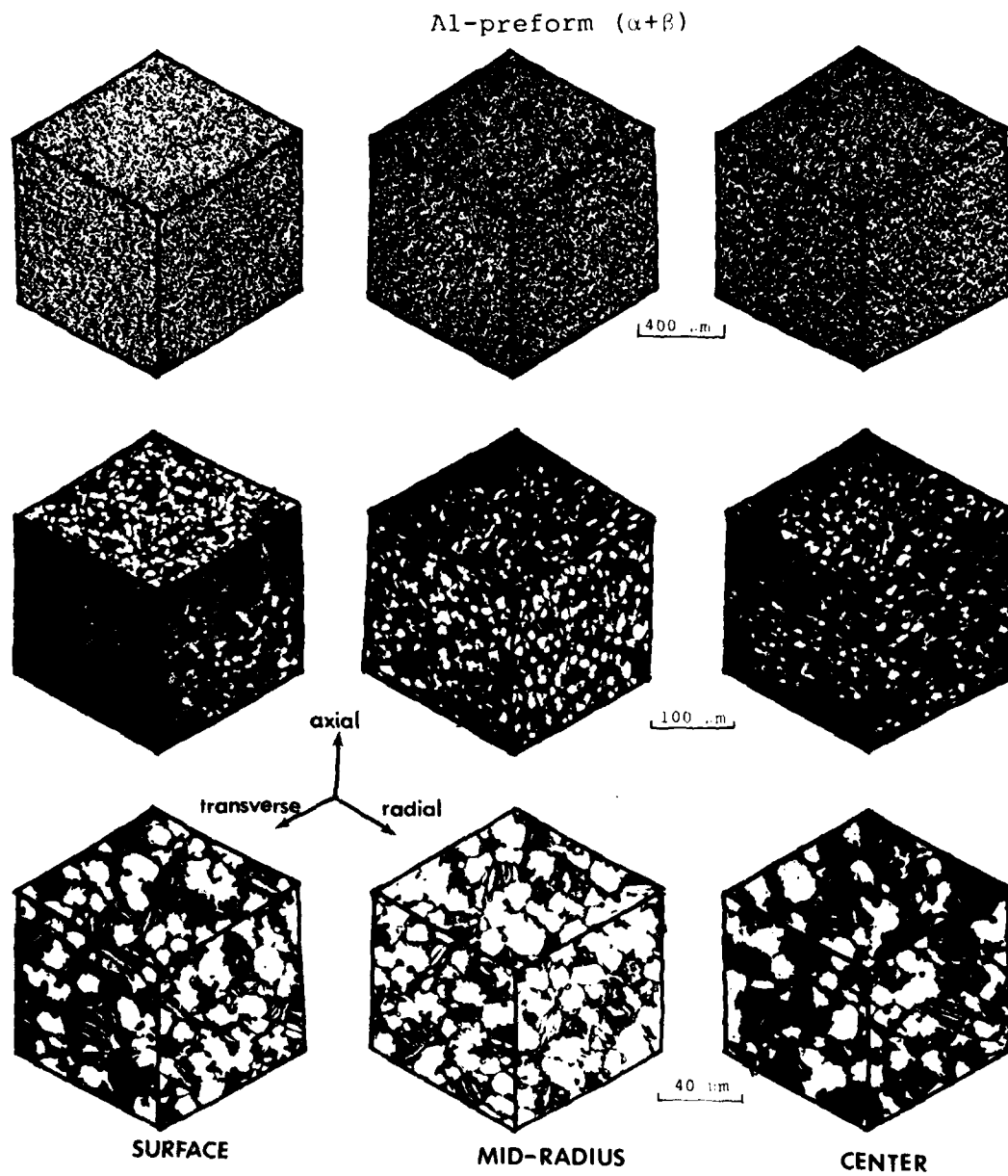


Figure E-25a Typical three-dimensional microstructures for the ($\alpha+\beta$) preforms produced from the present program

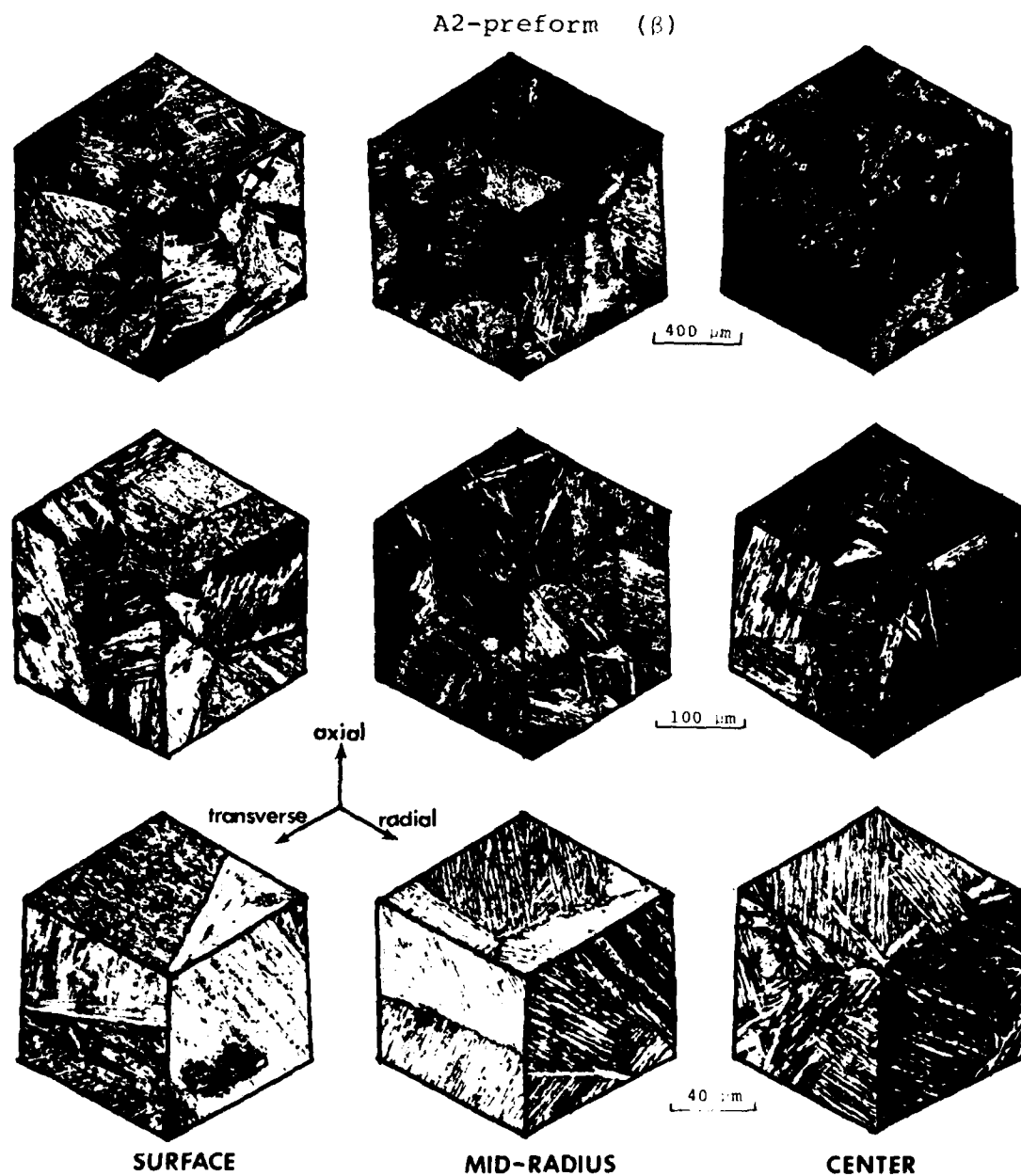


Figure E-25b Typical three-dimensional microstructures for the β -preforms produced from the present program

D1-preform ($\alpha+\beta$)

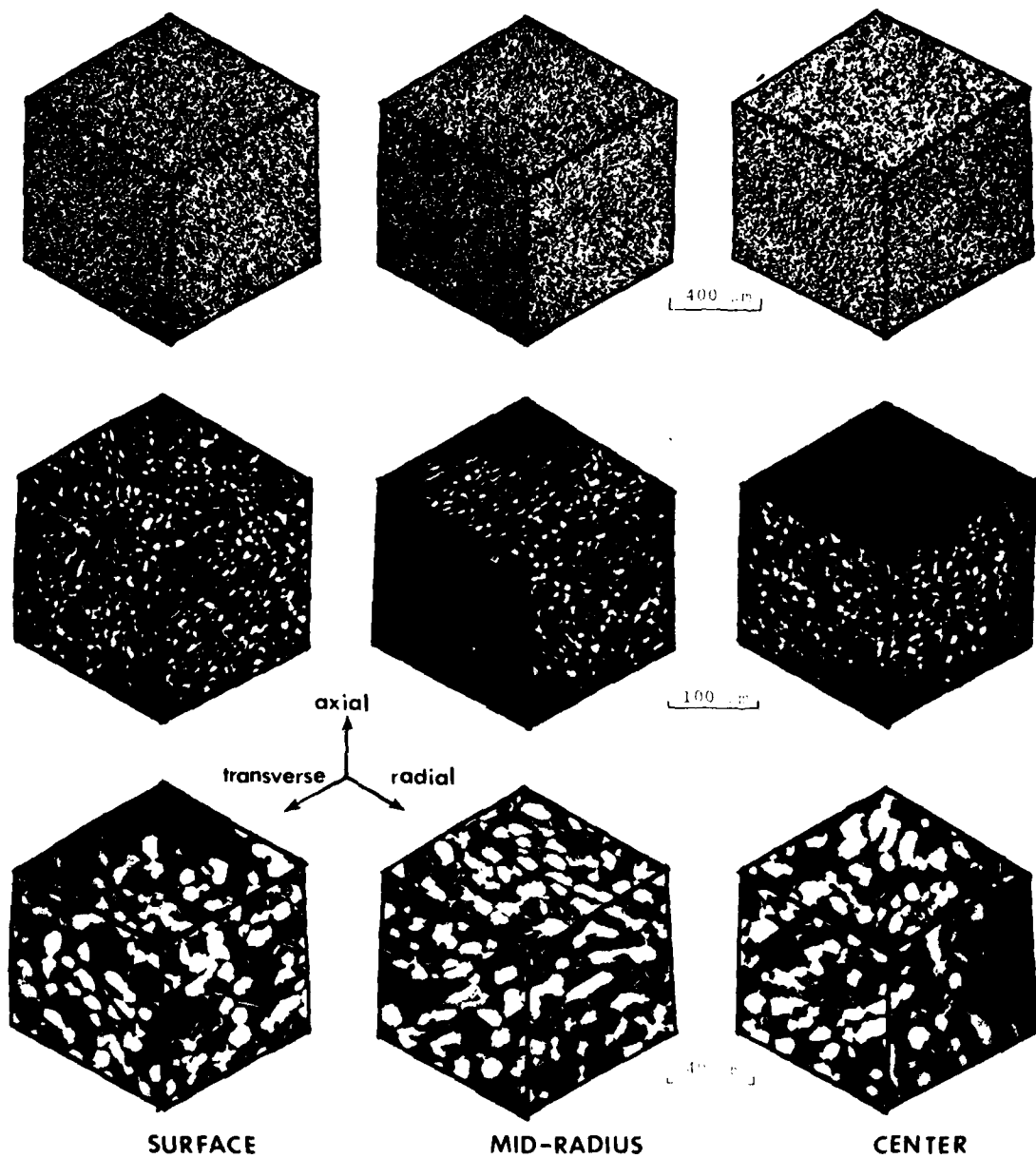


Figure E-25c Typical three-dimensional microstructures for the ($\alpha+\beta$) preforms produced from D-mult billet

D2-preform (β)

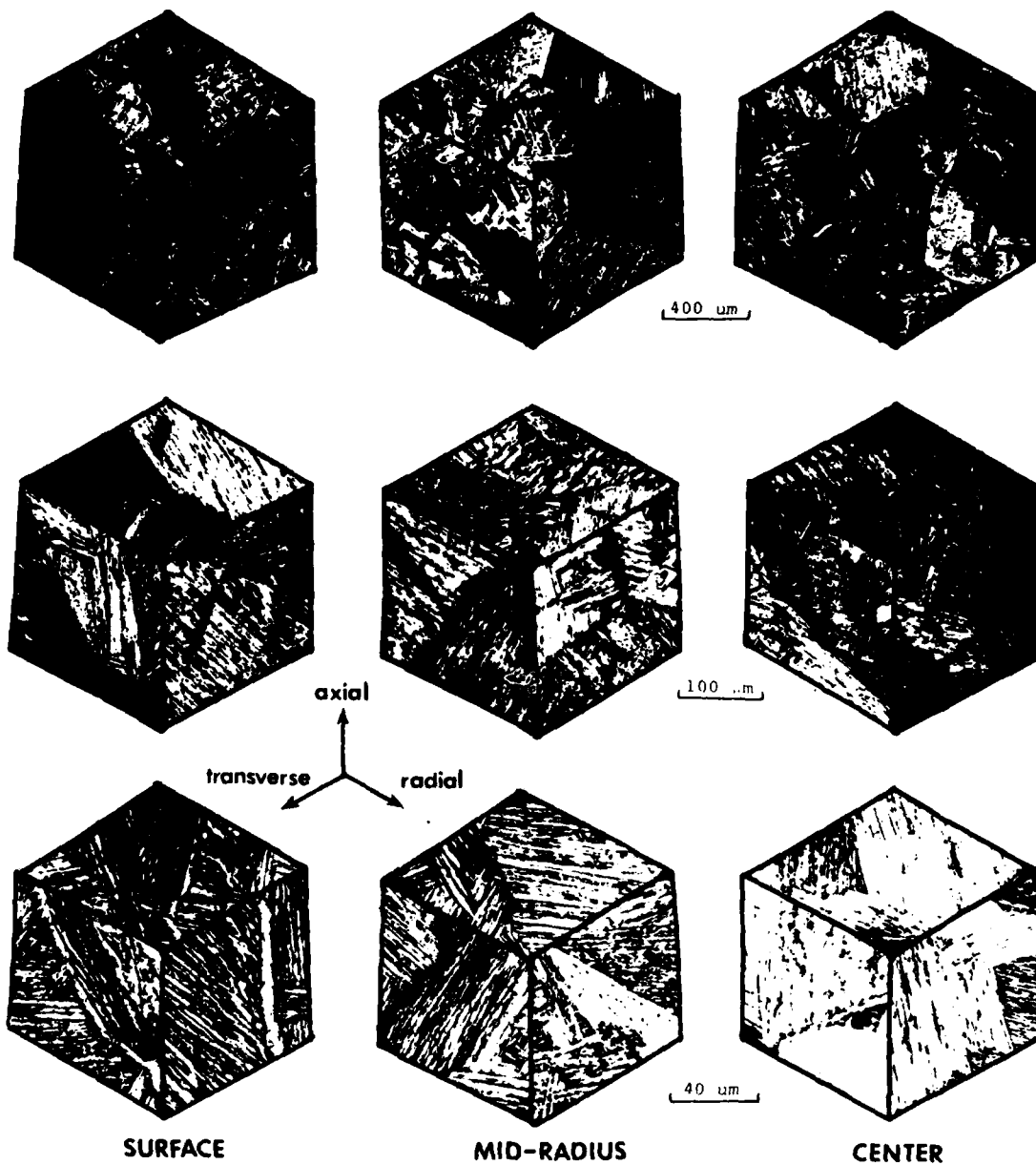
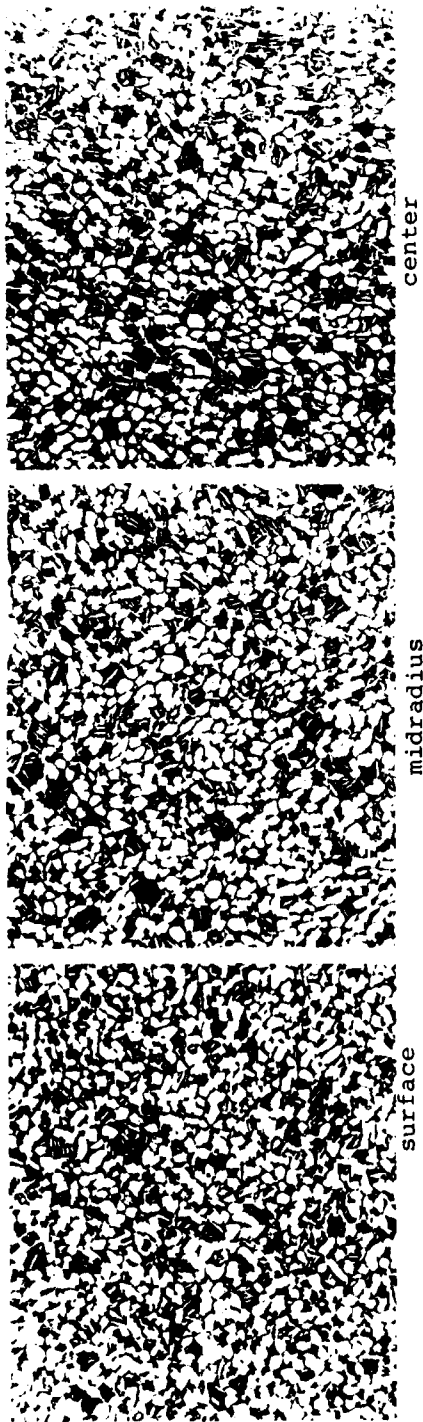


Figure E-25d Typical three-dimensional microstructures for the β -preforms produced from D-mult billet

(a) A1 preform: ($\alpha+\beta$)

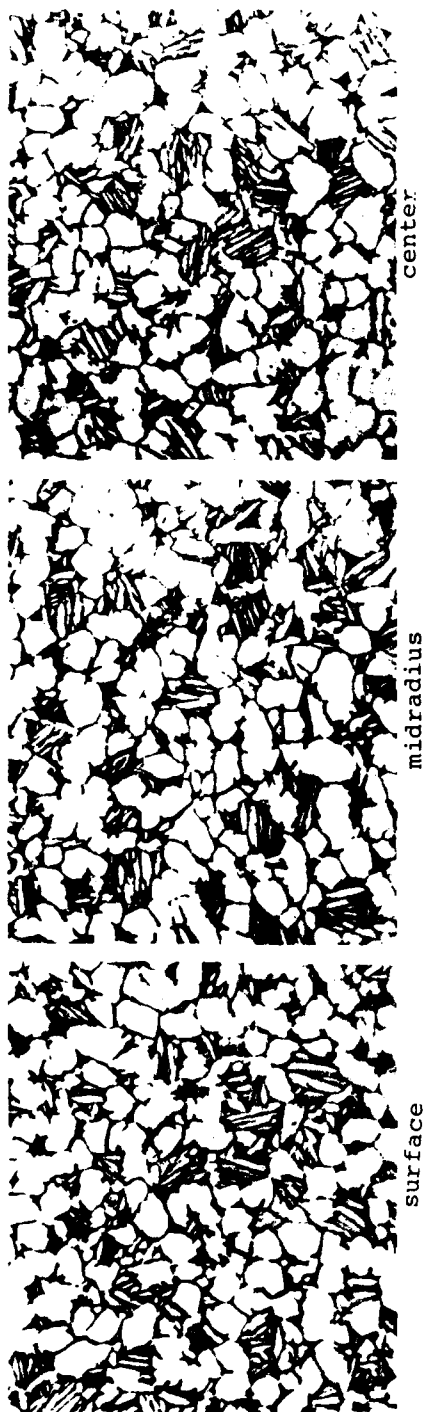


(b) A2 preform: β



Figure E-26a Transverse microstructures at various locations (surface, midradius, center) for (a) starting ($\alpha+\beta$) preforms, and (b) starting β -preforms produced from A-mult billet

(a) A1 preform: ($\alpha+\beta$)

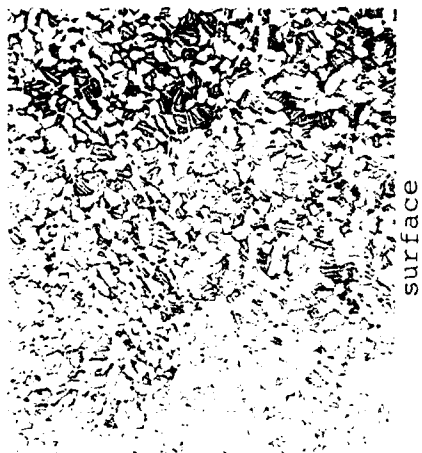


(b) A2 preform: β

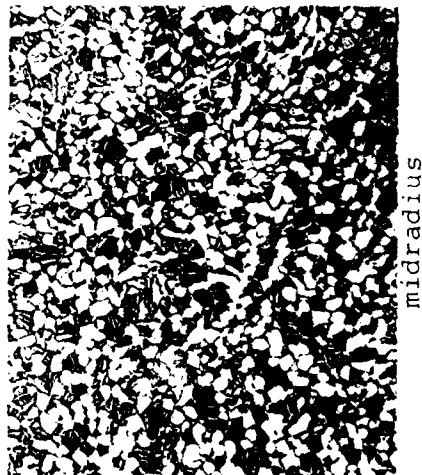


Figure F-26h
Transverse microstructures at various locations (surface, midradius, center) for (a) starting ($\alpha+\beta$) preforms, and (b) starting β -preforms produced from A-mult billet

(a) D1 preform: (+.)



surface



midradius



center

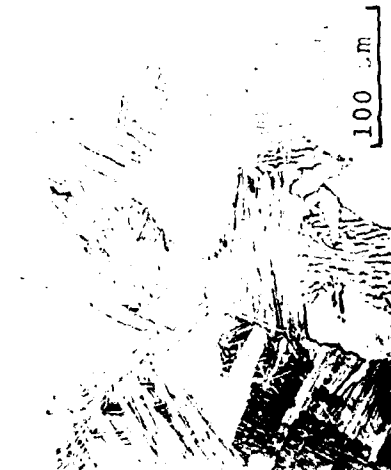
(b) D2 preform:



surface

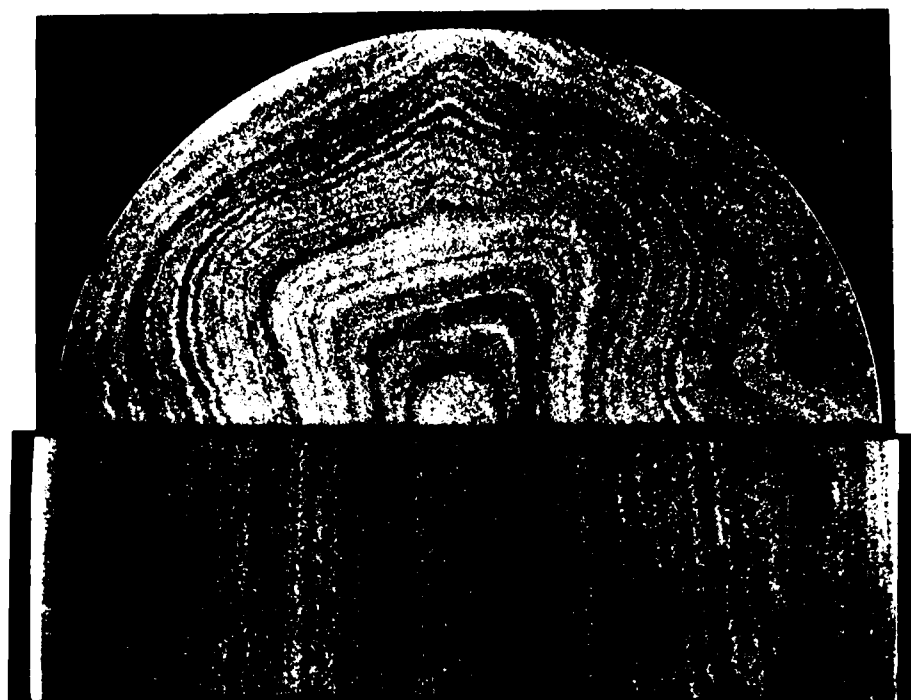


midradius



center

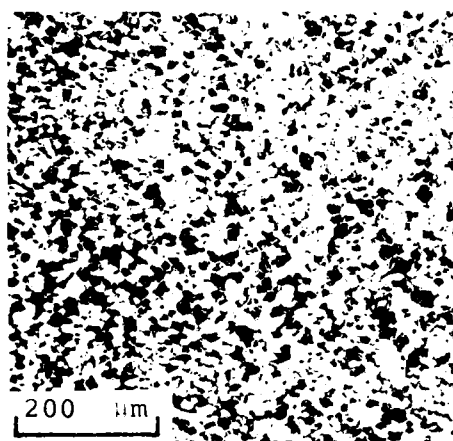
Figure E-26c Transverse microstructures at surface, midradius, and center locations for (a) starting (+) preforms, and (b) starting f-preforms produced from D-mult billet



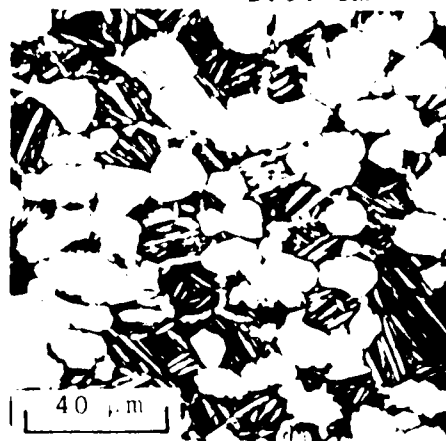
(α+ε)-preform

1 inch

2.54 cm

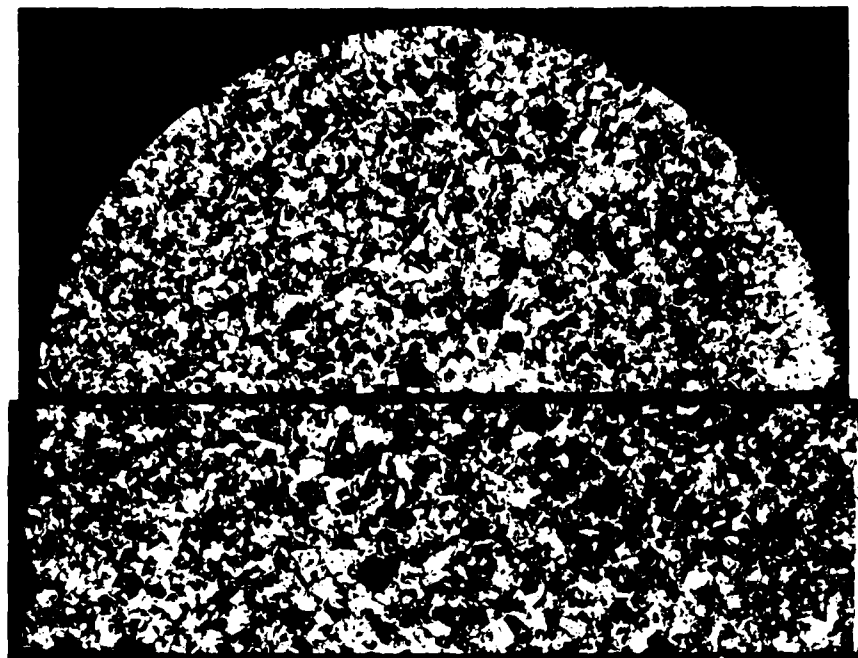


200 μm



40 μm

Figure E-27a Macro- and microstructures of the (α+ε) preforms used for producing pancake forstings



r-preform

1 inch

2.54 cm

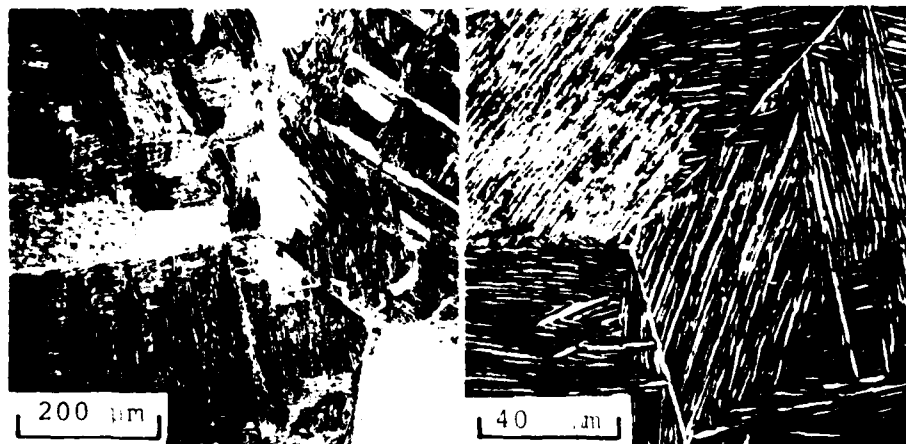


Figure E-27b Macro- and microstructures of the r-preforms used for producing pancake forgings

min.⁻¹ ($5.0 \times 10^{-2} \text{ s}^{-1}$) for conventional forging; these strain rates are comparable with those used in industrial press forging. The forge operations were accomplished by one-stage forging from 3.25 inches to a final thickness of about 1.25 inches. This is equal to a total deformation of 60% reduction in thickness. The thickness:diameter ratio of the initial preform is 1:1, an acceptable ratio for production preforms. After the forging operation, the forgings were air-cooled. The forgings have a diameter of 5-1/2 inches and a plan view area of 24 square inches. The forging variables used for the forge processings are given in Table E-5. Two pancakes per each condition were produced.

During forge processing, both forge load and displacement were recorded and the forgeability of the alloy were determined. The forge pressure as a function of percent reduction of pancake thickness were analyzed and the influence of processing variables was examined.

TABLE E-5
FORGING VARIABLES USED FOR THE 18 PANCAKES;
TWO PANCAKES PER EACH CONDITION WERE PRODUCED

S/N	Preform Micro- Structure	Stock Temp. (F)	Die Temp. (F)	Strain Rate ("/"/Min.)
P1	$\alpha+\beta$	1775	1775	0.1
P2	$\alpha+\beta$	1700	1700	0.1
P3	$\alpha+\beta$	1775	700	3.0
P4	$\alpha+\beta$	1875	1875	0.1
P5	$\alpha+\beta$	1875	700	3.0
P6	β	1775	1775	0.1
P7	β	1700	1700	0.1
P8	β	1775	700	3.0
P9	β	1775	1200	3.0

It should be mentioned that the mini-isothermal forge press is a bottom-acting, oil hydraulic unit, enclosed in an inert gas chamber (Figure E-28), and is capable of forging isothermally with operating die temperatures in excess of 2200F, and with strain rates ranging from 0 to 3 min⁻¹ for a 4-1/2 inch thick billet. The press head velocity is infinitely variable from zero to 5 inches/minute with a programmable flow control valve. Strain rate control is provided by an automatic valve controller and a Data-trak, Model 73211, microprocessor-based process programmer. The Data-trak programs the press ram to follow a displacement versus time curve for any given strain rate, and a Mosely X-Y1-Y2 recorder is used to record the ram position and press load as a function of time so that actual forging pressures and strain rates can be determined.



Figure E-28 200 tons mini-isothermal forging press at Wyman-Cordon

Figure E-29 illustrates examples of the pancakes produced through nine different combinations of forging variables. Heavy surface wrinkles are observable for isothermal ($\alpha+\beta$) forgings using β -preforms (s/n P6 and P7). Severity of surface cracking for conventional ($\alpha+\beta$) forgings using β -preforms depends strongly on the die temperatures used (P8 and P9).

Both the yielding and finish forge pressures for forging deformation have been previously defined (10). Examples of actual forge load-time curves processed at a constant strain rate for various forge temperatures are illustrated in Figures E-30a and E-30b for isothermal and conventional forging, respectively. The difference in the load-time variations for the two different preforms ($\alpha+\beta$ and β) are also compared. The serrated flow and anomalies in yield-softening for isothermal forgings are clearly observable; this appearance is more profound for ($\alpha+\beta$) forging as compared with β -forging. Similar to previous observations (1), the degree of yield-softening is higher for the forging using β -preforms than that of ($\alpha+\beta$) preforms.

The importance of die temperature and die temperature - ram rate interactions in determining the forge pressure required for forging Ti-6242Si alloy has been previously demonstrated (1). The forge pressure required depends strongly on the relative contributions of strain hardening and die-chilling, and the influence of die-chill becomes more profound as the die temperature is reduced. The effect of die temperature on the forge pressure required for producing the pancakes is also determined in the present investigation and the results are given in Figure E-30b.

Figure E-31a presents the average forge-load versus displacement curves for isothermally forged pancakes, illustrating the effect of forge temperatures and preform microstructures on the yielding and load-displacement behavior. The true stress-strain curves at various forge temperatures for pancake forgings using $\alpha+\beta$ and β -preforms are calculated from the average load versus displacement curves and are further illustrated in Figure E-31b. Briefly, the yielding forge pressure is the yielding forge load divided by the plan view area of the initial preforms, and the finish forge pressure is the finish forge load divided by the plan view area of the final pancakes. The true forge pressure (σ) was determined as the instantaneous forge load divided by the instantaneous plan view area of the pancake. The true plastic strain (ϵ) was calculated from the relationship of $\epsilon = - \ln(\frac{\lambda_i}{\lambda_0})$, where λ_i is the instantaneous pancake thickness and λ_0 is the initial thickness of the preform.

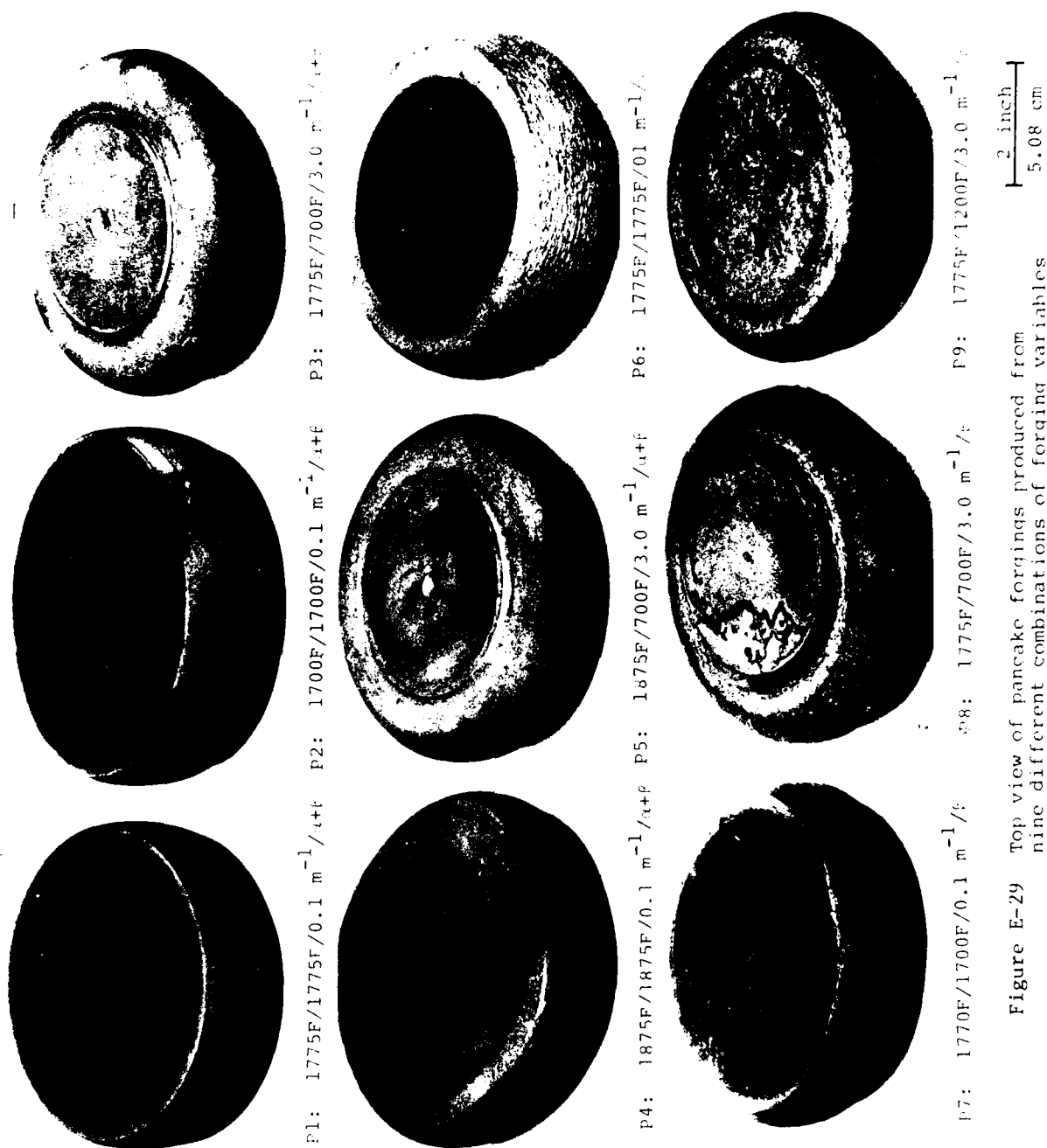


Figure E-29 Top view of pancake forgings produced from nine different combinations of forging variables

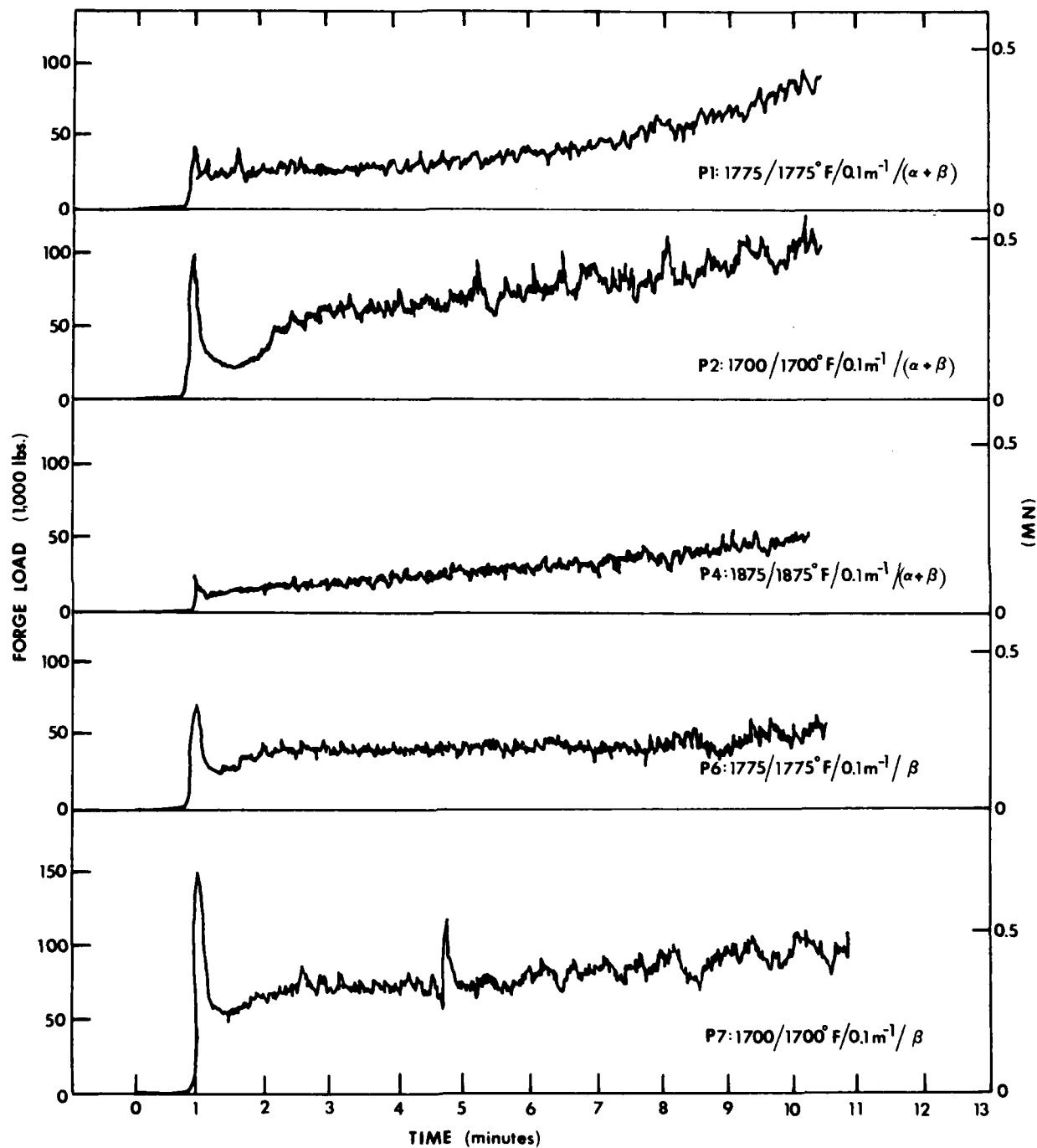


Figure E-30a Actual forge load-time curves for
pancake forgings made by isothermal forgings

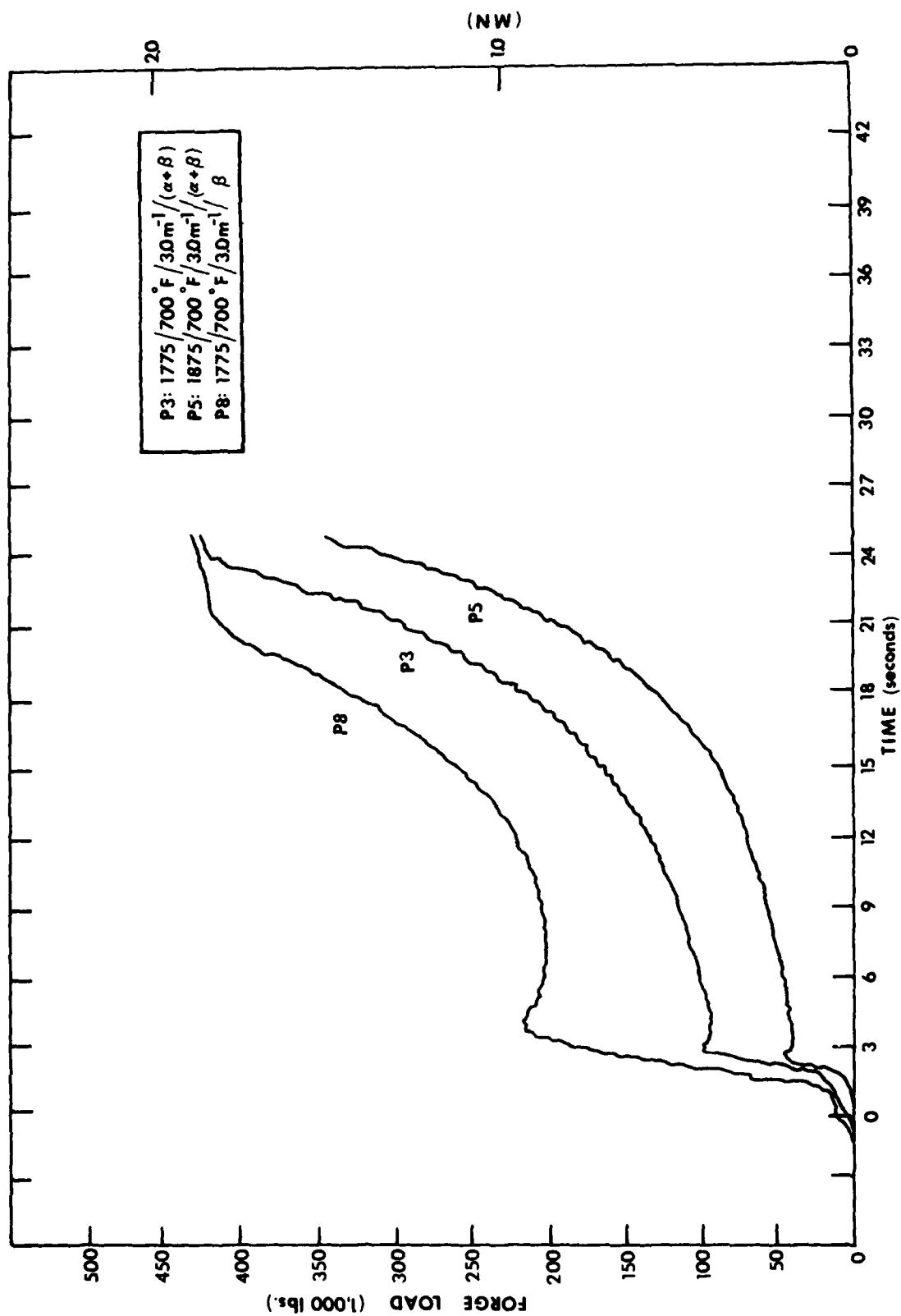


Figure E-30b Actual forge load-time curves for pancake forgings made by conventional forgings

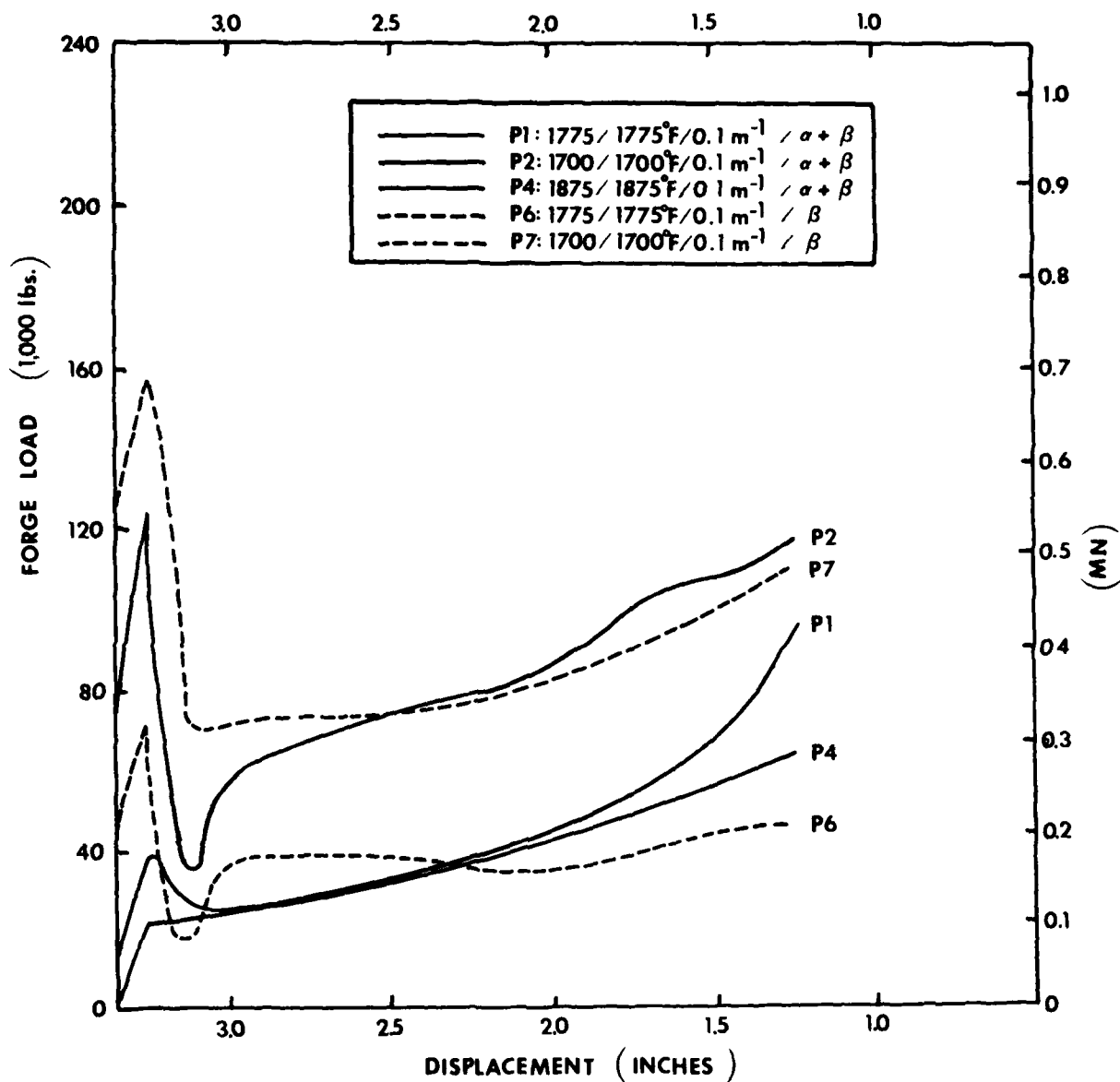


Figure E-31a Influence of forge temperatures and preform microstructures on the yielding and stress-strain behavior of isothermally forged pancakes

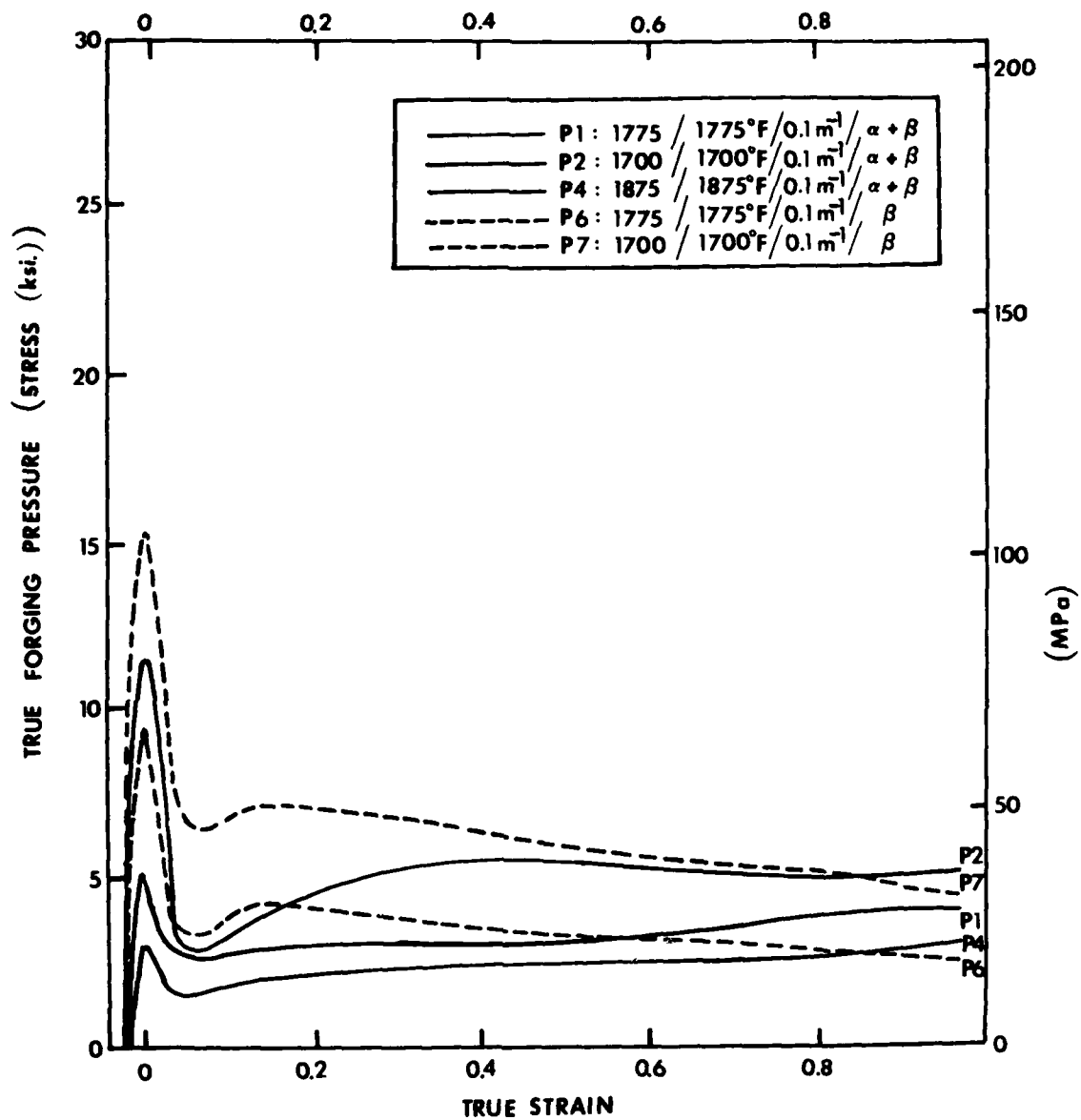


Figure E-31b Effect of forge temperatures and preform microstructures on the yielding forge pressure and stress-strain behavior of isothermally forged pancakes

It is seen from Figure E-31b that the true stress-strain curves obtained for $(\alpha+\beta)$ forgings were smooth and the deformation proceeded at relatively constant forge pressure for $(\alpha+\beta)$ preforms and at a continuous softening for β -preforms. The deformation for β -forgings continued at only a slight increase in forge pressure up to about a true strain of 1.0.

Figure E-31b also demonstrates that the values of yielding forge pressures for pancake forgings using β preforms are higher than those of $(\alpha+\beta)$ preforms. However, the stress-strain relationship showed that a more appreciable forge-pressure drop in the stress-strain curves for β -preform microstructures. The degree of softening during forging of $(\alpha+\beta)$ and β -preforms increases as the forge temperature decreases. At the end of the forging, the forge pressure required for $(\alpha+\beta)$ preforms is beyond that for β -preforms. The above observations are consistent with those previously observed in Ti-6Al-4V (4) and Ti-6242Si alloy (1).

(b) Structural Characterization

Figure E-32 illustrates the effects of forge temperature, die temperature, and preform microstructure on the macrostructures at the top surface of the pancakes. About 0.125 inch surface layers of top surface was removed by machining and the machined surface was then etched to reveal macrostructures.

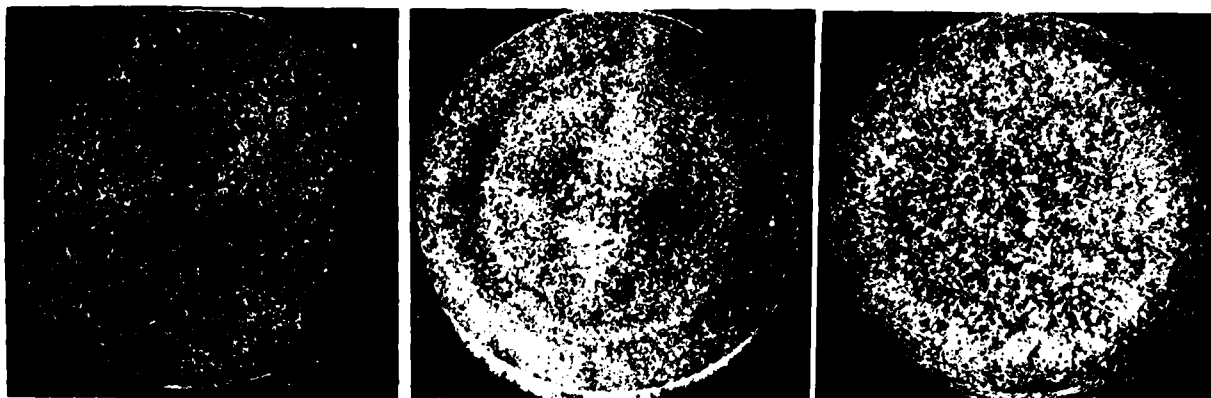
It is seen from Figure E-32 that microstructural uniformity of the forgings varies significantly with the forging variables, such as forge temperature, die temperature, and preform microstructure. In particular, the effects of lowering die temperature and/or using β -preforms are most obvious. As is expected, the fully recrystallized macrostructures of β -forgings are quite uniform throughout the forgings under isothermal forging conditions.

The variation of transverse macrostructures and microstructures with preform structure are given in Figures E-33a and E-33b for isothermal forging and conventional forging, respectively. It is seen that the preform structures have a significant influence on the flow characteristics and the microstructure of the $(\alpha+\beta)$ forgings. Good flow lines are observable for $(\alpha+\beta)$ preforms, and significant variations in microstructural features are seen for β -preforms from one location to another. Localized flow is clearly seen for conventional forgings.

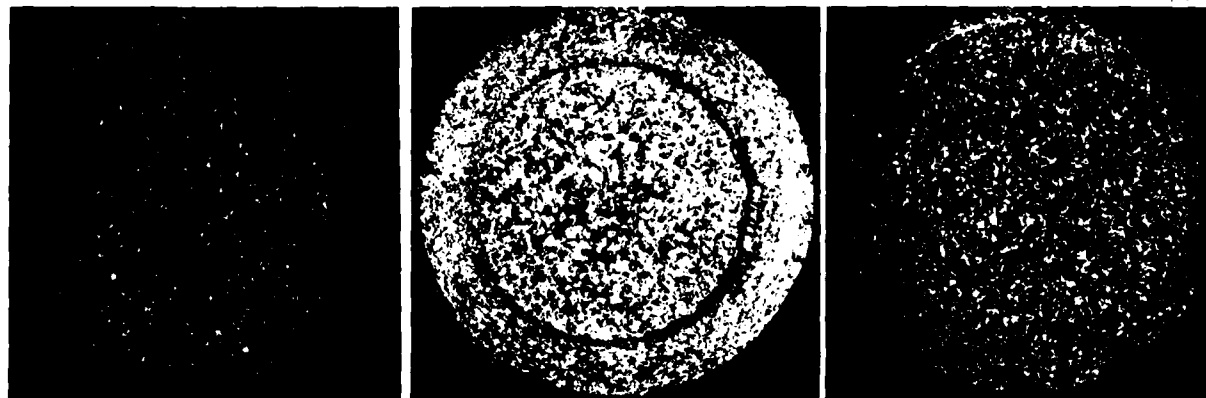
A direct comparison of the transverse macrostructures between isothermally forged and conventionally forged pancakes (Figures E-33c and E-33d) showed that excellent uniformity of macrostructure and microstructure for isothermal forgings. Very extended surface layers (characterized by large



P1: 1775F/1775F/0.1 m⁻¹/α+β P2: 1700F/1700F/0.1 m⁻¹/α+β P3: 1775F/700F/3.0 m⁻¹/α+β



P4: 1875F/1875F/0.1 m⁻¹/α+β P5: 1875F/700F/3.0 m⁻¹/α+β P6: 1775F/1775F/0.1 m⁻¹/α+β



P7: 1700F/1700F/0.1 m⁻¹/α+β P8: 1775F/700F/3.0 m⁻¹/α+β P9: 1775F/1200F/3.0 m⁻¹/α+β

2 inch
5.08 cm

Figure E-32 Macrostructures at the top surface of the pancake forgings produced from nine different combinations of forging variables

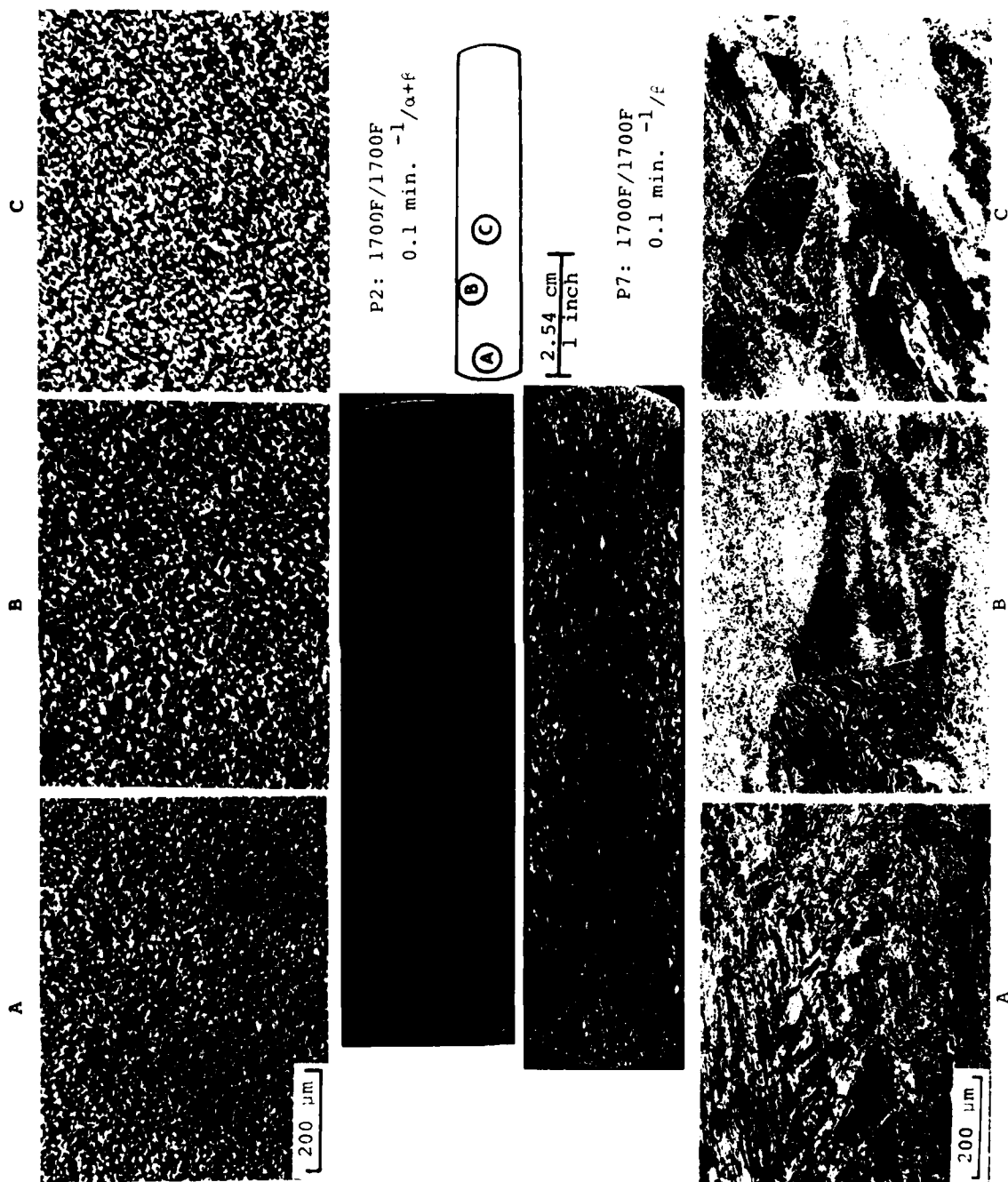
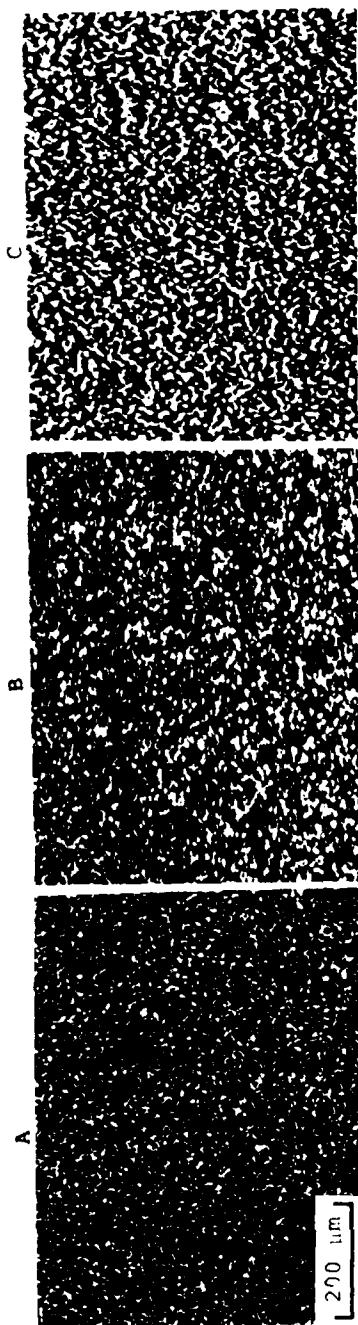


Figure E-33a Effect of preform structure on the macrostructures and microstructures of isothermally ($\alpha+\beta$) forged pancakes



P3: 1775F/700F

3.0 min. -1/1+2



2.54 cm
1 inch

P8: 1775F/700F

3.0 min. -1/1

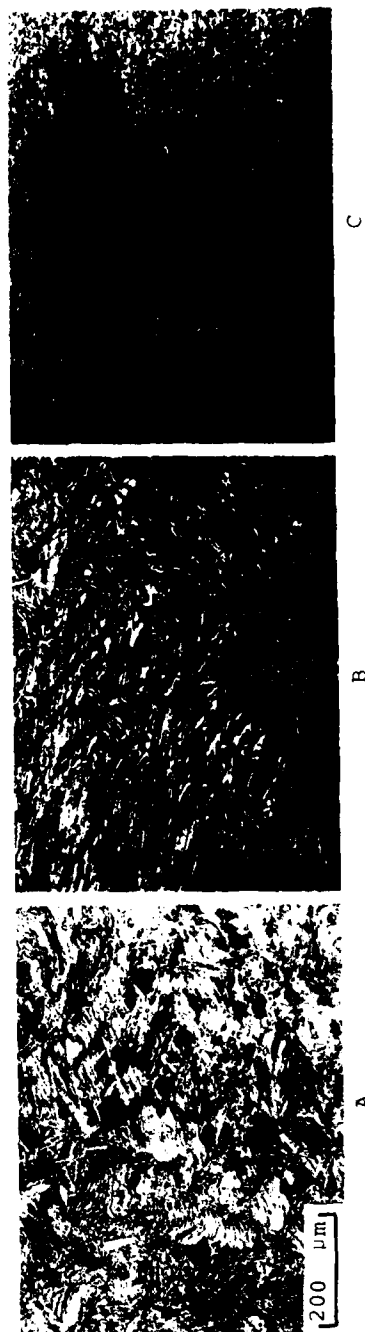


Figure E-32b Effect of preform structure on the macrostructures and microstructures of conventionally (a+B) forged pancakes

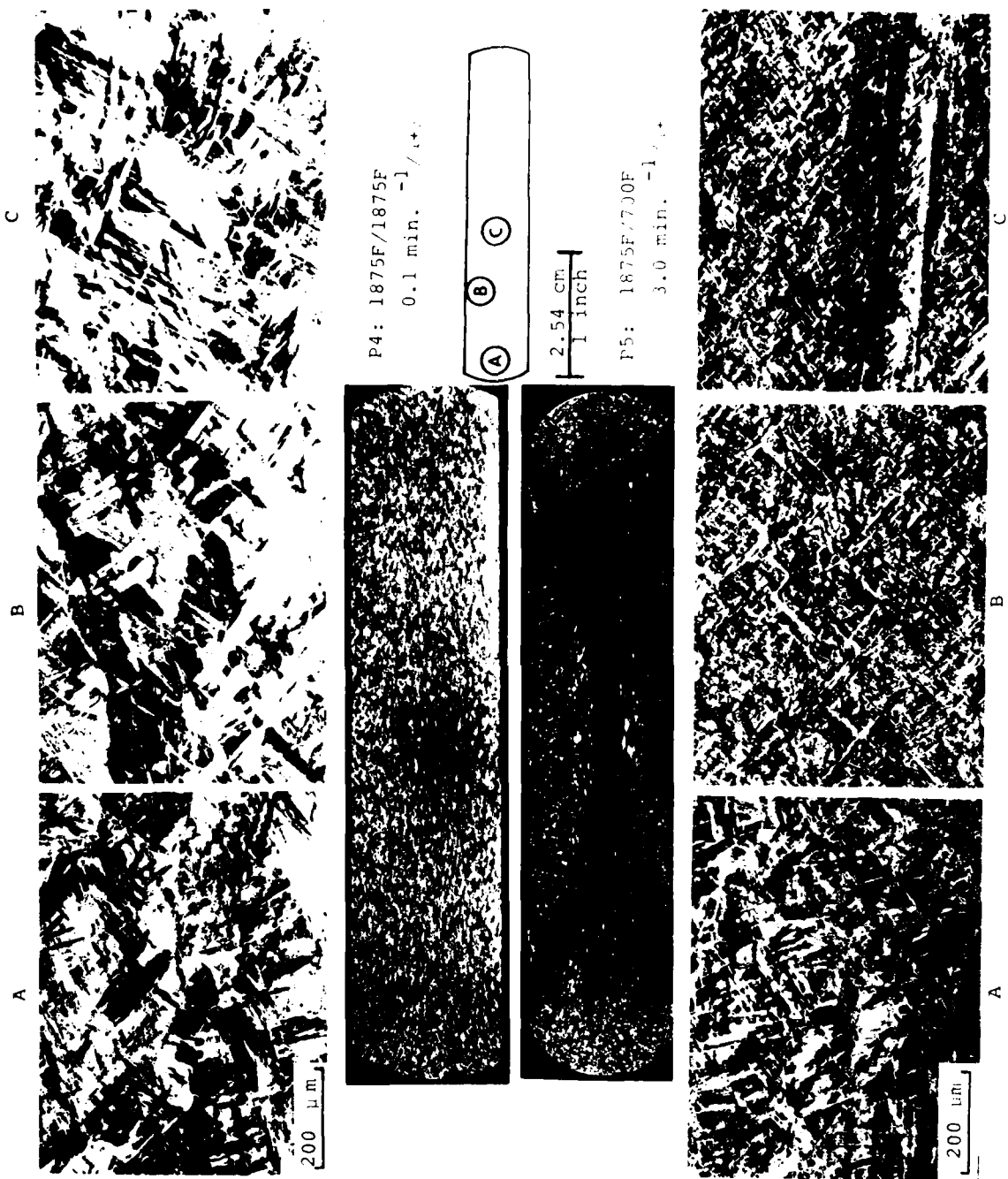


Figure E-33c Comparison of macrostructures and microstructures between isothermally and conventionally i-forged pancakes

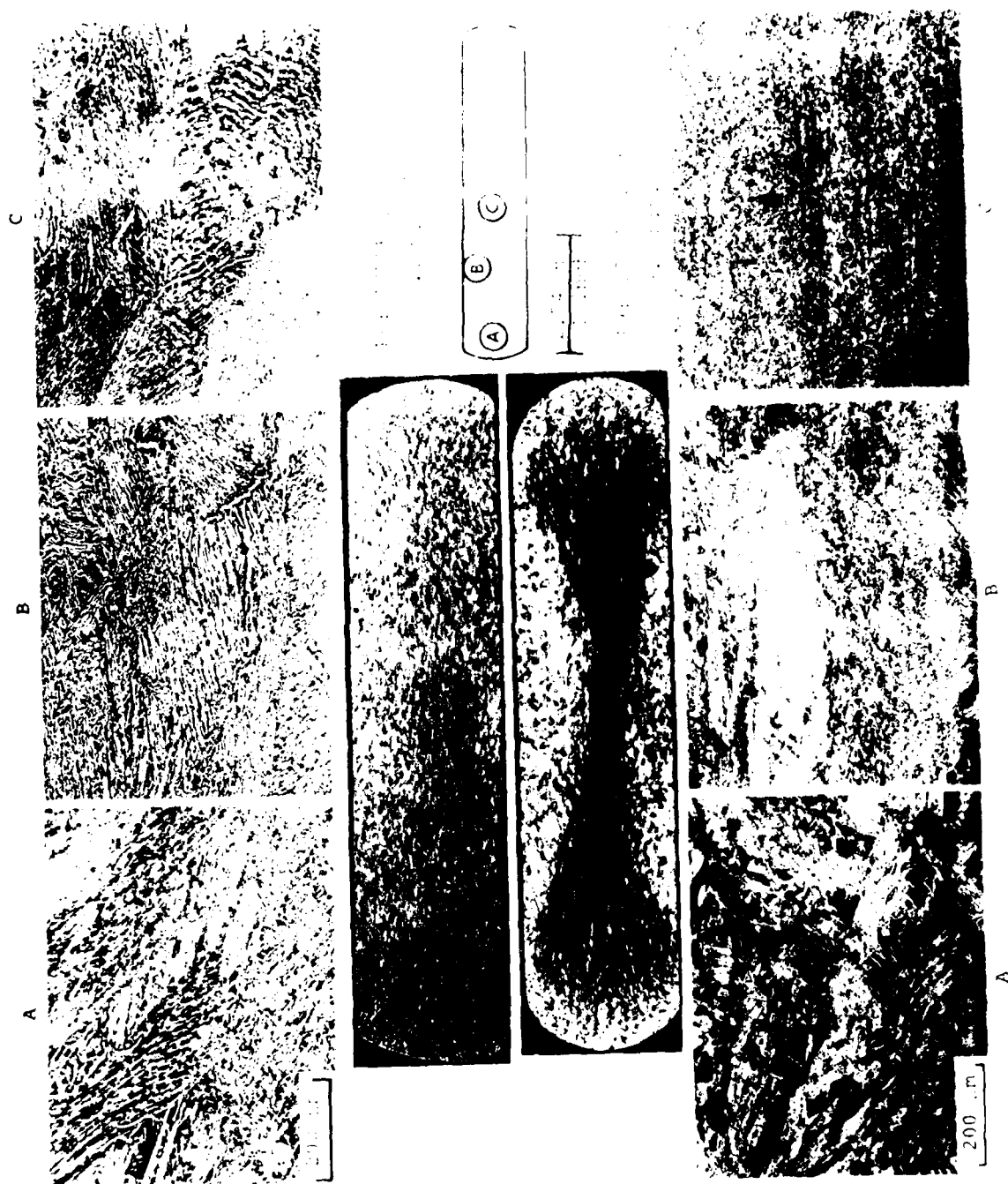


Figure E-33d Comparison of macrostructures and microstructures between isothermally and near-conventionally (u+f)-forged pancakes

recrystallized grains) are observable for conventional forgings. The increased shear band and reduced metal flow due to die chill are very profound.

(c) Heat Treatments

Sixteen pancake forgings (P1, P2, P3, P4, P5, P6, P7, P9) were sectioned into half-pancakes and subjected to five heat treat cycles; this gives a total of 32 forge-heat treat combinations for the 32 half-pancakes. The four half-pancakes per each forge condition were produced and identified as A, B, C, and D. The heat treatments included: * (a) direct age; (b) $(\alpha+\beta)$ -ST/AC + Age; (c) $(\alpha+\beta)$ -ST/WQ + Age; (d) β -ST/AC + Age; (e) β -ST/WQ + Age. Note that the solution-treatment was made in both $(\alpha+\beta)$ and β -phase regions, and the aging was done at 1100F/8 hours/AC for all conditions. After heat treatment, they were blast-cleaned to remove the coating. Details of heat treat variables are tabulated in Table E-6.

TABLE E-6
HEAT TREAT VARIABLES USED
FOR THE 32 HALF-PANCAKES

<u>Heat-Treat Condition</u>	<u>Half-Pancakes</u>
1100F/8 hrs/AC	P1-A, P2-A, P3-A, P4-A, P5-A, P6-A, P7-A, P9-A
1945F/1 hr/AC +1100F/8 hrs/AC	P1-B, P2-B, P3-B, P6-B, P7-B, P9-B
1795F/1 hr/AC +1100F/8 hrs/AC	P1-C, P2-C, P3-C, P6-C, P7-C, P9-C
1795F/1 hr/WQ +1100F/8 hrs/AC	P1-D, P2-D, P3-D, P6-D, P7-D, P9-D
1795F/1 hr/AC +1100F/8 hrs/AC	P4-B, P5-B
1795F/1 hr/WQ +1100F/8 hrs/AC	P4-C, P5-C
1845F/1 hr/WQ +1100F/8 hrs/AC	P4-D, P5-D

* $(\alpha+\beta)$ -ST= $(\alpha+\beta)$ solution treat; β -ST= β -solution treat
AC = air cool; WQ = water quench

(d) Property and Structural Characterizations

A series of mechanical property evaluations and microstructural characterizations of the heat-treated pancakes are being conducted, and the results will be compiled in the next reporting period. These results will include: (1) macro- and microstructural characterizations for the 32 half-pancakes (52 macros and 126 micros), (2) Room temperature tensiles (one per each for 32 conditions), (3) 950F tensiles (one per each for six conditions), (4) 1050F tensiles (one per each for six conditions), (5) creep at 950F/35 ksi/0.2% (one per each for six conditions), (6) creep at 1050F/25 ksi/0.2% (one per each for 32 conditions), (7) stress rupture at 950F/65 ksi (one per each for six conditions), and (8) post-creep tensiles (a total of 38 tests).

Based on the results of property testings, six best forge-heat treat cycles will be selected. Wyman-Gordon then will produce six more pancakes using the selected cycles. These pancakes will be delivered to BCL for $\frac{da}{dn}$ and LCF testings.

(e) Further Examination of Heat-Treatment
for Selected Forge Practice

In order to develop a successful processing model for manufacturing disk forgings with dual properties, an additional effort is necessary during Phase I effort to refine heat treat practice for the optimized forge cycles. A total of 12 pancake forgings will be produced to examine the two best forge-heat treat cycles. Both structural characterizations (macros and micros), and mechanical property testings (tensile, creep, stress rupture, post-creep tensile at Wyman-Gordon, and $\frac{da}{dn}$, LCF at BCL) will be subsequently carried out to determine optimum cycles for the best properties.

The results of Phase I effort will provide the information regarding the forging conditions and the preform shape required to produce subscale disk forgings in Phase IV. The part(Figure E-34) selected for this portion of the program is one of the subscaled compressor disk forgings with a projected plan view area of 23.76 square inches. This die set is made of TZM-moly, and has a die impression volume of 12 cubic inches, web thicknesses ranging from 0.26 to 0.52 inches, and rib thickness of 0.35 inch. This part represents a basic simple disk shape, and also characterizes a typical compressor disk production part for advanced turbine engine components. Furthermore, two TZM-moly rings (5-1/2 inch

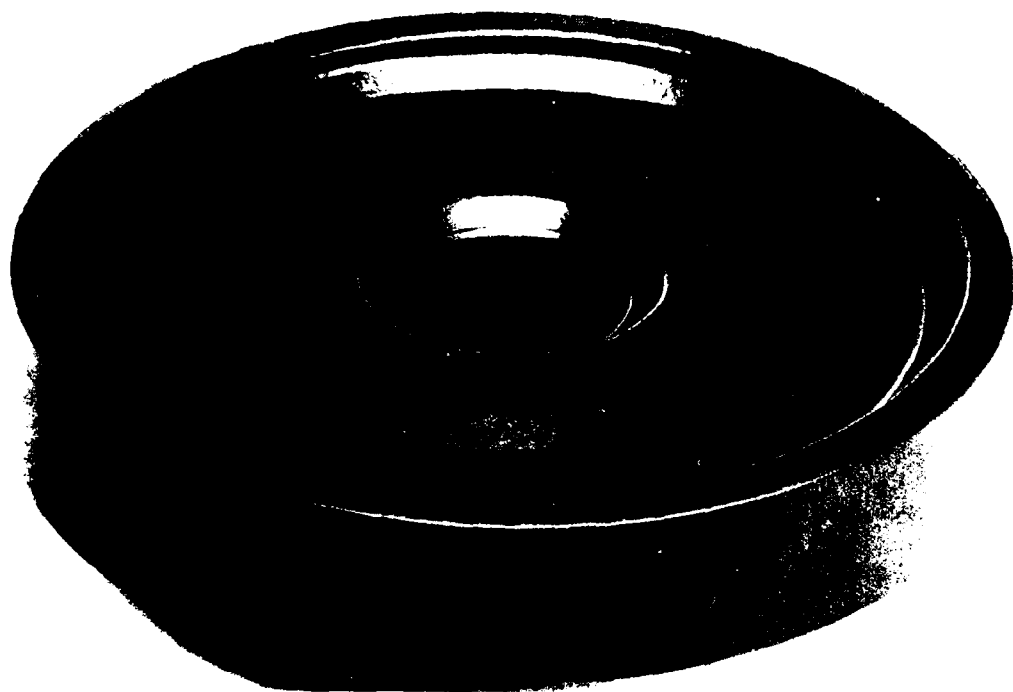
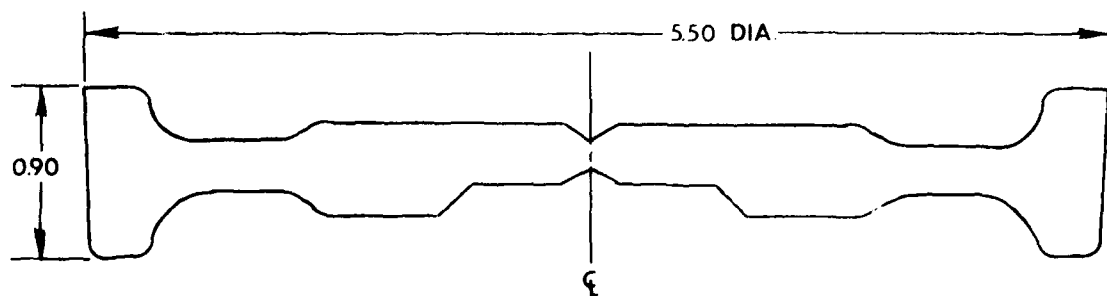


Figure E-34 Proposed subscale compressor disk forging for the program

diameter) are available to increase the web thickness of the disks for this die set, so that the web portion of the forging may be increased to cover the materials required for the fracture toughness, fatigue crack growth rate, and fatigue tests.

Isothermal Forging of Composite Ti-6242Si Preforms

In another phase of the program, Wyman-Gordon also performed isothermal forging of composite preform to demonstrate the capability of producing dual microstructure/ property pancake forging for Ti-6242Si alloy. Note that such a technical approach was initiated by AFML⁽¹⁴⁾. Here the basic concept was to investigate the stability of microstructural gradients and to obtain some mechanical properties.

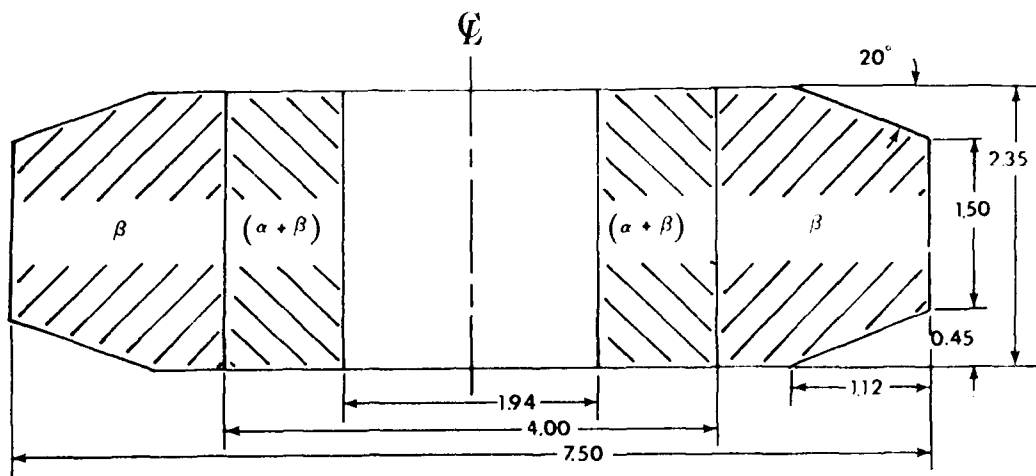
(a) Preform Preparation

The billet mult used for this portion of the program was 8 inch round billet, RMI heat number 803362. The chemical composition (wt.%) of the alloy heat, as provided by the melter is 6.1% Al, 2.0% Sn, 4.1% Zr, 1.9% Mo, 0.070% Si, 0.07% Fe, <0.01% Cu, 0.02% C, 0.008% N, <30 ppm B, 0.09 % O₂, and 0.0049% H₂.

The 8 inch round x 5 inch long (~40 pounds) billet mult was first upset and drawn at 1875F to produce β -preform microstructures. A center slot was removed from the mult by Elox and the slot was upset and drawn at 1750F to produce ($\alpha+\beta$) microstructures. They were then heat treated at 1845F/1 hour/WQ for outer ring and at 1775F/1 hour/WQ for center slot. The two preforms were then assembled by machining, chemically cleaning, electron beam welding, and finally, hiped at 1650F/1 hour/15 ksi condition. Special effort was made at each step to achieve a good, smooth, clean interface. Figure E-35 illustrates the initial preform used for making the dual microstructure/property pancake. As suggested by AFML⁽¹⁴⁾, the corner angle is added to reduce the die constraint during deformation and the center hole is used to indicate the amount of friction.

(b) Forge Processing

The forging operation was conducted on a 1500-ton hydraulic press, and IN-100 hot dies were used. The isothermal forge/die temperature used was 1750F. The preform was first coated with Acheson Deltaglaze-149 coating for about 6 mils thick per side, and then preheated for the aim temperature in an electric furnace for 1-1/2 hours prior to forging. The transfer time from the furnace to the dies was about 5 seconds. The strain rate used was comparable with those



Ti-6242Si Composite Preform

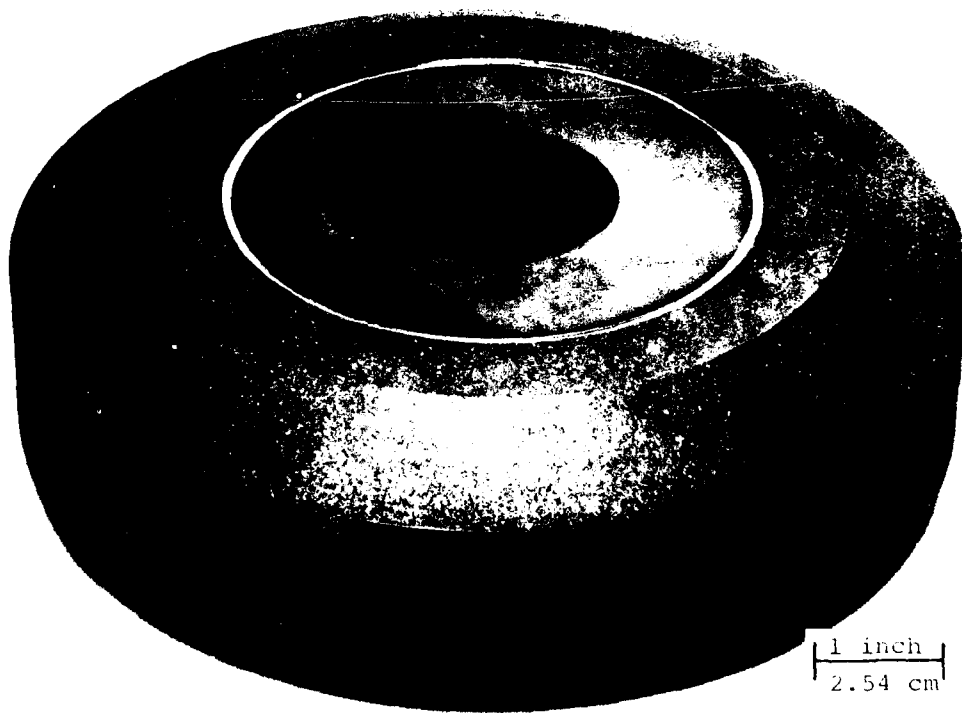


Figure E-35 A sketch and top view of composite preform used for producing dual microstructure pancake

used in industrial press forging with average ram rate of 0.2 in./min.; this corresponds to the initial strain rate of about $0.1 \text{ m}^{-1} (1.5 \times 10^{-3} \text{ s}^{-1})$.

The forge operation was accomplished by one-stage forging to a final thickness of about 1.32 inches, and 9.25 inches in diameter. This is equal to a total deformation of 44% reduction in thickness. The unit pressure applied was about 9 ksi. After the forging operation, the forging was air-cooled and sectioned for macro- and microstructural examinations. Figure E-36 gives the pancake forging produced from this composite preform.

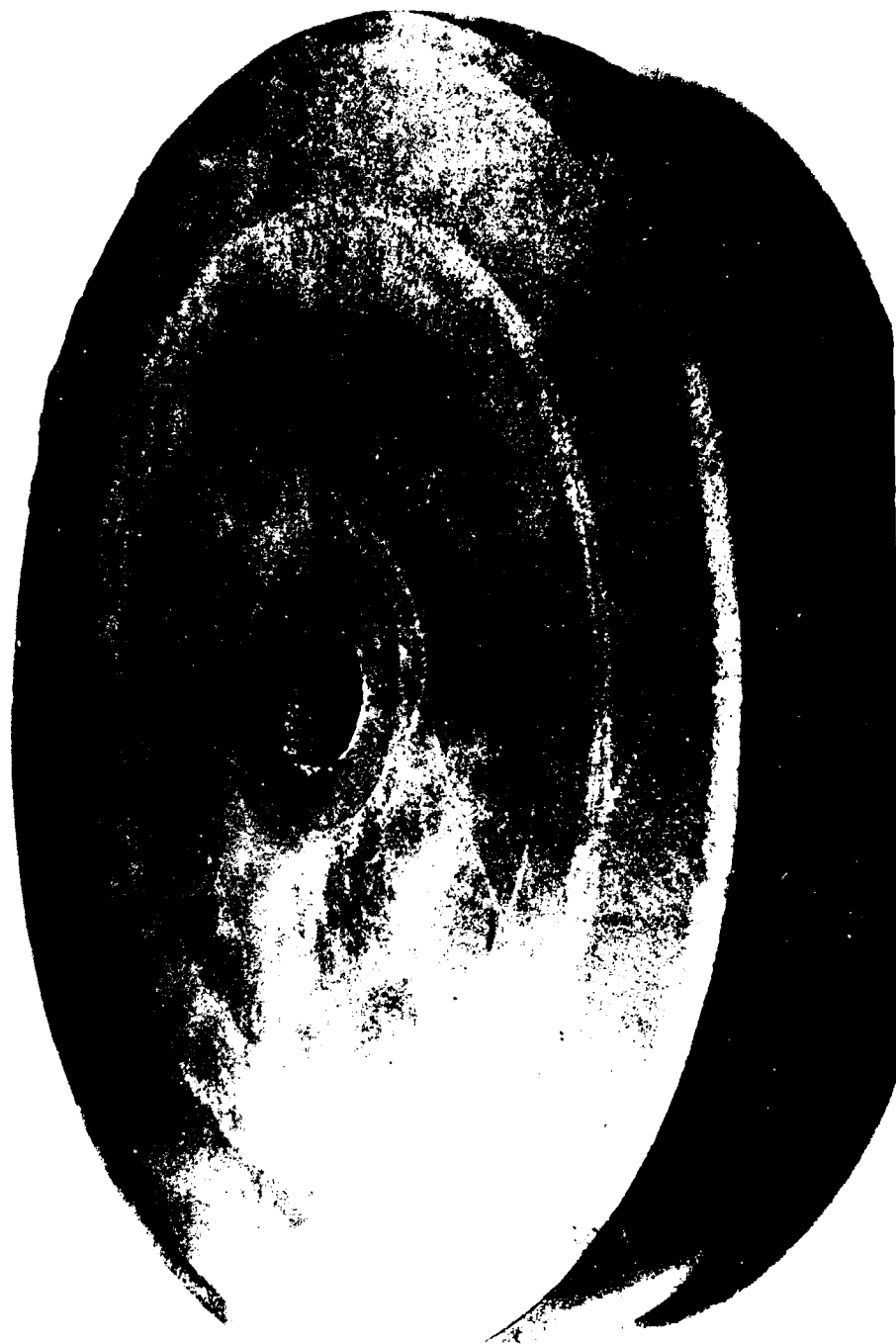
(c) Structural Characterizations

Figure E-37 presents the macro- and microstructures of the isothermally forged composite preform. The macroslice was cut just off the small center-hole. The micros were taken at five locations; two at rim portions (A, B), two at bore regions (C, D), and one at interface (C).

It is seen from Figure E-37 that the dual microstructure pancake is technically achievable; excellent macro- and microstructural characteristics were observed at optical magnifications. Good flow lines were observable without any evidence for the occurrence of plastic instability in $\alpha+\beta$ and β preform regions and also at interface. The rim area is characterized by pseudo- β microstructure, while the bore region contains highly globular- α in transformed- α matrix. This is a good dual microstructure for the present program since, metallurgically, the pseudo- β microstructure should provide excellent creep, fracture toughness, and stress rupture properties for the alloy forgings, while the globular- α should give better LCF, ductility, and strength.

The two half-pancakes were heat-treated at 1745F/4 hours/AC + 1100F/8 hours/AC and are being cut for microstructure and property evaluations. Note that this effort was designed purely from a technical standpoint, not from an economic viewpoint. Nevertheless, it has demonstrated the capability of forging dual microstructure preforms, and achievable stability of microstructural gradients by forging deformation. The results of property tests should also aid in determining appropriate processing variables for future effort.

In continuation of this portion of the effort, Wyman-Gordon will try to broadly define the preform shape requirements for controlling localized flow in the next reporting period. It is believed such a technical attempt is extremely important in order to achieve an economic and practical process-model for producing dual microstructure/property disks.



9.25 inch round X 1.32 inch thick

Figure E-36 Top view of Ti-6242Si pancake forging produced for this trial

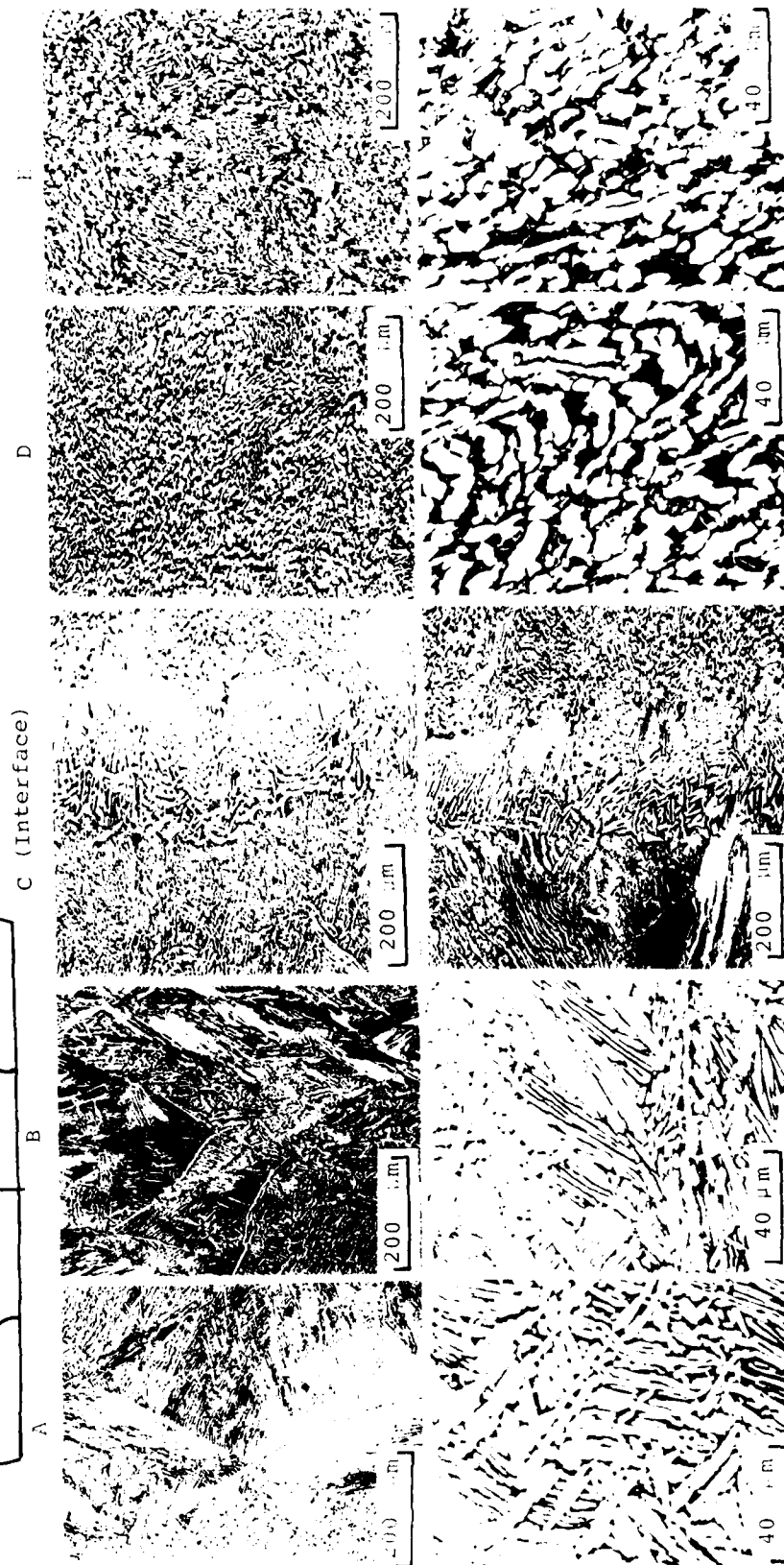
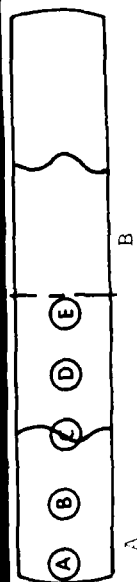


Figure E-3/ Macrostructures and microstructures of isothermally forged Ti-6242Si composite preform

References

1. C. C. Chen, "Metallurgical Fundamentals to Ti-6Al-2Sn-4Zr-2Mo-0.1Si Alloy Forgings: I. Influence of Processing Variables on the Deformation Characteristics and the Structural Features of Ti-6242Si Alloy Forgings", Wyman-Gordon Company Report RD-77-110, October 1977.
2. C. C. Chen, "Metallurgical Fundamentals to Ti-6Al-2Sn-4Zr-2Mo-0.1Si Alloy Forgings: II. Influence of Processing Variables on the Mechanical Properties of Ti-6242Si Alloy Forgings", Wyman-Gordon Company Report RD-77-111, October 1977.
3. C. C. Chen, "Metallurgical Fundamentals to Ti-6Al-2Sn-4Zr-2Mo-0.1Si Alloy Forgings: III. Relationships Between Microstructure and Mechanical Properties in Ti-6242Si Alloy Forgings", Wyman-Gordon Company Report RD-77-112, October 1977.
4. C. C. Chen, "Influence of Initial Microstructures on the Forgeability and Microstructure of Isothermally Forged Ti-6Al-4V Alloy", published at the proceedings of the Third International Conference on "Titanium", Moscow, Russia, May 1976.
5. C. C. Chen, "Evaluation of Lubrication Systems for Isothermal Forging of Alpha-Beta and Beta Titanium Alloys", Technical Report AFML-TR-77-181, November 1977.
6. "Ti-6Al-2Sn-4Zr-2Mo - Metallurgical and Mechanical Properties of Ti-6Al-2Sn-4Zr-2Mo Sheet, Bar, and Forgings", Technical Data Sheet, Titanium Metals Corporation of America, Pittsburgh, Pennsylvania (September 1966).
7. J. L. Shannon, Jr., "Ti-6Al-2Sn-4Zr-2Mo Chapter", Code 3718, Aerospace Structural Metals Handbook, Volume II, Nonferrous Light Metal Alloys, AFML-TR-68-115 (March 1968).
8. S. R. Seagle, G. S. Hall, and H. B. Bomberger, "High Temperature Properties of Ti-6Al-2Sn-4Zr-2Mo-0.09Si", Metals Engineering Quarterly, page 48, February 1975.
9. C. C. Chen, W. H. Coutts, Jr., C. P. Gure, and S. C. Jain, "Advanced Isothermal Forging, Lubrication and Tooling Process", Technical Report AFML-TR-77-136, August 1977.
10. C. C. Chen and J. E. Coyne, "Deformation Characteristics of Ti-6Al-4V Alloy Under Isothermal Forging Conditions", Metallurgical Transactions, Volume 7A, p. 1931, 1976.

11. T. Watmough, K. M. Kulkarni, and N. M. Parikh, "Isothermal Forging of Titanium Alloys Using Large Precision-Cast Dies", Technical Report AFML-TR-70-61, July 1970.
12. K. M. Kulkarni, N. M. Parikh, and T. Watmough, "Isothermal Hot-Die Forging of Complex Parts in a Titanium Alloy", Journal Inst. Metals, 1972, Volume 100, page 146.
13. C. C. Chen and R. R. Boyer, "Practical Considerations for Manufacturing High-Strength Ti-10V-2Fe-3Al Alloy Forgings", Journal of Metals, vol. 31, p. 33, July 1979.
14. H. L. Gegel, Air Force Materials Laboratory, Wright-Patterson Air Force Base, Ohio, Personal Letter, 12 June 1979.

APPENDIX F

FINITE-ELEMENT ANALYSIS OF
AXISYMMETRIC FORGING OF RATE-
SENSITIVE MATERIALS

S. Kobayashi
University of California
Berkeley, California 94720

APPENDIX F

FINITE-ELEMENT ANALYSIS OF AXISYMMETRIC FORGING OF RATE-SENSITIVE MATERIALS

Summary

The objective of the present research is to establish the finite-element formulation for the analysis of large plastic deformation of rate-sensitive materials. The behavior of the material is characterized as rigid-viscoplastic. First, an approach to the construction of constitutive equation for rigid-viscoplastic materials is described. Then, the extremum principle is presented as the basis for the finite-element formulation of flow behavior analysis. The finite-element method code is written and applied to the analysis of simple compression. The effect of rate-sensitivity of materials on flow behavior is revealed and computed results are compared with experiments found in the literature.

Introduction

The mathematical theory of plasticity adequately describes the time-independent aspect of the behavior of materials, but is inadequate for analysis of time-dependent behavior. An approach to achieving a satisfactory formulation for time-dependent behavior has been to generalize plasticity to cases within the strain-rate sensitive range. One such generalization has been provided by the theory of viscoplasticity. The history of this theory

dates back to as early as 1922 [1]. Since then, generalizations of early versions have been achieved and various forms of the theory of viscoplasticity have been provided (summarized, for example, by Perzyna [2] and by Cristescu [3]).

Considerable development of the finite-element method in recent years has removed many barriers in applying theories to various problems. A finite-element formulation of viscous materials, such as Bingham plastic or power law pseudoplastic, in isothermal processes, was given by Lyness et al. [4]. A finite-element formulation of elastic-viscoplastic materials was proposed by Zienkiewicz et al. [5] for the infinitesimal deformation and by Nagarajan and Popov [6], based on the finite strain theory. In the area of metal-working analysis, however, the treatment of time-dependent behavior of materials within the framework of the theory of viscoplasticity is still in its beginning [7] - [16].

The present research is aimed at establishing the finite-element formulation for the analysis of axisymmetric forging of rate-sensitive materials. Although the residual stress calculation is an important aspect in metal-working, equally important is the flow analysis during deformation. An accurate determination of flow-characteristics under various process parameters is a prime requirement for the proper design and control of any metal-working process. Therefore, an analysis method in this field of application can only be justified by its solution accuracy and computation efficiency. With this view, the behavior of materials is characterized as rigid-viscoplastic.

In this paper, we first describe an approach to the construction of a constitutive equation for rigid viscoplastic materials. Then, the extremum principle is presented as the basis for the finite-element formulation of flow behavior analysis. The finite-element method code is written and applied to

the analysis of simple compression.

Theoretical Foundations

Constitutive equations. What follows is based on work by Perzyna [12].

We consider a rigid viscoplastic material and apply the infinitesimal theory for each incremental deformation by successive updating of the coordinates.

A static yield function, assumed regular and convex,

$$F(\sigma_{ij}, \epsilon_{kl}^p) = \frac{f(\sigma_{ij}, \epsilon_{kl}^p)}{K} - 1 \quad (F-1)$$

is introduced, where $f(\sigma_{ij}, \epsilon_{kl}^p)$ is a function of the state of stress, σ_{ij} , and the state of plastic strain, ϵ_{kl}^p . The strain-hardening parameter, K , is given by

$$K = K(w_p) = K \left(\int_0^{\epsilon_k^p} \sigma_{ij} d\epsilon_{ij}^p \right) \quad (F-2)$$

The function F is such that for $F < 0$ the material is rigid, for $F = 0$, on the verge of yielding with practically zero strain-rate, and for $F > 0$, the material has yielded (with a certain strain-rate).

The constitutive equation, using the yield function and associated flow rule, is expressed as

$$\dot{\epsilon}_{ij} = \gamma'' \langle \phi(F) \rangle \frac{\partial F}{\partial \sigma_{ij}} \quad (F-3)$$

or

$$\dot{\epsilon}_{ij} = \gamma' \langle \phi(F) \rangle \frac{\partial f}{\partial \sigma_{ij}} \quad (F-4)$$

where

$$\langle \phi(F) \rangle = \begin{cases} 0 & \text{for } F \leq 0 \\ \phi(F) & \text{for } F > 0 \end{cases} \quad (F-5)$$

and γ is a viscosity constant of the material. The specific form of the function $\phi(F)$ is to be chosen according to the test results of material behavior. This constitutive relation simply states that strain-rate is a function of the excess of stress over the static yield stress.

Assuming isotropy (and isotropic work-hardening), incompressibility, and the Huber-Mises yield criterion, we have that

$$f = (J_2)^{1/2} \quad (F-6)$$

where $J_2 = \frac{1}{2} \sigma'_{ij} \sigma'_{ij}$ is the second invariant of the deviatoric stress tensor. Then, Eq. F-4 becomes

$$\dot{\epsilon}_{ij} = \gamma' \left\langle \phi \left(\frac{\sqrt{J_2}}{k} - 1 \right) \right\rangle \frac{\sigma'_{ij}}{2\sqrt{J_2}} \quad (F-7)$$

Using effective stress and strain, Eq. F-7 can be expressed as

$$\dot{\epsilon}_{ij} = \frac{3}{2} \frac{\dot{\epsilon}}{\sigma} \sigma'_{ij} \quad (F-8)$$

For metal-forming processes (excluding possibly explosive forming), experimental data found in the literature can be realistically represented in the form

$$\sigma = Y \left[1 + \left(\frac{\dot{\epsilon}}{Y} \right)^n \right] \quad (F-9)$$

$Y = Y(\epsilon)$ being the static yield stress. Then, from Eq. F-8,

$$\sigma'_{ij} = \frac{2}{3} Y \left[1 + \left(\frac{\dot{\epsilon}}{Y} \right)^n \right] \frac{\dot{\epsilon}_{ij}}{\dot{\epsilon}} \quad (F-10)$$

Extremum principle. The deformation process of the rigid-viscoplastic materials is associated with the following boundary value problems. At a generic stage in the process of quasistatic distortion, the shape of the body, the internal distribution of temperature, the state of inhomogeneity, and the current values of material parameters are supposed to be given or to have been determined already. The velocity vector, \underline{v} , is prescribed on a part of the surface, S_v , together with traction, \underline{F} , on the remainder of the surface, S_F . Equilibrium equations and compatibility equations are satisfied by the stress and velocity field solutions. To solve this boundary value problem, we consider the extremum principle derived by Hill [13].

Among all the possible constitutive equations, we will restrict our attention to the case where there exists the work function $E(\dot{\epsilon}_{ij})$, such that

$$\sigma'_{ij} = \frac{\partial E}{\partial \dot{\epsilon}_{ij}} \quad (F-11)$$

and where E is convex.

The existence of work function $E(\dot{\epsilon}_{ij})$ is ensured, if σ' is a single-valued function of $\dot{\epsilon}$, satisfying $\partial \sigma'_{ij} / \partial \dot{\epsilon}_{kl} = \partial \sigma'_{kl} / \partial \dot{\epsilon}_{ij}$. Also, E is a convex function, if

$$E(\dot{\epsilon}^*) - E(\dot{\epsilon}) \geq (\dot{\epsilon}^*_{ij} - \dot{\epsilon}_{ij}) \frac{\partial E}{\partial \dot{\epsilon}_{ij}} \quad (F-12)$$

With this restriction, we have the following relation, neglecting the body force,

$$\int E(\dot{\underline{\epsilon}}^*) dV - \int \underline{\underline{F}} \cdot \underline{\underline{v}}^* dS_F \geq \int E(\dot{\underline{\epsilon}}) dV - \int \underline{\underline{F}} \cdot \underline{\underline{v}} dS_F \quad (\text{F-13})$$

where $\dot{\underline{\epsilon}}$, $\underline{\underline{v}}$ are actual quantities and the starred quantities are kinematically admissible ones.

Finite-Element Formulation

The rigid-viscoplastic finite-element formulation is an extension of the rigid-plastic counterpart derived by Lee and Kobayashi [14]. According to the extremum principle, the minimum of the functional

$$\pi = \int_V E(\dot{\underline{\epsilon}}) dV - \int_F \underline{\underline{F}} \cdot \underline{\underline{v}} dS_F \quad (\text{F-14})$$

with respect to the admissible velocity field, $\underline{\underline{v}}$, with incompressibility constraint, is scratched. By introducing a Lagrangean multiplier, this problem is changed to the stationary value problem without constraints of

$$\pi = \int_V E(\dot{\underline{\epsilon}}) dV - \int_{S_F} \underline{\underline{F}} \cdot \underline{\underline{v}} dS_F + \int_V \lambda \dot{\epsilon}_{ii} dV \quad (\text{F-15})$$

The Lagrangean multiplier λ can be shown to be equal to the hydrostatic stress component. For interface friction the velocity-dependent frictional stresses developed by Chen and Kobayashi [15] were used:

$$f = -mk \left\{ \left(\frac{2}{\pi} \right) \tan^{-1} \left(\frac{|\underline{\underline{v}}_R|}{a|\underline{\underline{v}}_D|} \right) \right\} t \quad (\text{F-16})$$

where m is the friction factor ($0 \leq m \leq 1$);

k is the shear yield stress;

$|\underline{v}_R|$ is the magnitude of relative velocity between die and workpiece;

a is a constant several orders of magnitude less than the die velocity (was taken as 10^{-5});

$|\underline{v}_D|$ is the magnitude of die velocity;

and the functional F-15 was modified to

$$\pi = \int_V E(\underline{\dot{\epsilon}}) dV + \int_V \lambda \dot{\epsilon}_{ii} dV - \int_{S_F} \underline{F} \cdot \underline{v} dS_F - \int_{S_C} \left(\int_0^{|\underline{v}_R|} \underline{f} \cdot d\underline{v}_R \right) dS_C \quad (F-17)$$

S_C being the part of the boundary where frictional forces occur. The proof is identical to the one presented in [15].

The finite-element implementation was made for axisymmetric problems using 4-node quadrilateral isoparametric elements; the field variable is the velocity \underline{v} , and the Lagrangean multiplier was taken as a constant within each element. Accordingly, there were 8 nodal point velocity components u_i plus λ as unknowns in each element.

Applying the stationary condition, a set of algebraic nonlinear equations in \underline{u} and λ resulting from the assemblage for elements N of

$$\begin{aligned} \frac{\partial \pi^N}{\partial \underline{u}} &= 0 \\ \frac{\partial \pi^N}{\partial \lambda} &= 0 \end{aligned} \quad (F-18)$$

was obtained and solved in the following way: assume a solution \underline{u}_0 close to the actual solution. Then, using the first two terms of a Taylor expansion

$$\left. \frac{\partial \pi}{\partial u_i} \right|_{\underline{u}=\underline{u}_0} + \left. \frac{\partial^2 \pi}{\partial u_i \partial u_j} \right|_{\underline{u}=\underline{u}_0} \Delta u_j = 0$$

$$\left. \frac{\partial \pi}{\partial \lambda} \right|_{\underline{u}=\underline{u}_0} + \left. \frac{\partial^2 \pi}{\partial \lambda \partial u_j} \right|_{\underline{u}=\underline{u}_0} \Delta u_j = 0 \quad (F-19)$$

Δu and λ were obtained. The new approximation to the solution becomes $\underline{u}_0 + \Delta u$, and this process is repeated until the desired accuracy is reached.

The problem of non-uniqueness of stress in the rigid zones, and the difficulty in determining the minimum of Eq. F-14 under such conditions was numerically handled by considering an effective strain-rate offset, several orders of magnitude smaller than the average strain rates. Below that strain rate, the stress was considered to vary linearly down to zero, as shown schematically in Figs. F-1 and F-2. Whenever, $\dot{\epsilon} < \dot{\epsilon}_0$ in one element, Eq. F-10 becomes

$$\sigma'_{ij} = \frac{2}{3} \gamma \left(1 + \frac{\dot{\epsilon}_0}{\gamma^n} \right) \frac{\dot{\epsilon}_{ij}}{\dot{\epsilon}_0} \quad (F-20)$$

and Eqs. F-19 are accordingly modified. For all practical purposes, an element may be considered to be rigid if $\dot{\epsilon} < \dot{\epsilon}_0$.

Application

There are few available references in the literature where strain-rate effects in non-uniform deformation are explicitly put in evidence. Among them, the work by Klemz and Hashmi [16] on simple upsetting of lead cylinders at room temperature provides good experimental results for comparison with the finite-element solution, since lead is quite strain-rate sensitive at room temperatures. Thus, simulation of compression of a lead solid cylinder by a

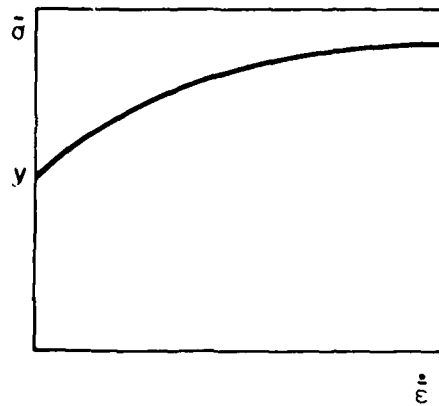


Fig. F-1 Schematic stress strain-rate curve for rigid-viscoplastic materials.

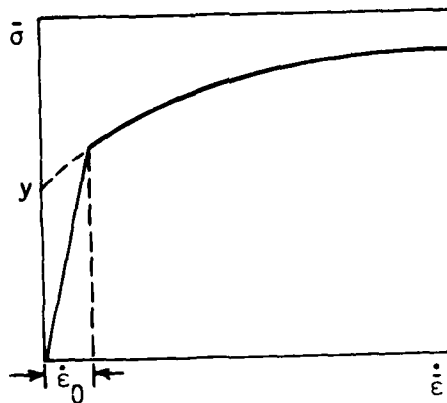


Fig. F-2 Modified stress strain-rate curve with offset strain rate.

drop hammer is performed.

A cylinder having a diameter of 1.00 (in.) and a height of 0.95 (in.) was considered. The stress strain strain-rate data for pure lead at room temperature were taken from [16] and from experimental results by Loizou and Sims [17]. The static stress-strain curve was approximated according to the expressions given in Table F-1. Then, for several strains, curves of the form $\sigma = Y[1 + (\dot{\epsilon}/\dot{\gamma})^n]$ were fitted to experimental data, and the obtained values of n and $\dot{\gamma}^n$ were interpolated in the program for intermediate strain values (Table F-1). The considered offset value $\dot{\epsilon}_0$ of Eq. F-20 was 1. The friction factor m of Eq. F-16 was taken as 0.06 (m = a fraction of the static yield shear strength), in agreement with the assumed value in [16].

TABLE F-1
Stress strain strain-rate properties of lead at room
temperature, used in calculations

ϵ	.105		.225	.6
$Y(\text{psi})$	1000+ +13212.4 ϵ	2387.3+6878.3(ϵ - .105)-28659.7(ϵ - .105) ²	2650+ +150cos[$\pi(\epsilon$ -.225)/.375]	2500
n	.015+.1525 ϵ		-.06+1.727-6.117 ϵ ² + +6.104 ϵ ³	.093
$\dot{\gamma}^n$	6.192-15.355 ϵ		6.67-24.54 ϵ +34.96 ϵ ² - -15.86 ϵ ³	1.105

The calculations simulate the deformation of the cylinder by a drop-hammer, whose tup mass is 35.5 lb, and hits the specimen at a speed of 30 ft s^{-1} . The assumption of a quasi-static process is justified for these velocities [18], [19]. Accordingly, the calculated work done by the contact forces between tup and workpiece in each step of deformation was subtracted to the tup kinetic energy, and the process ended when the tup came to a stop.

For comparison, the calculations were repeated without introducing strain-rate effects (making $\gamma = \infty$ in the formulation).

The non-steady-state deformation problem was analyzed in a step-by-step manner by treating it quasi-linearly during each incremental deformation. The reduction in height at each step is 1%. The solution of velocity field for uniform compression was used as an initial guess. The measure of the convergence is represented by the quantity $\|\Delta \underline{u}\|/\|\underline{u}\|$, where $\Delta \underline{u}$ is the error vector found during iterations and the Euclidean vector norm is defined by

$$\|\underline{u}\| = \sqrt{\sum_{i=1}^N |u_i|^2}, \text{ where } N = \text{total number of nodal points.}$$

The solution obtained from the previous step was then used as an initial guess for the subsequent step. Normally, 7 iterations were required for the first step to reach the accuracy of $\|\Delta \underline{u}\|/\|\underline{u}\| \leq 0.00005$. For subsequent steps, only 2 to 4 iterations were necessary to reach the same accuracy.

The calculated overall quantities are compared with experimental data and with the numerical dynamic analysis of Klemz and Hashmi [16] in Figs. F-3 and F-4. Some observations can be made from the figures. The result for non-strain-rate-sensitive analysis (Fig F-3) tends to follow those by the analysis of Klemz and Hashmi, which did not take into account strain-rate effects, but was based on a dynamic analysis. The agreement of the two indicates that the dynamic effect is negligible. However, both solutions show poor agreement with experiments. The analysis which includes strain-rate sensitivity shows good agreement with experiments (Fig. F-4). No "rigid" zones were formed at such a low value of friction in either rate-sensitive or rate-insensitive cases.

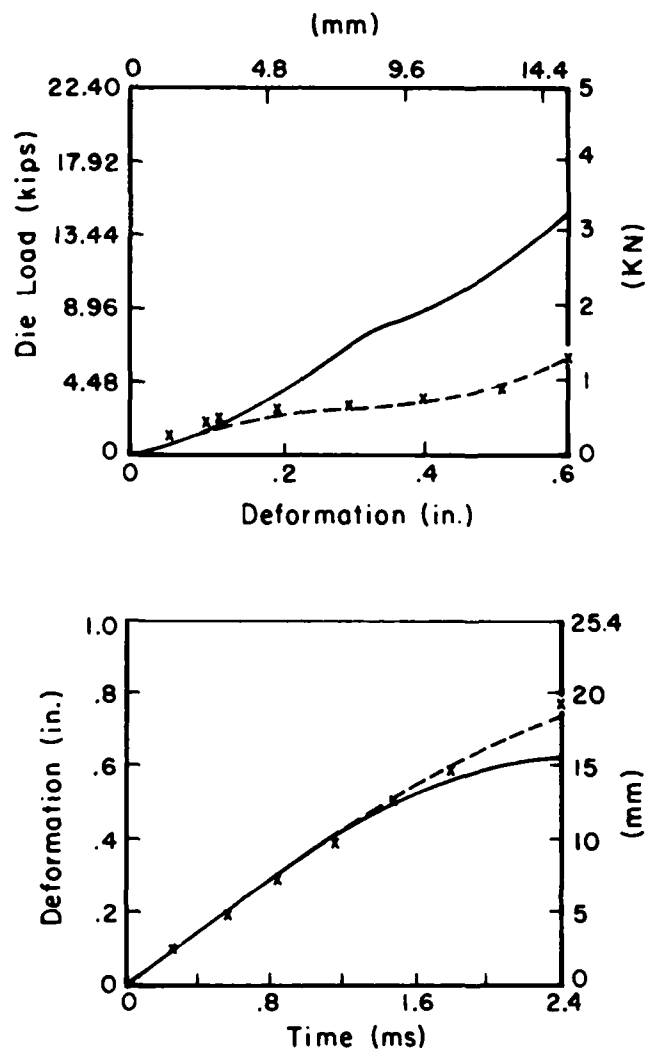


Fig. F-3. Comparison of the finite-element rigid-plastic analysis (xxxx) with the dynamic analysis (----) [16] and experiment (—) [16].

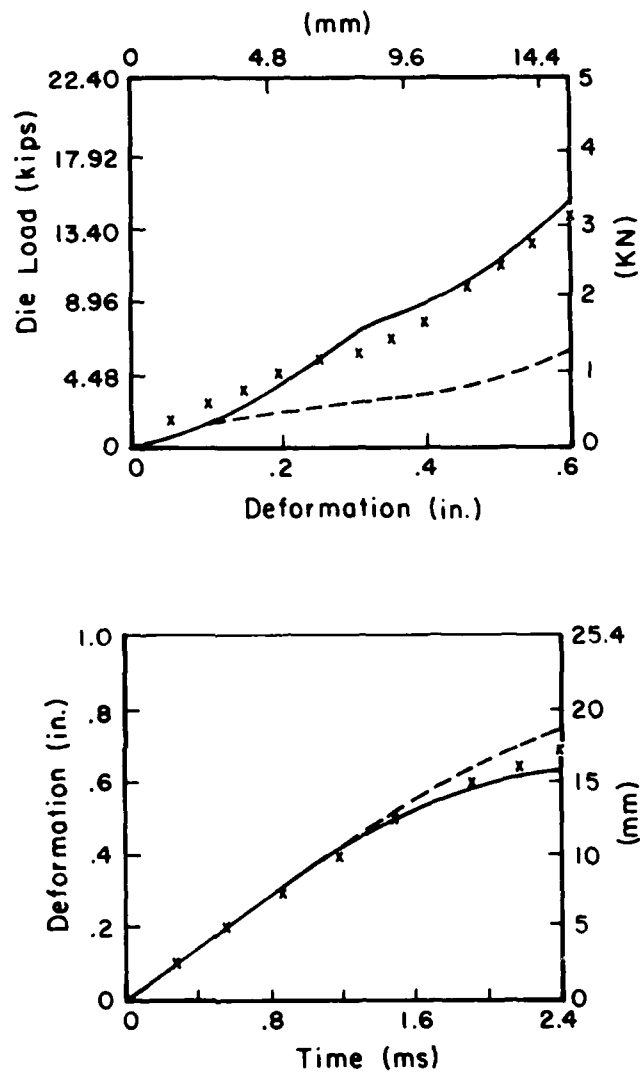


Fig. F-4. Comparison of the finite-element rigid-viscoplastic analysis (xxxx) with the dynamic analysis (----) [16] and experiment (—) [16].

Concluding Remarks

It is concluded that the rigid-viscoplastic finite-element formulation is adequate for flow analysis of rate-sensitive materials. The use of velocity-dependent frictional stress for the interface condition will be useful in analyzing the ring compression problem, where the direction of frictional stress is not known a priori. The next step is to include the temperature calculation in the finite-element scheme.

References

1. Bingham, E. C., Fluidity and Plasticity, New York, p. 125, 1922.
2. Perzyna, P., "The study of the dynamic behavior of rate-sensitive plastic materials," Arch. Mech. Stos., Vol. 15, p. 113, 1963.
3. Cristescu, N., Dynamic Plasticity, North Holland Press, Amsterdam, 1967.
4. Lyness, J. F., Owen, D. R. J., and Zienkiewicz, O. C., "Finite-element analysis of the steady-state flow of non-Newtonian fluids through parallel-sided conduits," Int. Sym. on Finite-element Method in Fluid Problems, Swansea, 1974.
5. Zienkiewicz, O. C., Owen, D. R. J., and Corneau, I. C., "Analysis of viscoplastic effects in pressure vessels by the finite-element method," Nuclear Engr. and Design, Vol. 28, p. 278, 1974.
6. Nagarajan, S. and Popov, E. P., "Plastic and viscoplastic analysis of axisymmetric shells," Int. J. Solids Structures, Vol. 11, p. 1, 1975.
7. Zienkiewicz, O. C. and Godbole, P. N., "Flow of plastic and viscoplastic solids with special reference to extrusion and forming processes," Int. J. Num. Meth. Engr., Vol. 8, p. 3, 1974.
8. Zienkiewicz, O. C., Jain, P. C., and Oñate, E., "Flow of solids during forming and extrusion: some aspects of numerical solutions," Int. J. Solids and Structures, Vol. 14, p. 15, 1978.
9. Price, J. W. H. and Alexander, J. M., "A study of the isothermal forming or creep forming of a titanium alloy," Proceedings of the 4th N.A.M.R.C., p. 46, 1976.
10. Price, J. W. H. and Alexander, J. M., "The finite-element analysis of two high-temperature metal deformation processes," 2nd Int'l. Symposium on F.E.M. in Flow Problems, p. 717, 1976.

11. Wang, N. M. and Wenner, M. L., "Elastic-viscoplastic analysis of simple stretch-forming problems," Proc. General Motors Research Symposium on Mechanics of Sheet-Metal Forming, Oct. 1977.
12. Perzyna, P., "Fundamental problems in viscoplasticity," Adv. in Applied Mechanics, Vol. 9, p. 243, 1966.
13. Hill, R., "New horizons in the mechanics of solids," J. Mech. Phys. of Solids, Vol. 5, p. 66, 1956.
14. Lee, C. H. and Kobayashi, S., "New solutions to rigid-plastic deformation problems using a matrix method," Trans. ASME, J. Engr. Ind., Vol. 95, p. 865, 1973.
15. Chen, C. C. and Kobayashi, S., "Rigid-plastic finite-element analysis of ring compression," ASME special publication, AMD-Vol. 28, pp. 163-174, 1978.
16. Klemz, F. B. and Hashmi, S. J., "Simple upsetting of cylindrical billets: experimental investigation and theoretical prediction," 18th MTDR Conference, London, 1977.
17. Loizou, N. and Sims, R. B., "The yield stress of pure lead in compression," J. of Mech. Phys. of Solids, Vol. 1, p. 234, 1953.
18. Lippman, H., Proc. 7th Int'l MTDR Conference, Birmingham, London, p. 53, 1966.
19. Samanta, S. K., "Resistance to dynamic compression of low-carbon steel and alloy steels at elevated temperatures and at high strain rates," Ind. J. Mech. Sci., Vol. 10, p. 613, 1968.

APPENDIX G

DESCRIPTION OF THE COMPUTER PROGRAM
'MATRIX'

S. I. Oh and G. D. Lahoti
Battelle-Columbus Laboratories
Columbus, Ohio 43201

APPENDIX G

DESCRIPTION OF THE SYSTEM OF COMPUTER PROGRAMS 'MATRIX'

The purpose of the system of computer program MATRIX is to obtain the mechanics of deformation during upset compression of a solid cylinder or a ring from either a rigid-plastic (invicid) or a rate-sensitive material under isothermal conditions. These programs were originally developed by Oh, Rabelo, and Kobayashi⁽¹⁾ at the University of California, Berkeley, and utilize the viscoplastic finite-element method for solution. The present programs are the modified version and were developed at Battelle to include interactive capabilities for easier input to the programs, and graphics capabilities for a simpler interpretation of the output from the programs.

The system of computer programs MATRIX consists of the following three programs:

- (1) Program MAIN
- (2) Program DATA
- (3) Program DRAWNG

The major portion of computations, input, output and handling of information is carried out under the program MAIN. Program DATA provides the guess values required for the initial run. All the graphical display is performed by the computer program DRAWNG. In addition, a binary file TAPE 1, initially generated by program DATA, and an output file TAPE 2, used for generating graphical displays, are needed.

The formal loading of the program MATRIX requires two input files. The first of the two files is the card input file, which also includes all the control information. The second file is a binary file, TAPE 1. For the initial run of the program, the binary file TAPE 1 is generated by the program DATA. At a later step, TAPE 1 is generated automatically from TAPE 2, which contains the output from the previous step. The information on TAPE 2 can be printed through a line printer for visual examination, and it also provides the input to the graphic display program DRAWNG.

⁽¹⁾ Oh, S. I., Rabelo, N. M., and Kobayashi, S., "Finite Element Formulation for the Analysis of Plastic Deformation of Rate-Sensitive Materials in Metal Forming", Proc. of IUTAM Symposium of Metal Forming Plasticity, 1978.

Input To and Output From Program MATRIX

The required input to the program MATRIX are:

- (a) Workpiece geometry through nodal point coordinates
- (b) Type of deformation process through boundary conditions
- (c) Process parameters, such as, die-workpiece friction, die speed, etc.
- (d) Workpiece material properties through subroutine HARD

Upon execution, these program provide the following output information at any stage of deformation:

- (a) the geometry of the deformed workpiece
- (b) the die pressure and deformation load
- (c) the complete distribution of strain, strain rate, and stress throughout the workpiece
- (d) the workpiece boundary reaction forces at the pre-assigned nodal points.

The various input variables, their explanation and format, to each of the three programs in MATRIX are given in the following.

Preparation of Input to Program MAIN

(1) First Data Set, FORMAT (12A6)

HED

where, HED: Headings (up to 72 characters),
which a user wants to be printed out

(2) Second Data Set, FORMAT (7I5)

ITER, NREAD, NFORM, NPUNCH, IPUNCH, IPUNST, NPRINT, IPROC

where, ITER: Number of maximum iterations allowed for a step solution.

NREAD : Input data is for the initial run if NREAD = 0
 Input data is for the subsequent run if NREAD = 1
 NFORM : Number of steps in the run
 NPUNCH: output information are written on Tape 2 if NPUNCH = 1
 output information will not be written if NPUNCH = 0
 IPUNST: If NPUNCH = 1, every IPUNCH - th step solution will be written
 on the Tape 2.
 NPRINT: Contracted output will be printed if NPRINT = 0
 Full output will be printed in NPRINT = 1
 IPROC : Constant ram speed hydraulic press type process is assumed if
 IPROC = 1, and mechanical type process is assumed for IPROC = 0

(3) Third Data Set, FORMAT (5I5)

IPLNAX, NUMNP, NUMEL, NUMPC, NBF

IPLNAX: Axisymmetric problem if IPLNAX = 0
 Plane strain problem if IPLNAX = 1
 NUMNP : Number of nodal points for the grid system used
 NUMEL : Number of elements for the grid system
 NUMPE : always 0 for this program
 NBF : Number of nodal points where the nodal point force calculation is
 required.

(4) Fourth Data Set, FORMAT (8F10.0)

ACFINI, FRICM, FLIMIT, TEST, ALPH

ACFINI: Deceleration coefficient for the convergence.
 $0.0 < ACFINI \leq 1.0$
 Recommended values of ACFINI are
 0.4 ~ 0.3 if friction is high and
 0.8 ~ 1.0 if friction is low
 FRICM : Constant coefficients of friction. Frictional traction is given by
 $\tau = (FRICM) * (\text{Local shear flow stress of the surface})$

FLIMIT: Convergence is assumed if

$$\|\Delta u\| / \|u\| \leq \text{FLIMIT where } u \text{ is nodal point velocity}$$

TEST : Maximum step displacement increment size.

ALPH : Some small positive number to improve numerical sealability.
Elements are assumed to be rigid if the effective strain rates of those elements become less than ALPH. This ALPH value will be automatically adjusted for the progress of the deformation.

(5) Fifth Data Set, FORMAT (4F10.0)

TVDMP, RPMNP, WSTAT, VO

TVDMP: Stroke of mechanical press in inches

RPMNP: RPM of mechanical press

WSAT : Initial distance of the ram head from the bottom position in inches

VO : Velocity of hydraulic press head in in/sec.

** TVDMP, RPMNP, WSTAT will be ignored if IPROC = 1, and VO will be ignored if IPROC = 0.

(6) Sixth Data Set, FORMAT (16I5)

(NF(I), I=1, NBF)

NF: Nodal point numbers where the force calculations are desired.

(7) Seventh Data Set, FORMAT (16I5)

(NE(I), I=1, NBF)

NE: Element numbers which contain the nodal points in NF array.

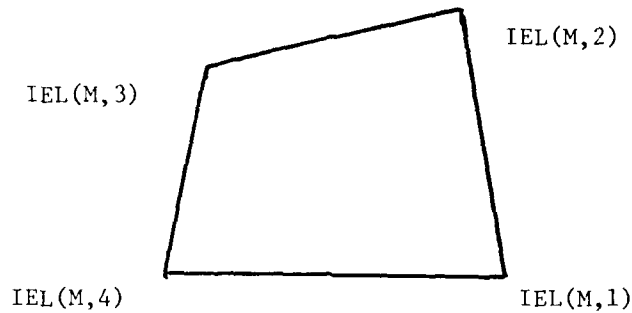
(8) Eighth Data Set, FORMAT (5I5)

M, (IEL(M, I), I=1, 4)

M : Elements number

IEL(M,I): I-th nodal point number of M-th element.

(IEL(M,I), I=1,4) should define the element in a counter clock-wise direction as in the figure.



In case where the grid system is regular rectangular system as shown in the input example, not all the element cards are required. For the best results, user is advised to use data preparation program described later.

The following input is prepared by PROGRAM DATA on TAPE 1.

(9) (HED(I), I=1,12), NSTEP, NCON

HED : Heading to identify the record up to 72 characters

NSTEP : 0 for the initial run

NCON : 0 for the initial run

(10) (R(N), Z(N), N=1, NUMNP)

R(N): R- or X-coordinate of nodal point N

Z(N): X- or Y-coordinate of nodal point N

(11) (UR(N), UZ(N), N=1, NUMNP)

UR(N): guess velocity of nodal point N in R- or X-direction

UZ(N): guess velocity of nodal point N in Z- or Y-direction

(12) (CODE(N), N=1, NUMNP)

CODE (N) : code number to define the boundary condition of nodal point N

if CODE = 0: force is prescribed in both directions

= 1: velocity is prescribed in R- or X- direction and force is prescribed in Z- or Y- direction

= 2: force is prescribed in R- or X- direction and velocity is prescribed in Z- or Y- direction

= 3: velocities are prescribed in both directions

(13) LEE, NFTOT, TIME

LEE : NF(LEE) is the right most nodal point number which touches die surface

NFTOT : NF(NFTOT) is the left most nodal point number which touches die surface

TIME : Elapse time in seconds. Zero for the initial run.

The data sets (1) - (8) make card input file and sets (9) - (13) binary input file, TAPE 1.

As an example, to the input file (1) - (8) are given in Figure G-1. The finite element grid system used are shown in Figure G-2.

T1 ALLOY ALPHA+BETA				ISOTHERM. M=0.05. MECH. PRESS										
10	1	13	1	1	1	0								
0	108	88	0	17										
0.8		0.05		0.0001		0.004875	0.002							
10.		7.7		0.4150										
37	28	19	10	1	2	3	4	5	6	7	8	9	18	
27	36													
45														
25	17	9	1	1	2	3	4	5	6	7	8	8	16	
24	32													
40														
1	11	2	1	10										
9	20	11	10	19										
17	29	20	19	28										
25	38	29	28	37										
33	47	38	37	46										
41	56	47	46	55										
49	65	56	55	64										
57	74	65	64	73										
65	83	74	73	82										
73	92	83	82	91										
81	101	92	91	100										
88	108	99	98	107										

FIGURE G-1 CODED INPUT FILE EXAMPLE

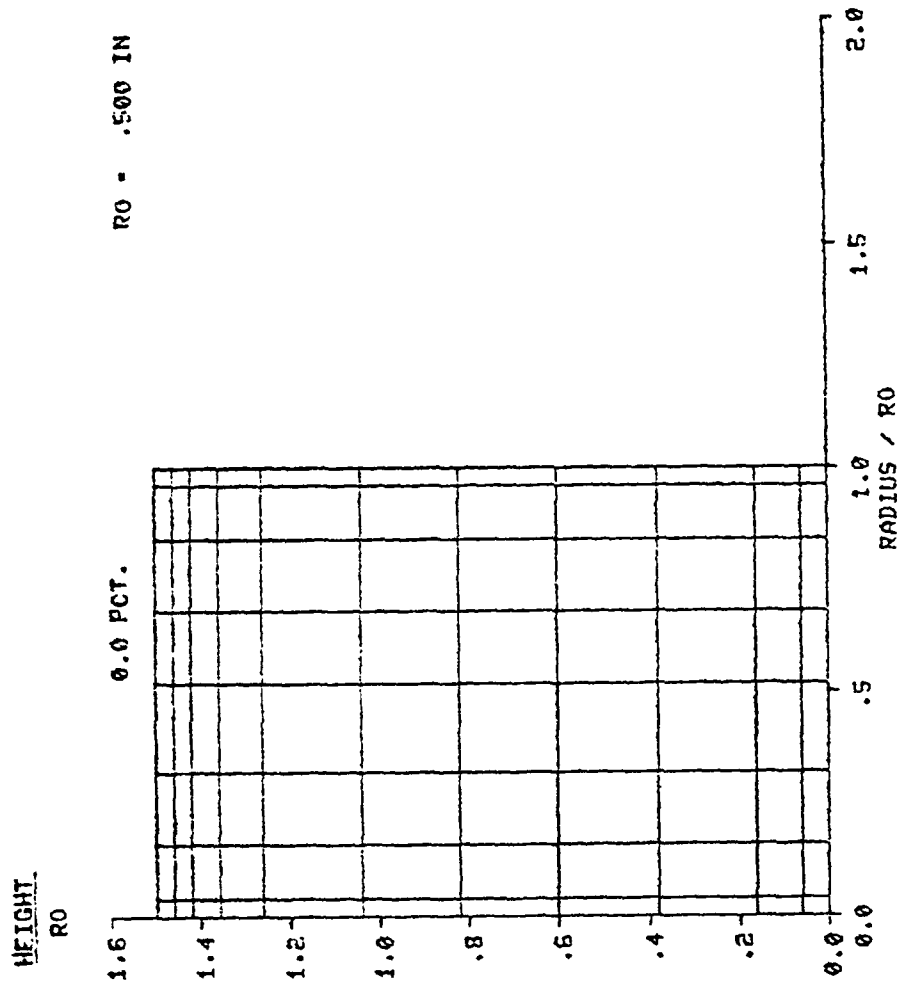


FIGURE G-2 TYPICAL EXAMPLE OF GRID SYSTEM USED FOR THE PROGRAM MATRIX.

Description of Program DATA

The purpose of this program is two fold. First, it provides the user with an easy, and error-free method to make the binary input file, TAPE 1, for the initial run. Second, it dictates certain nodal points and an elements numbering method. Even though program MATRIX does not require a specific numbering system, the graphic package DRAWNG is programmed to fit the one dictated by DATA.

The output of this program consists of three files, print output, TAPE 1 and TAPE 2. The print output contains nodal points coordinates, guess velocities, element arrangements and some additional information for visual inspection. TAPE 1 contains element card image (data set (8) of PROGRAM MATRIX) and TAPE 2 will make the binary input file for program MATRIX (data set (9)-(13) of PROGRAM MATRIX).

Input preparation for this program can be easily provided and it is explained below.

Data Input for Program DATA

(1) First Data Card, FORMAT (12A6)

(HED(1), I=1, 12)

HED: Same as data set (9)

(2) Second Data Card, FORMAT (I5)

IPLNAX

IPLNAX: Axisymmetric problem if IPLNAX = 0
Plane strain problem if IPLNAX = 1

(3) Third Data Card, FORMAT (4I5)

NX, NY, NBF, NBC

NX : Number of nodal points in R-direction
NY : Number of nodal points in Z-direction

NBF: Number of nodal points where the force calculation
is desired.

NBC: Number of nodal points whose "CODE" is other than zero

(4) Fourth Data Card, FORMAT (8F10.0)

(RX(I), I=1, NX)

RX(I): R- or X-coordinates of I-th vertical line in ascending
order

(5) Fifth Data Card, FORMAT (8F10.0)

(ZY(I), I=1, NY)

ZY(I): Z- or Y-coordinates of I-th horizontal line in ascending
order

(6) Sixth Data Card, FORMAT (F10.0)

W

W: refer to WSTAT in data (5) of PROGRAM MATRIX

(7) Seventh Data Card, FORMAT (2I5)

LEE, NFTOT

LEE : NF(LEE) is the right most nodal point number which is in
touch with die surface

NFTOT : NF(NFTOT) is the left most nodal point number which is
in touch with die surface

(8) Eighth Data Card, FORMAT (I5, F5.0)

NP, CODE(NP)*

NP : Nodal point number whose "CODE" is other than zero.

CODE: CODE for the boundary condition

* See footnote on the next page.

(9) Ninth Data Card, FORMAT (16I5)

(NF(I), I=1, NBF)*

NF: Nodal point number whose nodal point force is desired.

Description of the Program DRAWNG

This program is for plotting the matrix method solution of ring compression, or solid cylinder compression on a CRT screen interactively. This program uses the TEKTRONICS TCS graphic system. The program DRAWNG can provide:

- 1) Stress-strain or strain rate hardening curve
- 2) Load-displacement curve
- 3) Superimposed cross-sections of deformed work piece at different stages of deformation
- 4) Finite element grid distortions at any stages of the process. Rigid portions can be shaded if there is any.
- 5) Die-workpiece contact stress distributions at different stages of deformation.
- 6) Contour line plot for stress, strain and strain rate distribution will be implemented in the near future.

For the purpose of comparison, up to 4 plots of any combination of the above drawing can be shown in a screen.

The use of this program at the graphic terminal is self explanatory. The user can, however, enter the following commanding codes other than required input at any input stage:

END : to terminate the graphic session
HELP: to get necessary information for the input
RNEW: to restart the entire command

* Since the program DATA dictates a certain numbering system, user should verify the nodal point numbers used in data set (8) and (9).

BACK: to restart the current frame command

Except for the utility command input, such as described above, all graphic input command allows the leading blanks, so long as the whole command is within the first 10 character spaces. Also this program provides input error recovery routine. Whenever user enters wrong or unrecognizable command, the program gives error message and control returns to the same input phrase. The input error for command "YES" however, cannot be recovered. Any command other than "YES" and the utility command will be accepted as "NO".

Since the matrix method program usually takes large core memory space to load and substantial amount of computer time to run it is not practical to obtain matrix method solution while the graphic user is at the terminal. Instead, the program DRAWNG assumes that the complete matrix method solution has been obtained already and that all or parts of the solution information has been stored in a prearranged manner in TAPE 3. The TAPE 3 employs FTN random access file structure. The first record contains some preliminary information about finite elements grid system used by the matrix method and index for the subsequent record. The subsequent records contain the matrix method solution at a certain stage of deformation. This random access file TAPE 3 can be generated automatically by the small program EDITNG supplied with this graphic package.

For the better understanding of this graphic package user should refer the input and output examples listed below in Figure G-3 and G-4.

WELCOME TO A DRAWING SYSTEM PROGRAM
TO DISPLAY SOLID CYLINDER UPSETTING
BY
MATRIX METHOD.

... MATDRW VER. 1.0, JUL. 1979....

IF YOU NEED SOME ORIENTATION FOR THIS PROGRAM
ENTER YES >>>yes

** THE USE OF THIS PROGRAM IS SELF-EXPLANATORY.
YOU CAN, HOWEVER, ENTER FOLLOWING COMMANDING
CODE OTHER THAN REQUIRED INPUT AT ANY INPUT
STAGE.

END
TO TERMINATE THE PROGRAM
THIS IS THE ONLY WAY TO TERMINATE NORMALLY
HELP
TO GET SOME INFORMATION FOR THE INPUT
RNEW TO RESTART THE ENTIRE COMMAND
BACK TO RESTART THE CORRENT FRAME COMMAND.

NUMBER OF FIGURES IN A SCREEN, MAX.= 4

ENTER NUMBER >>> 4

*** INPUT PHASE FOR FIGURE NO. 1

*** ENTER COMMAND CY CODE WORD ***

COMMAND	CODE WORDS
STRESS-STRAIN-ITS RATE CURVE	STST
LOAD-DISPLACEMENT CURVE	LODP
SUPERIMPOSED CROSS SECTION	SUCS
GRID-DISTORTION	GRDS
DIE STRESS DISTRIBUTION	DSDS

ENTER CODE WORDS FOR PLOT = lodp

FIGURE G-3 EXAMPLE OF CRT COMMANDING INPUT FOR
GRAPHIC DISPLAY DRAWNG

*** INPUT PHASE FOR FIGURE NO. 2

ENTER CODE WORDS FOR PLOT = grds
DO YOU WISH TO HAVE THE RIGID PORTION SHADED.
IF THERE'S ANY. ENTER ANSWER... n

* ENTER PERCENT IN HEIGHT REDUCTION.

HAVE YOUR CHOICE AMONG THE FOLLOWINGS

0.0	1.3	2.5	5.0	7.5
10.0	12.5	15.0	17.5	20.0
22.5	25.0	27.5	30.0	32.5
35.0	37.5	40.0	42.5	45.0

ENTER REDUCTION = 45

*** INPUT PHASE FOR FIGURE NO. 3

ENTER CODE WORDS FOR PLOT = sucs
HOW MANY CROSS SECTIONS DO YOU WISH TO
HAVE SUPERIMPOSED. MAXIMUM = 15

ENTER NUMBER >>> 5
ENTER REDUCTION (1) = 0
ENTER REDUCTION (2) = 10
ENTER REDUCTION (3) = 20
ENTER REDUCTION (4) = 30
ENTER REDUCTION (5) = 40

*** INPUT PHASE FOR FIGURE NO. 4

ENTER CODE WORDS FOR PLOT = dsds
HOW MANY PRESURE PLOTS DO YOU WISH TO
HAVE SUPERIMPOSED. MAXIMUM = 15

ENTER NUMBER >>> 2
ENTER REDUCTION (1) = 1.3
ENTER REDUCTION (2) = 40

FIGURE G-3 (continued)

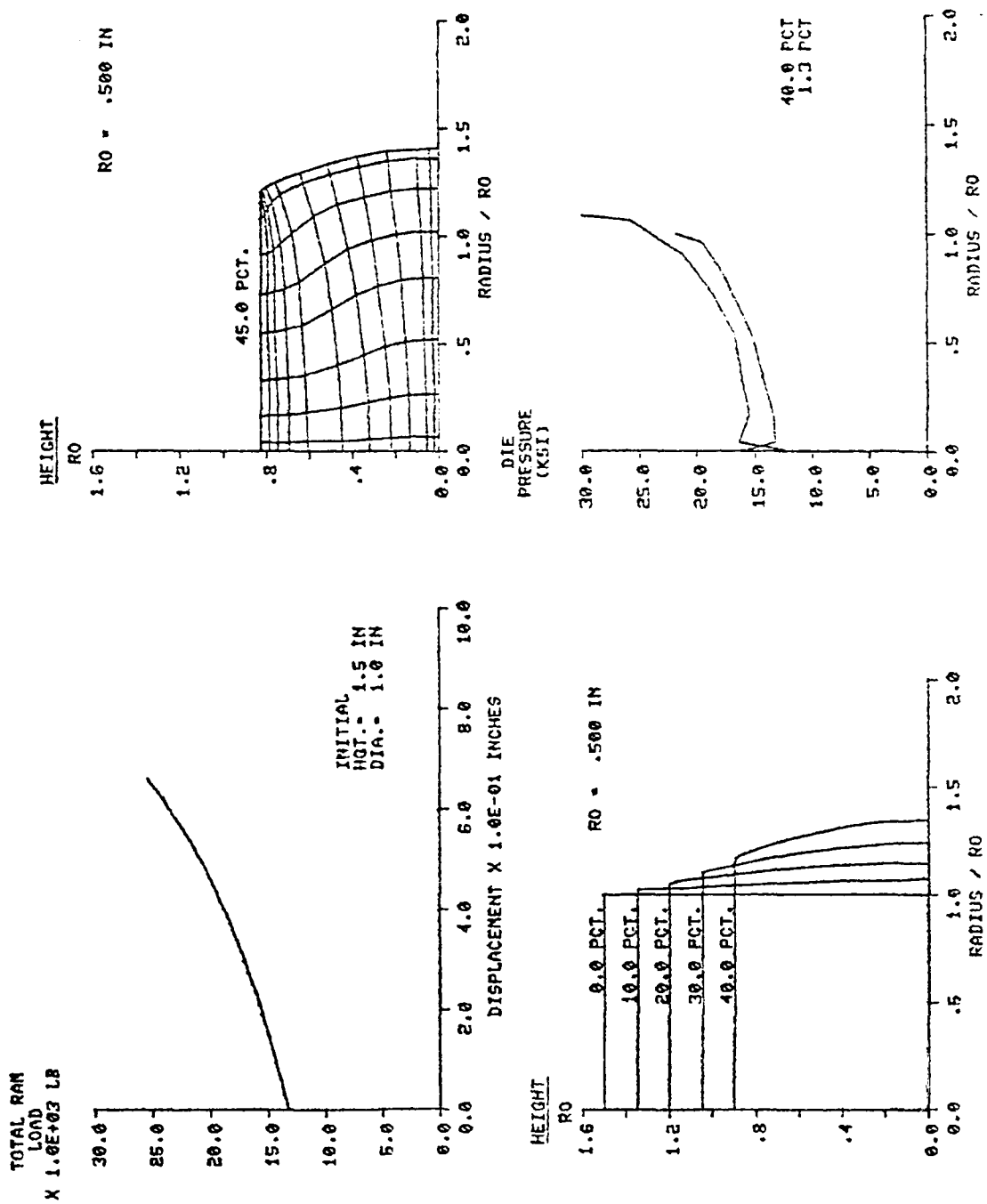


FIGURE G-4 EXAMPLE OF GRAPHIC OUTPUT BY INPUT COMMAND SHOWN IN FIGURE G-3

APPENDIX H

DESIGN OF THE HEAT TRANSFER EXPERIMENT

E. W. Collings
Battelle's Columbus Laboratories
505 King Avenue, Columbus, Ohio 43201

APPENDIX H

DESIGN OF THE HEAT TRANSFER EXPERIMENT

Introduction

By solving the equations for one-dimensional heat transfer between the surface and the interior of a block of high-temperature alloy IN 100, thermocouple placement depths commensurate with response times appropriate to those encountered in a typical forging operation can be calculated. In what follows, we will discuss the placement of thermocouples at several depths within the die. This redundancy leads to a more reliable determination of surface temperature than would be possible with a single surface thermocouple. Finally, we describe the thermocouples to be used and the design of the test fixture.

The Equations of Heat Transfer

The solution of heat-flow problems centers upon solutions of the general Fourier equation

$$\frac{\partial T}{\partial t} = \alpha \nabla^2 T \quad , \quad (H-1)$$

where T is temperature, t is time, and α is known as the thermal diffusivity. Generally, one is called upon to solve this equation in one of three situations:

- (a) The steady state $\frac{\partial T}{\partial t} = \alpha \nabla^2 T = 0$
- (b) Periodic heat flow - as for example in reciprocating heat engines
- (c) Transient heat flow, brought about by the sudden application of a heat source or sink.

Generalized Step Heating or Cooling

In this, the surface of a body at some initial temperature T_i , is raised to (step heating or up-quenching) or lowered to (quenching) and held at some constant temperature T_s . The temperature within the body as a function of time and distance from the surface is given by:

$$\frac{T - T_s}{T_i - T_s} = \phi, \text{ useful if } T_i > T_s, \quad (\text{H-2})$$

or

$$\frac{T_s - T}{T_s - T_i} = \phi, \text{ useful if } T_i < T_s$$

where $\phi \equiv \text{erf}(x\eta)$

x = distance from surface

η involves time measured
from the time of in-
stantaneous raising or
lowering of the surface
temperature

$$= 1/2\sqrt{\alpha t}.$$

This relationship can be used to determine the variation of temperature with time at some point x below the surface which is being held a fixed temperature T_s , Figure H-1. The same result can also be expressed as a set of isothermals representing T as function of distance below the surface for various times after the application of the heating step, Figure H-2.

Values of the error function are tabulated. However for the purposes of rough estimation it is instructive to note that over most of the range of interest $\phi(z) \approx z$, the equality holding for small z and for $z = 0.62$, Table H-1.

AD-A082 207

BATTELLE COLUMBUS LABS OH
RESEARCH TO DEVELOP PROCESS MODELS FOR PRODUCING A DUAL PROPERTY--ETC(U)
DEC 79 G D LAHOTI, T ALTAN

F/G 11/6

F33615-78-C-5025

UNCLASSIFIED

AFML-TR-79-4156

NL

SDF 5
AD
A082207



END
DATE
FILMED
4-80
DTIC

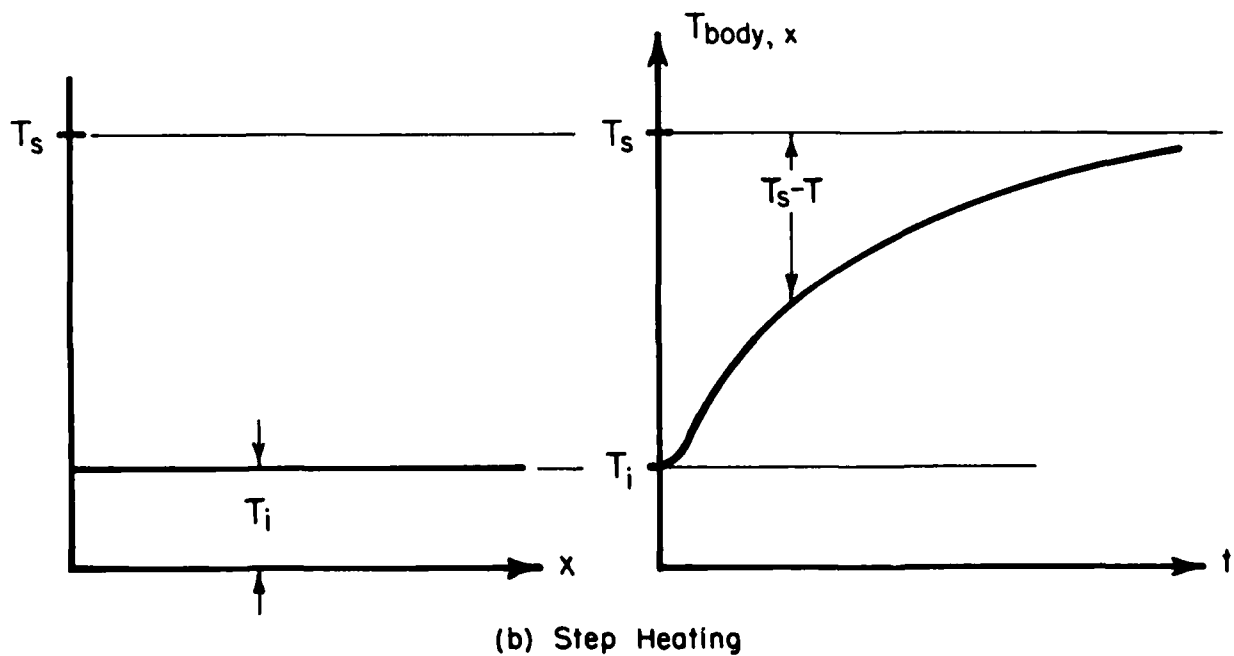
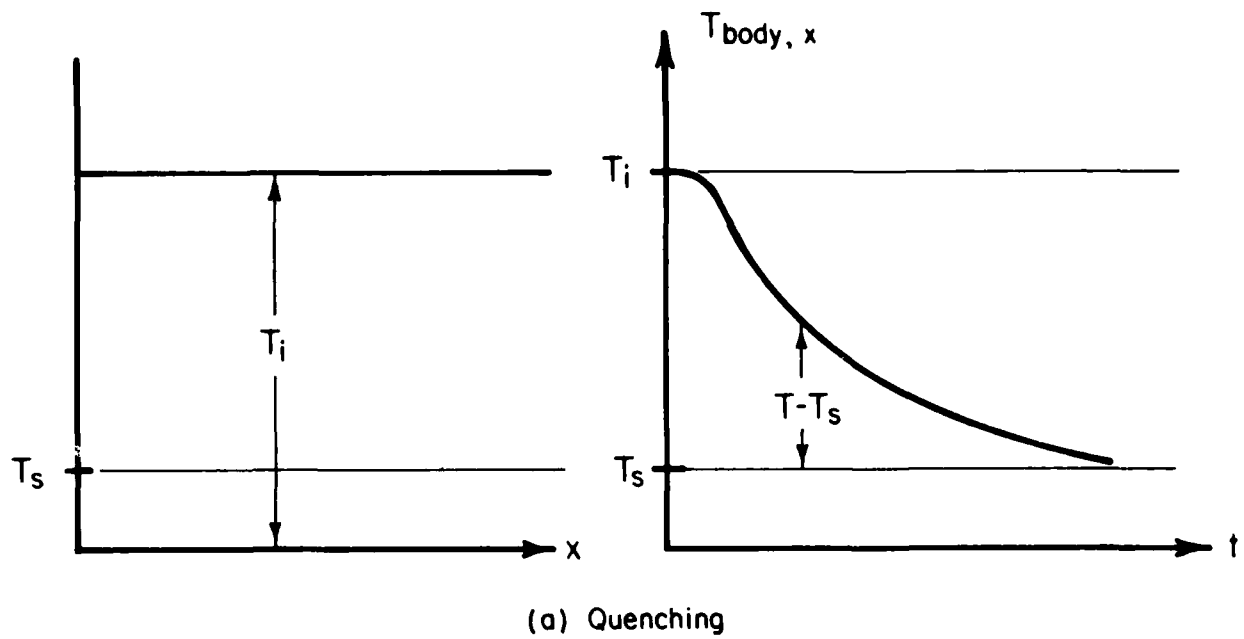


FIGURE H-1. Temperature at some point x within a body, initially at temperature T_i , as function of time as measured from the change in surface temperature.

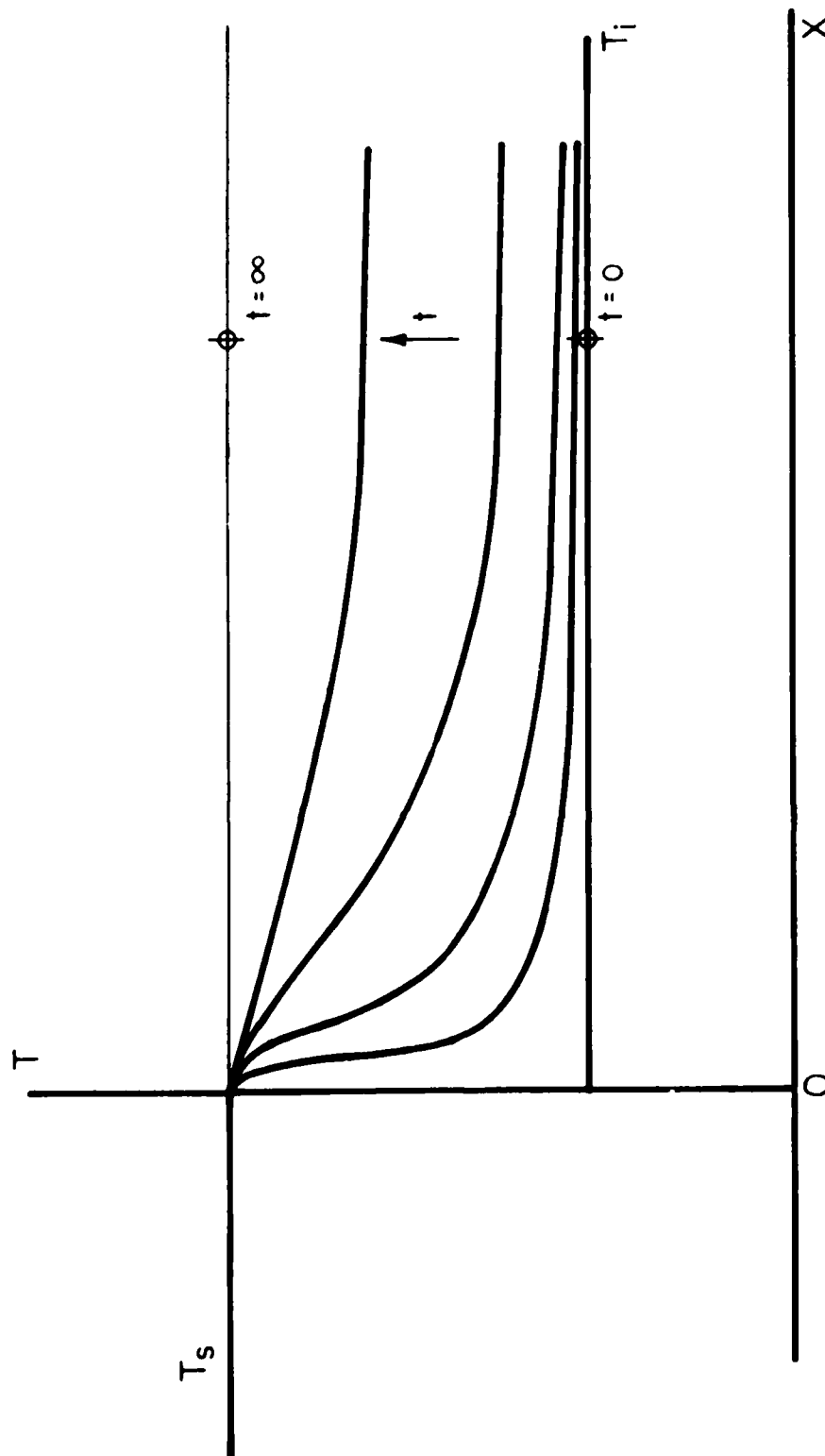


FIGURE H-2. Isotherms as function of distance from the surface for various times from the application of the temperature pulse.

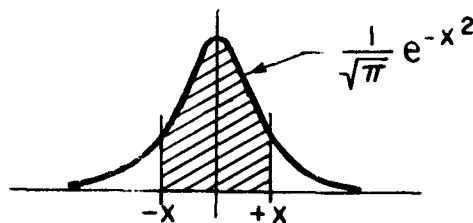


TABLE H-1
THE ERROR FUNCTION. NOTE THE EQUALITY
OF THE FUNCTION AND ITS KERNEL FOR
SMALL VALUES OF x (IN THIS CASE) AND
FOR VALUES OF x NEAR 0.62

$$\Phi(x) \equiv \frac{2}{\sqrt{\pi}} \int_0^x e^{-\beta^2} d\beta = \frac{2}{\sqrt{\pi}} \int_{-x}^0 e^{-\beta^2} d\beta$$

x	$\Phi(x)$	x	$\Phi(x)$	x	$\Phi(x)$
0.00	0.00000	0.25	0.27633	0.50	0.52050
0.01	0.01128	0.26	0.28690	0.51	0.52924
0.02	0.02256	0.27	0.29742	0.52	0.53790
0.03	0.03384	0.28	0.30788	0.53	0.54646
0.04	0.04511	0.29	0.31828	0.54	0.55494
0.05	0.05637	0.30	0.32863	0.55	0.56332
0.06	0.06762	0.31	0.33891	0.56	0.57162
0.07	0.07886	0.32	0.34913	0.57	0.57982
0.08	0.09008	0.33	0.35928	0.58	0.58792
0.09	0.10128	0.34	0.36936	0.59	0.59594
0.10	0.11246	0.35	0.37938	0.60	0.60386
0.11	0.12362	0.36	0.38933	0.61	0.61168
0.12	0.13476	0.37	0.39921	0.62	0.61941
0.13	0.14587	0.38	0.40901	0.63	0.62705
0.14	0.15695	0.39	0.41874	0.64	0.63459
0.15	0.16800	0.40	0.42839	0.65	0.64203
0.16	0.17901	0.41	0.43797	0.66	0.64938
0.17	0.18999	0.42	0.44747	0.67	0.65663
0.18	0.20094	0.43	0.45689	0.68	0.66378
0.19	0.21184	0.44	0.46623	0.69	0.67084
0.20	0.22270	0.45	0.47548	0.70	0.67780
0.21	0.23352	0.46	0.48466	0.71	0.68467
0.22	0.24430	0.47	0.49375	0.72	0.69143
0.23	0.25502	0.48	0.50275	0.73	0.69810
0.24	0.26570	0.49	0.51167	0.74	0.70468

* From "Tables of Probability Functions," Vol. I, Bureau of Standards, Washington, 1941, 1944

Application of the Heat Transfer Equations

Thermal Diffusivity

In order to be able to apply the above equations to material of interest, in this case IN 100, it is essential to have values of the thermal diffusivity over the appropriate temperature range.

Thermal diffusivity is given by $\alpha = K/\rho C$, where K is thermal conductivity, ρ is density, and C is the specific heat. Using tabulated values of K and C , and values of ρ estimated from the room temperature density and thermal expansivity, values of the thermal diffusivity have been calculated. These are given in Table H-2.

Example--Subsurface Time-Temperature of IN 100 Tooling

The time range to be considered must be compatible with the times encountered in a typical forging operation. With ram speed within the range 762 mm/s to 25.4 mm/s (30 to 1 in/sec), and an anticipated 50% deformation of a 12.57 mm (1/2 in) thick workpiece, the duration of the forging experiment is 10 ms to 0.25 sec.

Let us now consider the temperatures 0.76 mm (0.030 in) below the surface of IN 100 tooling initially at 371 C (700 F) whose surface is suddenly raised to and kept at 927 C (1700 F). We wish to determine the times at which our selected point rises to temperatures of 427, 538, and 816 C (800, 1000, and 1500 F). The calculational steps towards a solution are:

$$(a) \text{ Determine } \eta = (1/x) \phi^{-1} \left\{ \frac{T_s - T}{T_s - T_i} \right\}$$

$$(b) \text{ Determine } t = 1/4\alpha\eta^2.$$

These steps are shown in Table H-3.

TABLE H-2
THERMOPHYSICAL PARAMETERS FOR THE ALLOY IN 100

Temperature, T (°F)	Thermal Conductivity, K (Btu/ft/hr/°F)	Specific Heat, C (Btu/lb/°F)	Density, ρ^* (lb/cu ft)	Thermal Diffusivity ($\sigma=K/\rho C$)
200			482	
400			480	
600			477	
800			475	
1000	10.0	0.115	473	0.18
1200	11.0	0.12	470	0.20
1400	12.6	0.125	468	0.22
1600	14.6	0.13	467	0.24
1800	16.7	0.14	463	0.26
2000		0.145	461	

* Based on 0.280 lb/ cu in at room temperature taken as 100 F, and an average coefficient of linear expansion of $8.5 \times 10^{-6}/F$.

TABLE H-3
TIMES FOR A POINT 0.76 MM (0.30 IN) BELOW
THE SURFACE TO ACQUIRE TEMPERATURES OF
427, 538, and 816 C (800, 1000, and 1500 F,
RESPECTIVELY

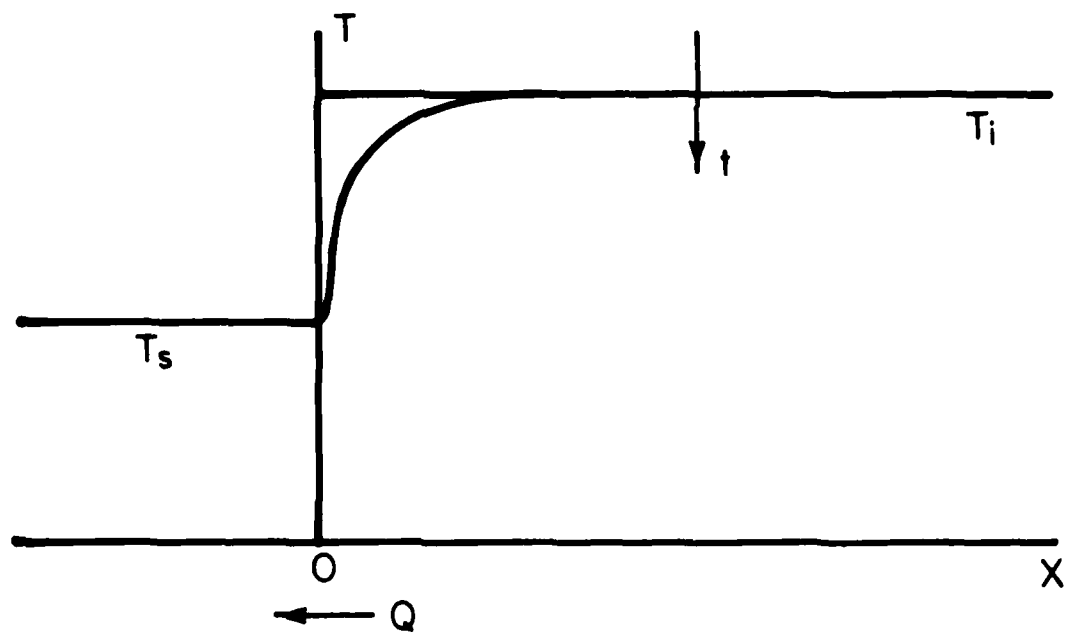
$\frac{T-T_s}{T_i-T_s}$ for $T_i-T_s = 1000$ F)	$x \eta^*$	t (sec)
0.9	1.16	21×10^{-3}
0.7	0.74	50×10^{-3}
0.2	0.18	860×10^{-3}

* From tables, since $\text{erf}^{-1} \left[\frac{T-T_s}{T_i-T_s} \right] = x \eta$.

Next, $x = 0.030$ in $= 2.5 \times 10^{-3}$ ft

and $t = 1/4\alpha\eta^2 = \left(\frac{x}{2(\eta x)} \right)^2 / \alpha$

where $\alpha \approx 0.20$ from thermal diffusivity table.



$$\dot{Q}/(x=0) = \frac{K(T_s - T_i)}{\sqrt{\pi a t}}$$

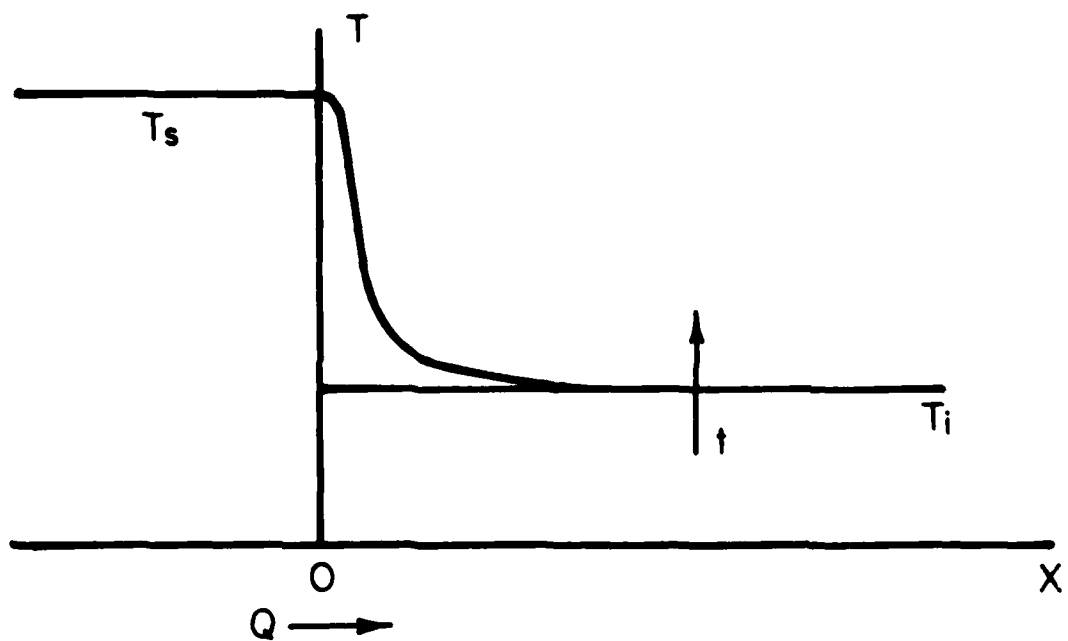


FIGURE H-3. Heat transfer during upquenching or downquenching.

Next, let us expand the calculation to include depths of 1.27, 2.54, 5.08, and 10.16 mm (0.05, 0.10, 0.20, and 0.40 in). We note that an isothermal is characterized by $\eta x = \text{const}$, that is $x/2\sqrt{at} = \text{const}$, $t \propto x^2$.

Hence, by knowing t for a given depth, in this case 0.76 mm (0.030 in) (Table H-3) the other times are calculated by proportion, as in Table H-4.

Conclusion

For the recording of temperatures during the 0.25 sec duration of a forging event, it is useful to place thermocouples down to a depth of 2.54 mm (0.10 in).

Heat Transfer--Perfect Interface

The rate at which heat flows by conduction between two points is proportional to the temperature difference, the constant of proportionality being the heat transfer coefficient. The rate of heat flow $\dot{Q} = -K \partial T / \partial x$ is obtained by differentiating Equation (H-2), thus:

$$\dot{Q} = -K \frac{\partial}{\partial x} (T_i - T_s) \phi = -K \frac{2(T_i - T_s)}{\sqrt{\pi}} \eta e^{-x^2 \eta^2},$$

hence $\dot{Q}/_{x=0} = \frac{K}{\sqrt{\pi at}} (T_s - T_i), \quad (H-3)$

Heat transfer in the upquenching or downquenching situation is illustrated in Figure H-3.

Heat Transfer--Boundary Layer Between Real Bodies

When heat source is finite, cooling takes place as heat flows out and raises the temperature of the sink. We thus have two heat-flow situations "back to back". Secondly, we can imagine a temperature drop to take place across a boundary layer governed by the temperature difference and the boundary

TABLE H-4
 THE SURFACE OF A BOYD AT AN INITIAL TEMPERATURE OF 371 C
 (700 F) IS SUDDENLY RAISED TO AND HELD AT 927 C (1700 F)
 [In the time intervals indicated, points at various
 depths rise in temperature by 38 C, 149 C, and 427 C
 (100, 300, and 800 F), respectively]

Depth, mm (in)	Times to Attain the Following Temperature Increments			Time Units
	38 C (100 F)	149 C (300 F)	427 C (800 F)	
0.76 (0.03)	21	50	860	ms
1.27 (0.05)	58	139	2.4	s
2.54 (0.10)	233	556	9.6	
5.08 (0.20)	933	2.2	38.2	
10.16 (0.40)	3.7	8.9	152.9	

heat transfer coefficient, α_{AB} . This situation is illustrated by Figure H-4 and the following associated relationship:

$$\dot{Q} = \frac{K_A (T_A - T_{SA})}{\sqrt{\pi \alpha_A t}} = \alpha_{AB} (T_{SA} - T_{SB}) = \frac{K_B (T_{SB} - T_B)}{\sqrt{\pi \alpha_B t}} \quad (H-4)$$

With the aid of thermocouples imbedded in both the source and the sink the temperature profiles can be reconstructed and true values of T_{SA} and T_{SB} and the other temperatures obtained. The interface heat transfer coefficient can be obtained by solving Equation (H-4).

Experimental Plan

Thermocouples

It is planned to use Medtherm coaxial thermocouples. These are suitable for use in the temperature range of the experiment (about 927 C [1700 F]) and will withstand if necessary pressure up to about 207 MPa (30,000 psi). The external sheath, which constitutes one of the thermoelements, occupies a large volume fraction of the thermocouple. Consequently, if its thermal characteristics match those of the material in which it is imbedded, very little disturbance of the heat flux will result. Typical appearance and standard dimensions of these thermocouples are given in Figure H-5. The hex-nut shown may be a high-temperature transition in which case signal is transmitted to the cool parts of the apparatus through high-temperature-insulated leads.

Instrumented Die

It is planned to imbed thermocouples in the die in such a way that they will lie directly underneath the alloy sample which is being plastically deformed. It has been suggested that the arrangement should be compatible with the use of standard ring specimens, which when deformed under lubricated conditions expand their external diameter, and contract their inner diameter in the manner shown in Figure H-6. Accordingly, the proposed die piece will be as shown in Figure H-7.

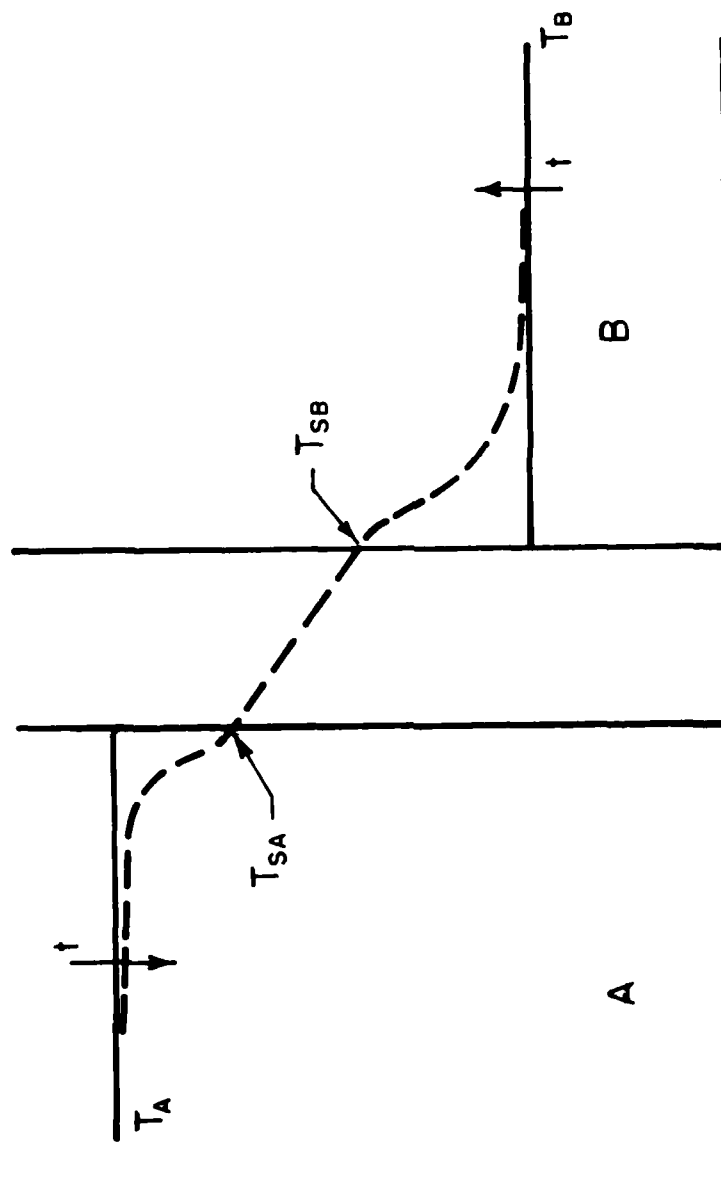
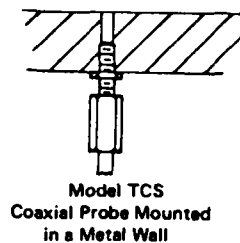
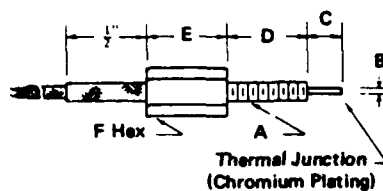


FIGURE H-4. Heat transfer across the boundary layer between a pair of finite bodies A and B.



Model No.	Mounting Thread A	Probe Diameter B	Probe Length C	Thread Length D	Terminal E	Cover F	Total Length
TCS-101	2-56NC	1/16	1/16	1/8	1/4	1/4 HEX	7/16
TCS-102	3-56NF	1/32	1/8	1/2	1/2	3/16 HEX	1-1/8
TCS-103	1/4-28NF	1/16	1/4	1-1/2	3/4	3/8 HEX	2-1/2
TCS-104	4-48NF	1/32	1.0	1/2	1/2	1/4 HEX	2

FIGURE H-5. SOME DETAILS OF THE MEDTHERM END-CONTACT COAXIAL THERMOCOUPLES (ALL DIMENSIONS ARE IN INCHES; INCH = 25.4 mm)

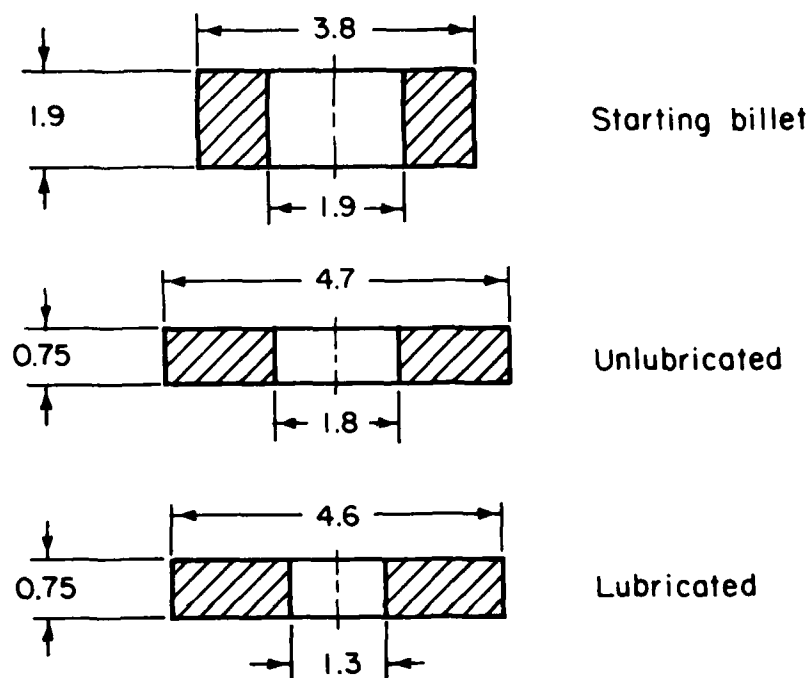


FIGURE H-6. Behavior of the standard ring-test specimen under lubricated and unlubricated conditions (All dimensions are in inches: 1 in.=25.4 mm)

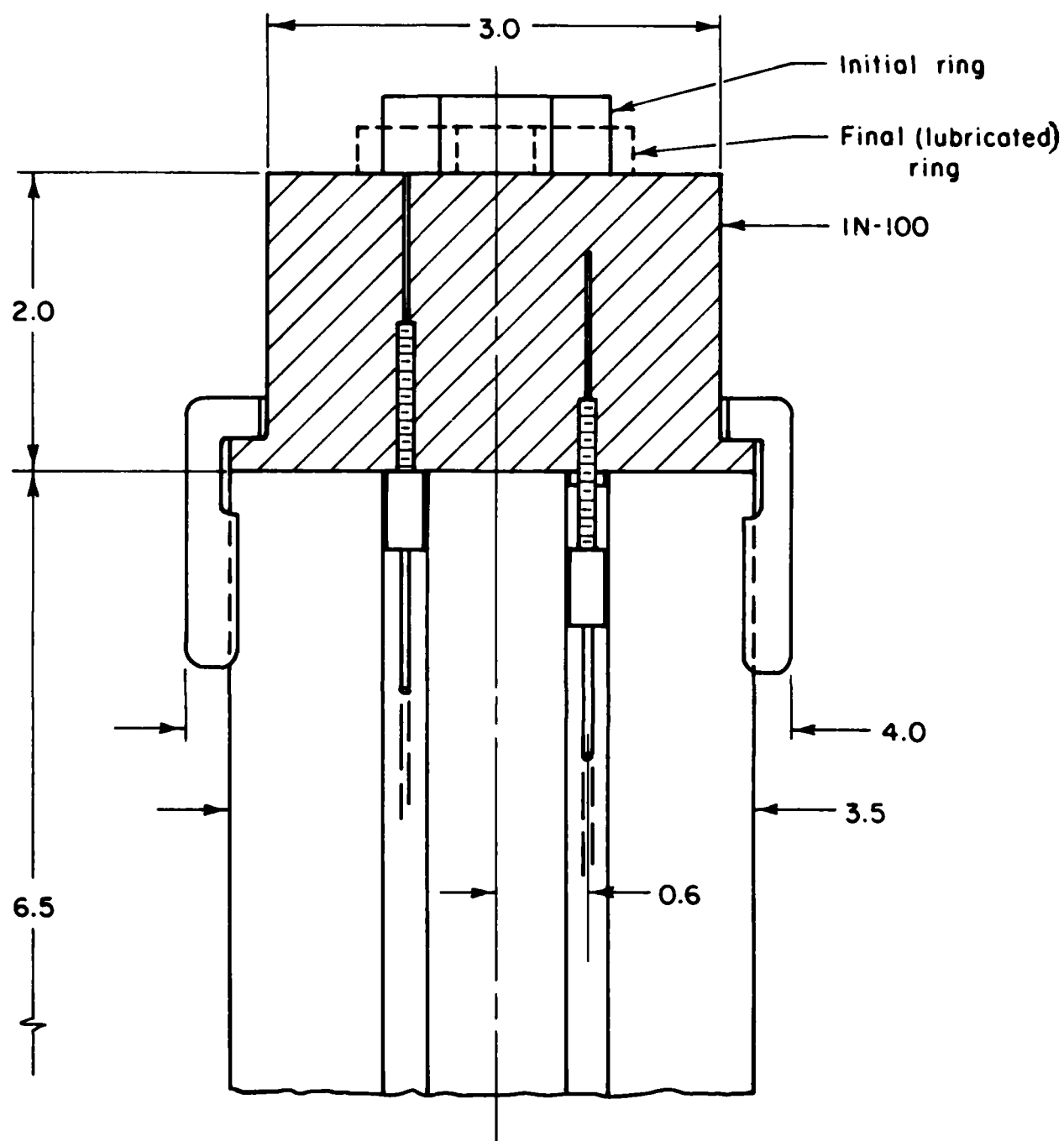


FIGURE H-7. Die and support arrangement with imbedded thermocouples.
(All dimensions are in inches: 1 in.=25.4 mm)

The Text Fixture

The upper and lower instrumented dies will be suitably located in a resistance furnace. The general mounting arrangement is shown, for one die, in Figure H-8.

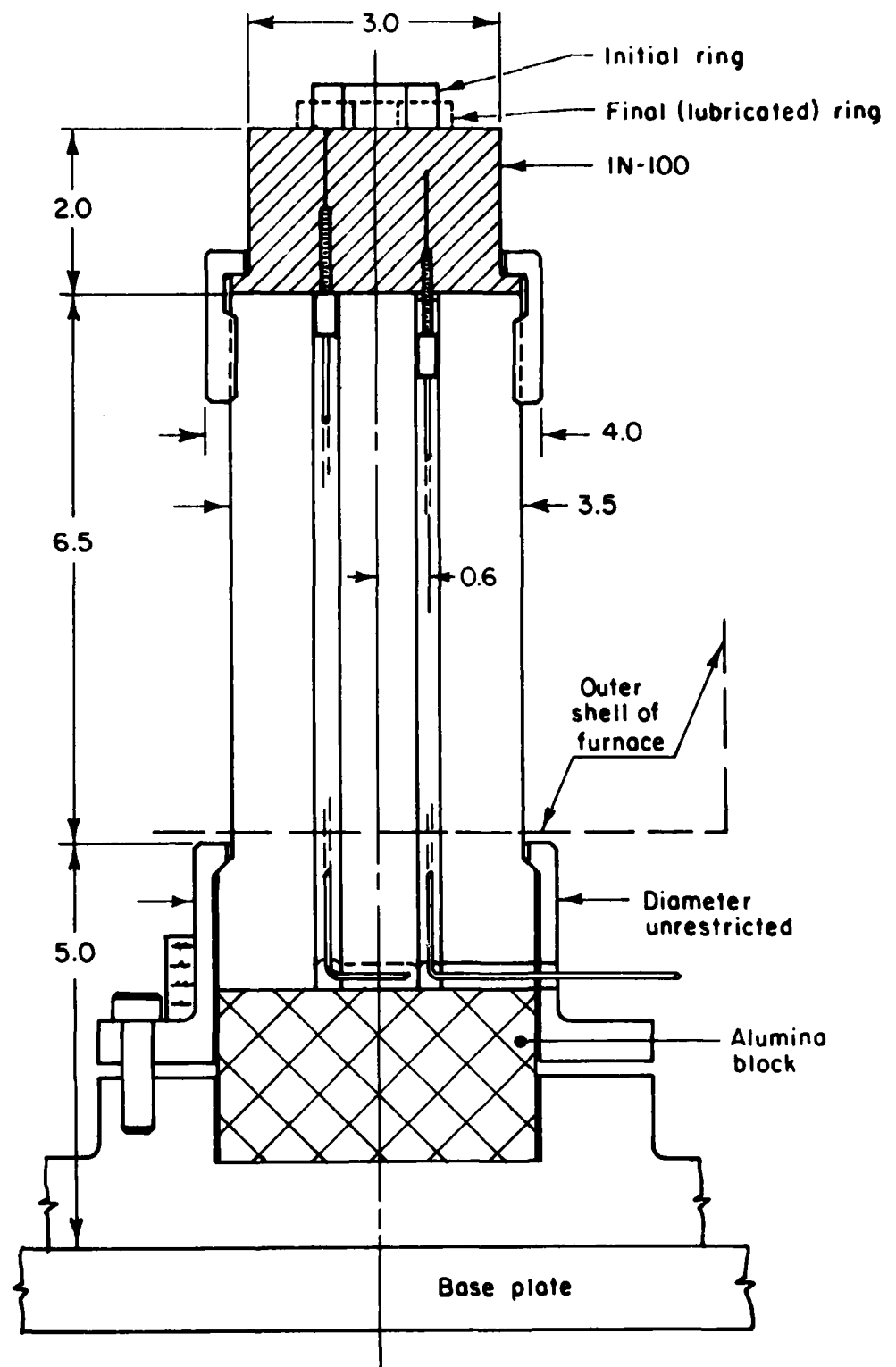


FIGURE H-8. The planned test fixture showing die with imbedded thermocouples mounted on heat resistant pedestal (all dimensions are in inches: 1 in.=25.4 mm)